

ARO 35188.1-PH-CF

TECHNICAL DIGEST

1 9 9 6

NONLINEAR OPTICS:
MATERIALS,
FUNDAMENTALS,
AND
APPLICATIONS

JULY 8-12, 1996
MAUI, HAWAII

1996 TECHNICAL DIGEST SERIES
VOLUME 11

19970521 027



COSPONSORED BY
OPTICAL SOCIETY OF AMERICA
IEEE/LASERS AND ELECTRO-OPTICS SOCIETY



DISTRIBUTION STATEMENT A

Approved for public release;
Distribution Unlimited

REPORT DOCUMENTATION PAGE			Form Approved OMB No. 0704-0188	
Public reporting burden for this collection of information is estimated to average 1 hour per response, including the time for reviewing instructions, searching existing data sources, gathering and maintaining the data needed, and completing and reviewing the collection of information. Send comments regarding this burden estimate or any other aspect of this collection of information, including suggestions for reducing this burden, to Washington Headquarters Services, Directorate for Information Operations and Reports, 1215 Jefferson Davis Highway, Suite 1204, Arlington, VA 22202-4302, and to the Office of Management and Budget, Paperwork Reduction Project (0704-0188), Washington, DC 20503.				
1. AGENCY USE ONLY (Leave blank)	2. REPORT DATE March 7, 1997	3. REPORT TYPE AND DATES COVERED Final 7/1/96-06/30/97		
4. TITLE AND SUBTITLE Organization of the 1996 Nonlinear Optics: Materials, Fundamentals and Applications Topical Meeting		5. FUNDING NUMBERS DAAH04-96-1-0335		
6. AUTHOR(S) David W. Hennage				
7. PERFORMING ORGANIZATION NAME(S) AND ADDRESS(ES) Optical Society of America 2010 Massachusetts Ave. NW Washington, DC 20036		8. PERFORMING ORGANIZATION REPORT NUMBER		
9. SPONSORING/MONITORING AGENCY NAME(S) AND ADDRESS(ES) US Army Research Office PO Box 12211 Research Triangle Park, NC 27709-2211		10. SPONSORING/MONITORING AGENCY REPORT NUMBER ARO 35188.1-PH-CF		
11. SUPPLEMENTARY NOTES				
12a. DISTRIBUTION/AVAILABILITY STATEMENT Approved for public release Distribution unlimited		12b. DISTRIBUTION CODE		
13. ABSTRACT (Maximum 200 words) The Nonlinear Optics topical meeting provided an international forum for discussion of all aspects of nonlinear optics: including new phenomena, novel devices, advanced materials, and applications.				
14. SUBJECT TERMS		15. NUMBER OF PAGES		
		16. PRICE CODE		
17. SECURITY CLASSIFICATION OF REPORT Unclassified	18. SECURITY CLASSIFICATION OF THIS PAGE Unclassified	19. SECURITY CLASSIFICATION OF ABSTRACT Unclassified	20. LIMITATION OF ABSTRACT UL	

CONFERENCE EDITION

*Summaries of the papers
presented at the topical meeting*

NONLINEAR OPTICS:
MATERIALS,
FUNDAMENTALS,
AND
APPLICATIONS

July 8-12, 1996
Maui, Hawaii

1996 Technical Digest Series
Volume 11



COSPONSORED BY
OPTICAL SOCIETY OF AMERICA
IEEE/LASERS AND ELECTRO-OPTICS SOCIETY



Optical Society of America
2010 Massachusetts Avenue NW
Washington DC 20011-1023

DTIC QUALITY INSPECTED 1

Articles in this publication may be cited in other publications. To facilitate access to the original publication source, the following form for the citation is suggested:

Name of Author(s), "Title of Paper," in *Nonlinear Optics: Materials, Fundamentals, and Applications*, Vol. 11, 1996 OSA Technical Digest Series (Optical Society of America, Washington DC, 1996), pp. xx-xx.

Optical Society of America

ISBN

Conference Edition 1-55752-446-7

Postconference Edition 1-55752-447-5

(Note: Postconference Edition
includes postdeadline papers.)

1996 Technical Digest Series 1-55752-417-3

Library of Congress Catalog Card Number

Conference Edition 95-72767

Postconference Edition 95-72768

Copyright © 1996, Optical Society of America

Individual readers of this digest and libraries acting for them are permitted to make fair use of the material in it, such as to copy an article for use in teaching or research, without payment of fee, provided that such copies are not sold. Copying for sale is subject to payment of copying fees. The code 1-55752-417-3/96/\$6.00 gives the per-article copying fee for each copy of the article made beyond the free copying permitted under Sections 107 and 108 of the U.S. Copyright Law. The fee should be paid through the Copyright Clearance Center, Inc., 21 Congress Street, Salem, MA 01970.

Permission is granted to quote excerpts from articles in this digest in scientific works with the customary acknowledgment of the source, including the author's name and the name of the digest, page, year, and name of the Society. Reproduction of figures and tables is likewise permitted in other articles and books provided that the same information is printed with them and notification is given to the Optical Society of America. In addition, the Optical Society may require that permission also be obtained from one of the authors. Address inquiries and notices to Director of Publications, Optical Society of America, 2010 Massachusetts Avenue, NW, Washington, DC 20036-1023. In the case of articles whose authors are employees of the United States Government or its contractors or grantees, the Optical Society of America recognizes the right of the United States Government to retain a nonexclusive, royalty free license to use the author's copyrighted article for United States Government purposes.

Printed in the U.S.A.

Contents

Agenda of Sessions	v
NMA Plenary Session	1
NMB Cascaded Optical Nonlinearities	3
NMC Frequency Conversion	11
NMD Molecular Nonlinear Optics	31
NME NLO Poster Session: 1	45
JTuA Joint Session on Holographic Systems	147
JTuB Joint Session on Holographic Materials & Fixing	165
JTuC Joint Session on Holographic Storage and Beyond	181
JTuD Joint Poster Session	197
NTuA NLO Poster Session: 2	237
NWA Coherent Effects in Semiconductor Structures	263
NWB Wavemixing in Semiconductors	277
NWC Nonlinear Probes of Materials and Devices	291
NWD Organic Nonlinear Optical Materials and Polymers	303
NThA Photorefractive Nonlinear Optics	315
NThB Thermal Nonlinear Optics and Mode Locking Mechanisms	335
NThC Fiber Nonlinear Optics	347
NThD Nonlinear Optics of Thin Films	361
NThE NLO Poster Session: 3	375
NFA NLO of Atomic Systems	455
NFB Optical Solitons	467
Key to Authors and Presiders	485

**1996 NONLINEAR OPTICS: MATERIALS, FUNDAMENTALS, AND APPLICATIONS
TECHNICAL PROGRAM COMMITTEE**

Richard Lind, *Hughes Research Laboratories, USA, General Co-Chair*
C. L. Tang, *Cornell University, USA, General Co-Chair*
Robert W. Boyd, *University of Rochester, USA, Program Co-Chair*
Ian C. McMichael, *Rockwell International, USA, Program Co-Chair*
Dana Z. Anderson, *University of Colorado, USA*
Christoph Bubeck, *Max Planck Institute, Germany*
Tallis Y. Chang, *Rockwell International, USA*
Daniel Chemla, *University of California, Berkeley, USA*
Gilbert Grynberg, *University of Paris, France*
Eiichi Hanamura, *University of Tokyo, Japan*
Stephen E. Harris, *Stanford University, USA*
Ravi Jain, *University of New Mexico, USA*
Wayne Knox, *AT&T Bell Laboratories, USA*
Jerry R. Meyer, *Naval Research Laboratory, USA*
John Ottusch, *Hughes Research Laboratories, USA*
Demetri Psaltis, *California Institute of Technology, USA*
Arthur L. Smirl, *University of Iowa, USA*
Robert Twieg, *IBM Almaden Research Center, USA*
Gary Wood, *Army Research Laboratory, USA*
Boris Zel'dovich, *University of Central Florida, USA*
John D. Harvey, *University of Auckland, New Zealand, IQEC Coordinator*

Domestic Advisory Committee

Christopher Clayton, *US Air Force Phillips Laboratory, USA*
L. N. Durvasula, *ARPA, USA*
Hyatt Gibbs, *University of Arizona, USA*
Robert Guenther, *Army Research Office, USA*
I. C. Khoo, *Pennsylvania State University, USA*
David Pepper, *Hughes Research Laboratories, USA*
Herschel Pilloff, *Office of Naval Research, USA*
Howard Schlossberg, *AFOSR, USA*
Y. R. Shen, *University of California, Berkeley, USA*
Pochi Yeh, *University of California, Santa Barbara, USA*

International Advisory Committee

H. J. Eichler, *Technische Universitaet Berlin, Germany*
W. J. Firth, *University of Strathclyde, UK*
Christos Flytzanis, *CNRS Lab., Palaiseau, France*
Peter Guenter, *ETH-Hoenggerberg, Switzerland*
Nikolai Koroteev, *Moscow State University, Russia*
B. Luther-Davis, *National University of Australia*
Seizo Miyata, *Tokyo University of Agriculture and Technology, Japan*
C. L. Pan, *National Chaio Tung University, China*
A. Persoons, *University of Leuven, Belgium*
Hiroyuki Sasabe, *RIKEN, Japan*
Francesco Simoni, *Universita di Ancona, Italy*
Daniel Walls, *University of Auckland, New Zealand*
Herbert Walther, *Max Planck Institute fur Quantenoptik, Germany*
Guo-Zheng Yang, *Academia Sinica, China*
Zhi-Ming Zhang, *Fudan University, China*

MONDAY

JULY 8, 1996

MAILE ROOM

7:55am-8:00am

Opening Remarks

Richard Lind, *Hughes Research Laboratories, General Chair*
C. L. Tang, *Cornell University, General Chair*

8:00am-8:45am

NMA • Plenary Session

Robert Boyd, *University of Rochester, Presider*

8:00am (Plenary)

NMA1 • Nicolaas Bloembergen, *Harvard Univ.* Abstract not available. (p. 2)

MAILE ROOM

8:45am-9:25am

NMB • Cascaded Optical Nonlinearities

David Pepper, *Hughes Research Laboratories, Presider*

8:45am (Invited)

NMB1 • *Experimental progress in cascading nonlinear optics*, G. I. Stegeman, W. E. Torruellas, R. Schiek, B. Lawrence, R. Fuerst, Y. Baek, C. Trevino-Palacios, D. Baboiu, *Univ. Central Florida*; I. Baumann, W. Sohler, *Univ. Paderborn, Germany*; G. Assanto, *Univ. Roma III, Italy*; L. Torner, *Polytechnic Univ. Catalunya, Spain*; P. Baldi, M. De Micheli, D. B. Ostrowsky, *Univ. Nice, France*. We discuss experimental progress using cascading for all-optical switching through nonlinear phase shifts and spatial solitary waves, beam clean-up and spatial instabilities, and unidirectional transmission. (p. 4)

9:10am

NMB2 • *Phase-insensitive, single wavelength, all-optical transistor based on cascaded second-order nonlinearities*, Z. Wang, D. J. Hagan, E. W. Van Stryland, *Univ. Central Florida*; G. Assanto, *Terza Univ. Rome, Italy*. We describe an all-optical transistor, based on cascaded second-order nonlinearities, in which the pump and signal waves may be incoherent. All inputs and outputs are at the same wavelength. (p. 7)

9:25am-9:55am

Coffee Break

MAILE ROOM

9:55am-12:10pm

NMC • Frequency Conversion

Jerry Meyer, *Naval Research Laboratory, Presider*

9:55am (Invited)

NMC1 • *Tailoring nonlinear optical interactions with microstructured materials*, M. M. Fejer, *Stanford Univ.* Microstructured ferroelectrics and semiconductors offer unprecedented flexibility in tailoring nonlinear materials to suit specific applications. Quasi-phases matching in conventional periodic structures, as well as in axially and transversely modulated structures, will be discussed. (p. 12)

10:20am

NMC2 • *Efficient ultraviolet light generation by LiNbO₃ waveguide quasi-phase-matched second-harmonic generation devices*, K. Kintaka, M. Fujimura, T. Suhara, H. Nishihara, *Osaka Univ., Japan*. LiNbO₃ waveguide QPM-SHG devices for ultraviolet light generation are fabricated for the first time by application of voltage. We obtain 1.9 mW output and 70%/W normalized efficiency. (p. 13)

10:35am (Invited)

NMC3 • *Quantum picture of nonlinear optical patterns*, A. Gatti, L. A. Lugiato, I. Marzoli, *INFN, Italy*; G. L. Oppo, S. M. Barnett, *Univ. Strathclyde, UK*; H. Wiedemann, *Univ. Ulm, Germany*. We show the complete phase transition of the quantum image in an optical parametric oscillator, covering the full range far below to above the threshold. For a cavity with spherical mirrors the quantum image in the far field well below threshold provides direct spatial evidence of the emission of twin photons, and it is formed by quantum correlated pairs of points, which constitutes a novel quantum effect. (p. 16)

11:00am

NMC4 • *Comparison of wide-band electro-optic frequency tuning in LiNbO₃ and KNbO₃ OPOs*, M. D. Ewbank, M. J. Rosker, *Rockwell Science Center*. Electro-optic index perturbations are compensated by wavelength detuning, dictated by index dispersion, to maintain phase matching in optical parametric oscillators (OPOs). Tuning ranges and rates for mid-infrared LiNbO₃ and KNbO₃ OPOs are compared. (p. 19)

11:15am (Invited)

NMC5 • *Ultrashort-pulse generation in the ultraviolet using ionization-induced harmonic generation*, H. C. Kapteyn, S. Backus, J. Peatross, E. Zeek, K. Read, M. M. Murnane, *Univ. Michigan*. Using harmonic generation in air and various gases, we generate 16-fs, microjoule energy pulses in the ultraviolet. (p. 22)

11:40am

NMC6 • *Third-harmonic generation in a plasma of self-induced optical breakdown in air using 80-fs laser pulses: Self-action of light beams and spectral broadening*, A. B. Fedotov, M. M. T. Loy, X. Xiao, *Hong Kong Univ. Science and Technology*; V. N. Krylov, A. K. Rebane, *Swiss Federal Institute of Technology*; N. I. Koroteev, A. M. Zheltikov, *Moscow State Univ, Russia*. Third-harmonic generation in self-induced optical breakdown with efficiency up to 0.15% is detected. Self-action of light is demonstrated to influence the harmonic-generation efficiency. (p. 25)

11:55am

NMC7 • *Nonlinear optics of nanostructured materials: Fractal nanocomposites and self-affine surfaces*, Vladimir M. Shalaev, *New Mexico State Univ.*; J. Mercer, *Sandia National Laboratories*; V. P. Safonov, *Institute of Automation and Electrometry, Russia*; R. Botet, *Univ. Paris-Sud, France*. Fractal nanostructured materials are shown to possess giant optical nonlinearities. The enhancement results from the subwavelength localization of dipolar modes and strong local field fluctuations. (p. 28)

12:10pm-7:00pm

Free Time

MAILE ROOM

7:00pm–8:20pm

NMD • Molecular Nonlinear OpticsChristoph Bubeck, *Max Planck Institute, Germany, Presider*

7:00pm (Invited)

NMD1 • From dipolar to multipolar systems: Opening new geometric and quantum dimensions in molecular NLO, Joseph Zyss, *France Telecom-CNET, France*. Recognition of 3D multipolar systems with multiple charge transfer as relevant candidates towards molecular NLO has permitted to enlarge traditional molecular engineering schemes in combination with new models and experiments. (p. 32)

7:25 pm (Invited)

NMD2 • Chirality in nonlinear optics, Thierry Verbiest, Martti Kauranen, Jeffery J. Maki, André Persoons, *Univ. Leuven, Belgium*. We give an overview of the investigation of chiral properties of thin films using second-harmonic generation. Theoretical and experimental results are presented. (p. 35)

7:50pm

NMD3 • Femtosecond to nanosecond dynamics in C_{60} : Implications for excited-state nonlinearities, D. McBranch, V. Klimov, L. Smilowitz, J. M. Robinson, A. Koskela, M. Grigorova, B. R. Mattes, *Los Alamos National Laboratory*. Results of excited-state dynamics of C_{60} in solution, solid, and sol-gel glasses are compared and implications for optical limiting are discussed. (p. 38)

8:05pm

NMD4 • Enhancement of second-order optical nonlinearity by supramolecular engineering, Martti Kauranen, Thierry Verbiest, Carlo Boutton, Stephan Houbrechts, André Persoons, Celest Samyn, *Univ. Leuven, Belgium*. Incorporation of second-order nonlinear chromophores as orientationally correlated side groups on a rigid polymer enhances the nonlinearity of chromophores by a factor of 35. (p. 41)

SOUTH PACIFIC BALLROOM

8:20pm–10:30pm

NME • NLO Poster Session: 1

NME1 • Vertical couplers: All-optical switch design, Rachel M. Geatches, Susan V. Dewar, *Univ. Wales College of Cardiff, UK*; Richard V. Penty, *Univ. Bristol, UK*. Vertical, asymmetric nonlinear directional couplers are investigated with use of spectral index and coupled mode theory methods to design low-power, all-optical switches for semiconductor integration. (p. 46)

NME2 • Experimental demonstration of an optical neural network using self-defocusing media, Steven R. Skinner, Alvaro A. Cruz-Cabrera, James E. Steck, Elizabeth C. Behrman, *Wichita State Univ.* The optical bench realization of an optical neural network using thermal self-defocusing material is presented. The network was trained to achieve several logic functions. (p. 49)

NME3 • Dynamics of a fiber laser with two-tone modulation, T. Newell, V. Kovanis, A. Gavrielides, D. Sukow, T. Erneux, *USAF Phillips Laboratory*. We investigate experimentally the dynamics of a fiber laser subject to two-tone sinusoidal modulation of the pump. (p. 52)

NME4 • Modeling cw, bulk periodically poled $LiNbO_3$ optical parametric oscillators with strong idler absorption, Dennis D. Lowenthal, *Aculight Corp.* An analytical model is developed to predict the performance of cw, singly resonant, optical parametric oscillators with strong idler absorption, strong pump depletion, and thermally induced dephasing. (p. 55)

NME5 • Recent advances in blue and green diode-pumpable upconversion fiber lasers, R. K. Jain, G. S. Feller, B. Srinivasan, M. C. Nostrand, *Univ. New Mexico*. We describe our recent work on several blue and green upconversion fiber lasers, including the demonstration of (i) high efficiency operation of a 544 nm Er:ZBLAN fiber laser, (ii) a novel pump source for and self mode-locking of a 482 nm Tm:ZBLAN laser, and (iii) new co-doped energy transfer systems for blue upconversion lasers with readily available pumps. (p. 58)

NME6 • Industrial laser ultrasonic inspection system using a DPCM for wave-front compensation, G. J. Dunning, D. M. Pepper, P. V. Mitchell, M. B. Klein, T. R. O'Meara, *Hughes Research Laboratories*. Using a double-pumped phase-conjugate mirror, we demonstrate compensation of optical wave-front distortions typical in an industrial environment, enabling the coherent detection of high-bandwidth laser-based ultrasound. (p. 61)

NME7 • Optical switching based on singlet-singlet excited state absorption, Miao Yang, Jinhai Si, Yuxiao Wang, Chunfei Li, *Harbin Institute of Technology, China*. All-optical switching in metallo-porphyrin-like solutions is demonstrated experimentally. Theoretical analysis shows that it is attributed to the singlet-singlet excited state absorption. (p. 64)

NME8 • Generalized dispersion equations for nonlinear waveguides with Kerr-type films, Jong-Sool Jeong, Seok Ho Song, El-Hang Lee, *Electronics and Telecommunications Research Institute, Korea*. We present a generalized form of nonlinear dispersion equations that can be applied to various nonlinear waveguide structures with Kerr-type films. (p. 67)

NME9 • All-optical switching in waveguide structures due to cascaded nonlinearities, R. Schiek, Y. Baek, G. Krijnen, G. I. Stegeman, *Univ. Central Florida*. All-optical switching caused by large intensity-dependent phase shifts as a result of cascading was observed in nonlinear directional waveguide couplers and integrated Mach-Zehnder interferometers. (p. 70)

NME10 • Coherent transient in optical lattices: Application to quasi-periodic optical structures, L. Guidoni, C. Triché, S. Guibal, P. Verkerk, G. Grynberg, *École Normale Supérieure, France*. Coherent transients greatly improve the experimental resolution in optical lattice spectroscopy. The relative distribution of atoms between the various potential wells in quasi-periodic structures is estimated. (p. 73)

NME11 • Localization and coupling dynamics in nonlinear waveguide arrays, Alejandro B. Aceves, Marco Santagiustina, *Univ. New Mexico*. A variational method is used to study pulse dynamics in asymmetric three-waveguide arrays. Predictions are confirmed by numerical solutions. Pulse-radiation interactions and localization are also studied. (p. 76)

NME12 • 39.5% conversion of low power Q-switched Nd:YAG laser radiation to 266 nm by use of a resonant ring cavity, Joachim Knittel, A. H. Kung, *Academia Sinica, China*. External resonance enhancement is used to obtain efficient fourth harmonic generation from a low-power Q-switched Nd:YAG laser. IR to UV energy conversion of >39% is achieved, providing 84 mW average power at 266 nm from 213 mW of 1064 nm radiation. (p. 79)

NME13 • Nonlinear optical microscopy for imaging thin films and surfaces, Laura Smilowitz, Duncan McBranch, Jeanne M. Robinson, *Los Alamos National Laboratory*. We use the inherent surface sensitivity of second harmonic generation to develop an instrument for nonlinear optical microscopy of surfaces and interfaces. (p. 82)

NME14 • Multiple wavelength generation in a picosecond optical parametric oscillator based on noncritically phase-matched LiB_3O_5 , S. French, M. Ebrahimzadeh, A. Miller, *Univ. St. Andrews, UK*. We describe the simultaneous generation of visible (500.1–511.6 nm) and infrared (1.1–2.26 μm) picosecond pulses from an optical parametric oscillator based on LiB_3O_5 . (p. 85)

NME15 • Mid-infrared femtosecond pulse generation using a 250 kHz Ti:sapphire-pumped BBO OPA and DFG in AgGaS_2 , Murray K. Reed, Michael K. Steiner-Shepard, *Coherent Laser Group*. A 100-fs Ti:sapphire 250-kHz regenerative amplifier pumping a BBO OPA generates 500-nJ infrared pulses with tuning from 1.1–2.5 μm . Difference frequency generation of the signal and idler in AgGaS_2 produces 60 nJ midinfrared pulses with tuning from 2.4–12 μm . (p. 88)

NME16 • Optical parametric device for efficient generation of radiation in the 3.9 μm range, Karl Koch, Gerald T. Moore, *USAF Phillips Laboratory*. We describe a Q-switched optical parametric oscillator incorporating difference-frequency mixing to enhance the generation of idler radiation at 3.9 μm . (p. 90)

NME17 • Energy characteristics of a loop laser with a thermal holographic mirror using millisecond pulses at 1.06 μm , A. A. Betin, S. C. Matthews, M. S. Mangir, *Hughes Research Laboratories*. Energy characteristics of a thermal nonlinearity loop operated at 1.06 μm indicate its viability for phase conjugation at input peak powers <100 W, coherence lengths <10 cm, with reflectivity >1. (p. 92)

NME18 • Degenerate backward optical parametric oscillators and amplifiers: Conversion efficiencies and gain saturation, Yujie J. Ding, *Bowling Green State Univ.*; Jacob B. Khurgin, *The Johns Hopkins Univ.* Degenerate backward optical parametric oscillators and amplifiers have been investigated for the first time, to the best of our knowledge. The oscillation can occur without an external feedback. (p. 94)

NME19 • Chaos stabilization via pulse train generation in dispersive optical parametric oscillators, Stefano Trillo, *Fondazione Ugo Bordon, Italy*; Marc Haelterman, *Univ. Libre de Bruxelles, Belgium*. We consider the role played by dispersion in optical parametric oscillators, and show that it allows stabilization of chaotic self-pulsation via a novel kind of dissipative modulational instability. (p. 97)

NME20 • Brillouin-enhanced four-wave-mixing vector phase-conjugate mirror, M. W. Bowers, R. W. Boyd, *Univ. Rochester*; A. K. Hankla, *Lawrence Livermore National Laboratory*. A Brillouin-enhanced four-wave-mixing vector phase-conjugate mirror is developed. Restoration of wave fronts and polarization is accomplished along with mechanically variable output coupling. (p. 100)

NME21 • Generalized master equation models for Kerr lens modelocking, A. M. Dunlop, W. J. Firth, *Univ. Strathclyde, UK*; E. M. Wright, *Univ. Arizona*. We present a generalized master equation for KLM lasers with ABCD cavities. Dynamical simulations of pulse compression are presented. Mode projection enables comparison with other KLM models. (p. 103)

NME22 • Highly repetitive generation of picosecond pulses at 1.57 μm using an optical parametric generator and amplifier, U. J. Greiner, T. Schröder, H. H. Klingenberg, *Institut für Technische Physik, Germany*. We present a KTP optical parametric generator-amplifier to generate picosecond pulses at 1.57 μm using an all-solid-state regenerative Nd:YAG amplifier. (p. 106)

NME23 • Effective suppression of amplified spontaneous emission by SBS phase conjugation, C. K. Ni, A. H. Kung, *Academia Sinica, China*. Amplified spontaneous emission is reduced from over 15% to less than 10^{-4} in a pulse-amplified cw Ti:sapphire laser by use of a phase-conjugate SBS mirror as a reflector in the amplifier chain. (p. 109)

NME24 • Quasi-phases-matched singly resonant parametric oscillation in periodically poled lithium niobate waveguides, M. A. Arbore, M. M. Fejer, *Stanford Univ.* We report singly resonant optical parametric oscillation in electric-field-poled lithium niobate waveguides. Gains as high as 250%/W, oscillation threshold of 1.6 W (peak), idler output of 220 mW, and a tuning range of 1270–1900 nm for pump wavelengths of 762–772 nm have been observed. (p. 112)

NME25 • Nonreciprocity of polarization rotary power, P. J. Bennett, S. Dhanjal, Yu. P. Svirko, N. I. Zheludev, *Univ. Southampton, UK*. First observation of weak natural nonreciprocity of polarization rotation in a crystal exhibiting conventional optical activity is reported. (p. 115)

NME26 • Cascaded optical nonlinearities: Microscopic understanding of it as a collective effect, Jacob B. Khurgin, S. J. Lee, *The Johns Hopkins Univ.* A general microscopic theory treating cascading of wide range nonlinear optical processes as a collective effect is developed. Important practical implications are discussed. (p. 118)

NME27 • Influence of mirror curvature on pattern formation in nonlinear optics, G. K. Harkness, J. Lega, G.-L. Oppo, *Univ. Strathclyde, UK*. The transition from mode-dominated to pattern-dominated transverse configurations of lasers and OPO with variable curvatures of cavity mirrors is discussed and numerically verified. (p. 120)

NME28 • Control of spatiotemporal dynamics in nonlinear optics, R. Martin, G.-L. Oppo, A. J. Scroggie, W. J. Firth, *Univ. Strathclyde, UK*. Spatiotemporal modulation of feedback fields leads to control of complex transverse dynamics of lasers and stabilization of homogeneous outputs of passive optical cavities. (p. 123)

NME29 • Absolute scale of the second-order nonlinear optical coefficients, I. Shoji, A. Kitamoto, M. Shirane, T. Kondo, R. Ito, *Univ. Tokyo, Japan*. Absolute magnitudes of the nonlinear optical coefficients of several important crystals are re-determined with improved accuracy by the second-harmonic generation, difference-frequency generation, and parametric fluorescence methods at several wavelengths. (p. 126)

NME30 • Comparison of molecular hyperpolarizabilities measured in gas and liquid phases, P. Kaatz, D. P. Shelton, *Univ. Nevada Las Vegas*. Hyperpolarizabilities of small molecules measured by hyper-Rayleigh scattering in the liquid are found to differ from gas-phase values by a factor of two. (p. 129)

NME31 • Computational modeling of ultrashort optical pulse propagation in nonlinear optical materials, Peter M. Goorjian, *NASA Ames Research Center*; Govind P. Agrawal, *Univ. Rochester*. The Maxwell-Bloch equations, governing pulse propagation in inhomogeneously broadened two-level media and in semiconductors are solved numerically without making slowly varying envelope and rotating-wave approximations. (p. 132)

NME32 • Lasers without inversion and Raman oscillators: Comparative analysis, Jacob B. Khurgin, *The Johns Hopkins Univ.*; Emmanuel Rosencher, *Thomson CSF, France*. Connection between the lasing without inversion (LWI) and Raman processes is established. It is shown that true LWI is feasible only in a system where pumping and relaxation rates are favorable for conventional lasing. (p. 134)

NME33 • Nondegenerate two-wave mixing in Kerr media, Andrei G. Skirtach, David J. Simkin, *McGill Univ, Canada*; Simon A. Boothroyd, *National Research Council, Canada*. Theory and experimental results for the nondegenerate two-wave mixing in nonlinear absorptive Kerr media including the contribution from nonlinear absorption are presented for the first time. (p. 137)

NME34 • Resonance and bright-dark solitons in group-velocity mismatched second-harmonic generation, Stefano Trillo, *Fondazione Ugo Bordon, Italy*. The existence and stability of solitons in second-harmonic generation dominated by walk-off is discussed. Both resonance soliton in gratings and coupled bright-dark pair in bulk are predicted. (p. 140)

NME35 • Soliton propagation in two-photon resonant region, R. Kitahara, J. Ishi, K. Ema, *Sophia Univ., Japan*. We examine the pulse propagation with dispersive nonlinearity and show that the solitonlike propagation of femtosecond pulses can be achieved at the two-photon resonant region. (p. 143)

HAKU ROOM

8:00am-9:50am

JTuA • Joint Session on Holographic SystemsGlenn Sincerbox, *IBM Almaden Research Center, Presider*

8:00am (Invited)

JTuA1 • Fundamental materials and device issues for digital holographic data storage, Lambertus Hesselink, John F. Heanue, Matthew C. Bashaw, *Stanford University and Optitek, Inc.* We discuss recent advances in digital holographic data storage in terms of fundamental tradeoffs between component, material characteristics and applications. Recent results, including stored and retrieved video clips will be presented. (p. 148)

8:25am (Invited)

JTuA2 • Prospects for fast access holographic memories, John H. Hong, Ian McMichael, Jian Ma, Tallis Chang, William Christian, David Pletcher, Monte Khoshnevisan, *Rockwell Science Center, USA.* A unique feature of holographic memory is its potential for fast random access if nonmechanical means for page addressing are implemented. It is possible to obtain 10 microsecond latency (equivalent to disk head seek time) by using acoustooptic deflectors to steer the address beam in an angularly multiplexed holographic memory system. When 1-100 GByte storage capacities are considered, however, the nonmechanical addressing constraint poses challenging design problems. In this paper, we describe fast access holographic memory architectures and discuss the critical design issues. We also describe recent Rockwell efforts to develop a fast access holographic memory system. (p. 151)

8:50am

JTuA3 • Error sources and performance limits in a digital holographic data storage system, John F. Heanue, Andrew Daiber, Ray Snyder, James Colvin, Matthew C. Bashaw, L. Hesselink, *Optitek Inc.* We describe error sources encountered in digital holographic storage and determine subsequent performance limits. Results obtained with our experimental system are presented. (p. 154)

9:05am

JTuA4 • Data detection for page-access optical memories with intersymbol interference, John F. Heanue, Korhan Gürkan, Lambertus Hesselink, *Stanford Univ.* We introduce a data detection technique that improves the bit-error-rate performance of page-access optical memories corrupted by intersymbol interference. (p. 156)

9:20am

JTuA5 • Statistics of cross-talk noise in holographic data storage, Claire Gu, Gregory Sornat, *The Pennsylvania State Univ.*; John Hong, *Rockwell International Science Center.* We analyze the statistics of cross-talk noise in holographic data storage and determine the corresponding signal-to-noise ratio, threshold value, and bit error rate. (p. 159)

9:35am

JTuA6 • Shift multiplexed holographic 3-D disk system, Allen Pu, Demetri Psaltis, *California Institute of Technology.* A holographic disk system has been demonstrated experimentally. Storage density of 4 bits/ μm^2 is achieved with 100- μm -thick photopolymer. (p. 162)

9:50am-10:20am

Coffee Break

HAKU ROOM

10:20am-12:15pm

JTuB • Joint Session on Holographic Materials & FixingTallis Chang, *Rockwell International, Presider*

10:20am (Invited)

JTuB1 • PRISM: Removing the materials bottleneck in holographic storage, Glenn T. Sincerbox, *IBM Almaden Research Center*; Lambertus Hesselink, *Optitek Inc.* This paper will review the demanding requirements placed on the recording material for holographic data storage and report on progress of the PRISM consortium in developing a suitable material for this application of the technology. (p. 166)

10:45am (Invited)

JTuB2 • Optically induced refractive index changes in glass, Turan Erdogan, *Univ. Rochester.* This talk will review photosensitivity in a variety of glasses in addition to current and potential applications of this phenomenon. (p. 169)

11:10am

JTuB3 • Multifunctional photorefractive chromophores with high transparency and optimized birefringence, R. Twieg, R. Wortmann, C. Poga, C. Geletneky, C. R. Moylan, P. Lundquist, R. G. DeVoe, P. M. Cotts, D. M. Burland, *IBM Almaden Research Center.* Novel organic chromophores useful for photorefractive optical storage are identified that produce high diffraction efficiencies by optimization of the Kerr susceptibility $\chi^{(3)}(-\omega, \omega, 0, 0)$ contribution. (p. 172)

11:25am (Invited)

JTuB4 • Electrical fixing of 1000 angle-multiplexed holograms in SBN:75, Jian Ma, Tallis Chang, John Hong, Ratnakar R. Neurgaonkar, *Rockwell International Science Center*; George Barbastathis, Demetri Psaltis, *California Institute of Technology.* Electrical fixing of 1000 angle-multiplexed holograms was demonstrated in a 1-cm³ Ce-doped SBN:75 crystal. The average diffraction efficiency was measured to be 0.005% and the uniformity was about 80%. (p. 175)

11:50am (Invited)

JTuB5 • Digital image storage by multiplexed holographic recording in Ce-doped SBN crystal, M. Yamamoto, K. Nonaka, T. Kume, *NTT Interdisciplinary Research Laboratories, Japan.* We show the results of multiplexed holographic recording characteristics of digital image data using SBN single crystal with a compact laser diode system. (p. 178)

12:15pm-7:00pm

Free Time

HAKU ROOM

7:00pm-8:25pm

JTuC • Joint Session on Holographic Storage and BeyondManabu Yamamoto, *NTT, Japan, Presider*

7:00pm (Invited)

JTuC1 • Large-scale holographic memory, Demetri Psaltis, Xin An, Geoffrey W. Burr, Fai H. Mok, *California Institute of Technology.* We designed and demonstrated a page-formatted random-access holographic memory capable of storing up to 160,000 holograms. The holograms stored were retrieved without any measured errors. (p. 182)

7:25pm

JTuC2 • Improved usable capacity for optical page-oriented memories with smart pixel interfaces, Wei-Feng Hsu, Alexander A. Sawchuck, *Univ. Southern California*. We describe Reed-Solomon error correcting codes implemented with smart pixel devices to improve the bit-error rate and capacity of optical page-oriented memories. (p. 185)

7:40pm

JTuC3 • A digital wavelength-multiplexed holographic data storage system, D. Lande, J. F. Heanue, M. C. Bashaw, L. Hesselink, *Stanford Univ.* We demonstrate the automated storage and retrieval of digital data in a novel holographic memory system using a diode laser. (p. 188)

7:55pm

JTuC4 • Novel system architectures for practical volume holographic memories, Feng Zhao, Koichi Sayano, *Accuwave Corp.* A novel lensless holographic memory architecture based on the phase-conjugation property of volume holograms is proposed. Optical read-only and write-once-read-many memories that use the new scheme are presented. (p. 191)

8:10pm

JTuC5 • Spectral-hole-and-angle multiplexed volume holographic memory, Xianmin Yi, Changxi Yang, Shiuan-Hui Lin, Pochi Yeh, *Univ. California-Santa Barbara*; Claire Gu, *Pennsylvania State Univ.* We investigate a 4-D spectral-hole-and-angle-multiplexed volume holographic storage system with spectral hole burning materials. Expressions for the cross-talk noise and storage density are obtained. (p. 194)

SOUTH PACIFIC BALLROOM

8:30pm-10:30pm

JTuD • Joint Poster Session

JTuD1 • Novel azo-dye-doped PMMA films as optical data storage media, V. P. Pham, A. Granger, T. Galstyan, R. A. Lessard, *Univ. Laval, Canada*. Optical information is holographically stored, retrieved, erased, and overwritten on new azo-dye-doped PMMA guest-host films. We present new data concerning the dynamic behavior of these films. (p. 198)

JTuD2 • Off-Bragg analysis of diffraction efficiency of photorefractive holograms, Koutarou Nonaka, *NTT Interdisciplinary Research Laboratories, Japan*. Diffraction efficiency versus angle mismatch from the Bragg condition is analyzed, taking into account the photorefractive phase shift and fringe bending effect. (p. 199)

JTuD3 • Theory of two-species transport in photorefractive crystals using two wavelengths for nondestructive readout, A. Y. Liu, M. C. Bashaw, L. Paraschis, L. Hesselink, *Stanford Univ.* We present a model of charge transport dynamics of holographic recording and nondestructive readout using two wavelengths sequentially in photorefractive media with two impurity species. (p. 202)

JTuD4 • Properties of resonant two-photon processes in photorefractive media, L. Paraschis, M. C. Bashaw, A. Liu, L. Hesselink, *Stanford Univ.* We develop a charge transport model to describe resonant two-photon processes establishing nonvolatile holograms in photorefractive media. We investigate the photorefractive behavior with respect to illumination and material parameters, and further evaluate the intermediate state occupancy and the saturation regime. (p. 205)

JTuD5 • Optical implementation of composite filters as volume holograms in LiNbO₃ for pattern recognition, Tracy D. Hudson, Amy S. Kransteuber, Deanna K. McMillen, *U.S. Army Missile Command*; Francis T. S. Yu, Shizhuo Yin, *Pennsylvania State Univ.* A composite filter for distortion-invariant object recognition is designed and implemented as a LiNbO₃ volume hologram located in a 4-f optical processor. (p. 208)

JTuD6 • Switchable diffractive elements and applications to holographic and multilayer optical storage, Lawrence H. Domash, Badri N. Gomatam, *Foster-Miller Inc.*; James Leger, Gregg Kilby, *Univ. Minnesota*. Storage applications of electrically switchable diffractive elements made from fine, grained polymer dispersed liquid crystal include beam steering, holographic ROM, and switchable lens aberration correction. (p. 211)

JTuD7 • Mobile ion compensation in photorefractive media for multiplex holography, M. C. Bashaw, J. F. Heanue, L. Hesselink, *Stanford Univ.* We evaluate operating points for mobile ion compensation in volume holography. (p. 214)

JTuD8 • Phase-conditioning techniques for leveling of the reference beam intensity in orthogonal phase-encoded multiplexing for holographic data storage, Peter B. Catrysse, Matthew C. Bashaw, John F. Heanue, Lambertus Hesselink, *Stanford Univ.* We present phase-conditioning techniques for orthogonal phase-encoded multiplexing, increasing spatial uniformity of the reference beam intensity and affecting storage capacity. (p. 217)

JTuD9 • Digital quasi-phaseshifted two-color nonvolatile holographic storage, E. S. Bjornson, M. Bashaw, L. Hesselink, *Stanford Univ.* Erasure can be reduced by writing at less sensitive wavelengths. We evaluate data magnification and optimization required to alleviate distortion resulting from the wavelength shift. (p. 220)

JTuD10 • Storage and readout of high-resolution holographic images for optical data storage and security applications, Koichi Sayano, Feng Zhao, *Accuwave Corp.* High spatial resolution images were recorded as wavelength multiplexed volume holograms and reconstructed without the need for imaging optics. 500 images were stored in a single volume by use of this approach. (p. 223)

JTuD11 • Optical correlation of phase- and amplitude-encoded objects using wavelength-multiplexed holographic storage elements, Koichi Sayano, Feng Zhao, *Accuwave Corp.* Wavelength multiplexed, holographic reference filters are used in optical correlators for both phase- and amplitude-encoded images. Applications in target recognition and security verification are demonstrated. (p. 226)

JTuD12 • Random phase diffuser design for holographic storage, Deanna McMillen, Tracy D. Hudson, Amy S. Kransteuber, *U.S. Army Missile Command*; Don A. Gregory, Peter S. Erbach, Cynthia G. Zabel, *Univ. Alabama-Huntsville*. A random phase diffuser is designed for use in storing multiplexed holograms. The design is reasonably independent of the type of input used. (p. 229)

JTuD13 • Pseudorandom codes for volume holographic storage application, V. Morozov, K. Johnson, A. Lahrichi, *Univ. Colorado*. We investigate the potentiality of pseudorandom codes for high capacity volume storage applications: hologram spatial multiplexing, multiplexing in storage based on image holograms, and keywords for associative memory. (p. 231)

JTuD14 • Holographic digital storage beyond the diffraction limit. Is it possible? Conceptual analysis of holographic digital storage with synthetic aperture, Valentine Morozov, *Univ. Colorado*. An architecture for holographic digital storage with synthetic aperture is discussed. Aperture synthesis allows for significant increase in holographic storage density beyond the classical diffraction limit. This conclusion results from previous efforts in superresolution technique development and *a priori* knowledge of the data pattern. (p. 234)

SOUTH PACIFIC BALLROOM

8:30pm–10:30pm

NTuA • NLO Poster Session: 2

NTuA1 • Multiwavelength optical computing using optical wave mixing in photorefractive media, Weishu Wu, Pochi Yeh, *Univ. California-Santa Barbara*. A multiwavelength fuzzy controller using optical wave mixing in photorefractive media is analyzed and demonstrated. Spectral parallelism is used to increase the processing throughput. (p. 238)

NTuA2 • Dye-doped liquid crystal films for potential wave-mixing, limiting, and photorefractive applications at 1320 nm, Peter G. LoPresti, Daniel Hemphill, *Univ. Tulsa*. Analysis of infrared self-limiting experiments in dye-doped nematics suggests the presence of galvanically enhanced molecular reorientation, with potential for holographic processing and storage applications. (p. 241)

NTuA3 • Dielectric photorefractive gratings in KLTN at the paraelectric phase, Aharon J. Agranat, Meir Razvag, Michal Balberg, *Hebrew Univ. Jerusalem, Israel*. We present experimental evidence indicating that in KLTN:Cu,V crystals slightly above the phase transition, photorefractive gratings are formed by spatial modulation of the low frequency dielectric constant. We attribute this phenomenon to the formation of dipolar clusters of locally shifted Li ions that screen the photorefractive space charge and create local changes in T_c . (p. 244)

NTuA4 • Optimization of rhodium-doped BaTiO₃ for high-power photorefractive applications in the near infrared, B. A. Wechsler, G. D. Bacher, C. C. Nelson, M. B. Klein, *Hughes Research Laboratories*; S. MacCormack, J. Feinberg, *Univ. Southern California*. For many high-power photorefractive applications using near-infrared laser diodes, large gain coefficients with small absorption loss are required. We have achieved this by varying the Rh dopant concentration and the post-growth annealing of the crystal. (p. 247)

NTuA5 • Measurement of photorefractive dynamics using time autocorrelation function, David Statman, Traci L. Rendulic, *Allegheny College*. We have developed a technique to measure the time autocorrelation function of the signal from two beam coupling in barium titanate. Linear response theory is applied to data analysis. (p. 250)

NTuA6 • Self-phase conjugation and hexagonal pattern formation in photorefractive potassium niobate, P. P. Banerjee, J. O. Dimmock, *Univ. Alabama-Huntsville*; N. V. Kukhtarev, H. J. Caulfield, *Alabama A&M Univ.*; T. Honda, *National Research Laboratory of Metrology, Japan*. We present a model for reflection-grating-dominated simultaneous self-phase conjugation and pattern formation, as well as hexagon rotation, observed in photorefractive potassium niobate. (p. 253)

NTuA7 • Two-color photorefractivity in LiNbO₃ waveguides, D. Eger, M. A. Arbore, M. M. Fejer, *Stanford Univ.*; M. L. Bortz, *New Focus Inc.* It is shown that photorefractive index changes are induced in titanium-poled waveguides of lithium niobate by the combined action of the infrared and blue light. (p. 256)

NTuA8 • Exact nonlinear full-field anisotropic analysis of higher-order diffraction in photorefractive barium titanate, J. M. Jarem, P. P. Banerjee, *Univ. Alabama-Huntsville*. The exact Kukhtarev equations along with rigorous coupled wave theory are used to study the time evolution of higher order diffraction in photorefractive barium titanate. (p. 259)

MAILE ROOM

8:00am–9:35am

NWA • Coherent Effects in Semiconductor StructuresRavi Jain, *University of New Mexico, Presider*

8:00am (Invited)

NWA1 • Nonlinear optics of semiconductor microcavities, Hyatt M. Gibbs, Ove Lyngnes, Jill D. Berger, John Prineas, Sahnggi Park, Galina Khitrova, *Univ. Arizona*. Time-resolved measurements of normal mode coupling oscillations show a strong decrease in the decay time with increased excitation power with little change in the oscillation period. (p. 264)

8:25am

NWA2 • Ultrafast time-resolved ellipsometry of four-wave-mixing signals: Measurement of coherent nonlinear processes in semiconductors, Arthur L. Smirl, A. E. Paul, J. A. Bolger, *Univ. Iowa*. A novel combination of ellipsometric and time-resolved pump probe techniques is used to completely determine the polarization state of the emitted four-wave-mixing signal from a GaAs/AlGaAs multiple quantum well. (p. 267)

8:40am

NWA3 • Coherent phonons as an ultrafast probe of optical nonlinearities in semiconductors, H. Kurz, G. C. Cho, T. Dekorsy, *RWTH Aachen, Germany*; S. Hunsche, H. J. Bakker, *FOM Institute for Atomic and Molecular Physics, The Netherlands*. Coherent phonons are shown to be an important tool for the investigation of optical nonlinearities in semiconductors, e.g., resonant coherent plasmon-phonon mode detection and optically induced lattice instabilities. (p. 270)

8:55am

NWA4 • Coherent-transient studies of ZnSe/ZnCdSe multiple quantum wells, I. J. Blewett, A. Tookey, A. K. Kar, I. Galbraith, G. Horsburgh, T. A. Steele, K. A. Prior, B. S. Wherrett, *Heriot-Watt Univ., UK*. Picosecond-timescale free-polarization decays exhibiting beats (with timescale independent of quantum-well width) are shown to have a biexcitonic and possibly a bipolaritonic contribution. (p. 273)

9:10am (Invited)

NWA5 • Exciton polariton Boser, Y. Yamamoto, S. Pau, H. Cao, G. Bjork, *Stanford Univ.* We observe the final-state stimulation in the microcavity exciton polariton emission when the pump laser is tuned a single longitudinal phonon energy above the polariton energy. (p. 276)

9:35am–10:00am

Coffee Break

MAILE ROOM

10:00am–11:20am

NWB • Wavemixing in SemiconductorsArthur Smirl, *University of Iowa, Presider*

10:00am (Invited)

NWB1 • Engineering the second-order optical nonlinearity in semiconductors, S. Janz, *National Research Council, Canada*. The material science aspects of the second-order optical nonlinearity in semiconductors are reviewed, with emphasis on nonlinear processes in the visible and near-infrared. (p. 278)

10:25am

NWB2 • Current induced second-harmonic generation in semiconductors, Jacob B. Khurgin, *The Johns Hopkins Univ.* Direct current in semiconductors is shown to be capable of doubling the frequency of the incoming optical radiation. $\chi^{(2)}$, proportional to the current, is found to be in the 10^{-14} – 10^{-13} m/V range. Applications in probing and mapping of the current in semiconductor devices are considered. (p. 281)

10:40am

NWB3 • Generation of terahertz radiation by difference-frequency mixing of femtosecond pulses in InSb and InAs, S. C. Howells, L. A. Schlie, *Phillips Laboratory*. The temperature dependence of terahertz radiation produced by difference-frequency mixing in (100)InAs and (111)InSb are measured and compared with theory. (p. 284)

10:55am (Invited)

NWB4 • Design of quantum well intersubband transitions for nonlinear difference frequency mixing, J. S. Harris, Jr., *Stanford Univ.* The use of intersubband transitions in quantum wells is discussed, particularly with application to difference frequency generation. The use of quasi-bound states is also explored. (p. 287)

11:20am–1:30pm

Lunch

MAILE ROOM

1:30pm–2:40pm

NWC • Nonlinear Probes of Materials and DevicesGeorge Stegeman, *University of Central Florida, Presider*

1:30pm (Invited)

NWC1 • Second harmonic spectroscopy of buried Si(001)/SiO₂ interfaces and Si(001) epitaxial growth surfaces, Michael Downer, *Univ. Texas*. Abstract not available. (p. 292)

1:55pm

NWC2 • Application of nonlinear optics for probing of silicon-based circuits, H. Kurz, C. Ohlhoff, C. Meyer, G. Lüpke, T. Löffler, T. Pfeifer, H. G. Roskos, *Rheinisch-Westfälische Technische Hochschule, Germany*. We present picosecond resolution SHG measurements of 2 GHz sinusoidal signals on a photoconductive silicon-on-sapphire antenna. Applications of the SHG technique for spatial mapping of free-running microwave signals in silicon are demonstrated. (p. 293)

2:10pm

NWC3 • Functional imaging of neurons with two-photon confocal microscopy using a saturable-Bragg-reflector-modelocked compact solid-state laser, W. H. Knox, S. Tsuda, K. Svoboda, W. Denk, *Bell Laboratories Lucent Technologies*. A compact 90-fs laser powers two-photon confocal microscopy, yielding morphological and functional images of living neurons with submicron 3D resolution deep in scattering tissue. (p. 296)

2:25pm

NWC4 • Observation of surface oxide properties by the second harmonic magneto-optic Kerr effect in $\text{Ni}_{81}\text{Fe}_{19}$ films, T. J. Silva, NIST; T. M. Crawford, C. T. Rogers, *Univ. Colorado*; Y. K. Kim, *Quantum Peripherals Colorado Inc.* We report on measurements of the second-harmonic magneto-optic Kerr effect in $\text{Ni}_{81}\text{Fe}_{19}$ films versus air-annealing time. We discuss the results and implications. (p. 299)

2:40pm–3:00pm

Break

MAILE ROOM

3:00pm–4:20pm

NWD • Organic Nonlinear Optical Materials and Polymers

Robert Twieg, *IBM Almaden Research Center, Presider*

3:00pm (Invited)

NWD1 • Theory of the third-order nonlinear optical response of organic materials, Shuji Abe, V. A. Shakin, *Electrotechnical Laboratory, Japan*. Resonant and nonresonant optical nonlinearity in organic conjugated polymers is theoretically studied by use of the configuration-interaction description of strongly interacting electrons. (p. 304)

3:25pm (Invited)

NWD2 • Novel high nonlinearity organic crystals, Peter Guenter, *Nonlinear Optics Laboratory*. We will present the most recent results on the growth and characterization of novel high quality molecular crystals for nonlinear optics. These crystals are based on ionic or hydrogen bonding of new and known chromophores with large second-order hyperpolarizabilities. Detailed results of optical, electro-optical and nonlinear-optical properties of high quality and large size DAST crystals, of hydrazone derivatives and new co-crystals will be presented. It will be shown that optimized parallel alignment of chromophores as well as optimum structures for phase-matched frequency mixing have been realized. In addition we report on the measurement of the highest known phase-matchable nonlinear susceptibility coefficient of 200 pm/V determined recently in our laboratory. (p. 307)

3:50pm

NWD3 • Nonlinear optical waveguide spectroscopy of Poly(p-Phenylenevinylene), K. Ueberhofen, R. O. Garay, K. Müllen, C. Bubeck, *Max-Planck-Institute for Polymer Research, Germany*. Thin films of PPV are investigated by intensity-dependent prism coupling. The near-infrared spectra of the nonlinear refractive and absorption index show interesting resonances. (p. 308)

4:05pm

NWD4 • Magnitude and sign of the third order optical nonlinearity in polydibutylstannane, Ardie D. Walser, Richard Priestley, Roger Dorsinville, *CUNY–City College*; W. K. Zou, D. Y. Xu, Nan-Loh Yang, *CUNY–College of Staten Island*. The magnitude of the third-order susceptibility of a new, transparent-in-the-visible, tin-based polymer polydibutylstannane is found to be two orders of magnitude larger than in polysilane. (p. 311)

4:20pm–7:30pm

Free Time

LUAU GARDENS

7:30pm–9:00pm

Conference Reception

MAILE ROOM

8:00am–9:30am

NThA • Photorefractive Nonlinear OpticsGary L. Wood, *US Army Research Laboratory, Presider*

8:00am

NThA1 • A powerful diffraction-limited semiconductor laser using photorefractive beam coupling, Stuart MacCormack, Jack Feinberg, *Univ. Southern California*; Steve O'Brien, Robert J. Lang, *SDL*; Marvin B. Klein, Barry A. Wechsler, *Hughes Research Laboratories*. We use a photorefractive crystal to transform 2.2 W of distorted light from a single-frequency semiconductor amplifier at $\lambda = 860$ nm into 1.1 W of diffraction-limited light. (p. 316)

8:15am

NThA2 • Two-wave mixing with partially coherent waves in photorefractive crystals, Xianmin Yi, Changxi Yang, Pochi Yeh, *Univ. California–Santa Barbara*. We investigate contradiirectional two-wave mixing with partially coherent waves in KNbO_3 photorefractive crystals. A general formulation based on linear system theory is provided. Both theoretical and experimental results are presented. (p. 319)

8:30am

NThA3 • Amplification of optical signals in $\text{Bi}_{12}\text{TiO}_{20}$ crystal by the fanned beam, Anatoli V. Khomenko, Alfonso García-Weidner, *Centro de Investigación Científica y de Educación Superior de Ensenada, México*; Alexei A. Kamshilin, *Univ. Joensuu, Finland*. Beam amplification by coupling between the signal and fanned beam internally reflected in the long $\text{Bi}_{12}\text{TiO}_{20}$ crystal with the gain of 16,000 is demonstrated experimentally. (p. 322)

8:45am

NThA4 • Demonstration of 3-D image reconstruction using a photorefractive storage media, Richard J. Anderson, *National Science Foundation*; Brian P. Ketchel, Gary L. Wood, *U.S. Army Research Laboratory*; Gregory J. Salamo, *Univ. Arkansas*. We demonstrate, using recorded observations from different perspectives, 3-D image storage and reconstruction with strontium barium niobate (SBN) as the photorefractive storage media. (p. 325)

9:00am

NThA5 • Self-compensating laser-based ultrasound sensors using photoinduced EMF detection, D. M. Pepper, G. J. Dunning, P. V. Mitchell, M. B. Klein, T. R. O'Meara, *Hughes Research Laboratories*. We demonstrate a self-compensating ultrasonic vibrometer using nonsteady-state photo-EMF in Cr:GaAs , which is laser-diode compatible. When integrated with a time-delay fiber-optic interferometer, a robust, high-bandwidth sensor is realized. (p. 328)

9:15am

NThA6 • Competition of hexagonal and square patterns in a photorefractive feedback system, Markus Sedlatschek, Torsten Rauch, Cornelia Denz, Theo Tschudi, *Institut für Angewandte Physik, Germany*; Tokuyuki Honda, *National Research Laboratory of Metrology, Japan*. Very recently, squares and squeezed hexagons have been discovered in a photorefractive feedback system. We present the competition of different patterns formed in that system. (p. 331)

9:30am–10:00am

Coffee Break

MAILE ROOM

10:00am–11:30am

NThB • Thermal Nonlinear Optics and Mode Locking MechanismsJohn Ottusch, *Hughes Research Laboratories, Presider*

10:00am (Invited)

NThB1 • Phase conjugation based on thermal nonlinearity, Alexander A. Betin, *Hughes Research Laboratories*. We review some ideas and achievements in use of the thermal nonlinear mechanism for phase conjugation. We conclude that it is very effective and suitable for different lasers (from 0.25–10.6 μm) and for different operating regimes. (p. 336)

10:25am (Invited)

NThB2 • Study of thermal nonlinear refraction in the transient regime, Pascale Brochard, Valérie Grolier, Régis Cabanel, *Thomson CSF Optronique, France*. The efficiency of thermal nonlinear refraction in the nanosecond regime is discussed. Acoustic waves and thermal effects are considered to evaluate the photoinduced index variation. (p. 340)

10:50am

NThB3 • Critical behavior of femtosecond nonlinearity of metallic indium on melting, N. I. Zheludev, S. V. Popov, I. R. Shatwell, *Univ. Southampton, UK*; V. E. Gusev, *Katholieke Univ. Leuven, Belgium*. We found a very strong ($\sim 10^{-7}$ esu) femtosecond cubic nonlinearity in indium that exhibits critical behavior on the melting of the metal. (p. 343)

11:05am (Invited)

NThB4 • Nonlinear optical processes in laser modelocking, Wilson Sibbett, *Univ. St. Andrews, UK*. Abstract not available. (p. 346)

11:30am–7:00pm

Free Time

MAILE ROOM

7:00pm–8:00pm

NThC • Fiber Nonlinear OpticsWayne Knox, *AT&T Bell Laboratories, Presider*

7:00pm

NThC1 • Electrostrictive intensity-dependent refractive index of silica fibers, Eric L. Buckland, Robert W. Boyd, *Univ. Rochester*. We identify electrostriction in optical fibers as the source of measured differences in the value of the nonlinear refractive index obtained using cw and modelocked pulses. (p. 348)

7:15pm

NThC2 • Phase-mismatched modulation instability in birefringent fibers, S. G. Murdoch, J. D. Harvey, *Univ. Auckland, New Zealand*. Modulation instability has been observed in optical fibers whose birefringence has been manipulated to generate phase mismatches. Periodic birefringence modulation generates tunable terahertz modulation. (p. 351)

7:30pm

NThC3 • Nonlinear liquid crystal optical fiber array, I. C. Khoo, M. Lee, K. Wang, M. Wood, B. D. Guenther, *Pennsylvania State Univ.* We have investigated several isotropic liquid crystals for use as nonlinear optical fiber array core materials that show very low switching/limiting thresholds for nanosecond laser pulses. (p. 354)

7:45pm

NThC4 • Theory of stretched pulse laser, S. Namiki, W. S. Wong, H. A. Haus, *MIT*. An analytic theory of the stretched pulse laser is compared with computer simulations and experimental results. Good agreement is found, except in highly overdriven operation, to which the analytic theory does not apply. (p. 358)

MAILE ROOM

8:00pm–9:00pm

NThD • Nonlinear Optics of Thin Films

Daniel Chemla, *Lawrence Berkeley Laboratory*, *Presider*

8:00pm

NThD1 • Phase-mismatched degenerate four-wave mixing: Measurement of the complex third-order nonlinear optical susceptibility in thin films, F. P. Strohkendl, L. R. Dalton, R. W. Hellwarth, *Univ. Southern California*. We demonstrate a method by which we determine all the elements of the complex third-order nonlinear optical susceptibility tensor of a C_{60} film at 768 nm. (p. 362)

8:15pm

NThD2 • Measuring weak laser pulses using frequency-resolved optical gating, David N. Fittinghoff, Marco A. Krumbügel, John N. Sweetser, Rick Trebino, *Sandia National Laboratories*; Thomas Tsang, *Brookhaven National Laboratory*. We use surface third-harmonic generation frequency-resolved optical gating to unambiguously measure pulses directly from a Ti:sapphire oscillator and demonstrate a technique for spatiotemporal pulse measurement. (p. 365)

8:30pm

NThD3 • Ultrashort pulse second-order frequency-resolved optical gating with thin poled nonlinear polymers, G. Taft, M. M. Murnane, H. C. Kapteyn, *Washington State Univ.*; D. R. Yankelevich, A. Knoesen, *Univ. California–Davis*; R. J. Twieg, *IBM Almaden Research Center*. A poled nonlinear polymer film is used to perform second harmonic frequency-resolved optical gating measurements of 13-fs pulses, eliminating the need for angle tuning associated with phase-matched crystals. (p. 368)

8:45pm

NThD4 • Nonlinear optical effects in the bulk and at the surface of acentric liquids demonstrating natural optical activity, N. I. Koroteev, V. A. Makarov, A. P. Shkurinov, A. V. Pakulev, A. A. Angelut, A. Yu. Resniansky, A. V. Balakin, *Moscow State Univ., Russia*. Three- and five-wave mixing processes in chiral liquids under single and multiple-wavelength irradiation with femtosecond laser pulses are reported. (p. 371)

SOUTH PACIFIC BALLROOM

9:00pm–11:00pm

NThE • NLO Poster Session: 3

NThE1 • Annealed proton exchange domain inversion erasure in electric-field poled $LiNbO_3$, K. Elhadi, M. Sundheimer, P. Baldi, P. Aschieri, M. DeMicheli, D. B. Ostrowsky, *Univ. Nice-Sophia Antipolis, France*; J. Webjörn, *Univ. Southampton, UK*. Comparison between bulk and guided parametric fluorescence using electric-field poled $LiNbO_3$ indicates erasure of domain inversion over a depth similar to that of the guide. (p. 376)

NThE2 • Electro-optic coefficients of thin layers of $BaTiO_3$, M. J. H. Niesten, *Eindhoven Univ., The Netherlands*; N. J. Pulsford, J. F. M. Cillessen, *Philips Research Laboratories, The Netherlands*. The electro-optic coefficients r_{13} and r_{33} have been determined for a strained $BaTiO_3$ layer grown by pulsed laser deposition. (p. 379)

NThE3 • Nonlinear optical properties of Au nanocrystals embedded in silicate thin films, Minyung Lee, *Ewha Womans Univ., Korea*. The third-order nonlinear optical coefficient of Au nanocrystals embedded in silicate thin films is measured in the surface plasmon absorption region, employing the degenerate four-wave mixing technique. (p. 382)

NThE4 • Third-order nonlinear optical properties of metal ion-implanted silica at 527, 800, and 1053 nm, Barry Luther-Davies, A. Samoc, M. Samoc, *The Australian National Univ.*; Robert H. Magruder, *Vanderbilt Univ.* We have measured the nonlinear optical response of fused silica implanted with gold, oxygen, titanium, or antimony ions using a low-repetition-rate laser to eliminate thermal effects. (p. 385)

NThE5 • Enhancement of χ^3 in nanoparticle composite media exhibiting electrostriction and quantum confinement, G. Flynn, C. Schwarze, D. A. Pomet, M. A. Fiddy, *Univ. Massachusetts–Lowell*. A new model is described that combines the interaction between quantum confinement in nanoparticles and electrostriction on the bulk optical nonlinearity of a medium. (p. 388)

NThE6 • Second harmonic generation studies of porous ice films: Quantitative measurements of multilayer physical adsorption on heterogeneous surfaces, Jeanne M. Robinson, Bryan F. Henson, Kevin R. Wilson, *Los Alamos National Laboratory*. Second-harmonic generation measurements of multilayer adsorption on polycrystalline, porous ice films of heterogeneous surface potential is quantitatively modeled by classical physical adsorption theories. (p. 391)

NThE7 • A comparison of chlorinated fluoride glasses for obtaining red upconversion fluorescence in praseodymium for a three-color solid-state 3D display, E. A. Downing, L. Hesselink, *Stanford Univ.*; R. M. Macfarlane, *IBM Almaden Research Center*; N. F. Borrelli, R. Bartholomew, M. Newhouse, *Corning Inc.* We have demonstrated an RGB solid-state 3D display based on two-step, two-frequency (TSTF) upconversion in bulk rare earth doped heavy metal halide glasses. (p. 394)

NThE8 • Excitonic enhancement of third-order optical nonlinearity in regioregular head-to-tail coupled poly(3-hexylthiophene), H. Kawahara, Y. Ueno, N. Morito, K. Ema, M. Rikukawa, N. Ogata, *Sophia Univ., Japan*. We measure the third-order nonlinearity of HT-PHT using degenerate four-wave mixing. We observe the enhancement of third-order optical nonlinearity around exciton resonance in HT-PHT. (p. 397)

NThE9 • Femtosecond nondegenerate four-wave mixing in C_{60} /polymer blends, Eric Maniloff, Duncan McBranch, Hsing Lin Wang, Ben Mattes, *Los Alamos National Laboratory*. Femtosecond nondegenerate four-wave mixing studies have been performed on C_{60} -doped poly(3-hexyl thiophene). By controlling the C_{60} concentration, it is possible to vary the incoherent contribution to $\chi^{(3)}$. (p. 400)

NThE10 • The optical polarizability of excited C_{60} molecules, Huapeng Guan, Robert W. Hellwarth, Jouni P. Partanen, Nansheng Tang, *Univ. Southern California*. Using pump-probe and degenerate four-wave mixing, we find that excited-state C_{60} molecules have absorption cross section at 532 nm nearly three times larger than their ground states, while their polarizabilities are less than 3% different. (p. 403)

NThE11 • Electric field thermopoling of high dipole guests when considered as oblate ellipsoids, G. H. Cross, D. Healy, *Univ. Durham, UK*. Local field correction factors considered when poling high dipole guest-host nonlinear optical polymers must account for the molecular shape and polarizability tensor components. (p. 406)

NThE12 • Molecular architectural approaches to nonlinear optical materials, DeQuan Li, Xiaoguang Yang, Duncan McBranch, *Los Alamos National Laboratory*. Ultra-high second-order nonlinearities are observed in calix[4]arene-based, chromophoric supermolecules, which form densely packed, highly ordered monolayers on silica surfaces. (p. 409)

NThE13 • Pump-probe experiments in organic solutions for optical limiting, Arthur Dogariu, Paul M. Buck, David J. Hagan, Eric W. Van Stryland, *Univ. Central Florida*. We characterize the nonlinear response of several organic solutions applicable for optical limiting using the pump-probe geometry at fixed wavelengths and with a femtosecond continuum probe. (p. 412)

NThE14 • Nonlinear effects in dye-doped liquid crystal waveguides, G. Abbate, L. De Stefano, P. Mormile, G. Scalia, E. Santamato, *INFN, Italy*. A theoretical and experimental study on a planar waveguide with a dye-doped liquid crystal core is presented. The experiment confirms some of the theoretical predictions, as mode self-splitting, but shows a number of interesting features that cannot be accounted for in the plane wave approximation. (p. 415)

NThE15 • Nonlinear cw pump-probe investigations for semiconductor microcavities exhibiting normal-mode coupling, T. R. Nelson Jr., G. Khitrova, E. K. Lindmark, D. V. Wick, J. D. Berger, H. M. Gibbs, *Univ. Arizona*; K. Tai, Y. Lai, *National Chiao Tung Univ., China*. Intensity-dependent cw pump-probe spectroscopy on semiconductor microcavities exhibiting normal-mode coupling results in disappearance of transmission peaks with negligible change in their splitting. (p. 418)

NThE16 • Strong optical nonlinearities and ultrafast carrier dynamics in luminescent and nonluminescent porous silicon, Victor I. Klimov, Duncan McBranch, *Los Alamos National Laboratory*; Vladimir A. Karavanskii, *Institute of General Physics, Russia*. Femtosecond dynamics of nonlinear transmission in luminescent and nonluminescent porous Si films suggest that the photoluminescence and the increased absorption from 1.2–2.65 eV originate from different species inside porous layers. (p. 421)

NThE17 • Ultrafast optical nonlinearities in Cu_xS nanocrystals, Victor I. Klimov, *Los Alamos National Laboratory*; Vladimir A. Karavanskii, *Institute of General Physics, Russia*. Femtosecond nonlinear transmission data indicate a drastic difference in mechanisms for optical nonlinearity in nanocrystals formed by direct and indirect-gap phases of copper sulfide. (p. 424)

NThE18 • Femtosecond nonlinear optical response of CuBr and CuCl nanocrystals in glass in the optically transparent region, N. Thantu, J. S. Melinger, D. McMorro, B. L. Justus, *US Naval Research Laboratory*. The nature of nonresonant optical nonlinearity in photodarkening and nonphotodarkening copper halide (CuBr and CuCl) nanocrystals embedded in borosilicate glass is investigated with use of heterodyne-detected optical Kerr effect and z-scan techniques. (p. 427)

NThE19 • Semiconductor amplifier as element of optical communication systems, Marina Settembre, Francesco Matera, *Fondazione Ugo Bordoni, Italy*; Volker Hägele, *Univ. Kaiserslautern, Germany*; Ildar Gabitov, Arnold Mattheus, *Telekom Forschungs- und Technologiezentrum, Germany*; Sergei K. Turitsyn, *Heinrich-Heine-Universität, Germany*. We study nonlinearities of semiconductor optical amplifiers and fibers in the field of high-capacity transmission systems. Intensity and polarized modulated soliton systems are considered. (p. 430)

NThE20 • High value of $\chi^{(3)}$ in fluorine-phosphate glass doped with CdS_xSe_{1-x} , B. Vaynberg, M. Matusovsky, M. Rosenbluh, *Bar-Ilan Univ., Israel*; A. Lipovskii, *St. Petersburg State Technical Univ., Russia*. We observe a very high value for $\chi^{(3)}$ in a novel semiconductor doped phosphate glass. Four- and six-wave mixing experiments are used to estimate $\chi^{(3)}$. (p. 433)

NThE21 • Waveguide-mode intersubband second-harmonic generation with separate active and phase-matching regions, I. Vurgaftman, J. R. Meyer, *Naval Research Laboratory*; L. R. Ram-Mohan, *Worcester Polytechnic Institute*. Separate active and phase-matching regions produce highly efficient and tunable second-harmonic generation from InGaAs/InAlAs asymmetric double quantum wells in waveguides that are up to 300 μm long. (p. 436)

NThE22 • Intersubband quantum box laser based on image charges, J. B. Khurgin, S. J. Lee, *The Johns Hopkins Univ.* We consider a novel lasing scheme in semiconductor quantum boxes. Ultralow threshold pumping power can be obtained as a result of image charges developed in surrounding layers. (p. 439)

NThE23 • Second-order nonlinear optical properties of wide-bandgap semiconductors, Takashi Kondo, Kaoru Morita, Ryoichi Ito, *The Univ. Tokyo, Japan*. Second-order nonlinear optical properties of wide-bandgap compound semiconductors, AlP, GaP, and SiC, have been characterized by the reflected second-harmonic generation technique. (p. 442)

NThE24 • Progress in reduction of loss of diffusion-bonded stacked GaAs for mid-infrared generation, Dong Zheng, Leslie A. Gordon, Robert C. Eckardt, Martin M. Fejer, Robert L. Byer, Y. S. Wu, R. S. Feigelson, *Stanford Univ.* Bonding of GaAs at 700 °C minimizes semi-insulating to p-type conversion, and reduces loss of a 15-layer stack to ~2% at 5 μm . (p. 445)

NThE25 • Near-bandgap time-resolved reflectivity studies of ion-implanted and MBE-grown GaAs:As, S. Janz, Z. R. Wasilewski, *National Research Council, Canada*; U. G. Akano, I. V. Mitchell, *Univ. of Western Ontario, Canada*. Time-resolved reflectivity experiments are used to compare the carrier-induced optical nonlinearities of GaAs, GaAs:As prepared by As⁺ implantation and MBE-grown GaAs:As. (p. 448)

NThE26 • Materials with bistable defects (DX centers) as Kerr-like media, Ian Redmond, Richard A. Linke, *NEC Research Institute*. We describe results of calculations of the third-order nonlinear susceptibility for tellurium-doped AlGaAs and report a measured phase conjugate reflectivity of 2.5%. (p. 451)

MAILE ROOM

8:00am-9:40am

NFA • NLO of Atomic SystemsChristopher Clayton, *USAF Phillips Laboratory, Presider*

8:00am (Invited)

NFA1 • Distinction between lasing without inversion and parametric nonlinear optics, Thomas W. Mossberg, *Univ. Oregon*. What makes an optical amplifier a laser rather than a parametric device? Fundamental distinctions are sought, identified, and applied to driven systems of current interest. (p. 456)

8:25am (Invited)

NFA2 • Bose Einstein condensation, Eric Cornell, *Univ. Colorado*. Abstract not available. (p. 459)

8:50am (Invited)

NFA3 • Nonlinear optics using electromagnetically induced transparency, K. Hakuta, *Univ. Electro-Communications, Japan*. Nonlinear optical processes using electromagnetically induced transparency are discussed theoretically and experimentally with an atomic hydrogen as a test medium. (p. 460)

9:15am (Invited)

NFA4 • Enhanced nonlinear optics using an atomic local oscillator, Maneesh Jain, H. Xia, A. J. Merriam, G. Y. Yin, S. E. Harris, *Stanford Univ.* We demonstrate a method of performing efficient, widely tunable, nonlinear four-frequency mixing by using an atomic local oscillator prepared by two high-quality lasers. (p. 463)

9:40am-10:00am

Coffee Break

MAILE ROOM

10:00am-11:40am

NFB • Optical SolitonsDana Z. Anderson, *University of Colorado, Presider*

10:00am (Invited)

NFB1 • Form-stable pulse propagation in three-level media: Adiabats and matched pulses, Michael Fleischhauer, *Ludwig-Maximilians-Univ. München, Germany*. The interaction of pulses with three-level atoms is discussed in a dressed-state-dressed-field basis. The quasi-formstable propagation of matched pulses, solitons, and adiabats is analyzed. (p. 468)

10:25am

NFB2 • Measurements of the nonlinear phase shift from orthogonally polarized soliton collisions, S. D. Koehler, J. N. Kutz, L. Leng, K. Bergman, *Princeton Univ.* We present theoretical predictions and experimental measurements of the cross nonlinear phase exchanged via collisions between orthogonally polarized solitons in a highly birefringent optical fiber. (p. 471)

10:40am

NFB3 • Optical bullet holes in semiconductors, W. J. Firth, A. Lord, A. J. Scroggie, *Univ. Strathclyde, UK*; M. Brambilla, L. A. Lugiato, R. Penco, R. Pregolato, L. Spinelli, *Univ. della Studi di Milano, Italy*. Bright soliton-like localized states occur in semiconductor cavity models. These stable bullet holes, created by address-pulses at target pixels, can be bits for optical memory. (p. 474)

10:55am

NFB4 • The bright future of darkness in nonlinear optics, G. A. Swartzlander Jr., *Worcester Polytechnic Institute*; C. T. Law, *Univ. Wisconsin-Milwaukee*. The dark side of nonlinear optics are reviewed, and our recent investigations and applications of optical vortices are discussed. (p. 477)

11:10am

NFB5 • Experiments on spatial solitons in saturating nonlinear media, Vladimir Tikhonenko, Jason Christou, Barry Luther-Davies, Yuri Kivshar, *The Australian National Univ.* We describe experiments demonstrating bright soliton repulsion; attraction and fusion as well as the creation of optical vortex solitons via an instability of a dark soliton stripe. (p. 480)

11:25am

NFB6 • (2+1)-D spatiotemporal solitary-wave dragging, Steve Blair, Kelvin Wagner, Robert McLeod, *Univ. Colorado*. The dragging interaction between two orthogonally polarized (2+1)-D spatiotemporal solitary waves using the full material dispersion relation and nonparaxial beam propagation is demonstrated numerically. (p. 482)

Monday, July 8, 1996

Plenary Session

NMA 8:00 am-8:45 am
Maile Room

Robert Boyd, *Presider*
University of Rochester

Plenary Speaker

Nicolaas Bloembergen
Harvard University

Summary not available.

Monday, July 8, 1996

Cascaded Optical Nonlinearities

NMB 8:45 am-9:25 am
Maile Room

David Pepper, *Presider*
Hughes Research Laboratories

Experimental Progress in Cascading Nonlinear Optics

G.I. Stegeman, W.E. Torruellas, R. Schiek, B. Lawrence, R. Fuerst, Y. Baek
C. Trevino-Palacios, and D. Baboiu
CREOL, Un. Central Florida, Orlando, FL 32816-2700 USA
Ph: 407-823-6915 Fax: 407-823-6955

I. Baumann and W. Sohler
Angewandte Physik, Universitaet Paderborn, D-33098 Paderborn, Germany

G. Assanto
Dipartimento di Ingegneria Electronica, University of Roma III, Italy

L. Torner
Dept. Of Signal Theory and Comm., Polytechnic University of Catalunya
08080 Barcelona, Spain

P. Baldi, M. De Micheli, and D.B.Ostrowsky
Laboratoire D'Electro-Optique, University of Nice, France

Cascading refers to phenomena associated with the multiple interchange of photons between beams which interact parametrically via second order nonlinearities.[1] Although second harmonic generation (SHG) is the most common example, it also involves sum and difference frequency mixing, optical parametric amplification etc. It has been known since the early days of nonlinear optics that two successive second order interactions can contribute to a third order nonlinearity via $\chi_{ijk}^{(2)}\chi_{kmn}^{(2)} \rightarrow \chi_{ijmn}^{(3)}$ (effective).[2,3] We have found that the effects are more subtle than this and they can give rise to many interesting effects in nonlinear optics. They are essentially of two types, one based on the nonlinear phase shift accumulated by the fundamental beam on transmission through a second order medium and the second is a consequence of the strong coupling which occurs at high intensities between the fundamental and harmonic beams. The second leads to the generation of spatial solitary waves.[4] Here we discuss our progress in studying these effects.

When light traverses a second order material, both the fundamental and second harmonic exit the crystal changed from their input values. In particular, the output fundamental field has the form:

$$E_0(\omega) = \frac{1}{2} |a_0(\omega, z)| \sqrt{\frac{2}{cn\epsilon_0}} \exp [i(\omega t - kz - \phi^{NL}(z))] + c.c.$$

where $|a_0(\omega, z)|\exp[-i\phi^{\text{NL}}(z)]$ is the complex amplitude resulting from the second order interaction. Both the amplitude and phase shift depend on the input intensity and detuning from phase-matching in a complicated way.[1] If modifying the fundamental is the purpose of cascading, one of the apparent disadvantages to this approach is the partial power conversion to the harmonic, a loss for the fundamental. We have found that by controlling the SHG wavevector mismatch locally as a function of distance into a sample (waveguide), phase shifts in excess of 2π could be achieved with less than 10% net conversion to second harmonic.[5] This was demonstrated in temperature tuned Type II phase matching in LiNbO_3 channel waveguides. Such local control of the effective nonlinearity is a very powerful aspect of the cascading nonlinearity. This feature has recently been used to also demonstrate all-optical switching in both a nonlinear directional coupler and a Mach-Zehnder interferometer fully integrated on a LiNbO_3 substrate. The throughput of these devices was $>80\%$, one half of the loss was due to conversion to second harmonic and one half to propagation loss.

An understanding of local control of the nonlinear phase shift and its detailed evolution with distance can also lead to unexpected transmission effects. An example is the non-reciprocal transmission through a second order active waveguide in the presence of SHG. That is, we found that by changing the wavevector matching condition half way through a channel waveguide, the fundamental transmission depends on which end of the waveguide is the input.

One feature of cascading which had actually been predicted over twenty years ago is the existence of spatial solitary waves for intensities above a threshold value, i.e. soliton-like beams. They consist of strongly coupled fundamental and harmonic beams which propagate together without spatial diffraction both in slab waveguides (1-dimensional beams) and bulk materials (2-dimensional beam cross-section).[4,6] We have verified experimentally the existence of such 2-D spatial solitary waves in KTP crystals near and at their phase-matching condition. This material is Type II birefringent and walk-off occurs naturally between the two fundamental beams, as well as the harmonic. We found that the three beams coalesce in space, producing one non-diffracting solitary wave. The "robustness" of such soliton-like beams has implications to reduced material and phase-matching tolerances in second order interactions.

The existence of spatial solitary waves has a number of interesting implications associated with it. For example in Type II SHG, a change in the relative intensity of the two orthogonally polarized input fundamentals sweeps in space the output position of the solitary wave. By using transmission through apertures this leads to phase-insensitive all-optical switching. Another consequence is the adiabatic evolution of beams with asymmetric profiles into a single circular beam, i.e. beam clean-up. If in fact the asymmetric beams are too intense to evolve into a single solitary wave, they break up into multiple solitary

waves due to modulational instabilities. This has also been observed experimentally.

In the US this research was sponsored by ARPA, ARO, AFOSR and NSF.

References:

- [1] reviewed in G.I. Stegeman, R. Schiek, L. Torner, W. Torruellas, Y. Baek, D. Baboiu, Z. Wang, E. VanStryland, D. Hagan, and G. Assanto, "Cascading: A Promising Approach to Nonlinear Optical Phenomena Revisited", book chapter in "Novel Optical Materials and Applications", edited by I.C. Khoo and F. Simoni, (Wiley Interscience, New York, 1995), in press
- [2] L. A. Ostrovskii, JETP Lett. **5**, 272-5 (1967)
- [3] for example Chr. Flytzanis and N. Bloembergen, Quant. Electron., **4**, 271-300 (1976); Chr. Flytzanis, in Quantum Electronics, ed. H. Rabin and C.L. Tang, (Academic, NY, 1975), Vol 1, Part A
- [4] W.E. Torruellas, Z. Wang, D.J. Hagan, E.W. VanStryland, G.I. Stegeman, L. Torner and C.R. Menyuk, Phys. Rev. Lett., **74**, 5036-9 (1995).
- [5] R. Schiek, M.L. Sundheimer, D.Y. Kim, Y. Baek, G.I. Stegeman, H. Suche and W. Sohler, Opt. Lett., **19**, 1949-51 (1994).
- [6] Y. N. Karamzin and A. P. Sukhorukov, JETP Lett. **20**, 339-42 (1974); Yu.N.Karamzin, A.P.Sukhorukov, Zh.Eksp.Teor.Phys **68**, 834 (1975) (Sov. Phys.-JETP **41**, 414-20 (1976))

Phase-Insensitive, Single Wavelength, All-Optical Transistor Based on Cascaded Second-Order Nonlinearities

Z. Wang, D.J. Hagan, S. Kim and E.W. Van Stryland

CREOL, University of Central Florida, Orlando Florida 32816-2700

Phone (407)823-6817, FAX (407)823-6880

G. Assanto, Terza University of Rome, 00184 Rome, Italy

The resurgence of interest in cascaded second order nonlinearities[1,2] has resulted in several schemes for applying cascading in second-harmonic generating (SHG) crystals to optical transistor-like devices[3-7]. Such devices allow a weak signal beam to impose a large amplitude modulation on a strong “pump” beam, through mixing in a $\chi^{(2)}$ crystal. However, all of the devices reported to date require the pump and signal beams to be temporally coherent, as the process is strongly dependent on the phase between these two beams. There have been some suggestions[6,7] that type II phasematched SHG may remove phase sensitivity, but the devices proposed still require that the signal must be in phase with approximately half of the pump intensity. In this letter, we describe how one may properly exploit type II phase matching to produce a truly phase-insensitive all-optical transistor (AOT) based on second order nonlinearities.

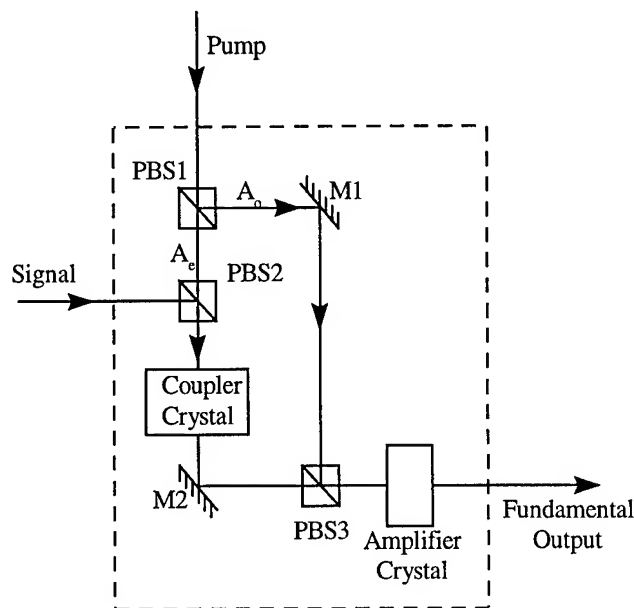


Figure 1. Schematic of All-optical Transistor device

The configuration of the proposed phase-insensitive AOT is shown schematically in Fig. 1. In a single device, two type II phase-matched second-order nonlinear crystals are used. The pump beam is split into two approximately equal, orthogonally polarized components. One of these passes through the first nonlinear crystal (Coupler), where it is modulated by the weak, incoherent signal with a gain of less than unity. This modulated pump is recombined with the other component of the pump and incident on the second crystal, (Amplifier), where the modulation is strongly amplified. The principle of the Amplifier has been described in reference [7]. The two orthogonally polarized input waves to the Amplifier have irradiances I_1 , the modulated pump, and I_2 , the fixed pump. If there is a small modulation on I_1 so that $I_1(t) = I_2 - \delta(t)$, the modulation of the total transmitted irradiance may greatly exceed δ . This is seen in Fig. 2, as a function of input “bias”, where we

define $\text{bias} = (I_1 - I_2)/I_t$. The data are the results of experiments in a 2 mm KTP crystal at a fundamental wavelength of $1.06\mu\text{m}$, for irradiances of 6.2 and $12 \text{ GW}/\text{cm}^2$. For small signals, the modulation of the transmitted irradiance is directly proportional to δ . Figure 2 shows that both inverting and noninverting amplifiers can be realized by adjusting the bias. It is shown below that the gain of the Amplifier is also exponentially dependent on L_2 and I_2 .

The key feature of the proposed device is the method of imposing a modulation on I_1 from a weak signal that is temporally incoherent. This is achieved by coupling I_1 to the signal in the Coupler, another type-II phasematched SHG crystal. This is inserted into the path of I_1 before it is incident on the amplifier crystal. The polarization of the signal field is perpendicular to that of I_1 . For a weak signal irradiance, $I_s \ll I_1$, the transmitted pump irradiance will be linearly modulated by the signal and is given by, $I_1(L_1) = I_1(0) - I_s(0) \sin^2(\gamma_1 L_1)$, where $I_1(0)$ and $I_s(0)$ are input intensities, $\gamma_1^2 = 16\pi^2 d_{\text{eff}}^2 I_1(0) / n_{\omega}^2 n_{2\omega}^2 \epsilon_0 c \lambda^2$ and L_1 is the length of the Coupler.

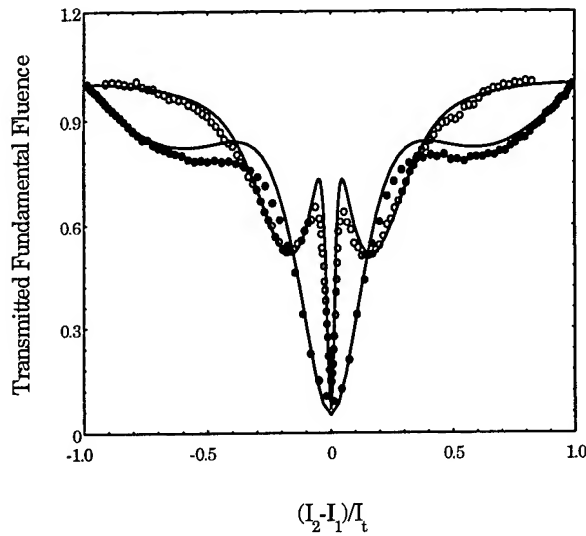


Figure 2: Transmitted irradiance in amplifier crystal versus bias.

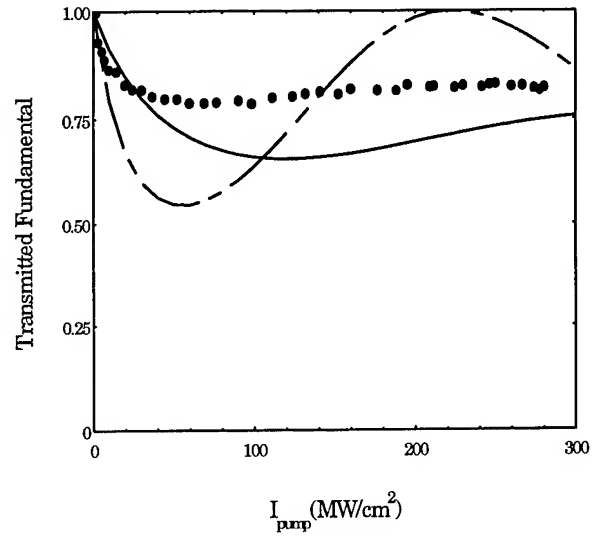


Figure 3: Modulated pump irradiance at the output of KTP coupler crystal vs. input pump irradiance, for a signal:pump ratio of 0.45

For plane waves, the maximum modulation efficiency is unity, which may be achieved for finite values of the fundamental intensity. However, when spatial and temporal irradiance distributions are taken into account, the modulation is reduced, as shown in Fig 3, where we plot the experimental and calculated signal modulation versus input irradiance for a 10 mm KTP crystal. We find that the maximum coupling occurs at $\gamma_1 L_1 = (2i+1)\pi/2$, where $i=0, 1, 2, 3, \dots$

The modulation imposed on I_1 in the Coupler is then amplified in the Amplifier crystal. The presence of the signal causes a modulation of I_1 which in turn produces an imbalance of $\delta = \sin^2(\gamma_1 L_1) I_s(0)$ between I_1 and I_2 incident on the Amplifying crystal. As described above and in reference[7], the interaction between these two fundamental waves in the amplifier results in amplification of this imbalance. It can be shown that the gain of the amplifier is given by, $G \propto \sin^2(\gamma_1 L_1) e^{\gamma_2 L_2}$, where $\gamma_2^2 = 16\pi^2$

$d_{\text{eff}}^2 I_2(0)/n_{\omega}^2 n_{2\omega} \epsilon_0 c \lambda^2$ and L_2 is the length of the Amplifier crystal. The constant of proportionality is a function of bias, itself proportional to the slope of the appropriate curve in Fig. 2.

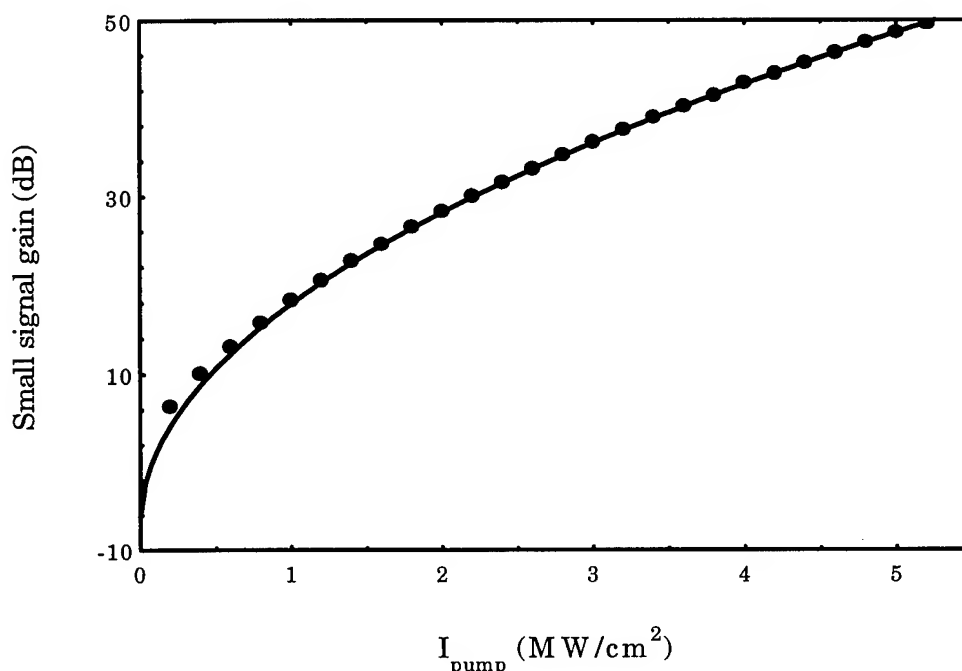


Figure 4: Small-signal gain of AOT versus total pump irradiance for a 10 mm NPP amplifier

The overall performance of the proposed AOT may be modeled by numerical simulation of the coupled equations governing the SHG process in both crystals.[1] The results are shown in Fig. 3, where we plot the overall transistor gain versus the input pump irradiance, for a 10 mm NPP crystal, with a d_{eff} of 85pm/V,[8] 40 dB of gain is achievable with an irradiance of $\sim 3.5 \text{ MW/cm}^2$. If a waveguide geometry were used, with an effective mode area of $25 \mu\text{m}^2$, the corresponding peak power would be less than 1 watt.

REFERENCES:

1. DeSalvo, R., *et. al.*, *Opt. Lett.*, 1992, **17**, pp. 28-30
2. Stegeman, G., *et. al.* in 'Novel optical materials and applications,' edited by I.C. Khoo and F. Simoni, (Wiley Interscience, New York, 1995)
3. Russell, P. St. J., *Electron. Lett.*, 1993, **29**, 1228
4. Hagan, *et al.* *Opt. Lett.*, **19**, 1305 (1994).
5. Kobayakov, A., *et.al.*, *Opt. Lett.*, 1995, **20**, pp. 1686-1688.
6. Lefort, L., and Barthelemy, A.: '*Electron. Lett.*, 1995, **31**, pp. 910-911
7. Assanto, G, *et. al.*, *Appl. Phys. Lett.*, 1995, **67**, pp. 2120-2122
8. W.E. Toruellas, *et.al.*, ACS Symposium Series 601, G.A. Lindsay and K.D. Singer, eds. (1994)

Monday, July 8, 1996

Frequency Conversion

NMC 9:55 am-12:10 pm
Maile Room

Jerry Meyer, *Presider*
U.S. Naval Research Laboratory

Tailoring Nonlinear Optical Interactions with Microstructured Materials

M.M. Fejer
Stanford University

Microstructured ferroelectrics and semiconductors offer unprecedented flexibility in tailoring nonlinear materials to suit specific applications. Quasi-phasematching in conventional periodic structures, as well as in axially and transversely modulated structures, will be discussed.

Efficient Ultraviolet Light Generation by LiNbO₃ Waveguide Quasi-Phase-Matched Second-Harmonic Generation Devices

K. Kintaka, M. Fujimura, T. Suhara, and H. Nishihara

Department of Electronic Engineering, Faculty of Engineering, Osaka University

2-1, Yamada-Oka, Suita, Osaka, 565 Japan

tel. : +81-6-879-7772, fax : +81-6-877-3544

INTRODUCTION Waveguide quasi-phase-matched second-harmonic generation (QPM-SHG) devices are being studied as a promising candidate for realization of a compact short wavelength coherent light source. Efficient LiNbO₃ waveguide QPM-SHG devices with ferroelectric-domain-inverted gratings for blue/green light generation have been reported so far [1,2]. Ultraviolet light generation can give further advantages in many applications such as optical data storage, optical information processing, and optical sensors. In this paper, we present the first fabrication of domain-inverted gratings of $\sim 2 \mu\text{m}$ period by applying voltage, and demonstrate efficient ultraviolet light generation in LiNbO₃ waveguide SHG device with the grating for 1st-order QPM.

ANALYSIS In ultraviolet region, light absorption in LiNbO₃ crystal is not negligible [3]. By taking account of the absorption, dependence of SHG efficiency η on the interaction length L was calculated. Fig. 1 shows an example of the calculated results at pump power P_0 of 100 mW. It was assumed that SHG coupling coefficient κ was $3.3 \text{ W}^{-1/2}\text{cm}^{-1}$, which was the value experimentally obtained in blue/green light generation devices [2], and the pump and harmonic waves were phase-matched. The result shows that there is an optimum interaction length that gives the maximum efficiency for each wavelength, and the efficiency degrades for interaction length longer than the optimum owing to the absorption of harmonic power. For example, a SHG efficiency of 11 % is expected with optimum interaction length of 8 mm at a harmonic

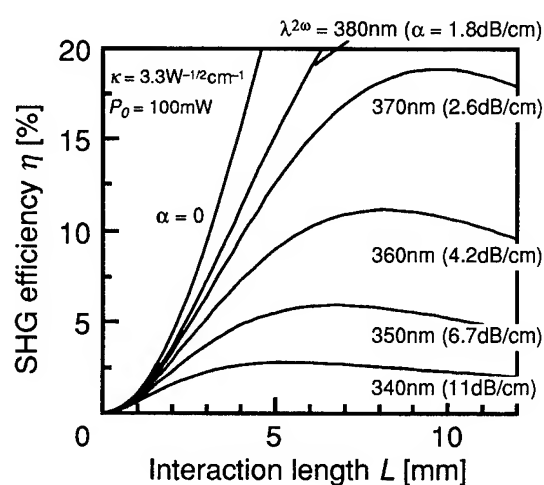


Fig. 1 Dependence of SHG efficiency on the interaction length for devices to generate harmonic wave of various wavelength (absorption factors).

wavelength of 360 nm.

FABRICATION LiNbO₃ waveguide 1st-order QPM-SHG devices for ultraviolet light generation require domain-inverted gratings of $\sim 2\ \mu\text{m}$ period, while blue light generation devices require $\sim 3\ \mu\text{m}$ period gratings. Voltage application method [1,2] was employed to fabricate such short period gratings in Z-cut LiNbO₃ crystals of 0.15 mm thickness. A corrugation electrode [2] of $2\ \mu\text{m}$ period ($0.3 - 1\ \text{mm}^2$ area) was formed on +Z surface and uniform electrode on -Z surface, and a single voltage pulse was applied between the electrodes in insulation oil at room temperature. The pulse duration was controlled automatically by a feedback circuit with inversion-charge monitor. Under the same condition as used in blue device fabrication, grating structures of $\sim 2\ \mu\text{m}$ period could hardly be obtained because of excess broadening of the domain-inverted region. To reduce such broadening, corrugation electrode with sharp cross-sectional structure was used, and electrical impedance and capacitance of voltage application system were reduced so that domain-inversion could be completed rapidly. These improvements enabled the fabrication of uniform grating suitable for efficient SHG devices. Fig. 2 shows +Z surface structure of domain-inverted grating of $2.0\ \mu\text{m}$ period after etching. The pulse voltage was 3.9 kV and the duration was $\sim 50\ \mu\text{sec}$.

For the fabrication of SHG devices, domain-inverted gratings of $2.0 - 2.2\ \mu\text{m}$ period and 1 – 3 mm interaction length were fabricated, and channel waveguides were fabricated by selective proton exchange in pure benzoic acid at $200\ ^\circ\text{C}$ for 20 min with Al mask of $3\ \mu\text{m}$ channel width followed by thermal annealing in dry oxygen at $350\ ^\circ\text{C}$ for 1 hour.

SHG EXPERIMENTS

SHG experiments were carried out using a Ti:Al₂O₃ laser. Ultraviolet light of 383 nm wavelength, which is the shortest value in our experiments, was obtained in fundamental guided-mode by a device with grating of $2.0\ \mu\text{m}$ period. Fig. 3 shows the dependence of SHG efficiency on the pump power for a device with grating of $2.2\ \mu\text{m}$ period and 3 mm interaction length. A maximum harmonic power as high as 1.9 mW at a wavelength of 393 nm was obtained at a pump power of 52 mW. The

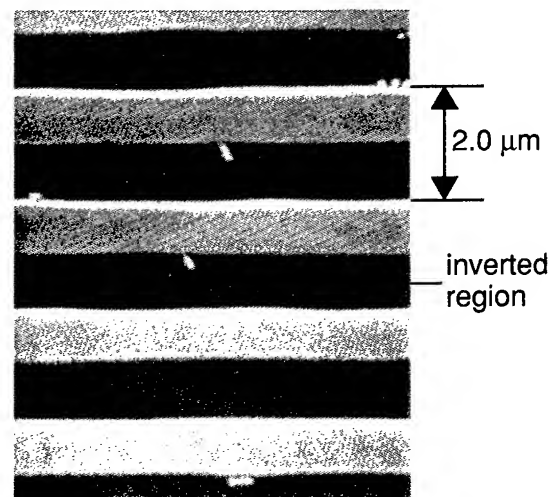


Fig. 2 Domain-inverted grating structure of $2.0\ \mu\text{m}$ period on +Z surface after etching.

maximum efficiency was 3.6 % and the normalized SHG efficiency was 70 %/W. The output power was higher by two orders of magnitude than the value reported in [4] with a device of 10 mm interaction length fabricated by Ti indiffusion method, although the normalized efficiency was comparable. The FWHM phase-matching bandwidth in terms of the pump wavelength deviation was 0.27 nm. SHG experiments were also carried out using a single-longitudinal-mode tunable laser diode. The dependence of SHG efficiency on the pump power is also shown in Fig. 3. A harmonic power of 72 μ W was obtained at a pump power of 13.5 mW. The normalized efficiency was 40 %/W. The reason why the normalized efficiency was lower than that by the Ti:Al₂O₃ laser was probably that the laser diode light was of single longitudinal mode while the Ti:Al₂O₃ laser light consisted of many longitudinal modes [5].

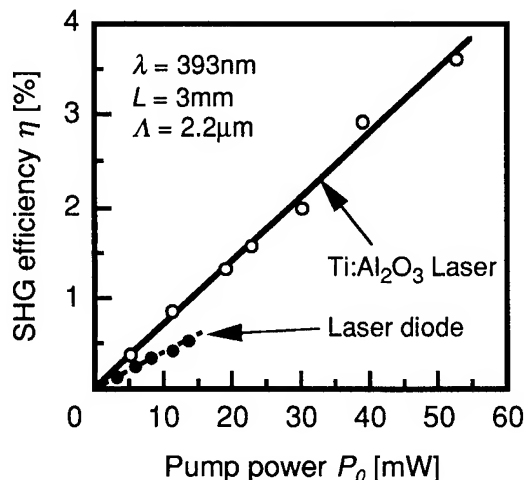


Fig. 3 Dependence of SHG efficiency on the pump power in SHG experiments using Ti:Al₂O₃ laser (open circles, solid line) and using laser diode (closed circles, dashed line) for pump wave.

CONCLUSION LiNbO₃ waveguide 1st-order QPM-SHG devices for ultraviolet light generation were fabricated by applying voltage for the first time. The shortest wavelength of 383 nm was obtained with grating of 2.0 μ m period. Milliwatt-order output of ultraviolet light and the normalized efficiency as high as 70 %/W were accomplished with an interaction length of 3 mm. Higher efficiencies will be realized by further optimization of a waveguide and/or interaction length.

REFERENCES

1. M. Yamada *et al.*, *Appl. Phys. Lett.*, **62**, pp.435-436 (1993).
2. K. Kintaka *et al.*, *Pacific Rim Conf. on Lasers and Electro-optics*, FE4, Chiba (1995);
K. Kintaka *et al.*, to be published in *J. Lightwave Technol.* (March 1996).
3. S. Kase *et al.*, *Ferroelectrics*, **8**, pp.419-420 (1974).
4. W. Wang *et al.*, *Appl. Phys. Lett.*, **68**, pp.729-731 (1996).
5. S. Helmfrid *et al.*, *J. Opt. Soc. Am. B*, **8**, pp.2326-2330 (1991).

QUANTUM PICTURE OF NONLINEAR OPTICAL PATTERNS

A. Gatti,¹ L. A. Lugiato,¹ I. Marzoli,¹G. L. Oppo,² S. M. Barnett,² and H. Wiedemann³¹*INFN, Dipartimento di Fisica, Via Celoria 16, 20133 Milano, Italy**Tel: +39 2 2392 264. Fax: +39 2 2392712*²*Department of Physics and Applied Physics, University of Strathclyde**107 Rottenrow, Glasgow G4 0NG, Scotland*³*Abteilung für Quantenphysik, Universität Ulm, D-89069 Ulm, Germany*

The recent investigations on quantum effects in nonlinear optical patterns and spatial aspect of squeezing have focused on the concept of quantum image [1,2,3]. These are very noisy images, dominated by quantum fluctuations and can be revealed either 1) by high frequency observation, which is able to reveal the fast dynamics of fluctuations, or 2) by low frequency observation, by measuring the spatial correlation function. This displays a regular modulation, which anticipates the stripe pattern that appear above threshold [4], while the intensity distribution is uniform on average.

We consider first a degenerate optical parametric oscillator (OPO) with a plane mirrors cavity. Using the Wigner representation, we approximate the exact Master Equation by a classical looking set of Langevin equations [5]. By solving these equations, we obtain stochastic realizations of the evolution of the system, which display the time-resolved dynamics of the quantum image. Well below threshold, the field distribution displays a totally noisy behaviour, in which the noise is white both in space and in time. Approaching threshold, one has the appearance of a spot pattern, with a notable presence of critical slowing down in time evolution. The pattern becomes more and more regular, as the pump intensity is increased to threshold, until it appears the stripe pattern which is known to be there above threshold. For the first time we bridge the entire passage from the below threshold to the above threshold behaviour. The features of this phase transition in a quantum optical system are studied in both the near and the far

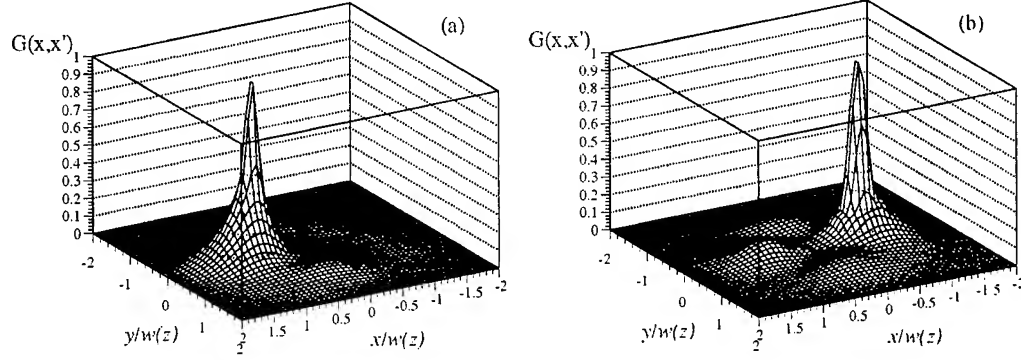


Figure 1: Intensity correlation function in the near field (a) and in the far field (b), for an optical parametric oscillator with spherical mirrors well below threshold.

field.

The standard OPO has a cavity with spherical mirrors. The features of the spatial correlation function below threshold in the near field were described in [3]. Here we focus on the far field behaviour, and we find a novel quantum effect. When the OPO is well below threshold the normally ordered intensity correlation function [6] $G(\vec{x}, \vec{x}')$ exhibits the presence of a high peak when the two points \vec{x} and \vec{x}' lie on opposite sides with respect to the optical axis (Fig. 1b). This represents a direct spatial manifestation of the correlated emission of twin photons pairs in the OPO. We demonstrate that this is a purely quantum effect, in the sense that no classical field can display a similar configuration for the correlation function. The quantum image in the far field can be subdivided into small regions; region opposite with respect to the system axis are quantum correlated in pairs.

REFERENCES

- [1] L. A. Lugiato and G. Grynberg, *Europhys. Lett.* **29**, 675 (1995)
- [2] A. Gatti and L. A. Lugiato, *Phys. Rev. A*, **52**, 1675 (1995)
- [3] L. A. Lugiato and I. Marzoli, *Phys. Rev. A* **52**, 4886 (1995)

- [4] G. L. Oppo, M. Brambila and L. A. Lugiato, *Phys. Rev. A* **49**, 2028 (1995).
- [5] H. Wiedemann, A. Gatti, L. A. Lugiato, S. M. Barnett, G. L. Oppo and I. Marzoli, in preparation.
- [6] For a measurement of the correlation in the far field on a classical level, see A. Maitre, A. Petrossian, A. Blouin, M. Pinard and G. Grynberg, *Opt. Comm.* **116**, 153 (1995)

Comparison of Wide-Band Electro-Optic Frequency Tuning in LiNbO₃ and KNbO₃ OPO's

M. D. Ewbank and M. J. Rosker

Rockwell Science Center

1049 Camino Dos Rios

Thousand Oaks, CA 91358

Phone: (805) 373-4443

FAX: (805) 373-4158

Email: mdewbank@scimail.risc.rockwell.com

Typically, wavelength tuning in a birefringently phase-matched optical parametric oscillator (OPO) is accomplished by adjusting the angle of propagation in the nonlinear optical crystal. However, angle tuning is not the only way to alter the wavelength of an OPO; other physical mechanisms such as temperature, pressure or electric field^{1,2} that change the refractive indices (or more specifically, the birefringence) will induce a corresponding dispersion-compensating change in wavelength to maintain phase matching. Electro-optically tuning an OPO is particularly attractive since it is non-mechanical (does not involving any moving parts) and can be done rapidly. Previously, electro-optic tuning was used to compensate for the phase mismatch from self-heating in CD*A during second-harmonic generation.³ More recently, frequency stabilization in a doubly-resonant OPO configuration with KTP was accomplished using electro-optic tuning.⁴ Here, we describe the first demonstration of broadband wavelength tuning in an OPO via the electro-optic effect in LiNbO₃. The method is then applied to KNbO₃ since it has much larger electro-optic coefficients. A comparison of electro-optic tuning range and tuning rate for LiNbO₃ and KNbO₃ are also discussed.

Figure 1 illustrates the configuration for a mid-infrared QPO using LiNbO₃ or KNbO₃. The collinear light propagation direction s_1 is given by $s_1 = \sin\theta\cos\phi x + \sin\theta\sin\phi y + \cos\theta z$ where x , y and z are the directions of the principal crystal axes while θ and ϕ are the conventional spherical coordinate angles. For Type I phase matching, the signal and idler waves are polarized along $s_2 = \sin\phi x - \cos\phi y$ while the pump wave is polarized along $s_3 = \cos\theta\cos\phi x + \cos\theta\sin\phi y - \sin\theta z$. The angle-tuning OPO phase-matching curves for LiNbO₃ or KNbO₃ with a 1064 nm pump are shown in Fig. 2; in both cases, $\theta \approx 45^\circ$. For an applied DC electric parallel to s_3 , the effective electro-optic coefficients for the pump and signal/idler polarizations (assuming $\theta = 45^\circ$) can be written as

$$r_{\text{eff}}^p = -(r_{22} + r_{13} + r_{33} + 2r_{51}) / (2\sqrt{2}) \approx 40 \text{ pm/V} \quad (1a)$$

and

$$r_{\text{eff}}^{s/i} = (r_{22} - r_{13}) / \sqrt{2} \approx 2.6 \text{ pm/V} \quad (1b)$$

for LiNbO₃ while

$$r_{\text{eff}}^p = -[r_{42} + (r_{23} + r_{33})/2] \sqrt{2} \approx 343 \text{ pm/V} \quad (1c)$$

and

$$r_{\text{eff}}^{s/i} = r_{13} / \sqrt{2} \approx 19.8 \text{ pm/V} \quad (1d)$$

for KNbO₃ where the expressions have been evaluated numerically using the following electro-optic tensors: $r_{13}=r_{23}=9.6\text{pm/V}$, $r_{33}=30.9\text{pm/V}$, $r_{22}=-r_{12}=-r_{61}=6.8\text{pm/V}$ and $r_{51}=r_{42}=32.6\text{pm/V}$ for LiNbO₃ and $r_{13}=34\text{pm/V}$, $r_{23}=6\text{pm/V}$, $r_{33}=63.4\text{pm/V}$ and $r_{42}=450\text{pm/V}$, $r_{51}=120\text{pm/V}$ for KNbO₃. The electro-optic change in refractive indices is simply $\delta n = -n_{\text{eff}}^3 r_{\text{eff}} E_3 / 2$ where E_3 is the magnitude of the DC electric field along s_3 .

These changes in the refractive indices of the pump, signal and idler due to the DC electric field cause a corresponding dispersion-compensating shift in signal and idler wavelengths to maintain phase matching. Using a linear perturbation approach,¹ the wavelength detuning can be determined analytically. Since the pump wavelength is fixed, the pump index depends only on applied DC field, whereas the signal and idler indices are functions of both applied DC field and wavelength detuning via dispersion. Substituting these perturbed refractive indices into the OPO phase-matching conditions

[i.e., conservation of energy $\lambda_p^{-1} = \lambda_s^{-1} + \lambda_i^{-1}$ and conservation of momentum $n_p \lambda_p^{-1} = n_s \lambda_s^{-1} + n_i \lambda_i^{-1}$] gives the following expressions for idler wavelength detuning $\Delta\lambda_i$:

$$\Delta\lambda_i \approx \lambda_{i0} \left(\frac{(\delta n_s - \delta n_i) - (\lambda_{i0}/\lambda_p)(\delta n_s - \delta n_p)}{(n_{s0} - n_{i0}) + \lambda_{i0} \dot{n}_i \lambda_{i0} - \lambda_{s0} \dot{n}_s \lambda_{s0}} \right) \quad (2a)$$

where second-order perturbation terms have been dropped and

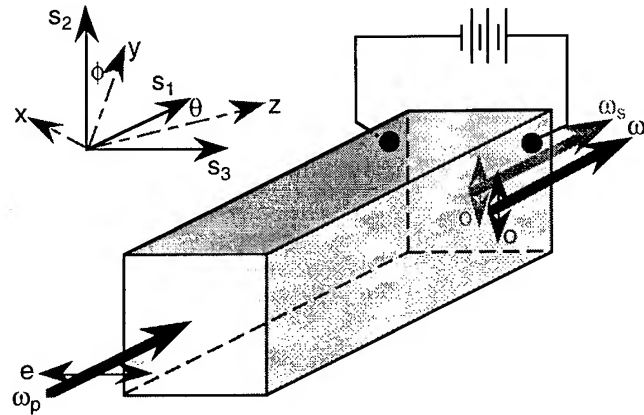
$$\begin{aligned} & \Delta\lambda_i^2 \left\{ \dot{n}_i \lambda_{i0} + (\lambda_{s0}/\lambda_{i0})^2 \dot{n}_s \lambda_{s0} \right\} - \\ & \Delta\lambda_i \left\{ n_{s0} - n_{i0} + \delta n_s - \delta n_i + \lambda_{i0} \dot{n}_i \lambda_{i0} - \lambda_{s0} \dot{n}_s \lambda_{s0} \right\} + \\ & \left\{ \lambda_{i0}(\delta n_s - \delta n_i) - (\lambda_{s0}^2/\lambda_p)(\delta n_s - \delta n_p) \right\} = 0 \end{aligned} \quad (2b)$$

when the second-order perturbation terms are included. Here \dot{n}_s and \dot{n}_i are the signal and idler wavelength dispersion coefficients (i.e., the change in refractive index with respect to wavelength) evaluated at the corresponding unperturbed wavelengths λ_{s0} and λ_{i0} . Note that the first-order approximation fails near degeneracy ($\lambda_{s0} = \lambda_{i0}$) hence the need to include the second-order terms. The idler wavelength detuning is linearly dependent on applied DC field. The predicted wavelength detuning rates for LiNbO₃ or KNbO₃ are compared in Fig. 3. The sizable detuning rate with KNbO₃ is clearly due to the much larger r_{eff} (see Eqs. 1a-d).

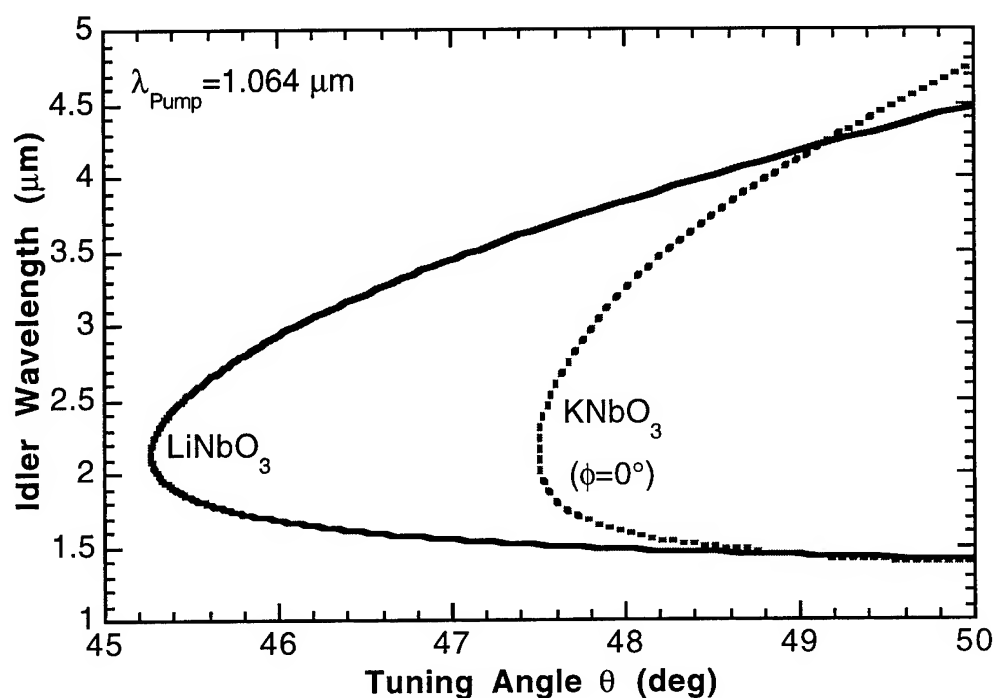
An electro-optic tuning range of ~90nm for the idler wavelength was observed in a LiNbO₃ OPO. This OPO had a wavelength detuning rate which varied from ~4 nm/[kV/cm] to ~9 nm/[kV/cm] for idler wavelengths between 4.2 μm and 3.4 μm , in agreement with the prediction in Fig. 3. Additional results on LiNbO₃ and KNbO₃ OPO's are presented.

1. A. Yariv, Quantum Electronics, (Wiley & Sons, New York, 1975) pp447-450.
2. R. C. Eckardt, C. D. Nabors, W. J. Kozlovsky, R. L. Byer, "OPO frequency tuning and control", *J. Opt. Soc. Am. B* **8**, 646 (1991).
3. D. T. Hon, "Electro-optical compensation for self-heating in CD*A during SHG", *IEEE J. Qu. Elect.* **QE-12**, 148 (1976).
4. D. Lee, N. C. Wong, "Stabilization and tuning of a doubly resonant OPO", *J. Opt. Soc. Am. B* **10**, 1659 (1993).

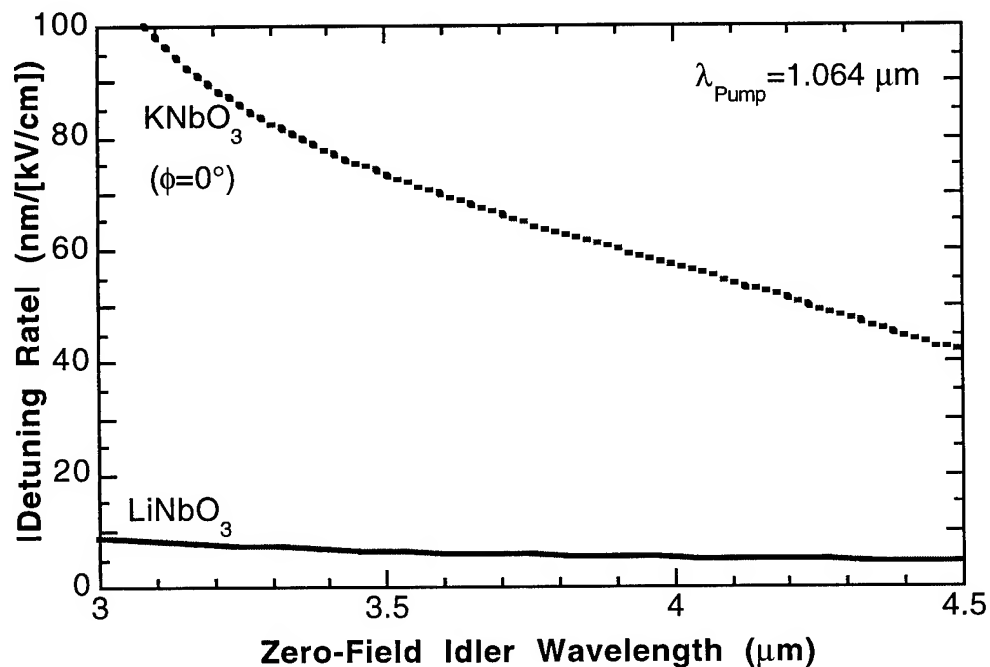
Figures



1. Configuration for a mid-infrared OPO using LiNbO₃ or KNbO₃ for electro-optic tuning.



2. OPO phase-matching curve for angle-wavelength tuning in LiNbO_3 and KNbO_3 .



3. Dispersion in idler detuning rate for LiNbO_3 or KNbO_3 OPO's.

Ultrashort-pulse generation in the ultraviolet using ionization-induced harmonic generation

H.C. Kapteyn, S. Backus, J. Peatross, E. Zeek, K. Read, and M.M. Murnane

Center for Ultrafast Optical Science

University of Michigan

2200 Bonisteel Boulevard

Ann Arbor, MI 48109-2099

Ph. (313) 763-4875; Fax: 313-763-4876; E-mail: kapteyn@eecs.umich.edu

In recent work, we have demonstrated that ionization-induced harmonic generation in gasses is a useful source of very short duration pulses in the ultraviolet and vacuum ultraviolet. Using millijoule-energy, 25 fs driving pulses at 800 nm wavelength, we can obtain a third harmonic pulse duration of under 16 fs, measured using the technique of self-diffraction frequency resolved optical gating. Microjoule pulse energy and milliwatt average power can be produced, and the conversion efficiency can be optimized by adjusting the chirp of the input pulse.

Many dynamic processes which occur on femtosecond time-scales can only be probed using ultrashort pulses at ultraviolet and vacuum ultraviolet wavelengths. For example, many chemical systems simply do not absorb visible-wavelength light, and shorter wavelengths are required for pump-probe experiments. Also, techniques such as ultrafast photoemission as a probe of electron dynamics in materials require uv or vuv light. Since no current ultrafast laser operates directly in the ultraviolet region of the spectrum, harmonic generation and other nonlinear techniques are used to produce the required pulses. In the past, harmonic generation in phase-matched crystals has been demonstrated to produce pulses in the deep ultraviolet.¹ However, in solid-state crystals such as BBO(beta-barium borate), complications such as finite phase-matching bandwidth and temporal walk-off severely limit the obtainable pulse duration. In contrast, these problems are completely avoided using a gas as a nonlinear medium for the production of odd harmonic orders. The efficiency of this third- or higher order process is generally expected to be low compared with second-order harmonic generation. However, in this work we show that using a very high peak-power, ultrashort laser source, we can produce microjoule energy pulses with conversion efficiency comparable to past work, and pulse duration an order of magnitude shorter than past work has demonstrated.² Furthermore, this process exhibits an optimization behavior which cannot yet be fully explained, and which may be fundamental to the intense laser-atom interaction which is used in the process.

The experimental setup for this work is straightforward. We use a laser which can produce pulses of 1 mJ energy at a wavelength of 800 nm, with a bandwidth of 38 nm and at a repetition rate of 1 kHz.³ This pulse is simply focused in air, forming a plasma channel \approx 1 cm long. After the focus, blue light can readily be observed copropagating with the red. This 3ω 266 nm light can be separated from the fundamental light using

dichroic mirrors. A beam with ~ 1 mW average power results, corresponding to a pulse energy of ~ 1 μ J and a conversion efficiency of $>10^{-3}$. Using argon gas in a pulse jet, the conversion efficiency approximately doubles, at the expense of experimental complexity.

We used the technique of self-diffraction frequency-resolved optical gating (SD-FROG) to characterize in time our third harmonic pulses.⁴ This technique is ideal for the measurement of very short uv light pulses, since it can be performed using a thin (100 μ m) sapphire plate, and does not suffer from phase-matching limitations. Figure 1 shows the pulse temporal profile of the 3rd harmonic retrieved by the FROG deconvolution algorithm. The average uv bandwidth observed is 6 nm, which can in principle support a pulse as short as 12 fs, in contrast to the 16 fs measured pulse width. However, the residual chirp can be explained by the dispersion of the air in the beam path between the generation region and the FROG measurement apparatus. These pulses are the shortest uv pulses generated to date. Work is in progress to characterize the fifth harmonic generated using this technique.

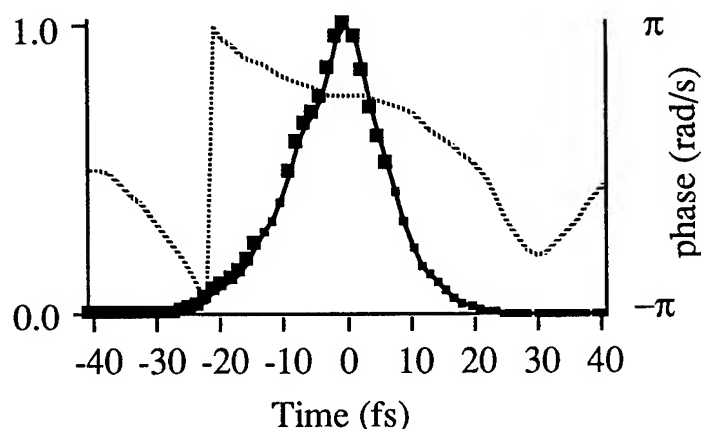


Figure 1: Temporal profile of the 3rd harmonic pulse retrieved using a self-diffraction FROG algorithm.

One intriguing observation we have made regarding this process is that the highest conversion efficiency and broadest spectral bandwidth are observed when the 800 nm excitation pulse is negatively chirped to 40 fs pulse duration, which is approximately double the transform-limited pulse width of 25 fs. This optimization occurs only for negative chirps, and is present even at very low gas pressures. For transform-limited 40 fs pulses, or for positive chirps, the observed uv conversion efficiency and bandwidths are significantly lower, as shown in figure 2. One possible explanation for this asymmetry in the chirp dependence of the data would be differences in the detailed pulse shape on the rising edge of the pulse, where the ionization and harmonic generation occur. However, by performing FROG measurements on the input excitation pulse, we confirmed that the shape of the excitation pulse does not change dramatically as chirp is introduced. These FROG measurements are challenging because of the broad bandwidth (38 nm FWHM) and substantial chirp of the pulse, but we were able to verify them by careful independent

checks of the consistency of the data. Pulse shapes were determined for the transform-limited 25 fs case, and for positively and negatively chirped pulses up to 100 fs.

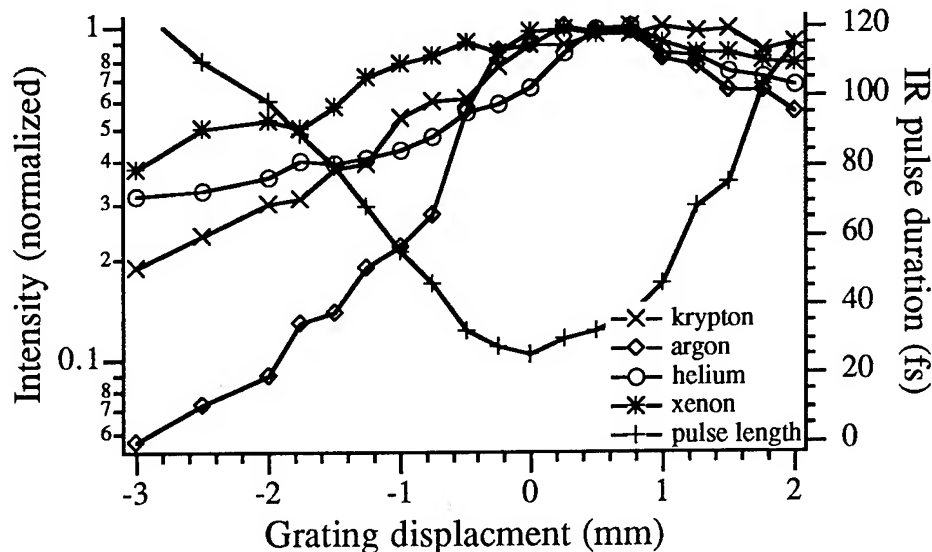


Figure 2: Conversion efficiency to third harmonic, along with pulse duration, as a function of chirp of the driving laser pulse. Negative values of grating displacement correspond to net positive dispersion on the pulse.

We also investigated the beam profiles of the generated harmonic light, to determine the optimum focusing and pressure conditions for good harmonic beam quality. We found that the optimal conversion efficiency occurs for the conditions which provide the best spatial and spectral quality of the 3rd harmonic beam.

The authors gratefully acknowledge funding by the Department of Energy. H. Kapteyn acknowledges support from a Sloan Foundation Fellowship.

References

- 1 J. Ringling, O. Kittelmann, F. Noack, *et al.*, Optics Letters 18, 2035-2037 (1993).
- 2 S. Backus, J. Peatross, E. Zeek, *et al.*, Optics Letters Accepted (1996).
- 3 S. Backus, J. Peatross, C. P. Huang, *et al.*, Opt. Lett. 20, 2000 (1995).
- 4 K. W. Delong, R. Trebino, and D. J. Kane, JOSA B 11, 1595-1608 (1994).

Third-Harmonic Generation in a Plasma of Self-Induced Optical Breakdown in Air Using 80-fs Laser Pulses: Self-Action of Light Beams and Spectral Broadening

A. B. Fedotov, M. M. T. Loy, X. Xiao,

Hong Kong University of Science and Technology

V. N. Krylov and A. K. Rebane

Swiss Federal Institute of Technology, Zurich, Switzerland

N. I. Koroteev, and A. M. Zheltikov

International Laser Center, Faculty of Physics, Moscow State University, Moscow, 119899
Russia; tel. (095) 9393959; e-mail: zhelt@ilc.phys.msu.su

1. Introduction

Recently, much attention has been focused on the generation of high-order harmonics using high-power laser pulses. Optical harmonics of extremely high orders were detected in experiments using high-power ultrashort laser pulses focused into rare-gas jets [1 - 4]. For the most part, experiments on harmonic generation both in rare gases [1 - 4] and in a laser-produced plasma [5 - 12] use pulsed high-power systems. First experiments on third-harmonic generation at a high repetition rate, which used 1-kHz laser pulses with a duration of 200 fs, demonstrated that the efficiency of third-harmonic generation (THG) in a plasma of self-induced optical breakdown can be as high as $7 \cdot 10^{-4}$ [13].

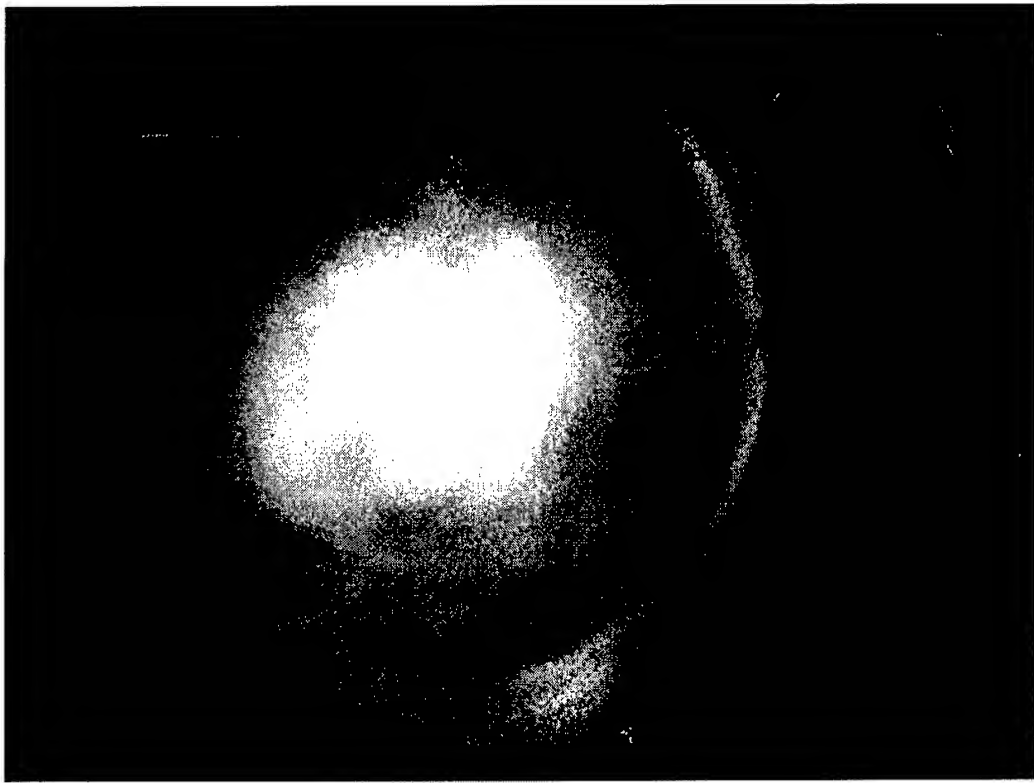
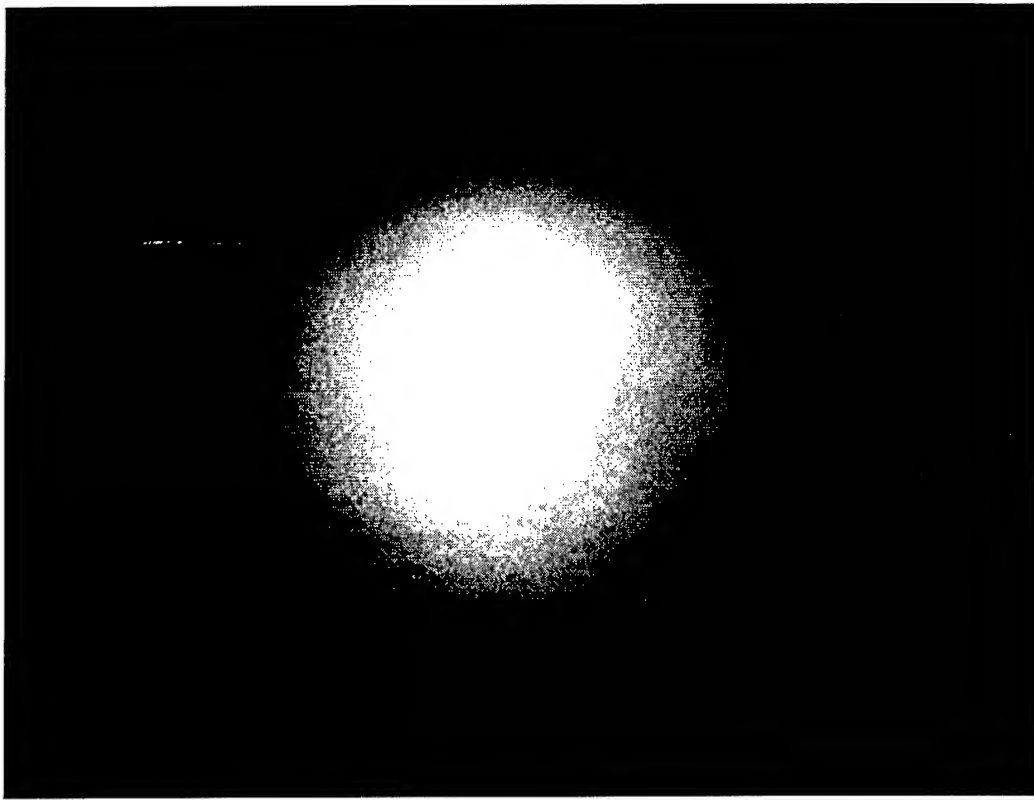
In this paper, we describe the experimental technique that provides the opportunity to efficiently generate the third harmonics of Ti:sapphire-laser radiation at a high repetition rate. For this purpose, we use plasma of self-induced optical breakdown in atmospheric air. We studied the spatial intensity distribution in the light beam emerging from the plasma and measured the spectra for fundamental radiation transmitted through the plasma and the third harmonic at the output of the plasma. The spatial distribution of light intensity in the beam emerging from the laser-produced plasma displayed qualitative changes with an increase in the energy of incident radiation. The maximum conversion efficiency of the power of fundamental laser radiation to the third harmonic achieved in our experiments was as high as $1.5 \cdot 10^{-3}$.

2. Experimental

The experimental setup for optical-harmonic generation was based on the Clark-MXR Inc. Ti:sapphire system with a regenerative amplifier. The laser system consisted of a Ti:sapphire oscillator, a stretcher, a regenerative amplifier pumped by the second harmonic of a Nd:YAG laser, and a compressor. The laser system generated 80-fs light pulses with a repetition rate of 1 kHz and the maximum energy up to 1 mJ per pulse. Radiation produced by this laser system was employed as a fundamental wave in the generation of the second and third harmonics. A lens with the focal length 5 cm focused the fundamental laser beam into a spot 30 - 35 μm in diameter. Thus, the maximum energy in the focus reached $1.5 \cdot 10^{15}$ W/cm². The focused fundamental beam induced a plasma of optical breakdown in the air.

3. Results and Discussion

We used the above-described experimental technique to investigate the intensity distribution in the beam emerging from the plasma of self-induced optical breakdown. For a



Spatial patterns of a light beam emerging from the laser-produced plasma for the energy of fundamental radiation of 0.08 (upper photo) and 0.8 mJ (lower photo).

relatively low incident power, the divergence of the light beam was close to the diffraction limit and the beam pattern was rather smooth. Starting from the average radiation power of approximately 0.2 W, noticeable distortions appeared in the beam. Beam patterns recorded for high powers of fundamental radiation displayed a noticeable spatial asymmetry and exhibited a complex internal structure and instabilities (see the figure). Simultaneously, the spectra of both fundamental radiation transmitted through the plasma and the third harmonic featured a considerable broadening indicative of self-phase modulation. The broadened spectra of fundamental radiation and of the third harmonic displayed a considerable asymmetry with respect to the central frequency. Specifically, at the intensity of incident radiation of about 800 μJ , the spectrum corresponding to fundamental radiation stretched from approximately 720 to 830 nm and had an asymmetric shape, whereas the initial spectrum of radiation at the output of a Ti:sapphire laser had the FWHM of about 13 nm and featured a symmetric profile.

In recent investigations [13], which employed 600- μJ pulses with the duration of 200 fs, the maximum THG efficiency was estimated as $7 \cdot 10^{-4}$. In the present study, the use of 80-fs pulses with the pulse energy up to 1 mJ made it possible to achieve the THG efficiency as high as $1.5 \cdot 10^{-3}$. Along with THG, we observed second-harmonic generation from the plasma of self-induced breakdown, which was approximately three orders of magnitude lower than the maximum THG efficiency. Analysis of the energy of the third harmonic as a function of the energy of incident light demonstrates that the self-action of laser pulses can be considered as one of the basic effects that limit the efficiency of frequency conversion in harmonic generation in a plasma of self-induced breakdown.

4. Conclusion

The performed investigations demonstrated a high efficiency of high-repetition-rate harmonic generation in a plasma of self-induced optical breakdown. Analysis of the spatial distribution of light intensity in the beam transmitted through the plasma revealed the presence of spatial structures characteristic of self-phase modulation. The above-discussed investigations show that the limiting efficiency of optical-harmonic generation in a plasma of self-induced breakdown is not achieved yet. However, when considering the possibility of increasing the harmonic energy by augmenting the energy of incident light, we should take into account the influence of self-action of ultrashort light pulses in a plasma.

References

1. McPherson A., Gibson G., Jara H., *et al.*, *J. Opt. Soc. Am. B*, 1987, **4**, 595.
2. L Huillier A. and Balcou P., *Phys. Rev. Lett.*, 1993, **70**, 774.
3. Macklin J.J., Kmetec J.D., and Gordon III C.L., *Phys. Rev. Lett.*, 1993, **70**, 766.
4. Kondo K., Sarukura N., Sajiki K., *et al.*, *Phys. Rev. A*, 1993, **47**, 2480.
5. Gladkov S.M., Zheltikov A.M., Koroteev N.I., *et al.*, *Sov. Tech. Phys. Lett.*, 1988, **14**, 610.
6. Fedotov A.B., Gladkov S.M., Koroteev N.I., *et al.* *J. Opt. Soc. Am. B*, 1991, **8**, 373.
7. Zheltikov A.M., Koroteev N.I., and Fedotov A.B. *Proc. SPIE*, 1993, **2097**, 308.
8. Kubodera S., Nagata Y., Akiyama Y., *et al.*, 1993, *Phys. Rev. A*, **48**, 4576.
9. Zheltikov A.M., Koroteev N.I., and Fedotov A.B., *Laser Phys.*, 1994, **4**, 569.
10. Theobald W., Wulker C., Schafer F.P., *et al.*, *Opt. Commun.*, 1995, **120**, 177.
11. Krushelnick K.M., Tighe W., and Suckewer S., 1995, Report of Princeton Plasma Physics Laboratory, no. PPPL-3105, Princeton University, Princeton, New Jersey, USA.
12. Von der Linde D., Engers T., Jenke G., *et al.*, 1995, *Phys. Rev. A* **52**, R25.
13. Rebane A.K., Krylov V.N., Koroteev N.I., *et al.*, *Kvantovaya Elektron.* (in press).

Nonlinear Optics of Nanostructured Materials: Fractal Nanocomposites and Self-Affine Surfaces

Vladimir M. Shalaev¹⁾, J. Mercer²⁾, V. P. Safonov³⁾, and R. Botet⁴⁾

¹⁾Department of Physics, New Mexico State University, Box 30001/Dept.3D, Las Cruces, New Mexico 88003, U.S.A. Tel: (505) 646-1932, fax: (505) 646-1934, e-mail: vshalaev@nmsu.edu

²⁾Sandia National Laboratories, Albuquerque, NM 87185, U.S.A.

³⁾Institute of Automation and Electrometry, 630090 Novosibirsk, Russia

⁴⁾Laboratoire de Physiques des Solides, Universite Paris-Sud, Cetre d'Orsay, 91405 Orsay, France

Optical phenomena experience a giant enhancement in metal nanocomposites and rough thin films consisting of small nm -sized particles and roughness features, respectively. The enhancement is associated with excitation of surface plasmons which are collective modes and strongly depend on the morphology (geometrical structure) of the material. Fractal structures are prevalent in composites and cold-deposited thin films. The emergence of fractal geometry was a significant breakthrough in the description of irregularity. Fractal objects do not possess translational invariance and, therefore, cannot transmit running waves. Accordingly, collective excitations, such as surface plasmons, tend to be localized in fractals [1,2]. Formally, this is a consequence of the fact that plane running waves are not eigenfunctions of the operator of dilation symmetry characterizing fractals.

Fractal aggregates of small particles embedded in a three-dimensional host are self-similar (scale-invariant) within a certain interval of sizes. Unlike fractal assemblies of particles, a self-affine surface reveals a scale-invariance if different scaling factors are applied in the (x, y) -plane of the surface and in the normal direction, z . We studied nonlinear optical properties of small-particle composites and rough thin films characterized by various random morphology. Nonlinear susceptibilities for fractal and non-fractal nanostructured materials were determined both theoretically and experimentally. Below, we first consider small-particle composites and then self-affine films.

As well known, there is only one dipolar mode that can be excited by a homogeneous field in a spherical object. For a 3-dimensional collection of small particles, such as the random close-packed sphere of particles (CPSP) and the random gas of particles (RGP), the absorption spectra are still peaked near the relatively narrow resonance of the individual particles, i.e., all eigenmodes of the collection of particles are located in a small spectral interval.

In contrast to conventional (non-fractal) 3-dimensional systems, the dipolar interactions in low-dimensional fractals are not long range, that results in localization of the corresponding eigenmodes at various random locations in the cluster. These modes form the broad optical spectrum of fractal aggregates which is characterized by strong inhomogeneous broadening. It is important that despite the asymptotically zero density of particles in a fractal cluster, there is always a high probability of finding a number of particles in close proximity to any given one (in fractals, the pair correlation $g \propto r^{D-3}$, where $D < 3$ is the fractal dimension; accordingly, g becomes large at small r). Therefore, there are strong interactions between neighboring particles, which lead to the formation of eigenmodes covering a broad spectral range. The large variety of different local configurations in a fractal cluster leads to the wide spectral interval covered by the eigenmodes. We emphasize that this behavior is different from non-fractal composites (such as RGP and CPSP) where dipolar eigenmodes are not localized and typically occupy a narrow spectral interval. Thus in objects with fractal morphology, the density-density correlation, $g(r) \propto r^{D-3}$, results in unusual combination of properties: whereas the volume fraction filled by N particles in a fractal is very small, $\propto N^{1-3/D} \rightarrow 0$, there are strong interactions between neighboring particles [1].

Localization of eigenmodes in fractals leads to a patchwork-like distribution of local fields associated with "hot" and "cold" zones [2]. This brings about large spatial fluctuations of local fields in fractal composites and giant enhancements of various optical effects [1].

In fractals formed by metal particles, the dipole eigenmodes cover the visible and infra-red parts of the spectrum; the mode quality-factors increase with the wavelength, i.e., the local fields are especially large in the long wavelength part of the spectrum [1].

In Fig. 1a we show the enhancement of the intensities of local fields, $G = \langle |E_i|^2 \rangle / |E^{(0)}|^2$, in silver cluster-cluster aggregates (for CCA, the fractal dimension $D \approx 1.78$), and non-fractal silver

RGP and CPSP, with $D = 3$. (E_i and $E^{(0)}$ are the local and applied fields, respectively, and the angular brackets denote an average over an ensemble of random clusters). As seen in the figure the local-field enhancements in fractal CCA are significantly larger than in non-fractal RGP and CPSP. In Fig. 1b, we also show electron micrograph of a typical silver fractal aggregate used in our experiments.

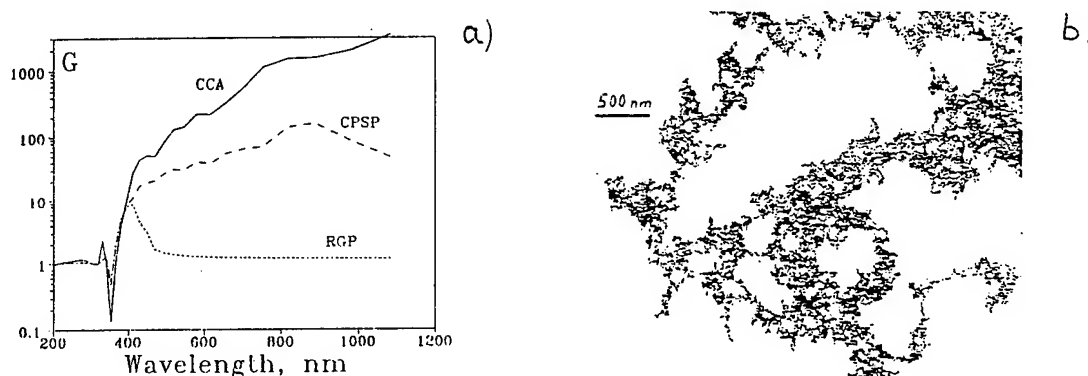


Fig. 1: a) Local-field enhancements, G , for fractal CCA ($D = 1.78$) and non-fractal RGP and CPSP ($D = d = 3$). b) Electron micrograph of a silver CCA.

High local fields result in giant optical nonlinearities for optical processes in small-particle composites. We found the enhancements associated with particle clustering for a number of optical phenomena, including degenerate four-wave mixing (DFWM), third-harmonic generation (THG), Raman scattering, and nonlinear refraction and absorption in Kerr media. The enhancement of optical processes is expressed in terms of the linear absorption by collective dipolar eigenmodes in a cluster, and quality-factors, q , of the modes ($q \gg 1$). It is shown that the susceptibility of a composite material consisting of random small-particle clusters is proportional to q^3 for Raman scattering and the Kerr optical nonlinearity, and to q^4 and q^6 for THG and FWM, respectively. For all of these processes, spectral dependences of the effective nonlinear susceptibilities are found.

In our earlier experiments, a million-fold enhancement of DFWM due to the clustering of initially isolated silver particles in a colloidal solution was obtained. In Fig. 2a we plot the experimental data for conversion efficiency $\eta = I_s/I_1 \propto I_0^2$ (I_s, I_1 and I_0 are the intensities of the DFWM signal, probe beam, and pump beam, respectively). As seen in the figure, similar values of η can be obtained in silver particles aggregated into fractal clusters at pump intensities $\sim 10^3$ times less than in the case of non-aggregated, isolated, particles. Since $\eta \propto I_0^2$, we conclude that the enhancement factor for silver fractal composites is $G \sim 10^6$ which is in good agreement with our calculations [1].

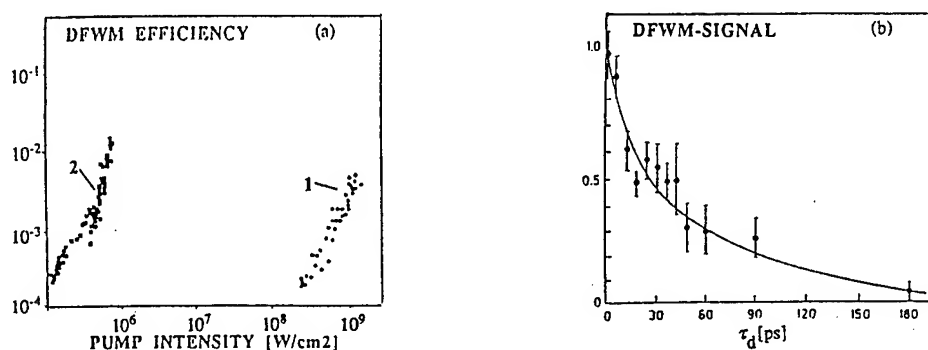


Fig. 2: a) DFWM efficiency vs pump intensity for Ag particles which are isolated (1) and aggregated into fractals (2). b) DFWM signal vs time delay of one of the pumps.

The obtained value for the nonlinear susceptibility in silver fractal composites is $\bar{\chi}^{(3c)} \sim p \times 10^{-5}$ e.s.u. at $\lambda = 532\text{nm}$. Even for the very small Ag volume fraction used in the experiment, $p \sim 10^{-5}$,

this gives $\bar{\chi}^{(3c)} \sim 10^{-10}$ e.s.u. (cf., a typical value of $\chi^{(3)}$ in crystals is $\sim 10^{-15}$ e.s.u. [3]). Moreover, p is a variable quantity and can be increased. We can assigned the value 10^{-5} e.s.u. to the nonlinear susceptibility, $\chi^{(3c)}$, of silver fractal clusters. Note that the obtained value $\chi^{(3c)} \sim 10^{-5}$ e.s.u. for *Ag* fractals is three orders of magnitude larger than the $\chi^{(3)}$ measured for non-aggregated *Ag* particles [4].

Rapid nonlinear response of silver CCA was tested in the OPC scheme when one of the input pulses was delayed by moving the mirror that reflected the input beam back to the sample. As follows from Fig. 2b, the DFWM signal is twice decreased with the time delay τ_d increasing up to 30 ps, which coincides with the pulse duration (pulse duration of the used laser, 30 ps, did not allow us to measure shorter nonlinear responses). Hence, the relaxation time of the nonlinear response does not exceed 30 ps. The huge nonlinearity, $\chi^{(3c)} \sim 10^{-5}$ e.s.u., with a time of the nonlinear response ≤ 30 ps, makes metal fractal aggregates very attractive for many potential applications.

We also studied linear and nonlinear optical properties of self-affine thin films. (Such films are formed by condensing atomic beams onto a low temperature substrate [1]). We observed that the eigenmodes of a self-affine surface manifest strongly inhomogeneous spatial distributions characterized by various degree of localization. On a metal self-affine film, the intensities in areas of high local fields ("hot" zones) exceed the applied field intensity by approximately three orders of magnitude. The spatial locations of the "hot" zones are very strong functions of the frequency and polarization of the incident light.

In Fig. 3a, we show a computer-generated self-affine film obtained within the restricted solid-on-solid model ($D = 2.6$) which is a good model for *Ag* cold-deposited films. The field distribution on *Ag* self-affine film for the s-polarized light at the wavelength $\lambda = 500$ nm is shown in Fig. 3b. As seen in the figure, the field in the hot zones is much larger than the applied field. $E^{(0)} = 1$. Our simulations also showed that a change of the wavelength or/and the polarization strongly affects the field distribution. A similar strong dependence on frequency and polarization of the applied field was obtained in our experiments on near-field scanning optical microscopy of localized optical modes in *Ag* fractal aggregates deposited onto a surface [2].

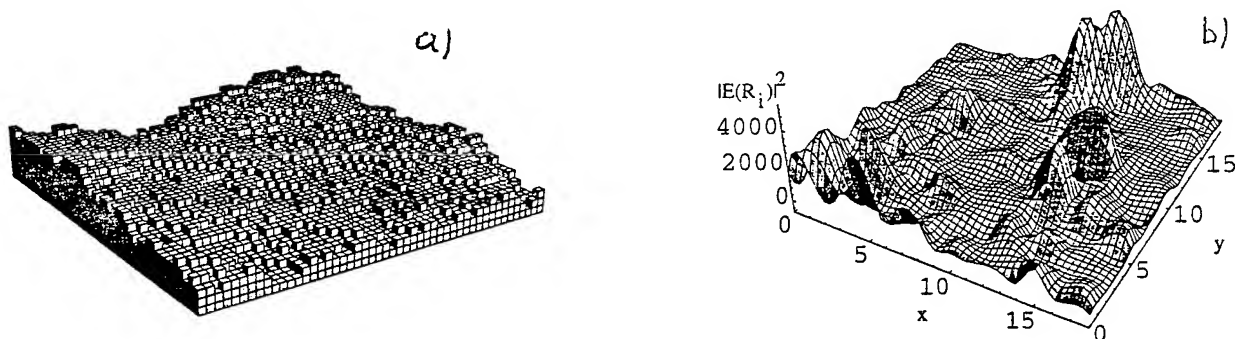


Fig. 3: a) Self-affine film ($D = 2.6$). b) Local field distribution on the *Ag* self-affine film.

To summarize, dipole-dipole interactions in fractals are not long-range (as they are in conventional three-dimensional media) and many of the collective eigenmodes are strongly localized in different parts of a fractal object with various random structures. This ultimately leads to strong spatial fluctuations of the fields. Optical nonlinearities emphasize the role of fluctuations leading to giant enhancements.

References:

- [1] V. M. Shalaev, Phys. Reports (in press); V. M. Shalaev, E. Y. Poliakov, V. A. Markel, Phys. Rev. B **53**, (1996).
- [2] D. P. Tsai, J. Kovacs, Z. Wang, M. Moskovits, V. M. Shalaev, J. Suh, R. Botet. Phys. Rev. Lett. **72**, 4149 (1994); V. M. Shalaev, M. Moskovits, Phys. Rev. Lett. **75**, 2451 (1995).
- [3] R. W. Boyd, Nonlinear Optics, Academic Press, 1992.
- [4] D. Ricard, Ph. Roussignol, C. Flytzanis, Opt. Lett. **10**, 511 (1985).

Monday, July 8, 1996

Molecular Nonlinear Optics

NMD 7:00 pm-8:20 pm
Maile Room

Christoph Bubeck, *Presider*
Max-Planck-Institute for Polymer Research, Germany

**FROM DIPOLAR TO MULTIPOLAR SYSTEMS :
OPENING NEW GEOMETRIC AND QUANTUM DIMENSIONS
IN MOLECULAR NONLINEAR OPTICS**

Joseph ZYSS

France Telecom-CNET

Laboratoire de Bagnex (UA CNRS 250), *Molecular Quantum Electronics* Dept^t
196, Avenue Henri Ravera, 92225-Bagnex, FRANCE

The field of Molecular Nonlinear Optics¹ has been seeded in the mid-seventies by the all pervading *molecular diode* template as exemplified by paranitroaniline derivatives exhibiting the now well recognized features of a rod-like dipolar structure with quasi-one dimensional intramolecular charge transfer between a single donor-acceptor pair via a delocalized π electron linkage. A highly consistent body of experiments in solutions, crystals and polymers as well as related models have come to reinforce the validity of this approach which has been further substantiated by a series of conceptual as well as application oriented developments. NLO measurements are now well acknowledged and currently used in Chemistry as sensitive probes of such basic features as intramolecular charge transfer or π -electron delocalization in conjugated systems whereas recent demonstrations of high bandwidth electrooptic modulation in polymer based modulators² or low threshold near IR infrared parametric oscillation in molecular crystals³ evidence the application potential of the field. The existence of a large ground state dipole moment and the possibility to couple it to a poling electric field via a Langevin-Boltzmann distribution stands-out as the major cornerstone responsible for the development of the field. A two-level model pointing-out the difference between excited and ground state dipoles as a basic underlying parameter further strengthens the relevance of a dipolar geometry. However, such highly consistent interplay of dipolar models, experiments and technologies may have lead to ignore broader possibilities as recently recognized in the form of octupolar (see Fig.1) and more generally, multipolar systems⁴.

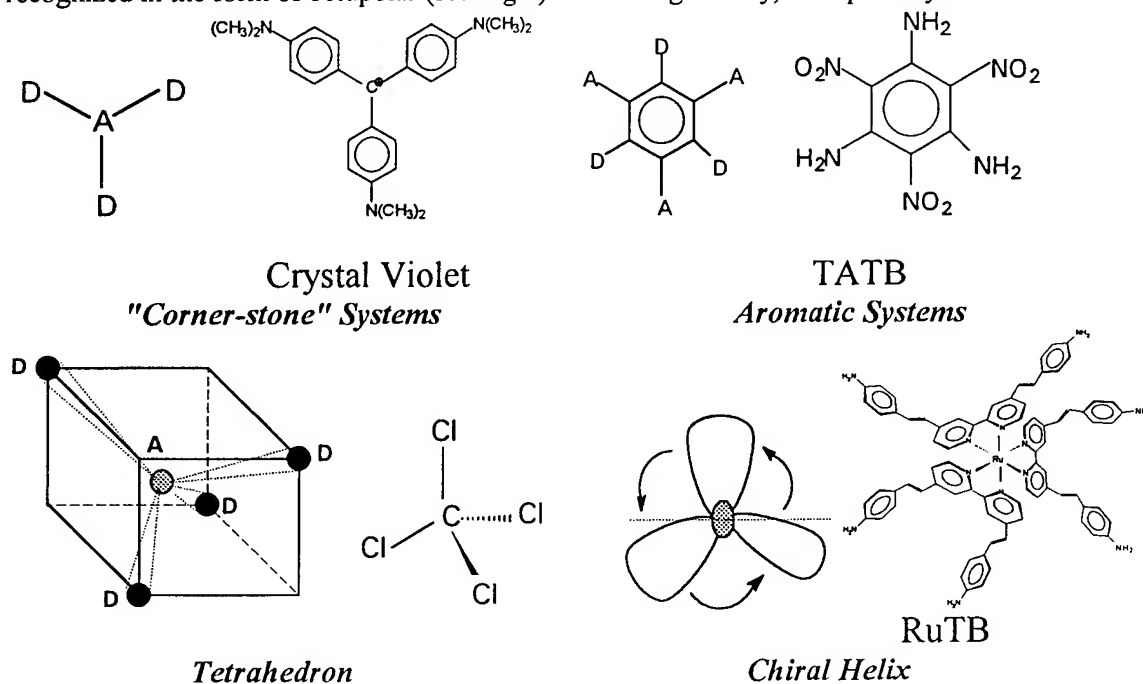


Fig.1: Basic patterns and selected examples of 2-D (first row) and 3-D (second row) octupolar systems. A record high value of $800 \cdot 10^{-30}$ esu has been measured by HLS⁵ for the chiral propeller RuTB ion⁶.

Fig.1 exemplifies some basic patterns of octupolar systems which have been conceived in search of a compromise between isotropy and polarity resulting in cylindrical, spheroidal or twisted chiral shapes exhibiting multiple charge transfer substitution patterns while being deprived of dipole moments although still non-centrosymmetric.

This has lead over the past five years to revisit traditional techniques and propose new approaches towards systematic measurements in solutions and films. Revival of Maker's Harmonic Light Scattering experiment⁵ has indeed permitted to perform such systematic measurements in unoriented solutions with the additional benefit, as opposed to EFISH, of an informative polarization response permitting to infer both octupolar and dipolar components of the quadratic hyperpolarizability tensor β (with $\beta = \beta_{J=1} \oplus \beta_{J=3}$). An adequately defined *nonlinear anisotropy ratio* can be inferred, as illustrated in Fig.2, from the harmonic scattering depolarization ratio with minima (resp. maxima) occurring precisely for purely dipolar (resp. octupolar) systems.

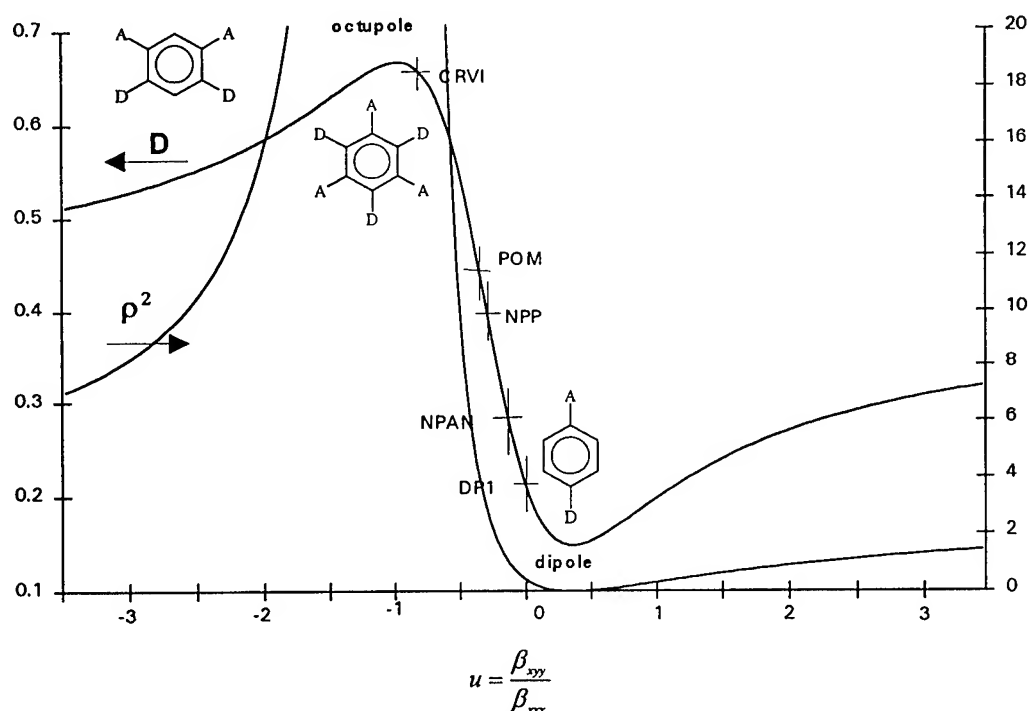


Fig.2: Depolarization ratio D as from a Variable Incident Polarization (VIP) configuration⁷ in Harmonic Light Scattering⁵. The nonlinear anisotropy ρ is inferred from D . The various acronyms correspond to different charge transfer aromatic molecular systems as in Ref 1.

The significant nonlinear anisotropies evidenced therefrom, even for paranitroaniline derivatives such as NPP³, cannot be accounted for by a two-level quantum model. A more general n -level ($n \geq 3$) model has been developed⁷ and is being confronted to coherent SHG Nonlinear Spectroscopy performed on poled polymer samples whereas two-photon fluorescence presently precludes the use of HLS for such resonant studies.

A recently achieved crucial subsequent step is the demonstration of permanent octupolar macroscopic orientation by an *all-optical poling* bichromatic scheme whereby a guest-host thin film is poled via polarized $\omega, 2\omega$ illumination⁸. This scheme rests on the orientationally selective transient pumping of molecules towards an electronically excited metastable state followed by relaxation through a reversible conformational change entailing partial orientational randomization.

Fig.3 illustrates the specific polarization features of such induced octupolar macroscopic order in comparison with dipolar order, as from comparative polarized SHG from optically poled samples. An original formalism, whereby irreducible tensorial decomposition is applied in a parallel way to both susceptibility (e.g. $\chi^{(2)}$) and field tensor (e.g. $(E^{2\omega})^* \otimes E^\omega \otimes E^\omega$) is shown to be relevant for both Optical Poling and Harmonic Light Scattering.

In the former case, this parallelism helps evidence the correspondance between the irreducible components of the field tensor (namely the ellipticity of the writing beams) and that of the molecular susceptibility (i.e. the nonlinear anisotropy) with optimal interaction and poling ensured by matching these, such as shining octupoles (resp. dipoles) with circularly polarized ω and 2ω beams with same

(resp. opposed) handedness.

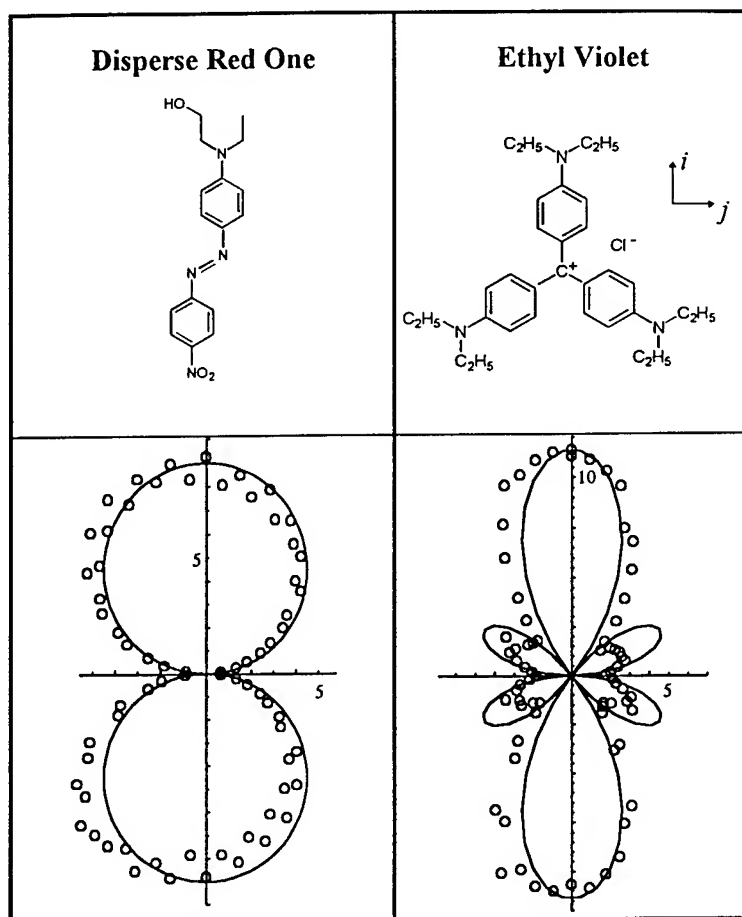


Fig.3: Compared coherent polarized SHG response of DR1 (~dipolar) and Ethyl Violet (octupolar) systems embedded in an optically poled guest-host sol-gel thin film⁸.

Adaptation of the multipolar anisotropy of the write/read field tensor to that of the molecular susceptibility may thus drive the imprinted multipolar macroscopic order to a desired level of nonlinear anisotropy with the additional benefit of a quasi-phase-matched patterning.

In conclusion, new quantum and geometric dimensions have been consistently introduced in Molecular Engineering for NLO following the design of highly efficient 2-D and 3-D multiple charge transfer systems aiming at an optimal trade-off between isotropy and polarity. Enlarged perspectives for organic materials in NLO are being envisioned therefrom, all the way from molecular design to micropatterned multipolar nonlinear structures for device applications.

References

- 1) *Molecular Nonlinear Optics: Materials, Physics and Devices* J.Zyss Ed. (Academic Press, Boston, 1994)
- 2) W.Wang, D.Chen, H.Fetterman, Y.Shi, W.H.Steier, L.R.Dalton and P.M.D.Chow, *Appl.Phys.Lett.* 67,1806(1995)
- 3) S.Khodja, D.Josse, I.D.W.Samuel and J.Zyss, *Appl.Phys.Lett.* 67,3841(1995)
- 4) J.Zyss, *Nonlinear Optics* 1,3(1991); J.Zyss, *J.Chem.Phys.* 98,6583(1993)
- 5) P.D.Maker, *Phys.Rev.A* 1,923(1970); K.Clays and A.Persoons, *Phys.Rev.Lett.* 66,2980(1991)
- 6) C.Dhenaut, I.Ledoux, I.D.W.Samuel, J.Zyss, H.Bourgault and H.Le Bozec, *Nature* 374,339(1995)
- 7) S.Brasselet and J.Zyss, to appear in *The Journal of Nonlinear Optical Physics and Materials* (Proceedings of FRISNO'4, the 4th French-Israeli Symposium on Nonlinear and Quantum Optics)
- 8) C.Fiorini, F.Charra, J.M.Nunzi, I.D.W.Samuel and J.Zyss, *Optics Lett.* 20,2469(1995)

Chirality in Nonlinear Optics

Thierry Verbiest, Martti Kauranen, Jeffery J. Maki, and André Persoons
 University of Leuven, Laboratory of Chemical and Biological Dynamics
 Celestijnenlaan 200 D, B-3001 Leuven, Belgium
 Tel. : +32-16-32.71.71 Fax : +32-16-32.79.82

Second-harmonic generation (SHG) can be used to study the chiral properties of isotropic thin films¹. The efficiency of SHG is highly dependent on the handedness of incoming circularly-polarized light. This phenomenon is referred to as nonlinear optical activity. In addition, linearly-polarized fundamental light can also be used as a probe of chirality. Recently, we showed experimentally that the second-harmonic efficiency is different upon radiation with fundamental light that is linearly-polarized -45° and $+45^\circ$ with respect to the p-polarized direction². We also developed a theory of SHG from isotropic chiral surfaces that includes contributions of electric- and magnetic-dipole transitions to the surface nonlinearity³. In this model, the nonlinear polarization is taken to be of the form :

$$P_i(2\omega) = \chi_{ijk}^{eee} E_j(\omega) E_k(\omega) + \chi_{ijk}^{eem} E_j(\omega) B_k(\omega) \quad [1]$$

where the subscripts refer to cartesian coordinates and E and B are the electric field and the magnetic induction field, respectively. Analogously, we define the nonlinear magnetization as :

$$M_i(2\omega) = \chi_{ijk}^{mee} E_j(\omega) E_k(\omega) \quad [2]$$

In eq. [1] and [2], superscript e (m) implies that the respective subscript refers to a cartesian component of an electric (magnetic) transition moment. χ^{eee} is the usual second-order nonlinear susceptibility, which depends only on electric-dipole transitions, and χ^{eem} and χ^{mee} are susceptibilities that account for the

contributions of magnetic-dipole transitions to the nonlinearity. The nonlinear polarization and magnetization act as sources for the second-harmonic field.

The intensity of the second-harmonic light generated by a surface upon radiation with circularly-polarized fundamental light can always be expressed in the general form :

$$I(2\omega) = |-f + g \pm ih|^2 I^2(\omega) \quad [3]$$

where the upper and lower signs correspond respectively to right-hand circular (RHC) and left-hand circular (LHC) polarizations. The coefficients f, g and h are combinations of the different surface susceptibility components and are different for the reflected and transmitted s- and p-polarized components of the second-harmonic field. For the case of isotropic chiral surfaces, these coefficients are functions of 4 independent χ^{eee} components, 4 independent χ^{mee} components and 7 independent χ^{eem} components. From eq. [3] it is clear that circular-difference effects (i.e different second-harmonic response to left-hand circular and right-hand circular polarizations) can only occur when a phase-difference exists between the coefficient h and the two other coefficients (f and g). Furthermore, for the case of isotropic films, $(-f + g)$ and h are nonvanishing only for chiral surfaces and hence a circular-difference effect can occur only for chiral surfaces. For the case of $\pm 45^\circ$ linearly-polarized incident light, the intensity of the second-harmonic field is :

$$I(2\omega) = |f + g \pm h|^2 I^2(\omega) \quad [4]$$

where the upper and lower signs correspond respectively to the $+45^\circ$ and -45° linear polarizations. In contrast to the previous case (circularly-polarized excitation), difference effects for $\pm 45^\circ$ linear excitation (linear-difference effects) will occur even if there is no phase-difference between h and the other coefficients.

In general we can express the magnitude of both circular- (SHG-CD) and linear-difference (SHG-LD) effects as :

$$\Delta I_{\text{SHG-CD}} = I_{\text{LHC}}(2\omega) - I_{\text{RHC}}(2\omega) = 4Im[(f - g)h^*] I^2(\omega) \quad [5]$$

$$\Delta I_{\text{SHG-LD}} = I_{-45^\circ}(2\omega) - I_{+45^\circ}(2\omega) = 4Re[(f + g)h^*] I^2(\omega) \quad [6]$$

From these equations it is clear that circular- and linear-difference effects are nearly complementary ; one measuring the real part and the other the imaginary part of a bilinear function of f , g , and h .

Both circular- and linear-difference effects can be studied experimentally in isotropic Langmuir-Blodgett films of chiral polymers. Infrared light from a Q-switched and injection-seeded Nd:YAG laser (1064 nm, 10 ns pulses, 50 Hz) is used as the fundamental beam and is incident at the sample at an angle of 45° . The polarization of the fundamental beam is continuously varied by rotating a half-wave or a quarter-wave plate and the intensity of the second harmonic (p- or s-polarized) is recorded in reflection and transmission. Sufficient polarization purity of the experiment is verified by making sure that no difference effects (circular or linear) are observed in the second-harmonic intensity generated from isotropic achiral samples.

Langmuir-Blodgett films of our chiral polymers show a strong response to both the circular and linear probes of chirality. The magnitudes of the circular -and linear-differences are comparable in value and on the order of 10-100 %, but orders of magnitude higher than circular-difference effects observed in ordinary linear-optical circular dichroism, which are typically on the order of 0.1 %. These results are remarkable considering that only a thin layer of the chiral material is required. We also experimentally verified the complementarity of circular- and linear-difference effects in SHG by determining the real and imaginary parts of the expansion coefficients f , g , and h . In addition, by determining the values of f , g , and h for the reflected and transmitted p- and s-polarized components of the second-harmonic field, we were able to extract relative values for all nonvanishing χ^{eee} , χ^{mee} and χ^{eem} components. An interesting result is the finding that the magnitude of some of the χ^{eem} components is on the order of 20 % of the highest electric-dipole components. This is in contrast to the common belief that magnetic-dipole contributions are negligible in nonlinear optics.

References

1. M. Kauranen et al., *Adv. Mater.* **7**, 641 (1995)
2. T. Verbiest et al., *J. Chem. Phys.* **103**, 8296 (1995)
3. J.J. Maki et al., *Phys. Rev. B* **51**, 1425 (1995)

Femtosecond to nanosecond dynamics in C_{60} : implications for excited-state nonlinearities

D. McBranch, V. Klimov, L. Smilowitz, J. M. Robinson,
A. Koskelo, M. Grigorova and B. R. Mattes

*Mail Stop J567
Los Alamos National Laboratory
Los Alamos, NM 87545
phone: (505) 665-4836; FAX (505) 665-4817*

Recently, many studies have emerged on optical power limiting (OL) in buckminsterfullerene (C_{60}).¹ OL occurs when the absolute transmittance of a material decreases with increasing laser fluence; in C_{60} , the dominant mechanism for OL is reverse saturable absorption (RSA), in which the absorption cross section from excited-state electronic energy levels is significantly higher than the ground state absorption cross section. For limiting of nanosecond pulses, the lifetime of the excited-state responsible for the nonlinear absorption is a crucial parameter. In this work, we provide a detailed study of the relaxation dynamics of the excited-state absorption for C_{60} in toluene solution, as a thin solid film, and entrapped within an inorganic sol-gel glass matrix. Our results demonstrate that the microscopic morphology of the C_{60} molecule plays a crucial role in determining the relaxation dynamics. We find that the dynamics of the C_{60} -glass composite occur on long (ns) timescales, comparable to those in solution; thin film samples, by contrast, show rapid decay (<20 picoseconds). Combined with intensity-dependent transmission measurements on the same samples, these results demonstrate that the C_{60} /sol-gel glass composites contain C_{60} in a molecular dispersion, and are suitable candidates for solid-state optical limiting.

Time-resolved excited-state absorption spectra are measured using a femtosecond (fs) pump-probe technique. The samples are excited at 405 nm by 100 fs pulses from a frequency-doubled regeneratively amplified modelocked Ti:Sapphire laser (Clark-MXR). The pump pulse energy is 5 μ J, corresponding to an excitation density of 12 mJ/cm², and the repetition rate is 1 kHz. Femtosecond white light pulses are generated in a 1 mm sapphire window. The transmission of the sample is measured using a 0.15 m spectrometer and CCD array with the pump beam on (T_{on}) and off (T_{off}), and the differential transmission $\Delta T/T$ is determined from the expression: $\Delta T/T = (T_{on} - T_{off})/T_{off}$. Each spectrum is the average of 500-1000 pulses. Alternately, single wavelength dynamics are monitored with much higher sensitivity by mechanically chopping the pump beam, and using a balanced reference beam and signal beam differential amplification, followed by lock-in detection. C_{60} samples were prepared in toluene solution in 2 mm path length cells, with concentration adjusted to yield optical density approximately 1 at the pump wavelength. Thin films were prepared by vacuum sublimation, and no attempt was made to preserve them from exposure to oxygen. C_{60} /sol-gel composites were prepared by mixing C_{60} solutions together with the precursor sols in a conventional silicate sol-gel glass synthesis, as previously described.²

Excited-state absorption spectra were measured from 450–1000 nm. Following photoexcitation, a broad excited-state absorption feature peaking near 975 nm with a tail extending to 450 nm appears, due to the excited singlet state.^{3,4} With a one ns intersystem crossing time, a new peak near 750 nm due to the triplet state emerges.

The photoexcitation dynamics are most accurately revealed in the time-dependence at different wavelengths, as shown for C_{60} in toluene solution in Figure 1. At a wavelength of 920 nm, we observed a 1.0 ± 0.1 ns exponential decay of the singlet excited-state absorption (Fig. 1, solid circles). The complementary increase of absorption at 750 nm with the same time constant provides a direct measurement of the intersystem crossing time (Fig. 1, solid triangles). The decay observed at earlier times indicates that the singlet absorption also contributes at this wavelength. At intermediate wavelengths, the temporal behavior varies smoothly between these two values (Fig. 1, open squares). Hence, for ns pulses, the spectral region in the vicinity of 750 nm should be the most promising one for optical limiting in C_{60} solutions, as is observed experimentally.^{3,4}

In addition, we monitored the dynamics on much shorter timescales. Figure 2 shows the early evolution of the singlet excited-state absorption band. In this case, a very fast (230 fs) initial decay was observed at lower wavelengths (570 nm, open squares). A complementary increase with a 260 fs rise time (dashed line)

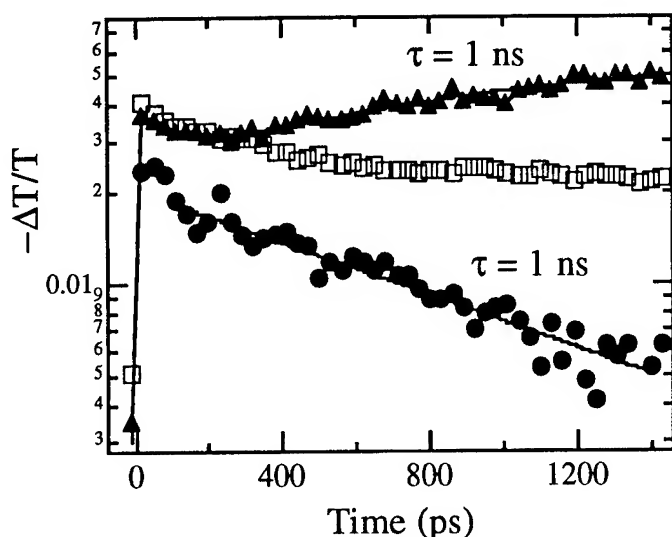


Figure 1. Time-dependence of $-\Delta T/T$ for C_{60} in toluene solution at three wavelengths: 750 nm (solid triangles), 820 nm (open squares), and 920 nm (solid circles). Solid lines are fits to the decay and rise, respectively, of the singlet and triplet states, with the same time constant 1.0 ± 0.1 ns.

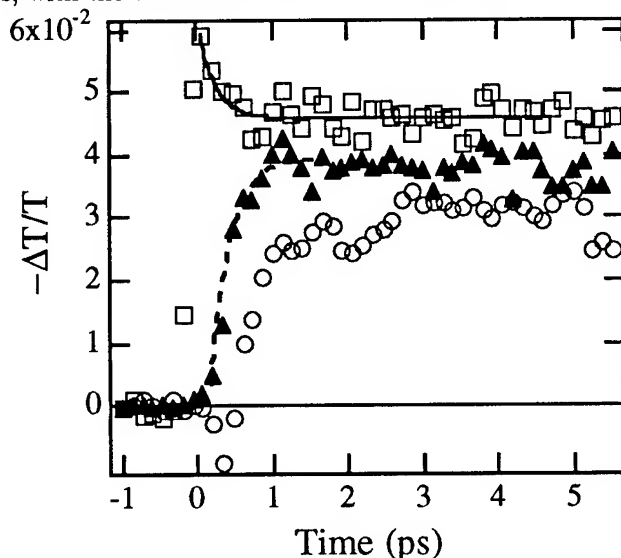


Figure 2. Early time-dependence of $-\Delta T/T$ for C_{60} in toluene at 570 nm (open squares), 750 nm (solid triangles), and 920 nm (open circles). The initial decay at 570 nm occurs with 230 fs time constant (solid line), accompanied by a rise of the lowest singlet excited-state absorption (260 fs, dashed line).

excited-state absorption peaks are also broadened, with no distinct singlet or triplet features, in contrast to the spectra in solution. The strongest evidence that the fullerenes are dispersed in the glass on a molecular scale comes from the relaxation dynamics. Figure 3 shows the dynamics at three different wavelengths, together with fits to single exponential decays (solid lines). The decay at long wavelengths dominated by the singlet excited-state absorption in solution (850 nm, Fig. 3, squares) shows an exponential time constant

is observed at 750 nm (solid triangles) and 920 nm (open circles). This is the first direct measurement of the fs relaxation from higher singlet excited-states (at the 3.1 eV pump photon energy) to the lowest singlet excited-state (≈ 2.3 eV); such rapid relaxation has been proposed as essential to explain both the significant optical limiting for ps pulses, and the intensity-dependent recombination in C_{60} thin films.⁵ The relative delay between the onset of the photoinduced absorption is due to the dispersion, or chirp on the white light continuum. The variation of the rising edges in Figure 2 shows that the chirp over the entire spectral range measured is less than one ps.

In sharp contrast to the relaxation dynamics solution, the dynamics in thin films of C_{60} show a very rapid and intensity-dependent decay on picosecond timescales.⁵ Under similar excitation conditions, a thin film shows a nearly complete decay of the excited-state absorption within 20 ps.³ The rapid and nonlinear recombination dynamics for C_{60} thin films at high fluences has been attributed to bimolecular recombination due to exciton-exciton annihilation.⁵ Hence, for ns pulses, the excited-state absorption remains large in solution over a broad wavelength range for the duration of the pulse, while the decay back to the ground-state in the solid thin film is much more rapid than the pulsewidth. Consequently, RSA on the nanosecond time scale is not observed in the thin film. This is confirmed by intensity-dependent transmission measurements of C_{60} films using ns pulses, in which optical limiting is not observed.³

Since most applications of optical limiters require solid-state samples, solid-state solutions of C_{60} in a sol-gel glass matrix were prepared.² The optical absorption in the resulting doped porous glasses is broadened relative to that of the fullerenes in solution, and the samples are brown (similar in color to the thin film). The

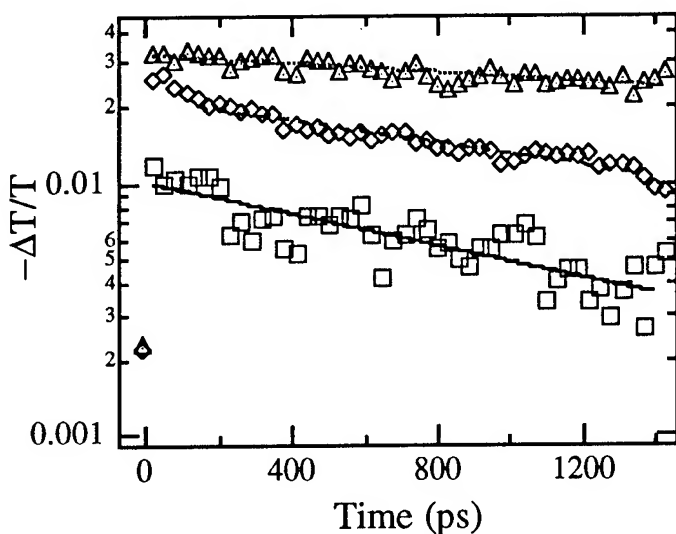


Figure 3. Time-dependence of $-\Delta T/T$ for C_{60} /sol-gel glass 750 nm (open triangles), 820 nm (open diamonds), and 850 nm (open squares). Solid lines are exponential decays with time constants 4.8 ns, 2.0 ns, and 1.4 ns, respectively.

with the the FCC crystalline thin films. The results also confirm that the primary mechanism for rapid relaxation in the thin films is the close proximity of adjacent fullerenes, not additional nonradiative relaxation pathways introduced by the disordered solid-state (as is seen, for example, in conjugated polymers).

From our measurements of the detailed relaxation dynamics of the excited-state absorption at several wavelengths in C_{60} in toluene, thin films, and encapsulated within sol-gel glass matrices, we conclude the following. First, the relaxation rates from the initial excited-state are important experimental parameters which must be determined to understand the utility of these materials for applications in optical limiting of ps to ns pulses. We have directly measured the intersystem crossing time in solution (1.0 ns), and have shown that the initial decay from higher excited-states to the lowest excited state takes place in about 250 fs. We have highlighted the difference between the rapid recombination seen in a thin film and that for liquid or solid-state solutions. Finally, we have shown that in C_{60} /sol-gel glass composites, the dynamics indicate that the fullerenes are molecularly dispersed within the glass matrix, with additional inhomogeneous broadening of ground and excited-state transitions due to the solid-state environment. These composites are promising for solid-state optical limiting of ns pulses over a broad spectral range.

This work was supported by Los Alamos National Laboratory LDRD funds, under the auspices of the U.S. Department of Energy.

of 1.4 ns; dynamics at longer wavelengths were not measured due to reduced signal-to-noise owing to larger scattering in the porous glass sample. The decay at the position of the triplet peak in solution (750 nm, Fig. 3, triangles) shows a slow 4.8 ns decay in the glass. At the intermediate wavelength of 820 nm (Fig. 3, diamonds) an intermediate decay of 2.0 ns is observed. The fact that no increase was observed in the magnitude of the excited-state absorption at 750 nm (associated with the growth of triplet population) is attributed to the broadening of the excited-state absorption peaks in the glass, so that there is a relatively larger contribution from the singlet at this wavelength. This is due to inhomogeneous broadening from the variable local environment seen by individual C_{60} molecules in the solid state, and is similar to the inhomogeneous broadening seen in the thin film. However, the dynamics show clearly that the C_{60} molecules in the composite glass are well separated compared

1. L. Tutt and A. Kost, "Optical Limiting Performance of C_{60} and C_{70} Solutions," *Nature* **356**, 225-226 (1992).
2. B. R. Mattes, D. McBranch, J. M. Robinson, A. Koskelo, and S. P. Love, "Fullerene/glass composites," U.S. Patent 5,420,081 (1995).
3. D. McBranch, L. Smilowitz, V. Klimov, J. Robinson, B. Mattes, A. Koskelo, J. Hummelen, F. Wudl, N. Borrelli, and J. Withers, "Optical Limiting in Fullerene Solutions and Doped Glasses," *SPIE Proceedings, Fullerenes and Photonics II* **2530**, 196 (1995).
4. L. Smilowitz, V. Klimov, D. McBranch, J. Robinson, M. Grigorova, B. Mattes, A. Koskelo, H. Wang, and F. Wudl, "Enhanced Optical Limiting in Substituted Fullerenes," *Opt. Lett.* (in press).
5. S. L. Dexheimer, W. A. Varecka, C. V. Shank, D. Mittelman, and A. Zettl, "Nonexponential relaxation in solid C_{60} via time-dependent singlet exciton annihilation," *Chem. Phys. Lett.* **235**, 552 (1995).

Enhancement of Second-Order Optical Nonlinearity by Supramolecular Engineering

Marti Kauranen, Thierry Verbiest, Carlo Boutton, Stephan Houbrechts, and André Persoons
*Laboratory of Chemical and Biological Dynamics, University of Leuven, Celestijnenlaan
200 D, B-3001 Heverlee, Belgium, Tel. +32-16-327508, Fax. +32-16-327982*

Celest Samyn

*Laboratory of Macromolecular and Physical Organic Chemistry, University of Leuven,
Celestijnenlaan 200 F, B-3001 Heverlee, Belgium,
Tel. +32-16-327438, Fax. +32-16-327990*

Only noncentrosymmetric molecules can possess a second-order nonlinear response, i.e., they have a nonvanishing first molecular hyperpolarizability. Polar molecules with donor and acceptor groups connected by a conjugated π electron system are traditional organic second-order materials. For macroscopic noncentrosymmetry, such molecules are incorporated in, e.g., a polymer host and poled with a static electric field. The nonlinear coefficients of poled materials are proportional to the product $\mu\beta$ where μ is the permanent dipole moment of the molecules and β is the vectorial part of the first hyperpolarizability [1].

In this paper, we consider polar molecules that are introduced as orientationally-correlated chromophores into a rigid supramolecular structure. In such a structure, supramolecular hyperpolarizability and dipole moment are obtained as coherent superpositions of the chromophoric quantities and can lead to enhanced nonlinear properties. Such principles have been demonstrated [2,3] but only with modest enhancements. In the present work, we utilize nonlinear chromophores organized as side groups on a polypeptide [4] backbone and show that this structure gives rise to a very large enhancement of the second-order nonlinear response.

We consider the schematic structure of Fig. 1 in which n chromophores make an equal angle θ with respect to the axis (z direction) of the supramolecular structure but are randomly

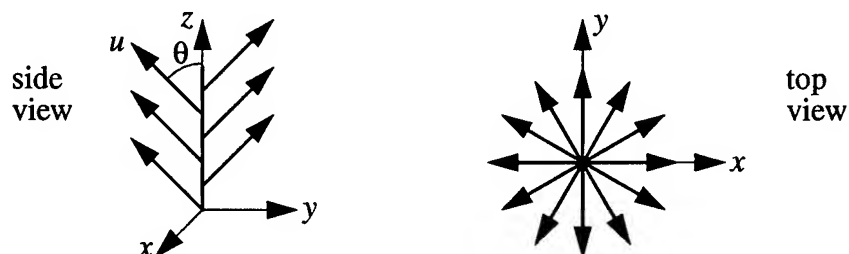


Figure 1. Supramolecular structure with orientationally-correlated chromophores. The coordinate systems uvw and xyz define the chromophoric and supramolecular frames of reference, respectively. In the side view, the chromophores pointing to the front and back have been omitted for clarity.

oriented in the transverse (x - y) direction. We assume that the hyperpolarizability of the chromophores has only one dominant tensor component $\beta_{uuu} \equiv \beta_u$ where u is along the direction of conjugation. The vectorial part of the supramolecular hyperpolarizability is

$$\beta = n\beta_u \cos \theta \quad (1)$$

In addition, the dipole moment of the supramolecular structure is

$$\mu = n\mu_u \cos \theta \quad (2)$$

where μ_u is the dipole moment of a single chromophore.

The above analysis implies that the hyperpolarizability *per* chromophore of the supramolecular structure is actually reduced compared to individual chromophores. However, the product characterizing nonlinear coefficients of poled materials is

$$\mu\beta = n^2\mu_u\beta_u \cos^2 \theta \quad (3)$$

Hence, the nonlinear response of the supramolecular structure *per* chromophore is enhanced whenever $n\cos^2 \theta > 1$.

In our experiments, we used the synthetic polypeptide poly(γ -methyl-L-glutamate) functionalized with the nonlinear chromophore 6-[4-[(2-methyl-4-nitrophenyl)azo]phenoxy]-1-hexanol (Fig. 2). Hydrogen bonds between the NH and CO groups fold the polypeptide backbone into an α -helix configuration [4], which can be further stabilized by appropriate side groups. The degree of functionalization of our polypeptides was 16 mol % and the average degree of polymerization was 77. The structure of the polypeptide is equivalent to that of Fig. 1 with the nonlinear side groups distributed along the helical backbone.

We determined the product $\mu\beta$ of our compounds by electric-field-induced second-harmonic generation using a Q-switched and injection-seeded Nd:YAG laser (1064 nm, 10 ns, 10

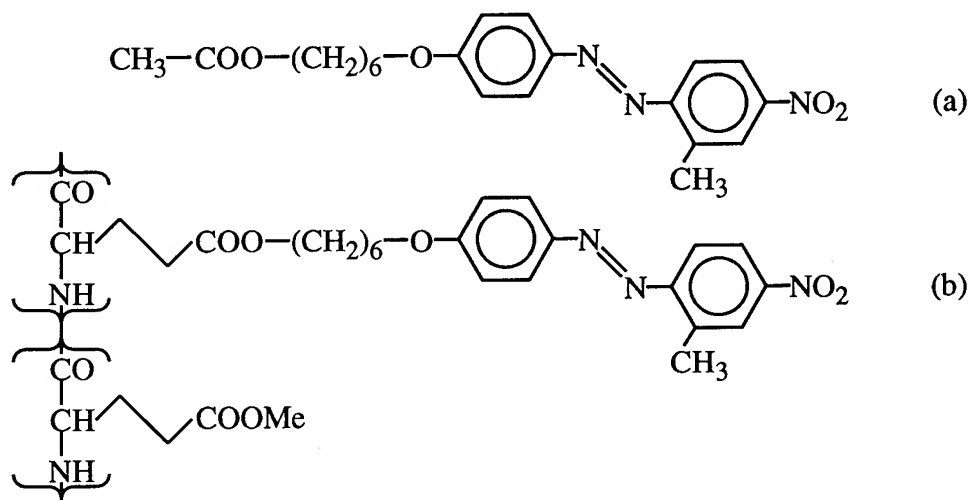


Figure 2. Chemical structures of the model chromophore (a) and the polypeptide (b).

Hz). The measurements were performed in chloroform solutions with 4.3% of hexafluoro-isopropanol to increase the solubility of the polymer. Dipole moments were determined from capacitance measurements.

Table 1: Properties of the model chromophore and the polyglutamate. λ_{\max} (nm) is the wavelength of maximum absorption, μ (D) the dipole moment, $\mu\beta$ (10^{-48} esu) the product characterizing nonlinear response of poled materials, and β (10^{-30} esu) the hyperpolarizability at 1064 nm. The zero-frequency quantities $\mu\beta_0$ (10^{-48} esu) and β_0 (10^{-30} esu) were obtained by extrapolating the measured values using the two-level model [1].

	λ_{\max}	μ	$\mu\beta$	$\mu\beta_0$	β	β_0
model chromophore	369	9.6	581	277	60.5	28.8
polyglutamate (<i>per</i> chromophore)	365	460	248000 (20200)	119000 (9690)	539 (43.8)	259 (21.1)

The hyperpolarizability of the polyglutamate *per* chromophore was ~30% lower than that of the individual chromophores (Table 1). This result suggests that the angle θ between the chromophoric and polymeric axes was ~45°. However, the product $\mu\beta$ of the polymer *per* chromophore was a factor of 35 higher than that of the individual chromophores. This enhancement factor is even higher than predicted by our model and implies that the backbone contributes significantly to the dipole moment of the polymer structure [4] and further improves its nonlinear response. Note also that the efficiency of frequency conversion devices is proportional to $(\mu\beta)^2$. Hence, a poled frequency converter utilizing our polymer instead of free chromophores would give rise to a factor of 1200 increase in the conversion efficiency at the same total chromophore concentration.

The off-resonant value of $\mu\beta_0 = 9690 \times 10^{-48}$ esu *per* chromophore is more than an order of magnitude higher than reported values for single chromophores with similar (near UV) absorption characteristics. Hence, our supramolecular strategy has given rise to a structure with strongly enhanced second-order nonlinear response without altering the favorable absorption characteristics of the individual chromophores.

References

1. See for example, P. N. Prasad and D. J. Williams, *Introduction to Nonlinear Optical Effects in Molecules and Polymers* (Wiley, New York, 1991).
2. E. Kelderman *et al.*, Adv. Mater. **5**, 925 (1993).
3. M. Kauranen *et al.*, Science **270**, 966 (1995).
4. See for example, *Poly- α -Amino Acids*, G. D. Fasman, Ed., (Marcel-Dekker, New York, 1967).

Monday, July 8, 1996

NLO Poster Session: 1

NME 8:20 pm-10:30 pm
South Pacific Ballroom

Vertical couplers: all-optical switch design

Rachel M Geatches, Susan V Dewar

Department of Physics and Astronomy, University of Wales College of Cardiff
PO Box 913, Cardiff, CF2 3YB, UK
Tel: +44 1222 874458, Fax: +44 1222 874056

Richard V Penty

Department of Electrical and Electronic Engineering, University of Bristol
Queen's Building, University Walk, Bristol, BS8 1TR, UK
Tel: +44 117 928 8183, Fax: +44 117 925 5265

1 Introduction

Nonlinear directional couplers (NLDCs) have been shown to have great potential as the basis for all-optical switching devices (reviewed, for example by Agrawal and Boyd [1]). The potential for nonlinear switching has been demonstrated in InGaAsP NLDCs, by utilizing resonant nonlinearities near the band gap, *i.e.*, $\lambda = 1.55\mu\text{m}$, thereby requiring moderate switching powers [2]. However, the required switching power is higher than that ideally required for semiconductor laser optical sources and so it is important that this is minimised. Significant reductions in switching power have been predicted in coupled fibers with asymmetric configurations when compared to corresponding symmetric designs [3]. Chen *et al* also forecast further reductions in switching power by matching gain in one guide to loss in the other. We have studied the design of asymmetric semiconductor couplers, where the coupling is finely balanced, and predict the switching power to be substantially reduced when compared with symmetric designs. These investigations are now being extended to vertical configurations, which are expected to have significant advantages over the more conventional horizontal designs. By adopting a vertical configuration, the waveguiding regions can be realistically closer together, thereby reducing the coupling length, which will allow for a minimum of loss over the distance required for switching. Furthermore, the geometrical asymmetry of the coupler can be maximized, by coupling a planar-guide to a rib-guide. Likewise material asymmetry can be introduced easily into a vertical configuration. Finally, by having the guides in different planes, the doping requirements needed for biasing in order to induce gain (at transparency), can be more easily realised.

2 Design methods

To design vertical, asymmetric NLDCs as all-optical switching devices, we have adopted two modelling techniques: the Spectral Index (SI) method [4] to calculate the linear propagation modes; and Coupled Mode Theory (CMT) [3] to evaluate nonlinear switching.

The SI method is a fast and accurate linear 2D technique for modelling semiconductor rib waveguides, both as single waveguides and as directional couplers. The technique has been successfully employed as a design tool for wavelength filters, spatial switches, etc. More recently, it has been adapted to include multi-layer structures as well as incorporating optical loss and gain (by operating in the complex plane). In this paper we have adopted the Discrete SI method, described in detail by Burke [5]. In order to calculate the complex modal propagation constant (and corresponding quasi-TE or quasi-TM mode profiles), the SI method solves the wave equation for a given structure, in the form:

$$\frac{\partial^2 E}{\partial x^2} + \frac{\partial^2 E}{\partial y^2} + (k^2(x, y) - (\beta + i\alpha)^2)E = 0 \quad (1)$$

where the wavenumber $k(x, y) = (2\pi/\lambda)n(x, y)$, with λ as the wavelength of operation and

$n(x, y)$ is the complex refractive index profile in the cross section of the structure. It is assumed that the mode has a z -dependency of the form $\exp[-i(\beta + i\alpha)z]$, where $(\beta + i\alpha)$ is the complex modal propagation constant: β is the real propagation constant; and α is the attenuation (loss or gain depending on sign).

The coupled mode theory (CMT) equations used to model the nonlinear switching characteristics can be written in terms of modal amplitudes ($a_{1,2}$) for each waveguide as [3]:

$$-i \frac{da_1}{dz} = (\beta_1 + i\alpha_1)a_1 + \Delta\beta_1(|a_1|^2)a_1 + \kappa a_2 \quad (2)$$

$$-i \frac{da_2}{dz} = (\beta_2 + i\alpha_2)a_2 + \Delta\beta_2(|a_2|^2)a_2 + \kappa a_1 \quad (3)$$

where $\beta_j + i\alpha_j$ are the propagation constants for the individual waveguides in isolation, modelled using the SI method. κ is the linear coupling coefficient determined from the modal propagation constants of the coupled symmetric (β_s) and antisymmetric (β_{as}) modes (*supermodes*) of the structure, i.e., $\kappa = (\beta_s - \beta_{as})/2$. The nonlinearity induced refractive index change $\Delta\beta_j(|a_j|^2)$, can be written as:

$$\Delta\beta_j(|a_j|^2) = \pm \frac{4\kappa |a_j|^2}{P_c} \quad (4)$$

where P_c is the critical power required to decouple the waveguides sufficiently, so that light intensity is equally shared between them at a distance equal to the linear coupling length, $L_c = \pi/2\kappa$.

3 Results

A vertical NLDC has been designed, whereby the linear modal propagation constants of the individual waveguides modelled in isolation, are equal (figure 1). To create a switch, the intensity of the light acts on the resonant material nonlinearity, thereby changing the refractive index and thus creating mismatch between the waveguides. In this way a coupling-decoupling mechanism is induced in the structure dependent on the intensity of light. Realistically, it may be difficult to match the linear waveguides exactly. However, this is not a problem: if the waveguides are mismatched in the linear regime, then the waveguides can be electrically tuned to obtain a matched configuration. A schematic diagram of this design is given in figure 1, together with the corresponding TE-mode profiles for the coupled symmetric and antisymmetric *supermodes*. The coupling length for the vertical structure shown here is approximately $L_c < 200\mu\text{m}$. We have endeavoured to design a switch using realistic criteria, i.e., by adopting a

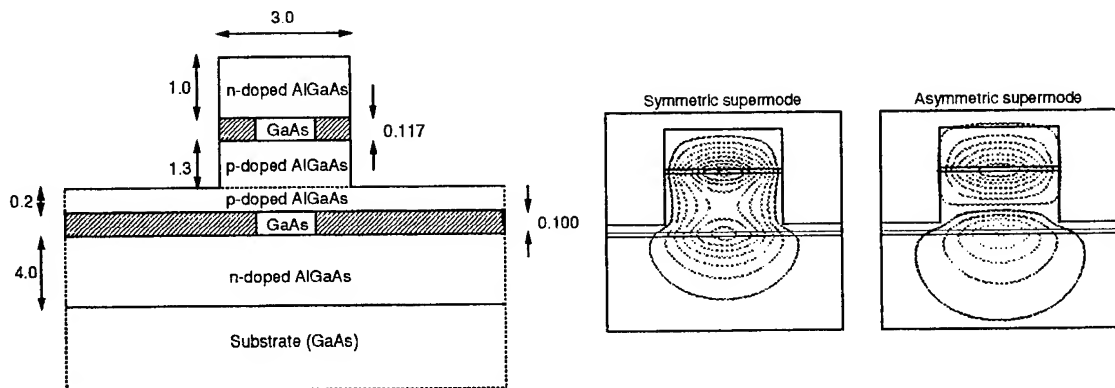


Figure 1: Schematic diagram of the vertical coupler design ($\lambda = 0.88\mu\text{m}$, and all dimensions are in μm), together with the symmetric and antisymmetric TE supermode profiles.

vertical design, it is realistic to incorporate appropriately doped layers around the waveguiding regions, to create regions that can be electrically biased at transparency to induce gain. Figure 2 indicates the switching characteristics of a vertical coupler when the predicted induced gain in the first guide is matched to the material loss in the second guide. As indicated in the figure, the reduction in switching power requirement is considerable, as $\alpha/\kappa \rightarrow \pm 0.7$ (as α/κ becomes much greater than ± 0.7 , the coupling characteristics begin to break down [3]). In

FIGURE 2: COUPLING CHARACTERISTICS WITH MATCHED GAIN TO LOSS

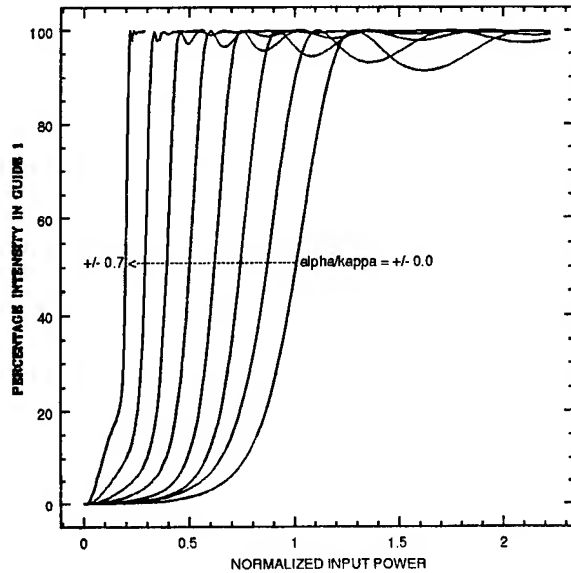
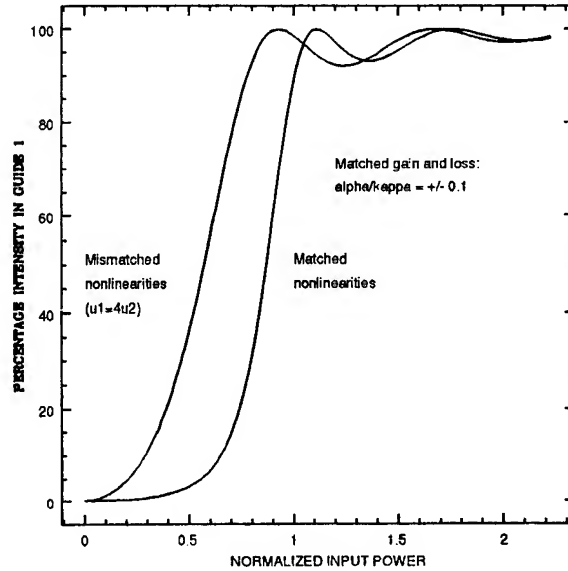


FIGURE 3: COUPLING CHARACTERISTICS WITH MISMATCHED NONLINEARITIES



addition to the above, we have predicted an additional switching power reduction associated with mismatch in the nonlinearities of the two guides (Figure 3). Nonlinearity mismatch can be achieved by using different materials (and therefore different nonlinearities) in each of the waveguides: a vertical configuration is an ideal structure to achieve this realistically. It will be extremely difficult to achieve a similar mismatch with a horizontal coupler design, where the growth processes dictate that the waveguides must be made of the same material. Furthermore, in order for the effect of the nonlinearity to be maximized, the effective area (A_{eff} , which can be estimated from the mode-profiles), should be minimized. We have found that A_{eff} can be made suitably small ($1 - 2\mu m^2$) using the vertical NLDC designs.

4 Conclusions

We have reported here for the first time semiconductor, vertical NLDC designs for use in all-optical switching devices. The structures have all been designed with realistic end-goals *i.e.*, realisable dimensions, doping levels and material compositions. It is predicted that substantial switching power reductions are achievable, and while the actual power will depend on the nonlinearity of the material, we predict that a ten-fold reduction in switching power can be attained by matching loss and gain, and creating nonlinearity mismatch in these structures.

- [1] G P Agrawal and R W Boyd (eds.) *Contemporary Nonlinear Optics* Acad. Press, Inc, 1992
- [2] D A O Davies, M A Fisher, D J Elton, S D Perrin, M J Adams, G T Kennedy, R S Grant, P D Roberts and W Sibbett *Elec. Lett.* **29** 1710-1711 (1993)
- [3] Y Chen, A W Snyder and D N Payne *IEEE J. Quant. Elect.* **28**(1) 239-245 (1992)
- [4] P N Robson and P C Kendall (eds.) *Rib Waveguide Theory by the Spectral Index Method* Research Studies Press and Wiley, New York, 1990)
- [5] S V Burke *Optical and Quantum Elect.* **26** 63-77 (1994)

Experimental Demonstration of an Optical Neural Network Using Self-Defocusing Media

Steven R. Skinner

Department of Electrical Engineering, Wichita State University, Wichita, KS 67260-0044
Phone: (316) 689-3415 FAX: (316) 689-3853 Email: srs@ee.twsu.edu

Alvaro A. Cruz-Cabrera

Department of Electrical Engineering, Wichita State University, Wichita, KS 67260-0044
Phone: (316) 689-3415 FAX: (316) 689-3853 Email: aacruz@ee.twsu.edu

James E. Steck

Department of Mechanical Engineering, Wichita State University, Wichita, KS 67260-0035
Phone: (316) 689-3402 FAX: (316) 689-3236 Email: steck@me.twsu.edu

Elizabeth C. Behrman

Department of Physics, Wichita State University, Wichita, KS 67260-0032
Phone: (316) 689-3990 FAX: (316) 689-3770 Email: behrman@wsuhub.uc.twsu.edu

Introduction

Artificial neural networks are becoming more common because they can do tasks that are difficult, or even impossible, for a common numerical processor. Their strength, compared with normal numerical processors, resides in the use of a very large number of simple processing elements that are highly interconnected. A typical artificial neural network mimics some behavioral characteristics of a brain, for example it is trained not programmed.

This paper describes an experimental demonstration of an optical neural network where a thermal self-defocusing material was used to steer light through cross phase modulation between a weight beam and a co-propagating information beam¹. The training of the network was accomplished on-line by storing the weights in a computer while presenting them to the network through a liquid crystal display (LCD)². The weights were modified in the computer by using a reinforcement learning algorithm which trained the network to realize several logic functions. Computer simulations have shown that this type of network can also solve a variety of benchmark classification problems¹.

Experimental Setup

The network realized, shown in Fig. 1, can be described as a sandwich of two thick linear layers of free space with a thin nonlinear layer between them. The thin layer is a self-defocusing thermal nonlinear material (NLM)³. The NLM index of refraction can be ideally described by $n(x,y) = n_0 + n_2 I(x,y)$ where n_0 is the linear index of refraction, $I(x,y)$ is the irradiance applied to the material and n_2 , the nonlinear coefficient, is negative. The NLM layer acts as a continuum of neurons and is where the processing takes place, while the linear layers are considered the connection layers¹. The material used as the NLM is a microscope slide melt-mount material encapsulated between two sapphire windows. The melt-mount is tinted red to absorb the green argon weighting beam. The thickness of the NLM layer is 0.45 mm with a nonlinear index of refraction measured to be $n_2 = -4.4 \times 10^{-4} \text{ cm}^2/\text{W}$ with a measured coefficient of absorption of 56.35 cm^{-1} . This thermal material is slow but permits the testing of some of the concepts described in Skinner et al¹, without having to use the amount of power required by electronic nonlinearities. The drawback with these types of materials is their high thermal diffusivity which limits the spatial resolution of the applied irradiance patterns to the material.

The network, shown in Fig. 1, uses a spatial light modulator (SLM) placed in the path of the forward beam. The SLM encodes the inputs on the forward beam by changing the irradiance spatial

profile of the beam. The set up used a HeNe laser as the forward beam, with a 15 mW output and a 3.54 mm $1/e^2$ irradiance diameter. The input SLM is a 64 gray level liquid crystal display (LCD). The input mask is encoded as two dark bars located in the center of the screen, each bar representing one of two logic states: the presence of a bar indicates a logic "1," and the absence a logic "0." The source of the weighting beam is an argon ion laser with an output power of 800 mW and is cross polarized with respect to the forward beam to prevent interference. The weighting beam diameter is 5.22 mm $1/e^2$ at the location of the NLM layer, placed 53 cm after the input mask. A pinhole and photo-detector are placed 74 cm after the NLM layer, where the output of the system is the average irradiance measured by the detector. In order to take out high frequency noise, the output is averaged over 200 samples. The output is then normalized according to: $O_{out} = 10(O_i/N - 1)$ where O_i is the output power obtained for i^{th} input and N is the average output power for all four inputs.

The weighting mask is stored and changed in a computer by using a training algorithm developed specifically for this network. The algorithm is based on a paradigm known as reinforcement learning. The method is slow but simple: the network is trained by altering the irradiance profile of the weighting beam by changing the transmittance at a certain location of the LCD. If a change in the transmittance decreases the overall error of the network, then the change is kept, otherwise the LCD is returned to its former transmittance value.

The network was trained using two desired values, -1 for a logic "0" and 1 for a logic "1". If the desired value for a certain output were a logic "1" and the actual value were larger than 1, then the error for that value was considered 0. The same applies to the case where the desired value was -1 and the obtained value was less than -1.

Results

The network was able to train five basic logic functions (AND, NAND, OR, NOR and XOR) with results depicted in Table 1. All gates were trained starting with the same hardware setup and initial conditions. Any variation on the initial values was due to the small alignment adjustment between experiments. For each set of inputs the table shows the starting and the obtained output values associated to each of the gates. The results illustrate the capabilities of the network to be trained, in spite of the problems originating from thermal diffusivity of the nonlinear material.

Acknowledgments

This work was supported in part by the National Science Foundation under grant ECS-9312345 and by the University of Kansas Center for Research, Inc.

References

- 1 S.R. Skinner, E.C. Behrman, A.A. Cruz-Cabrera, and J.E. Steck, "Neural network implementation using self-lensing media," *Appl. Opt.* **34**, 4129-4136 (1995).
- 2 F.T.S. Yu, T. Lu, X. Yang, and D.A. Gregory, "Optical neural network with pocket-size liquid-crystal television," *Opt. Lett.* **15**, 863-865 (1990).
- 3 P. L. Kelley, "Thermally self-induced phase modulation of laser beams," *Appl. Phys. Lett.* **16**, 362-365 (1970).

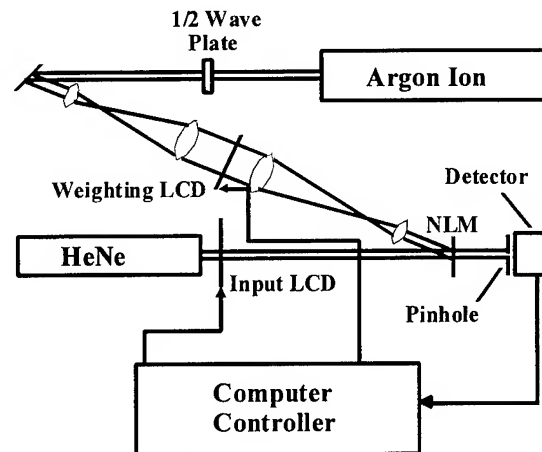


Fig. 1 - Schematic of the neural network setup

INPUT (A B)		0 0	0 1	1 0	1 1
GATE		OUTPUT			
OR	Start	0.640	0.422	0.483	-1.733
	End	-0.887	0.541	0.629	0.716
	Thresholded	0	1	1	1
NOR	Start	0.697	0.536	0.465	-1.900
	End	0.648	-0.914	-0.828	-4.082
	Thresholded	1	0	0	0
AND	Start	0.644	0.570	0.466	-1.653
	End	-1.977	-0.404	-1.395	0.323
	Thresholded	0	0	0	1
NAND	Start	0.771	0.607	0.463	-1.860
	End	1.651	1.081	1.336	-1.573
	Thresholded	1	1	1	0
XOR	Start	0.618	0.501	0.521	-1.762
	End	-0.557	0.428	0.425	-0.542
	Thresholded	0	1	1	0

Table 1 - The results of the training of five standard logic functions. Any output value greater than zero is considered a logic "1" and any value less than zero a logic "0". The table shows the normalized starting and ending output values for each of the four inputs, and the obtained thresholded output.

Dynamics of a fiber laser with two tone modulation

T. Newell, V. Kovanis, A. Gavrielides, D. Sukow, and T. Erneux
 Phillips Laboratory Nonlinear Optics Center PL/LIDN
 3550 Aberdeen Ave. SE Kirtland AFB, NM 87117-5776
 Tel: (505) 846-4750 Fax: (505) 846-1191
 email: newell@hpruby.plk.af.mil

In addition to their connection with communication networks, fiber lasers provide a rich system for the study of nonlinear dynamics. These lasers are slow in the sense that their relaxation oscillations range in the tens of kilohertz. As a result, we can study in the time domain fluctuations in the output intensity as changes occur in the pump laser. Under the influence of an oscillating pump beam, a neodymium fiber laser shows period doubling bifurcations, quasiperiodicity, chaos, coexisting attractors, and hysteresis [1-3].

Concurrently, theoretical studies in nonlinear dynamical systems have investigated the shifting of bifurcation points (possibly delaying instabilities) and the potential creation of new attractors in a system when a two tone sinusoidal modulation term is incorporated in the dynamical equations of motion. Recently, experiments in CO₂ lasers subject to two independent sinusoidal modulations have shown the bifurcation structure caused by the second modulation [4,5] but concentrated on the first period doubling transition. By contrast, our fiber laser experiments allows a systematic investigation of different transitions.

Specifically we study a neodymium doped fiber laser when the pump is modulated with a primary frequency, f , and a second frequency, $f/2$. The amplitude of the second term is on the order of 10% to 15% of the primary. We find that the bifurcation points shift with respect to a phase difference between the two waves and also shift as a function of their relative amplitudes.

A schematic diagram of the experimental setup is shown in Fig. 1. The active

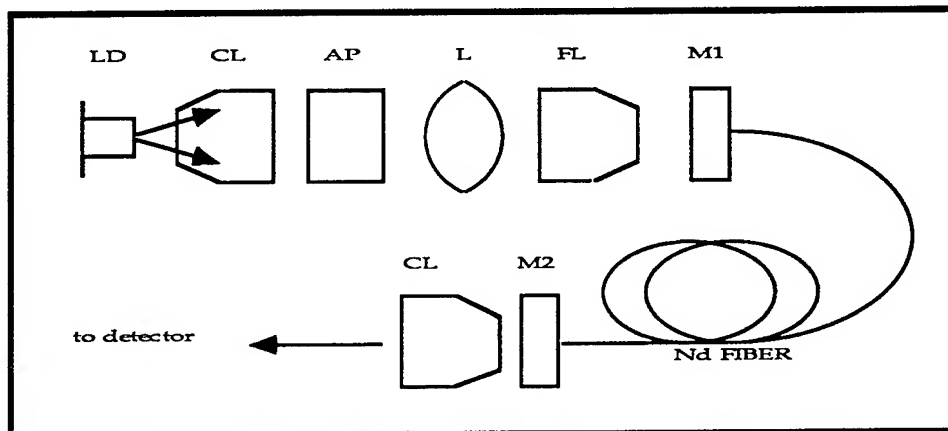


Figure 1. Experimental setup. LD laser diode, CL collimating lens, AP anamorphic prism, L lens, FL focusing lens, M1 input coupling mirror, M2 output coupling mirror.

medium is a neodymium doped silica core single mode fiber. The fiber is 3m long and has a core diameter of 3.5 mm. The medium is strongly absorbing at 810nm and lases at $\lambda=1088$ nm. Mirrors at the ends of the fiber form the cavity. The input coupling mirror is highly reflective at 1088nm and highly transmitting at 810nm. The output mirror is highly reflective at 810nm and 95% reflective at 1088nm. The output intensity is recorded with a 10-bit resolution digitizer. When the laser pump current is modulated sinusoidally in a frequency range from 12kHz to 25kHz, the CW output of the laser is replaced by a pulse train that period doubles on the drive wave as the frequency is increased (See Fig. 2) and displays complex behavior indicative of chaos.

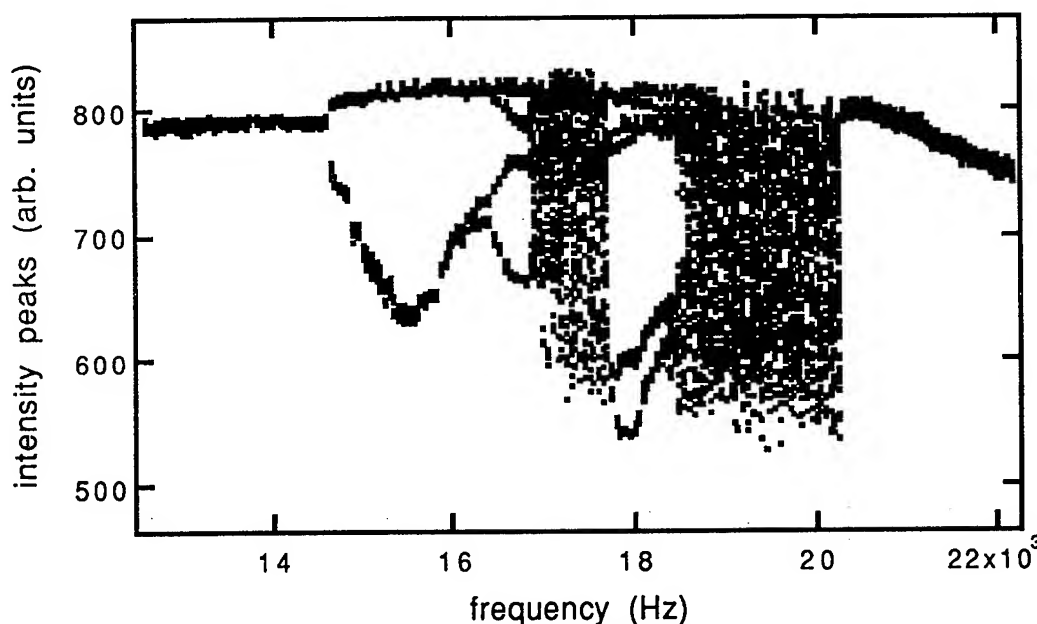


Figure 2. Bifurcation diagram of the peaks of the intensity as a function of a single tone drive frequency. The driving frequency is near the relaxation oscillation of the laser.

The experiment examines the behavior of the system and its bifurcation points when the system is subjected to a near-resonant perturbation. That is, we normally drive the system through the pump field with a signal such as $A_0 + A_1 \cos(2\pi f_1 t)$. A subharmonic oscillation, $A_2 \cos(2\pi f_2 t + \phi)$, where $f_2 = f_1/2$ and ϕ is a relative phase difference between the driving term and the perturbation term, is then added to the primary driver. We fix A_0 , A_2 , and f_1 then observe the effect of varying ϕ and A_1 on the dynamics of the system. The experiment shows the shifting of bifurcation points across the two dimensional parameter space. Periodic orbits may be stable over a region in which they were previously unstable, or they may become unstable in a previously stable region.

A compact way to represent the various regions of periodicity along with the bifurcation points is to generate a two-dimensional bifurcation diagram. For this type of diagram, we determine the periodicity of the laser dynamics on a grid of the two parameters, A_1 and ϕ . A data acquisition algorithm would set a value for ϕ , sweep through values of A_1 incrementally, then increment ϕ , and so on. At each point (A_1, ϕ) the program would examine the peaks of the time series and determine the periodicity of the wave. The results are shown in Fig. 3. On this two-dimensional grid, we have drawn

contours to distinguish the borders between regions of different periodicity. While there is complex behavior occurring, the effect of shifting the bifurcation point is quite apparent. There is a large island of period-2 behavior in the upper left half of the figure. As A_1 increases along the horizontal axis, the system eventually bifurcates into a period-4 regime. However, the particular value of A_1 at which the bifurcation occurs depends smoothly on the phase.

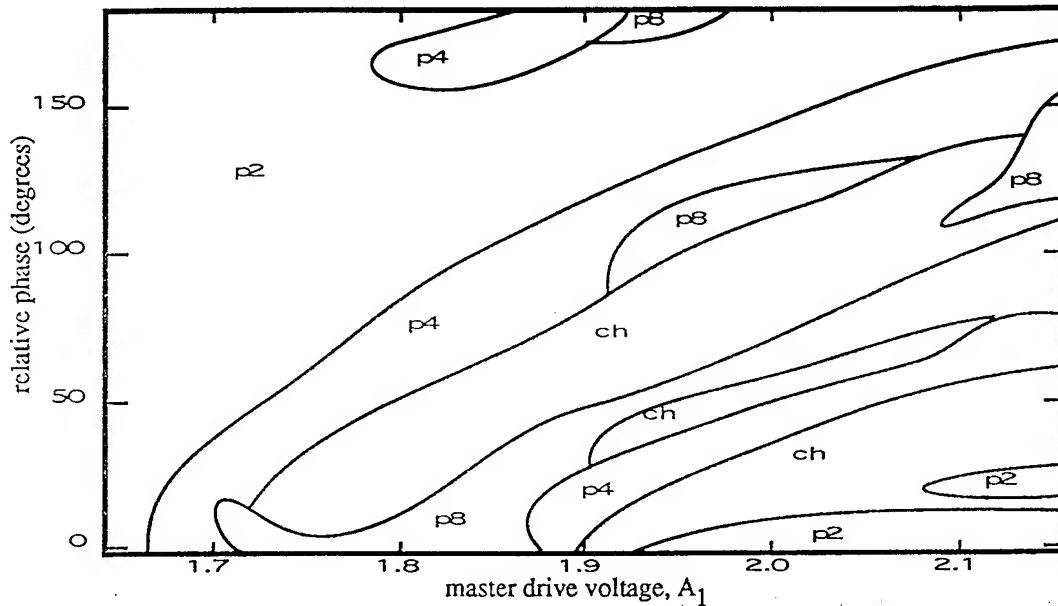


Figure 3. A two dimensional bifurcation diagram showing the different regions of periodicity. The vertical axis ϕ between the two drive terms while the horizontal axis plots A_1 . Bifurcation points are seen as the dividing lines.

In conclusion, we have investigated the nonlinear dynamical behavior in a driven Nd-doped fiber laser system. We have found that the application of a small subharmonic perturbation, with a period twice that of the drive, has dramatic effects on the system dynamics. Bifurcation points can be shifted positive or negative, depending on the amplitude of the perturbation and the relative phase between the perturbation and the master driving signal. By using this procedure, the fiber laser can be stabilized in a periodic orbit at pump amplitudes that would otherwise render the fiber laser in a chaotic state.

- [1] M.W. Phillips, H. Gong, A.I Ferguson, and D.C. Hanna, *Optics Comm.* **68**, 215 (1987).
- [2] D. Derozier, S. Bielawski, and P. Glorieux, *Optics Comm.* **83**, 97 (1991).
- [3] S. Bielawski, D. Derozier, and P. Glorieux, *Phys. Rev. A* **46**, 2811 (1992).
- [4] R. Corbalan, J. Cortit, A.N. Pisarchic, V.N. Chizhevsky and R. Vilaseca, *Phys. Rev. A* **51**, 663 (1995).
- [5] P. Glorieux, C. Lepers, R. Corbalan, J. Cortit, A.N. Pisarchic, *Opt. Comm.* **118**, 309 (1995).

Modeling CW, Bulk Periodically Poled LiNbO₃ Optical Parametric Oscillators With Strong Idler Absorption

Dennis D. Lowenthal

Aculight Corporation
40 Lake Bellevue, suite 100
Bellevue, WA 98005

(206) 451-9558 Ph (206) 451-9438 Fax
e-mail: dlowen@aculight.com

Abstract

An analytical model was developed to predict the performance of cw, singly resonant, optical parametric oscillators with strong idler absorption, strong pump depletion and thermally induced dephasing. Optimum beam sizes for a given crystal length are chosen consistent with the Boyd and Kleinman approach. Comparisons are presented with existing data and full diffraction code modeling with good agreement. In some cases idler absorption enhances the pump depletion by impeding back conversion.

Introduction

Analytical solutions have been reported for cases with no pump depletion and absorption; and pump depletion and no absorption. Here a solution is described that includes: strong pump depletion, strong idler absorption and thermal induced dephasing effects. The results indicate that materials like bulk periodically poled LiNbO₃ (PPLN) can generate significant powers at idler wavelengths of 4.5 μm , with reasonable efficiencies, where the idler absorption is strong at $\sim 35\%/cm$

Analytical Model

Because this is a cw model, the power of the resonated (signal) wave will be at least one order of magnitude larger than the power of the pump or idler waves. Further, the resonated (signal) wave will not change magnitude more than a few percent within the OPO crystal. Under these conditions the three wave equations can be reduced to two: the pump and the non-resonated (idler) wave. The signal wave is approximately constant. The resulting equations are

$$\frac{dE_p(z)}{dz} = iK_p E_s(0) E_l(z) \exp(-i\Delta kz), \quad \frac{dE_l(z)}{dz} = iK_l E_s^*(0) E_p(z) \exp(+i\Delta kz) - \frac{\alpha}{2} E_l(z)$$

Taking the second derivative of these two equations and then combining (requires lengthy algebraic manipulation) one obtains a solution for the idler wave output 'power' as

$$|E_I(\ell)|^2 = \left[K_I^2 |E_S(0)|^2 |E_P(0)|^2 \ell^2 \right] \left[\exp(-\alpha \ell / 2) \frac{(\exp(-a\ell) + \exp(+a\ell) - 2\cos(bZ))}{4\rho\ell^2} \right]$$

In these expressions, α is the intensity absorption coefficient, and a , b , and ρ are listed below.

$$a = 2\sqrt{\rho} \sin\left(\frac{\theta}{2}\right), \quad b = 2\sqrt{\rho} \cos\left(\frac{\theta}{2}\right), \quad \cos(\theta) = \left(\frac{a}{\rho}\right)$$

$$\rho = \sqrt{\left[K_I K_P |E_S(0)|^2 + \left(\frac{\Delta k}{2}\right)^2 - \left(\frac{\alpha}{4}\right)^2 \right]^2 + \left[\frac{\alpha \Delta k}{4} \right]^2}$$

The change in the circulating signal power can now be obtained from the Manley-Rowe relations modified for idler absorption as

$$|E_S(\ell)|^2 - |E_S(0)|^2 = \frac{\lambda_s}{\lambda_I} \left[|E_I(\ell)|^2 + \alpha \int_0^\ell |E_I(Z)|^2 dZ \right]$$

From these expressions a complete solution for the singly resonant OPO with idler absorption can be found. However, it is useful, in terms of understanding how these expressions are used, to take the limit where there is no absorption or dephasing. In this limit the equation for the idler output power becomes:

$$|E_I(\ell)|^2 = \frac{\lambda_s}{\lambda_I} \left[K_S K_I |E_P(0)|^2 \ell^2 \right] \left[|E_S(0)|^2 \text{Sinc}^2\left(\sqrt{K_I K_P |E_S(0)|^2} \ell\right) \right].$$

The first term in square brackets is the nonlinear drive ($C^2 L^2 I_P$), and the second terms in square brackets represents the effects of pump depletion. As the nonlinear drive increases the idler output power cannot increase without limit, and it is the pump depletion term that provides this control by setting the circulating signal power level, $|E_S(0)|^2$. This becomes clearer when we note that the signal gain in the OPO must be equal to the signal losses. In a ring cavity this loss is the output coupling, other ring cavity losses and signal absorption in the crystal. This is expressed as

$$\frac{|E_S(\ell)|^2 - |E_S(0)|^2}{|E_S(0)|^2} = \left[K_S K_I |E_P(0)|^2 \ell^2 \right] \text{Sinc}^2\left(\sqrt{K_I K_P |E_S(0)|^2} \ell\right) = \text{SigLoss}.$$

This equation, and its equivalent with idler absorption and dephasing included, is the key to a solution. When the circulating signal power is low, the Sinc function is unity and the nonlinear drive must equal the signal loss to reach threshold. Above threshold, the

circulating signal power increases until the Sinc function and nonlinear drive product is equal to the signal losses. Once the circulating signal power is found, then the signal output and the idler output power is determined from the above expressions. With idler and signal absorption included the solution must be found using an iterative approach. This is because the heat generated in the absorption process causes dephasing, which

impacts the conversion efficiency. Absorption of the circulating signal power is also important because it is a primary contributor to temperature variations in the crystal. The absorption at the signal wavelength is weak compared to the idler, but the circulating signal power reaches several hundred watts compared to 2-10 Watts for the idler. Our results provide: efficiency, circulating signal power, output signal power, output idler power, idler power absorbed, signal power absorbed, temperature variations across the optical beams in the crystal and an estimate of the resulting dephasing based on the nonlinear material temperature sensitivity. Beam size and crystal length are chosen consistent with the Boyd and Kleinman approach that sets the effective nonlinear drive through the $h(\xi, B)$ parameters.

Results

An interesting example is an OPO pumped at $1.49 \mu\text{m}$ and producing $2.23 \mu\text{m}$ and $4.5 \mu\text{m}$ power. In this case there is considerable absorption at the idler wave of 25-35% per cm. Without idler absorption loss, the predicted output idler power is, of course, greater; however, the analysis presented here shows that it appears feasible to obtain significant $4.5 \mu\text{m}$ output even with the large idler absorption. Figure 1 illustrates this effect where we plot the signal and output power vs. the PPLN length. In this case the pump power at $1.49 \mu\text{m}$ is taken as 20 Watts, and the signal output coupling was chosen at 3%. Figure 1 shows the results with 1%/cm and 35%/cm idler absorption. As expected, the idler output

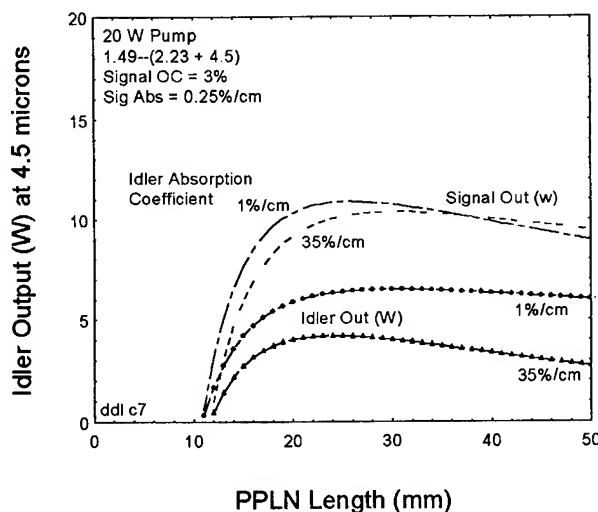


Figure 1a, The output power is not severely impacted by the 25%/cm idler absorption still providing >10 W output.

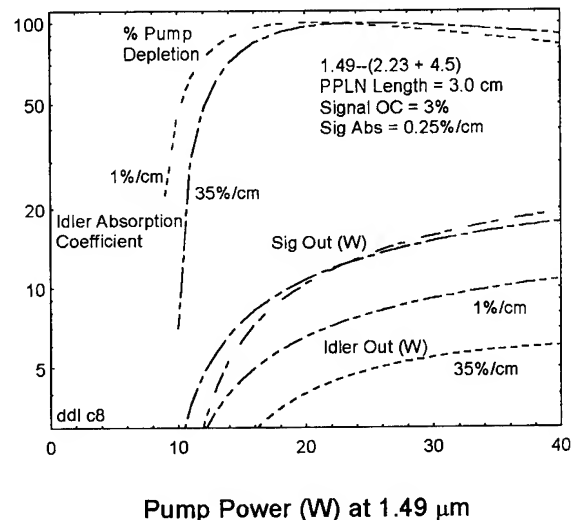


Figure 1b, Predictions show the power is sensitive to losses in the resonated signal wavelength.

power peaks at different PPLN lengths depending on the degree of idler absorption. Also, the idler output power drops from about 7 Watts to 4 Watts when idler absorption is added. It is quite interesting to note that at about 3 times threshold the signal output is larger for the case where there is only 1%/cm idler absorption. However, above this pump power level, the signal power output is greater for the case where the idler absorption is 35%/cm. This is because the idler absorption delays the onset of back conversion.

Recent Advances in Blue and Green Diode-Pumpable

Upconversion Fiber Lasers

R. K. Jain, G. S. Feller, B. Srinivasan, and M. C. Nostrand*

Center for High Technology Materials, Univ. of New Mexico, Albuquerque, NM 87131

Phone: (505) 277-2610 Fax: (505) 277-4853

**Presently at U.C. Davis, Livermore, CA*

Upconversion fiber lasers appear as promising candidates of infrared diode pumpable sources of blue and green radiation^{1,2} at moderate output power levels (~50 - 200 mW). Despite significant technological advances made by direct doubled-diode sources and doubled diode-pumped solid state lasers, recent improvements in the reliability and cost of fluoride fibers have made upconversion fiber lasers competitive as compact blue and green sources, particularly with regard to choices of specific wavelengths and power levels needed for numerous applications such as full color displays, high performance imaging and printing (e.g. for digital radiography), high capacity optical storage, satellite-to-satellite communications, semiconductor wafer inspection systems, and biotechnology (specifically for flow cytometry and phase fluorometry systems).

In this talk we will describe our recent results in several areas related to blue and green upconversion fiber lasers, including:

1) 50 mW Er:ZBLAN fiber laser at 544 nm. We have demonstrated the highest combination of slope efficiency (37%) and output power levels yet demonstrated for a 544 nm Er:ZBLAN fiber laser (see Figure 1 for output power characteristics) by appropriate choice of dopant density, material quality and fiber design (core diameter, NA and length). Mechanisms leading to the saturation of the output power at high pump intensities, and possible solutions for their alleviation will be discussed in the presentation.

2) Use of novel Raman fiber laser pump sources for 480 nm operation of a Tm:ZBLAN laser. We have used a Raman fiber laser³⁻⁵ based on standard silica fiber to access the 1120 - 1140 nm 3-photon upconversion pump band of Tm, a spectral region in which high power diodes are not readily available. In our initial experiments, the Raman fiber (see Figure 2) was a first Stokes 1118 nm laser pumped by a 6 W Nd:YAG laser; an output power of 1.4 W was obtained from such an 1118 nm fiber Raman laser, well above the 120 mW threshold pump power for our

480 nm Tm:ZBLAN fiber laser. We are currently designing and constructing a second Stokes Raman fiber laser operable at the optimized pump wavelength of 1130 nm when pumped by a 2 W 980 nm diode laser. The advantage of using fiber Raman lasers as pumps is their relative easy scalability to Watt-level 1130 nm pump powers with the use of diode pumps at 980 nm, a wavelength at which very reliable high power diode pumps are readily available.

3) Mode-locked operation of Tm laser. We will describe results on the self-mode-locking of an upconversion fiber laser; more specifically, a CW mode-locked pulse train of a repetition rate of 300 MHz was obtained from the Raman fiber laser (1118 nm) pumped 482 nm Tm:ZBLAN fiber laser of 33 cm length (see Figure 3). Competition between the pump-induced photodarkening and absorption saturation is believed to be the most likely mode-locking mechanism. We will also describe details of our studies of the multiphoton absorption (1118 nm) induced photodarkening of the Tm:ZBLAN fiber at 482 nm, and on the "healing" or saturation of this 482 nm absorption with the use of blue (482 or 488 nm argon ion laser) radiation.

4) New co-doped rare-earth systems for blue upconversion. We will describe our work on the study of excitation transfer in new rare-earth co-doped fluoride glasses to enable blue laser sources that are pumpable directly by relatively convenient high power diode pump wavelengths (i.e., 800 nm or 980 nm). Figure 4 depicts an example of such a system in which the blue emission (at 482 nm) occurs from Tm subsequent to appropriate excitation transfer of energy from the $^4F_{3/2}$ level of Nd to the $^3F_4 \rightarrow ^1G_4$ transition of Tm. Details of this and other promising co-doped candidate systems, as well as calculations based on a rate-equation analysis of such systems will be presented in the talk.

Work is currently in progress on improvement of a 491 nm Pr/Yb:ZBLAN upconversion fiber laser (pumped near 800 nm) by reducing the role of gain competition from other laser lines originating from the 3P_0 upper laser level (common to the desired 491 transition and the competing 520 nm and 635 nm transitions). We anticipate also being able to present results of such work in this presentation.

References

1. S. Sanders et al. "Laser diode pumped 106 mW blue upconversion fiber laser" *Applied Physics Letters*. **67**, 1815 (1995)
2. D. Piehler et al. "Green laser diode pumped erbium fiber laser" Compact Blue Green Lasers '94, Paper CFA2, Salt Lake City (1994)
3. R.K. Jain et al. "A high-efficiency tunable cw Raman oscillator" *Applied Physics Letters*. **30**, 162 (1977)
4. S.G. Grubb et al., "1.3 μ m cascaded Raman amplifier in germanosilicate fibers" Optical Amplifiers and Applications Technical Digest, PD3-2 (1994)
5. We thank Drs. S. G. Grubb and A. M. Vengsarkar of Lucent Technologies (Bell Labs) for fabrication and splicing of the in-line fiber gratings to the 2 km long fused silica fiber that constitutes the gain medium for this Raman fiber laser.

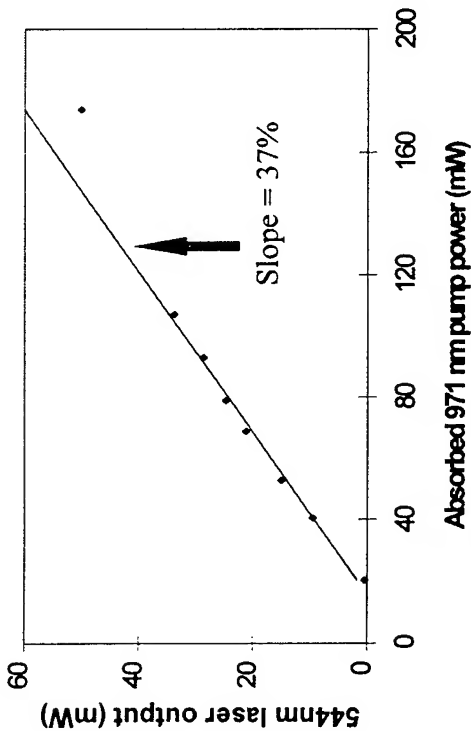


Fig 1: Output power of the 544 nm Er:ZBLAN fiber laser as a function of the absorbed pump power

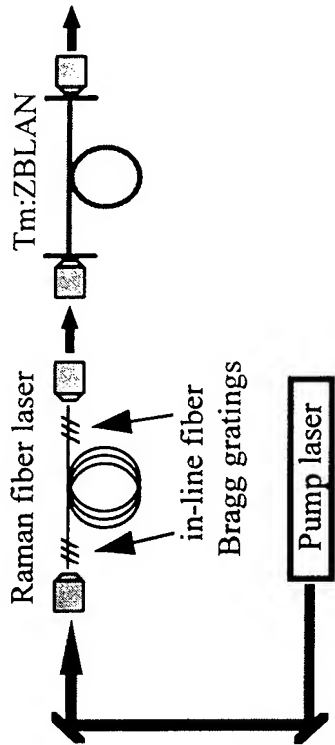


Fig 2: Schematic of experimental setup depicting a Raman fiber laser-pumped blue (482 nm, Tm:ZBLAN) fiber laser

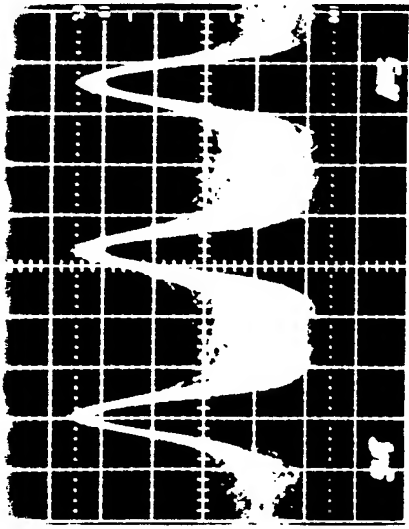


Fig 3: Oscilloscope trace depicting 300 MHz rep. rate pulse train from a 482 nm self-mode-locked Tm:ZBLAN laser

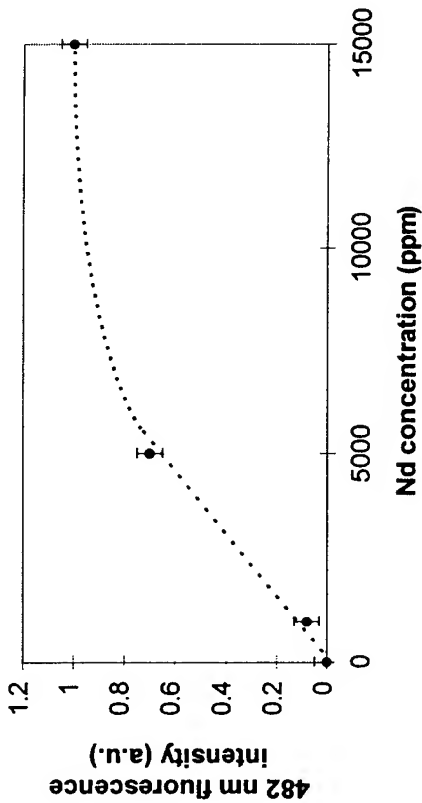


Fig 4: 482 nm fluorescence intensity as a function of Nd concentration in 800 nm-pumped Tm/Nd co-doped system

Industrial Laser Ultrasonic Inspection System Using A DPCM for Wavefront Compensation

**G.J. Dunning, D.M. Pepper*, P.V. Mitchell,
M.B. Klein, and T.R. O'Meara
Hughes Research Laboratories
3011 Malibu Canyon Road
Malibu, CA 90265 USA**

***Point-of-contact: 310/317-5125 310/317-5679 (FAX)
dpepper@msmail4.hac.com (e-mail)**

We present the results of a prototype laser-based ultrasound inspection system combining a wavefront-scrubbed laser receiver with a pulsed laser ultrasonic generator. Laser-based ultrasound [1] represents a noncontact, long-standoff-distance technology to remotely inspect materials for integrity of bonds, surface treatments, thickness, defects, microcracks, and temperature. The ability to employ lasers for the diagnostic enables one to perform the inspection under harsh industrial conditions, including high temperature, radiation, and vacuum environments. The basic system involves one laser to generate acoustic modes in a material via thermoelastic and/or ablative excitation, and a second laser to sense the resultant, transient surface displacements of the workpiece, induced by the ultrasound. Neural network post-processing or rule-based algorithms can be employed to classify the detected ultrasonic signatures.

The bandwidth of the ultrasound can be in the 1 MHz to 100 MHz range, with a large fractional bandwidth (> 99%). Moreover, the induced surface displacements are typically small, in the range of nanometers. In an industrial environment, these parameters pose formidable technical challenges when using optical sensing techniques, since surface roughness of typical parts (leading to speckle noise), coupled with whole-body mechanical vibrations, can compromise the performance of coherent optical detection systems. A variety of schemes [1,2,3] have been considered to deal with these real-world scenarios, while enabling the detection of the desired ultrasound, including actively stabilized time-delay interferometers (e.g., Fabry Perots) using electro-mechanical feedback control for cavity stabilization [2,3], and reference-beam interferometers (e.g., Michelson) using phase conjugation [4] or two-wave mixing [5] for wavefront compensation.

In our approach, we employ a double-pumped phase-conjugate mirror (DPCM) [6,7] to enable wavefront scrubbing (beam cleanup) of the wavefront-distorted probe beam, while preserving high-bandwidth, global phase shifts imposed by the ultrasound. Our system has the benefit of requiring only a single pass of the workpiece undergoing inspection, thereby improving the diagnostic performance for low-reflectivity components. Moreover, the DPCM-based system does not require collection of all the scattered light for wavefront beam cleanup, thereby enabling the use of finite field-of-view collection systems, including optical fibers.

Our basic system is shown in Figure 1 and consists of a Co-doped single-crystal of barium titanate as the DPCM; a 200 mW cw diode-pumped, 2xNd:YAG laser (532 nm) as the probe; and a 100 mJ, 10 Hz, Q-switched Nd:YAG laser (1.06 microns) to generate the ultrasound. A high-speed custom f#1 optical collection system, in conjunction with polarization

decoupling techniques, was used to optimize the collection of the highly diffuse light scattered by the workpiece under inspection. The collected light was directed onto one port the DPCM, with a frequency-shifted plane-wave entering the other port. The wavefront-scrubbed beam exiting the DPCM (and preserving the ultrasonic phase modulation) was then directed to a coherent detection system, which included a dual-Si detector for common-mode rejection of the heterodyne-detected signal. A phase-lock-loop post-processor was employed to track out low-frequency, background whole-body vibrations (< 100 kHz), while passing the desired high-bandwidth ultrasound, with a bandpass of about 25 MHz. A computer-controlled data acquisition system, in conjunction with a programmable precision translation and rotation stage, enabled signal averaging as well as reproducible spatial positioning of the workpiece undergoing evaluation.

One important application of laser-based ultrasound is in the detection and spatial mapping of corrosion pits, voids, or inclusions in critical components, including airframe structures, composites, adhesive bonds, and extruded metallic stock. In Figure 2, we show an example of the capability of our system to detect spatial defects in a 30 mil steel plate. For this demonstration, small holes (15 mil in diameter) of varying depth were partially drilled into one surface of the plate at random locations to simulate corrosion pits. This sample was then placed in our system and raster scanned (with 100 micron step-size increments) across the pair of opposing "pitch-and-catch" laser beams. Good signal-to-noise was realized through the use of the DPCM-based compensated detection system. In the figure, the ultrasonic time scale is shown emerging from the page, while the transverse coordinates are shown in the plane of the figure. The defects are clearly seen as "spots" in the acoustic return, indicating the spatial location (in the transverse dimension), as well as the depth of the drilled-out hole (by virtue of the arrival time of the acoustic return).

References

1. C. Scruby and L. Drain, *Laser Ultrasonics: Techniques and Applications* (Hilgar Press, Bristol, 1990).
2. J.-P. Monchalín, IEEE UFFC 33, 485 (1986);
ibid., Rev. Prog. Quant. NDE, Vol. 12 (Plenum, New York, 1993), pp. 495-506.
3. J.W. Wagner, "Optical Detection of Ultrasound," in *Physical Acoustics, Vol. XIX*, W.P. Mason, Ed. (Academic Press, New York, 1990), pp. 201-265.
4. M. Paul, B. Betz, and W. Arnold, Appl. Phys. Lett. 50, 1569 (1987);
Y. Matsuda, H. Nakano, and S. Nagai, Jpn. J. Appl. Phys. 31, L987 (1992).
5. R.K. Ing and J.-P. Monchalín, Appl. Phys. Lett. 59, 3233 (1991);
A. Blouin and J.-P. Monchalín, Appl. Phys. Lett. 65, 932 (1994);
T. Honda, T. Yamashita, and H. Matsumoto, Jpn. J. Appl. Phys. 34, 3737 (1995).
6. S. Sternklar, S. Weiss, M. Segev, and B. Fischer, Opt. Lett. 11, 528 (1986).
A.M. Smout and R.W. Eason, Opt. Lett. 12, 498 (1987);
M. Ewbank, Opt. Lett. 13, 47 (1988).
7. D.M. Pepper, P.V. Mitchell, G.J. Dunning, S.W. McCahon, M.B. Klein, and
T.R. O'Meara, 7th Int. Sym. on Nondestr. Char. of Mat., Prague, June, 1995;
P. Delaye, A. Blouin, D. Drolet, and J.-P. Monchalín, Rev. Prog. in Quant. NDE Conf.,
Seattle, WA, August 2, 1995; ibid., Appl. Phys. Lett. 67, 3251 (1995);
H. Nakano, Y. Matsuda, S. Shin, and S. Nagai, Ultrasonics 33, 261 (1995).

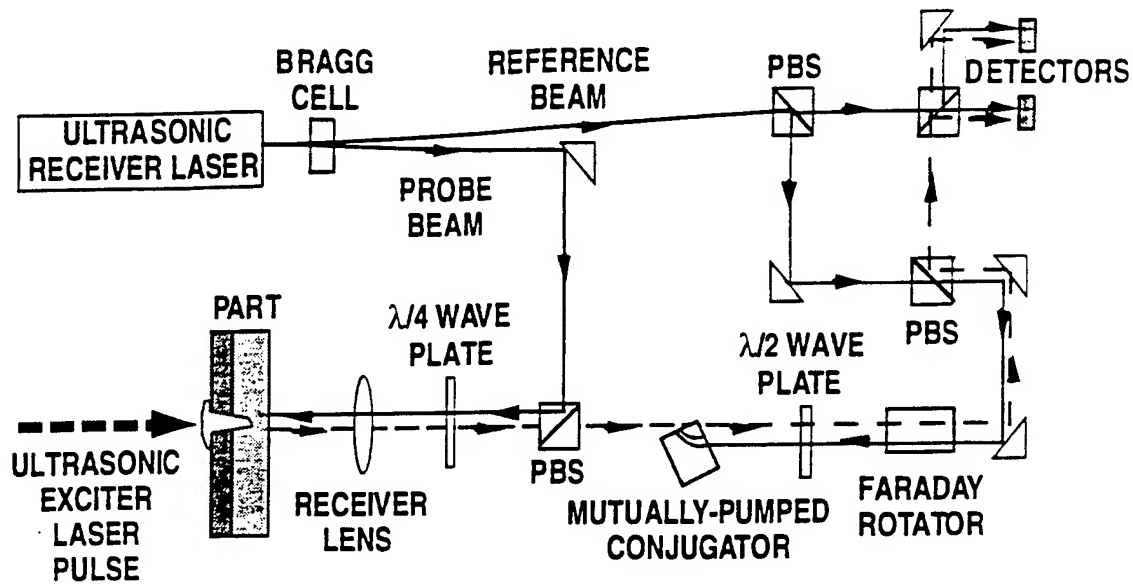


Figure 1. Schematic of laser ultrasonic receiver based on a double conjugator and heterodyne detector.

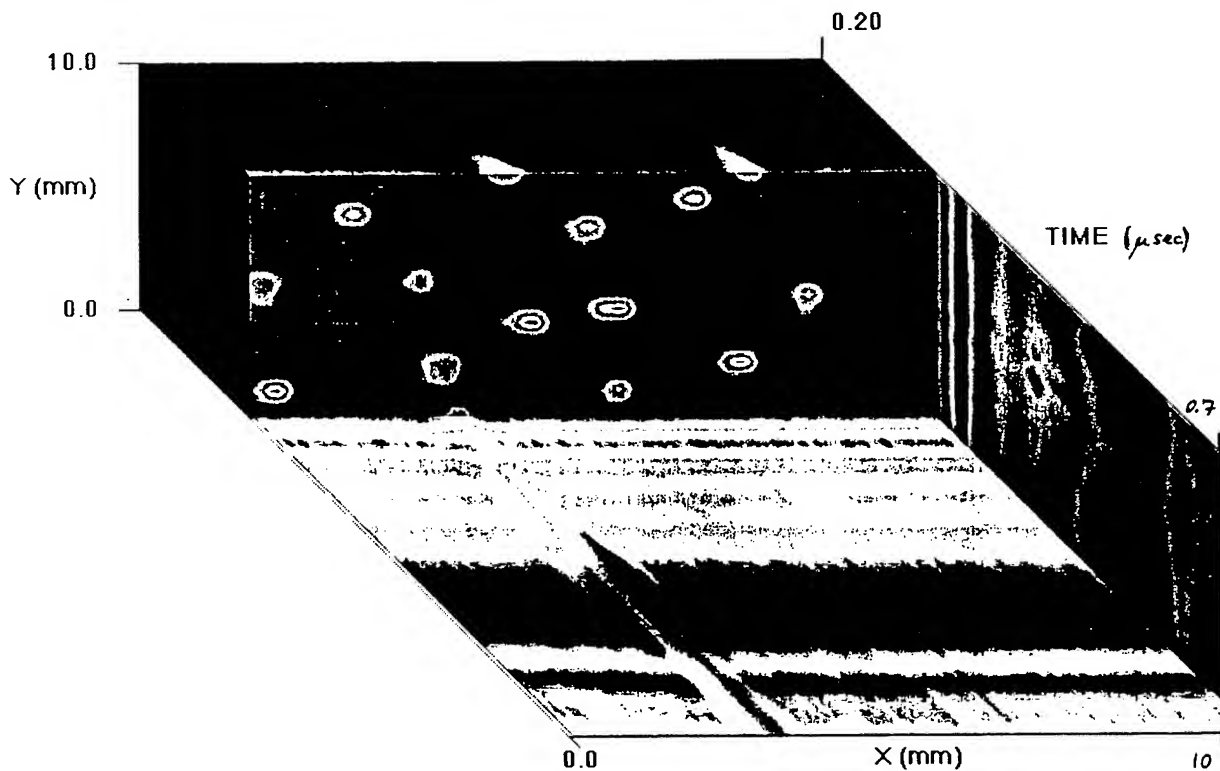


Figure 2. Raster-scanned output of the DPCM-compensated laser-based ultrasound system, demonstrating the ability to spatially locate (simulated) corrosion pits in a metallic component.

Optical switching based on singlet-singlet excited state absorption

Miao Yang, Jinhai Si, Yuxiao Wang, and Chunfei Li

Department of Physics, Harbin Institute of Technology, Harbin 150001, P. R. CHINA

Tel: 86-451-3621000 ext. 4127

Fax: 86-451-3621048

Progress in optical computing, optical communication and optical information processing depends on a large extent of the availability of fast all-optical switches. Most of the all-optical switches utilize nonlinear FP cavity^{1,2,3}. Its absorptive loss is very large because of working on the resonant wavelength, and the switching time is restricted by the response time of cavity. In 1990 K. W. Beeson⁴ presented a novel all-optical switch based on the triplet-triplet absorption in Eosin Y using a CW laser as a pump beam, and obtained μs scale switching time. We developed this kind of switches in C_{60} ⁵ whose switch off time was about 250 ns which depends on the lifetime of the first triplet excited state.

In this paper we present a new absorptive optical switching in metallo-porphyrin-like materials based on the singlet-singlet excited state absorption. The switch off time is shorter than that of the former one in one order, because the lifetime of the singlet excited state is much shorter than that of triplet excited state.

In our experiment, a pulse laser (8 ns, 355 nm) was employed as a pump beam, a CW laser (632.8 nm) as a signal beam. When the sample is excited by a strong pump laser, the output intensity of the signal laser will be suddenly switched off. The experimental result of transient optical switching is shown in Fig.1, which indicated the transmittance of the signal laser versus time within one pump pulse duration. The switch on and switch off time are both about 35 ns.

To analyze the mechanism of the all-optical switching, we present here a six-level model which is shown in Fig.2. In which S_0 is the ground state; S_1 and S_m are the first and an upper excited state in singlets, respectively; T_1 and T_m are the first and an upper excited state in triplets, respectively⁶.

The photons of the pump light (with the frequency ν_p , intensity I_p) are absorbed by molecules in the ground state; that result in the transition of molecules from S_0 to S_1 with the absorption cross section σ_0 , most of molecules in S_1 with the lifetime τ_S ($\sim\text{ns}$) transit to T_1 with the intersystem lifetime τ_{ISC} , the molecules in T_1 with the lifetime τ_T ($\sim\mu\text{s}$) return to the S_0 by the nonradiative transition. During the action of pump beam, the populations in S_1 and T_1 will accumulate, and will absorb the photons of the signal light (with the frequency ν_S off

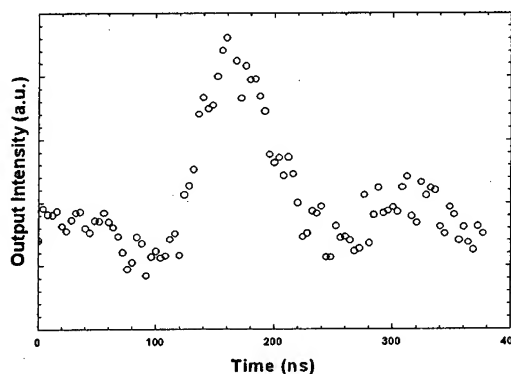


Fig.1 All-optical switching characteristic in (TXP)Gd: the transmittance versus time for the signal laser.

the absorption peak of the ground state but just near a absorption peak of the excited state) with the absorption cross sections σ'_S and σ'_T , respectively.

The variation of populations during the exciting of pump pulse in each energy-level can be described using following rate equation:

$$\frac{dN}{dt} = RN, \quad (1)$$

where N is a population vector matrix, whose component expression is

$N = (n_0, n_{S1}, n_V, n_{Sm}, n_{T1}, n_{Tn})$, where n_i indicates the population density of the i -level.

R is a 6×6 rate operator matrix,

$$R = \begin{bmatrix} -\frac{\sigma_0 I_p}{h\nu_p} & 0 & \frac{1}{\tau_s} & \frac{1}{\tau_T} & 0 & 0 \\ 0 & \frac{1}{\tau_v} & -\frac{\sigma_s I_p}{h\nu_p} - \frac{1}{\tau_s} - \frac{1}{\tau_{ISC}} & 0 & \frac{1}{\tau_{SS}} & 0 \\ 0 & 0 & \frac{1}{\tau_{ISC}} & -\frac{\sigma_T I_p}{h\nu_p} - \frac{1}{\tau_T} & 0 & \frac{1}{\tau_{TT}} \\ \frac{\sigma_0 I_p}{h\nu_p} & -\frac{1}{\tau_v} & 0 & 0 & 0 & 0 \\ 0 & 0 & \frac{\sigma_s I_p}{h\nu_p} & 0 & -\frac{1}{\tau_{SS}} & 0 \\ 0 & 0 & 0 & \frac{\sigma_T I_p}{h\nu_p} & 0 & -\frac{1}{\tau_{TT}} \end{bmatrix}, \quad (2)$$

where τ_{SS} and τ_{TT} are the lifetimes of upper excited state in singlets and triplets, respectively. Here we ignore the action of the signal light to the populations of each level, because its intensity is very weak than that of pump light.

The solutions of equations (1)-(2) and light-propagation equation give the variation of populations in each energy-level during the action of pump beam, which will cause the variation of transmittance of signal beam

$$T_s = \exp[-(\sigma'_0 n_0 + \sigma'_s n_{S1} + \sigma'_T n_{T1})L], \quad (3)$$

where σ'_0 is the ground state absorption cross section of S_0 for signal laser, L is the thickness of sample. Equation (3) indicates the variation of transmittance of the CW signal laser versus time during the action of pump pulse laser. The switch on and off times depend on the pulse width of pump laser and the lifetimes of S_1 or T_1 , respectively.

To determine the state whose absorption cause all-optical switching, we calculate the variation of transmittance of signal light versus time in different conditions, which are shown in Fig.3. Fig.3(a) and 3(b) are the results in conditions for pulse width $\tau_L > \tau_{ISC}$ and $\tau_L < \tau_{ISC}$, respectively, where curves 1, 2, 3, 4 correspond to the conditions of $\sigma'_S > \sigma'_T > \sigma'_0$, $\sigma'_S > \sigma'_0 > \sigma'_T$, $\sigma'_S > \sigma'_T \approx \sigma'_0$ and $\sigma'_T > \sigma'_S, \sigma'_0$, respectively.

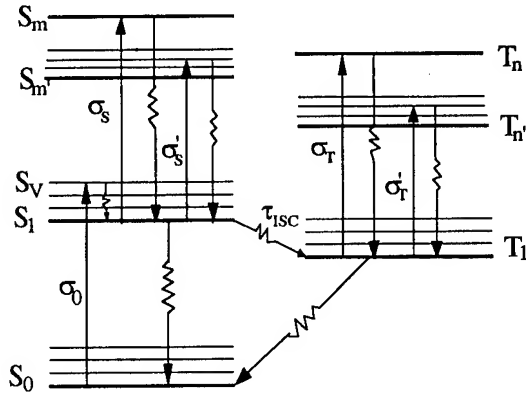


Fig.2 Energy-level diagram of metallo-porphyrin-like.

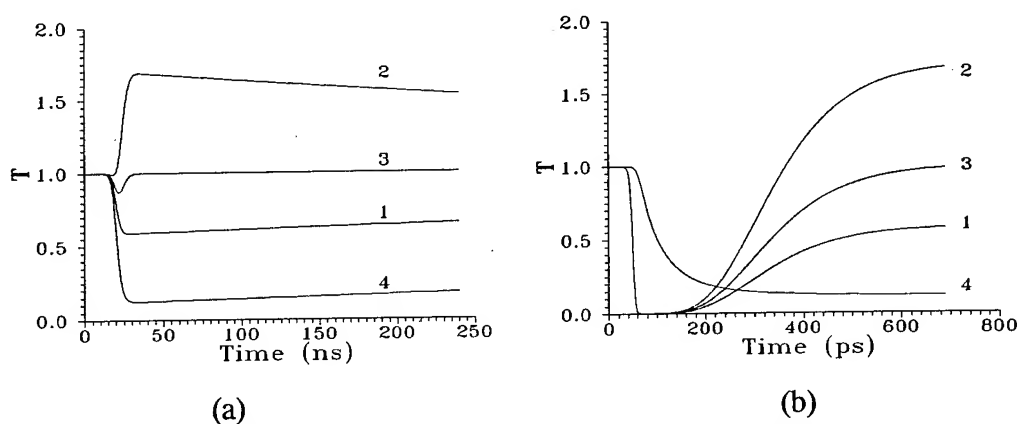


Fig.3 Theoretical calculations of all-optical switching behavior, curves 1,2,3,4 correspond to the conditions of $\sigma'_S > \sigma'_T > \sigma'_0$, $\sigma'_S > \sigma'_0 > \sigma'_T$, $\sigma'_S > \sigma'_T \approx \sigma'_0$ and $\sigma'_T > \sigma'_S$, σ'_0 , respectively, and (a) $\tau_L > \tau_{ISC}$, (b) $\tau_L < \tau_{ISC}$.

Fig.3 clearly shows that, if σ'_S is larger than σ'_T and σ'_0 , and σ'_T is close to σ'_0 (see curve 3), the singlet excited state play an important role in all-optical switching based on excited state absorption, no matter whether the pulse width is larger or smaller than the intersystem lifetime. Curve 4 shows the effect of the triplet excited state on the absorption, curve 1 shows the combination effect of the singlet and triplet excited state on the absorption, and curve 2 shows the combination effect of the excited state and ground state on the absorption.

In conclusion, a novel all-optical switching based on the singlet-singlet excited state absorption was presented and demonstrated experimentally by using (TXP)Gd. The switch on and off times are both 35 ns. Usually, the lifetime of singlet excited state is much shorter, therefore we can obtain much faster all-optical switches through selecting pump laser with short pulse and material with short lifetime of singlet excited state. Theoretical analyses show that if the absorption cross section of triplet excited state for signal light is close to that of the ground state and smaller than that of the singlet excited state, the all-optical switching will be mainly attributed to the singlet-singlet excited state absorption.

References

- [1] D. A. B. Miller, T. H. Wood, *Opt. News*, **10**, (1986)345.
- [2] D. Jager, F. Forsmann and B. Wedding, *IEEE J. Quantum Electron.*, **QE-21**, (1988)1453.
- [3] G. L. Wood, W. W. Clark, J. J. Miller et.al, *Proc. SPIE*, **1105**, (1989)154.
- [4] K. W. Beeson, J. T. Yarkley and S. Speiser, *Proc. SPIE*, **1337**, (1990)364.
- [5] Chunfei Li, Miao Yang, Fengyun Guo et.al, *Int. J. Nonlinear Optical Physics*, **2**, (1994)551.
- [6] Chunfei Li, Lei Zhang, Miao Yang, Hui Wang and Yuxiao Wang, *Phys. Rev. A*, **49**, (1994)1149.
- [7] B. G. Maiya, A. Harriman, J. L. Sessler, G. Hemmi, T. Murai and T. E. Mallouk, *J. Phys. Chem.*, **93**, (1989)8111.

Generalized Dispersion Equations for Nonlinear Waveguides with Kerr-type Films

Jong-Sool Jeong, Seok Ho Song, and El-Hang Lee

Research Department, Electronics and Telecommunications Research Institute,

Yusong P.O.Box 106, Taejon, 305-600, KOREA

(FAX: +82-42-860-5033, e-mail: jeong@utopia.etri.re.kr)

The characteristics of planar waveguides with nonlinear layers has been extensively studied due to their potential application as all-optical switching and signal-processing element [1-3]. Here we present a generalized form of nonlinear dispersion equations for various nonlinear waveguide structures with Kerr-type films. By using the relation of the interface electric fields, we obtain the generalized form of nonlinear dispersion equations as an analytic form. The "generalized" means that the equation can represent most of nonlinear waveguide structures with up to five linear and/or nonlinear layers. For example, we apply the generalized dispersion equation to 4-types of nonlinear waveguide structures: I) the waveguides with a nonlinear core layer, II) the waveguides with two nonlinear core layers, III) the planar structures having a linear core with nonlinear surrounding media, and IV) the five-layer nonlinear waveguides having symmetric or asymmetric structures.

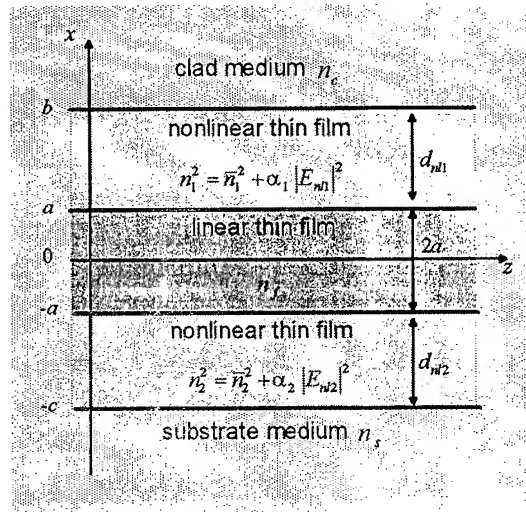


Fig. 1. Schematic drawing of the nonlinear waveguide bounded by two nonlinear layers.

The electric field $E_{nli}(x)$ of the i th nonlinear thin film having Kerr-like refractive indices of $n_i^2 = \bar{n}_i^2 + \alpha_i |E_i|^2$ ($i=1,2$) with self-focusing nonlinear coefficient, α_i , can be expressed by Jacobian elliptic function

$$E_{nli}(x) = p_i \text{cn}[k_0 q_i (x + x_{0i}) | m_i], \quad (1)$$

where k_0 is the free-space wavenumber, x_{0i} is an integration constant indicating the location of the maximum field, $p_i = q_i \sqrt{2m_i/\alpha_i}$, $q_i^2 = (\bar{n}_i^2 - \beta^2)/(1 - 2m_i)$, $m_i = (|\Gamma_i| - (\bar{n}_i^2 - \beta^2))/2|\Gamma_i|$, $\Gamma_i^2 = (\bar{n}_i^2 - \beta^2)^2 + 2\alpha_i C_{nli}$, and $C_{nli} = (\bar{n}_i^2 - n_{c,s}^2)E_{0i}^2 + \alpha_i E_{0i}^4/2$ with the mode index β , the interface electric field E_{0i} , and the clad (substrate) refractive index n_c (n_s). The integration constant x_{0i} can be obtained from the relation of

$$\text{sn}^2(k_0 q_i x_{0i} | m_i) = \frac{(1 + \zeta_i) - \left[(1 + \zeta_i)^2 - 4m_i \zeta_i \right]^{1/2}}{2m_i} \quad (2)$$

with $\zeta_i = (2m_i - 1)(\beta^2 - n_{c,s}^2)(\beta^2 - \bar{n}_i^2)^{-1}$.

After appropriately manipulating the conservation constants, we can obtain the relation between the interface electric fields E_{01} and E_{02} in the five-layer waveguides with either symmetric or asymmetric structure, shown in Fig. 1. With the help of the relation between the interface electric fields and the boundary conditions at each interface, we find a generalized form of the dispersion equation as follows:

$$\tan \theta = \frac{U_1(\beta, E_{01}) - U_2(\beta, E_{02})}{(-1)^h + U_1(\beta, E_{01}) U_2(\beta, E_{02})}, \quad (3)$$

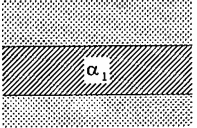
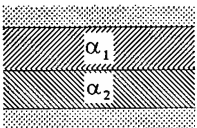
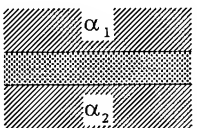
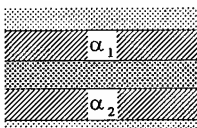
where

$$U_i(\beta, E_{0i}) = \frac{q_i}{\gamma_f} \frac{\text{sn}(u_i | m_i) \text{dn}(u_i | m_i)}{\text{cn}(u_i | m_i)} \quad (4)$$

with $\theta = 2ak_0\gamma_f$, $\gamma_f = \sqrt{n_f^2 - \beta^2}$, $u_1 = k_0 q_1(a - b + x_{01})$, and $u_2 = k_0 q_2(c - a - x_{02})$. Eq.(3) is valid with $h = 0$ for $n_f > \beta$. In case of $n_f < \beta$, it can be readily shown that Eq.(3) is valid with \tan replaced by \tanh and $h = 1$. Since Eq.(3) is based on the relation between the electric fields of E_{01} and E_{02} at the interface of the upper nonlinear layer and the lower nonlinear layer, the equation can be readily applied to the various nonlinear waveguide structure. First, in case of $a = b = c$, $U_i(\beta, E_{0i})$ becomes q_i/γ_f with $m_i = 1$ and $x_{0i} \rightarrow \infty$, and therefore Eq.(3) becomes the dispersion equation for the three-layer linear waveguide. And in case of $a = c = 0$, the five-layer waveguide becomes the three-layer waveguide with the nonlinear core layer and Eq. (3) becomes $\text{sn}(u_1 | m_1) \text{dn}(u_1 | m_1) / \text{cn}(u_1 | m_1) = q_2/q_1$, which is similar to the unified nonlinear dispersion equation by Li *et al.* [2]. Similarly, there is readily obtained the dispersion equation for the waveguide having two nonlinear core layers, $\text{sn}(u_1 | m_1) \text{dn}(u_1 | m_1) \text{cn}(u_2 | m_2) / \text{sn}(u_2 | m_2) \text{dn}(u_2 | m_2) \text{cn}(u_1 | m_1) = q_2/q_1$. And in case of $b, c \rightarrow \infty$, $U_i(\beta, E_{0i})$ approaches $q_i \tanh(u_i) / \gamma_f$ with $m_i \rightarrow 1$, $(b - x_{01}) \rightarrow x'_{01}$, and $(c - x_{02}) \rightarrow x'_{02}$, and Eq.(3) is simplified to the dispersion equation of the planar waveguides

having a linear core with nonlinear surrounding media, presented by Seaton *et al.* [3]. The dispersion equations for the various nonlinear waveguide structures are presented in Table I.

Table I. Nonlinear dispersion equations of the various nonlinear waveguides.

Case	Waveguide Structures	Nonlinear Dispersion Equations
I		$\frac{\text{sn}(u_1) \text{dn}(u_1)}{\text{cn}(u_1)} = \frac{q_2}{q_1}$
II		$\frac{\text{sn}(u_1) \text{dn}(u_1) \text{cn}(u_2)}{\text{sn}(u_2) \text{dn}(u_2) \text{cn}(u_1)} = \frac{q_2}{q_1}$
III		$\tan \theta = \frac{\gamma_f [q_1 \tanh(u_1) - q_2 \tanh(u_2)]}{(-1)^h \gamma_f^2 + q_1 q_2 \tanh(u_1) \tanh(u_2)}$
IV		$\tan \theta = \frac{\gamma_f [q_1 \text{sn}(u_1) \text{dn}(u_1) \text{cn}(u_2) - q_2 \text{sn}(u_2) \text{dn}(u_2) \text{cn}(u_1)]}{(-1)^h \gamma_f^2 \text{cn}(u_1) \text{cn}(u_2) + q_1 q_2 \text{sn}(u_1) \text{dn}(u_1) \text{sn}(u_2) \text{dn}(u_2)}$

In conclusion, we have obtained a novel, generalized nonlinear dispersion equation for various nonlinear waveguides with Kerr-type films. The analytic form of nonlinear dispersion equations has been derived by using the relation between the interface fields. The dispersion equation shows a generalized form, which can be applied to I) the waveguides with a nonlinear core layer, II) the waveguides with two nonlinear core layers, III) the planar structures having a linear core with nonlinear surrounding media, and IV) the five-layer nonlinear waveguides having symmetric or asymmetric structures. Similarly, our method can be also applied to the analysis of nonlinear waveguide systems with self-defocusing nonlinear thin films.

REFERENCES

1. J.-S. Jeong, C. H. Kwak, and E.-H. Lee, *Opt. Commun.*, **116**, 351 (1995).
2. Y.-F. Li and K. Iizuka, *IEEE J. Quantum Electron.*, **QE-31**, 791 (1995).
3. C. T. Seaton *et al.*, *IEEE J. Quantum Electron.*, **QE-21**, 774 (1985).

All-Optical Switching in Waveguide Structures Due to Cascaded Nonlinearities

R. Schiek, Y. Baek, G. Krijnen, and G. I. Stegeman

Center for Research and Education in Optics and Lasers, University of Central Florida

4000 Central Florida Blvd., Orlando, FL 32816-2700, USA

Fax: 407 823 6955, email: roland@soliton.creol.ucf.edu

Introduction:

The second-order nonlinear interaction between a fundamental light wave and its second harmonic causes energy transfer between the interacting waves (second harmonic generation (SHG)) and modifies their phases nonlinearly (cascaded nonlinearity) [1]. This implies that all-optical switching can be implemented on the basis of cascading in phase-sensitive waveguide structures [2].

This idea was experimentally verified using Ti-indiffused LiNbO₃ waveguide devices. In order to generate an intensity-dependent phase shift for the fundamental light wave via the cascaded nonlinearity, SHG was implemented by coupling fundamental TM-modes to second harmonic TE-modes. Phase shifts are the largest near phase-matching. For a fundamental with a wavelength of 1.32μm the two modes are phase-matched around 340°C for our geometry and material. Due to a nonuniform wavevector mismatch along the propagation length (caused by the temperature profile in the waveguide and a slight waveguide inhomogeneity), we can obtain large nonlinear phase shifts along with only small fundamental depletion [3]. Phase shifts larger than π were measured with less than 10% net conversion to second harmonic, ideal for an efficient all-optical switching device such as directional couplers and Mach Zehnder interferometers [4]. We simulated the intensity-dependent wave propagation in two linear coupled straight waveguides and in asymmetric integrated waveguide Mach Zehnder interferometers taking into account the details of the experimental conditions. Based on the simulations sets of nonlinear directional couplers (NLDC) and Mach Zehnder interferometers (MZ) were designed and fabricated. The Y-cut samples were 5cm long with propagation along the X-axis.

Nonlinear Directional Coupler:

We obtained half-beat-, full-beat- and one-and-a-half-beat-length couplers. In order to characterize the nonlinear switching light was incoupled in only one coupler arm. The output at the fundamental wavelength from both coupler branches was separated and measured independently. The nonlinear switching was verified by two separate sets of measurements. First, we kept the input power constant. By ramping the temperature through phase-matching, the wavevector mismatch was varied, which in turn changed the magnitude of the effective nonlinearity, i.e. the phase shift. Fig. 1 shows a typical result for a half-beat-length coupler. Far below the phase-matching temperature of $T_{PM} \approx 345^\circ\text{C}$ weak cascading does not influence the coupling. At the device output all the incoupled light has coupled over into the cross coupler branch. Approaching the phase-matching temperature the induced nonlinear phase shift decreases the coupling and some light stays in the input waveguide, the coupler begins to switch. For temperatures above T_{PM} large phase shifts still detune the coupling but the nonlinear switching is accompanied by strong second harmonic generation and signal depletion. In a second set of measurements we also measured the output dependent on the input power at fixed temperatures. Fig. 2 shows a switching curve at a crystal temperature of 343.5°C. In the low fundamental depletion region below phase-matching the switching curves

are comparable to switching curves of $\chi^{(3)}$ -based NLDCs. We observed increasing switching power for increased wavevector-mismatch, i.e. decreased cascaded nonlinearity. Also the full-beat-length coupler showed the expected nonlinear switching.

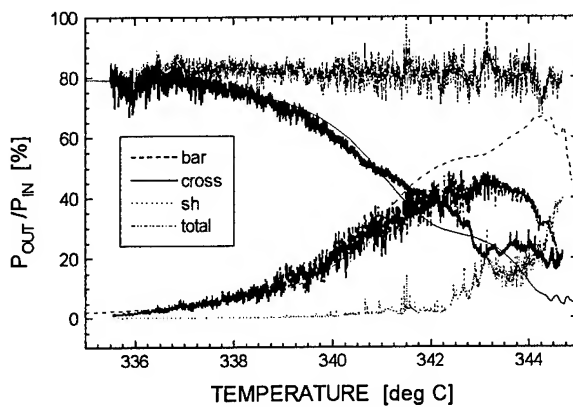


Fig. 1: Temperature-dependence of the normalized output of a NLDC for an input of 6000W.

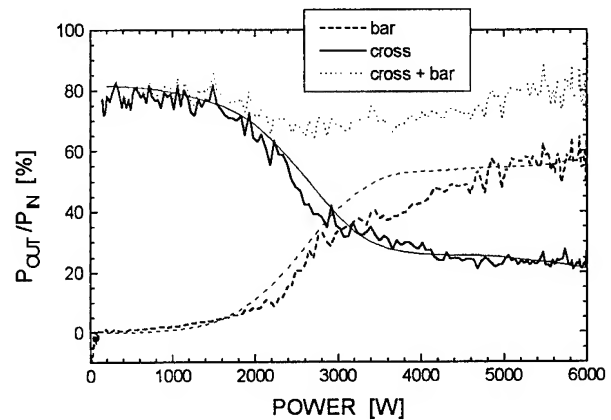


Fig. 2: Power-dependence of a NLDC fundamental output for a temperature of 343.5 °C.

Mach Zehnder Interferometer:

The integrated Mach Zehnder interferometer consists of two symmetric Y-junctions (Fig. 3). At the first Y-junction, the input beam is equally split into each of the two arms. In one arm, the width of the channel waveguide is tapered down from 15 μ m to 11 μ m. The separation between two arms is 80 μ m which is wide enough to prevent linear coupling. At the second Y-junction, the light from two channels is recombined, causing interference effects. With small variations in the radius of the Y-junction bends we were able to obtain MZs with different initial linear phase differences between the channels of approximately zero and π .

Because of the difference in the widths of the two interferometer arms the phasematching temperatures in both arms are different. A typical SHG tuning curve in Fig. 4 shows the two resonance temperatures separated by 2.5K.

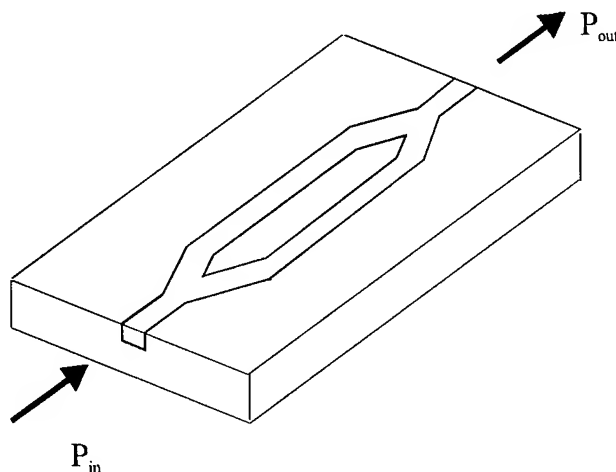


Fig. 3: Configuration of the integrated Mach Zehnder interferometer.

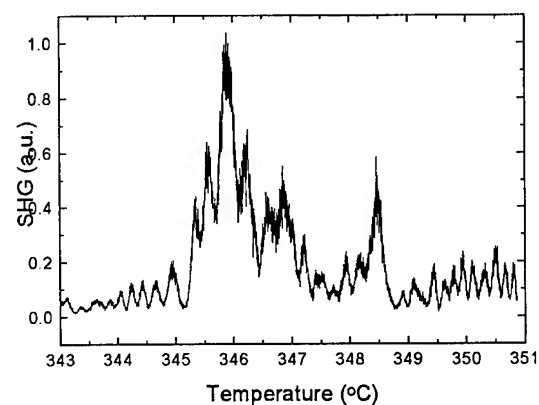


Fig. 4: Measured temperature dependence of SHG for a peak input power of 150W. (The first peak around 346°C corresponds to the 15 μ m arm and the second one around 348.5°C corresponds to the 11 μ m arm.)

This yields different amounts of the nonlinear phase shift due to different strong cascading in each arm at a fixed temperature. The resulting intensity-dependent interference in the second Y-junction enables all-optical switching. We chose the temperature of the switching experiments around 344°C which is in the low depletion region below both phase-matching temperatures. Figure 5 shows the fundamental output of the Mach Zehnder interferometer, normalized to the input power. Due to the differences in the effective length of the arms, the switching curves start either in the "on" or "off" conditions. As we increased the input power, due to the cascaded second-order nonlinearity the difference in amounts of the induced phase shift of each arm increases. Therefore, the output is changed from "on" to "off" or vice versa. Pulse break-up is responsible for the incomplete switching. But because of the nonlinear dependency of the phase shift on the input power in the cascaded second-order nonlinearities we obtained a better switching ratio than usually achieved with third-order nonlinear materials. In our waveguide geometry the actual length of the arms which contribute to the generated phase differences is only 18 mm. Also, because the separation of the two resonances is only 2.5K, the nonlinear phase shift from the 11μm wide arm is not zero and is still significant at the switching temperature. Consequently, the switching power was much higher than for the previous hybrid switching case [4].

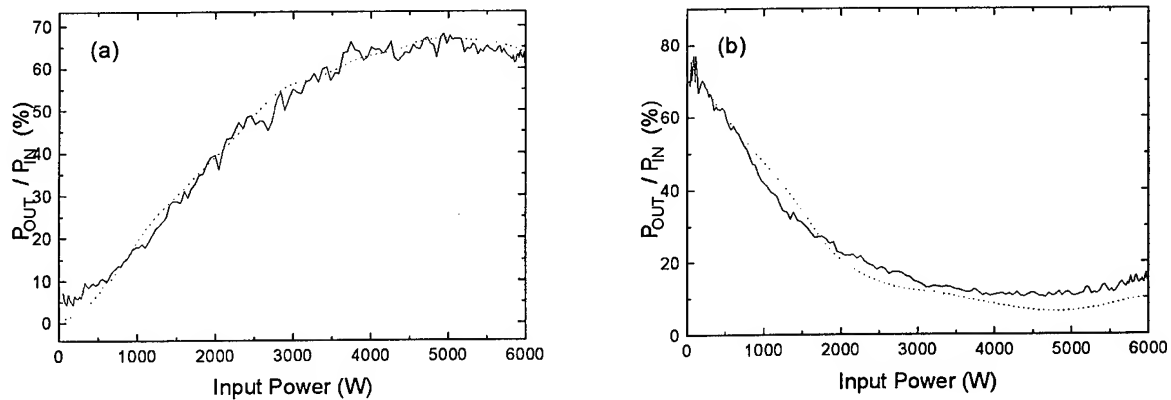


Fig. 5: Measured transmittance of a LiNbO₃ integrated Mach Zehnder interferometer as a function of the peak input power, (a) initial relative phase between the interferometer arms of ≈ 0 , (b) initial phase of $\approx \pi$ (solid curves: experiment; dotted curves: theory).

Conclusion:

In summary, we have reported all optical switching in fully integrated directional couplers and Mach Zehnder interferometers due to the cascaded second-order nonlinearity. We reached switching ratios of up to 8:1. To the best of our knowledge, these represent the first integrated all-optical switching devices using cascaded second order nonlinearities.

We thank Dr. Sohler from the University Paderborn for the preparation of the excellent waveguides.

References:

- [1] A. Armstrong, N. Bloembergen, J. Ducuing, and P. S. Pershan, *Phys. Rev.* **127**, 1918 (1962)
- [2] R. Schiek, *J. Opt. Soc. Am. B* **10**, 1848 (1993)
- [3] R. Schiek, M. L. Sundheimer, D. Y. Kim, Y. Baek, G. I. Stegeman, H. Seibert, and W. Sohler, *Opt. Lett.* **19**, 1949 (1994)
- [4] Y. Baek, R. Schiek, and G. I. Stegeman, *Opt. Lett.* **20**, 2168 (1995)

Coherent transient in optical lattices : Application to quasi-periodic optical structures

L. Guidoni, C. Triché, S. Guibal, P. Verkerk and G. Grynberg

Laboratoire Kastler-Brossel; Département de Physique de l'Ecole Normale Supérieure

24 rue Lhomond, 75231 Paris Cedex 05, France

(Tel: 33 1 44 32 34 55; Fax: 33 1 45 35 00 76)

We present a new method of spectroscopy for atoms cooled and trapped in an optical lattice. This method which makes use of *coherent transients* permit to improve the signal to noise ratio by more than one order of magnitude by comparison with the previous optical detection methods such as probe transmission or atomic fluorescence [1]. We apply this method to the spectroscopy of cesium atoms first in a *four-beam lattice* [2] and second in a *quasi-periodic* structure obtained by adding supplementary incident beams. These structures are strongly connected with the field of quasi-crystals [3] which is very active in solid-state physics. Because of the *topological invariance* of the optical potential, the same spectra are obtained whatever the phases of the incident beams. Additional information about distribution of atoms among the potential wells can be deduced from the analysis of the coherent transients.

We first describe the principle of the experiment. We consider a standard four beam optical lattice consisting of two *x*-polarized beams propagating in the *yOz* plane and making an angle 2θ , and two *y*-polarized beams propagating in the *xOz* plane and making the same angle 2θ . The lattice beams have a frequency ω . A probe beam of frequency ω_p is applied along the *z*-axis. At a certain time, the frequency of the probe beam is suddenly switched from ω_p to another value $\omega_p + \omega_s$ and the transient variation of the beat note due to superposition of probe and coherently diffused light is recorded. The value of ω_s is sufficiently large so that the medium is almost transparent to the probe after the frequency jump. We present in Figs 1.a and 1.b the time dependence of the light emitted in the probe direction for two values of ω_p . The double selectivity at the excitation and at the detection thus permits to achieve almost pure Rayleigh (Fig 1.c) and vibrational Raman (Fig 1.d) spectra.

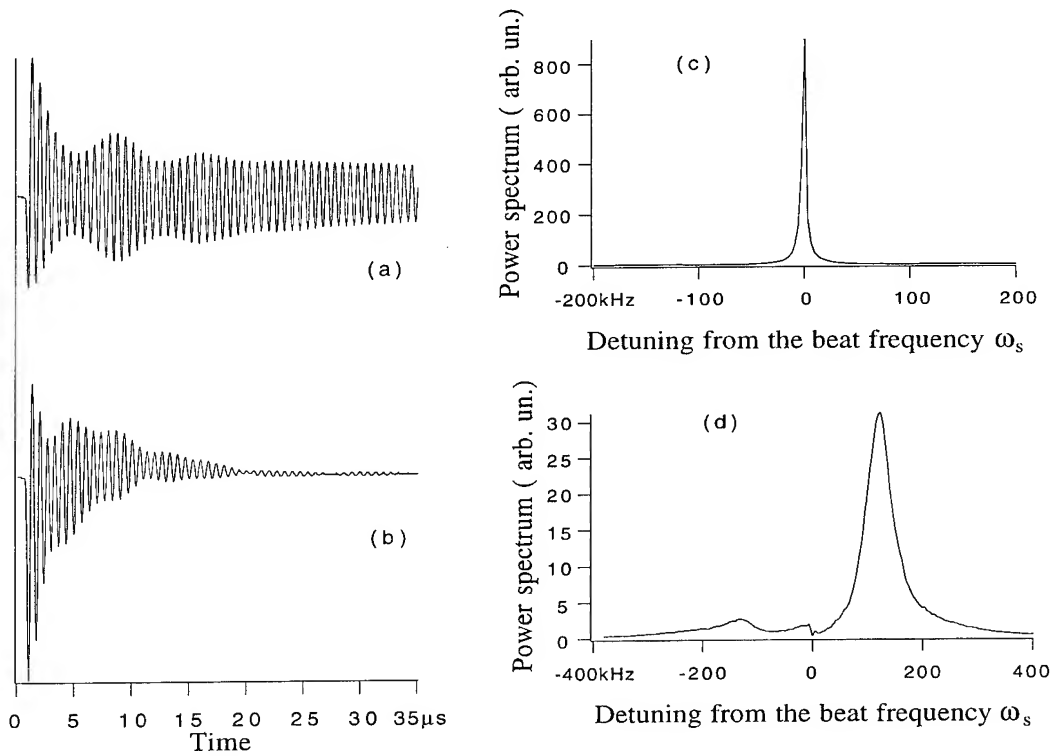


Figure 1 : Time dependence of the light emitted in the probe direction after a probe frequency jump, in the case where initially $\omega_p = \omega$ (a) and when $\omega_p - \omega$ is close to the vibration frequency of the atoms at the bottom of the optical potential wells (b). The square modulus of the Fourier transforms of these signals are shown in (c) and (d).

If the probe intensity is increased, a *saturated dip* centered around the probe excitation frequency appears in the Raman line when an *inhomogeneous* broadening occurs (Fig.2). Such a dip is extremely useful when the depths of the optical potential wells vary over a large range. This is, for instance, the case when one considers a quasi-periodic lattice obtained by adding to the four beams of the lattice a standing wave along the z axis. In this case, the optical potential obtained from the superposition of the six travelling waves depends on the relative phases between the beams. However, it can be shown that all the potentials obtained by changing the phases, although different, are topologically equivalent in the sense that they lead to the same statistical distribution of wells. Indeed, we have checked that the vibration spectrum is always the same independently of the relative phases of the incident beams. Furthermore, with an intense probe, we use the saturated dip of Fig.2 to test selectively various classes of potential wells corresponding to different vibrational frequencies. In this way we can have an estimate of the relative atomic populations in these different potential wells.

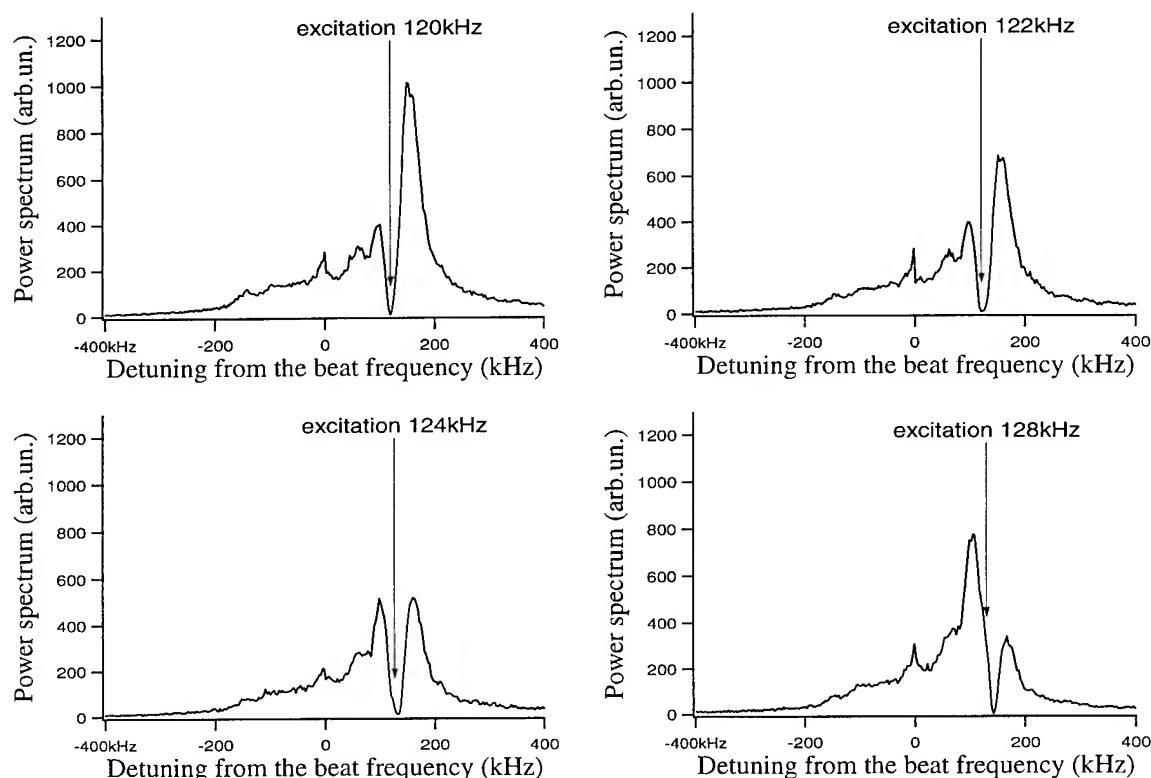


Figure 2 : Square of the Fourier transform of the light emitted in the probe direction in the case of a quasi-periodic structure. The saturated dip occurring at the probe excitation frequency ω_p shows the occurrence of an inhomogeneous broadening. The four spectra correspond to different excitation frequencies.

References:

- [1] Verkerk P., Lounis B., Salomon C., Cohen-Tannoudji C., Courtois J.-Y. and Grynberg G., *Phys. Rev. Lett.* **68** (1992) 3861 ; Jessen P. S., Gerz C., Lett P., Phillips W. D., Rolston S., Spreuw R. and Westbrook C., *Phys. Rev. Lett.* **69** (1992) 49
- [2] Verkerk P., Meacher D. R., Coates A. B., Courtois J.-Y., Guibal S., Salomon C. and Grynberg G., *Europhys. Lett.* **26** (1994) 171
- [3] Hippert F. and Gratias D., *Lectures on quasicrystals* (Les Editions de Physique, 1994); Axel F. and Gratias D., *Beyond quasicrystals* (Springer-Verlag and Les Editions de Physique, 1995)

Localization and coupling dynamics in nonlinear waveguide arrays

Alejandro B. Aceves and Marco Santagiustina

*Department of Mathematics, University of New Mexico,
Albuquerque, New Mexico 87131, tel 505 277 2114, fax 505 277 5505*

Several efforts have been made to study the pulse dynamics in nonlinear waveguide (WG) arrays. Steady-state solutions are known for N-periodic WG arrays [1] and the dynamics of 2-coupled WG's have been investigated by means of variational methods [2, 3].

The dynamics of N-coupled WG's has been studied mostly through numerical solutions, due to the difficulty of applying any analytical approach because of the great number of parameters that must be used. However these numerical results demonstrate that energy localization may take place [4], thus the dynamics becomes predominant in a few (mainly three) WG's [5, 6].

In the presentation we will show, to our knowledge for the first time, a variational approach to an asymmetric coupled system of three WG's, which besides its own merit, may mimic under certain conditions the N-WG array. The governing equation for this problem can be derived from the Lagrangian density, which reads $L = L_q + L_u + L_v + L_{int}$, where: $L_f = i/2(f^* f_z - f f_z^*) - 1/2|f_t|^2 + 1/2|f|^4$, $f = q, u, v$ and $L_{int} = -K(uq^* + u^*q + vq^* + v^*q - 2(|q|^2 + |u|^2 + |v|^2))$. First, we calculate a reduced Lagrangian density \mathcal{L} , by integrating L over t and by approximating the solutions with the following simple trial functions $f(z, t) = \eta_f \text{sech}(\eta_f t) \exp(i\phi_f)$, $f = q, u, v$. We then obtain a set of ODE for the parameters $\eta_{q,u,v}$ and $\phi_{q,u,v}$. If the initial conditions are symmetric in the lateral WG's we can impose $u(z, t) = v(z, t)$ and remove the eqs. for η_v and ϕ_v . Moreover, the remaining eqs. are invariant with only phase shifts thus we may consider only the differential phase $\phi = \phi_q - \phi_u$. Finally, a conserved quantity ($P = \eta_q + 2\eta_u$) is found, allowing us to take into account only a normalized amplitude difference $\eta = (\eta_q - 2\eta_u)/P$. The complete analysis leads to the equations,

$$\begin{aligned} \eta_Z &= \frac{\partial H}{\partial \phi} = (\eta^2 - 1) \sin(\phi) I(\eta) \\ \phi_Z &= -\frac{\partial H}{\partial \eta} = \beta(3 + 10\eta + 3\eta^2) + \frac{d}{d\eta} [(\eta^2 - 1) \cos(\phi) I(\eta)] \end{aligned} \quad (1)$$

where the Hamiltonian is $H(\eta, \phi) = \beta(3\eta + 5\eta^2 + \eta^3) + (\eta^2 - 1) \cos(\phi) I(\eta)$, $I(\eta)$ is an overlap integral that can be analitically calculated only in special cases, $\beta = P/(16K)$ and $Z = KPz$.

This system can be studied through the topology of its phase space. In particular we note there are two unstable (saddle) fixed points at $\eta = \pm 1$ and $\phi_+ = \cos^{-1}(-P^2/2\pi K)$, $\phi_- = \cos^{-1}(-P^2/16\pi K)$, provided that $K > P^2/2\pi$ and $K > P^2/16\pi$ respectively. Note that for $K \rightarrow \infty$ these phases tend to $\pm\pi/2$. Physically these points represent the conditions $\eta_q = P, \eta_u = 0$ and $\eta_q = 0, \eta_u = P/2$. Note that, like in the case of a two-core waveguide [3], for each value of K there exists a (switching) threshold value of the input power for a single WG (in our case P_{th}) beyond which almost all the power remains localized in the same WG. In practice the phase space is divided for each possible P into two main regions: the first characterized by a possible net flux of energy among the WG's, the second by a localized state with almost fixed amplitude, though the phase may vary.

Additional critical points are found at $\phi = 0$ or $\phi = \pi$; the values of η can be found solving a trascendental equation that can be obtained by setting to zero the second of eqs. (1) with $\phi = 0, \pi$. The bifurcation diagram for $P = 3$ of the critical points is presented in fig. 1; note that it has been transformed back into the parameter space (η_0, ϕ) for the sake of clarity. Observe that as $K \rightarrow 0$ the critical point approaches the soliton solution of the uncoupled WG's (the amplitude in the other two WG's are in fact given by $\eta_u = \eta_v = (P - \eta_q)/2$) as clearly predictable.

An example of the orbits of the phase plane ($P = 3 \ll P_{th}$) is given in fig. 2 for $K = 10$. On the same figure, we projected some of the solutions of the governing equations, obtained by a finite-difference numerical integration scheme, with transparent boundary conditions. This must be used due to radiation emanating from the pulse.

Numerical solutions confirm the validity of the approach, regarding the position of the fixed points in the infinite-dimensional space and the estimate of the period of coupling.

In fig. 3 we present the wavenumber spectrum of the central WG pulse amplitude in the propagation direction, obtained by Fourier transforming the peak amplitude waveform as a function of Z . The peak on the right hand side is the coupling frequency, which compares well with the predicted value of 5.75. Observe also that other features appear in the low frequency range; they represent a weak modulation that we interpret as a result of the pulse-radiation interaction. In fact, the governing equations are not integrable and using as an initial condition the soliton solution of the unperturbed equation, leads to the generation of radiation which interacts [7] with the pulse. Assuming that the coupled system will reach at its final steady-state ($Z \rightarrow +\infty$) the solution indicated by the variational approach (the center of the ODE model becomes an attractor due to radiation emission), i.e. $\eta_q = 1.22$ and $\eta_u = \eta_v = 0.89$ we can calculate an approximate frequency of the oscillations due to the pulse-radiation interaction. It is in fact known [7] that if the initial condition is an amplified or damped soliton of the form $\gamma\eta_0 \text{sech}(\eta_0 t)$ ($K \rightarrow 0$) the final state will be $\eta_{fin} = (2\gamma - 1)\eta_0$ which will be approached with oscillations of frequency $\nu = \eta_{fin}^2/2\pi$. In our case, the final state is imposed by the coupling structure and we may use the values of the critical points obtained through the variational approach to estimate the frequencies of oscillation. The result is $\nu_q = 0.23$ and $\nu_u = 0.12$, which are very close to those observed in fig. 3. They are both present in the q pulse because of the coupling among the WG's.

We finally comment on the localization effect; numerical solutions indicate it may occur when the power is above a certain K -dependend threshold, as we mention above. For initial conditions different from a soliton, eg. a strongly amplified soliton $\gamma\eta_0 \text{sech}(\eta_0 t)$ ($\gamma/K \gg 1$), self-focusing prevails and a different dynamics appears. This can be observed in fig. 4, where we show that the pulse amplitude starts to oscillate very rapidly around a new final state, which cannot be inferred through a variational approach since it is not due to coupling. In this case we can define a total variance of the energy distribution as

$$\theta = \sum_n \int_{-\infty}^{+\infty} (n^2 + t^2) |f_n|^2 dt \quad (2)$$

where $f_{-1,0,1} = u, q, v$, and derive a dynamics for θ , using a virial-like model. We find an equilibrium point, which determines the amplitude (inverse width) of the localized state. Details of this theory will be given at the presentation, but the prediction is

$$\eta_c = \left(\frac{9}{4}P - \frac{3}{2}H \right)^{\frac{1}{3}} \quad (3)$$

where P, H are the initial power and energy. In fig. 4, we compare the average amplitude value and the prediction of eq. (3); this good agreement occurs for a wide range of initial conditions.

References

- [1] A.V. Buryak, N.N. Akhmediev, IEEE JQE, QE-31, 682 (1995).
- [2] C. Paré, M. Florjańczyk, Phy. Rev. A, 41, 6287 (1990).
- [3] P.L. Chu, B.A. Malomed, G.D. Peng, JOSA B, 10, 1379 (1993).

- [4] A.B. Aceves, G.G. Luther, C. De Angelis, A.M Rubenchik, S.K. Turitsyn, Phys. Rev. Lett., 75, 73 (1995).
- [5] A.B. Aceves, C. De Angelis, S. Trillo, S. Wabnitz, Opt. Lett., 19, 332 (1994).
- [6] A.B. Aceves, C. De Angelis, A.M Rubenchik, S.K. Turitsyn, Opt. Lett., 19, 329 (1994).
- [7] A.Z. Kuznetsov, A.V. Mikhailov, I.A. Shimokhin, to be published, Opt. Comm. (1996).

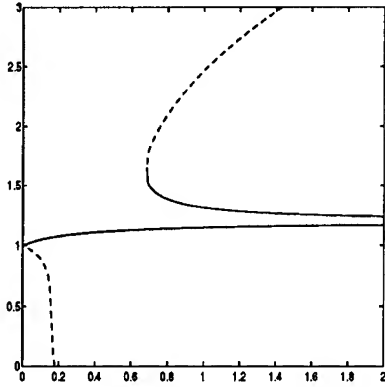


Figure 1: Bifurcation diagram (η vs. K) of the critical point of eqs. (1) ($P = 3$)

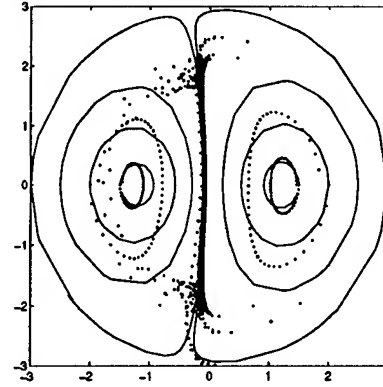


Figure 2: Phase plane ($\eta_0 \cos(\phi)$ vs. $\eta_0 \sin(\phi)$) for $K=10$, of the Hamiltonian system (1) (solid lines) and projection of the numerical solution (dots).

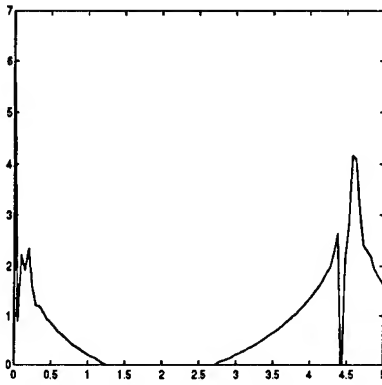


Figure 3: Spectral amplitude (log scale) vs. wavenumber of $\eta_0(z)$ as a result of the numerical solution ($P = 3, K = 10, \eta_0(0) = 2, \phi(0) = 0$).

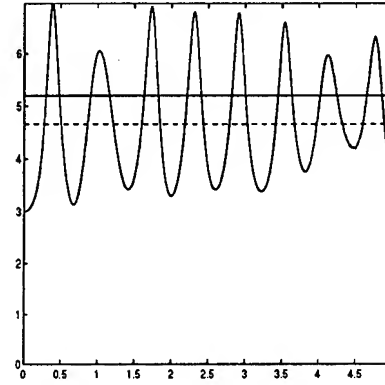


Figure 4: Peak amplitude vs. z plot for initial condition that leads to pure localization dynamics ($K = 1, P = 3, \eta_0(0) = 1, \gamma = 2.99$). The dashed straight line is the amplitude average, while the solid straight line is the predicted steady-state (eq. (3)).

39.5% conversion of low power Q-switched Nd:YAG laser radiation to
266 nm by use of a resonant ring

Joachim Knittel and A. H. Kung

Institute of Atomic and Molecular Sciences

Academia Sinica

P.O. Box 23-166, Taipei 10764

Taiwan, R.O.C.

High power UV radiation is very attractive for many industrial applications including ultrahigh-density optical disk mastering, photolithography, material processing, marking, as well as for medical surgery and science¹. While the excimer laser is the leading candidate for the UV source in these applications, fourth harmonic generation (FHG) from solid state lasers, with their compactness and availability of diode-laser pumping, offers a viable alternative to excimer lasers. For solid state lasers, efficient frequency conversion methods must be used to generate high UV power. For low power high-repetition-rate lasers the most promising approach is to use external resonant cavities.²⁻⁴ In this paper we report the use of a single resonant optical cavity to generate the fourth harmonic from the fundamental. The idea is to generate the second harmonic and the fourth harmonic both in one cavity consisting of mirrors that are highly reflecting at the second harmonic only. Hence the fundamental IR radiation is

coupled into the cavity simply by a dichroic mirror. Energy is out-coupled from the cavity in the form of fourth harmonic UV radiation. The need for impedance matching is thus eliminated. This idea was put forward by Giordano and Matone for FHG from mode-locked lasers.^{5,6} In that case, in order to gain high conversion, it was necessary to match the length of the ring cavity to the IR laser length of 3.96 m with tight tolerance. The small beam size on the crystals led to thermal distortion and complex spatial mode pattern for the UV output. In this paper, we demonstrate that high UV conversion can be achieved from nanosecond IR pulses of energy in the mJ range using a single resonant ring cavity of arbitrary length and consisting of flat mirrors that are highly reflecting at the second harmonic. Using a Q-switched Nd:YAG laser running at 30 Hz with 213 mW of average IR power, we obtained 84 mW in the fourth harmonic at 266 nm. This corresponds to an internal IR to UV conversion of 39.5% (see figure 1). The output UV beam had a near-TEM₀₀ mode with a 95% fit to a Gaussian profile. Enhancement of >65 by the ring over single pass UV generation was measured.

Q-switched lasers have relatively high peak powers compared with CW lasers. So it is not usually the case that large resonant enhancement is needed in order to reach high conversion efficiency into the UV. However, use of a resonant ring for pulsed lasers will be beneficial when available peak power is low, such as in the case of high-repetition-rate diode-pumped lasers. This approach will also elevate the usefulness of crystals that have small nonlinear coefficients or size.

This research was supported by the National Science Council of the Republic of China under contract NSC 85-2113-M-001-027.

References:

- (1) W. H. Arnold, P. Haglestein, M. Obara, and R. Waynant, J. Spec. Topic. Quantum Electron. 1, 765 (1995).
- (2) A. Ashkin, G.D. Boyd, and J. M. Dziedzic, IEEE J. Quantum Electron. QE-2, 109 (1966).
- (3) M. Oka, L. Y. Liu, W. Wiechmann, N. Eguchi, and S. Kubota, J. Spec. Topic. Quantum Electron. 1, 859 (1995).
- (4) Yushi Kaneda and S. Kubota, Opt. Lett. 20, 2204 (1995).
- (5) G. Giordano and G. Matone, Nuovo Cimento 12D, 927 (1990).
- (6) S. C. Tidwell, J. F. Seamans, D. D. Lowenthal, G. Matone, and G. Giordano, Opt. Lett. 18, 1517 (1993).

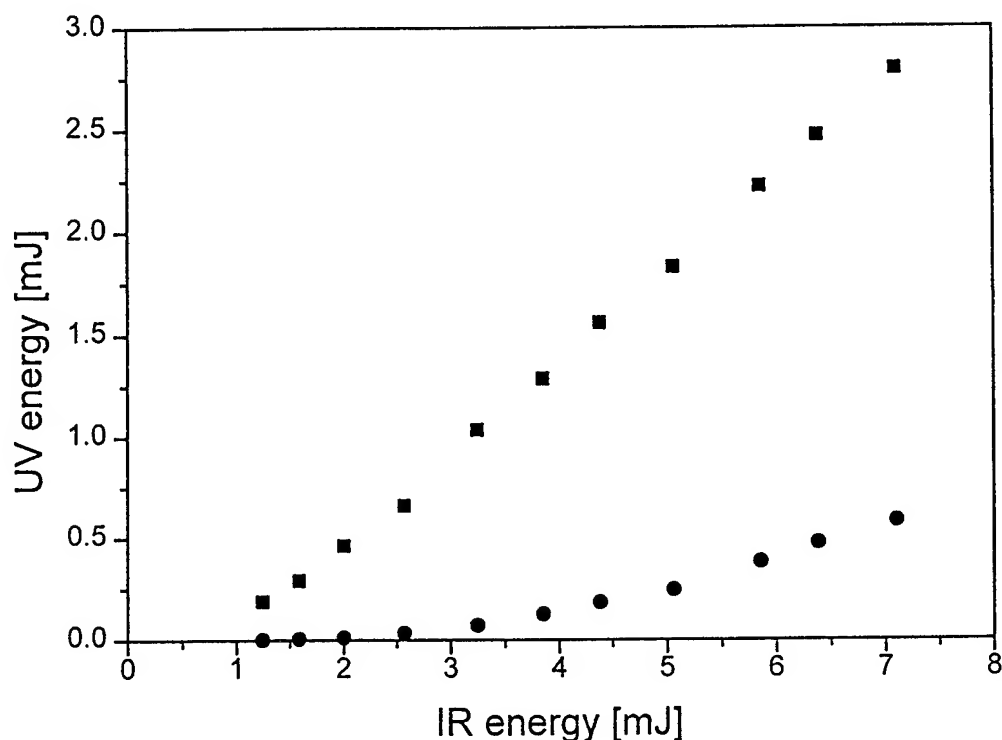


Figure 1. Generated single pulse UV energy vs IR input . Circles: single-pass results; squares: resonantly enhanced results.

Nonlinear Optical Microscopy for Imaging Thin Films and Surfaces

Laura Smilowitz, Duncan McBranch, and Jeanne M. Robinson

Chemical Sciences and Technology Division
CST-6, MS J585, Los Alamos National Lab
Los Alamos, NM 87545
phone: (505) 665-6186, fax: (505) 665-4817

Introduction

In the electric dipole approximation, an intense laser beam incident on a centrosymmetric material will not generate any even ordered harmonics. In particular, there will be no second harmonic response generated by the bulk of the material. At the surface of a centrosymmetric medium, the inversion symmetry is broken, allowing for a second order response characterized by the second order nonlinear susceptibility, $\chi^{(2)}$ ¹. Thus, $\chi^{(2)}$ has an inherent surface sensitivity which we utilize in order to image surfaces, interfaces, and thin films.

Instrument and Results

We have constructed two different systems for SHG imaging. The first system uses a CCD camera and laser beam diameter on the order of 5 mm (Figure 1).

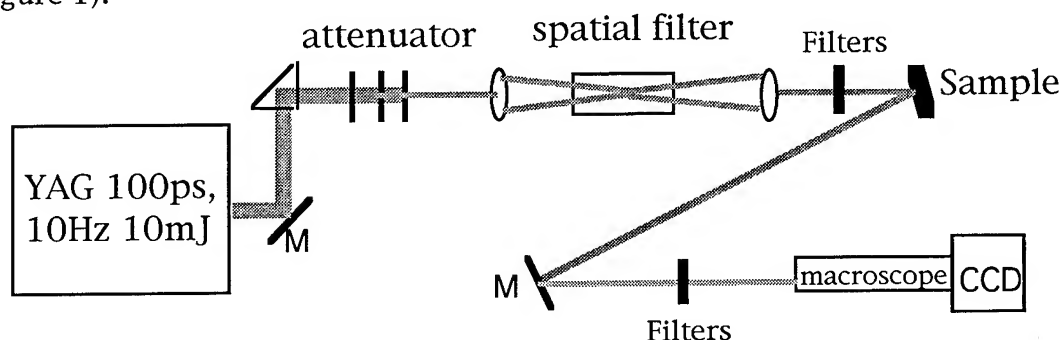


Figure 1: Experimental setup using CCD camera for imaging.

This system has the advantage of high speed image collection. The camera we use is a Photometrics liquid nitrogen cooled CCD with $18\text{ }\mu\text{m} \times 18\text{ }\mu\text{m}$ pixels with a dark current on the order of 1 electron per pixel per hour and read noise on the order of several electrons per pixel per read. The combination of the pixel size and the magnification used determines the system resolution. With a magnification of 2, we are able to resolve $7\text{ }\mu\text{m}$ features on a test pattern resolution target. The very low read noise allows us to perform long signal integrations without being swamped by detector noise buildup. This is important for our application, in which we expect on the order of 10-100 counts per pixel per hour at the detector. We typically integrate between 20 minutes and 1 hour to build up images. Our pump light is the 1064 nm output of a Nd:YAG laser which produces 100 ps pulses at 10 Hz. We typically use about 10 mJ per pulse with a beam diameter of about 5 mm. Optical filters are used to separate the fundamental and harmonic light. The images discussed below are taken with a p-polarized fundamental beam; polarization studies are currently underway.

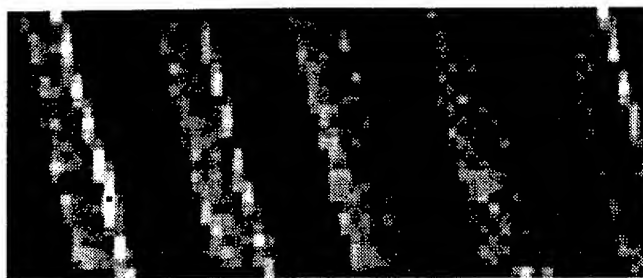
We have successfully used this system to image SHG from thin films of C_{60} and the conjugated polymer MEHPPV. Figure 2 shows the SHG image obtained from a patterned thin film of C_{60} with lines of C_{60} 300-400 microns wide separated by millimeter spaces made by vacuum sublimation of C_{60} through a mask onto a Suprasil substrate. The films produced this way are several thousand angstroms thick as determined by Dektak Profilometer measurements. We have also used this setup to take an image of the two photon light induced fluorescence from a thin film of Rhodamine 6G laser dye. The TPF is imaged by removing the 532 nm notch filter. A second image is taken with the 532 nm notch filter in place in order to determine what part of the image is from SHG and what part from longer wavelength emission.



Figure 2: SHG image of C_{60} lines using CCD camera.

The second NLO microscope design uses a focused pump beam and builds up an image pointwise by rastering the sample. In this case, the time required to build up an image is the product of the integration time per point (typically on the order of a 20 shots/point at 10 Hz) and the number of points taken. The tradeoffs here are between sensitivity and image acquisition time. The ultimate resolution of the image is limited by the spot size at the sample. This is diffraction limited in theory. In practice, it is limited by signal to noise which will depend on the peak damage threshold of the sample (which is improved by having the sample in vacuum). The image shown in Figure 3 is obtained using a 7.5 cm focal length lens which gives a spot size of 200 μm at the sample. The second harmonic goes as the square of the spot size which gives a FWHM of 140 μm . The second harmonic generated by the sample is collimated and then collected by a PMT with filters to separate the fundamental and harmonic frequencies.

The rastering setup has the advantage of being more flexible than the CCD experiment. By removing the focusing lens and using a collimated excitation beam, a larger area can be probed at once and a larger signal obtained. This makes it easier to map out the parameter space in order to obtain more quantitative information about the sample.



Resolution:
 y-axis 25 pixels, 100 μm step size
 x-axis 60 pixels, 100 μm step size

Figure 3: SHG image of C₆₀ lines using rastering setup.

Applications

We are currently studying photoinduced charge transfer reactions using second harmonic generation. Photoinduced charge transfer in a heterojunction configuration should produce a large local dipole moment by separating charges across an interface.¹² Second harmonic is sensitive to these local dipole moments. We have also applied our microscope to imaging patterned self-assembled monolayers of NLO molecules.

References

1. K.A. Schultz, I.I. Suni, E.G. Seebauer, J. Opt. Soc. Am. B, **10**, pp. 546, 1993.
2. G.T. Boyd, Y.R. Shen and T.W. Hansch, Optics Lett., **11**, pp. 97, 1986.
3. Y.R. Shen, Surface Science, **299/300**, pp. 551-562, 1994.
4. Y.R. Shen, The Principles of Nonlinear Optics, John Wiley and Sons, New York, 1984.
5. Bert Koopmans, Anna-Maria Janner, Harry T. Jonkman, George A. Sawatzky and Folkert van der Woude, Phys. Rev. Lett., **71**, pp. 3569, 1993.
6. P. Guyot-Sionnest and Y.R. Shen, Phys. Rev. B, **38**, pp. 7985, 1988.
7. N. Bloembergen and P.S. Pershan, Phys. Rev., **128**, pp. 606, 1962.
8. G.L. Richmond, J.M. Robinson and V.L. Shannon, Progress in Surface Science, **28**, pp. 1-70, 1988.
9. Y.R. Shen, **40**, pp. 327, 1989.
10. Robert M. Corn and Daniel A. Higgins, Chem. Rev., **94**, pp. 107-125, 1994.
11. T.F. Heinz and G.A. Reider, Trends in Analytical Chemistry, **8**, pp. 1989.
12. M.S. Yeganeh, J. Qi, A.G. Yodh and M.C. Tamargo, PRL, **69**, pp. 3579, 1992.
13. N.S. Sariciftci, L. Smilowitz, A.J. Heeger and F. Wudl, Science, **258**, 1992.
14. Tony Wilson, Theory and Practice of Scanning Optical Microscopy, Academic Press, London, 1984.

Multiple wavelength generation in a picosecond optical parametric oscillator based on noncritically-phase-matched LiB_3O_5

S. French, M. Ebrahimzadeh, and A. Miller

The J. F. Allen Research Laboratories, School of Physics and Astronomy,
University of St. Andrews, Fife KY16 9SS, Scotland, United Kingdom

Tel: 01334-463158 Fax: 01334-463104

E-mail: sf@st-andrews.ac.uk

The Ti:sapphire-pumped optical parametric oscillator (OPO) based on noncritically phase-matched LiB_3O_5 (LBO) has been shown to be a versatile source of high-repetition-rate picosecond pulses for the near-infrared¹. It is capable of providing signal and idler output pulses with durations of 1-2 ps over the continuous wavelength range 1-2.5 μm . Here we present results that demonstrate that this system is also capable of directly producing visible picosecond pulses in the green spectral region.

The configuration of the Ti:sapphire-pumped picosecond LiB_3O_5 OPO is similar to that described previously in ref. 1. The LiB_3O_5 crystal was 30 mm in length and 3 mm x 3 mm in aperture. The crystal was cut for noncritical type I phase-matching along x-axis ($\theta=90^\circ$, $\phi=0^\circ$).

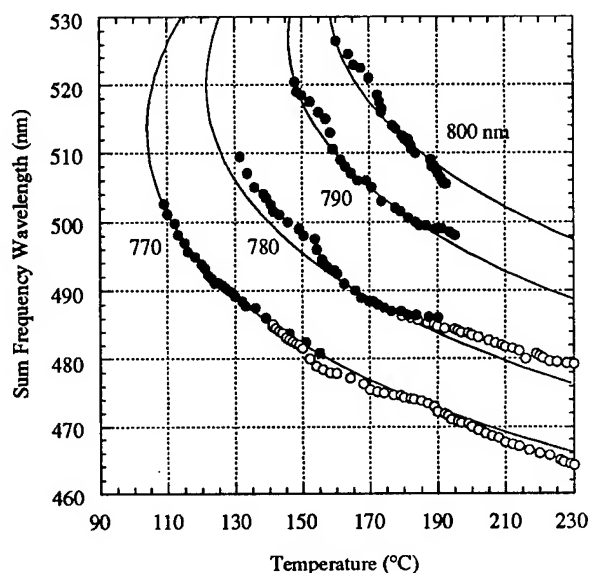


Figure 1. Visible SFM tuning as a function of Ti:sapphire pump wavelength. The solid lines represent the theoretical curves derived from the Sellmeier equations of ref. 2 and the temperature dependence of the refractive indices given in ref. 3.

In addition to the signal and idler beams, our OPO also generates tunable output in the visible green-blue spectral region. This phenomenon which has also been observed in femtosecond oscillators based on KTP, is a result of non-phase-matched sum-frequency mixing (SFM) between the resonated signal and the single-pass pump. Since this radiation exits the OPO cavity in the same forward direction as the pump and idler beams, it can be used as a visual aid for optimisation of the resonator. The polarisation direction of the sum-frequency light is the same as the pump (parallel to y-axis) and perpendicular to that of the signal.

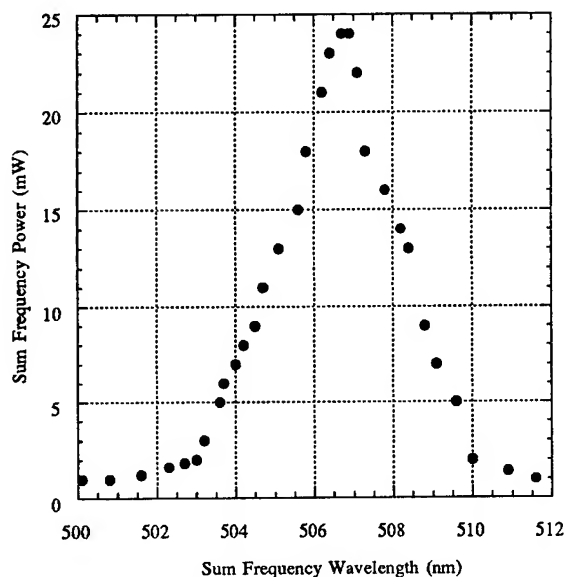


Figure 2. Visible SFM power as a function of SFM wavelength for a pump wavelength of 780 nm.

By using a combination of pump and/or temperature tuning, the SFM output can be tuned from 472-528 nm in the blue-green, for Ti:sapphire pump wavelengths covering 770-800 nm and temperature tuning from 100 to 230 °C see Fig. 1. Interestingly, however, at a pump wavelength of 780 nm, this SFM process becomes phase-matched over a temperature range of 134.9-142.5°C which corresponds to a wavelength range of 500.1-511.6 nm.

When the OPO was operating in a non-phases-matched regime up to 2 mW of visible output over a wavelength range of 472-528 nm in the blue-green region was produced. However over the phase-matched SFM wavelength range of 500.1-511.6 nm, we obtained intense generation in the green, with powers of up to 25 mW being produced, see Fig. 2. this is an indication that simultaneous parametric conversion of pump to signal and idler and sum frequency mixing between the pump and signal is taking place. This has been verified theoretically. This interesting feature results in competition between the parametric conversion and SFM process, with the maximum conversion oscillating between the two processes. The SFM process as expected had a different synchronous cavity length than the parametric process and so the desired process was easily selected by the choice of the appropriate cavity length. The output of the SFM was stable enough so that it could be used as a reliable source of green picosecond pulses.

The spectrum of one of these phase-matched SFM pulses at a wavelength of 506 nm is depicted in Fig. 3, this can be seen to have a spectral width of 0.28 nm, if this represented a

transform limited pulse then the corresponding pulse duration would be 1.02 ps. The spectrum can be seen to have no evidence of chirp, with the smooth profile also indicative of a lack of self phase modulation.

Our results demonstrate that systems based solely on noncritically phase-matched LBO are capable of producing picosecond pulses in 1.1-2.26 μm spectral range as well as in the visible from 500.1-511.6 nm. Few systems are capable of such wide tunability and transform-limited performance.

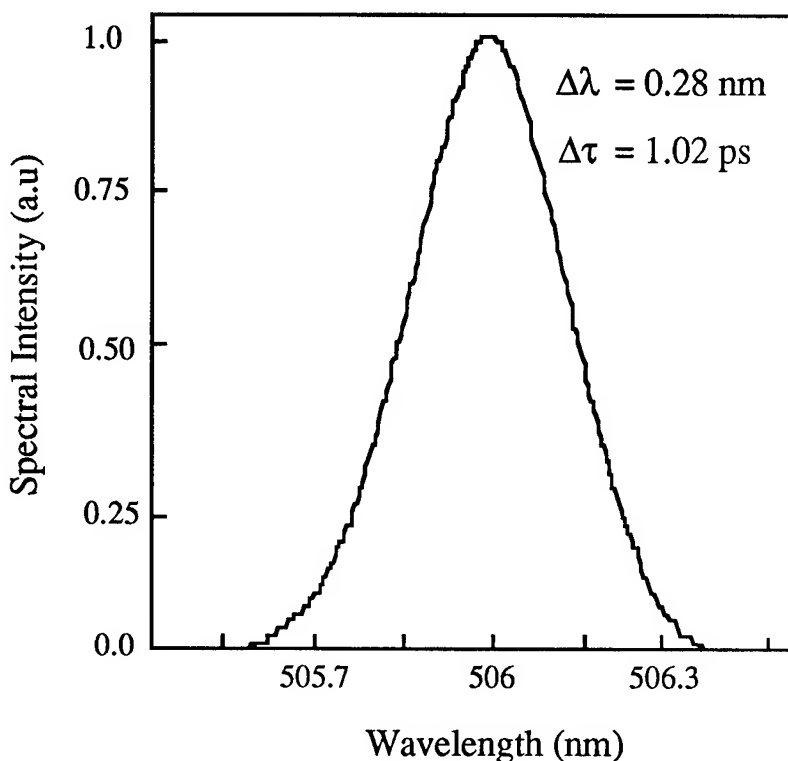


Figure 3. Spectrum of a phase-matched SFM pulse at a wavelength of 506 nm, the spectrum has a bandwidth of 0.28 nm, indicating a transform limited 1.02 ps pulse.

References.

1. M. Ebrahimzadeh, S. French, and A. Miller, J. Opt. Soc. Am. B 12, 2180 (1995)
2. S. Lin, J. Y. Huang, C. Chen, and Y. R. Shen, Appl. Phys. Lett. 59, 2805 (1991)
3. S. P. Velsko, M. Webb, L. Davis, and C. Huang, IEEE J. Quantum Electron. 27, 2182 (1991)

Midinfrared Femtosecond Pulse Generation Using a 250 kHz Ti:Sapphire pumped BBO OPA and DFG in AgGaS₂

Murray K. Reed and Michael K. Steiner-Shepard

Coherent Laser Group, 5100 Patrick Henry Drive, Santa Clara, CA 95054 U.S.A.

(408) 764-4305 fax (408)764-4818 email murray_reed@cohr.cam

Extending the tuning range of Kerr lens modelocked Ti:sapphire lasers into the visible, ultraviolet and near infrared by using ultrafast optical parametric amplifiers (OPA) is now common. A high power source of sub-picosecond light pulses tunable to longer wavelengths in the midinfrared is attractive for applications in the ultrafast spectroscopy of molecular vibrations and intersubband absorption in semiconductors. In this talk we describe a low energy 800 nm pumped, BBO Type-II infrared OPA and demonstrate the conversion of the output of this OPA through difference frequency generation (DFG) in AgGaS₂ to the midinfrared from 2.4 μm to beyond 12 μm with more than 10 mW of power from 3 μm to 6 μm .

The pump for this system was a compact Ti:sapphire modelocked oscillator and regenerative amplifier system, the Coherent RegA, which uses a single argon-ion laser to pump both the oscillator and the amplifier components. This produces 800 nm wavelength, 100 fs pulses with μJ level pulse energies at repetition rates up to 300 kHz.

The OPA architecture involves splitting the 800 nm wavelength RegA output into two portions: one part (25%) generates a broadband whitelight continuum to seed the OPA while the other part (75%) is rotated in polarization by 90° to provide the pump for the OPA. The two pulses, the 800 nm OPA pump and the whitelight OPA seed, are recombined on a dichroic mirror and focused into a 3 mm long Type II BBO OPA crystal cut at $\theta = 32^\circ$. The signal output from the OPA is tunable across the infrared by just rotating the OPA crystal for phase matching and then slightly varying the whitelight to pump relative optical delay to allow the appropriate seed wavelength to temporally overlap with the pump pulse. For efficient operation the OPA crystal is double-passed by both the pump and signal beams. The OPA signal and idler energy versus wavelength measured at 250 kHz repetition rate with 4 μJ pump energy from the RegA is shown in Fig. 1. The output pulsewidth is less than 100-fs and the time-bandwidth product was better than 2

times transform limited over most of the range except around the phasematching curve inflection point near $1.15\text{ }\mu\text{m}$.

We achieved conversion to the midinfrared by DFG of the signal and idler output from the OPA. The signal idler pair generated by the OPA were separated with a dichroic mirror designed to reflect the signal so that an adjustable relative optical delay could be introduced, recombined with an identical dichroic and focused with a 50 mm focal length lens into a 1.1 mm thick Type I AgGaS₂ crystal cut at 50° . The crystal angle was adjusted from 33° to 46° to achieve efficient DFG as the OPA signal was tuned from $1.2\text{ }\mu\text{m}$ to $1.55\text{ }\mu\text{m}$. The resulting DFG power at 250 kHz, measured with a pyroelectric detector, is shown versus wavelength in Fig 2. Beyond $2.6\text{ }\mu\text{m}$ the DFG power is greater than that of the OPA idler, peaking at more than 15 mW around $4\text{ }\mu\text{m}$ and then decreasing exponentially with wavelength to beyond $12\text{ }\mu\text{m}$.

Figure 1. OPA output tuning curve.

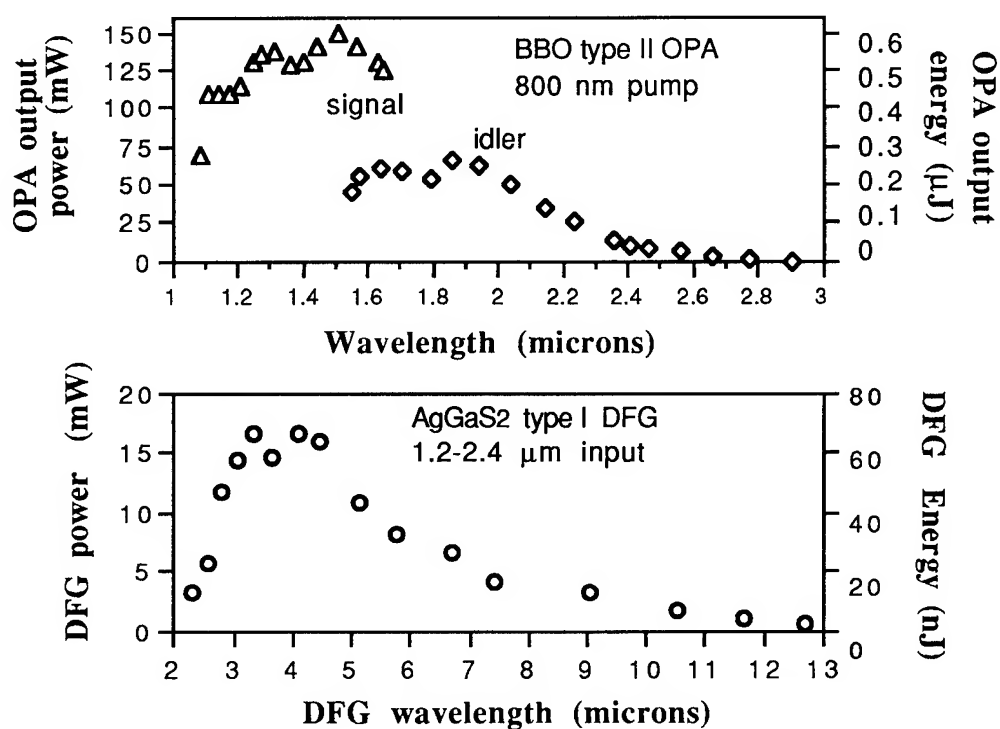


Figure 2. DFG output tuning curve.

Optical Parametric Device for Efficient Generation of Radiation in the 3.9 Micrometer Range

Karl Koch and Gerald T. Moore

Nonlinear Optics Center, Phillips Laboratory
3550 Aberdeen Ave., SE, Kirtland AFB, NM 87117-5776
Phone: (505) 846-4750. Fax (505) 846-1191.

In this paper we describe a device for efficiently converting pump radiation, such as the $\lambda_p = 1.064 \mu\text{m}$ radiation from a Nd:YAG laser, to idler radiation at a desired wavelength λ_i , using an optical parametric oscillator (OPO) which incorporates additional stages of three-wave mixing. In the conventional OPO each converted pump photon produces only one idler photon. We can extract a second idler photon by internally converting a signal photon of frequency $\omega_s = \omega_p - \omega_i$ using difference-frequency mixing (DFM). We suppose that the OPO is singly resonant at ω_s and insert a DFM crystal in the cavity after the OPO crystal. The DFM crystal is phase-matched for the process $\omega_s - \omega_i \rightarrow \omega_d$. The DFM interaction also plays the role of an optical parametric amplifier (OPA) for the idler radiation. Thus, the ideal output of the OPO-DFM device consists of two photons of frequency ω_i and one photon of frequency ω_d per pump photon. If $\omega_d > \omega_i$, one or more additional idler photons can be extracted by successive DFM/OPA stages outside the cavity, the first such external conversion being pumped at ω_d and generating a frequency $\omega_{d2} = \omega_d - \omega_i$. For conversion of $1.064 \mu\text{m}$ radiation to $3.9 \mu\text{m}$ radiation one internal and one external DFM process are possible. The other wavelengths generated are $\lambda_s = 1.463 \mu\text{m}$, $\lambda_d = 2.342 \mu\text{m}$, and $\lambda_{d2} = 5.861 \mu\text{m}$. The OPO and internal DFM process can be carried out using two successive quasi-phasematched $\chi^{(2)}$ gratings on a wafer of periodically poled LiNbO₃ (PPLN). The external DFM process can be carried out using AgGaS₂, with the ω_{d2} radiation polarized orthogonally to the other two waves.

The plane-wave theory of the OPO-DFM device has been developed previously [1]. Here we present the results of detailed numerical modeling and preliminary results of experiments for the PPLN OPO-DFM $3.9 \mu\text{m}$ frequency converter. This device has a cavity length of about 16 mm and is pumped by 140 ns, 4 mJ Q-switched pulses. The two $\chi^{(2)}$ gratings are each about 3 mm long, providing sufficient nonlinear drive for a good overlap with the expected dynamic range for high efficiency predicted by plane-wave theory [1]. Using a numerical integrator that models the two transverse dimensions [2] we have computed OPO-DFM quantum efficiency for generation of $3.9 \mu\text{m}$ idler photons to be about 1.7, which can be further increased by adding an external DFM process.

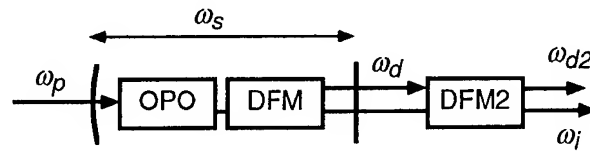


Figure 1: Schematic design of the $1.064 \mu\text{m} \rightarrow 3.9 \mu\text{m}$ frequency converter.

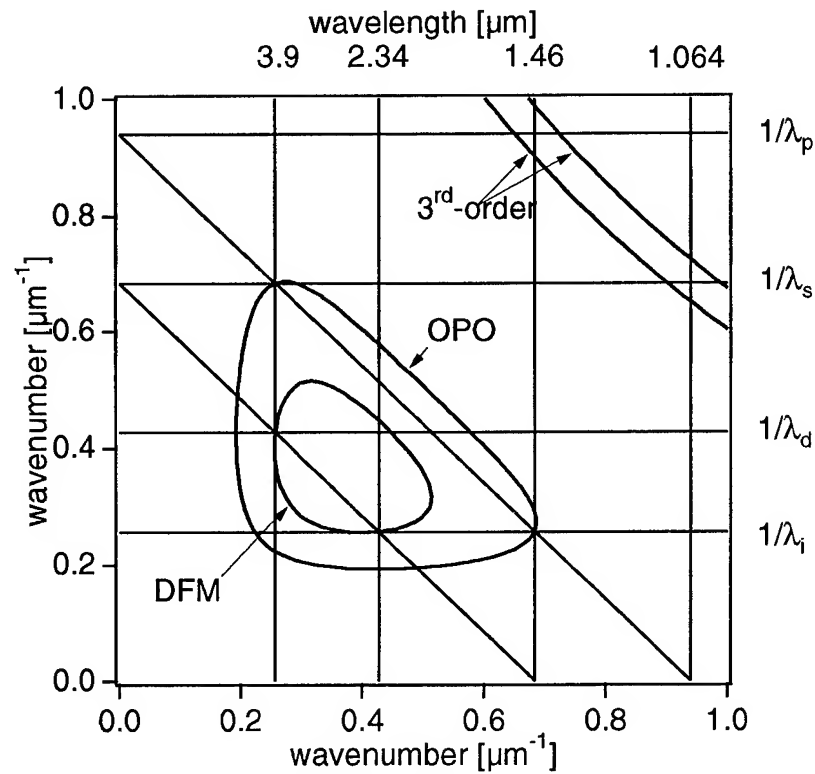


Figure 2: Grating contours for OPO-DFM quasi-phase matching at $T = 200^\circ\text{C}$.

Reference

1. K. Koch, G. T. Moore, and E. C. Cheung, "Optical parametric oscillation with intracavity difference-frequency mixing," J. Opt. Soc. Am. B. **12**, 2268–2273 (1995).
2. G. T. Moore, K. Koch, and E. C. Cheung, "Theory of multi-stage intracavity frequency conversion in optical parametric oscillators," SPIE **2379**, 84–94 (1995).

Energy characteristics of a loop laser with a thermal holographic mirror using millisecond pulses at 1.06 μm

A. A. Betin, S. C. Matthews, and M. S. Mangir

Optical Physics Laboratory
Hughes Research Laboratories
3011 Malibu Canyon Road
Malibu, CA 90265

Telephone: (310) 317-5028
FAX: (310) 317-5679

We report on experimental studies of a four-wave mixing thermal nonlinearity loop (TNL) conjugator for Nd: YAG laser operating at 1.06 μm with a 1 msec pulse format.

As shown in Fig. 1, the loop is composed of an interaction cell, an optical diode, and an internal amplifier¹. The cell is made up of thin layers of an absorbing liquid as a nonlinear medium. The input beam E_1 and its initial round trip counterpart E_3 mix to create a holographic grating that acts to scatter E_2 into E_4 which is the conjugate of E_3 . The optical diode, using a Faraday rotator and polarizing elements, prevents a saturation of the amplifier by the input, and favors oscillation in the reverse direction, giving rise to a strong return E_0 which is the conjugate of E_1 . Wave E_2 starts from spontaneous noise and grows if the generation condition is fulfilled: $|RG| > 1$, where $R = E_4/E_2$ is reflectivity of the holographic grating, and $G = E_2/E_4$ is the net gain inside the loop.

The input consisted of 1 ms pulses from a master oscillator, operating in a single transverse mode, but several longitudinal modes (coherence length ~ 10 cm), with a beam diameter of 3 mm. Adjusting the loop length to equal one resonator round trip ensured an optimum fringe contrast in the interaction zone (the cell). The decay time τ of the grating depends on the convergence angle θ between waves E_1 and E_3 . In our experiments we chose $\theta \sim 30$ mrad, with $\tau < 0.3$ msec. We therefore operated at a condition where the input pulse was of greater duration than the decay time of holographic mirror, and of upper level lifetime of the Nd:YAG gain medium (~ 0.25 msec).

The generated return started after a small delay time from the start of the input pulse, the length of this delay depending on how much the input power exceeded the threshold. The loop was not self-generating, i.e., when the E_1 field was turned off, the generated field decayed, even though there was still gain in the loop. Thus the envelope of the reflected pulse closely followed the input pulse. The temporal behavior of the output (Fig. 2) consisted of ~ 1 μs wide subpulses separated by 10-30 μs .

The threshold input power for the 1 ms pulse was 20 W, with a reflectivity ranging from less than unity to several times unity, depending on input level and the loop gain and loss configuration. Fig. 3 shows typical input-output data for two settings of the transmission γ of the optical diode in the input direction, and in this case with the loop amplifier at a double pass small signal gain of 23 dB.

The input beam had a coherence length of < 10 cm. The generated return had a coherence length ~ 2 cm. This confirms our expectations that the TNL can perform well with short coherence length inputs. This provides an advantage over the use of a long SBS lightguide² for obtaining a low peak power (< 100 W) conjugator for near infrared radiation.

This work was supported by a contract from ARPA (MDA972-94-3-0020).

REFERENCES

- ¹M.S. Barashkov, et. al., "Strong reflection of a series of pulses from a four wave mirror with thermal nonlinearity under parametric feedback conditions," Sov. J. Quantum Electron. **19** (4), p.518 (1989).
- ²D.C. Jones, et. al., "Aberration and depolarization compensation of a 10-m large-core (up to 1-mm) fiber by using a Brillouin phase-conjugate mirror," Proc. CLEO '95, p.23.

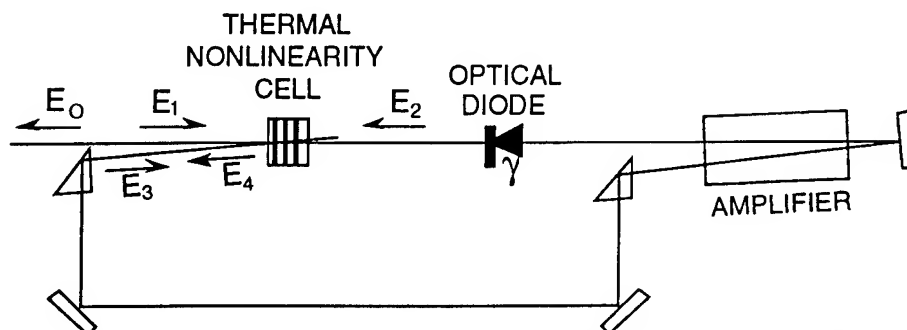


Figure 1. Four-wave mixing scheme for thermal nonlinearity loop laser.

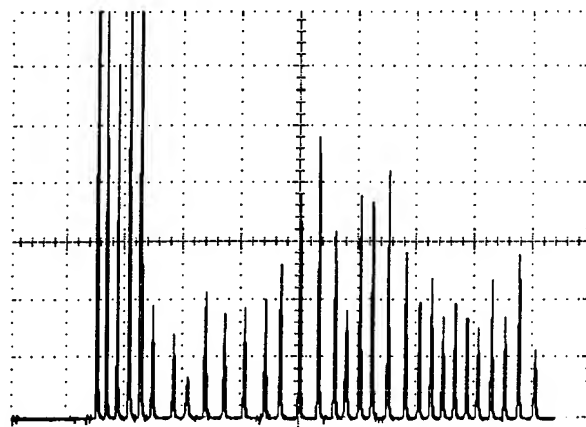


Figure 2. Temporal output from loop laser (100 μ s/div)

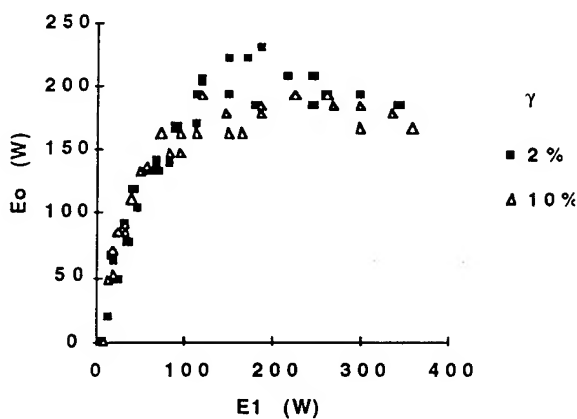


Figure 3. Input-output data for loop laser. Powers are averages over the 1 ms input pulse duration.

Degenerate Backward Optical Parametric Oscillators and Amplifiers: Conversion Efficiencies and Gain Saturation

Yujie J. Ding

Department of Physics and Astronomy and Centers for Materials and Photochemical Sciences
Bowling Green State University, Bowling Green, OH 43403

Jacob B. Khurgin

Department of Electrical and Computer Engineering
The Johns Hopkins University, Baltimore, MD 21218
Telephone: (419) 372-8785; Fax: (419) 372-9938

Since quasi-phase matching (QPM) was proposed in Ref. [1], there have been many demonstrations [2] of achieving second-harmonic generation (SHG) based on QPM. Recently, due to rapid development of poled nonlinear materials such as LiNbO₃, optical parametric oscillators (OPOs) and amplifiers (OPAs) have been intensively studied [3]. In these investigations, the thickness of each domain is usually much larger than the wavelengths of the parametric and pump wave based on QPM. Recently, GaAs/AlGaAs multilayers [4] and asymmetric coupled quantum-well domain structures [5] were used to achieve SHG. Most recently, we proposed transversely-pumped counter-propagating OPOs and OPAs (TPCOPOs and TPCOPAs) based on semiconductor structures [6], which is the reverse process of surface-emitting sum-frequency generation. In this configuration, the parametric waves counter-propagate in a waveguide along the epitaxial layer plane while pump waves propagate along the surface normal. Oscillation can occur without an external feedback. Such a concept was first introduced for nondegenerate backward OPO based on conventional phase-matching [7]. Recently, we investigated the conversion efficiency vs. the pump intensity in this configuration, however, based on QPM [8]. Here, we present our result of the first study of the degenerate backward optical parametric oscillators (DBOPOs) and optical parametric amplifiers (DBOPAs) in a waveguide based on QPM. DBOPO can occur without an external feedback. This is fundamentally different from conventional OPO. A second-order nonlinear optical material consists of many domains in which the adjacent domains have the opposite signs of second-order susceptibilities, but the same magnitude [$\chi_0^{(2)}$], see Fig. 1. The spatial period of the domains is $l_0 = \lambda_0/n_0$, where n_0 is the effective refractive index the domains at the wavelength λ_0 . A pump wave at the wavelength in vacuum $\lambda_{2\omega} = \lambda_0$ propagates along the positive z axis and is reflected by a mirror attached to the right-side facet with the reflectivity $R_{2\omega}$. These two counter-propagating pump waves interact with the nonlinear medium. As a result, DBOPOs can occur in the nonlinear medium, i.e. forward and backward parametric waves are generated and propagate along the positive and negative z axes, respectively, see Fig. 1(a). All the waves propagate in a waveguide. The conversion efficiency from the pump wave to parametric waves is $I_{\text{out}}/I_p = 2(1 + \sqrt{R_{2\omega}})(I_{\text{th}}/I_p)(\sqrt{I_p/I_{\text{th}}} - 1)$, where I_{th} is the threshold pump intensity for DBOPO:

$$I_{\text{th}} = \frac{\pi^2 \lambda_0^2 n_{\omega}^2 n_{2\omega}}{8[\chi_0^{(2)}]^2 L^2 (1 + \sqrt{R_{2\omega}})^2 n_0} \quad (1)$$

Compared with the nondegenerate BOPO [8], for the output wavelengths of the parametric waves being close to each other, I_{th} decreases by a factor of 16. Fig. 2 shows the dependence of the conversion efficiency on the normalized pump power. The efficiency reaches a maximum value when $I_p = 4I_{\text{th}}$. Such a unique behavior is quite different from that of the conventional OPOs, but is somewhat similar to that of TPCOPO [6]. DBOPO can occur

without an external feedback. This is similar to TPCOPO [6] and nondegenerate BOPO [7,8]. This is an advantage of DBOPOs compared with conventional OPOs. In all three configurations, there is, however, a distributed feedback due to the opposite directions of the two parametric waves. Consider a GaAs/AlAs asymmetric-coupled quantum-well domain structure [4]: $\chi_0^{(2)} \approx 30 \text{ nm/V}$, $L \approx 20 \mu\text{m}$, and $\lambda_{2\omega} \approx 10 \mu\text{m}$, $I_{\text{th}} \approx 0.61 \text{ GW/cm}^2$. For a poled LiNbO_3 : $\lambda_0/n_0 \approx 0.5 \mu\text{m}$, $\lambda_{2\omega} \approx 1 \mu\text{m}$, $\chi_0^{(2)} \approx 14 \text{ pm/V}$, and $L \approx 2.6 \text{ cm}$, $I_{\text{th}} \approx 4.9 \text{ MW/cm}^2$. For a poled KTP: $\lambda_0/n_0 \approx 0.7 \mu\text{m}$ and $\lambda_{2\omega} \approx 1.3 \mu\text{m}$, $I_{\text{th}} \approx 2.8 \text{ MW/cm}^2$. For LiNbO_3 with $\lambda_0/n_0 \approx 4 \mu\text{m}$ and for $\lambda_{2\omega} \approx 1.1 \mu\text{m}$, one can use one term of $\chi^{(2)}(z)$ with the spatial period of $\lambda_0/7n_0$ to achieve QPM. Assuming $\lambda_{2\omega} \approx 1.1 \mu\text{m}$, $I_{\text{th}} \approx 0.29 \text{ GW/cm}^2$. One should note that the dependence of the conversion efficiency on the pump intensity for DBOPO is quite different from that for nondegenerate BOPO [8]. This is because for each pump wave propagating along the positive z axis in DBOPO there are two counter-propagating degenerate parametric waves. Due to degeneracy, these two parametric waves efficiently generate a wave at the pump frequency which propagates along the negative z axis. This wave and incident pump wave are strongly coupled with each other. On the other hand, for nondegenerate BOPO, each incident pump wave propagating along the positive z axis can also generate two counter-propagating parametric waves, though the frequencies of these two waves are different. However, these two parametric waves cannot efficiently generate a wave at the pump frequency that propagates along the negative z axis due to phase-mismatch. Because of this fundamental difference between two processes, the dependence of the conversion efficiency on the pump intensity is quite different between these two processes. Fig. 1(b) shows the configuration for DBOPA. The gain for the backward parametric wave can be expressed as $G = |A_{\omega}^-(0)|^2/|A_{\omega}^-(L)|^2 = \sec^2 \gamma$, where γ is determined by $\sqrt{I_p/I_{\text{th}}} = 2\gamma/\pi + [\pi \tan^2 \gamma / 2(1 + \sqrt{R_{2\omega}}) \gamma] (I_{\text{in}}/I_{\text{th}})$, with I_{in} the input intensity of the backward parametric wave. Fig. 3 shows the dependence of the gain on the pump intensity for different input intensities. When $I_{\text{in}} \gg I_{\text{th}}$, $G \approx 1$ even for $I_p \gg I_{\text{th}}$. On the other hand, if $I_{\text{in}} \ll I_{\text{th}}$, the gain increases rapidly as the pump intensity increases. For even lower input intensity, the gain becomes very large. Eventually it approaches infinity, which corresponds to DBOPO. Fig. 4 shows the dependence of the gain on the input intensity for different values of pump intensities. The gain always decreases dramatically as the input intensity increases regardless of the level of the pump intensity. Therefore, to achieve large values of gain, I_{in} should be much less than I_{th} .

This work is supported by AFOSR and NSF.

- [1] J. A. Armstrong *et al.*, Phys. Rev. 127, 1918 (1962).
- [2] M. M. Fejer *et al.*, IEEE J. Quant. Electr. 28, 2631 (1992).
- [3] Special issue on optical parametric devices: J. Opt. Soc. Am. B. Dec. 1995.
- [4] R. Normandin, R. L. Williams, and F. Chatenoud, Electr. Lett. 26, 2088 (1990).
- [5] J. B. Khurgin, Phys. Rev. B 38, 4056 (1988); S. Li and J. Khurgin, Appl. Phys. Lett. 62, 1727 (1993); S. Janz, F. Chatenoud, and R. Normandin, Opt. Lett. 19, 622 (1994).
- [6] Y. J. Ding, S. J. Lee, J. B. Khurgin, Phys. Rev. Lett. 75, 429 (1995); IEEE J. Quant. Electr. 31, 1648 (1995).
- [7] S. E. Harris, Appl. Phys. Lett. 9, 114 (1966).
- [8] Y. J. Ding and J. B. Khurgin, submitted to Phys. Rev. Lett.

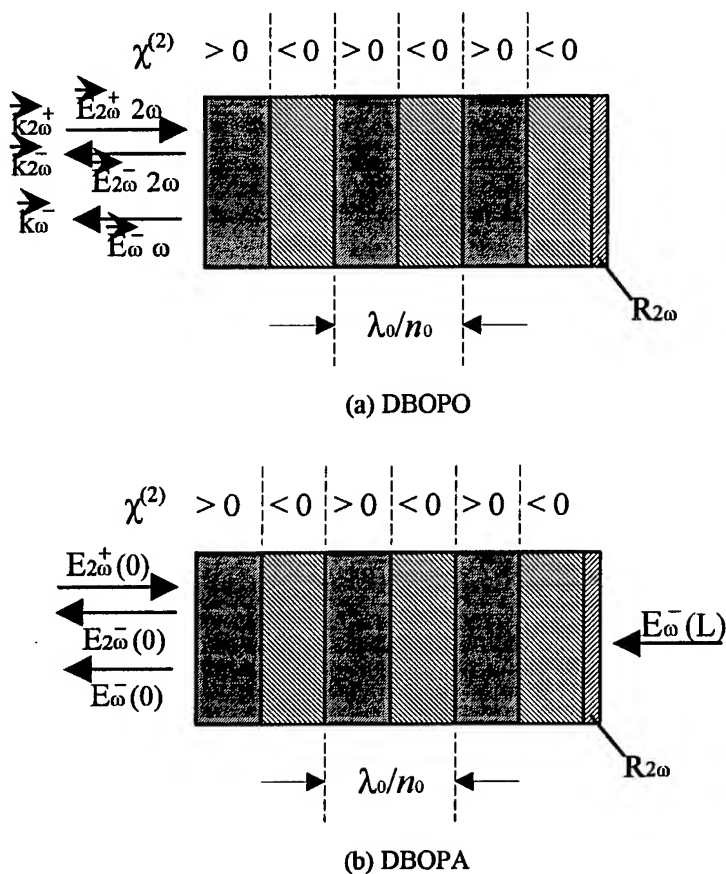


Fig. 1

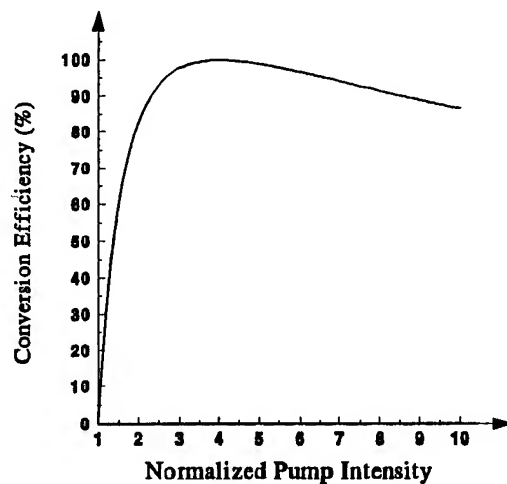
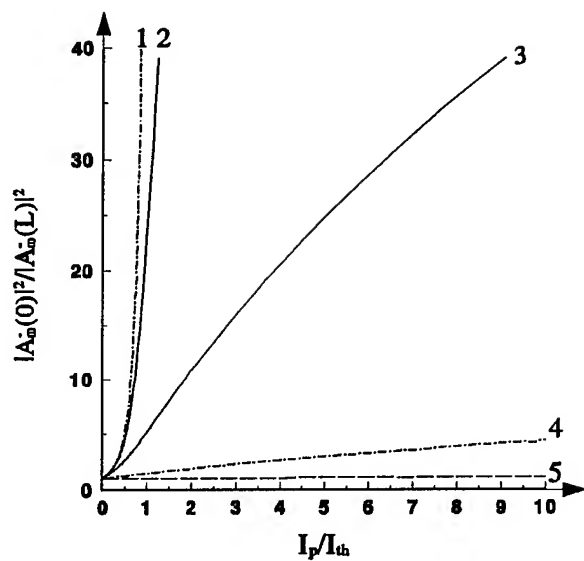
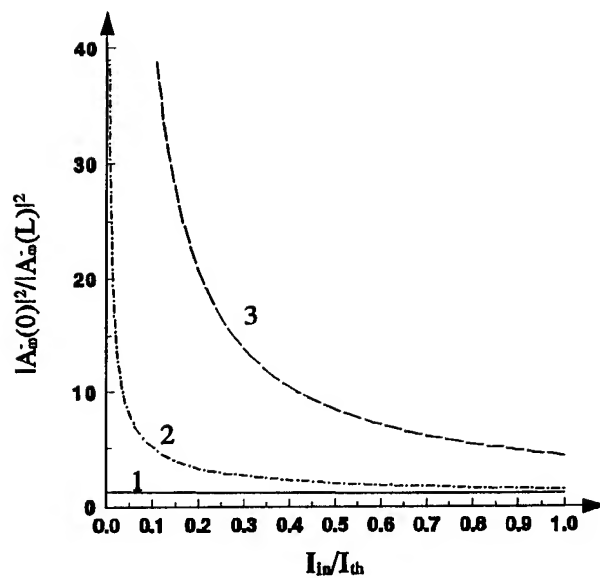


Fig. 2 Conversion efficiency from the pump wave to the parametric waves vs. normalized pump intensity for DBOPO.

Fig. 3 Gain vs. normalized pump intensity for $I_{in}/I_{th} = 0.001$ (Curve 1); 0.01 (2); 0.1 (3); 1 (4); and 10 (5).Fig. 4 Gain vs. normalized input intensity for $I_p/I_{th} = 0.1$ (Curve 1); 1 (2); and 10 (3).

Chaos stabilization via pulse train generation in dispersive optical parametric oscillators

Stefano Trillo

*Fondazione Ugo Bordoni, Via B. Castiglione 59, 00142 Rome, Italy
tel: +396-5480-2223; fax: +396-5480-4402; e-mail: strillo@fub.it*

Marc Haelterman

*Service d'Optique et Acoustique, Université Libre de Bruxelles,
50 Av. F. D. Roosevelt, CP 194/5, B-1050 Bruxelles, Belgium
phone: + 322-650-2801; fax: + 322-650-4496; e-mail: mhaelter@is1.ulb.ac.be*

Optical parametric oscillators (OPOs) are devices of growing importance for several applications [1]. In the degenerate configuration OPOs permit to enhance the conversion between the pump ($2\omega_0$, SH) and the subharmonic or fundamental (ω_0 , FF) fields, both being close to two resonance modes of the cavity. However, cw-operating degenerate OPOs undergo different instabilities, such as bistability and self-pulsing. These instabilities, predicted in the framework of the dispersionless mean field model, give rise to hysteresis and chaotic self-pulsing, respectively [2-4]. In this communication we are aimed at showing that *this scenario changes drastically as long as dispersion is included in the mean-field description*. In particular dispersion allows for nonlinear phase-matching of nondegenerate processes, which results into a novel instability of the OPO steady-states, namely the build-up of sideband pairs equally detuned (say, by $\pm\Omega$) from both the FF and SH carriers. This novel mechanism is analogous to modulational instability recently predicted for cavityless parametric amplification [5]. In the OPO, however, the dissipative nature of the problem favours the stable formation of periodic patterns (i.e., pulse trains) at a repetition rate Ω . The stability analysis reveals that these periodic trains are stable at power much larger than the threshold for the competing chaotic self-pulsing, and hence constitute an intrinsic mechanism of stabilization of the OPO. Moreover the formation of periodic trains via modulational instability turns out to be a preferential mechanism even when the OPO is bistable, or, unexpectedly, even when it operates below the cw threshold for conversion to the subharmonic.

Assuming that the FF and SH intracavity fields $u_{1,2}$ at $\omega_0, 2\omega_0$ are close to two modes of a high-finesse cavity, we reduce the system of propagation equations and boundary conditions to the path-averaged equations (in dimensionless units)

$$i\frac{\partial u_1}{\partial \xi} - \frac{\beta_1}{2}\frac{\partial^2 u_1}{\partial \tau^2} + u_2 u_1^* = (\Delta_1 - i)u_1 ; \quad i\frac{\partial u_2}{\partial \xi} - \frac{\beta_2}{2}\frac{\partial^2 u_2}{\partial \tau^2} + \frac{u_1^2}{2} = (\Delta_2 - i\alpha)u_2 + iS, \quad (1)$$

where ξ is a propagation distance in units of the cavity buildup length, τ is time, and the dimensionless quantities $\Delta_{1,2}, \beta_{1,2}, \alpha, S$ represent cavity detunings, dispersion coefficient, SH to FF absorption ratio, and pumping, respectively (we assumed group-velocity matching in the crystal). We investigate the linear stability of the OPO cw steady-state solutions against sideband

perturbation $a_j(\xi, \tau) = \epsilon_{js}(\xi)e^{i\Omega\tau} + \epsilon_{ja}(\xi)e^{-i\Omega\tau}$ ($j = 1, 2$). Below the pump cw threshold $(S_{th})^2 = (1 + \Delta_1^2)(\Delta_2^2 + \alpha^2)$ the SH to FF conversion is zero and the steady-state is $\bar{u}_1 = 0, \bar{u}_2 = S/(\alpha + i\Delta_2)$, whereas above threshold the OPO generates a mixed mode steady-state with FF $\bar{u}_1^\pm = \pm[\bar{u}_2 P_1/(\Delta_1 - i\alpha_1)]^{1/2}$ where $P_1 = |\bar{u}_1|^2$ is the FF intensity, and \bar{u}_2 is the above threshold SH, whose intensity remains locked at the threshold value $P_2 = |\bar{u}_2|^2 = 1 + \Delta_1^2$.

In Fig. 1 we show the results of the stability analysis for the qualitatively different regimes of operation: we report the instability gain g against modulation frequency Ω and steady-state intensity P_2 (below cw threshold) or P_1 (above cw threshold). As shown, the dominant mechanism is always a Turing or dissipative modulational instability (MI), which is associated with the parametric generation of sidebands (i.e., high gain bandwidths at nonvanishing frequency detunings Ω). Below the cw threshold (see Fig. 1(a)) this is the only mechanism expected to build up. Above the cw threshold, depending on the detunings, this instability competes with the low frequency instabilities associated with either the negative slope branch of the bistable response (see Fig. 1(b)), or a self-pulsing instability associated with a Hopf bifurcation (see Fig. 1(c)). Consider, e.g., the latter case occurring for $\Delta_1\Delta_2 < -1$. In this case, as shown in Fig. 2, when the intensity grows larger than the Hopf threshold ($P_1 = P_{1th} = 2.5$ in Fig. 1(c)-2) a dispersionless OPO is expected to exhibit a transition to chaotic self-pulsation through a sequence of subharmonic bifurcations [3]. Conversely numerical simulations of Eqs.(1) show that, in a dispersive OPO, chaos is inhibited by the buildup of stable temporal patterns (with periodicity corresponding to the most unstable frequency Ω), even for powers much larger than the Hopf threshold P_{1th} . Fig. 3 shows the case of a OPO starting from noise, reaching the above threshold steady state, and showing the formation of the periodic solution. Analogous results are obtained below threshold, and in the bistable case.

In conclusions we have shown that dispersion may deeply affect the operation of degenerate OPOs, allowing for the buildup of dissipative modulational instability, which is in turn responsible for the generation of stable pulse trains. This operation regime is expected to self-stabilize the chaotic self-pulsing, to dominate over bistability, and to allow for operation below threshold.

References

- [1] Optical Parametric Devices, J. Opt. Soc. Am. B, feature issue, November 1995.
- [2] K.J. McNeil, P.D. Drummond, and D.F. Walls, Opt. Commun. **27**, 292 (1978). P. D. Drummond, K.J. McNeil, and D.F. Walls, Opt. Acta **27**, 321 (1980); Opt. Acta **28**, 211 (1981).
- [3] L.A. Lugiato et al., Il Nuovo Cimento **10D**, 959 (1988).
- [4] N. P. Pettiaux, R. D. Li, and P. Mandel, Opt. Commun. **72**, 256 (1989).
- [5] S. Trillo and P. Ferro, Opt. Lett. **20**, 438 (1995); Phys. Rev. E **51**, 4994 (1995).

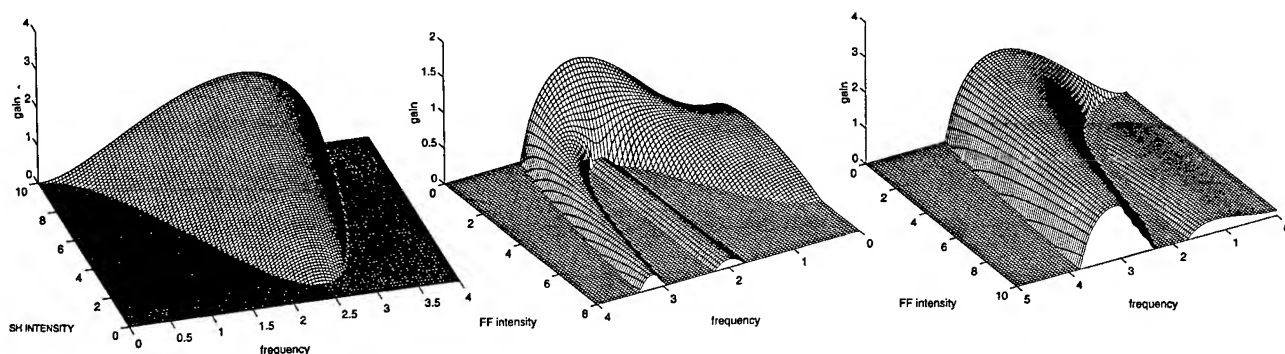


Figure 1: Instability gain g vs. intensity and frequency detuning Ω in the normal dispersion regime ($\beta_{1,2} = 1$), $\alpha = 1$. (left) below cw threshold ($\Delta_1 = 3, \Delta_2 = -1$); (middle) above cw threshold, bistable case ($\Delta_{1,2} = 2$); (right) above cw threshold, monostable case ($\Delta_1 = 3, \Delta_2 = -1$).

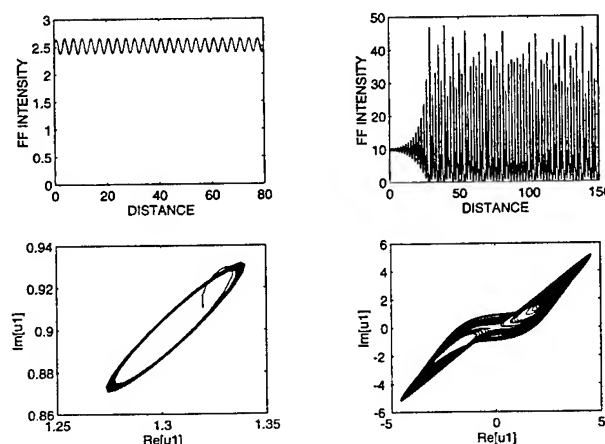


Figure 2: Evolution and phase-plane picture of self-pulsing in dispersionless OPOs, $\Delta_1 = 3, \Delta_2 = -1, \alpha = 1$: (left) close to Hopf threshold ($P_1 \sim 2.5$); (right) chaos well above threshold ($P_1 = 10$).

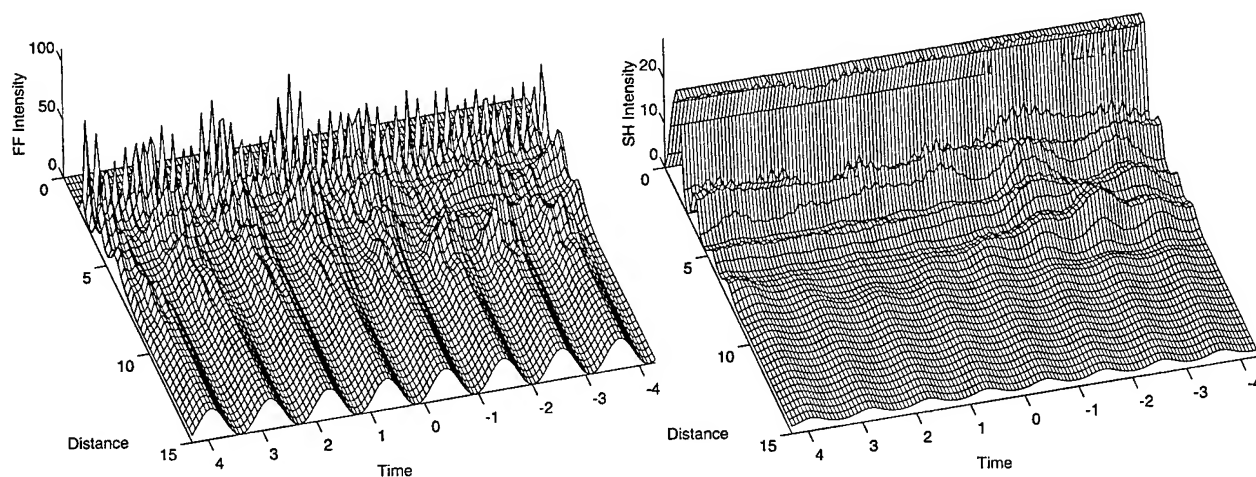


Figure 3: Stable formation of periodic solutions from noise due to dissipative modulational instability: $\Delta_1 = 3, \Delta_2 = -1, \alpha = 1, P_1 = 5$, normal dispersion.

Brillouin-Enhanced-Four-Wave-Mixing Vector Phase Conjugate Mirror

M. W. Bowers,

Institute of Optics, University of Rochester, Rochester, NY 14627
Tel. (716)275-5030, Fax (716)244-4936

R. W. Boyd

Institute of Optics, University of Rochester, Rochester, NY 14627
Tel. (716)275-2329, Fax (716)244-4936

A. K. Hankla

Lawrence Livermore National Laboratory, L-054, 7000 East Ave., Livermore, CA 94550
Tel. (510)424-4326, Fax (510)423-2505

Most laser applications require very good beam quality. Many components in lasers and laser systems can degrade the laser quality below what is acceptable. Optical phase conjugation is one method in which a highly aberrated optical beam can be restored to near diffraction limited quality. Stimulated Brillouin scattering (SBS) is a nonlinear process which can produce a phase conjugated optical wave. Simple SBS phase conjugators typically cannot correct for polarization distortions. Polarization restoration has been accomplished by phase locking orthogonal polarizations together in an SBS cell^{1,2,3,4}. We have designed and tested a new method of polarization restoration which is easy to implement and can passively alter the phase or polarization of the return beam for output coupling.

In our arrangement, shown in Figure 1, both the pump and probe beams are generated by the same Nd:YAG oscillator. The pump beam is circularly polarized and contains 200 mJ of energy in 10 ns. The probe beam is split using either a beam splitter or a combination consisting of a polarizer, a half wave plate, and a second polarizer. The reason for the polarizer combination will become apparent later in this paper. The two beams pass through separate amplifiers and are split again into two orthogonal polarizations. All five beams, the pump and four probe beams, are focused into a cell containing a Brillouin medium. The four probe beams need only come to focus inside the conical volume formed by the pump beam as it converges to a focus inside the Brillouin cell. The four probe beams need not have any other relationship with respect to each other once inside the cell. Each of the conjugated probe beams has a phase directly related to the input probe, the pump beam, and the conjugate of the pump beam. The phase of each of the probe beam conjugates at the beamsplitter can therefore be calculated⁵ by:

$$\Delta\phi = \Delta k(\Delta L) - \Delta\beta + \Delta\psi \quad (1)$$

where Δk is the Brillouin frequency shift measured in cm^{-1} times 2π , and ΔL is the path length difference. The contribution of $\Delta\beta$ and $\Delta\psi$ arise from the phase difference between the two polarizations of the probe and pump beams respectively as defined by the polarizers in Figure 1. From Equation 1 it is evident that we want $\Delta k\Delta L + \Delta\psi = m2\pi$ since $(-\Delta\beta)$ is the conjugate of the input phase difference. By adjusting the path length of one probe beam with respect to its orthogonal polarization, ΔL_1 or ΔL_2 , it is possible to meet this condition and thus reconstruct the

original wavefronts and polarizations as they pass back through the amplifiers. This reconstruction has been demonstrated and the resulting data is shown in Figure 2 for an individual amplifier leg. Path length errors of more than a centimeter are found to have acceptable depolarization levels.

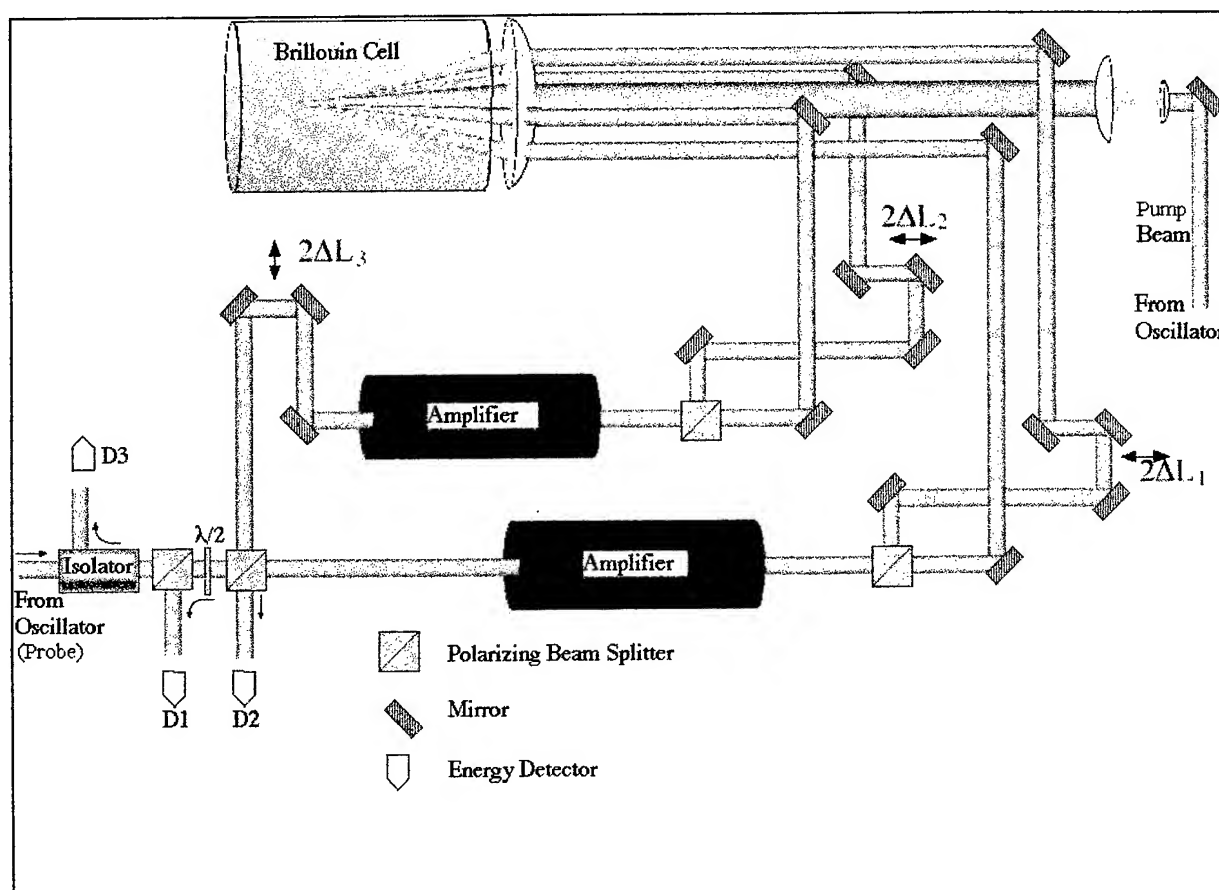


Figure 1. A schematic of the laser amplifier system that employs the BEFWM phase conjugate mirror. The path lengths ΔL_1 and ΔL_2 are used to adjust depolarization while ΔL_3 is used to adjust the percent of the output coupled to detector D1. Detector D2 is used to measure the amount of depolarized light and detector D1 measures the amount of light that is coupled back toward the oscillator.

By adjusting the path length between the two amplifier chains, ΔL_3 , it is possible to adjust the relative phase of the two probe beams. The phase shift between the two probe beams can again be calculated using Equation 1. If this phase shift is π radians then the beam polarization is effectively rotated $\pi/2$ radians compared to its input state as it passes back through the waveplate. The beam is then coupled out towards detector D1 while the depolarized light from each leg is coupled out to detector D2. Using this phase shift produced by ΔL_3 it is possible to direct the back reflected probe beam towards the oscillator, and is thus coupled out to detector D3 via the Faraday rotator, or is coupled out of the system to detector D1 directly.

The system described above has been tested in both double and four pass configurations and with more than two parallel amplifier chains. Results will be shown for Brillouin reflectivities

greater than 70%, depolarization of less than 2%, and better than 1.5x diffraction limited for a system running at 10 Hz.

1. N. G. Basov, V. F. Efimkov, I. G. Zubarev, A. V. Kotov, S. I. Mikhailov, M. G. Smirnov, *JETP Lett.* **28**, 197 (1979)
2. D. A. Rockwell, D. S. Sumida, *SPIE Phase Conjugation; Beam Combining and Diagnostics*, **739** (1987)
3. I. D. Carr, D. C. Hanna, *Appl. Phys. B.* **36** (1985)
4. J. J. Ottusch, D. A. Rockwell, *CLEO* (1991)
5. N. G. Basov, I. G. Zubarev, A. B. Mironov, S. I. Mikhailov, A. Y. Okulov, *Sov. Phys. JETP* **52** (5) Nov. (1980)

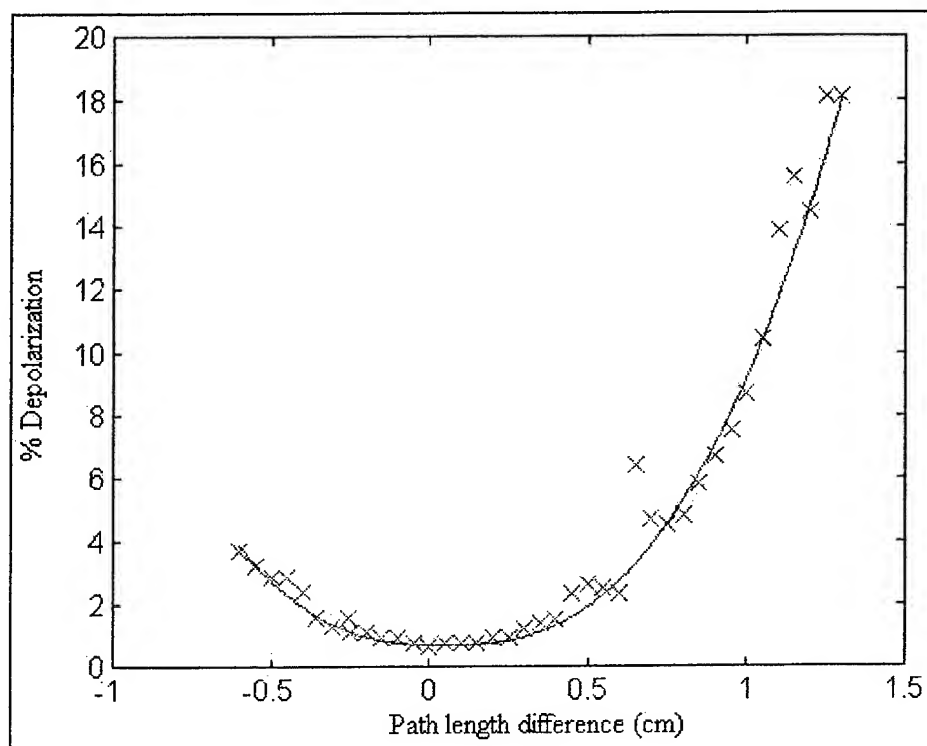


Figure 2. The polarization can be restored in each amplifier leg by adjusting the path lengths ΔL_1 or ΔL_2 . Percent depolarization is defined as the amount of energy (D2) as a function of total backward going energy (D1+D2).

Generalized Master Equation Models for Kerr Lens Mode-Locking

A. M. Dunlop and W. J. Firth
Department of Physics & Applied Physics
University of Strathclyde, Glasgow G4 ONG, Scotland
Tel: + 44 141 552 4400 x3354 ; Fax: + 44 141 552 2891

E. M. Wright
Optical Sciences Center
University of Arizona, Tucson, AZ 85721, USA

We recently presented [1] the following “master equation” [2] applicable to any nonlinear cavity with linear properties describable by an ABCD matrix and with one nonlinear interaction per round trip:

$$\begin{aligned} \frac{\partial E}{\partial T} = & g \left(1 + \frac{1}{\Omega_g^2} \frac{\partial^2}{\partial t^2} \right) E + i \left(\phi + \beta \frac{\partial^2}{\partial t^2} \right) E + N(E) \\ & + \frac{i\psi}{2T_R \sin \psi} \left(\frac{B}{k} \nabla_{\perp}^2 E + i(A - D)(\vec{r}_{\perp} \cdot \nabla_{\perp} E + E) + kCr_{\perp}^2 E \right), \end{aligned} \quad (1)$$

The intra-cavity field E is a function of fast (t) and slow (T) times, as well as \vec{r}_{\perp} , the transverse position vector. ∇_{\perp} is the transverse gradient operator, and $\cos \psi = S$. Here $S = (A + D)/2$. We have included typical operators for gain and dispersion [2], and so the round-trip time T_R is that based on the group velocity. To describe KLM, we specialize the nonlinear function $N(E)$ to the Kerr form $N(E) = i\eta|E|^2 E$, which requires that the ABCD elements be calculated *at the Kerr lens*.

In the low-power limit this master equation has the correct transverse mode and related properties, including e.g the differential attenuation of higher-order modes in cavities with a gaussian aperture, for which the ABCD elements, and thus ψ , are complex. It also correctly reproduces both the mode spectrum and gain of the cavity.

The unusual $\vec{r}_{\perp} \cdot \nabla_{\perp} E$ term is non-zero for almost all locations of the nonlinear medium, but is essential for matching the mode structure of the linear cavity. It can be removed, so giving an equation suitable for split-step integration, by transforming to a new field $F(T, t, \vec{r}_{\perp})$, leading to a fully equivalent form:

$$\begin{aligned} \frac{\partial F}{\partial T} = & g \left(1 + \frac{1}{\Omega_g^2} \frac{\partial^2}{\partial t^2} \right) F + i \left(\phi + \beta \frac{\partial^2}{\partial t^2} \right) F + i\eta|Fe^{-ar_{\perp}^2}|^2 F \\ & + \frac{i\psi}{2T_R} \left\{ \frac{B}{k \sin \psi} \nabla_{\perp}^2 F - \frac{k \sin \psi}{B} r_{\perp}^2 F \right\}, \end{aligned} \quad (2)$$

where

$$a = \frac{ik(A-D)}{4B} \text{ and } F = E \exp\left(\frac{ik(A-D)r_{\perp}^2}{4B}\right)$$

Note that the location-sensitive $(A-D)$ term transforms into a kind of profile in the Kerr lens term.

Using (2) we can simulate both quasi-cw and pulse dynamics in KLM ring lasers, figure 1. We find cw nonlinear mode-resaping in a system previously studied by us [3], broadly consistent with these earlier results. We demonstrate directly that mode-resaping alone is enough to saturate the output power and stabilize it at a finite level, without the necessity for gain saturation. This power level is strongly dependent on the Kerr lens location in the cavity, through the ABCD elements. The simulation results also show that the laser frequency (figure 1) is both power dependent and depends on the Kerr lens location.

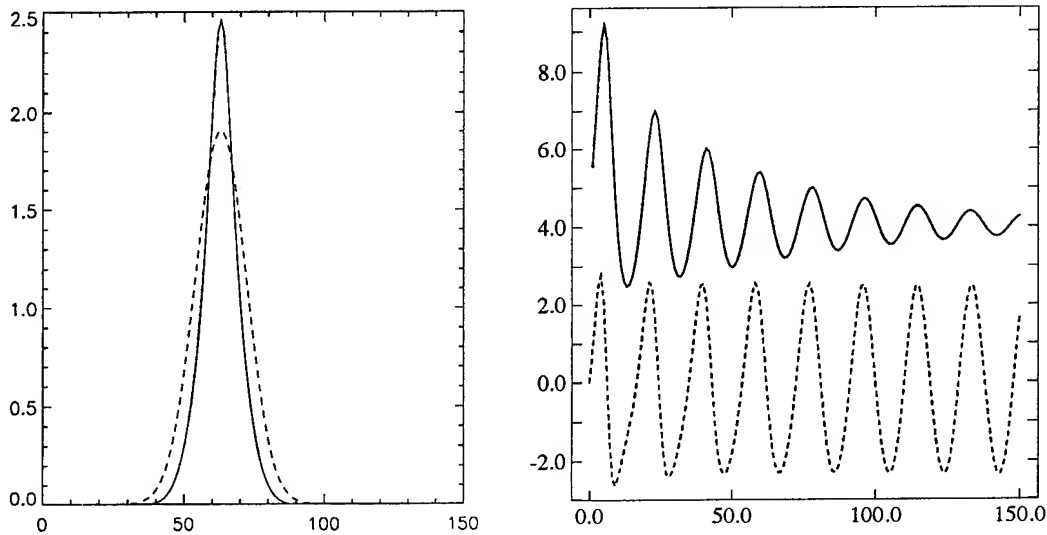


Figure 1: The diagram on the left shows the linear (dashed) and nonlinear (solid) beam profiles. That on the right shows the beam power (solid line) and the imaginary part of the central field (dashed line) as a function of the number of cavity roundtrips.

As a first full KLM simulation, we consider a cavity in which KLM is initiated by an amplitude modulator. This can be described by adding a term proportional to t^2 to our master equation. In the linear limit this gives an output gaussian in both space and time, as expected from Kuizenga-Siegman theory [4]. We will show how the Kerr term leads to a mutual compression in both space and time, giving KLM-type output pulses and profiles at high enough gain. Stable pulses are generated even with linear, unsaturable gain.

Our master equation for KLM fully incorporates the transverse effects of the cavity along with the effects of group velocity dispersion. It must, therefore, include as special cases several previous KLM master equations based on a purely time domain description. To reduce our space-time description to an effective time domain equation we project out the spatial dimension. We choose to expand the cavity field in terms of

the linear cavity modes $\{u_0\}$. Since this involves transversely varying losses the linear modes of (1) are not orthogonal in the usual Hermitian sense but are rather biorthogonal to an adjoint set of modes $\{u_0^\dagger\}$ which are physically the modes for propagation in the reverse direction around the cavity at the selected reference plane. Performing this projection onto the gaussian fundamental mode, we find the reduced temporal master equation

$$\frac{\partial C_0}{\partial T} = (g - \alpha_0 + i\phi) C_0 + i\beta \frac{\partial^2 C_0}{\partial t^2} + i\eta \kappa_0 |C_0|^2 C_0 \quad (3)$$

where $|C_0|^2$ is the circulating power, and the *complex* coefficient κ_0 describes how the self-phase modulation due to the Kerr medium is transferred into nonlinear amplitude modulation. Equation (3) is of precisely the form of the usual master equations and has the same type of complex *sech* solutions. Unlike these equations, however, it is sensitive, through the ABCD dependence of the effective Kerr coefficient, to the precise location in the cavity of the Kerr lens and the gaussian aperture. We will compare these projection results with the above full dynamical simulations, and discuss optimization of KLM cavity design on this basis.

Mode projection allows us to go beyond the restriction to a single nonlinear interaction per round trip, and we will present models and results for typical Z-fold Fabry-Perot cavities, again discussing implications for KLM cavity design.

References

- [1] A. M. Dunlop, W. J. Firth, E. M. Wright, and D. R. Heatley, Opt. Lett., accepted for publication (1996).
- [2] H. A. Haus, J. G. Fujimoto, and E. P. Ippen, J. Opt. Soc. Am. B **8**, 2068 (1991).
- [3] D. R. Heatley, A. M. Dunlop, and W. J. Firth, Opt. Lett. **18**, 170 (1993).
- [4] D. J. Kuizenga and A. E. Siegman, IEEE J. Quantum Electronics **QE-6**, 694 (1970).

Highly repetitive generation of picosecond pulses at 1.57 μm using an optical parametric generator and amplifier

U. J. Greiner, T. Schröder, H. H. Klingenberg
 Institut für Technische Physik
 Deutsche Forschungsanstalt für Luft- und Raumfahrt
 Pfaffenwaldring 38-40, 70569 Stuttgart, Germany
 Tel: +49 711 6862 742, E-mail: ulrich.greiner@dlr.de

The generation of parametric fluorescence with picosecond pulses has recently enjoyed a revival. This is partly due to the availability of suitable pump sources, namely regenerative amplifiers, capable of producing picosecond pulses with pulse energies on the order of millijoules at repetition rates of several kilohertz. With such lasers it is easy to generate high power densities necessary for an efficient conversion in a nonlinear crystal^{1, 2, 3}.

We have build an all-solid-state Nd:YAG regenerative amplifier capable of delivering pulses with energies up to 1.3 mJ at a repetition rate of 1 kHz with a pulse duration of 25 - 30 ps^{4, 5}. This laser served as the pump source for an optical parametric generator and amplifier. The nonlinear crystal used was a KTP crystal cut for noncritical phase matching to generate a signal wave at 1.57 μm when pumped at 1.064 μm .

At first we used a double pass arrangement (Fig. 1). The generated signal wave as well as the pump pulse not completely converted on the first pass are reflected and passed through the crystal a second time. The conversion efficiency reached only 5% with a doughnut shaped mode at 1.57 μm .

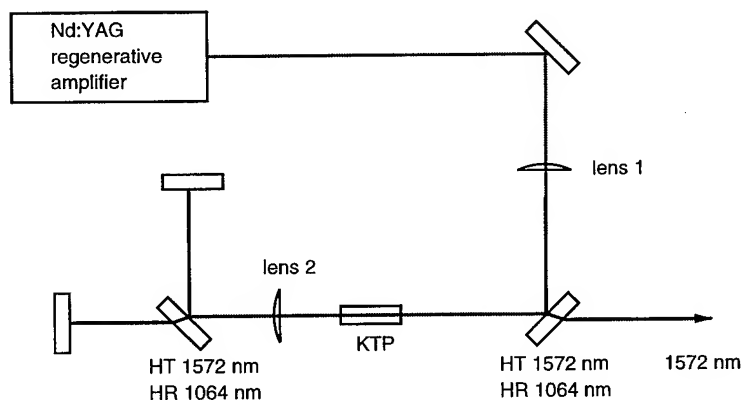


Fig. 1 Experimental setup for a simple double pass optical generator amplifier. Lens 1 focuses the pump light into the crystal and lens 2 is used to collimate and re-focus the signal and the pump light.

Simple models for parametric conversion, however, suggest a much higher conversion efficiency. With the high power densities reached with the picosecond pulses pump depletion, temporal and spatial pulse shapes can not be neglected^{6, 7}. Subsequent numerical simulations including the mentioned effects revealed that low conversion efficiency and the ring mode is to be expected in a double pass arrangement.

Pump depletion and back conversion at the center of the beam where the power density is highest lead to the ring mode (Fig 2). Furthermore, pump depletion starts at a different crystal length for different radial parts of the beam profile. At any given crystal length only a fraction of the complete pulse will therefore actually contribute to an efficient

conversion. The same effect needs to be considered in the temporal pulse evolution. The leading edge and the trailing edge will not contribute to an efficient conversion at the same location in the crystal as the center of the pulse. This effect will lower the maximum achievable efficiency which might be expected.

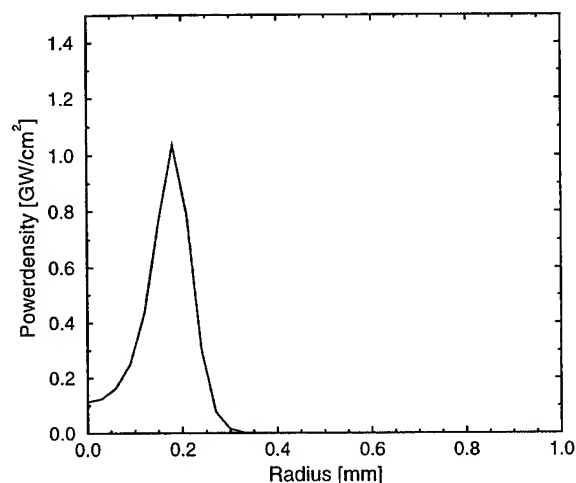


Fig. 2 Calculated transverse pulse profile for a simple double pass experiment for a pump pulse energy of 250 μJ .

According to our numerical simulation this problem can partly be reduced if one uses a generator - amplifier (OPG / OPA) setup (Fig. 3). In this case part of the pump pulse is split off and used to generate a small signal with a low efficiency but good beam profile. The signal wave will then be amplified by the rest pump pulse with no depletion at the center as in the case of a simple double pass. This will lead to a nearly Gaussian pulse profile and much higher conversion efficiencies (Fig. 4).

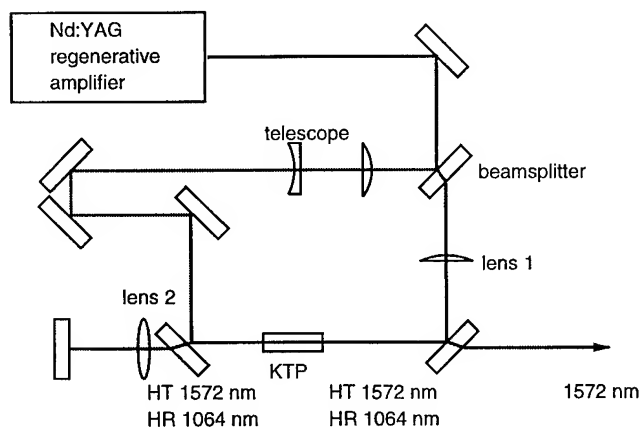


Fig. 3 Experimental setup of the optical parametric generator and amplifier. Lens 1 focuses the pump pulse of the generator into the crystal. With the telescope the beam diameter of the pump pulse for the amplifier can be adjusted to get the best performance. With lens 2 the signal generated with the generator can be collimated.

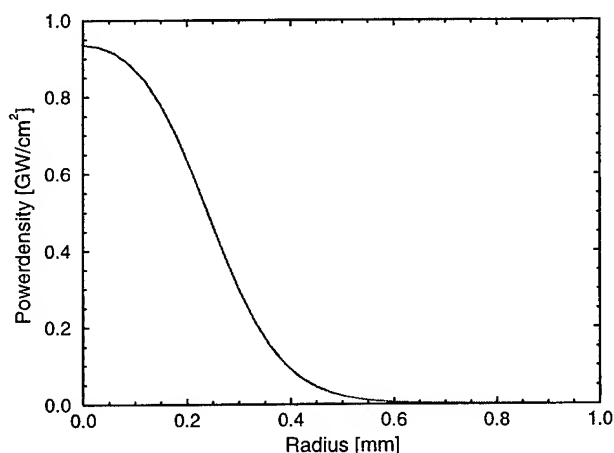


Fig. 4 Calculated transverse beam profile for the OPG / OPA with an pump puls energy of 250 μJ .

In first experiments with an optical parametric generator - amplifier configuration we confirmed the improved beam profile expected from our numerical simulations. A conversion efficiency of 10 % with a Gaussian beam profile was obtained so far. However, from the model we expect higher efficiencies which we are currently trying to achieve experimentally.

1. J. Y. Huang, J. Y. Zhang, and Y. R. Shen *Appl. Phys. Lett.*, vol. 57, no. 19, p. 1961, 1990.
2. D. R. Walker, C. J. Flood, and H. M. van Driel *Opt. Lett.*, vol. 20, no. 2, p. 145, 1995.
3. H.-J. Krause and W. Daum *Appl. Phys. Lett.*, vol. 60, no. 18, p. 2180, 1992.
4. D. R. Walker, C. J. Flood, H. M. van Driel, U. J. Greiner, and H. H. Klingenberg *Appl. Phys. Lett.*, vol. 65, p. 1992, 1994.
5. U. J. Greiner, H. H. Klingenberg, D. R. Walker, C. J. Flood, and H. M. van Driel *Appl. Phys. B*, vol. 58, p. 393, 1994.
6. R. Danelyus, G. Dikchyus, V. Kabelka, A. Piskarskas, A. Stabinis, and Y. Yasevichyute *Sov. J. Quantum Electron.*, vol. 7, no. 11, p. 1360, 1977.
7. T. Nishikawa and N. Uesugi *J. Appl. Phys.*, vol. 78, no. 11, p. 6361, 1995.

Effective Suppression of Amplified Spontaneous Emission by SBS Phase Conjugation

C. K. Ni and A. H. Kung

Institute of Atomic and Molecular Sciences, Academia Sinica

P.O. Box 23-166, Taipei 10764, Taiwan, R.O.C.

Optical phase conjugation using stimulated Brillouin scattering (SBS) is widely used in high average power solid state lasers and multipass amplifiers for correction of problems brought on by thermally induced birefringence and depolarization and for pulse compression.¹ Multi-kilowatt average power with diffraction-limited beams are now routinely obtained in Nd:YAG laser systems where a SBS mirror is an integral part of the system. The pump lasers used in these systems all have narrow bandwidths, typically <1 GHz. The reason for this is well-known^{2,3}: the SBS threshold for a noisy (multi-frequency) pump is higher than that for a single-longitudinal-mode pump or one with just a few modes. So, in order to obtain high reflectivity for the SBS mirror using minimal power, narrow-bandwidth lasers are used. We have taken note of this property of SBS and explored its utility to solve another important problem in laser amplifiers: the suppression of amplified spontaneous emission.

Amplified spontaneous emission (ASE) is the primary limiting factor in efficient amplification using high gain media⁴ and in maintaining high spectral purity and broad tuning in pulse-amplified CW lasers.⁵ In large amplification, very often elaborate dispersion or spatial filtering schemes are used to suppress the significant ASE content. Since ASE in general has

a broad spectral width (poor monochromaticity), the SBS gain from focused ASE is lower than from the amplified seeding pulse under similar focusing conditions by the ratio of the seeder bandwidth to the ASE bandwidth.² Insertion of a SBS phase-conjugate mirror in the amplifier chain could therefore provide effective discrimination between the signal pulse and the uncorrelated ASE background. In the most favorable case when SBS gain due to ASE is below threshold, the ASE can be eliminated. The simplicity of a SBS mirror is also advantageous over four-wave mixing methods, and methods using dispersion or spatial filtering. In addition, the phase-conjugated pulse will retrace the beam path through the amplifier chain, allowing additional amplification and efficient extraction of the stored energy in the amplifier.

We have tested this ASE suppression scheme using a single-mode CW Ti:sapphire laser and a Ti:sapphire amplifier pumped by the second harmonic of a Q-switched Nd:YAG laser. The CW laser at 821 nm was first passed through a dye pre-amplifier with a gain of 3×10^4 to produce a narrowband pulse. This pulse was then sent through a 4-pass Ti:sapphire amplifier before being focused into a SBS cell containing a fluorocarbon liquid. The phase-conjugated beam is extracted after it has retraced through the 4-pass amplifier. The energy and ASE content of the output pulse were monitored for the case of using phase-conjugation and without phase-conjugation.

ASE content is found to be reduced from 15% of the total output when a regular mirror is used to less than 1 part in 10^4 with phase-conjugation. The ASE level is below the detectable noise of our photodiode detector. A reflectivity of up to 40% is achieved for the SBS mirror. Total output energy is 25 mJ when the phase-conjugate mirror is used, as

opposed to 35 mJ when a regular mirror is used. It is expected that by operating the Ti-sapphire amplifier in saturation the difference in output energy between the two cases will diminish. The threshold for SBS is ~ 2 mJ which is similar to that observed for 1064 nm in the SBS medium. Duration of the pulse is compressed from 10 ns to 3.7 ns. The temporal profile of the output pulse has a single peak with a smooth profile. The spatial profile has a $>90\%$ Gaussian fit, similar to that of the input.

These results show that phase conjugation is effective in suppressing ASE. Use of phase-conjugating mirror permits additional amplification of the output without enhancing ASE content. It will be important for tunable systems where the output wavelength is far from the central gain wavelength of the amplifying medium. Results on tuning characteristics and use of additional amplifiers will also be presented

This research was supported by the National Science Council of the Republic of China under contract NSC 85-2113-M-001-027.

References

- (1) D. A. Rockwell, IEEE J. Quantum Electron. **24**, 1124 (1988).
- (2) S.A. Akhmanov, Yu.E. D'yakov, L.I. Pavlov, Sov. Phys. JETP **39**, 249 (1974).
- (3) R. A. Fisher, editor, "Optical Phase Conjugation", Academic Press, New York (1983).
- (4) J.T. Verdeyen, "Laser Electronics" p179, Prentice Hall, Inc., New Jersey, publisher (1981).
- (5) E. Cromwell, T. Trickl, Y.T. Lee, and A.H. Kung, Rev. Sci. Instrum. **60**, 2888 (1989).

Quasi-Phasematched Singly Resonant Parametric Oscillation in Periodically-Poled Lithium Niobate Waveguides

M. A. Arbore and M. M. Fejer

E.L.Ginzton Laboratory, Stanford University, Stanford California 94305

(415) 725-2282 , Fax: (415) 723-2666

Email: marbore@loki.stanford.edu

Diode-based sources of near or mid-IR radiation are finding applications in communications, spectroscopy, and process monitoring. Nonlinear optical frequency conversion to shift diode laser outputs to the desired wavelength has attracted significant attention as a means to meet these needs. Periodically-poled lithium niobate (PPLN) has proven to be a nonlinear material offering an excellent combination of efficiency, wavelength accessibility, ease of fabrication, reproducibility, and cost. Waveguide geometries significantly increase conversion efficiencies of nonlinear devices by tightly confining the optical fields over long interaction lengths. Combining annealed proton-exchanged (APE) waveguide technology with PPLN allows the application of nonlinear frequency conversion to low power sources.

Optical parametric oscillators (OPOs) offer high conversion efficiency and wide tunability while requiring only a single pump laser. The oscillation threshold for nearly degenerate parametric oscillation is¹

$$P_{th} = \frac{1}{\eta_{nor}} \left[\frac{\alpha_p}{1 - \exp(-\alpha_p L)} \ln \left(Q + \sqrt{Q^2 - 1} \right) \right]^2 \quad \text{with} \quad Q = \frac{1 + R_s R_i \exp(-4\alpha L)}{(R_s + R_i) \exp(-2\alpha L)} \quad (1)$$

where α_p is the field loss coefficient at the pump wavelength, $R_{s,i}$ and α are the effective mirror power reflectivities and field loss coefficients at the signal and idler wavelengths, and η_{nor} is the normalized small-signal parametric gain (%/Wcm²). While doubly resonant oscillators (DROs), with feedback at both the signal and idler wavelength, can have low thresholds, their tuning behavior is complicated by the required double resonance condition. Singly resonant oscillators (SROs), with feedback only at the signal wavelength, offer simplified tuning at the expense of higher thresholds. One current challenge for SROs is reducing the oscillation threshold to levels attainable with diode lasers.

A significant difference between bulk and waveguide OPOs is that the waveguide modes are generated and depleted in a spatially homogeneous fashion, so that their evolution in the OPO follows the same mathematical description used for plane wave devices, e.g. 100% pump depletion for pumping at $(\pi/2)^2$ times above threshold power.

Low threshold doubly resonant OPOs^{2,3} have been previously demonstrated in LiNbO₃ waveguides. These devices were based on titanium diffused waveguides and birefringent

phasematching. They operated at temperatures between 200 - 300 °C with pump wavelengths limited to ≈ 600 nm, and normalized parametric gains⁴ of $\eta_{\text{nor}} = 0.03$ %/Wcm². Since our first demonstration of a quasi-phasematched⁵ (QPM) waveguide OPO⁶, processing improvements have resulted in an order of magnitude improvement in gain. We report these device improvements and more detailed characterization of OPO performance.

The channel waveguide device used in the experiments reported here was 2.7 cm long and two-moded at the degeneracy wavelength of 1543 nm. The periodically-poled substrate, with a domain period of 14 μm , was fabricated by electric field poling⁷ of a 0.5-mm-thick z-cut wafer of congruent LiNbO₃. The waveguide was designed using the model for linear and nonlinear properties of APE-LiNbO₃ given in reference 8. The sample was proton exchanged at 177 °C for 4 hours to a depth of 0.55 μm through a lithographically defined mask of sputtered SiO₂ with 5 μm wide channel openings. The sample was then iteratively annealed in air at 340 °C for a total of 11.5 hours, resulting in phasematching at the desired wavelength. An SHG tuning curve for the best waveguide on the sample exhibited a 0.5 nm FWHM bandwidth and a peak conversion efficiency, η_{nor} , of 250 %/W as shown

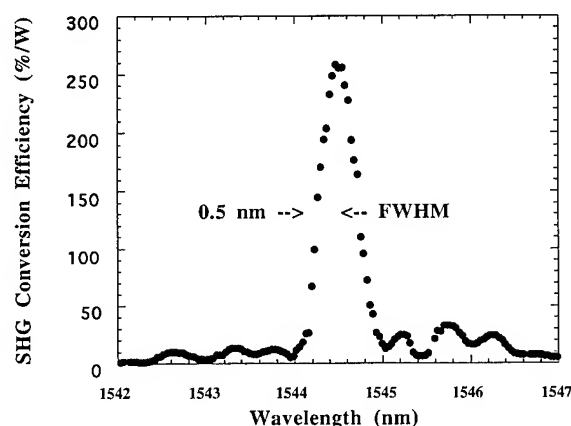


Figure 1. Single-frequency SHG tuning curve. Peak efficiency is identical to near-degenerate parametric gain.

in Figure 1. Small-signal parametric gain at degeneracy is the same as the SHG conversion efficiency. A similar waveguide with gain of 175%/W was used for the OPO experiments. Waveguide losses at 1.32 μm of 0.6 dB/cm were measured by the Fabry-Perot method. Dielectric mirrors with high reflectivity from 1100-1475 nm and < 5% reflectivity for $\lambda > 1600$ nm (to ensure SRO operation) were contacted to the polished waveguide endfaces. Equation 1 indicates a 600 mW threshold for this device, assuming equal waveguide losses at all wavelengths.

Using an acousto-optically-Q-switched Ti:sapphire laser with ~ 100 ns FWHM output pulses as a pump source, we observed a threshold of 1.6 (peak) watts of launched pump. By tuning the pump wavelength from 762-771.5 nm, the SRO output wavelengths tuned over 1270-1900 nm, as shown in Figure 2. The phasematching data near degeneracy were measured by SHG and single-pass parametric amplification. The solid line is the theoretical prediction based on the theoretical waveguide dispersion, with the degeneracy wavelength set to the measured value.

Figure 3 shows pump transmission (unity minus pump depletion) and peak idler output power as a function of peak launched pump power. The maximum pump depletion, observed at 1700 nm, was 40%, with peak idler output power of 220 mW for a peak launched pump power of 3.7 W.

A waveguide supporting one mode at the idler wavelength is of necessity highly multi-moded at the pump wavelength. Even with careful input coupling, it is difficult to avoid significant coupling

of the pump power into higher order modes, so the major uncertainty in comparing experiment to theory is the fraction of the pump power launched into the fundamental mode of the waveguide. The observed threshold is consistent with the theoretical prediction if 38% of the pump power is properly coupled. A check of the consistency of this assumption is fitting the pump depletion data to theoretical prediction. The best fit, shown in Fig. 3, is obtained for 43% coupling, in good agreement with the value obtained from the threshold calculation. Note that with 43% coupling, the maximum depletion of the pump power in the fundamental mode is ~95% for pumping at 2 times above threshold, approaching the complete pump depletion expected for a plane wave SRO.

Our modeling indicates that an optimally processed device would have an SRO threshold < 100 mW, accessible to CW diode pumping. The major experimental difficulty, coupling into the desired pump mode, can be addressed with an adiabatically tapered waveguide, as demonstrated in Ref. 10. Future work will investigate such optimized devices.

We acknowledge generous donation of materials from Crystal Technology and mirrors from Spectra Physics.

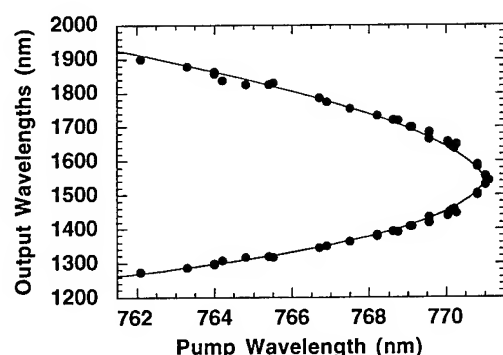


Figure 2. Parametric tuning curve for waveguide SRO. Data near degeneracy was measured by SHG and single-pass parametric gain, rather than by OPO.

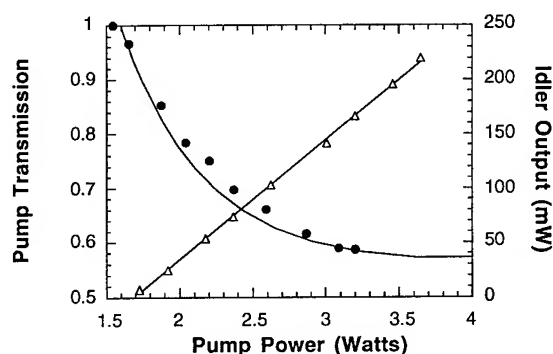


Figure 3. OPO pump depletion and output power. Nearly 100% of pump in phasematched transverse mode is depleted at twice threshold.

- 1 G. P. Bava, I. Montrosset, W. Sohler, and H. Suche, *IEEE J. Quantum Electron.*, **QE-23**, 42 (1987).
- 2 W. Sohler and H. Suche, *Tech. Dig. 3rd Int. Conf. Integrated Opt. and Opt. Fiber Commun.*, 1981, San Francisco, Ca, p. 89.
- 3 H. Suche and W. Sohler, *Integrated and guided wave optics*, IGWO, 1988, Santa Fe, USA, OSA Technical digest series Vol. 5, paper MF15 (1988), p. 176.
- 4 W. Sohler and H. Suche, *Appl. Phys. Lett.*, **37**, 255-277 (1980).
- 5 J. A. Armstrong, N. Bloembergen, J. Ducuing, and P. S. Pershan, *Phys. Rev.*, **127**, 1918 (1962).
- 6 M. L. Bortz, M. A. Arbore, and M. M. Fejer, *Opt. Lett.*, 49-51 (1995).
- 7 L. E. Myers, R. C. Eckardt, M. M. Fejer, R. L. Byer, W. R. Bosenberg and J. W. Pierce, *J. Opt. Soc. Am B* **12**, 2102 (1995).
- 8 M. L. Bortz and M. M. Fejer, *Opt. Lett.* **16**, 1844-1846 (1991); M. L. Bortz, L. A. Eyres and M. M. Fejer, *Appl. Phys. Lett.* **62**, 2012-2014 (1993).
- 9 J. E. Bjorkholm, *IEEE Jour. Quan. Elec.*, **QE-7**, 109 (1971).
- 10 M. H. Chou, M. A. Arbore and M. M. Fejer, submitted for publication.

NON-RECIPROCITY OF POLARIZATION ROTATORY POWER

P.J.Bennett, S.Dhanjal, Yu.P.Svirko and N.I.Zheludev

Department of Physics
University of Southampton
Southampton SO17 1BJ
UK

phone: +44.1703.593566; fax: +44.1703.593910; e-mail: (n.i.zheludev@soton.ac.uk)

It was commonly believed that polarization plane rotation in a non-magnetic, optically active media is reciprocal. Here we report, what is to the best of our knowledge, the first observation of nonreciprocal polarization plane rotation in an optically active, non-magnetic crystal. We saw that a light wave which passed through the crystal, $B_{12}SO_{20}$, and which was then reflected exactly back through it, did not recover its initial polarization azimuth. The nonreciprocal component of rotation was of the order of 7×10^{-3} of the reciprocal rotation. The effect is unambiguous evidence of broken reversality of the light-matter interaction process. Our interest in this research was motivated by the fundamental importance of the topic, and because time non-reversal effects may be exploited in unidirectional valves for electromagnetic radiation.

The crystal, $B_{12}SO_{20}$, belongs to the cubic, noncentrosymmetric 23 crystal point group. Its optical properties may be described by the constitutive equation $D_i = \epsilon_{ij}(\omega)E_j + \nabla_m[\gamma_{ijm}(\omega)E_j]$. This symmetry does not support birefringence, that is the dielectric tensor $\epsilon_{ij}(\omega)$ is diagonal: $\epsilon_{ij}(\omega) = \epsilon(\omega)\delta_{ij}$. However, the crystal symmetry supports conventional isotropic optical activity. It is described by the *anti-symmetric* part of the nonlocality tensor $\gamma^a_{ijm} = -\gamma^a_{jim} = \gamma_{ijm} - \gamma_{jim}$. Only taking into account these two contributions, the wave propagation in this crystal is reciprocal and polarization plane rotation is compensated for on the return propagation. However, the 23 crystal symmetry also supports the *symmetric* part of the nonlocality tensor $\gamma^s_{ijm} = \gamma^s_{jim} = \gamma_{ijm} + \gamma_{jim}$. It was commonly believed that the microscopic time-reversality of the light-matter interaction process forbids the existence of the symmetric component γ^s_{ijm} of the nonlocality tensor in non-magnetic crystals [1]. Recently, by analyzing the light-matter interaction Hamiltonians, we have shown that taking the non-local relativistic effects into account the light matter interaction is not necessarily invariant under time-reversal, T [1]. In fact it obeys the more rigid relativistic symmetry with respect to simultaneous inversion of the process in time and space, PT. According to the analysis in [1], nothing forbids the symmetric nonlocality tensor $\gamma^s_{ijm} = \gamma^s_{jim}$ in crystals lacking an inversion centre. This is the part of the nonlocal response which gives rise to the nonreciprocal polarization plane rotation.

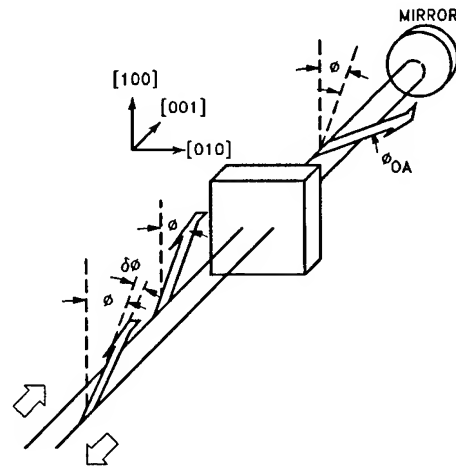


Fig. 1. *Experimental setup to study nonreciprocity in polarization rotatory power*

Indeed if no restriction is imposed on the existence of the symmetric part of the nonlocality tensor, one can readily obtain the following formula for the change, $\delta\phi$, of the polarization state after a consecutive forward and backward propagation through the 23 crystal along the [001] direction [2].

$$\delta\phi = - \frac{2\phi_{TNOA}}{\phi_{OA}} \cos(2\phi + \eta) \sin(\phi_{OA}) \quad (1)$$

ϕ is the incident polarization azimuth measured from the [100] direction, η is the offset parameter, which is exactly equal to the conventional optical activity polarization plane rotation, $\phi_{OA} = (\omega^2/4c^2) \text{Re}\{ \gamma_{xyz} - \gamma_{yxz} \} z$. Here, $\phi_{TNOA} = (\omega^2/4c^2) \text{Re}\{ \gamma_{xyz} + \gamma_{yxz} \} z$, which is a figure of merit for the nonreciprocal effect. Note that the nonreciprocal effect is proportional to $\text{Re}\{ \gamma_{xyz} + \gamma_{yxz} \}$, which is a dissipative susceptibility, and should only be noticeable in the spectral range of significant absorption.

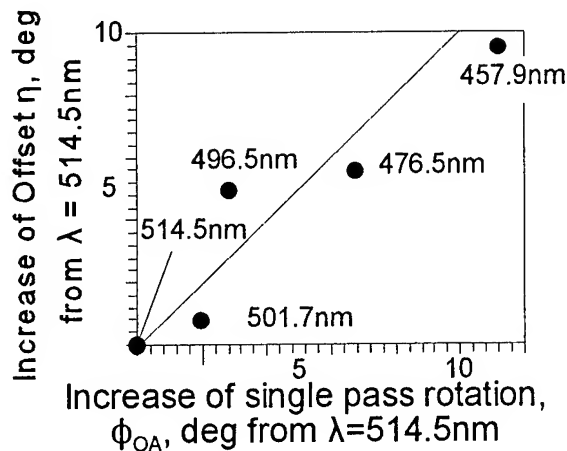


Fig. 3. Dependence of the orientation offset η on the single pass optical activity ϕ_{OA} shows that the offset steadily follows the single pass rotation at all five available wavelengths

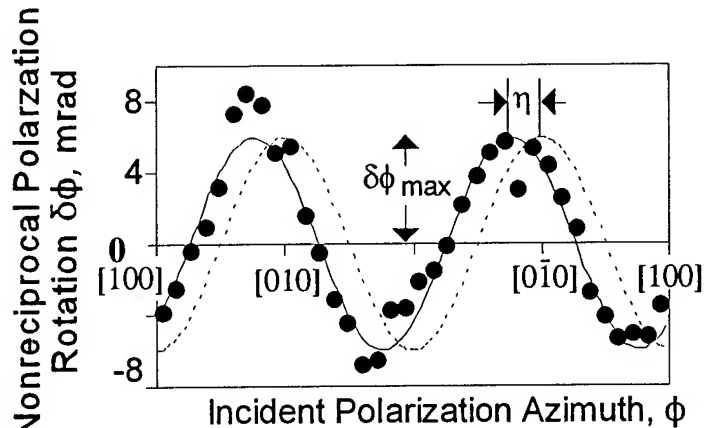


Fig. 2. Dependence of the nonreciprocal component of the polarization azimuth rotation, $\delta\phi$, on the polarization azimuth of the incident light wave with respect to the crystal axes.

Although the optical properties of $B_{12}SO_{20}$, and the optical rotatory power in particular, have been studied comprehensively in this crystal, there have not been any attempts to examine the reciprocity of optical activity. We have set-up an experiment to detect this nonreciprocal rotation in an unambiguous, retroreflecting, double pass experiment (see fig.1). Since some absorption was important we chose a beam-stabilized argon-ion laser as the optical source. With this laser we were able to do measurements at different wavelengths (514.5, 501.7, 496.5, 476.5 and 457.9nm) in the proximity of the edge of the transparency spectral gap. Because the nonreciprocal rotation should have an oscillatory dependence on the crystal thickness (see formula (1)), there was no reason to go for long samples. We chose a

high grade, virtually stress-free, sample of $B_{12}SO_{20}$, of approximately 0.63mm thickness and $5 \times 5 \text{mm}^2$ square. Using a special polarimetric configuration we ensured that the light propagates though the crystal along exactly the same pass forwards and backwards.

The laser was protected from the returning light by an optical isolator. The measurement technique was solely sensitive to the polarimetric azimuth rotation and has been described elsewhere [3].

We saw clearly measurable, nonreciprocal polarization plane rotation in the $B_{12}SO_{20}$ crystal. In order to compare this rotation with the theoretical predictions we have done the following set of experiments:

- (i) We measured the nonreciprocal polarization rotation, $\delta\phi$, as a function of ϕ , i.e. the incident polarization azimuth. A clear oscillatory dependence was observed, which accurately follows the $\cos(2\phi + \eta)$ function as predicted by formula (1) (see fig.2);
- (ii) We compared the orientational offset η of the oscillatory dependence in $\cos(2\phi + \eta)$ with the directly measured value of the single-pass optical activity ϕ_{OA} . The theory predicts that they must be equal. They correlate very well across the whole measured spectral range. (see fig.3);
- (iii) We measured the dependence of the nonreciprocal rotation on the wavelength. As would be anticipated for a dissipative effect, the nonreciprocal effect due to the dissipative susceptibility $Re\{\gamma_{xyz} + \gamma_{yxz}\}$ increases for shorter wavelengths, i.e. with absorption (see fig.4);
- (iv) In order to see if there were any contributions to the polarization rotation which could appear due to imperfections of the sample, such as residual stress, we measured the nonreciprocal rotation at different points of the crystal over the whole crystal surface. No significant change of the effect has been observed.

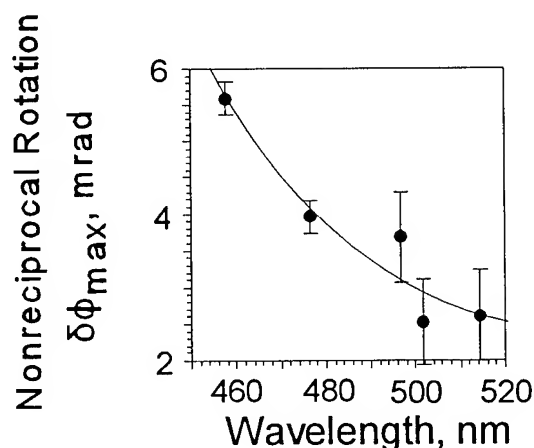


Fig. 4. Dependence of the nonreciprocal rotation $\delta\phi$ on the wavelength

We consider the results above are the first explicit evidence of the existence of natural nonreciprocal polarization rotation on the background of the reciprocal optical activity, which unambiguously and positively indicate broken time reversality of the light matter interaction process.

- [1] Yu.P.Svirko, N.I.Zheludev. Reversality of optical interactions in noncentrosymmetric media. *Optics Letters*, **20**, 1809, (1995).
- [2] A.Malinowski, Yu.P.Svirko, N.I.Zheludev. Reciprocity in nonlocal optics. *JOSA-B*, in press 1996.
- [3] A. R. Bungay, Yu.P. Svirko, N.I. Zheludev. Experimental observation of specular optical activity. *Physical Review Letters*, **70**, 3039, (1993).

Cascaded Optical Nonlinearities: Microscopic Understanding of It as a Collective Effect.

Jacob B. Khurgin and S.J. Lee

*Department of Electrical and Computer Engineering
The Johns Hopkins University, Baltimore MD 21218*

The third-order optical nonlinearities, whose potential for optical processing and switching has been understood for many years, have not found wide applications, for the simple reason that typical $\chi^{(3)}$ is too small to make the devices based on it practical. Recently, however, a significant progress has been made on the way to change this unfortunate situation, by using cascaded second order nonlinear processes in order to achieve the effective third-order nonlinearity. This method, first realized in [1],[2] suggests the use of the parametric interaction between fundamental and second-harmonic waves in order to obtain effective $\chi^{(3)}$ proportional to $|\chi^{(2)}|^2$. More recently, a number of cascading schemes utilizing surface-emitting second-harmonic generation in a resonator have been proposed [3].

A completely different approach to implementing artificial $\chi^{(3)}$ have been taken by the developers of all-optical processing devices using the self-electro-optic-device (SEED) [4], where the optical signal is first detected and then modulated. A closer look at the SEED, however, reveals that its nonlinear action is nothing but cascading, but this time consisting of subsequent application of optical rectification (detection) and linear electro-optic effect - both of them $\chi^{(2)}$ processes. Similarly, it is not difficult to see that the photo-refractive effect can also be considered as a sequence of detection and modulation.

In this presentation we develop a very simple general microscopic theory of cascading effects, showing that in general the enhancement of the $\chi^{(3)}$ due to cascading can be described by the factor

$$K_{casc} = \frac{NQ | \langle \mu \rangle |^2}{\epsilon_0 \langle \delta E \rangle} \quad (1)$$

where N is a density of active atoms or molecules involved in the nonlinear process, $\langle \mu \rangle$ is an average dipole moment, $\langle \delta E \rangle$ is an average detuning energy, and Q is either $Q = \omega\tau$ of the resonator cavity, or, in the absence of latter, simply $\omega L/c$.

We point out that microscopically cascading is a *collective* effect, whose meaning lies in the extending the lifetime of the virtual states by coupling them together with the electro-magnetic wave of intermediate frequency. Based on our theory we describe cascading equivalents of all major third-order nonlinear effects, including nonlinear index, phase conjugation, four-wave mixing, Raman and other two-photon effects, evaluate relative efficiencies of various cascading schemes, and stress their advantages and weaknesses. We also consider innovative schemes that include amplification on the intermediate frequency.

This work is supported by the AFOSR.

References

- [1] R. DeSalvo, D. J. Hagan, M. Sheik-Bahae, G. Stegeman, and E. W. VanStryland, Opt. Lett. **17** , 28 (1992).
- [2] G. I. Stegeman, M. Sheik-Bahae, E. W. VanStryland, and G. Assanto, Opt. Lett. **18** , 13 (1993).
- [3] J. B. Khurgin and Y. J. Ding, Opt. Lett. **19** , 1016 (1994).
- [4] A. L. Lentine and D. A. B. Miller, IEEE J. Quantum Electron., **QE-29**, 655 (1993)

Influence of Mirror Curvature on Pattern Formation in Nonlinear Optics

G. K. Harkness, J. Lega[†] and G.-L. Oppo

*Department of Physics and Applied Physics,
University of Strathclyde, 107 Rottenrow, Glasgow G4 0NG, UK
Tel: + 44 - 141 - 552 - 4400 x3354 ; Fax: + 44 - 141 - 552 - 2891*

Study of pattern formation in the transverse section of lasers with plane cavity mirrors of infinite size shows that the fundamental solutions are transverse travelling waves [1]. In the case of Optical Parametric Oscillators (OPO), instead, rolls [2] or squares, or hexagons [3] are the fundamental patterns close to threshold. With curved cavity mirrors, however, both cases of lasers and OPO produce outputs which look like a combination of empty cavity modes, generally of Gauss-Laguerre type. These are the most commonly observed experimentally; a typical example of output intensity is shown in Figure 1 for the laser case.

We have shown that, although the mirror curvature introduces a singular perturbation to the diffractive nonlinear equations [4,2], the mechanisms behind the selection of either patterns (flat mirrors) or cavity modes (curved mirrors) are analogous [5]. In fact, numerical simulations show that even when the mirrors are curved, patterns of a travelling-wave nature are recovered in the laser case and patterns of the roll type are obtained for the OPO for large enough input energies (pump).

For both the laser and the OPO cases, we have reduced the diffractive nonlinear equations to modified Swift-Hohenberg equations by introducing a new perturbation parameter η inversely proportional to the square root of the radius of curvature R of the cavity mirrors. We show in Figure 2 how, for example, the laser threshold versus the detuning δ is modified for increasing values of η . The limit of plane mirrors is recovered when $\eta = 0$. Two cases are of interest for finite η . The first corresponds to detuning values close to the bottom of the parabola of Figure 2 where the excitation of just one family of modes takes place. The second corresponds to the intersection of two adjacent parabola where separate families of modes can be excited. For both cases, we have derived suitable amplitude equations for the modal competition just above threshold. Stability of the solutions above the laser/OPO threshold is studied both analytically and numerically.

We focus now on the laser case. By moving away from the laser threshold, we have found a new transition from mode dominated spatial structures to patterns of a travelling-wave nature as shown in panel 1 of Figure 3. As the radius of curvature of the mirrors, R , decreases the threshold values of the pump increase. In the shaded region there is bistability between target and Gauss-Laguerre pattern types. We believe that the difficulty of observing travelling-wave patterns in real lasers is related to the fact that for typical experimental configurations with curved cavity mirror η is of order 1 and the pump value corresponding to the transition of Figure 3 becomes quite large.

Above such threshold, the laser patterns take the form of the cylindrically symmetric travelling waves shown in panel 2 of Figure 3. The waves are generated at the edge and travel inwards. We have analysed these structures using amplitude equations derived in the Gauss-Laguerre basis, and a numerical shooting method. This method allows us to study the stability of these target patterns; complex spatio-temporal behaviour

is predicted for specific parameter ranges. In particular we have found an instability of the source of travelling waves which leads to a weak turbulence characterised by the erratic emission of vortices. Moreover, the stability of these new solutions to externally induced breaking of the cylindrical symmetry is also investigated.

Analogies and differences between the laser and OPO cases are also discussed. Target patterns and other fascinating laser/OPO spatio-temporal structures will be presented with the aid of video displays. This work is, in part, supported by EPSRC grant GR/J/30998.

References

- [1] P. K. Jakobsen *et al.*, Phys. Rev. A, **49**, 4189 (1994) and references therein.
- [2] G.-L. Oppo, M. Brambilla, and L. A. Lugiato, Phys. Rev. A, **49**, 2028 (1994).
- [3] M. Brambilla, D. Camesasca, G.-L. Oppo and W.J. Firth, preprint (1996).
- [4] L. A. Lugiato *et al.*, J. Opt. Soc. Am. B, **7**, 6, 1019 (1990).
- [5] G. K. Harkness, J. Lega and G.-L. Oppo, submitted to Phys. Rev. A (1996).

([†]) Permanent address: INLN, 1361 Route des Lucioles, 06560 Valbonne, France.

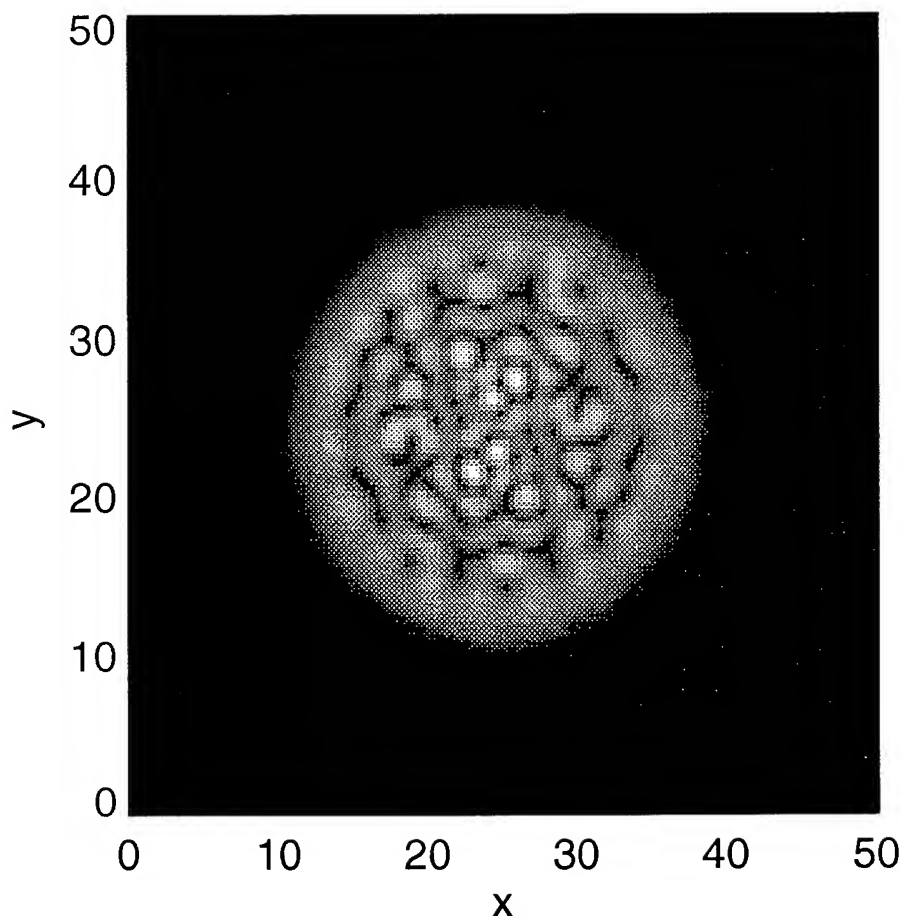


Figure 1: Typical laser output intensity dominated by Gauss-Laguerre modes.

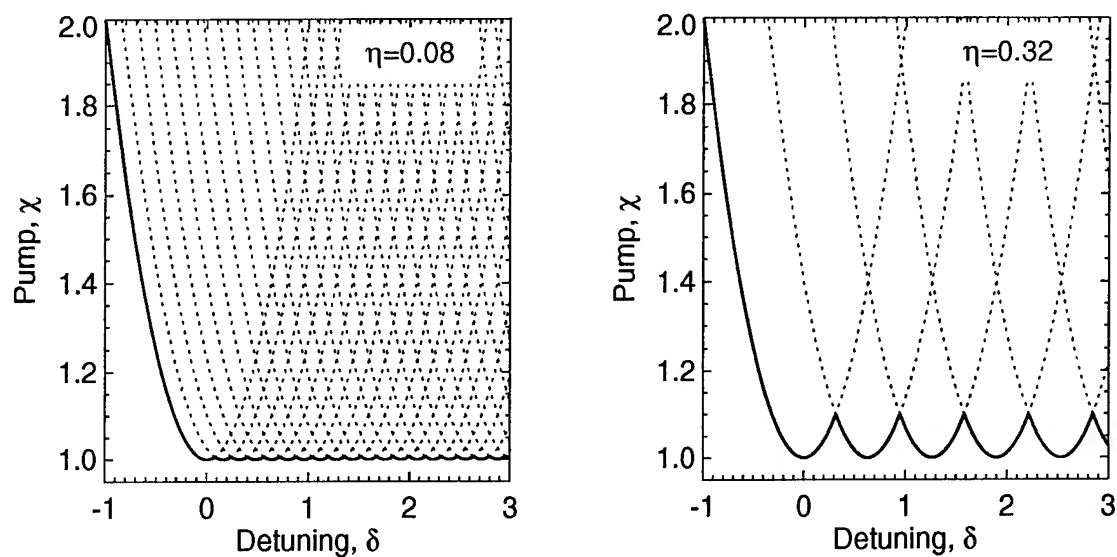


Figure 2: Laser threshold (solid line) versus the detuning δ for two values of the mirror curvature η . Each dashed line correspond to the threshold for a specific family of Gauss-Laguerre modes.

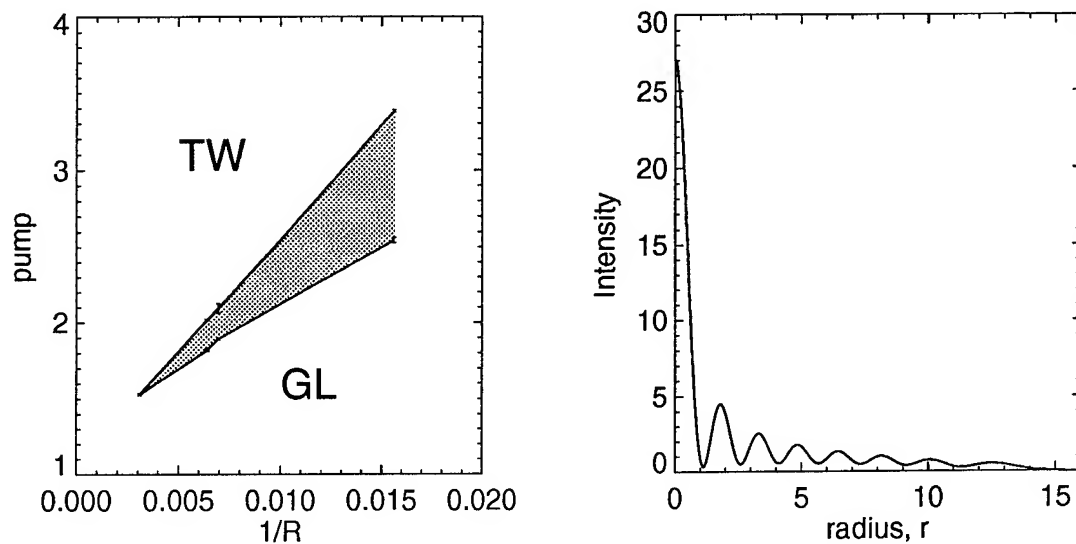


Figure 3: Transition between Gauss-Laguerre dominated structures (GL) to travelling-wave dominated patterns (TW) in lasers. The radial intensity profile of a cylindrically symmetric travelling-wave pattern is shown on the right.

Control of Spatio-Temporal Dynamics in Nonlinear Optics

R. Martin, G.-L. Oppo, A.J. Scroggie and W.J. Firth

Department of Physics and Applied Physics, University of Strathclyde
107 Rottenrow, Glasgow, G4 0NG, Scotland, UK

Tel + 44 - 141 - 552 - 4400 (ext. 3761) ; Fax + 44 - 141 - 552 - 2891

The ability to control spatio-temporal dynamics of nonlinear optical systems is of great interest due to the possibilities of obtaining stable outputs without losing essential power and also to achieve pattern selection for information processing purposes.

We consider first the case of multi transverse mode lasers by using a diffractive Maxwell-Bloch model for a single longitudinal mode ring cavity [1] where the electric field variable is projected onto a finite set of Gauss-Laguerre modes. For certain parameter regimes, chaotic behaviour results in complex dynamics of the output profile of the laser. By applying both incoherent and coherent control techniques, we have been able of achieving regular oscillations without losing the overall output power.

Using a method introduced by Roy and collaborators [2], we have controlled the dynamics of diffractive laser equations in a weakly disordered regime by applying small periodic parameter variations at the frequency of the relaxation oscillations, for models including as many as twenty one cavity modes (corresponding to 1972 coupled ordinary differential equations) [3]. Control signals determined by a simple feedback law [2], have been added to either the pump or the cavity losses with magnitudes of the order of a few percent. We have been able, however, to obtain regular oscillations only from weakly disordered regimes characterised by a low dimension density [4,5] where the fractal dimension appears to diverge slowly with embedding dimension (see Figure 1) [3]. It is important to note that this technique allowed us to control the dynamics temporally, but provided no tools for pattern or mode selection [3]. In regimes corresponding to the steeper curve in Figure 1, we were unable to obtain control. This has led us to introduce new techniques which add a spatial element to the temporal one. In particular, we have used feedback fields with specific spatial configurations. For example, by feeding back a small percentage of the fundamental gaussian mode, we show that steady state behaviour can be obtained along with a degree of mode selection. Stable dynamics are observed right throughout the otherwise chaotic regime of the laser for as little as 1% feedback of the gaussian intensity (see Figure 2). Stability analysis of the three mode case confirms that under the action of injection, the region where the gaussian mode is stable with respect to neighbouring modes, is greatly increased.

Secondly, we have focused on the use of spatio-temporal control techniques applied to optical systems that display the formation of rolls or hexagons at threshold. In particular we have integrated model equations describing a two-level atomic medium in a ring cavity under the action of an external pump and diffraction in the resonator [6,7]. By selecting the parameters within the regime where the roll pattern is the only stable attractive solution close to threshold, we are able to stabilise the originally unstable homogeneous solution as shown in Figure 3. Stabilisation is attained by employing a technique which extends a control method suggested by Ott, Grebogi and Yorke [8] to the spatio-temporal domain. We apply a spatial and temporal control modulation

to the input pump beam, obtained by a suitable analysis of the stable and unstable directions in the spatial Fourier domain. One of the major interests of our procedure is that the control method can be easily implemented in the optical domain since it is based on information contained in the far-field images. The possibility of extending this control technique to pattern states (such as hexagons) will also be discussed. Support from EPSRC (GR/J/30998) is gratefully acknowledged.

References

- [1] L. Lugiato et al., J. Opt. Soc. Am. B **7**, 1019 (1990).
- [2] R. Roy et al., Phys. Rev. Lett. **68**, 1259 (1992).
- [3] R. Martin et al., Optics Communications, to appear (1996).
- [4] M. Bauer et al., Phys. Rev. Lett. **71**, 521 (1993).
- [5] G. Steinmeyer et al., Phys. Rev. E, to appear (1996)
- [6] L. Lugiato and C. Oldano, Phys. Rev. A **37**, 3896 (1988).
- [7] W.J. Firth and A.J. Scroggie, Europhys. Lett. **26**, 521 (1994).
- [8] E. Ott, C. Grebogi, and J.A. Yorke, Phys. Rev. Lett. **64**, 1196 (1990).

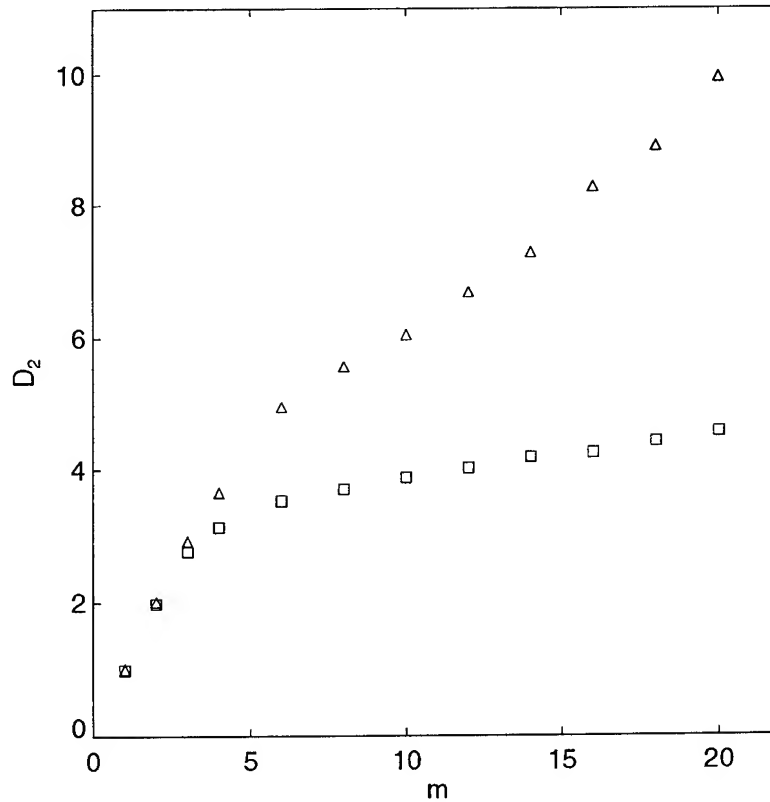


Figure 1: Calculated fractal dimension D_2 versus embedding dimension m . The lower plot marked by squares, corresponds to the controllable case and the upper plot, marked by triangles, corresponds to the uncontrollable case.

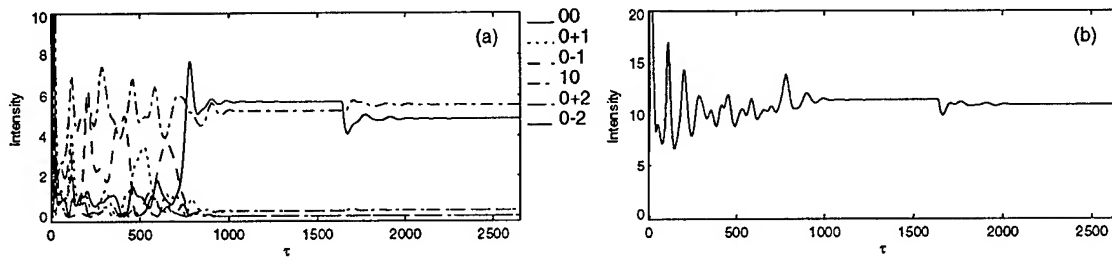


Figure 2: (a) Laser mode amplitudes before and after feedback is switched on. A small change in feedback strength inverts the roles played by the $(0,0)$ and $(1,0)$ modes. (b) The corresponding total power of the laser.

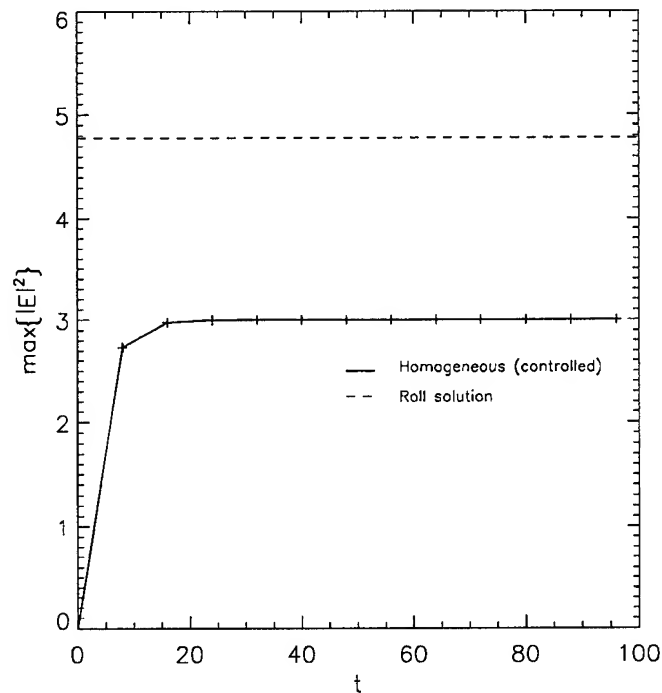


Figure 3: Controlled evolution of the maximum of the output intensity of the homogeneous solution (solid curve). The dashed line indicates the maximum of the output intensity for the roll pattern which is attained if no control is applied.

Absolute Scale of the Second-Order Nonlinear Optical Coefficients

I. Shoji, A. Kitamoto, M. Shirane, T. Kondo, and R. Ito

Department of Applied Physics, Faculty of Engineering,

The University of Tokyo

7-3-1 Hongo, Bunkyo-ku, Tokyo 113, Japan

Tel. : +81-3-3812-2111 ext. 6842

Fax : +81-3-3816-7805

E-mail : ishoji@photonics.rcast.u-tokyo.ac.jp

The second-order nonlinear optical coefficients are essential material parameters that determine the performance of nonlinear optical devices. Unfortunately, however, there have been considerable discrepancies among their absolute values reported to date [1]. This confusion, we believe, arises from the following factors. First, quite different values have been reported between parametric fluorescence (PF) and second-harmonic generation (SHG) measurements; e.g., $d_{31}(\text{LiIO}_3)$ measured by PF method is 70 % larger than by SHG method [2, 3]. Second, wavelength scaling of nonlinear optical coefficients has been made based on the constancy of Miller's Δ , although it has not been experimentally confirmed in what wavelength region and to what accuracy Miller's Δ is constant. Moreover, the interference effect caused by multiple reflection effect in (nearly) plane-parallel samples has been overlooked in almost all the previous measurements, which can be the source of considerable error.

The purpose of this work is to establish a more accurate absolute scale of the nonlinear optical coefficients of some of the most important materials. We performed absolute and relative measurements using SHG, difference-frequency generation (DFG), and PF methods. The measurements were carried out at several wavelengths to investigate the dispersion of nonlinear optical coefficients and verify Miller's rule. Besides, we took full account of the influence of the multiple reflection effect in all the measurements.

In the SHG measurement, we employed the wedge technique to redetermine the absolute nonlinear optical coefficients of several important crystals: congruent LiNbO_3 , MgO-doped LiNbO_3 , LiTaO_3 , KNbO_3 , KTP, $\alpha\text{-ZnS}$, CdS, CdTe, GaP, and GaAs. As fundamental light sources we used single-longitudinal-mode laser diodes oscillating at 1.548 μm , 1.533 μm , 1.313 μm , and 0.852 μm , respectively, and a diode-pumped single-longitudinal-mode Nd:YAG laser oscillating at 1.064 μm . Relative measurement, which included quartz and KDP in addition to the above crystals, was made to $d_{33}(\text{congruent LiNbO}_3)$ at 1.064 μm using a Q-switched Nd:YAG laser. In the analysis of these measurements, the multiple reflection effect was fully taken into account [4].

The DFG method was used for the first time to determine the absolute value of $d_{31}(\text{congruent LiNbO}_3)$ [5]. The input wavelengths were 0.532 μm and 1.314 μm . On the other hand, d_{31} of congruent and 5 % MgO-doped LiNbO_3 were absolutely measured by the PF method at two pump wavelengths, 0.488 μm and 0.532 μm . In these measurements we used anti-reflection coated samples to minimize the end reflection and took great care to isolate signal waves from stray light.

Table 1 The absolute magnitudes of the second-order nonlinear optical coefficients in pm/V. The wavelengths shown are the fundamental wavelengths for SHG and the pump wavelengths for DFG and PF. The overall accuracy is estimated to be better than 10 %. In indicating d tensor of KNbO_3 and KTP (mm2 class crystals) we obey the recommendation by Roberts [6]. †The value measured at $1.533 \mu\text{m}$.

Crystal	d_{ij}	$1.548 \mu\text{m}$ (SHG)	$1.313 \mu\text{m}$ (SHG)	$1.064 \mu\text{m}$ (SHG)	$0.852 \mu\text{m}$ (SHG)	$0.532 \mu\text{m}$ (DFG)	$0.488 \mu\text{m}$ (PF)
Congruent LiNbO_3	d_{33}		19.5	25.2	25.7		
	d_{31}		3.2	4.6	4.8	4.3	4.3
1%MgO: LiNbO_3	d_{33}		20.3	24.9	27.5		
	d_{31}		3.2	4.6	4.8		
5%MgO: LiNbO_3	d_{33}		20.3	25.0	28.4		
	d_{31}		3.4	4.4	4.9		4.9
LiTaO_3	d_{33}		10.7	13.8	15.1		
	d_{31}			0.85			
KNbO_3	d_{33}		16.1	19.6	22.3		
	d_{31}		9.2	10.8	11.0		
	d_{15}			12.5			
KTP	d_{33}		11.1	14.6	16.6		
	d_{31}			3.7			
	d_{32}			2.2			
	d_{15}		2.6	3.0	3.9		
	d_{24}		1.4	1.9	1.9		
quartz	d_{11}			0.30			
KDP	d_{36}			0.39			
$\alpha\text{-ZnS}$	d_{33}	9.0		12.5			
	d_{31}	4.8		6.2			
	d_{15}	4.3		5.8			
CdS	d_{33}	14.2	16.8	19.1			
	d_{31}	7.4	8.3	10.1			
	d_{15}	8.0	8.8	10.7			
CdTe	d_{36}	73		109			
GaP	d_{36}		36.8	70.6			
GaAs	d_{36}	119 [†]		170			

The absolute magnitudes of the nonlinear optical coefficients determined from our measurement are summarized in Table 1. The results show that DFG and PF values of d_{31} (congruent LiNbO_3) are in agreement with SHG value, which indicates that the previous PF value, $d_{31} = 5.8 \text{ pm/V}$ [2], was overestimated. Table 2 lists Miller's Δ at the measured wavelengths. It shows that Miller's Δ is hardly constant and the wavelength dependence of Δ is different for different materials and different tensor components; e.g., $\Delta(0.85 \mu\text{m})/\Delta(1.31 \mu\text{m})=1.36$ for Δ_{15} (KTP), while $\Delta(1.06 \mu\text{m})/\Delta(1.31 \mu\text{m})=0.90$ for Δ_{33} (CdS).

Although currently accepted standard values have been mostly determined from SHG methods, many of these values are larger than the values obtained from this work. For example, the standard value of d_{33} (congruent LiNbO_3) [6] is 7.1 % larger than our value. This fact, we believe, indicates that the currently accepted values have been overestimated, which is mainly caused by neglect of the multiple reflection effect. The multiple reflection effect has been overlooked because the interference apparently disappears in measurement using multi-longitudinal-mode lasers and/or large fundamental beam spots, although the effect does exist

Table 2 Experimentally determined Miller's Δ 's in ($10^{-2}\text{m}^2/\text{C}$). †The value measured at $1.533\text{ }\mu\text{m}$.

Crystal	Δ_{ij}	1.548 μm (SHG)	1.313 μm (SHG)	1.064 μm (SHG)	0.852 μm (SHG)	0.532 μm (DFG)	0.488 μm (PF)
Congruent LiNbO ₃	Δ_{33}		4.43	5.35	4.90		
	Δ_{31}		0.61	0.82	0.76	0.77	0.77
1%MgO:LiNbO ₃	Δ_{33}		4.65	5.34	5.29		
	Δ_{31}		0.61	0.83	0.77		
5%MgO:LiNbO ₃	Δ_{33}		4.73	5.43	5.55		
	Δ_{31}		0.66	0.80	0.78		0.85
LiTaO ₃	Δ_{33}		2.58	3.14	3.12		
	Δ_{31}			0.20			
KNbO ₃	Δ_{33}		4.16	4.69	4.73		
	Δ_{31}		1.74	1.88	1.67		
KTP	Δ_{15}			2.21			
	Δ_{33}		9.48	11.8	11.9		
	Δ_{31}			3.9			
	Δ_{32}			2.4			
	Δ_{15}		2.9	3.3	3.8		
	Δ_{24}		1.6	2.1	1.9		
quartz	Δ_{11}			1.3			
KDP	Δ_{36}			2.5			
α -ZnS	Δ_{33}	1.3		1.61			
	Δ_{31}	0.69		0.80			
	Δ_{15}	0.62		0.75			
CdS	Δ_{33}	1.82	1.96	1.76			
	Δ_{31}	0.99	1.0	0.96			
	Δ_{15}	1.1	1.1	1.0			
CdTe	Δ_{36}	2.5		2.86			
GaP	Δ_{36}		0.60	0.96			
GaAs	Δ_{36}	0.96 †		1.07			

and enhances second-harmonic power. This overestimation amounts to 5.7 % for d_{33} (congruent LiNbO₃), for instance, which agrees well with the discrepancy between the currently accepted value and ours. On the other hand, our values of quartz and KDP are in good agreement with the standard values, in which the enhancement by the multiple reflections hardly occurs because of their low refractive indices. It is concluded that many of the accepted standard values of the second-order nonlinear optical coefficients should be revised.

References

- [1] See, for example, S. Singh, "Nonlinear Optical Materials", in *Handbook of Laser Science and Technology*, M. J. Weber Ed., (CRC, Boca Raton, 1986), Vol. III.
- [2] M. M. Choy and R. L. Byer, Phys. Rev. B **14**, 1693 (1976).
- [3] R. C. Eckardt, H. Masuda, Y. X. Fan, and R. L. Byer, IEEE J. Quantum Electron. **26**, 922 (1990).
- [4] R. Morita, T. Kondo, Y. Kaneda, A. Sugihashi, N. Ogasawara, S. Umegaki, and R. Ito, Jpn. J. Appl. Phys. **27**, L1134 (1988).
- [5] A. Kitamoto, T. Kondo, I. Shoji, and R. Ito, Opt. Rev. **2**, 280 (1995).
- [6] D. A. Roberts, IEEE J. Quantum Electron. **28**, 2057 (1992).

Comparison of Molecular Hyperpolarizabilities Measured in Gas and Liquid Phases

Philip Kaatz and David P. Shelton

Physics Department
University of Nevada Las Vegas
Las Vegas, NV 89154-4002
tel: (702) 895-3564, fax: (702) 895-0804

Hyper-Rayleigh Scattering (HRS) measurements have become an important method for measuring the first hyperpolarizabilities β of organic chromophores [1]. This technique is more flexible and much simpler than the alternative Electric-Field-Induced Second Harmonic Generation (EFISH) method for determining β . However, unresolved difficulties with the absolute calibration of solution EFISH measurements [2] have not been avoided, but only compounded, because the uncertain EFISH values are used to calibrate HRS, and because different combinations of tensor components are measured in the two experiments. Furthermore, HRS signals from liquid phase samples can include large intermolecular contributions [3], which have usually been ignored.

To address these issues we have made gas-phase EFISH, gas-phase HRS, and liquid -phase HRS measurements of β for several molecules, all at $\lambda = 1064$ nm. The gas-phase EFISH measurements give accurate unequivocal absolute hyperpolarizabilities, which can be used to calibrate the gas-phase HRS measurements. The EFISH measurements are made by comparing the harmonic signal for N_2 reference gas with the harmonic signal for a mixture of sample vapor and N_2 buffer gas. The measurements are made in a single gas cell, using the periodic phase matching technique [4,5]. Measurements are made over a range of temperature, as shown in Figure 1, yielding β_z with an uncertainty of $\pm 5\%$. The gas-phase values of β_{HRS} are obtained from β_z by making use of the ratios of the components of the tensor β for each molecule. For acetonitrile the ratios of tensor components are adequately known from ab initio calculations [4], while for nitrobenzene we have used HRS polarization ratio measurements to determine the ratios of the largest components [6].

HRS intensity measurements for vapor and liquid samples are combined to determine the ratio β_L/β_G , where β_L is the effective hyperpolarizability of molecules in the liquid. The hyperpolarizability is related to the measured HRS intensity by the expression [6]

$$\beta^2 \propto I / (\rho \ell^6 T^3 n^{-1}), \quad (1)$$

where n is the sample refractive index, ℓ is the Lorentz local field factor, and T is the Fresnel transmission factor. The value of the effective hyperpolarizability β_L is obtained by applying

$$(\beta_L)_{\text{HRS}} = \left(\frac{\beta_L}{\beta_G} \right)_{\text{HRS}} \left(\frac{\beta_{\text{HRS}}}{\beta_{z,\text{EFISH}}} \right)_G (\beta_{z,\text{EFISH}})_G \quad (2)$$

to the results of the EFISH and HRS measurements. Thus, the measurements provide both the value of β in the liquid, and a measure of the influence of the liquid environment on the value of β . As a final step, the liquid HRS intensity ratios $(I_X/I_{\text{CCl}_4})_L$ were measured and combined with the β_X to make independent estimates of β_{CCl_4} . These independent estimates of β for CCl_4 should all agree, so this serves as a consistency check on the overall calibration procedure.

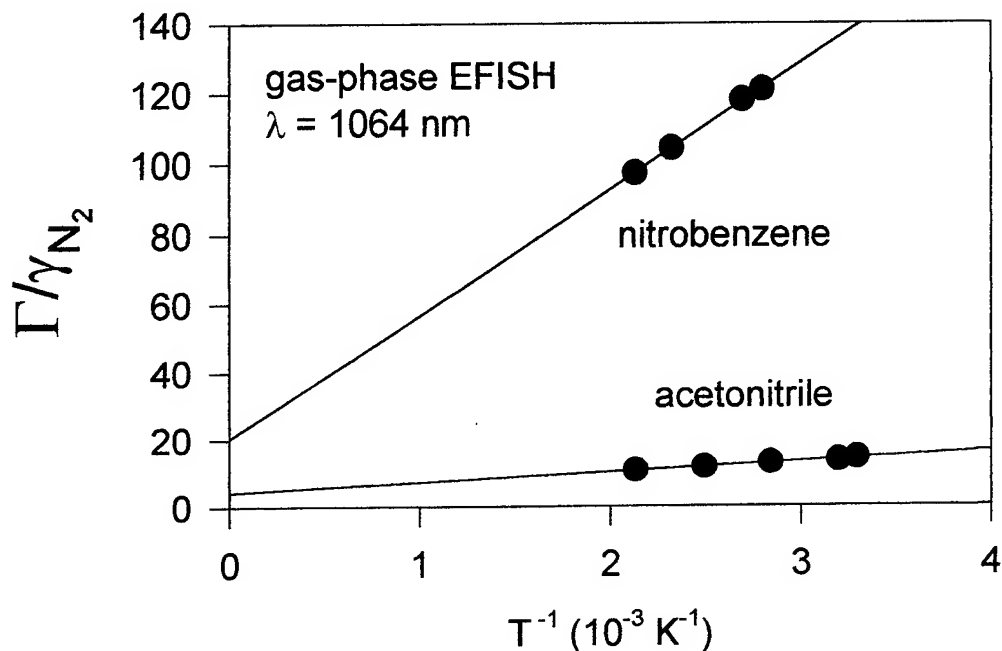


Figure 1. Measurement of the temperature dependence of $\Gamma = \gamma + \mu\beta_z/5kT$ allows both β_z and γ to be determined.

Table 1 shows the results obtained for several molecules by the above procedure. The uncertainties of the HRS results are estimated to be about ± 5 -10%. The last column of Table 1 shows that the three independent determinations of β_{xyz} for CCl_4 in the gas-phase, obtained using the data in the table, agree to within $\pm 3\%$. These values also agree with the value of β_{xyz} obtained previously in a less direct way [3], further supporting the accuracy of the present results.

The third column of Table 1, β_L/β_G , shows that the effective β of molecules in the liquid is enhanced over the gas-phase value by a factor which varies from 0.4 to 2.0. Previous study of CCl_4 HRS spectra [3] has identified two main intermolecular interaction effects which modify β in the liquid. They are orientational correlations between neighboring molecules, and distortion of the molecule by the permanent multipolar fields of its nearest neighbors. For CCl_4 , the unimolecular, orientational

correlation, and multipolar contributions to the liquid HRS intensity are all comparable (40%, 20%, 40%, respectively). The interaction effects are even larger for the other small molecules in Table 1, but the relative importance of orientational correlations as compared to multipolar fields for these molecules is unknown. Because EFISH measurements are insensitive to short-range orientational correlations, liquid EFISH and HRS results may be expected to differ when orientational correlations contribute significantly to the HRS signal. In the case of a very dilute solution of a chromophore with a very large β , it may be that orientational correlations and multipolar fields of the surrounding solvent molecules have a weak effect on β of the chromophore, but this remains to be demonstrated.

Table 1. Gas-phase EFISH measurements and liquid/gas HRS intensity ratios are combined to determine values of the effective β for HRS in the liquid. These $\beta_{L,HRS}$ values are combined with liquid HRS intensity ratios to make three estimates of β_{xyz} for CCl_4 . Hyperpolarizabilities β are given in atomic units ($1 \text{ au} = 3.206361 \times 10^{-53} \text{ C}^3 \text{ m}^3 \text{ J}^{-2} = 8.6392 \times 10^{-33} \text{ esu}$, with $\mu = 1/2 \beta E^2$).

molecule	$(\beta_z)_{G,EFISH}$ (au)	$(\beta_L/\beta_G)_{HRS}$ (-)	$\beta_{L,HRS}$ (au)	$(I_X/I_{\text{CCl}_4})_{L,HRS}$ (-)	$(\beta_{xyz})_{G,\text{CCl}_4}$ (au)
CCl_4		1.53		1	
CH_3CN	29.9	2.0	21.5	1.70	20.3
CD_3CN	30.0	1.9	20.4	1.65	19.5
nitrobenzene	329.	1.3	158	95.	20.8
p-nitroaniline	1972.				
CDCl_3		1.7		0.82	
D_2O		1.5		0.78	
CH_3NO_2		0.55		0.42	
CD_3OH		0.40		0.22	

References

1. J. Zyss, I. Ledoux, Chem. Rev. **94**, 77 (1994); K. Clays, A. Persoons, L. De Maeyer, Adv. Chem. Phys. **85**, 455 (1994).
2. A. Willetts, J.E. Rice, D.M. Burland, D.P. Shelton, J. Chem. Phys. **97**, 7590 (1992).
3. P. Kaatz and D.P. Shelton, Mol. Phys., in press.
4. M. Stahelin, C.R. Moylan, D.M. Burland, A. Willetts, J.E. Rice, D.P. Shelton, E.A. Donley, J. Chem. Phys. **98**, 5595 (1993).
5. D.P. Shelton, Phys. Rev. A **42**, 2578 (1990).
6. P. Kaatz and D.P. Shelton, Rev. Sci. Instrum., in press.

Computational Modeling of Ultrashort Pulse Propagation in Nonlinear Optical Materials

Peter M. Goorjian

NASA Ames Research Center, M.S. T27B-1, Moffett Field, CA 94035-1000

Phone: (415) 604-5547, Fax: (415) 604-1095, Email: goorjian@nas.nasa.gov

Govind P. Agrawal

Institute of Optics, University of Rochester, Rochester, NY 14627

Phone: (716) 275-4846, Fax: (716) 244-4936, Email: gpa@optics.rochester.edu

Recent progress in ultrafast technology has led to the generation of optical pulses as short as 8 fs. The propagation of such short pulses in nonlinear optical media requires new computational techniques in which the standard approximations such as the slowly-varying envelope approximation (SVEA) and rotating-wave approximation (RWA) are not made while using the Maxwell-Bloch equations [1]. Previous calculations, which used the finite-difference time-domain (FDTD) method, found that for a Kerr-like instantaneous nonlinearity [2] significant differences can occur when the full vector Maxwell equations are used instead of the nonlinear Schrodinger equation. Recently, the FDTD method has been extended to the case of a homogeneously broadened two-level atomic system [3].

In this paper, we apply the FDTD method to an inhomogeneously broadened two-level atomic system. Such an extension also permits one to apply the new algorithm to studies of ultrafast optical pulse propagation in nonlinear semiconductor materials including semiconductor lasers and amplifiers. In essence, this new method solves the semiconductor Bloch equations [4] together with the Maxwell equations without making the SVEA and the RWA. One can also include many-body effects, which occur when the Coulomb interaction is taken into account. Since the full vector Maxwell equations are solved exactly, all higher-order effects are automatically accounted for in these simulations. Although the results are valid down to a single-cycle pulse in the case of atomic systems, their validity for nonlinear semiconductor materials is limited to time scales over which the relaxation-time approximation holds for various intraband scattering processes.

This computational model solves the coupled Maxwell-Bloch equations without making the SVEA and RWA. Assuming that the electric field of a pulse propagating along the z direction is polarized along the x axis and ignoring the transverse effects, the Maxwell equations becomes

$$\frac{\partial D_x}{\partial t} = -\frac{\partial H_y}{\partial z} \quad , \quad \mu_0 \frac{\partial H_y}{\partial t} = -\frac{\partial E_x}{\partial z} \quad , \quad D_x = \epsilon_0 \epsilon_r E_x + P_x \quad , \quad (1)$$

where P_x is the induced polarization. In the case of semiconductors, P_x is calculated by using the semiconductor Bloch equations [4]

$$\begin{aligned} \frac{dn_k^e}{dt} &= -\frac{n_k^e - \bar{n}_k^e}{\tau_e} - \frac{n_k^e - \bar{n}_k^e}{\tau_c} + \frac{2\mu}{\hbar} p_{2,k} E(t) \quad , \quad \frac{dn_k^h}{dt} = -\frac{n_k^h - \bar{n}_k^h}{\tau_e} - \frac{n_k^h - \bar{n}_k^h}{\tau_v} + \frac{2\mu}{\hbar} p_{2,k} E(t) \quad , \\ \frac{dp_{1,k}}{dt} &= -\frac{p_{1,k}}{\tau_2} + \omega_k p_{2,k} \quad , \quad \frac{dp_{2,k}}{dt} = -\frac{p_{2,k}}{\tau_2} - \omega_k p_{1,k} - \frac{\mu}{\hbar} (n_k^e + n_k^h - 1) E(t) \quad , \end{aligned} \quad (2)$$

where n_k^e and n_k^h are the occupation probabilities for electron and holes of the wave vector k in the conduction and valence bands respectively, $p_{1,k}$ and $p_{2,k}$ are the dispersive and absorptive components of the dipole moment, and the τ parameters govern various decay processes. The transition frequency ω_k is varied over a sufficiently large range to accurately describe the interaction of an ultrashort optical pulse with the semiconductor. The induced polarization P_x is calculated by integrating $p_k = p_{1,k} + ip_{2,k}$ over all values of k . In the case of an inhomogeneously broadened two-level atomic system, the subscript k labels various atomic transition frequencies and P_x is calculated by integrating over the atomic density distribution function.

The computer model has been checked against several known results for the case of two-level systems. The simplest case considered was the phenomenon of self-induced transparency. It is well known [1] that optical pulses, whose electric field at the entrance to the material is described by

$$E(t) = 2E_0 \text{sech}(t/T_0) \cos(\omega_c t) \quad (3)$$

where ω_c is the optical carrier frequency and T_0 is the pulse width, can propagate undistorted in the form of a soliton when the pulse energy corresponds to a 2π pulse. This analytic result is, however valid only when both the SVEA and the RWA hold. It is not obvious *a priori* how short a 2π pulse may be before it ceases to propagate as a soliton. To answer this question, we have solved Eqs. (1) and (2) for the case of homogeneous broadening for a 10-ps pulse ($T_0 = 5.7$ fs) at a carrier frequency ω_c corresponding to an input wavelength of $0.87 \mu\text{m}$. The calculations were performed over a propagation distance of $35 \mu\text{m}$. Figure 1 shows the electric field of the pulse at several moments during its propagation inside the medium. Notice that the pulse is propagating undistorted. Figure 2 shows the corresponding population inversion $w = (n^e + n^h) - 1$. The fine structure seen in Fig. 2 can occur only when the carrier is retained [3] and is absent in conventional models based on the SVEA and the RWA.

During the conference we shall present results on self-induced transparency of femtosecond pulses in inhomogeneously broadened two-level atomic systems and explore the limit at which the SVEA and RWA begin to break down. We are applying the newly developed computer algorithm for studying the amplification of femtosecond (as short as 30 fs) pulses in a semiconductor optical amplifier. These results will also be presented.

We would like to thank Rolf Binder, Optical Sciences Center, University of Arizona, for his many helpful comments concerning algorithm development for the semiconductor Bloch equations.

References

1. Allen, L. and Eberly, J. H., *Optical Resonance and Two-Level Atoms*, Dover Press, 1987.
2. Goorjian, P. M. and Taflove, A., "Direct Time Integration of Maxwell's Equations in Nonlinear Dispersive Media for Propagation of Femtosecond Electromagnetic Solitons," *Optics Letters*, Vol. 17, No. 3, Feb. 1, 1992.
3. Ziolkowski, R. W., Arnold, J. M., and Gogny, D. M., "Ultrafast pulse interactions with two-level atoms," *Phys. Rev. A*, Vol. 52, No. 4, pp. 3082-3094, Oct., 1995.
4. Haug, H., and Koch, S. W., *Quantum Theory of the Optical and Electronic Properties of Semiconductors*, World Scientific Press, 2nd Ed., 1993.

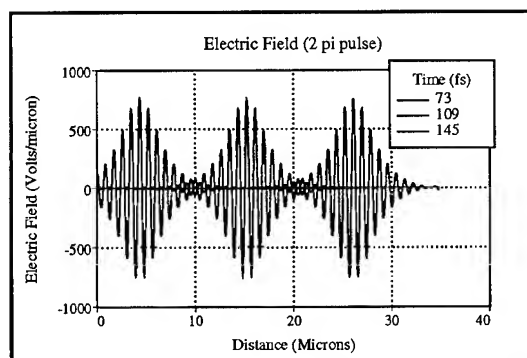


Fig. 1 Two-level atom.
Self induced transparency

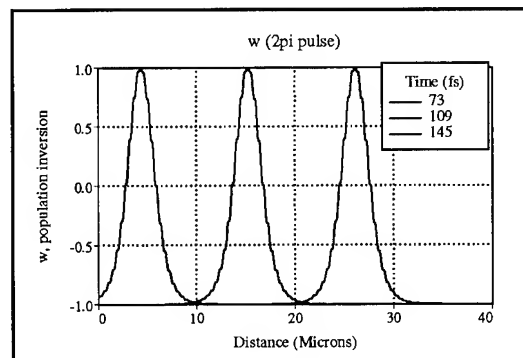


Fig. 2 Two-level atom.
Population inversion

Lasers Without Inversion and Raman Oscillators Comparative Analysis

Jacob B. Khurgin

Department of Electrical and Computer Engineering
The Johns Hopkins University, Baltimore MD 21218
and

Emmanuel Rosencher

Thomson CSF, Laboratoire Central de Recherches,
Domaine de Corbeville, 91404, Orsay Cedex France

In the last few years there has been substantial interest in the lasers capable of operation without inversion (LWI). Numerous schemes have been suggested [1],[2], which, if realized in practice, can expand the range of laser devices in spectral regions where for various reasons inversion is difficult to achieve - among them vacuum UV, using atomic vapors as an active medium, and mid-to-far IR., using intersubband transitions in quantum wells. Until recently, the research has been mostly limited to the theoretical work, but lately there had been a conclusive report of laser oscillation without inversion in Rb [3]. A number of LWI proposals based on intersubband transitions in quantum wells, that seem to be ideally suited for the practical implementation of LWI concept, have also been made.

Therefore, it seems to be a right time to attempt an in-depth investigation of the applicability of the LWI concept to the intersubband transitions in QW's. There seems to be a lack not only of the experimental data, but also of a concise treatise of the LWI in terms familiar to the laser community, i.e. pumping rate, lasing threshold, slope efficiency and saturation intensity. There is an uncertainty of using the different terminology, such as electro-magnetically induced transparency, amplification, or lasing without inversion to describe various manifestations of the same phenomena. There is also an opposite, yet equally misleading trend of using the same term, LWI to describe what is an odd assembly of well-known and fundamentally distinct nonlinear optical phenomena - Raman and parametric processes, and dynamic Stark Effect. But by far, the most important is the fact that most of the theoretical research has concentrated on the ability to *prepare* the lasing state, while from the practical point of view, it is the ability to *sustain* the lasing that matters the most.

In our work we develop density matrix formalism for the LWI that can be applied to the intersubband transitions in QW's - including the relaxation, broadening and pumping mechanism. We obtain the rate equations and analytical expressions for the lasing threshold and input/output characteristics. Using this approach one can easily estimate the performance of the potential LWI using experimentally-available data. We perform such estimates and make some conclusions.

Among our most important conclusions are the following:

In most cases the so-called LWI is nothing but resonant Raman or two-photon process, modified by the AC-Stark splitting of the absorption line. Therefore, in

order to achieve gain it is necessary to maintain a population inversion associated with the two-photon coupled states. In the so-called Λ scheme (Fig.1) the two upper levels (2) and (3) are coupled by the coherence inducing field of frequency ω_c , while the signal is emitted by the transition $2 \rightarrow 1$. We show that it is necessary to maintain population inversion between levels 3 and 1. In the so-called V -scheme (Fig.2) the two lower levels (1) and (3) are coupled by the coherence inducing field of frequency ω_c , while the signal is emitted by the transition $2 \rightarrow 1$. We show that it is necessary to maintain population inversion between levels 2 and 3.

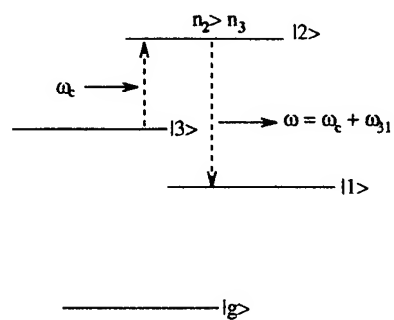
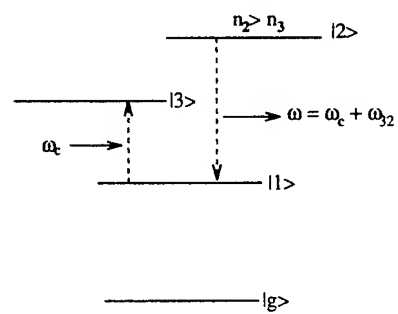
This should be in no way understood as something questioning practicality of the proposed scheme - quite the opposite, since the level 3 is not optically-coupled with the level 1, achieving the population inversion between levels 3 and 1 shall be easier than between levels 2 and 1, and the stimulated emission may be attained with the reasonable values of pump and coupling intensities [4], but that will amount to nothing but the demonstration of Raman lasing, modified by AC Stark shift, and it shall be treated as such.

There are also additional conditions under which "true LWI" can occur without Raman inversion. They are, however require that the upper laser level does not decay to the lower state, which is very difficult to implement in practice. Moreover, we actually calculated the threshold and slope efficiency of the "true LWI", and found out that they are at least two orders of magnitude worse than for conventional lasing. in the pumping and relaxation conditions. Therefore, from the practical point of view it appears that non-Raman LWI is an extremely interesting concept but one shall not expect it to find wide applications with the possible exception of the UV and soft X-ray region.

This research is supported by the AFOSR

References

- [1] O. Kocharovskaya and P. Mandel Phys. Rev. **A42**, 52 (1990)
- [2] M. O. Scully and S-Y Jhu, Phys. Rev. Lett., **62**, 2813 (1989)
- [3] A. S. Zibrov, M. D. Lukin, D. E. Nikonov, L. Hollberg, M. O. Scully, V. L. Velichansky, and H. G. Robinson, Phys. Rev. Lett., **75**, 1499 (1995)
- [4] J. B. Khurgin, G. Sun, L. R. Friedman and R. A. Soref, to be published in J. Appl. Phys., 1995

Figure 1: Λ LWI schemeFigure 2: V LWI scheme

Non-degenerate two wave mixing in Kerr media

Andrei G. Skirtach and David J. Simkin,

McGill University, Department of Chemistry, 801 Sherbrooke Str.
West, Montreal, Quebec, Canada, H3A 2K6,
tel.: (514) 398-6909, fax: (514) 398-7378

Simon A. Boothroyd,
National Research Council, Institute for Information Technology,
Ottawa, Ontario, Canada K1A 0R6

The analysis here applies to a nonlinearity with the refractive index represented by $n=n_0+(n_2'+in_2'')I$, where n_2' is the real (dispersive) and n_2'' is the imaginary (absorptive) part of the nonlinear refractive index n_2 . An exact theoretical treatment has been given for the NDTWM including only the dispersive nonlinearity ($n_2''=0$)¹. This has been extended to include nonlinear absorption through a holographic or grating term².

We analyze the solution of the NDTWM problem including both holographic and bias nonlinear absorption terms. The coupled set of equations describing NDTWM in a Kerr medium³ can be solved exactly in the approximation of $I_2(z)/I_1(z) \approx I_2(0)/I_1(0) = C$, where C is a constant:

$$\frac{I_{\frac{1}{2}}(L)}{I_{\frac{1}{2}}(0)} = \frac{(1+A^{\pm 1})e^{-\alpha L}}{1+A^{\pm 1}\exp(\pm\gamma)} \quad (1)$$

where α is the linear absorption coefficient,

$$\gamma = \beta(1+A)\Gamma_2 I_1(0) \frac{1-e^{-\alpha L}}{\alpha} \quad (2)$$

$$\Gamma_{\frac{1}{2}} = n_2' \frac{\delta \pm r(C^{\pm 1} + 2 + C^{\pm 1}\delta^2 + \delta^2)}{1 + \delta^2} \quad (3)$$

$\beta = 4\pi/\lambda \cos(\theta/2)$, λ is the wavelength of the pump, I_1 , and probe, I_2 , beams, θ is the angle between them, $\delta = (\omega_1 - \omega_2)\tau$ is the frequency detuning, τ is the grating decay time, $A = \Gamma_1 \cdot \Gamma_2^{-1} \cdot C$, $r = n_2''/n_2'$.

This enables us to account for a peak in the symmetric component of NDTWM gain near a detuning $\delta=1$ reported previously as an unexplained result for ruby⁴. The peak in the symmetric component of NDTWM gain Γ_{sym} at $\delta=1$ is also seen in the data of Ref. [2]. The data for the NDTWM gain measurements in ruby at $\lambda=488$ nm were digitized and are shown in Fig. 1. In contrast to existing theory, which predicts no extremum in this case, the peak at $\delta=1$, which arises from the influence of nonlinear absorption, is well

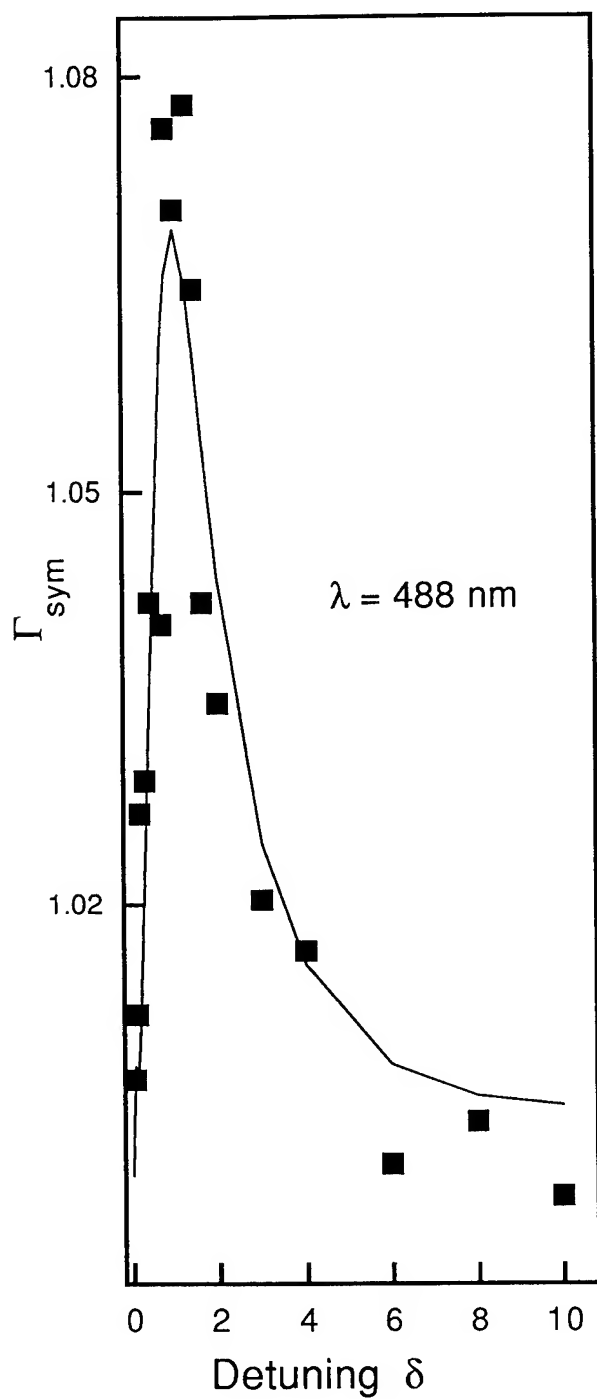
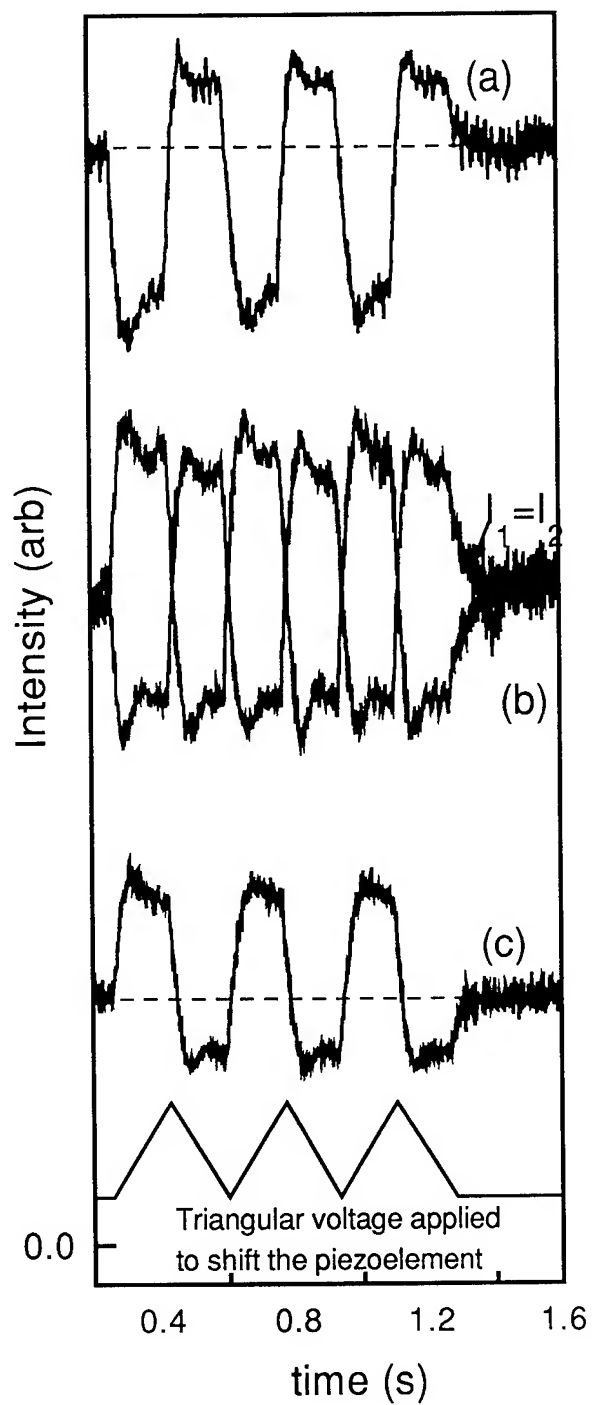
accounted for by our model. When $I_1 > I_2$, the bias terms in the coupled wave equations, $\propto n_2 I_1^2$ for the pump beam and $\propto n_2 I_2^2$ for the probe beam, are not comparable. This gives rise to nonsymmetrical energy exchange between the interacting beams.

Experimental confirmation of that is presented in Fig. 2, where the NDTWM signal for $\text{Cr}^{3+}:\text{YAlO}_3$ is shown for both the pump and the probe beams at $\lambda = 514.5 \text{ nm}$, $I_1(0) = 0.25 \text{ kW/cm}^2$, and different values of $I_2(0)$. When $I_2(0) = I_1(0)$, the "pump" and the "probe" beams exchange energy symmetrically, which is illustrated in Fig. 2, curves (b). When $I_2 = I_1/5$, the NDTWM signal appears nonsymmetric as seen in Fig. 2, curves (a) and (c). In the previous theory the holographic ($\propto n_2 I_1 I_2 / (1 + \delta^2)$) term was the only term giving rise to a nonsymmetrical energy exchange between the beams. Since in the coupled wave equations³ this term is positive for both the pump and the probe beams, it contributes to the departure from the symmetry in energy exchange similarly for both beams. However, as can be clearly seen from Fig. 2, the DC ($\delta = 0$) signal for the pump beam (dashed line in curve (a)) is up-shifted, while that for the probe beam is down-shifted (dashed line in curve (c)). This confirms the influence of nonlinear absorption on the unsymmetrical energy exchange between the beams.

We also note that for the case of $I_1(0) = I_2(0)$ the energy exchange between the two beams is symmetrical and the output behaves exactly like a bistable element (flip-flop). In $\text{Cr}^{3+}:\text{YAlO}_3$ this is so pronounced, because of high gain, that the flip-flop is easily observed by the naked eye.

REFERENCES

1. P. Yeh, J. Opt. Soc. Am. **B 3**, 747 (1986).
2. I. McMichael, P. Yeh, and P. Beckwith, Opt. Lett. **13**, 500 (1988).
3. M. A. Kramer, W. R. Tompkin, and R. W. Boyd, Phys. Rev **A 34**, 2026 (1986).
4. S. A. Boothroyd, J. Chrostowski, and M.S. O'Sullivan, J. Opt. Soc. Am. **B 6**, 766 (1989).

Fig. 1. Γ_{sym} for rubyFig. 2. NDTWM signal in Cr:YAlO_3 

Resonance and bright-dark solitons in group-velocity mismatched second-harmonic generation

Stefano Trillo

Fondazione Ugo Bordon, Via B. Castiglione 59, 00142 Rome, Italy

tel: +396-5480-2223; fax: +396-5480-4402; e-mail: strillo@fub.it

Waves interacting parametrically in quadratic media experience nonlinear phase changes which, under appropriate conditions, may be compensated for by dispersion or diffraction, resulting into mutually trapped (temporal or spatial) solitary envelopes or solitons. Although this trapping was predicted in the seventies [1], it was observed only recently for second-harmonic generation (SHG) in the 3D spatial case [2], motivating renewed interest for applications oriented to all-optical processing. Usually these solitons survive in the presence of moderate walkoff [3]. Here we investigate the opposite case for which *the group-velocity difference or walk-off dominates over dispersion (or diffraction)*. This occurs whenever the beam widths are large enough so that the walkoff length z_w is much shorter than dispersion length z_d . The purpose of this communication is to show that, in this case, group-velocity difference may be offset by velocity-locking due to new types of solitons. We consider two specific cases of SHG. First, we show that type I bulk SHG, supports only dark-bright pairs whereas bright-bright solutions are not permitted. Conversely we show that when type II forward SHG occurs in a grating structure which couples the two fundamental polarization components, new types of stable solitons which fulfill the Bragg condition (i.e. resonance solitons) are supported.

Let us consider the former case (bulk SHG) described by the usual coupled dimensionless equations

$$i \left(\frac{\partial u_1}{\partial \xi} + \delta_1 \frac{\partial u_1}{\partial \tau} \right) - \frac{\beta_1}{2} \frac{\partial^2 u_1}{\partial \tau^2} + u_2 u_1^* e^{i\delta k \xi} = 0; \quad i \left(\frac{\partial u_2}{\partial \xi} + \delta_2 \frac{\partial u_2}{\partial \tau} \right) - \frac{\beta_2}{2} \frac{\partial^2 u_2}{\partial \tau^2} + \frac{u_1^2}{2} e^{-i\delta k \xi} = 0, \quad (1)$$

where we considered the most general mismatched case ($\delta k \neq 0$). Whenever $\beta_{1,2} \ll \delta_{1,2}$ group-velocity effects prevail, and it is possible to construct all the possible velocity-locked solitary waves of Eqs. (1) by means of the Hamiltonian formulation [5] of Eqs. (1). These are constituted by a bright wave (fundamental envelope) coupled to a dark (harmonic envelope, which is reminiscent of the grey soliton in Kerr defocusing media) of the following form (take the zero velocity for simplicity)

$$\begin{aligned} u_1 &= \sqrt{2a\delta_2/\delta_1} \operatorname{sech}(\alpha\tau) \exp[i b\tau + i\mu\xi], \\ u_2 &= \sqrt{1 - a \operatorname{sech}^2(\alpha\tau)} \exp[i 2b\tau + i(2\mu - \delta k)\xi + i\psi]; \quad \psi = \tan^{-1} \left[\sqrt{a/(1-a)} \tanh(\alpha\tau) \right] + \phi_0 \end{aligned}$$

where the parameters μ, b, α, a depend on the velocities $\delta_{1,2}$ and mismatch δk . We studied the domain of existence, and the stability of this soliton pair (against both cw perturbation or para-

metric nondegenerate decay), and show that stable propagation is possible. We also discuss the generalization of this solution to type II SHG.

Consider now forward propagation in the presence of a periodic variation of the linear index (grating with spacing $2\pi/\beta_0$). Here we focus on the case of type II SHG where the grating couples the two polarization components (u_{1x}, u_{1y}) of the fundamental frequency. When Bragg resonance is fulfilled (i.e., $\delta\beta = k_{1x} - k_{1x} - \beta_0 = 0$), the grating does not affect the behavior of the harmonic field and the propagation is reasonably described by the following model

$$\begin{aligned} i \left(\frac{\partial u_{1x}}{\partial \xi} + v_1 \frac{\partial u_{1x}}{\partial \tau} \right) + \kappa u_{1y} + u_2 u_{1y}^* = 0 ; \quad i \left(\frac{\partial u_{1y}}{\partial \xi} - v_1 \frac{\partial u_{1y}}{\partial \tau} \right) + \kappa u_{1x} + u_2 u_{1x}^* = 0 , ; \\ i \left(\frac{\partial u_2}{\partial \xi} + v_2 \frac{\partial u_2}{\partial \tau} \right) + \delta k u_2 + u_{1x} u_{1y} = 0. \end{aligned} \quad (2)$$

where κ is the coupling strength, and v_1 is the mean group-velocity at fundamental. For large wavevector mismatches δk , the second-harmonic beam adiabatically follows the fundamental fields, and the third of Eqs. (2) reduces to $u_2 = -u_{1x}u_{1y}/\delta k$. In this regime, it is easy to show that the two FF envelope amplitudes obey the so-called integrable massive Thirring model [5], which possess exact closed-form bright solitons, which are supported also in gratings with Kerr-like nonlinearity [6]. At low power the group-velocity difference quickly disperse the two input FF beams (see Fig. 1). However, as shown in Fig. 2, at high powers SHG works as a mechanism which permits soliton formation (with minor oscillations depending on δk) and group-velocity locking. For sake of brevity we do not report the explicit expressions for the solitons. However it is possible to show that the velocity is related to the unbalance of the fundamental components, whereas the phase profile of the soliton depends on an other internal parameter. We discuss the possibility to observe these solitons in practice, even without initial second-harmonic seeding.

In summary we have shown that new types of group-velocity locked solitons may propagate in parametric amplification, when the dominant term is group-velocity difference. The generation, stability, and practical application of such solitons will be discussed.

References

- [1] Y.N. Karamzin, A.P. Sukhorukov, JETP Lett. **20**, 339 (1974); Sov. Phys. JETP **41**, 414 (1976).
- [2] W. E. Torruellas et al., Phys. Rev. Lett. **74**, 5036 (1995).
- [3] L. Torner, C.R. Menyuk, G.I. Stegeman, Opt. Lett. **19**, 1615 (1994).
- [4] S. Trillo et al., Opt. Lett. **17**, 637 (1992); S. Trillo, P. Ferro, Phys. Rev. E **51**, 4994 (1995).
- [5] E.A. Kuznetsov, A.V. Mikhailov, Teor. Mat. Fiz. **30**, 193 (1977).
- [6] S. Wabnitz, Opt. Lett. **19**, 1071 (1989).

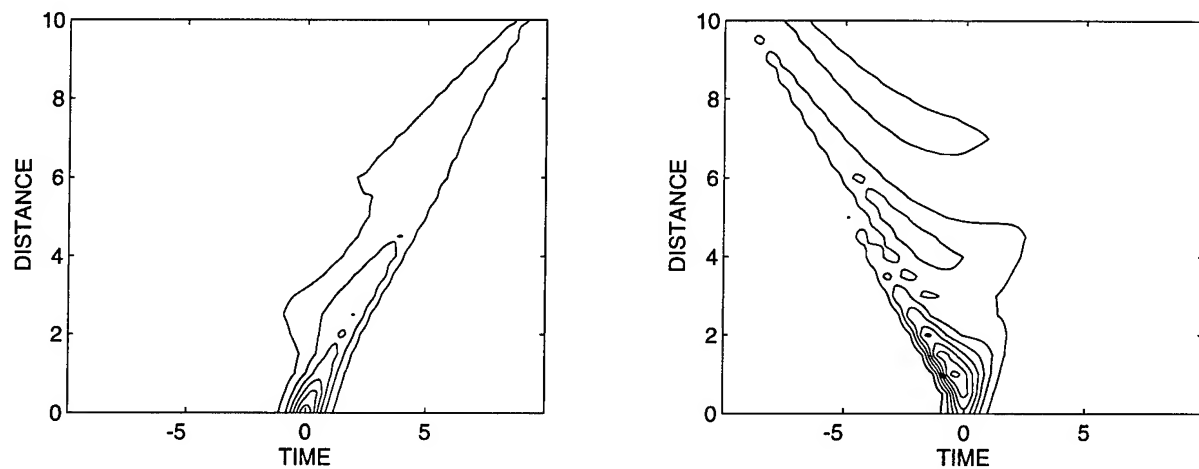


Figure 1: Contour plot of the fundamental frequency fields propagating in the grating at low intensity, when walk-off prevails over nonlinearity ($\delta k = -10$).

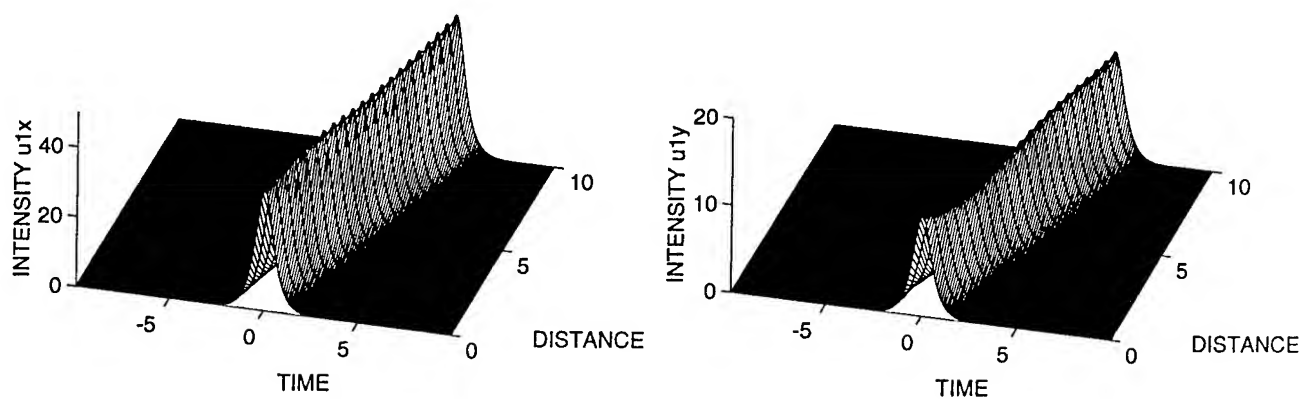


Figure 2: High intensity, group-velocity locking due to a resonance soliton ($\delta k = -10$).

Soliton Propagation in Two-Photon Resonant Region

R. Kitahara, J. Ishi, and K. Ema

Department of Physics, Sophia University, 7-1 Kioi-cho, Chiyoda-ku, Tokyo 102, Japan

phone;81-3-3238-3432, fax;81-3-3238-3341

1. Introduction

The stability of soliton propagation in nonresonant region has been studied extensively. The temporal and spatial evolution of pulses in such region can be analyzed with the nonlinear Schrödinger equation (NSE). The effects of the third-order dispersion term can be analyzed in the frame of NSE, however the dispersion of nonlinearity is usually ignored except for some extreme cases such as shock term.¹⁾ When we consider the propagation of ultrashort pulse or the propagation in resonant region, the effects of nonlinear dispersion reveal themselves remarkably. Nevertheless, the dispersion of nonlinearity have not been fully explored. In this paper, we examine the pulse propagation characteristics with dispersive nonlinearity using nonlinear wave equation in frequency domain. We show that, when pulses propagate at the two-photon resonant region, the effects of the third-order dispersion is compensated by the dispersive nonlinearity and solitonlike propagation of femtosecond pulses can be achieved.

2. Frequency domain analysis for optical solitons

First, we show that the fundamental soliton solution in nonresonant region is easily obtained by frequency domain analysis. Fourier components of the electric field of the pulse in the form of running wave is

$$E(\omega, z) = \hat{E}(\omega, z)e^{ik(\omega)z}, \quad k^2(\omega) = \left(1 + \chi^{(1)}(\omega)\right)\omega^2/c^2, \quad (1)$$

Within a slowly varying envelope approximation, we obtain the following derivative of $\hat{E}(\omega, z)$:²⁾

$$\begin{aligned} \frac{\partial}{\partial z}\hat{E}(\omega, z) = & i \frac{1}{2k(\omega)} \left(\frac{\omega}{c}\right)^2 \int d\omega_1 \int d\omega_2 \chi^{(3)}(\omega; \omega_1, \omega_2, \omega_1 + \omega_2 - \omega) \\ & \times \hat{E}(\omega_1, z) \hat{E}(\omega_2, z) \hat{E}^*(\omega_1 + \omega_2 - \omega, z) e^{i\Delta k \cdot z}, \end{aligned} \quad (2)$$

where Δk is the phase mismatch. For soliton propagation in nonresonant region, we give two following conditions to above equation; (i) $\chi^{(3)}$ is a real constant, and nonlinear refractive index n_2 is introduced as $3\chi^{(3)}(\omega/c)^2/(8k(\omega)) = \omega_0 n_2/c$. (ii) $k(\omega)$ is expanded up to the second order,

$$k(\omega) = k_0 + k_1(\omega - \omega_0) + \frac{1}{2}k_2(\omega - \omega_0)^2. \quad (3)$$

In this case, if the solution of Eq.(2) is expressed as

$$\hat{E}(\omega, z) = \hat{E}(\omega, 0) \cdot \exp \left[-i \left\{ k_0 + \frac{1}{2} k_2 (\omega - \omega_0)^2 \right\} z \right] = \hat{E}(\omega, 0) \cdot \exp \left\{ -i k^{NL}(\omega) z \right\} \quad (4)$$

then total wave number $k^T(\omega)$ is

$$k^T(\omega) = k(\omega) + k^{NL}(\omega) = k(\omega_0) - k_0 + k_1(\omega - \omega_0) \quad (5)$$

where we define nonlinear wave number $k^{NL}(\omega)$, and k_0 is constant with ω (but k_0 is dependent on the pulse intensity and the pulse width as seen later). Because $k^T(\omega)$ is linear respect to ω , the pulse propagates with velocity k_1^{-1} and envelope function does not change along z in this condition. This change of dispersion curve is illustrated in Fig.1. The gray curve shows the linear dispersion $k(\omega)$, the dotted curve shows the nonlinear dispersion $k^{NL}(\omega)$, and the solid line shows the total dispersion $k^T(\omega)$. In order to confirm that Eq.(4) is the solution of Eq.(2), we insert it into Eq.(2);

$$\int d\omega_1 \int d\omega_2 \hat{E}(\omega_1, 0) \hat{E}(\omega_2, 0) \hat{E}^*(\omega_1 + \omega_2 - \omega, 0) = \left\{ \frac{ck_0}{\omega_0 n_2} + \frac{ck_2}{2\omega_0 n_2} (\omega - \omega_0)^2 \right\} \hat{E}(\omega, 0). \quad (6)$$

This integral equation is analytically solved if $k_2/n_2 < 0$ and $k_0/n_2 < 0$. The solution is

$$\hat{E}(\omega, 0) = \sqrt{\frac{c}{4\omega_0} \left| \frac{k_0}{n_2} \right|} \operatorname{sech} \left\{ \pi \sqrt{\left| \frac{k_2}{8k_0} \right|} (\omega - \omega_0) \right\}. \quad (7)$$

We obtain electric field $E(t, z)$ at $z = z$ by Fourier transformation,

$$E(t, z) = \sqrt{\frac{2c}{\omega_0} \left| \frac{k_0}{n_2} \right|} \operatorname{sech} \left\{ \sqrt{\left| \frac{2k_0}{k_2} \right|} (t - k_1 z) \right\} \cdot \exp \left[-i \left\{ \omega_0 t - (k(\omega_0) + k_0) z \right\} \right]. \quad (8)$$

This is well known fundamental soliton pulse.

3. Propagation at two photon resonant (TPR) region

Although $k^{NL}(\omega)$ derived from constant $\chi^{(3)}$ compensates the second-order dispersion term, dispersion still remains if $k(\omega)$ has third-order term. We show that the third-order dispersion is also compensated at TPR region. $\chi^{(3)}$ can be divided into resonant term $\chi_r^{(3)}(\omega, \omega_1, \omega_2)$ and nonresonant constant term $\chi_{nr}^{(3)}$; $\chi^{(3)} = \chi_r^{(3)} + \chi_{nr}^{(3)}$. Correspondingly, we write $k^{NL}(\omega)$ as $k^{NL}(\omega) = k_r^{NL}(\omega) + k_{nr}^{NL}(\omega)$. The definite form of $\chi_r^{(3)}(\omega, \omega_1, \omega_2)$ is

$$\chi^{(3)} \propto \frac{1}{\Omega - \omega_1 - \omega_2 - i\gamma} \cdot \frac{1}{\Omega - \omega - i\gamma} \cdot \left(\frac{1}{\Omega - \omega_1 - i\gamma} + \frac{1}{\Omega - \omega_2 - i\gamma} \right), \quad (9)$$

where Ω denotes the upper-state energy and γ is the dephasing constant. At TPR frequency ($\omega_0 = \Omega/2$), $k_r^{NL}(\omega)$ is derived by inserting Eq.(9) into Eq.(2)

$$k_r^{NL}(\omega) = \frac{-G(\omega - \omega_0)}{(\omega - \omega_0)^2 + \Gamma^2} = \frac{-G}{\Gamma^2} (\omega - \omega_0) + \frac{G}{6\Gamma^4} (\omega - \omega_0)^3 + \dots, \quad (10)$$

where the magnitude G is determined by the pulse intensity and the oscillator strength of TPR, and Γ is the constant determined by γ and the spectral width of the pulse. The third-order term of $k_r^{NL}(\omega)$ can compensate the third-order dispersion of $k(\omega)$. Fig.2 shows schematically that the total wave number $k^T(\omega) = k(\omega) + k_{nr}^{NL}(\omega) + k_r^{NL}(\omega)$ becomes almost linear under certain condition. Consequently soliton propagation is possible even in presence

of third-order dispersion. It is noted that the first-order term of $k_r^{NL}(\omega)$ increases group velocity of the pulse.

We observe soliton propagation of this scheme at biexciton TPR in CuCl. Figure.3 shows the obtained transmitted pulse shapes through 10 μ m sample.³⁾ Input pulse width is 300fs and center frequency is tuned to biexciton TPR frequency (3.186eV). At weak intensity, we observe distortion of pulse shape because of the group velocity dispersion. With increasing the intensity, we clearly see the narrowing of the pulse duration and the increase in the velocity. These results are good agreement with our theoretical consideration.

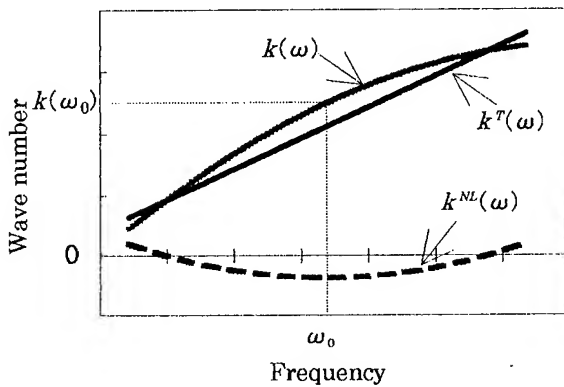


Fig.1. $k(\omega)$ is the linear dispersion with the second-order term (gray curve), $k^{NL}(\omega)$ and $k^T(\omega)$ are the nonlinear dispersion (dotted curve) and the total dispersion (solid line) respectively. The nonlinear dispersion compensates the quadratic group velocity dispersion for the frequency region of the input pulse.

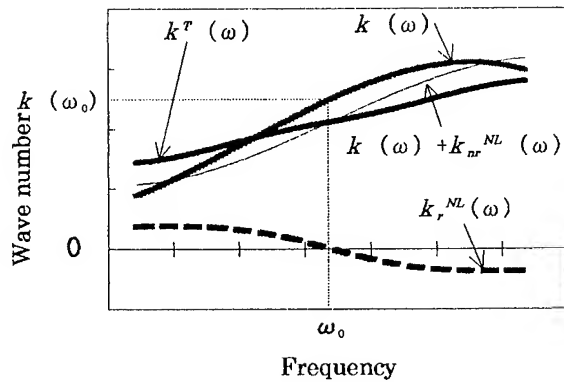


Fig.2. $k(\omega)$ is the linear dispersion with the third-order term (gray curve), $k(\omega) + k_r^{NL}(\omega)$ represents the curve compensated only second-order term (thin curve), and $k_r^{NL}(\omega)$ is the nonlinear dispersion of TPR (dotted curve). Total dispersion $k^T(\omega)$ is almost linear around ω_0 .

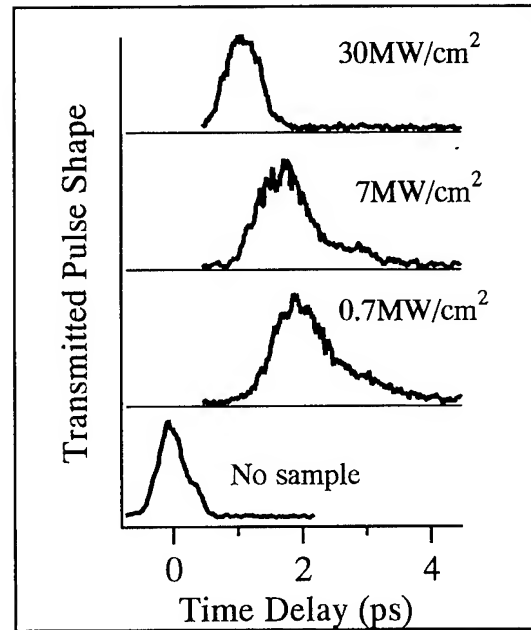


Fig.3. The measured transmitted pulse shape. The thickness of the sample is 10 μ m. The pulse width and frequency of the input pulse are 300fs and 3.186eV. The time delay zero point is the time when the pulse peaks without the sample.

Reference

- 1) A. Hasegawa, *Optical Solitons in Fibers* (Springer-verlag, Berlin, 1989); G.P Agrawal, *Nonlinear Fiber Optics* (Academic Press, Boston, 1989), Chap. 2.
- 2) P. N. Butcher and D. Cotter, *The Elements of Nonlinear Optics* (Cambridge University Press, Cambridge, 1990))
- 3) K. Ema, and M. Kuwata, Phys. Rev. Lett. 75,227 (1995)

Tuesday, July 9, 1996

Joint Session on Holographic Systems

JTuA 8:00 am-9:50 am
Haku Room

Glenn T. Sincerbox, *Presider*
IBM Almaden Research Center

Fundamental materials and device issues for digital holographic data storage

Lambertus Hesselink, John F. Heanue, Matthew C. Bashaw, A. J. Daiber, R. Snyder
Stanford University
Optitek, Inc.

Phone: 415-723-4850
Fax: 415-966-3200
email: bert@kaos.stanford.edu

Abstract.

The performance of digital holographic data storage (DHDS) systems is primarily limited by the recording medium, as other components have been developed for consumer applications. In this invited paper we review state-of-the-art DHDS systems, fixing issues, and fundamental tradeoffs between materials and device characteristics. Recent results, including stored and retrieved video clips will be presented.

Introduction.

During the recording process, a laser is split into two branches: a signal beam, which is used to encode data, and a reference beam.

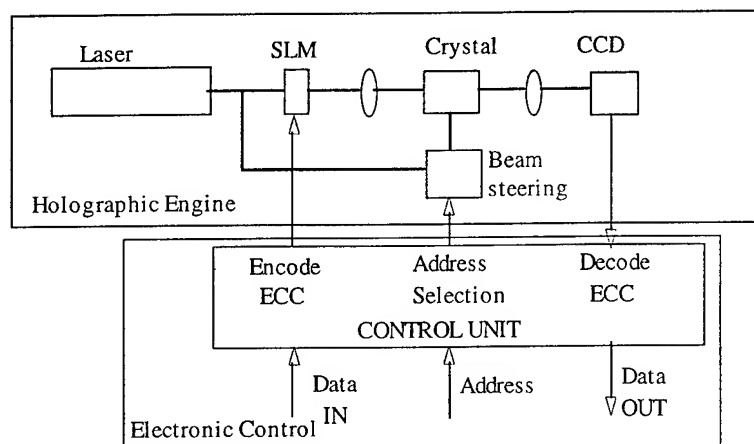


Figure 1. Optical setup for digital holographic data storage system.

The signal beam passes through a spatial-light modulator, that represents data with a matrix of squares; each square can be directed to transmit light, corresponding to a binary 1, or to block light, corresponding to a binary 0. The signal beam is then focused onto the holographic medium, typically a crystal, where it intersects with the reference beam to create a modulation in index of refraction. During the readout process, the original reference beam is incident on the medium by itself. It interacts with the index perturbation to regenerate the original signal beam, which is then refocused onto a detector array similar to that used in electronic cameras. By using a large number of pixels in the input SLM and the readout CCD array, large data transfer rates can be achieved approaching 1 Gb/sec using a commercially available laser sources and other components. By superimposing

hundreds of holograms, the capacity of a stack of pages can be made large; capacity can be further increased by using multiple volumes of media.

In the past, much work has been carried out on investigating the limits of certain aspects of the technology, using analog recording of gray scale images or checker board patterns. At Northrop, for example, Mok has stored 5000 holograms of greyscale images in a crystal of LiNbO₃ (Ref 1).

Although much valuable information was gained from these experiments, in a practical system it is necessary to evaluate the bit error rate for a given capacity at a certain data transfer rate. In general, this requires one to make tradeoffs between the performance of individual components and that of the overall system. At Stanford University we performed the first of such an experiment by demonstrating that a modest *digital* holographic data

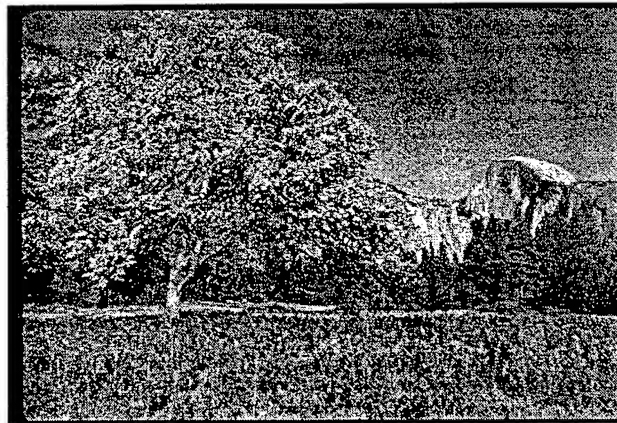


Figure 2 High resolution image, stored and retrieved from digital holographic storage system at Optitek, 1.2 MB file size.

storage system (DHDS) could be built with off-the-shelf technology (Science, Ref 2)

To a large extent, the number of photons reaching a CCD detector element is the overriding consideration for system tradeoff studies. We have modeled and studied experimentally the processes responsible for the signal to noise ratio at the detector. Page size, laser power during readout, the number of holograms, and the optical efficiency of the readout system determine the number of collected photons; noise models have been used to investigate scatter noise in the medium, and at the detector. From this model and experimental results, overall system performance can be evaluated. For discussion we consider LiNbO₃, for which a key parameter is the diffraction efficiency of fixed holograms. In previous work large diffraction efficiencies have been reported for fixed holograms in the transmission geometry, but little research has been carried out in the perpendicular geometry which affords the highest angular selectivity and lowest scatter of noise into the signal beam. We demonstrate recent results of high diffraction efficiency of fixed digital data in the 90 degree geometry. In summary, there is a strong interrelationship between capacity, data transfer rate and signal to noise ratio or raw bit error rates.

In practice it is difficult to achieve raw bit error rates much less than 10^{-5} to 10^{-6} . For commercial devices bit error rates less than 10^{-12} are typically required. Therefore modulation codes and error control codes are added to the data pages, further decreasing capacity. In conventional disk drives, Reed-Solomon codes are often used for this purpose, and may be modified for use in DHDS systems. Holographic recording,

however, offers the opportunity to exploit the page organization of the data, giving rise to novel encoding and decoding schemes. (Ref 3, 4).

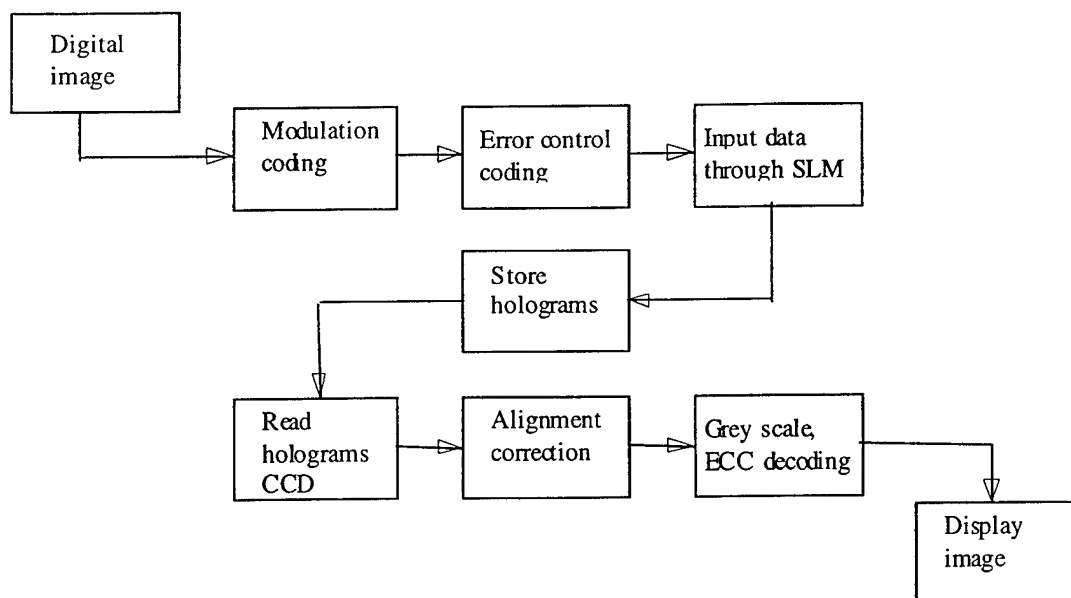


Figure 3. Data flow in the Optitek DHDS system

To demonstrate the performance of a state-of-the-art DHDS system, we show how digital images can be stored and retrieved, as well as video, sound clips and numeric data.

Acknowledgments:

This research has been financially supported in part by the Advanced Research Projects Agency through the PRISM and HDSS programs. We are grateful to Jim Colvin, Ingolf Sander, and Bill Phillips at Optitek for providing the image of Yosemite valley stored in the digital holographic data storage system.

References:

1. F.H. Mok, "Angle-multiplexed storage of 5000 holograms in lithium niobate", *Opt. Lett.* 18: 915-917 (1993)
2. J.F. Heanue, M.C. Bashaw, L. Hesselink, Volume Holographic Storage and Retrieval of Digital Data, *Science* 5 August 1994, Vol 265, pp. 749-752
3. B. Olsen and S. Esener, "Multi-dimensional partial response precoding for parallel readout optical memories", *SPIE Symposium on Optics, Imaging, and Instrumentation*, San Diego, CA (1994), paper 2297-39
4. J.F. Heanue, K. Gurkan, and L. Hesselink, "Signal detection for page-access optical memories with intersymbol interference", *Applied Optics*, to be published 1996

Prospects for Fast Access Holographic Memories

John Hong, Ian McMichael, Jian Ma,
Tallis Chang, William Christian, David Pletcher, Monte Khoshnevisan

Rockwell Science Center
1049 Camino dos Rios, A25A
Thousand Oaks, CA 91360
(805) 373 4193

Abstract

A unique feature of holographic memory is its potential for fast random access if nonmechanical means for page addressing are implemented. It is possible to obtain 10 microsecond latency (equivalent to disk head seek time) by using acoustooptic deflectors to steer the address beam in an angularly multiplexed holographic memory system. When 1-100 GByte storage capacities are considered, however, the nonmechanical addressing constraint poses challenging design problems. In this paper, we describe fast access holographic memory architectures and discuss the critical design issues. We also describe recent Rockwell efforts to develop a fast access holographic memory system.

Mass memory systems serve computer needs in providing archival data storage as well as some emerging applications involving network data and multimedia services. In general, mass memory implies capacities larger than 10 GBytes with other performance factors such as random data access latency (the time lag for data to appear at output after address is set), data transfer time, cost and system size dictated by specific application needs. Archival storage, for example, can tolerate relatively long data access latency but is extremely sensitive to system cost and size. In contrast, network server and multimedia applications typically stress the speed aspect (both data access latency and transfer) and is less sensitive to the system cost.

A variety of hardware approaches are currently available as illustrated in Figure 1 where they are classified with respect to two important performance measures: storage capacity and effective data transfer time. The latter metric measures the time required to fully retrieve an arbitrarily located data block (e.g., 10 KB block) from the system and is a combination of the data transfer rate (the rate at which data is transferred from the mass memory to the user or CPU) and the data latency (the time lag between the address set-up and the appearance of valid data at the output). If D is the data block size (in bytes), R is the data transfer rate and τ_{latency} is the data latency, the data access time is given by

$$\tau_{\text{access}} = \tau_{\text{latency}} + D/R.$$

For specific comparisons, the block size must of course be chosen with care depending on the application of interest. No matter how fast the data transfer may be (e.g., high speed tape), a fundamental limitation exists for all approaches involving mechanical motion of either the head or the medium.

To achieve fast access, a holographic mass memory system must be capable of providing not only fast tuning of the reference beam for read-out (in angle, wavelength, or other characteristic) but also provide fast conversion of the optical reconstruction into electronic data and sufficient signal processing and correction to yield usable output data for the application. The fast optical to electronic data conversion goal (data transfer rate) can be achieved by using parallel electronic approaches involving, for example, multiple output channel CCD arrays to yield raw data transfer rates in the neighborhood of 1 Gbit/sec. The signal processing and correction will require digital signal processing that implement algorithms that are optimized for the holographic memory technology.

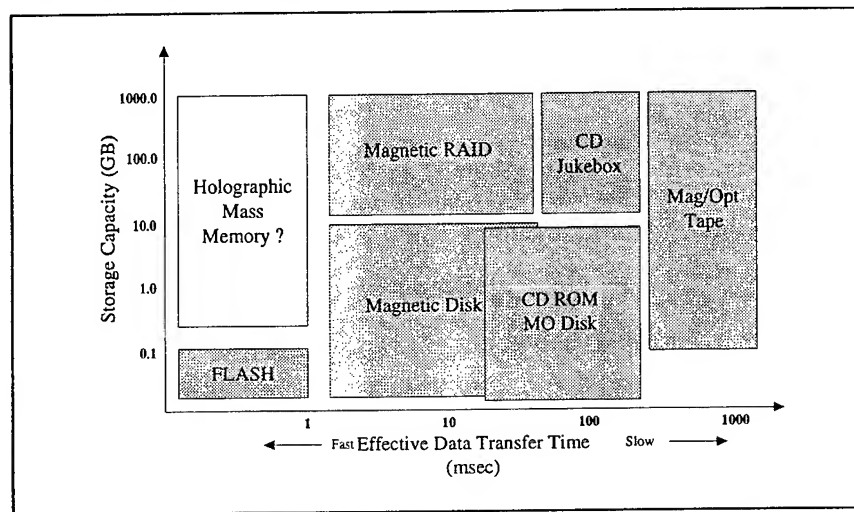


Figure 1 Mass Storage Technologies

The current method of choice for tuning the reference beam rapidly is the acousto-optic deflector which has high efficiency and extremely rapid switching time between random angular positions. We have made this selection for our current development work, exploiting the relatively high maturity of this technology and its compatibility with the shorter visible wavelengths at which the photorefractive materials respond best. Future progress may, however, focus on wavelength tunable lasers with sufficiently fast and stable tuning characteristics.

The basic architectural approach (fast access, angularly multiplexed) is illustrated in Figure 2 which incorporates both spatial and angular multiplexing for high capacity, both implemented using acousto-optic to maintain rapid access. The first acousto-optic deflector in the address beam path deflects the beam vertically to select spatially distinct layers in the crystal. A two-dimensional approach can also be adopted in which distinct cells are addressed by using a pair of acousto-optic deflectors. A second deflector is then used to yield fine angular deviations in the horizontal direction to allow angular multiplexing within each layer (or cell). The memory is thus organized into angularly

Error Sources and Performance Limits in Digital Holographic Data Storage

John F. Heanue, Andrew Daiber, Ray Snyder, James Colvin,
Matthew C. Bashaw, and L. Hesselink

Optitek, Inc., 100 Ferguson Dr., Mailstop 5G61, Mountain View, CA 94039

Starting with the work of van Heerden¹, many estimates of the potential storage capacity of a holographic data storage system have been made. While some effort has been made to theoretically predict^{2,3} and to measure^{4,5} the practical limits imposed by noise sources, most results deal with fundamental limits imposed by the finite spatial frequency resolution of the recording medium and the optical system. We are interested in characterizing the noise statistics in a typical holographic storage system and using these statistics to predict the ultimate limits on system performance. Toward this end, we have developed theoretical models to describe several fundamental noise sources. These models are used to predict limits on the storage capacity and transfer rate achievable in a practical device. We have constructed an experimental system that is used to obtain data on bit-error-rate performance and to verify theoretical predictions. Finally, we are using the experimental system to develop efficient techniques for overcoming noise sources so that we can achieve performance closer to the theoretical limits.

A real holographic storage system will be affected by optical noise caused by scatter of the reference beam, by thermal noise at the detector, by random fluctuations in the recording process, and by photon shot noise. The statistics that describe the behavior of each of these noise sources are different. For example, the performance of a system dominated by optical scatter can be described by Rician statistics⁴, whereas detector noise can frequently be modeled using Gaussian statistics. We identify the operating regimes that apply to each of the various statistical models and describe conditional statistical models that are appropriate when no single noise source is dominant. In each case, we present experimental results to examine the validity of the theoretical predictions.

Our experimental system utilizes angular multiplexing in the perpendicular recording geometry. Scatter of the reference beam into the signal beam is minimized in this geometry. The recording medium we are currently examining is iron-doped LiNbO₃. This medium introduces noise induced by scatter, by fanning, and by photovoltaic damage. In addition to the standard additive noise sources, inter-pixel cross-talk is introduced due to aberrations in the imaging optics. The imperfect overlap of the signal and reference beams introduces spatial frequency filtering effects because recording is done near the Fourier plane. These filtering effects also lead to inter-pixel cross-talk.

Given the various noise sources, it is necessary to take steps toward maximizing system performance and controlling the occurrence of errors. The steps can be broadly

categorized into three groups: modulation coding, error-correction-coding (ECC), and signal detection. The modulation code defines the way in which a binary one or zero is represented in the system. One use of modulation codes is to reduce inter-pixel cross-talk for example. The use of ECC entails adding redundant information to a string of binary data so that errors in the string can be detected and corrected. The particular error-correction code implemented in the system can be selected to protect against burst errors. Signal detection concerns the method used for converting the output of the CCD array from a measure of intensity levels to a binary data stream. Signal detection methods range from simple techniques such as binary threshold detection to more complex techniques like maximum likelihood sequence estimation.

Knowledge of the error sources and the governing statistics is critical in understanding the limitations of a practical system. In addition, this knowledge is necessary for determining effective error-control strategies so that good digital storage performance can be achieved. We have characterized our system in terms of the main sources of error and compared the error characteristics to theoretical models. We have used this information to develop efficient error-control strategies so that digital storage demonstrations can be carried out. To date, we have been able to demonstrate storage of digital data, such as digitized video, sound, and text. The latest results will be presented.

REFERENCES

- [1] P. J. van Heerden. "Theory of optical information storage in solids." *Appl. Opt.*, **2**:393-400 (1963).
- [2] W. Lee. "Effect of film-grain noise on the performance of holographic memory." *J. Opt. Soc. Am.*, **62**:797-801 (1972).
- [3] K. Blotekjaer. "Limitations on holographic storage capacity of photochromic and photorefractive media." *Appl. Opt.*, **18**:57-67, (1979).
- [4] J. E. Weaver and T. K. Gaylord. "Evaluation experiments on holographic storage of binary data in electro-optic crystals." *Opt. Eng.* **20**:404-411 (1981).
- [5] R. M. Shelby *et al.* "Defining materials limits to holographic data storage: holographic storage tester." In *1995 OSA Annual Meeting*, Portland, OR, Paper MP2 (1995).

Data Detection for Page-Access Optical Memories with Intersymbol Interference

John F. Heanue^{*†}, Korhan Gürkan[†], and Lambertus Hesselink[†]

^{*}Department of Applied Physics, Stanford University, Stanford, CA 94305-4090

[†]Department of Electrical Engineering, Stanford University, Stanford, CA 94305-4035

Page-access optical memories are being investigated for the next generation of digital storage due to their potential for simultaneously achieving high capacity, fast transfer rates, and short access times. Examples of such memories are systems based on volume holography[1], two photon 3D recording[2], and spectral hole burning[3]. A common feature of these systems is that data is input using a spatial light modulator (SLM) and the output signal is imaged onto a CCD array. A typical arrangement for a digital volume holographic memory is shown in Fig. 1. To meet the capacity and transfer rate goals of a commercial system, page sizes on the order of one million pixels are required. The need to image pixel-to-pixel from the SLM to the CCD array over such a large page imposes tight tolerances on the optical design. Deviations from ideal imaging typically result in degraded performance. In future systems, signal processing methods will be required to overcome the limitations of the optical components. We describe a technique for data detection in page-access memories that extends the well-known method of sequence detection from digital communications to two dimensions. The technique, which we term Decision Feedback Viterbi Algorithm (DF-VA) Detection improves the bit-error-rate (BER) performance of systems without ideal optics. Use of such a detection scheme can allow the use of less expensive, lower-complexity imaging optics, or, alternatively, can lead to higher information density per data page.

Deviations from ideal imaging, such as those caused by misalignment or by optical aberrations, result in interpixel crosstalk, where the measurement of one data value is affected by the surrounding data bits. In the digital storage literature, this crosstalk is known as intersymbol interference (ISI). A system corrupted by ISI generally exhibits degraded BER performance. In the case of ideal imaging, the system is free of ISI and the optimum detector is one that performs bit-by-bit threshold detection. When ISI occurs, the signal is said to have memory, and the optimum detector is one that bases its decisions on observations of a sequence of received values[4]. Such a detector can be implemented using the Viterbi algorithm. Our DF-VA detector combines Viterbi detection on a row-by-row basis with feedback of previous row decisions, thereby extending this inherently one-dimensional technique to two dimensions. This detection scheme has the advantage that it operates on data row-by-row as it is typically output from a CCD array. In addition, the decision feedback allows information about the progression of data in the vertical dimension to be used in the decision process.

To experimentally investigate our 2-D Viterbi detection scheme, we used a system similar to that in Fig. 1. A chrome-on-glass mask with 512×512 pixels was used in place of a SLM. The optics are of sufficient quality that each data pixel can be imaged onto one effective pixel on the CCD with minimal ISI. In order to generate ISI, the mask was translated with respect to the CCD array. Both bit-by-bit threshold detection and DF-VA detection were performed on the data output by the CCD. Histograms of the detected intensities for the well-aligned and the significantly misaligned system are shown in Fig. 2. It is evident that threshold detection is incapable of distinguishing many of the zeroes and ones in the misaligned system. With the same data for the misaligned system, the DF-VA detector achieved a BER of 3.4×10^{-4} compared to 1.8×10^{-1} for threshold detection. While these experimental results can not be expected to accurately predict actual BER performance in a system, they do give an indication of the ability of the DF-VA detector to compensate for the effects of ISI.

Additional evidence for the effectiveness of our detection scheme was obtained by numerical simulations of the detection process for typical examples of ISI-corrupted page-access memories. In each case, DF-VA detection was compared to bit-by-bit threshold detection and other detection schemes. We present the results of these simulations as well as additional experimental data. In addition, we discuss the feasibility of a hardware implementation and the possibility of increasing parallelism by incorporation of multiple DF-VA detectors in a system with a multiple-channel CCD array.

This research has been supported in part by the Advanced Research Projects Agency through the ARPA-University-Industry Photorefractive Information Storage Materials (PRISM) Consortium (MDA972-94-2-0008). We gratefully acknowledge the holographic storage group at the IBM Almaden Research Center for some of the experimental data.

[†]Present address: Optitek, Inc., 100 Ferguson Dr., MS 5G61, Mountain View, CA 94039.

References

- [1] J. F. Heanue, M. C. Bashaw, and L. Hesselink. "Volume holographic storage and retrieval of digital data". *Science*, **265**:749-752, (1994).
- [2] B. H. Olson and S. C. Esener. "Partial response precoding for parallel-readout optical memories". *Opt. Lett.*, **19**:661-663, (1993).
- [3] E. S. Maniloff, S. B. Altnier, S. Bernet, F. R. Graf, A. Renn, and U. P. Wild. "Recording of 6000 holograms by use of spectral hole burning". *Appl. Opt.*, **34**:4140-4148, (1995).
- [4] G. D. Forney. "Maximum-likelihood sequence estimation of digital sequences in the presence of intersymbol interference". *IEEE Trans. Inf. Theory*, **IT-18**:363-378, (1972).

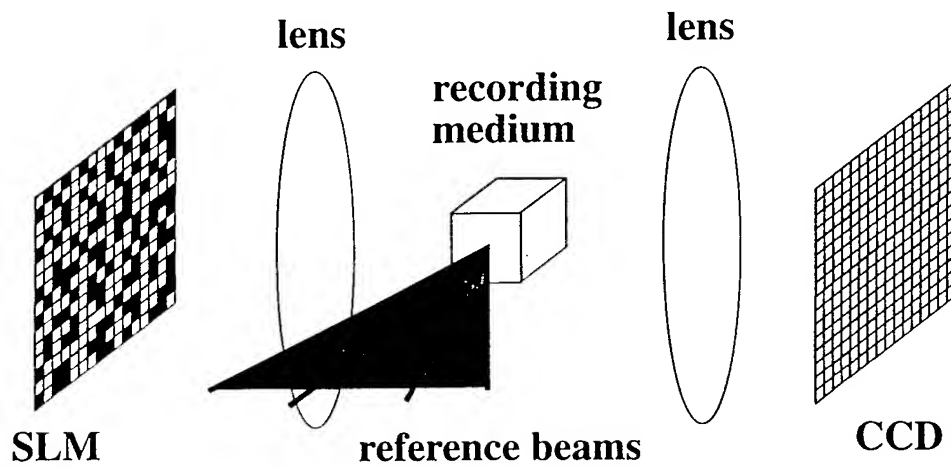


Figure 1: Typical arrangement of a digital holographic data storage system.

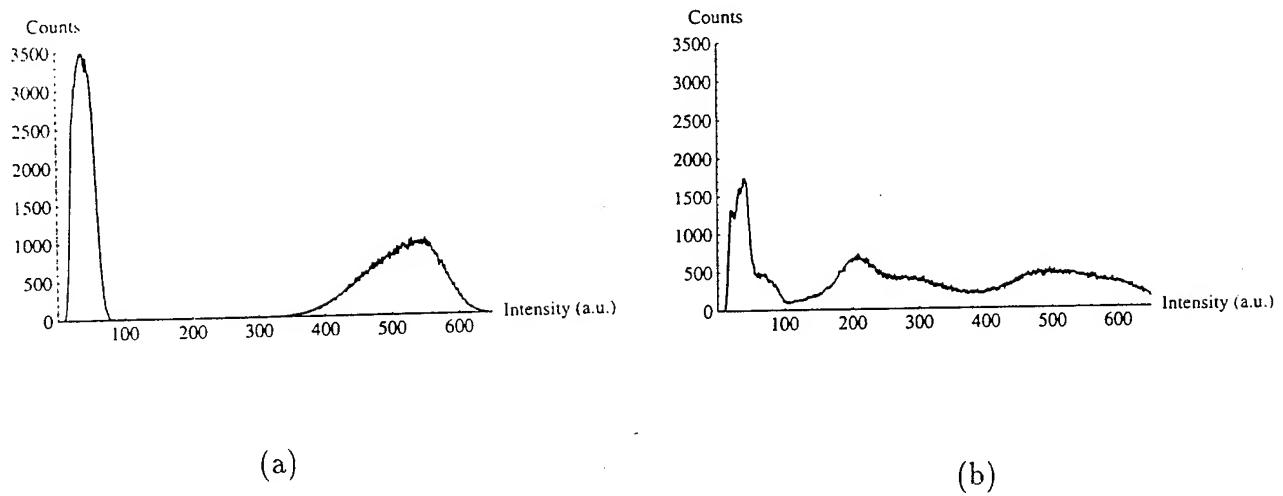


Figure 2: Histograms of the measured intensities for (a) a well-aligned system, and (b) a significantly misaligned system.

Statistics of Cross-Talk Noise in Holographic Data Storage

Claire Gu and Gregory Sornat

Department of Electrical Engineering

The Pennsylvania State University, University Park, PA 16802

Phone: (814) 863-2946, Fax: (814) 865-7065, E-Mail: gxc@ecl.psu.edu

John Hong

Rockwell International Science Center

1049 Camino Dos Rios, Thousand Oaks, CA 91360

Digital holographic data storage is becoming increasingly important because of its potential for optical memory systems with high storage density and fast parallel access. One of the important parameters of a digital system is its accuracy, which is usually characterized in terms of bit-error-rate (BER) defined as the probability of error for each bit. To determine the BER of a holographic storage system, one needs to know the statistics of the noise. There are several noise sources including cross-talk noise, scattering noise, shot noise, and thermal noise from the detector, etc. In this paper, we will concentrate on the discussion of the statistics of the cross-talk noise.

Previously, BER related to the cross-talk noise has been calculated using various statistics. If the noise amplitude is assumed to be a real random variable with Gaussian probability density function (PDF), then the intensity PDF will be a first-order χ^2 distribution (for the off bit). The BER can be calculated either by integrating the intensity PDF (non-Gaussian) with respect to the threshold value or by integrating the amplitude PDF (Gaussian) over corresponding regions [1,2]. However, this approach can not be used to calculate the BER when the noise amplitude is complex, which is the case when the cross-talk noise from each pixel (or page) has a random phase. Another approach used to analyze the statistics of noise is to fit the pixel value histogram obtained by numerical simulation with a Gaussian distribution [3]. This approach is complicated by the fact that although the center of the histogram may fit well with a Gaussian profile the tails do not. However, the BER is determined mainly by calculating the areas covered by the tails of the PDF. A poor fit of the tails may lead to orders of magnitude difference in the estimation of the BER.

In this paper, we analyze the statistics of cross-talk noise in holographic data storage assuming the noise amplitude is a complex random variable. Then we determine the threshold value for distinguishing binary bits (e.g., 1 or 0). Finally, we calculate the BER. Explicit expressions of the threshold value and the BER are obtained analytically. Our analytical results show excellent agreement as compared with our numerical calculations.

Consider the output amplitude from the readout of a holographic memory. Let a be the signal component of the holographically read-out wave and n be the noise component of the same. For simplicity, a is assumed to be real and for binary memory takes on the values 1 or ε where $1/\varepsilon^2$ is the intensity contrast ratio of the on/off pixel values. The complex noise amplitude $n = n_r + in_i$ where the statistics are assumed to be circularly Gaussian, i.e., n_r and n_i are statistically independent and have the same standard deviation σ . The amplitude at the output is a random variable consisting of both the signal and the noise, $u = u_r + iu_i = (a + n_r) + in_i$. The PDF of the amplitude is given by

$$p_u(u_r, u_i | a) = \frac{1}{2\pi\sigma^2} \exp\left\{-\frac{1}{2\sigma^2}[(u_r - a)^2 + u_i^2]\right\}. \quad (1)$$

During the detection process which converts the optical energy into an electronic form a square law operation is involved. The random variable $v = |u|^2 = u_r^2 + u_i^2$ represents the intensity arriving at the detector (proportional to the pixel value). Its corresponding PDF can be obtained from the above equation by a change of variables. The calculation yields

$$p_v(v|a) = \begin{cases} \frac{1}{2\sigma^2} \exp\left[\frac{-1}{2\sigma^2}(v+a^2)\right] I_0\left(\frac{a\sqrt{v}}{\sigma^2}\right) & \text{for } v \geq 0, \\ 0 & \text{for } v < 0, \end{cases} \quad (2)$$

where $I_0(x)$ is the zeroth order modified Bessel function. Fig. 1 shows the PDFs of both on and off pixels with $a_{on} = 1$ for the on pixel and $a_{off} = 0.1, 0.2, 0.4, 0.5$, for the off pixel, respectively. The corresponding intensity contrast ratios are 100, 25, 6.25, and 4, respectively. As can be seen in Fig. 1, the variance of the intensity distribution depends on the signal value. It is easier to calculate the mean and variance of the intensity by using the amplitude Gaussian distribution [Eq. (1)] and the relation $v = |u|^2 = u_r^2 + u_i^2$. The results are listed as

$$\langle v \rangle = a^2 + 2\sigma^2, \quad (3)$$

$$\sigma_v^2 = \langle v^2 \rangle - \langle v \rangle^2 = 4\sigma^2(a^2 + \sigma^2). \quad (4)$$

The signal-to-noise ratio (SNR) can be defined as the ratio between the mean value and the standard deviation of the intensity in terms of the on pixel. These values are measurable from the experimental pixel value histogram. Using Eqs. (3) and (4) we obtain the SNR

$$SNR = \frac{\langle v \rangle}{\sigma_v} = \frac{1 + 2\sigma^2}{2\sigma\sqrt{1 + \sigma^2}} \approx \frac{1}{2\sigma}, \quad (5)$$

where the last approximation is valid when $\sigma^2 \ll 1$.

In order to calculate the BER, we need to decide the threshold value v_{th} . When $v > v_{th}$, the output pixel is said to be on, and vice versa. The BER is defined as the total probability of error, i.e.,

$$BER = P(a=1)P(v < v_{th}|a=1) + P(a=\varepsilon)P(v > v_{th}|a=\varepsilon), \quad (6)$$

where $P(a=1)$ and $P(a=\varepsilon)$ are the probabilities for the input pixel to be on or off, respectively,

$$P(v < v_{th}|a=1) = \int_0^{v_{th}} p_v(v|a=1)dv, \quad P(v > v_{th}|a=\varepsilon) = \int_{v_{th}}^{\infty} p_v(v|a=\varepsilon)dv. \quad (7)$$

When $P(a=1) = P(a=\varepsilon) = 1/2$, in other words, the probability for any input pixel to be on or off is equal, the condition for minimizing the BER is given by $p_v(v_{th}|a=1) = p_v(v_{th}|a=\varepsilon)$.

We can obtain explicit expressions for the threshold value v_{th} by using asymptotic approximations for the modified Bessel function in Eq. (2). The threshold value is obtained as

$$\sqrt{v_{th}} = \frac{1 + \delta}{2} \quad \text{where} \quad \delta = \text{Max}\{\varepsilon, \sigma^2 \ln(\pi / \sigma^2)\}. \quad (8)$$

Once the threshold value is decided, we can calculate the BER by carrying out the integrations in Eq. (7). Further approximation is used in the integration in order to obtain an analytical expression for BER. Assuming equal probability for a pixel to be on or off and substituting the appropriate threshold values, we obtain the BER defined by Eq. (6)

$$BER \approx \frac{\sqrt{\varepsilon+1}}{4\sqrt{2}} \left[\text{erfc}\left(\frac{1-\varepsilon}{2\sqrt{2}\sigma}\right) - \text{erfc}\left(\frac{1}{\sqrt{2}\sigma}\right) \right] + \frac{\sqrt{\varepsilon+1}}{4\sqrt{2}\varepsilon} \left[\text{erfc}\left(\frac{1-\varepsilon}{2\sqrt{2}\sigma}\right) \right] \quad \text{for } \varepsilon > \sigma^2 \ln(\pi / \sigma^2), \quad (9)$$

$$BER = \frac{\sqrt{1 + \sigma^2 \ln(\pi / \sigma^2)}}{4\sqrt{2}} \left[\text{erfc}\left(\frac{1 - \sigma^2 \ln(\pi / \sigma^2)}{2\sqrt{2}\sigma}\right) - \text{erfc}\left(\frac{1}{\sqrt{2}\sigma}\right) \right] + \frac{1}{2} \exp\left\{ -\frac{[1 + \sigma^2 \ln(\pi / \sigma^2)]^2}{8\sigma^2} \right\} \quad \text{for } \varepsilon < \sigma^2 \ln(\pi / \sigma^2), \quad (10)$$

where $\text{erfc}(x)$ is the complimentary error function.

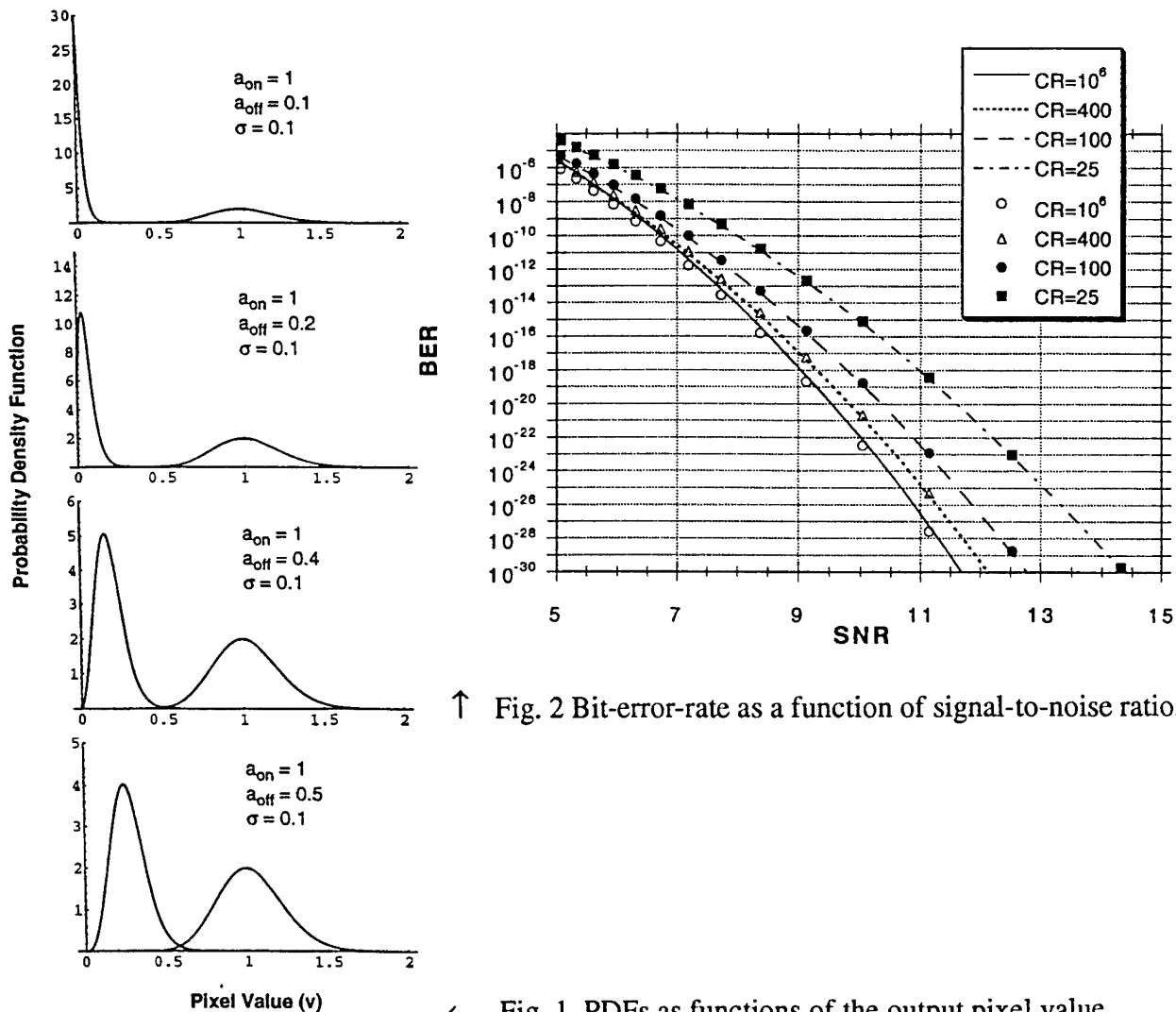
In Fig. 2, we plot the BER as a function of the SNR for various values of the contrast ratio. The lines are calculated using Eqs. (9) and (10), and the scattered data points are calculated by direct integration of the PDF in Eq. (2). The plots show excellent agreement between the analytical and numerical results. The difference in the range of SNR in Fig. 2 and that in previous papers [1] is a result of different definitions of SNR.

In conclusion, we have analyzed the statistics of cross-talk noise in holographic data storage and determined the corresponding bit-error-rate. Explicit expressions of the threshold value for distinguishing binary bits and of the bit-error-rate have been obtained analytically. Comparison between the analytical and the numerical results shows excellent agreement. Further work will be conducted to include the noise contributions from the electronic detectors, such as shot noise and thermal noise.

We acknowledge support by National Science Foundation under NYI program, No. ESC-9358318, and by Rockwell International Science Center.

References

1. X. Yi, P. Yeh, and C. Gu, *Opt. Lett.*, **19**, 1580, (1994).
2. A. Pu and D. Psaltis, "High density recording in photopolymer-based holographic 3-D disks," to appear in *Appl. Opt.*
3. G. P. Nordin and P. Athana, *Opt. Lett.*, **18**, 1553, (1993).



↑ Fig. 2 Bit-error-rate as a function of signal-to-noise ratio.

← Fig. 1 PDFs as functions of the output pixel value.

Shift Multiplexed Holographic 3-D Disk System

Allen Pu and Demetri Psaltis

California Institute of Technology

Department of Electrical Engineering

136-93 CALTECH

Pasadena, CA 91125

Tel : (818) 395-2231 Fax : (818) 568-8437

Internet : allenpu@sunoptics.caltech.edu

We have demonstrated for the first time a fully functional holographic disk system using shift multiplexing. The architecture of our system is similar to the compact disc, but with higher storage density and data transfer rate. Figure 1 shows the experimental setup. An amplitude data mask containing 590,000 random bits (pixels) is imaged to the detector plane by a pair of Nikon F/1.4 50mm camera lenses. A 120mm glass substrate coated with a holographic recording medium (DuPont's HRF-150 100 micron thick photopolymer) is placed slightly after the Fourier plane of the camera lenses. The photopolymer disk is rotated by a microstepping motor capable of 125,000 steps per revolution. A F/1.4 CCD camera lens is used to create the spherical reference beam necessary for shift multiplexing [1]. The stored data is retrieved by a CCD camera placed at the detector plane.

During data storage, the overlapping signal and reference beams create an interference pattern which is recorded in the photopolymer as localized index change. Additional holograms can be recorded on top of the existing hologram by rotating the disk by a few steps (the number of steps required between holograms is inversely proportional to the thickness of the photopolymer). Figure 2 shows how the holograms can be placed to overlap laterally as well as radially on the disk. Since several holograms share the same physical location, the effective storage density is increased.

For readout, the same spherical reference beam used in recording is used to illuminate the stored holograms. As the disk spins, the wave front of the reference beam matches one of the stored holograms and the data contained within that particular hologram is read out by the CCD camera. The wavefront of the reference beam at the current location is shifted with respect to the wavefront used to record adjacent holograms and therefore, their reconstruction will be suppressed even though they are illuminated. As the disk spins, sequential holograms become matched and entire pages of data can be retrieved, achieving high data throughput rate.

Other than using the spherical reference beam for shift multiplexing holograms, another interesting benefit of using a spherical reference beam to record Fresnel plane holograms is the ability to correct for the shrinkage of the photopolymer [2]. After exposure to light, the polymerization causes the photopolymer to shrink by about 3% in the direction parallel to the surface normal. What this means for high bandwidth holograms is that only a portion of the hologram can be Bragg matched and reconstructed with a given reference beam. The rest of the hologram can be reconstructed by slightly detuning the reference beam angle. However, by positioning the spherical reference beam properly, this shrinkage effect can be avoided completely. Figure 3 shows two spherical beams created from lenses with the same F/#. For the signal beam, the focal point is placed in front of the recording material and for the reference beam, the focal point is behind. By matching the center ray of the two spherical beams so that they are incident at the same location on the photopolymer and are symmetric with respect to the surface normal (both have angle β), the hologram created by these two rays doesn't suffer from the shrinkage effect (it has been shown experimentally and theoretically that for symmetric rays, shrinkage does not effect the Bragg condition). Since both lenses have the same F/#, they can be adjusted so that the spherical beams overlap each other completely on the photopolymer and each reference ray has a complementary signal ray such that they record a symmetric hologram which does not suffer from the shrinkage effect (this is approximately true for thin materials like the photopolymer). We have done experiments proving this method by recording high bandwidth holograms and reconstructing the entire hologram without detuning

the reference beam. This would not be possible if a plane wave reference beam was used to record the high bandwidth hologram.

At the time this summary is written, we have achieved a surface density of $4 \text{ bits}/\mu\text{m}^2$ along a single track with the setup shown in Figure 1. 60 holograms were recorded in the 100 micron thick photopolymer with 36 steps (100 microns) between holograms. A portion of a reconstructed hologram is shown in Figure 4. Each hologram occupies the area of a circle with a diameter of 1.5 mm. We can calculate the surface density by dividing the total number of bits per page (590,000) by the area, that is the diameter of the recording spot on the medium (1.5 mm) times the shift distance between holograms (.1mm). This yields $590,000 \text{ bits}/(1.5 \text{ mm} * .1 \text{ mm}) = 4 \text{ bits}/\mu\text{m}^2$. This means that with the active area of a CD-ROM disk, a raw (un-compressed) storage capacity of 4 Gbytes per disk is possible. Furthermore, instead of reading a single bit at a time, 590,000 pixels is presented simultaneously per hologram. By the time of the conference, we aim to have more than double the surface density to $10 \text{ bits}/\mu\text{m}^2$ by using inter-track recording (overlapping in the radially direction) and lower F/# lenses. Density in excess of $100 \text{ bits}/\mu\text{m}^2$ can then be achieved with a recording medium of 1 mm in thickness.

Figure 5 shows one possible practical implementation of a holographic 3-D disk using spherical reference beam. The system consists of two major components: the read/write head and the holographic 3-D disk. The read/write head is mounted on a mechanical slide so that the spherical reference beam can access different tracks on the disk. The holographic 3-D disk spins so that different stored holograms get reconstructed by the spherical reference beam. Notice that there are no moving parts inside the read/write head and only about ten components are required. Furthermore, holograms are read out in a continuous fashion by the spinning motion of the disk. The holographic 3-D disk setup shown in Figure 5 offers the simple compact-disk-like architecture, high surface density, and high speed page access.

References

- [1] D. Psaltis, M. Levene, A. Pu, G. Barbastathis, and K. Curtis, "Holographic storage using shift multiplexing," *Opt. Lett.* **20**(7), pg 782-784 (1995).
- [2] U. Rhee, H. J. Caulfield, J. Shmir, C. S. Vikram, and M. M. Mirsalehi, "Characteristics of the Du Pont photopolymer for angularly multiplexed page-oriented holographic memories," *Opt. Eng.* **32**(8), pg 1839- 1847 (1993).

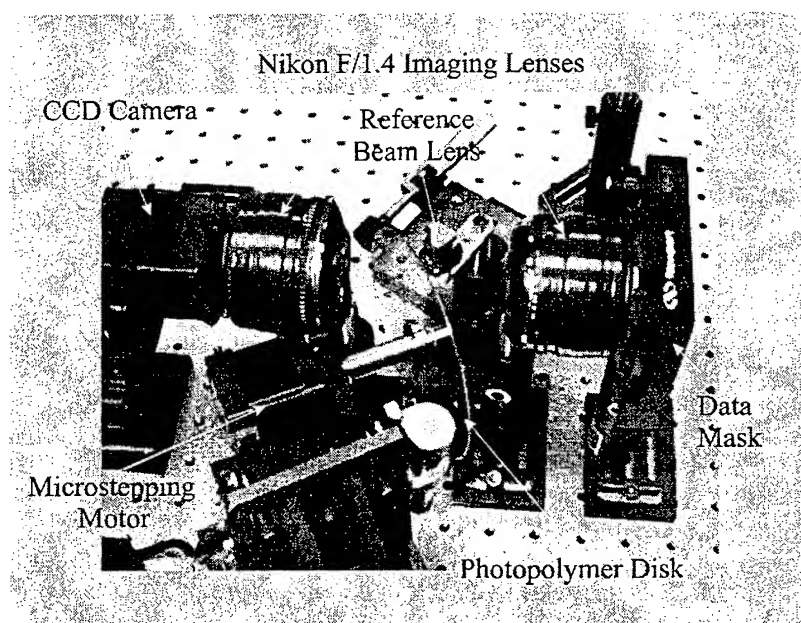


Figure 1 : Current implementation of a shift multiplexed holographic 3-D disk.

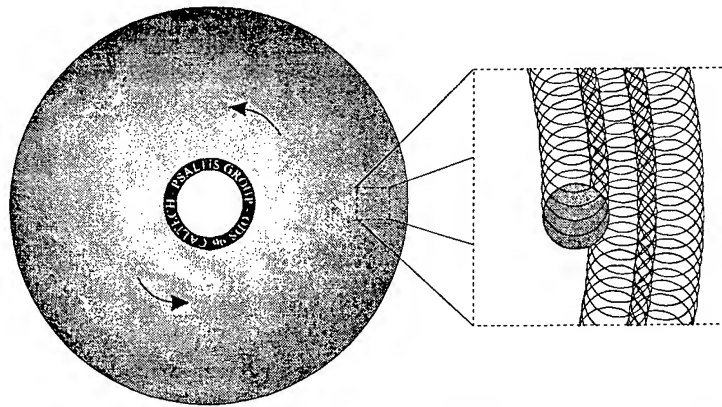


Figure 2 : A photopolymer disk with blowup showing how the holograms overlaps.

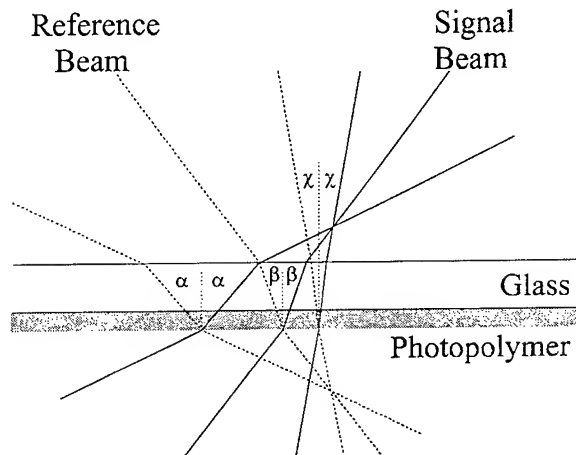


Figure 3 : Geometry using a spherical reference beam to avoid the shrinkage effect.

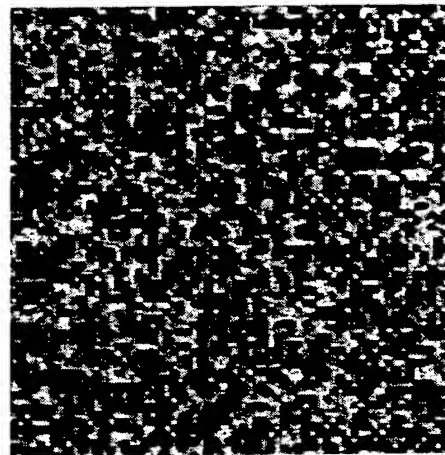


Figure 4 : A sample reconstruction of a hologram from the 4 bits/μm² experiment.

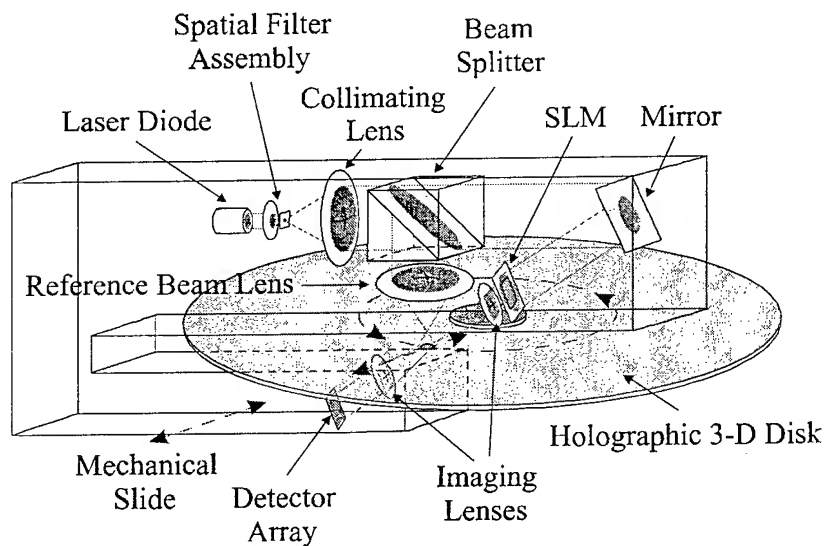


Figure 5 : Compact holographic 3-D disk system using spherical reference beam.

Tuesday, July 9, 1996

Joint Session on Holographic Materials & Fixing

JTuB 10:20 am-12:15 pm
Haku Room

Tallis Chang, *Presider*
Rockwell International Science Center

PRISM: Removing The Materials Bottleneck In Holographic Storage

Glenn T. Sincerbox

IBM Research Division, Almaden Research Center, 650 Harry Road
San Jose, CA 95120-6099

Lambertus Hesselink

Optitek, Inc., 100 Ferguson Drive
Mountain View, CA 94039

The lack of a suitable recording material has long been the Achilles heel of holographic storage. In contrast to the other system components (such as SLM, laser and detector array) which are generally available, although they may not be optimized for this particular application, the ideal material has yet to be developed. As a result, after 30 years of on-and-off development, no commercial digital holographic storage system has yet been deployed. To address this bottleneck, the PRISM (photorefractive information storage materials) consortium was formed in 1994 to focus on the development of a suitable recording material and to understand how storage system trade-offs are affected by each candidate material system.

In contrast to other applications of holography where there are numerous material candidates, a practical data storage material must meet very stringent requirements to insure success as measured by the cost/performance competitiveness of the final product and reliability of the stored data. The ideal material would have the following properties: a) high optical quality, b) thick: 500 μm - 10 mm, c) exhibit large Δn : 10^{-4} - 10^{-3} , d) have a high writing sensitivity: 1- 10 $\text{cm}^3/\text{kJoule}$, e) near-ir sensitivity, f) be self-processing, g) be fixable (and unfixable), h) have a long shelf life, inert, and i) be cheap. This, of course, is the ideal world. The real world will necessitate some compromises. The near-ir sensitivity, for example, would enable us to use compact laser diodes for system cost and size considerations. This is a relatively soft requirement as we could design a system with 530 nm sensitivity using a doubled-NdYAG laser. The large Δn , in combination with a thick material enables us to store many holograms in a common recording volume, 1,000-10,000 for example, by one of several multiplexing techniques. This permits rapid access to a large number of pages with fast devices like acousto-optic deflectors and is an important distinguishing feature in comparison to other storage technologies.

A high writing sensitivity is important in order to minimize the laser power and/or the time required for writing. Defined as the index change per absorbed energy per unit volume, typical values (in units of cm^3/kJ) are 15 for BSO, 6 for BaTiO_3 , 0.11 for SBN and 0.017 for LiNbO_3 . These values can vary as much as 10x with grating period and orientation, applied voltage, dopant concentration, etc. Ideally, one would like to write holograms in a few msec with power densities of less than 100 $\text{mWatts}/\text{cm}^2$. Remembering that the diffraction efficiency of an individual hologram falls off as $1/N^2$, where N is the number of multiplexed holograms in the same recording volume, the diffraction efficiency of a single hologram in a set of 1000 will be on the order of 10^{-6} . This represents an index change of $\delta n = 1 \times 10^{-8}$ for a 1 cm long sample at the 90° recording geometry. The resulting sensitivity requirement as defined above is 0.1 cm^3/kJ although a more conservative estimate would be 2-5 cm^3/kJ to allow for overexposing the first holograms to

achieve uniform diffraction efficiency. This is obviously an oversimplification of a very complex issue as these materials will have to be fine-tuned to provide for other features such as fixing.

While photorefractive materials come closest to having all the requisite properties, they exhibit one severe problem that has been a particular focus of the PRISM program - data volatility. The self-developing nature of the photorefractive process creates a situation whereby; a) there is partial erasure of previously recorded holograms when the next hologram in a sequence is recorded, b) there is partial erasure of all holograms when one hologram is read out and c) there is a slow decay of the holograms in the dark. There have been many novel engineering solutions to these problems, many involving re-recording the data, but they do so at a price which ultimately impacts (or at least limits) the overall performance of the system. The elegant solution is to fix the holograms or in some way render them insensitive to the reading/recording illumination. This fixing may be permanent, creating a WORM-type (write-once-read-many) of storage, or reversible permitting a fully read/write capability. Emphasis within the consortium has centered on thermal and electrical fixing, two-photon recording and the development of a WORM type of photochromic recording material.

Thermal fixing studies, conducted at Stanford, involve elevation of the materials temperature ($>100^{\circ}\text{C}$) to allow mobile ions to form a complementary grating which is subsequently revealed by erasure of the electronic grating with uniform illumination. The hologram may be recorded at an elevated temperature with simultaneous formation of the complementary grating and read at a lower temperature, or the hologram can be recorded at a low temperature with subsequent creation of the complementary grating at elevated temperature after which it is revealed and read at the original lower temperature. While the first method produces larger fields and stronger complementary gratings, the grating formed during writing at high temperatures can become distorted as the temperature is lowered.¹ Caused by anisotropic thermal expansion or contraction and refractive index variations, only a portion of the image field can be recovered by adjusting the Bragg angle. If the effects are isotropic, the recorded grating changes uniformly and the entire image can be recovered by wavelength tuning. The second, classical, method of fixing is therefore preferred although there is a loss in diffraction efficiency between the electronic grating and the complementary grating.

Formation of complementary gratings by the application of an electric field to produce ferroelectric domain reversal can be accomplished in materials having a low phase transition temperature such as SBN and BaTiO_3 . A study of electrical fixing of 1000 holograms in SBN:75 has been performed at Rockwell and is reported in another paper at this conference.²

The most elegant solution to the problem of image volatility is to *gate* the recording process so that hologram formation occurs only when (and where) both the recording light and gating signals are present. In the same way, nondestructive reading can be performed in the absence of the gating signal. The PRISM program is exploring mechanisms by which a beam of light at one wavelength is used to sensitize the medium for absorption of the hologram-forming beams at another wavelength.³ Depending on the lifetime of the intermediate state caused by the sensitization process, these exposures can be simultaneous or sequential. In addition, illumination with the gating wavelength and one of the recording beams at the second wavelength provides a

mechanism by which the holograms can be erased. We will discuss various sensitization processes and report on results with various host and dopant combinations.⁴

Organic materials offer the advantages of ease-of-fabrication and low cost. Photochromic and photorefractive material systems have been developed at IBM that show exceptionally high refractive index modulations ($\sim 10^{-3}$) with diffraction efficiencies approaching 100% in samples as thin as a few hundred microns.^{5,6} The photochromic material is particularly suited for use in WORM applications. At issue is the fabrication of thick sample with the requisite optical quality - this is the subject of an ongoing study and progress will be reported..

In order to test and compare the many material parameters, the effectiveness of fixing methods and determine performance trade-offs, a precision teststand was developed and constructed at IBM.⁷ The teststand records and retrieves high density digital pages under computer control and is designed to not introduce any significant errors on its own as an imaging system. That is, comparing the CCD image of a 256Kbit chrome-on-glass mask transmitted through a fused silica optical blank produces a bit error rate (ber) of 10^{-14} . The same image transmitted through the best LiNbO₃ crystal we could obtain exhibits a ber of 10^{-7} and a hologram made in the same material reconstructs an image with a ber of 8×10^{-7} . Using bit error rate as the metric is an excellent means for comparing materials, their optical quality and quantifying image behavior with time and readout conditions. It is a singularly important factor in determining the ultimate applicability of this technology to storage. Knowledge gained in these teststand experiments will form the basis for development of a demonstration platform at Optitek.

Finally, it should be noted that the holograms must be recorded and evaluated in a manner similar to their intended end-use. The multiplexing of many holograms into a common volume and the $1/N^2$ scaling of diffraction efficiency produces holograms with efficiencies approaching 10^{-6} . Retrieval and analysis of data in such a photon-poor environment will highlight problems much faster than if one were to evaluate holograms with efficiencies on the order of 0.1 to 0.5.

We acknowledge our partners in the PRISM Consortium, the National Storage Industry Consortium and partial funding support from ARPA through agreement MDA972-94-2-0008.

References

1. J. Heanue et al., private communication
2. J. Ma, "Electrical fixing of 1000 angle-multiplexed holograms in SBN:75," ISOM/ODS/NLO Joint Session on Holographic Storage, Maui, Hawaii, July 1996.
3. Bai et al., "Resonant two-photon photorefractive gratings in Pr:SBN using cw lasers," accepted for publication in Optics Letters
4. G. Bacher, et al., "Ultralong dark decay measurements in BaTiO₃," Opt. Lett., **21**, 18 (1996).
5. R. Wortmann et al., in preparation
6. R. Twieg et al., "Multifunctional photorefractive chromophores with high transparency and optimized birefringence," ISOM/ODS/NLO Joint Session on Holographic Storage, Maui, Hawaii, July 1996.
7. M.-P. Bernal, et. al., "A precision tester for the studies of holographic optical storage materials and recording physics," accepted for publication in Applied Optics.

Optically Induced Refractive Index Changes in Glass

Turan Erdogan

The Institute of Optics, University of Rochester, Rochester, NY 14627

Tel: (716) 275-7227 Fax: (716) 244-4936

Light can permanently change the optical properties of glass. The change is desirable for "photosensitive" glass, in which an induced refractive index change is used to write optical-fiber gratings and volume holograms in glass. But "optical damage," which generally includes induced index change and absorption, is undesirable when manifested as reduced transmission in expensive ultraviolet (UV) photolithography lenses. These effects are linked to each other, but researchers have only recently begun to exploit this connection.

Germanium-doped silica ($\text{Ge}:\text{SiO}_2$) in particular is known to exhibit photosensitivity that is associated with a broken Ge-O-Si linkage; some of these defects cause a strong absorption around 240 nm. Direct exposure of the glass to UV light can permanently alter the refractive index. This effect is used to make photo-induced diffraction gratings in optical fibers for optical communications, including fiber-grating filters and fiber lasers, and for sensors, including medical and environmental sensing and smart materials and structures. The index change appears to be quite permanent at room temperature [1]. Fig. 1 shows the growth of the refractive index change δn vs. UV exposure time during writing of a typical fiber grating in a standard $\text{Ge}:\text{SiO}_2$ -core fiber. The inset shows the transmission spectrum through the grating after 180 sec of exposure, demonstrating greater than 95% reflection with a bandwidth of about 3 Å.

Recently researchers have discovered that by "loading" molecular hydrogen into a variety of doped silicas (including GeO_2 , P_2O_5 , and other dopants) via a high-pressure, low-temperature diffusion process, it is possible to greatly enhance the photosensitivity of the glass [2]. It has been shown that in H_2 -enhanced photosensitivity the UV light initiates a reaction at every dopant atom, rather than only at the defect sites as in the case of standard photosensitivity. In many cases the achievable index change is increased by roughly two orders of magnitude over that obtainable in similar unloaded glass. We have measured peak index changes exceeding 2×10^{-2} [3]. H_2 -enhanced photosensitivity is practically important for a number of reasons. Hydrogen loading enables ultrastrong gratings with broadband spectral characteristics to be produced, and it enables nearly any Ge-doped silica glass to be photosensitized (including low-loss, low- Δ communications fibers that are otherwise not very photosensitive). Fig. 2 shows transmission through gratings fabricated in the same type of fiber and using identical conditions without hydrogen loading (a), and with hydrogen loading (b). The reflectivity of the grating in Fig. 2(b) is practically 100% over a spectral bandwidth of 4 nm. For potential applications such as volume-holographic data storage, hydrogen loading can be used to sensitize the glass for the writing process, after which the hydrogen can be diffused out of the glass rendering the material highly immune to subsequent readout degradation.

The current speculation on possible mechanisms for standard photosensitivity is mainly centered in two camps, which are not necessarily mutually exclusive. In the first, the mechanism involves creation of deep color centers (i.e., electron traps) [4,5]. The index change is related to the modified absorption spectrum using a Kramers-Kronig analysis [6]. The experimental basis for this camp comes from correlation of UV/visible absorption spectra with measured index

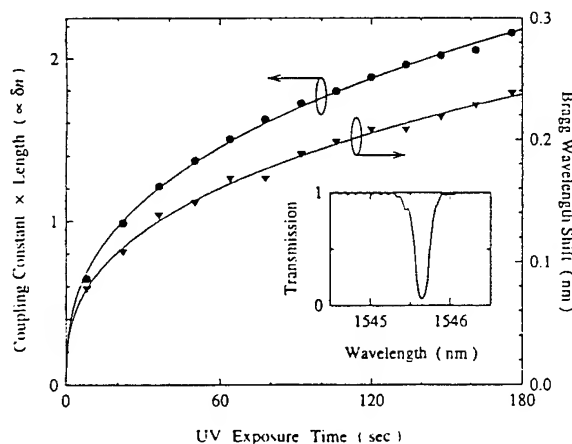


Figure 1: Growth of fiber grating parameters proportional to UV-induced index change for a typical fiber grating. Inset shows transmission spectrum.

changes. The problem with this picture is that the predicted index changes according to the Kramers-Kronig analysis frequently do not fully account for the measured index changes. This shortcoming does not, of course, disprove this picture.

The second camp holds that standard UV photosensitivity is related to compaction of the glass matrix due to reorganization of bonds and bond angles. Such compaction is known to exist even in undoped silica. Presumably it is enhanced in Ge-doped silica due to the significantly higher absorption of UV light that results from the oxygen-deficiency defect absorption band at 240 nm. Currently experimental evidence for compaction is not conclusive. It has been directly measured in thin films [7], and has been inferred from stress measurements of UV-induced gratings in optical fibers [8]. This theory has only very recently been considered, and there is some confusion surrounding it. For example, the fiber grating measurements indicate that an overall tension is imparted to the core, which would seem to lower the refractive index. But, since it is known that the index increases, it is inferred that the illuminated regions of the fiber core undergo compaction while the unilluminated regions experience stronger tension, but have less influence on the refractive index [8].

The possible mechanisms occurring in H_2 -enhanced photosensitivity appear significantly different from those in standard photosensitivity. Currently the understanding involves evidence for what types of species are created. In particular, it appears that the UV-induced reaction breaks Ge-O bonds and cracks H_2 molecules, and then forms GeH and SiOH. The modified glass structure then has a higher index of refraction. It is not clear what role the oxygen-deficiency defects play in this scenario, other than to provide a means for the actinic energy to be coupled to the material.

The UV-induced index change is primarily of interest for Bragg grating applications, wherein substantial optical effects can be achieved with index changes less than fractions of a percent. Most research has centered on fiber gratings and related devices over the past half-dozen years since the first reports of UV photosensitivity (for review articles see [9-13]). Numerous applications are being developed, including: rare-earth-doped and Raman fiber lasers; fiber-coupled external-cavity semiconductor lasers; filters for wavelength-division-multiplexed fiber-optic communications systems; and distributed arrays of grating-based sensors, in which dynamic maps of temperature and strain variations can be made in civil structures, such as bridges and dams, and "smart" materials. Recently UV-induced gratings have also been demonstrated for integrated-optical applications, including interferometric add-drop filters, Er-doped waveguide lasers.

Volume gratings in glass are also attracting increasing attention. It is possible that volume gratings could form the basis for such technologies as archival holographic data storage and static free-space interconnection in glass. High storage capacity (implying high dynamic range and short read/write wavelength), robustness (implying long storage times and immunity to readout), and low cost are all items of paramount importance for holographic data storage to compete with the rapidly advancing 2-dimensional technologies. Utilization of UV or a related

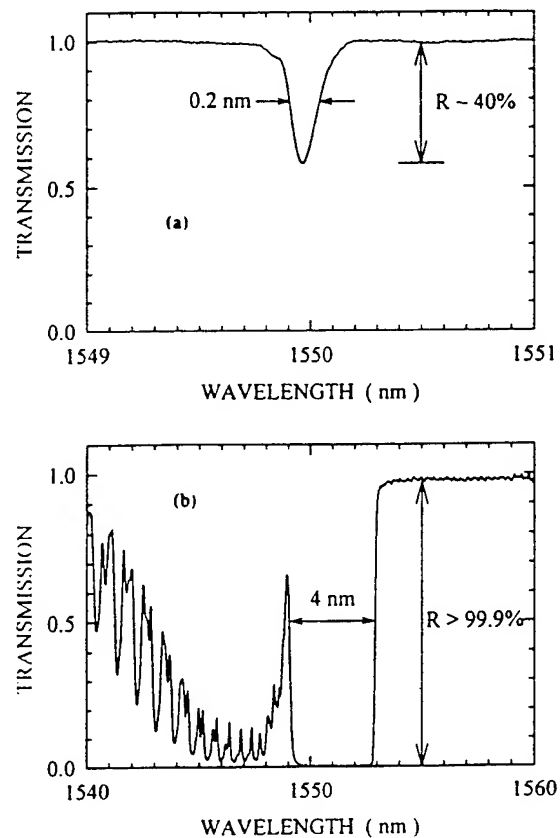


Figure 2: Transmission spectra of fiber gratings fabricated under identical conditions in a standard telecommunications fiber with (a) and without (b) H_2 enhancement of UV photosensitivity.

photosensitivity in glass media might provide advantages in all of these areas. Fig. 3 shows the measured diffraction efficiency vs. exposure time and readout angle (inset) typical of volume gratings we have written in bulk glass [14].

A number of applications of UV photosensitivity not based on gratings have also surfaced recently. One of these is the use of glass photosensitivity to form the basis for an all-dry integrated-optical fabrication platform. Here planar waveguides are fabricated by standard techniques, but the definition of waveguides and devices associated with the two planar dimensions is accomplished simply with appropriate masks and ultraviolet exposure, potentially taking advantage of existing silicon wafer-handling and lithography-exposure machinery. To this end, demonstrations of the fabrication of channel waveguides, Mach-Zehnder interferometers, and planar-waveguide Fresnel lenses by direct UV exposure have been made.

The list of applications described above is by no means an exhaustive one — it is intended to provide a flavor for the potential impact of technologies based on UV photosensitivity in communications, computers, military, industry, medicine, and other areas. Many clever ideas that take advantage of this physical phenomenon have surfaced in the last half-decade or so. However, most of the research focusing on this area has been concentrated on applications. Relatively little comprehensive research has been concerned with the physical mechanisms responsible for UV photosensitivity. There is both fertile and vital physics lurking behind the flashy applications of glass photosensitivity.

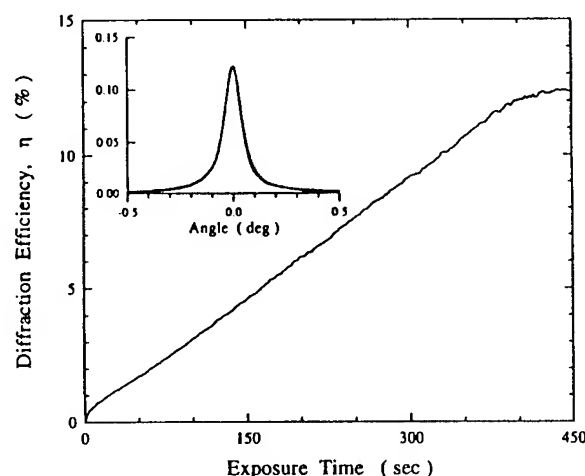


Figure 3: Measured volume grating diffraction efficiency vs. exposure and readout angle in glass.

- [1] T. Erdogan, V. Mizrahi, P. J. Lemaire, and D. Monroe, *J. Appl. Phys.*, **76**, 73 (1994).
- [2] P. J. Lemaire, R. M. Atkins, V. Mizrahi, and W. A. Reed, *Electron. Lett.*, **29**, 1191 (1993).
- [3] V. Mizrahi, P. J. Lemaire, T. Erdogan, W. A. Reed, D. J. DiGiovanni, and R. M. Atkins, *Appl. Phys. Lett.*, **63**, 1727 (1993).
- [4] R. M. Atkins, V. Mizrahi, and T. Erdogan, *Electron. Lett.*, **29**, 385 (1993).
- [5] L. Dong, J. L. Archambault, L. Reekie, P. St. J. Russell, and D. N. Payne, *Appl. Opt.*, **34**, 3436 (1995).
- [6] D. P. Hand and P. St. J. Russell, *Opt. Lett.*, **15**, 102 (1990).
- [7] I. Riant, S. Borne, P. Sansonetti, and B. Poumellec, paper SaD3, Conf. on Photosensitivity and Quadratic Nonlinearity in Glass Waveguides, Portland, OR (September 9-11, 1995).
- [8] H. G. Limberger, P. Y. Fonjallaz, and R. P. Salathe, paper SaD4, Conf. on Photosensitivity and Quadratic Nonlinearity in Glass Waveguides, Portland, OR (September 9-11, 1995).
- [9] K. O. Hill, B. Malo, F. Bilodeau, and D. C. Johnson, *Annu. Rev. Mater. Sci.*, **23**, 125 (1993).
- [10] W. W. Morey, G. A. Ball, and G. Meltz, *Opt. and Photon. News*, **5**, 8 (1994).
- [11] T. Erdogan and V. Mizrahi, *Laser Focus World*, February issue, 73 (1994).
- [12] R. J. Campbell and R. Kashyap, *Int. J. of Optoelectron.*, **9**, 33 (1994).
- [13] P. St. J. Russell, J.-L. Archambault, and L. Reekie, *Physics World*, October issue, 41 (1993).
- [14] T. Erdogan, A. Partovi, V. Mizrahi, P. J. Lemaire, W. L. Wilson, T. A. Strasser, and A. M. Glass, *Appl. Opt.*, **34**, 6738 (1995).

Multifunctional Photorefractive Chromophores with High Transparency and Optimized Birefringence

R. Twieg, R. Wortmann, C. Poga, C. Geletneky, C. R. Moylan,

P. Lundquist, R. G. DeVoe, P. M. Cotts, D. M. Burland

IBM Almaden Research Center 650 Harry Road San Jose, CA 95120

(tel) 408-927-1630 (fax) 408-927-3310 (email) twieg @ almaden.ibm.com

The photorefractive (PR) effect gives rise to a variety of two and four wave mixing phenomena and is of potential technological importance for applications including holographic storage and optical signal processing. The photorefractive effect is very familiar in inorganic media but only relatively recently observed in organic media.[1] Although initial studies of the organic media were guided by what was known about the properties of inorganic systems more recent effort has evolved which instead explores and exploits behavior unique to these organic compositions. Among the most important differences between the inorganic and organic systems is the additional contribution to grating formation from the birefringence of oriented chromophores.[2] Here we describe unique chromophore systems intentionally designed to enhance this birefringence contribution which have produced very promising results.

The local mechanism of the PR effect in organic composites with low glass transition temperature (T_g) involves the formation of refractive index gratings through a space-charge field modulated Kerr effect. A tensorial formulation of the macroscopic aspects of the PR Kerr effect reveals that the second-order dipole orientation term containing the anisotropy of the first-order polarizability $\alpha(-\omega;\omega)$ produces the dominant contribution to the Kerr susceptibility $\chi^{(3)}(-\omega;\omega,0,0)$. In order to optimize this term a class of special chromophores with vanishing second-order polarizability $\beta(-\omega;\omega,0)$ and large ground state dipole moment (μ_g)

have been discovered. Since these new chromophores are not subject to the efficiency transparency trade-off encountered with conventional second order NLO chromophores now highly transparent materials with a very large PR Kerr effect result.[3]

As a typical example the constituents of a PR composition (Figure 1) include 30% of the novel chromophore DPDCP [2,6-di-n-propyl-4H-pyran-ylidene-dinitrile] : 15% of the charge transport agent TPD [N,N'-bis-(3-methylphenyl)-N,N'-bis-phenyl-benzidine] : 55% of the inert glassy polymer host PMMA [polymethylmethacrylate] : 0.3% of the sensitizer C₆₀ [buckminsterfullerene]. A 100 μm thick film of the material exhibits a steady state diffraction efficiency of $\eta = 25\%$ and a net two-beam coupling efficiency of $\Gamma = 50 \text{ cm}^{-1}$ with a bias field of 100 V/ μm at a wavelength of 676 nm. In Figure 2 is found a plot of Δn and Γ as a function of the bias field. The chromophore DPDCP is relatively transparent (compared to other typical more highly conjugated PR systems) and has an intense absorption at $\lambda_{\text{max}} = 352 \text{ nm}$ and $\lambda_{\text{cutoff}} < 400 \text{ nm}$ with a transition dipole of $\mu_{\text{Z}}^{\text{ag}} = 21 \times 10^{-30} \text{ Cm}$. The ground state dipole moment and the Kerr anisotropy of the first-order optical polarizability are both large, $\mu_{\text{g}} = 24.4 \times 10^{-30} \text{ Cm}$ and $\delta\alpha_{\text{K}}(-\omega;\omega) = 22 \times 10^{-40} \text{ CV}^{-1}\text{m}^2$, while the second-order polarizability is almost vanishing $\beta_{\text{ZZZ}}(-2\omega;\omega,\omega) = 1.8 \times 10^{-50} \text{ CV}^{-2}\text{m}^3$. The DPDCP chromophore is a prototype and other related chromophores with still superior properties are presently being evaluated.

References:

- [1] W. E. Moerner, S. M. Silence, *Chem. Rev.*, **94**, 127 (1994).
- [2]. W. E. Moerner, S. M. Silence, F. Hache, G. C. Bjorklund, *J. Opt. Soc. Am. B.*, **11**, 321 (1994).
- [3] R. Wortmann, C. Poga, R. J. Twieg, C. Geletneky, C. R. Moylan, R. G. DeVoe, P. M. Cotts, D. M. Burland, manuscript in preparation.

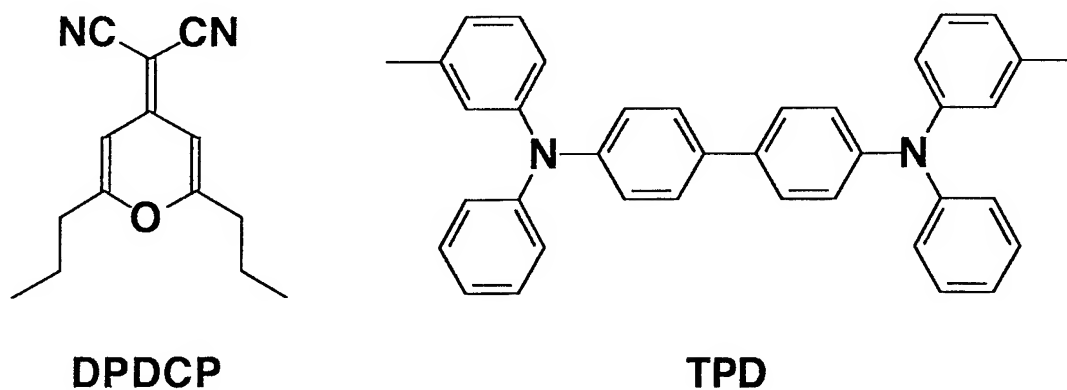


Figure 1. An organic photorefractive composition optimized for birefringence contains the chromophore DPDCP, the transport agent TPD and (not depicted) the host polymer PMMA and sensitizer C60.

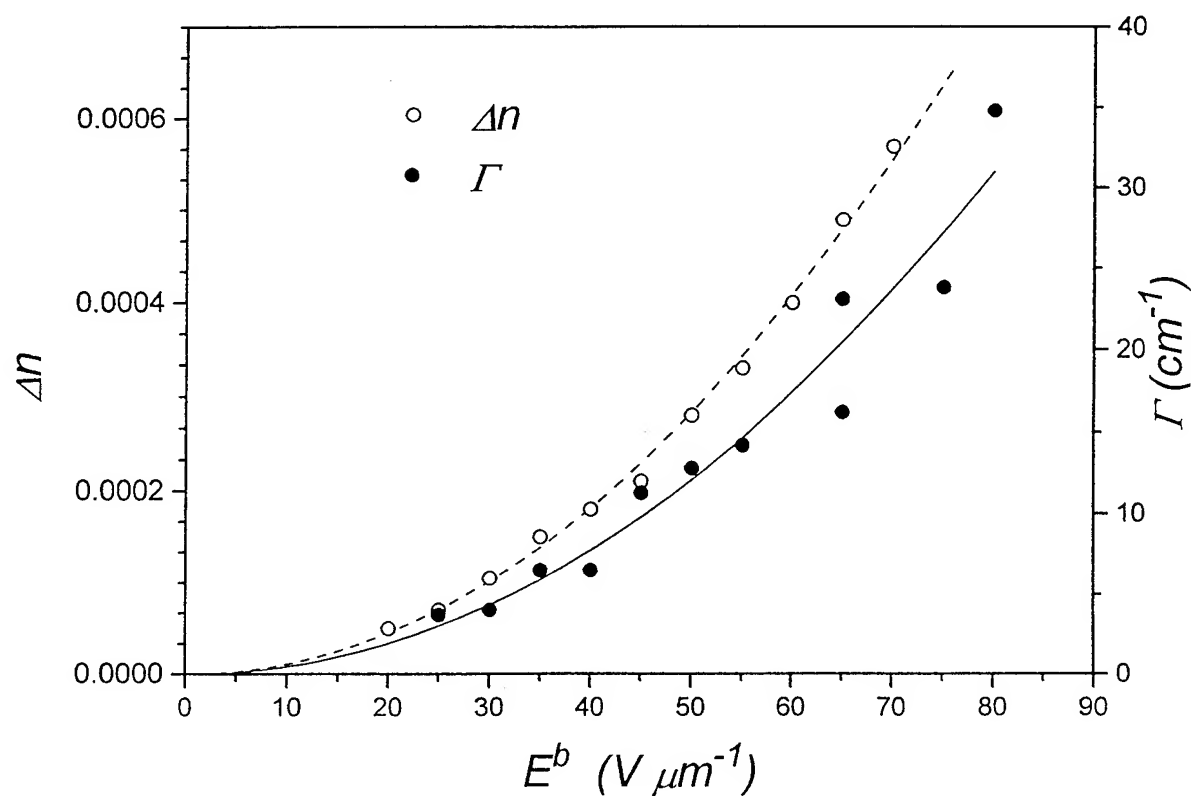


Figure 2. The dependence of refractive index Δn and two-beam coupling efficiency Γ as a function of the bias field applied to the sample.

Electrical Fixing of 1000 Angle-Multiplexed Holograms in SBN:75

Jian Ma, Tallis Chang, John Hong, and Ratnakar R. Neurgaonkar
 Rockwell International Science Center, MS A25A
 1049 Camino Dos Rios, Thousand Oaks, CA 91360
 jian@prism.risc.rockwell.com

George Barbastathis, and Demetri Psaltis
 Department of Electrical Engineering, MS 116-81
 California Institute of Technology, Pasadena, CA 91125

Electrical fixing of holograms in SBN:75 has been demonstrated by applying a negative electrical pulse after recording [1-4]. In this presentation, we report the experimental investigation of electrical fixing of angle-multiplexed holograms in SBN:75.

The exposure schedule for recording and fixing angle-multiplexed hologram can be implemented by either single-cycle exposure or multiple-cycle exposure. In the single-cycle exposure, the fixing electrical pulse is applied after all the holograms are recorded; while in the multiple-cycle exposure, as the term implies, the entire exposure is divided into multiple cycles, and the electrical fixing and revealing pulses are applied at the end of each cycle. We found that the diffraction efficiency of multiplexed fixed holograms are much higher using multiple-cycle exposure, primarily due to two effects. First, the holograms recorded in the previous exposure cycle have better resistance to the erasure of the successive exposure when the fixing pulse is applied. Second, multiplexed holograms of larger diffraction efficiency can be recorded when a negative pulse (such as fixing pulse or preparation pulse which will be described below) is applied prior to recording.

We found in our experiments that a significant improvement in diffraction efficiency of multiplexed and fixed holograms were obtained by applying a negative pulse prior to recording. The similar phenomenon was also found in BaTiO₃ [5]. We call this pulse the preparation pulse that prepares the crystal for fixing. We have achieved an 8-time enhancement in diffraction efficiency of 100 multiplexed holograms by applying a negative 2kV/cm, 0.2 second preparation pulse. The enhancement was somewhat different from BaTiO₃ in that we did not observe enhancement in diffraction of a single hologram. The exact physical mechanism for this enhancement is under study presently. The initial negative pulse obviously depletes the crystal to a degree. However, the main contribution for the enhanced diffraction of the multiplexed holograms is from the increased erasure time constant that effectively increase the diffraction efficiency of the multiplexed holograms. Fig. 1 shows the erasure characteristic of the gratings recorded with and without a preparation pulse. The situation is somewhat complicated by the fact that there seem to be two time constants. We describe the erasure of the holograms by

$$\eta = r_1^2 \exp\left(-\frac{2t}{\tau_s}\right) + r_2^2 \exp\left(-\frac{2t}{\tau_L}\right) + 2r_1r_2 \exp\left[-t\left(\frac{1}{\tau_s} + \frac{1}{\tau_L}\right)\right], \quad \text{and } r_1 + r_2 = 1, \quad (1)$$

where η is the normalized diffraction efficiency, τ_s is the short time constant, and τ_L is the long time constant. Concentrating on the long time constant term that affects the multiplexing schedule, one can clearly see from Fig.1 the significant increase in r_2 (the weight or contribution of long time constant) with the application of the preparation pulse. The fixing pulse in the multiple-cycle exposure schedule plays the exactly the same role as the preparation pulse for the successive exposure cycle.

An exposure schedule that takes into account the two time constants was used to obtain the uniform diffraction efficiency of multiple holograms at each cycle, which is described by

$$t_{m-1} = -\tau_w \ln \left\{ 1 - \left(1 - e^{-\frac{t_m}{\tau_w}} \right) e^{-\frac{t_{m+1}}{\tau_s}} \left[\frac{r_1 + r_2 e^{S_{m+1} \left(\frac{1}{\tau_s} - \frac{1}{\tau_L} \right)}}{r_1 + r_2 e^{S_m \left(\frac{1}{\tau_s} - \frac{1}{\tau_L} \right)}} \right] \right\}, \text{ and } S_m = \sum_{i=m}^M t_i, \quad (2)$$

where t_m is the exposure time for m th hologram, τ_w is the writing time constant, and M is the total number exposures in each cycle.

Another important concern in multiple-cycle exposure is to maintain a uniform diffraction efficiency among holograms recorded at different exposure cycles since the holograms recorded in the previous cycle will be partially erased by the exposure of the successive cycles although fixing pulse is applied before starting a new exposure cycle. The erasure characteristic of fixed hologram was measured by illuminating the crystal with a constant erasure intensity of 50 mW/cm². The degradation of the hologram was observed and is shown in Fig.2. As a comparison, the degradation of a hologram without fixing is also shown in the same figure. The erasure of the grating has two time constants whether it is fixed or not. However, the ratio of the magnitudes of these two time constants changes significantly between the fixed and unfixed states. The relationship between exposure time of successive cycles is determined by the observed time constants (from Fig.2) using Eq. (2).

The experimental setup for recording and fixing angle-multiplexed holograms is shown in Fig.3. The crystal used was a Ce-doped (0.02%) SBN:75 with dimension of approximately 1-cm³, which was located near the Fourier plane of the input image displayed on a SLM (frame size: 640x480). The angle between object and reference beams was about 7° outside the crystal, which provides an angular selectivity about 0.15° (measured with negligible crosstalk between the adjacent holograms). Angle multiplexing was achieved by rotating crystal in horizontal plane (0.15° separation). Fractal (off-plane) multiplexing was achieved by rotating mirror (M1) to change the angle of incidence of the reference beam in the vertical direction (2° separation). 200 holograms were multiplexed on every fractal row, and 5 fractal rows were used for a total of 1000 holograms. Recording was performed in 5 exposure cycles (i.e. one fixing pulse was applied after recording the 200 holograms of each row). The preparation pulse and fixing pulse was both -2kV/cm in amplitude and 0.2 second duration, and the revealing pulse was 5kV/cm in amplitude and 1 second duration. The average diffraction efficiency of the fixed/revealed holograms was about 0.005% with a uniformity about 80% among different holograms. Fig.4 shows the sample of images reconstructed from fixed/revealed holograms.

In summary, electrical fixing of 1000 angle-multiplexed holograms was demonstrated in a 1-cm³ Ce-doped SBN:75 crystal. The average diffraction efficiency was measured to be 0.005% and the uniformity was about 80%. Two erasure time constants were observed for the holograms recorded with the application of a negative electrical pulse prior to recording; two time constants makes hologram multiplexing schedule more complicated. In addition, multiple-cycle exposure/fixing schedule was used for achieving higher diffraction efficiency.

- [1] F. Micheron and G. Bismuth, Appl. Phys. Lett. **20**, 79(1972).
- [2] F. Micheron and G. Bismuth, Appl. Phys. Lett. **23**, 71(1973).
- [3] Y. Qiao, S. Orlov, D. Psaltis, and R. R. Neurgaonkar, Opt. Lett. **18**, 1004(1993).
- [4] M. Horowitz, A. Bekker, and B. Fischer, Opt. Lett. **22**, 1964(1993).
- [5] R.S. Cudney, J. Fousek, M. Zgonik, P. Gunter, M.H. Garrett, and D. Rytz, Phys. Rev. Lett. **72**, 3883(1994).

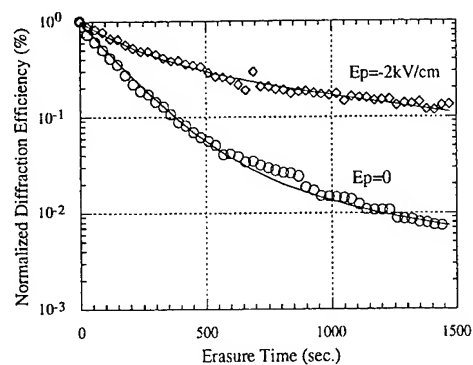


Fig.1. Measurement of erasure time constant of the holograms recorded with and without a preparation pulse. Without a preparation pulse: curve fitted with $r_1=0.85$, $r_2=0.15$, $\tau_s=250$ sec, $\tau_L=2500$ sec. With a preparation pulse: $r_1=0.40$, $r_2=0.60$, $\tau_s=250$ sec, $\tau_L=2500$ sec.

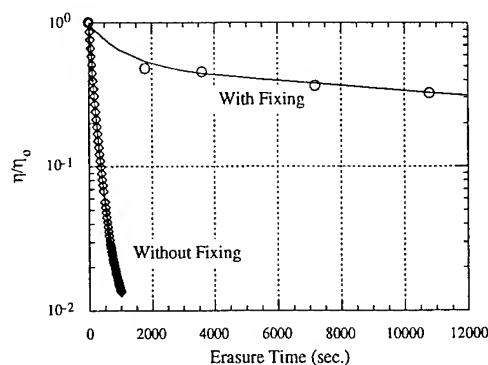


Fig.2. Erasure of an unfixed hologram: curve fitted with $r_1=0.85$, $r_2=0.15$, $\tau_s=250$ sec. $\tau_L=2500$ sec. Erasure of a fixed hologram: curve fitted with $r_1=0.293$, $r_2=0.707$, $\tau_s=1000$ sec, $\tau_L=50000$ sec.

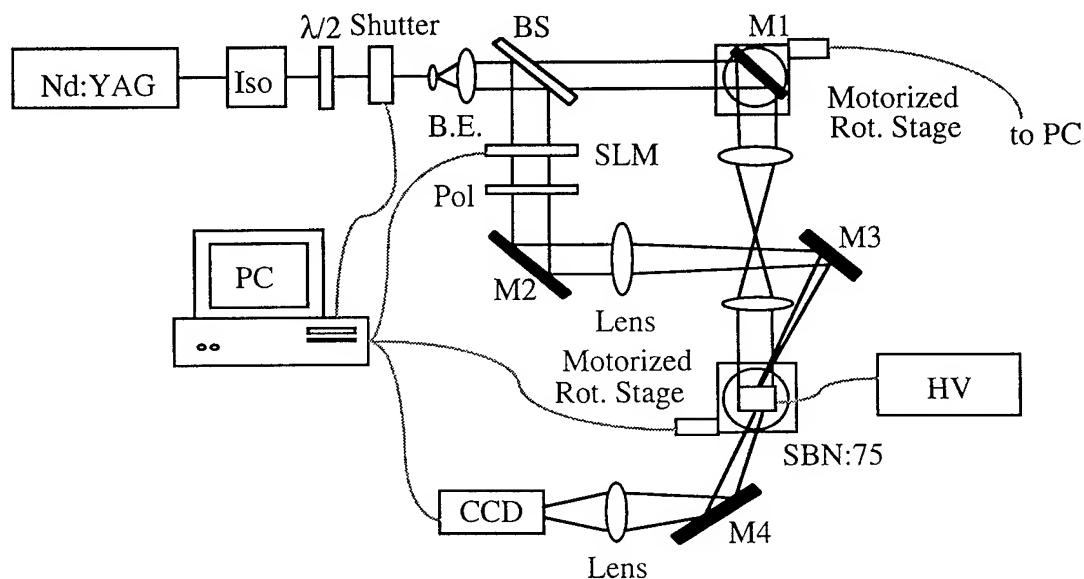


Fig.3 Experimental setup for recording and fixing angle-multiplexed holograms.

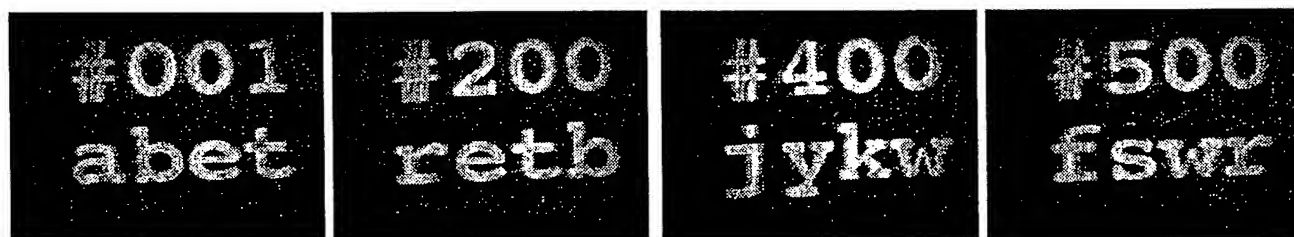


Fig.4. Samples of reconstructed images.

Digital image storage by multiplexed holographic recording in Ce-doped SBN crystal

M.Yamamoto K.Nonaka and T.Kume

NTT Interdisciplinary Research Laboratories
3-9-11 Midori-cho, Musashino-shi, Tokyo 180, Japan

1.Introduction

In the future, in order to popularize multimedia network services into the home, the network file storage systems will have to possess a huge storage capacity and an ultra-high data transfer rate¹⁾. Various studies have recently been undertaken to increase the recording density using short wavelength lasers²⁾ and super resolution technologies.³⁾ Data transfer rates have been increased using multiple beams.⁴⁾ However, it still might be difficult to attain these goals by conventional optical disk recording method.

Holographic memory has been researched, and various multiplexed holographic recording methods have been reported⁵⁾⁶⁾. However, practical applications of holographic memory are few due to limited number of suitable light sources and storage media have not yet been manufactured at reasonable prices. Recently, the lifetime of cerium doped SBN single photorefractive crystal has been improved⁷⁾ as a rewritable optical storage medium. In addition, high power compact laser diode system has been developed, thereby making laser systems compact and easy to operate. These advantages have made holographic memory more practical for high-density, high speed data storage.

This paper shows the results of multiplexed holographic recording characteristics of digital data using SBN single crystal with a compact laser diode system.

2. Diffraction efficiency analysis

In order to select the most suitable recording method, we investigated the theoretical results of angle-multiplexed and wavelength-multiplexed holographic recording characteristics using an SBN single crystal.

The theoretical results of diffraction efficiency of a Bragg mismatched holographic grating have been reported⁸⁾⁹⁾. However, these analyses were not enough to design the read/write conditions of the lossy case, such as using SBN single crystal medium. Our analysis¹⁰⁾¹¹⁾ uses coupled-wave theory for mixed (phase and absorption) holograms grating that consider light absorption during writing and reconstructing. Using this analysis, it is possible to evaluate the optimum medium parameters and read/write conditions for high diffraction efficiency. The angle and wavelength mismatch from the Bragg condition was also quantified by the derived formula.¹⁰⁾¹¹⁾ Figure 1 shows the theoretical results of crosstalk between wavelength-multiplexed and angle-multiplexed holograms. The angle resolution becomes 0.02 degree and the wavelength resolution becomes 0.04nm, in which the adjacent multiplexed holograms can not be

reconstructed. For conventional optical setup or wavelength range of a tunable LD, the multiplexity becomes 1000 for both angle multiplexed and wavelength multiplexed recording. These results indicate that if the wavelength resolution of tunable LD becomes lower than 0.04nm, the multiplexity becomes same for both case. But the write power becomes very weak and the data recording can not be attained. Therefore, we select the angle-multiplexing method for data recording.

3. Digital image recording experiment

The basic arrangement of digital data holographic recording is shown in Fig.2 and the experimental conditions are shown in Table 1. A hologram corresponding to the digital data on the SLM is recorded in a photorefractive medium. The recording medium was a Ce-doped $\text{Sr}_{0.6}\text{Ba}_{0.4}\text{Nb}_2\text{O}_6$ single crystal. Multiple holograms, each corresponding to one page of digital data, are written in the medium using angular multiplexing. The holograms are written with reference beams separated by 0.2 degree. The angle is changed by mechanical rotation of galvano-diffractor on which the storage medium was set. The stored digital data was reconstructed by imaging the diffracted optical signal on to a CCD array.

The crystal was cooled to -4°C by Peltier device tip to ensure the storage life of 10 years. We used the two wavelength techniques for writing and reading to avoid the destructive readout. The laser for writing data had a wavelength of 532nm, a power of 30mW, while laser for reading had a wavelength of 630nm, a power of 5 mW. We controlled the rotation angle of the SBN crystal for data readout to realize the Bragg matching condition during reconstructing and slite movement of imaging digital data from the CCD pixel map is corrected by redundant bits mapping and software correction. By using these methods, we investigated the signal to noise ratio and the recording density for multiplexed holographic recording.

We will describe in more detail the analysis and experimental results of multiplexed holographic recording for digital data at the conference.

References

- 1)H.Yamaguchi:NTT Review, Vol.1, No.1, May(1989)6.
- 2)S.Nakamura:Tech.Digest of Int.Symp. Optical Memory(1995)9.
- 3)K.Aratani, A.Fukumoto, M.Ohta, M.Kaneko, and K.Watanabe:SPIE vol.1499(1991)209.
- 4)R.Arai, and K.Itao:Digest IEEE MSS Sympo.(1990)149.
- 5)L.Hesselink, and M.C.Bashaw:Optical and Quantum Electronics 25(1993)611.
- 6)G.A.Rakuljic, V.Leyva, and A.Yariv:Opt. Lett., vol.17, no.20(1992)1471.
- 7)S.Yagi, Y.Sugiyama, and I.Hatakeyama:Proc. IEEE Nonlinear Optics, 200(1994).
- 8)N.Uchida:J. Opt. Soc. Am. 63, 280(1973).
- 9)R.Hofmeister, A.Yariv, and S.Yagi:J. Opt. Soc. Am., A, 1342(1994).
- 10)K.Nonaka:J.Appl.Pys.78(7),1 4345(1995).
- 11)T.Kume, K.Nonaka, and M.Yamamoto:IEICE TRANS.ELECTRON, Vol.E78-C, NO.11 NOVEMBER(1995).

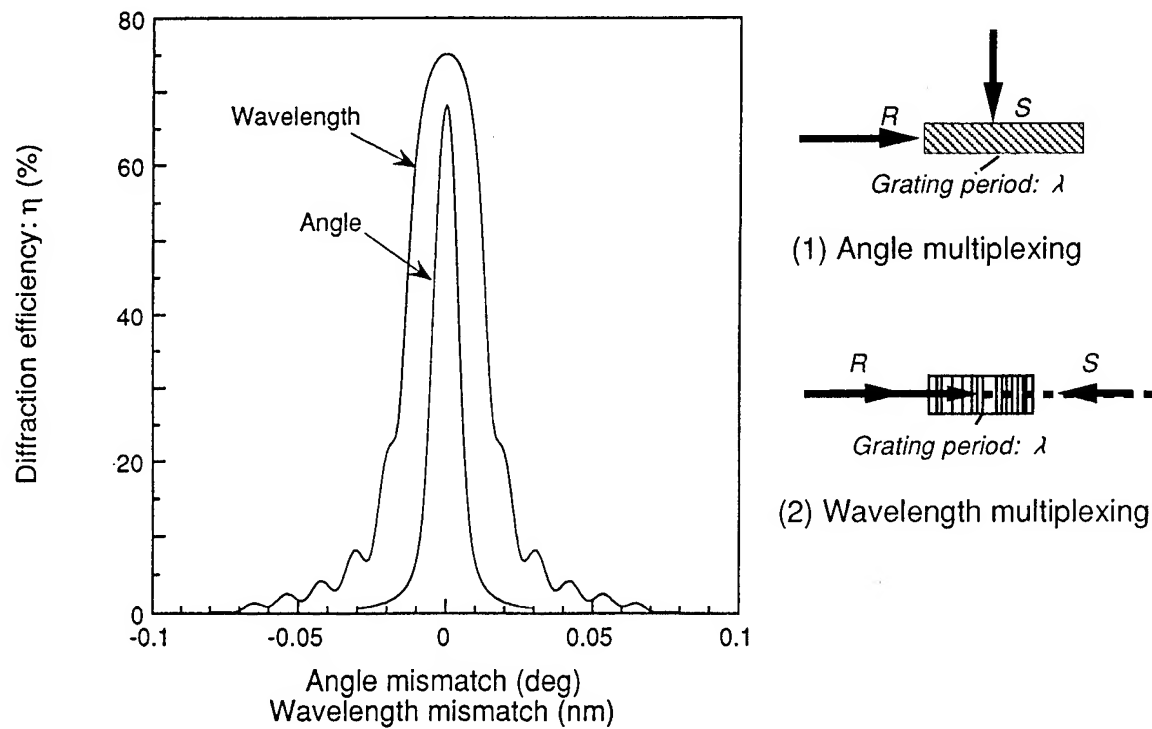


Fig.1 Diffraction efficiency of a Bragg mismatched holographic gratings

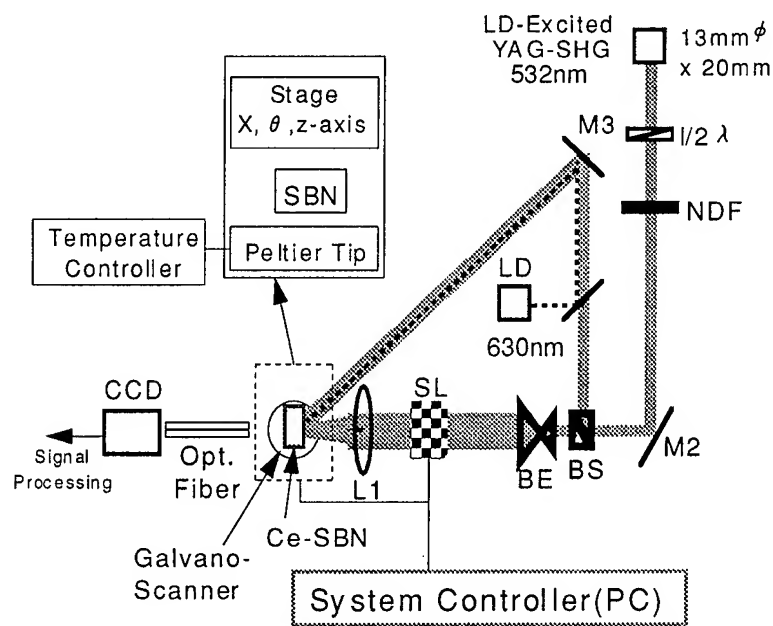


Fig.2 Experimental Setup

Table 1 Experimental conditions

Medium size	3x3x5mm 10x10x2mm
Laser power	
write	30mW
read	5mW
SLM	640x480 pixcell
Recording time	5ms~500ms
Laser(write)	LD-excited YAG-SHG (532nm)
Laser(read)	LD(630nm)
Medium	
Temperature	-4C°

Tuesday, July 9, 1996

Joint Session on Holographic Storage and Beyond

JTuC 7:00 pm-8:25 pm
Haku Room

Manabu Yamamoto, *Presider*
NTT Interdisciplinary Research Laboratories, Japan

Large-scale holographic memory

Demetri Psaltis, Xin An, Geoffrey W. Burr, and Fai H. Mok[†]

Department of Electrical Engineering
California Institute of Technology, MS 116-81, Pasadena, CA 91125

[†]Also affiliated with Holoplex, Inc.,
600 S. Lake Avenue, Suite 102, Pasadena, CA 91106
e-mail: psaltis, axin, goffbo, fai@sunoptics.caltech.edu

Holographic memory has attracted a lot of interests because of its high storage capacity and fast parallel access.¹ In volume holographic memories data is stored as interference patterns formed by coherent beams of light. The information is imprinted on the object beam. Multiple pages of data are superimposed within the same volume of a storage medium. These pages, stored as separate holograms, can be independently accessed by changing either the angle,² wavelength^{3,4} or phase code^{5,6} of the reference (non-information-bearing) beam. The storage capacity C achievable with each of these methods can be written as $C = NM$, where N is the number of bits in each stored page, and M is the number of pages superimposed in the same volume. Assuming one bit per pixel, current spatial light modulator (SLM) technology can provide 10^5 – 10^6 bits per stored page. Because these pixels are recalled in parallel by a single reference beam, very high read-out rates can be achieved.

The system design is shown in Figure 1. A laser beam is split in two parts and then brought together at a storage location within a photorefractive crystal. Information is imprinted on the object beam using a spatial light modulator (SLM), while the reference beam contains no information. A segmented mirror array and two mechanical angle scanners allow the reference arm of the system to control both the position and angle of incidence of this reference beam. Another pair of mechanical stages is used to deflect the object beam to control the position of the information-bearing object beam on the crystals. In order to store 160,000 holograms, we need 16 different vertical positions on the crystal where we store 10,000 holograms each.

The key element in the realization of angle and spatial multiplexing is the segmented mirror array which is placed at the center of a 4F system. For angle and fractal multiplexing, the horizontal and vertical angle scanning of the reference beam is controlled by two orthogonal angle scanners. The vertically tilted mirror facets on the mirror array provide the vertical deflection of the reference beam to address distinct storage locations.^{7,8} In order to avoid overloading the space-bandwidth product of the horizontal scanner, we used 4 fractal rows,

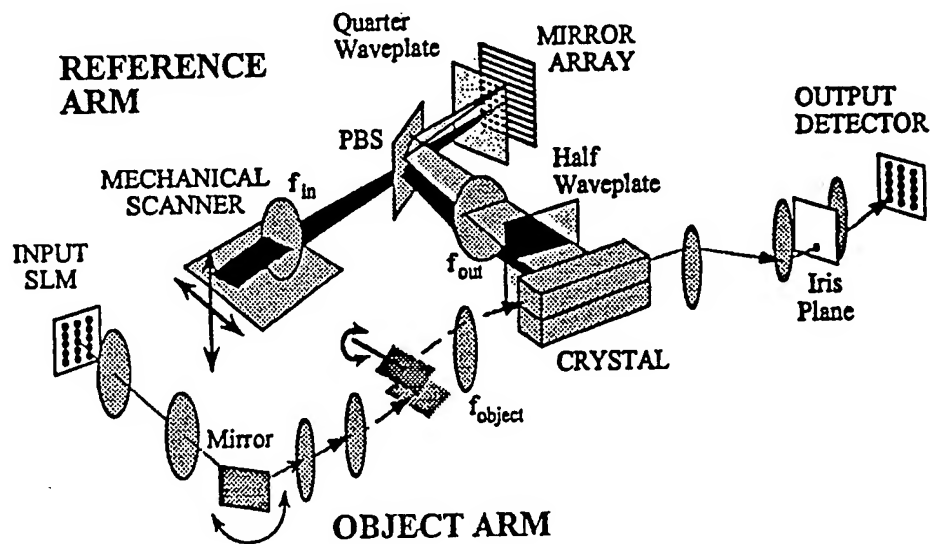


Figure 1: diagram of 160,000 hologram memory system.

with 2,500 holograms on each row. Figure 2a shows the schematic of the mirror array and Figure 2b shows the implementation of fractal and spatial multiplexing using the mirror array.

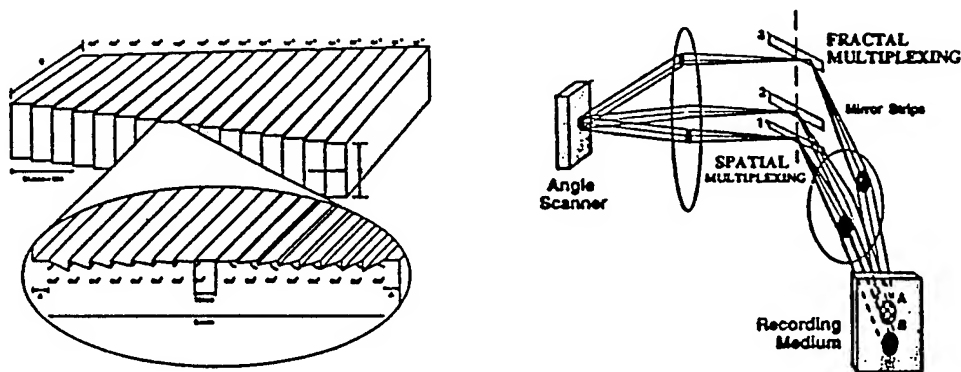


Figure 2: Fractal multiplexing, spatial multiplexing shown for comparison.

We experimentally demonstrated the storage of 30,000 holograms at 3 out of 16 locations on the crystal—top edge, center and bottom edge. We used random-bit patterns consisting of 3,000 ON/OFF pixels. The pixel map is divided into regions which were expected to be bright (or dark). In this process, edge pixels which were near a dark/bright transition were discarded. The two resulting histograms serve as estimates of the probability density functions (PDF) for storage of binary data. In this experiment, we detected no measured errors and an estimated probability of error ranging from 10^{-6} to 10^{-4} .

We also demonstrated the capability of the system to store data simultaneously by storing 16,000 holograms,

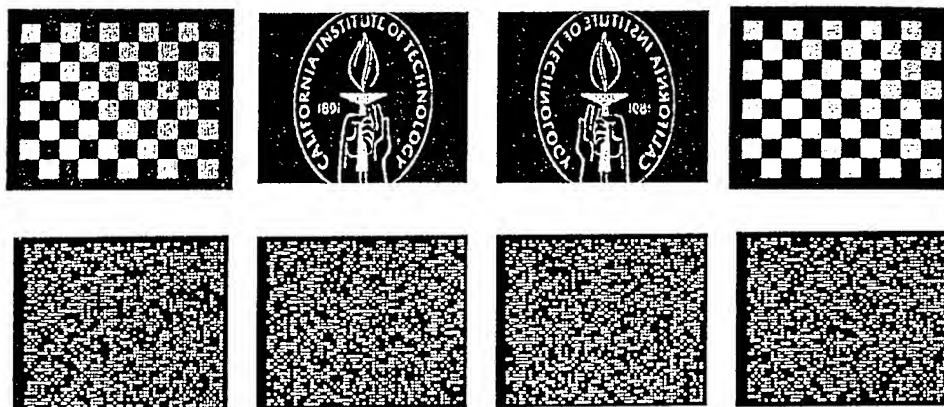


Figure 3: Sample reconstructions

1,000 at each location. There were no measured errors in the reconstructed holograms.

REFERENCES

- [1] D. Psaltis, and F. H. Mok, "Holographic memories", *Scientific America*, 273(5):70-76, November 1995.
- [2] D. L. Staebler, J. J. Amodei, and W. Philips, "Multiple storage of thick phase holograms in LiNbO_3 ", In *VII International Quantum Electronics Conference*, Montreal, May 1972.
- [3] F. T. S. Yu, S. Wu, A. W. Mayers, and S. Rajan, "Wavelength multiplexed reflection matched spatial filters using LiNbO_3 ", *Opt. Commun.*, 81:343, 1992.
- [4] G. A. Rakuljic, V. Leyva, and A. Yariv, "Optical data storage by using orthogonal wavelength-multiplexed volume holograms", *Opt. Lett.*, 17:1471, 1992.
- [5] T. F. Krile, M. O. Hagler, W. D. Redus, and J. F. Walkup, "Multiplex holography with chirp-modulated binary phase-coded reference-beam masks", *Appl. Opt.*, 18:52, 1979.
- [6] J. E. Ford, Y. Fainman, and S. H. Lee, "Array interconnection by phase-coded optical correlation", *Opt. Lett.*, 15:1088, 1990.
- [7] F. H. Mok, "Angle-multiplexed storage of 5000 holograms in lithium niobate", *Optics Letters*, 18(11):915-917, June 1993.
- [8] F. H. Mok, D. Psaltis, and G. W. Burr, "Spatially- and angle- multiplexed holographic random access memory", *SPIE Proc.*, 1773c:1, 1992.

Improved Usable Capacity for Optical Page-Oriented Memories with Smart Pixel Interfaces

Wei-Feng Hsu and Alexander A. Sawchuk

Signal and Image Processing Institute, University of Southern California
EEB 400 MC 2564, 3740 McClintock Avenue, Los Angeles, CA 90089-2564 USA
phone: 213-740-4622, fax: 213-740-4651, email: whsu@sipi.usc.edu; sawchuk@sipi.usc.edu

Novel digital information applications such as multimedia and video-on-demand require the storage of a large amount of data at very low bit-error rates (BER), fast access to this data, and the efficient interface of the storage system to high speed (gigabit per second) networks [1]. Optical page-oriented memory (OPOM) technology [2], [3] is one candidate that simultaneously provides large capacity (10^{12} bits/cm³ theoretically) and high data access rate (10^9 bits/second or more). Unfortunately, the high raw BER (10^{-4} - 10^{-7}) of the retrieved data is a limitation. The use of error detecting/correcting coding is one way to reduce the BER to a desirable rate (10^{-15} or better) while improving the overall memory capacity and maintaining high data access rates. In holographic memories, for example, recording a large data page, consisting of perhaps $10^3 \times 10^3$ bits (a megabit), yields a low signal-to-noise ratio (SNR) and thus high BER because of the low distributed power per bit and inter-pixel crosstalk. By adding a small number of redundant (parity) bits, the BER of the decoded data can be reduced to desirable levels while maintaining the same data access rate [4]. This paper is concerned with the design of data encoding and decoding procedures for OPOMs which provide high effective storage capacity and output data rates, along with parallel-to-serial conversion and reformatting. These functions are implemented with optoelectronic smart-pixel interfaces.

Reed-Solomon (RS) codes are frequently used for error correction because they can effectively correct both random and burst errors, and because its codewords have a variety of lengths and maximal separation in the code space [5]. Using interleaving and combining methods, RS codes can distribute large burst errors (hundreds to thousands of bits) over many smaller codewords and correct them. Encoding of the RS codes involves vector-matrix multiplication and addition performed over a finite field. Decoding of the RS codes involves these procedures and along with complicated logic operations [6], [7]. Because of the complicated electrical circuitry, the large number of inputs/outputs (discussed later), and parallel decoding needed to provide a high data rate, we explore the use of smart pixel technology to perform the error correction and high speed network interface functions.

Figure 1 shows a schematic of the SP interface. At the left is a 2-D input from an OPOM, which may produce 10^6 bits every $10 \mu\text{s}$, or an aggregate raw data rate of 0.1 Tb/s. The output of the photodetector array goes to SP nodes consisting of one or more RS decoders. Several parallel decoders may be required because a single decoder might not be able to complete decoding in a given time period. Smart pixels combining electronic circuitry with optical input/output (I/O) are needed because the decoding logic is too complicated for current all-optical systems. The optical I/O of the SP devices is needed because electrical bandwidth and crosstalk limitations restrict the needed spatial channel density (channels/cm²) and information spatial channel density (bits/sec/cm²).

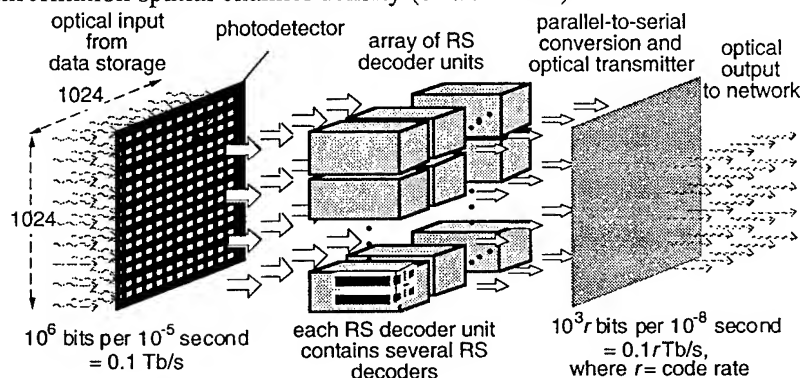


Figure 1. Schematic model of the smart pixel interface.

We have analyzed a particular RS decoding scheme, the transform decoding algorithm (TDA) [7], that uses 1-D and 2-D pipeline structures [8]. The finite field multiplier (FFM) used in decoding the RS codes was implemented by serial/parallel systolic arrays and compound VLSI gates. We studied six different design variations of the TDA RS decoder: bit-serial-symbol-serial (BSSS); bit-parallel-symbol-serial (BPSS-P

and BPSS-C) where P denotes the parallel systolic FFM and C denotes the compound-gate FFM; bit-serial-symbol-parallel (BSSP); and bit-parallel-symbol-parallel (BPSP-P and BPSP-C). In order to compare the performance of these implementations, a VLSI circuit simulation model, SUSPENS [9], was

applied to estimate the decoder area, the maximum clock frequency, and the power dissipation. In the simulations, a 0.25- μm CMOS process was assumed.

To find the RS code and the TDA decoder which result in the largest data rate, the input spatial channel density, d_{scin} , defined as the number of inputs in a unit area, was first determined, and is shown on the vertical axes in Fig. 2. The two horizontal dashed lines in Fig. 2 show 1-D and 2-D electrical limits given by the maximum numbers of input pins on the edge of the chip and through the chip, respectively. The horizontal axes are the codeword length n in symbols, and the parameter m is the order of the RS codes, equal to the bits/symbol. The dotted lines that link symbols for the six decoding methods denote primitive RS codes, in which all $2^m - 1$ possible symbols are used. The other types of lines represent TDA decoders and RS codes with the same order m , but different n . All the RS codes shown in Figs. 2 and 3 reduce the BER from 10^{-4} to 10^{-15} or better. Except for the BPSP-P and BSSP decoders for the $m = 8$ RS codes, most RS codes and TDA decoders are limited by the electrical I/O. We then assume that all the fabricated decoders in a given area operate at a speed limited by the maximum power density. We compute the information spatial channel density, d_{info} , defined as the number of decoded bits per unit time and area, i.e., the average data rate in a unit area at the output of the interface. Thus d_{info} is equal to the product of the code rate r (defined as the ratio of the number of valid information bits to the total number of bits including parity check bits) and the input data rate. Figure 3 shows d_{info} versus codeword length for the primitive families of $m = 5$ and $m = 8$ RS codes. The maximum d_{info} is obtained by the (27,17) RS code (with code rate $r = 0.63$) having $m = 5$ implemented by the BPSS-C design.

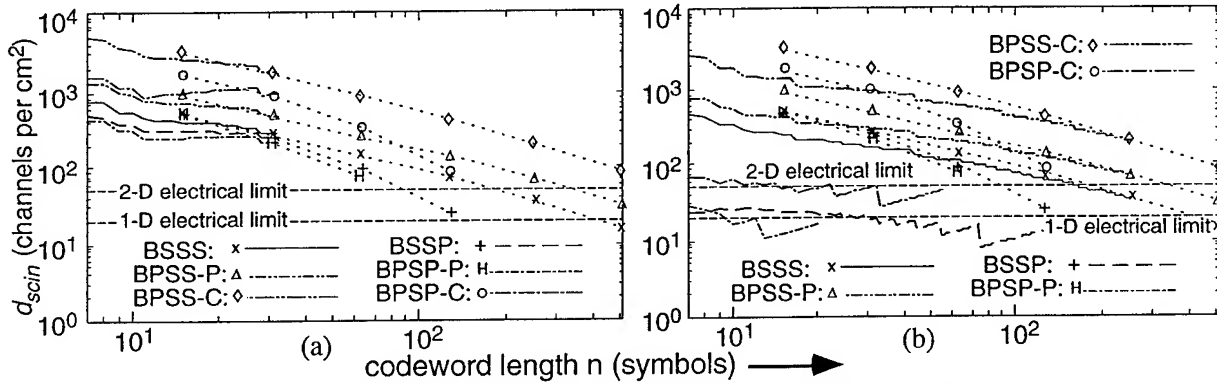


Figure 2. Input spatial channel density for the TDA decoders and the primitive RS codes (dotted lines), (a) $m = 5$ RS codes, and (b) $m = 8$ RS codes (all codes reduce BER from 10^{-4} to 10^{-15} or better).

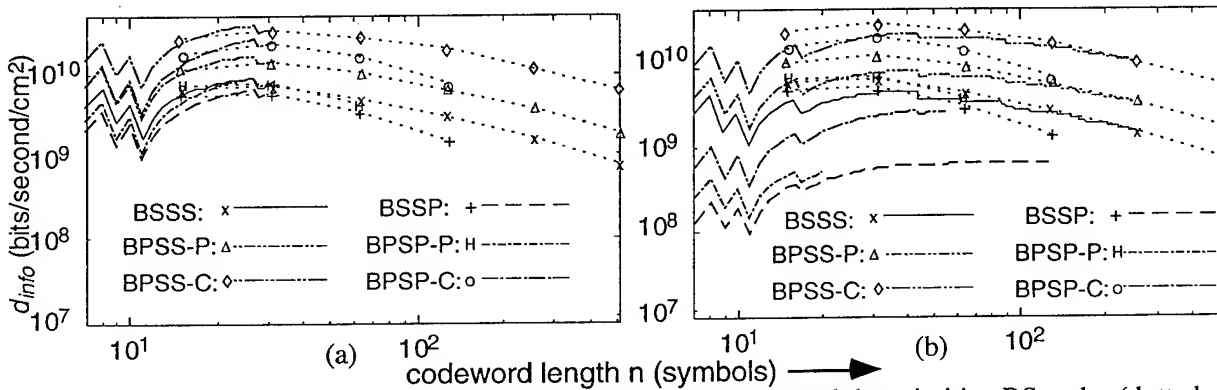


Figure 3. Information spatial channel density for the TDA decoders and the primitive RS codes (dotted lines), (a) $m = 5$ RS codes, and (b) $m = 8$ RS codes (all codes reduce BER from 10^{-4} to 10^{-15} or better).

When the size and the maximum access rate of a data page are known for an OPOM, the input data rate to the SP interface (given by the product of the two) is determined. We then want to choose the RS code with the highest r along with a decoder design that provides the necessary processing rate because the usable memory capacity is proportional to r . When designing a SP interface, two categories of interface constraints were considered to determine the possible RS codes and decoders. The first category includes two constraints regarding the properties of the RS codes only: one of them selects RS codes which reduce the BER from 10^{-4} to 10^{-15} or better (as assumed previously); another selects the RS codes with r higher

than a specified minimum. In Fig. 4, a dashed line shows the upper bound of the code rate constraint for r set above 0.75, and a dash-dotted line shows the lower bound for the codes satisfying the BER constraint. The RS codes in the shaded region satisfy both constraints simultaneously. In the second category, the VLSI specifications are imposed to determine the possible RS codes and decoders. Feasible RS codes and decoders are then specified as limited by the decoding delay, buffer length, interface area, and power density. The dotted lines in Fig. 4 show the upper bound on the maximum number of correctable errors t for the six implementations of the primitive RS codes. The BPSS-C designs for some primitive codes with $n = 63, 127$ and 255 , and the BPSS-P and the BPSP-C designs for some $n = 63$ codes are located in the shaded region and satisfy all the constraints.

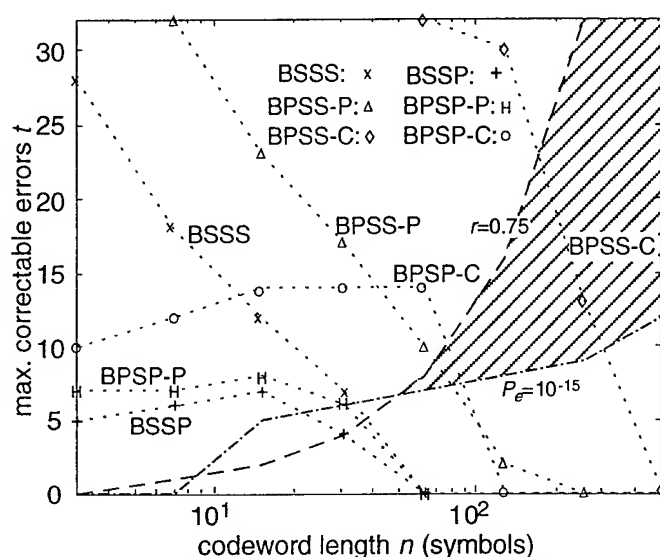


Figure 4. Feasibility analysis of the TDA decoder and RS codes - search for the RS code and the decoder design which provide the highest code rate.

From Figs. 3 and 4, the RS codeword length n tends to approach two extremes: achieving either high data throughput (shorter n); or large capacity (longer n). One possible way to extend the envelope of these conflicting requirements is to use 3-D VLSI packaging (interconnection of multiple stacked chips) to implement long-length RS pipelined decoders. Another possibility is the use of product codes in which two RS codes with shorter n are combined. The product codes provide a higher combined code rate than a regular RS code of the same error-correcting capability, and the design of the decoder for short-length codes is easier.

Acknowledgement

This research was supported by the National Center for Integrated Photonic Technology (NCIPT) program funded by ARPA under Contract No. MDA972-94-1-0001 and by the DOD Focused Research Initiative/BMDO

through the Air Force Office of Scientific Research (AFOSR) under Grant No. F49620-95-1-0531.

References

1. J.F. Heanue, M.C. Bashaw, and L. Hesselink, "Volume holographic storage and retrieval of digital data," *Science* **265**, 749-752 (1994).
2. D. Psaltis and A. Pu, "Holographic 3-D disks," *Optoelectronics- Devices and Technologies* **10**, 333-342 (1995).
3. M.-P. Bernal, et al, "A precision tester for studies of holographic optical storage materials and recording physics," submitted to *Applied Optics*.
4. M.A. Neifeld and M. McDonald, "Error Correction for Increasing the Usable Capacity of Photorefractive Memories," *Optics Letters* **19**, 1483-1485 (1994).
5. S.B. Wicker and V.K. Bhargava, Eds., *Reed-Solomon Codes and Their Applications*, IEEE Press, New York, 1994.
6. S. Lin and D.J. Costello, Jr., *Error Control Coding: Fundamentals and Applications*, Prentice-Hall, Englewood Cliffs, New Jersey, 1983.
7. H.M. Shao, et al "A VLSI design of a pipeline Reed-Solomon Decoder," *IEEE Trans. Computers*. C-**34**, 393-403 (1985).
8. W.-F. Hsu and A.A. Sawchuk, "Volume optical memory smart pixel interfaces with 0.1-1.0 terabit per second performance," *OSA Annual Meeting* (1995) paper TuE4; W.-F. Hsu and A.A. Sawchuk, "Design of smart pixel interfaces for volume optical memories," *1996 International Topical Meeting on Optical Computing*, Sendai, Japan, April 21-25, (1996) paper OWB3.
9. H.B. Bakoglu, *Circuits, Interconnections, and Packaging for VLSI*, (VLSI Systems Series), Addison Wesley, Reading, MA, 1990.

A Digital Wavelength-Multiplexed Holographic Data Storage System

D. Lande[†], J. F. Heanue[†], M. C. Bashaw[‡], and L. Hesselink[‡]

[†]Department of Applied Physics, Stanford University, Stanford, CA 94305-4090

[‡]Department of Electrical Engineering, Stanford University, Stanford, CA 94305-4035

Phone: (415) 723-9127

Fax: (415) 725-3377

We have implemented what we believe to be the first wavelength-multiplexed digital holographic data storage system. The fully automated storage and retrieval of digital data in an iron-doped lithium niobate crystal, using an external-cavity tunable diode laser operating in the red, was demonstrated.

The system is shown in Fig.1. The wavelength of the Spectra Diode Labs diode laser is automatically tuned by the computer to access the different data pages. Pages are written with a VGA-format liquid crystal spatial light modulator (SLM) from Kopin, and read with a Kodak CCD camera, which also acts as an optical feedback control for the laser tuning. The feedback control allows the system to tune to the correct wavelengths despite the common problems of mode-hopping and frequency drift in diode lasers. Unlike previous wavelength multiplexing schemes which use counter propagating beams [1], we used a 90 degree geometry to eliminate excess noise commonly associated with reflection geometry experiments, after we calculated that such non-optimal geometry actually did not reduce

wavelength selectivity significantly. Furthermore, the use of a laser diode demonstrates for the first time the feasibility of more compact and less expensive holographic digital systems, and wavelength multiplexing eliminates the need for moving parts in the optical setup, as opposed to previous data storage experiments using angular and spatial multiplexing [2].

As a preliminary experiment, we stored a 60 Kbyte digital image file in a single hologram stack in the lithium niobate crystal and retrieved the data back to an output file. By comparing both files, we found the raw bit error rate to be 10^{-4} . With the addition of error-correcting codes, data interleaving to eliminate burst errors, and optimization of the optical feedback to fine-tune the laser at readout, significant improvement in bit error rates is expected. Even though wavelength multiplexing by itself is limited by the tuning range and linewidth of the diode laser, we have also combined spatial and angular multiplexing to create multiple stacks and multiply the storage capacity, using the technique of sparse-angle wavelength multiplexing.

This research has been supported in part by the Advanced Research Program Agency through the ARPA-University-Industry Holographic Data Storage Systems (HDSS) Consortium.

References

- [1] G. A. Rakuljic *et. al.*, "Optical data storage by using orthogonal wavelength-multiplexed volume holograms," *Optics Letters* **17**, p.1471 (1992).
- [2] J. F. Heanue *et. al.*, "Volume Holographic Storage and Retrieval of Digital Data," *Science* **265**, p.749 (1994).

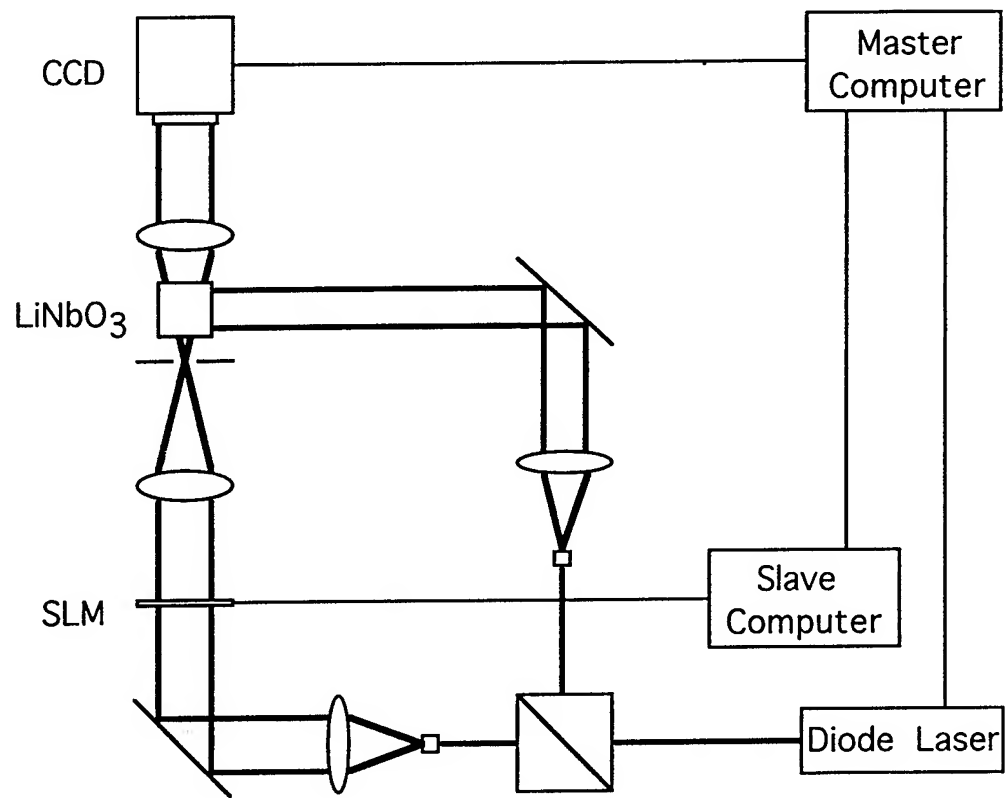


Figure1: Wavelength-multiplexing experimental setup

Novel system architectures for practical volume holographic memories

Feng Zhao and Koichi Sayano

Accuwave Corporation

1651 19th Street, Santa Monica, California 90404

Tel: (310)449-5540 Fax: (310)449-5539

The potential advantages of volume holographic data storage have long been recognized -parallel fashion of data transfer and large storage density ($\sim V/\lambda^3$). However, whether the technology will succeed or fail in commercialization also depends on practical issues such as system size and cost. Ever in its early days, volume holographic data storage has basically relied on one of the two fundamental system architectures, i.e., Fourier transform and imaging holograms. In these conventional systems, the reference beam reconstructs the hologram by forming a virtual holographic image and thus a lens is needed to form a real image on the CCD detector. With the increasing demand for high resolution ($> \text{Mbits per hologram}$) for the goal of terrabyte memories, conventional systems are starting to show limitations such as lens-limited resolution, alignment difficulties and too large a size for practical holographic memories.

In this paper, we present a novel system architecture, the "Lensless Phase-Conjugate Hologram (LPCH)" [1,2], as an alternative for practical volume holographic memories. Unlike the conventional architecture, the LPCH approach uses (1) holographic recording of the data array in the near-field, and (2) phase-conjugate reference beam during readout to reconstruct real images which can be picked up directly by a CCD, eliminating the use of lenses during both recording and readout. The LPCH is illustrated in Fig. 1, in which the SLM containing the input data S is placed next to the recording material and the data are recorded by forming a permanent hologram with a plane reference wave R . For readout, a collimated plane wave traveling in the opposite direction (which is a phase conjugate of R) is used to reconstruct a real and time-reversed replica S^* of the original object field [3], shown in Fig.1(c). The reconstructed S^*

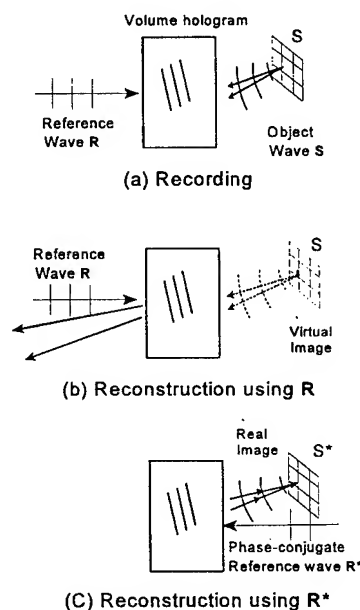


Figure 1. A diagram illustrating the concept of the LPCH.

compensates in its reverse propagation for any phase distortions undergone by S during recording, leading to distortion-free 1:1 imaging. Unlike the case of 3-D objects, where a phase-conjugate image has a pseudoscopic effect, the two-dimensional nature of the data array allows complete reproduction of the holographic data to a square-law detector.

Compared with conventional holographic systems, the phase-conjugation property of volume holograms provides enormous advantages for practical volume holographic memories. The advantages include:

(1) Compact and simplified system. No bulky and expensive lenses are needed in either recording or reconstruction processes and the reduced number of optical elements offers ease in alignment and

robustness. The use of near-field holography makes it possible to construct a compact 20cm×20cm×10cm memory with Gbytes capacity.

(2) High resolution. Since there is only one optical element, i.e., the recording material involved, the spatial resolution of the reconstructed array data is limited only by the holographic medium, which include hologram aperture recording material resolution. The spatial resolution of the recording material, using LiNbO₃ for example, is about 10⁵ lp/mm for moderate doping levels (~10¹⁸/cm³), which is sufficient for any holographic applications. Thus the image resolution is essentially limited by the hologram aperture P . The diffraction-limited image resolution δ can be approximately described by the Rayleigh criterion [3]:

$$\delta \approx \lambda \frac{z}{P},$$

where λ is the laser wavelength, and z is the distance between the SLM (also the CCD) and the recording material. For example, let $P \approx 25$ mm, $\lambda = 0.5\mu\text{m}$, and $z = 20$ mm, then the diffraction limited resolution is about 2500 lp/mm (i.e., Airy disk size is $\sim 0.4\mu\text{m}$). Thus the LPCH provides the necessary resolution for >Mbytes/page which are very beneficial to high capacity memories.

(3) Low optical noise. The phase-conjugation property of the hologram tends to cancel any aberrations and phase distortions including coherent speckle noise which is especially troublesome for near diffraction-limited high resolution coherent systems. Assuming that the aberrations can be described by $\exp[j\varphi(x,y)]$, then the aberrations are recorded in the hologram, i.e., $S(x,y)\exp[j\varphi(x,y)]$. Now, if the aberrations remain unchanged in the readout, the reconstructed phase-conjugate image wavefronts retrace back to its original object,

$$S_o^*(x,y)\exp[-j\varphi(x,y)]\exp[j\varphi(x,y)] \equiv S_o^*(x,y).$$

Thus, any aberrations will be canceled due to the “undoing” property of phase-conjugation, leading to distortion-free 1:1 imaging.

The improvement in bit-error rate (BER) by using the LPCH is significant. We experimentally examined the inter-pixel (inner-page) cross-talk noise of a reconstructed phase-conjugate

holographic image. A Chrome-on-glass photomask of 512×512 pixels with 24μm×24μm pixel size was used as the object data array. The reconstructed phase-conjugate readout was imaged pixel-to-pixel onto a CCD, where the pixel dimensions were matched to those of the camera. The raw BER of a single data array of 24μm pixels was estimated to be about 10⁻¹². Figure 2 shows the histogram of the reconstructed binary data from the 8-bit (256 gray levels) CCD.

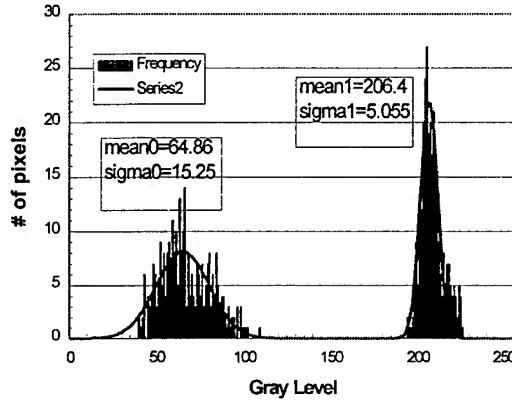


Figure 2. Histogram of reconstructed binary data.

Various optical layout configurations are possible based on the LPCH, depending on the preferred writing angle, multiplexing techniques, etc. Existing multiplexing techniques, such as wavelength-multiplexing and angle-multiplexing, can be incorporated in the LPCH, as in the case of conventional holographic systems. Here we describe two architectures for holographic read-only memory (ROM) and write-once-read-many (WORM) memory. Figure 3 illustrates the schematic of the ROM optical player, in which Fig.3(a) shows how the “optical cube” (i.e., the volume hologram) is fabricated with the ● indicating its orientation. In this scheme, we assume using angle-multiplexing and recording of multiple data pages is done by varying the reference beam angle using an A-O deflector. The “optical cube” is then inserted into the ROM player shown in Fig.3(b), in which the stored data is recalled using a collimated read beam entering from the opposite direction (phase-conjugate reference beam). The

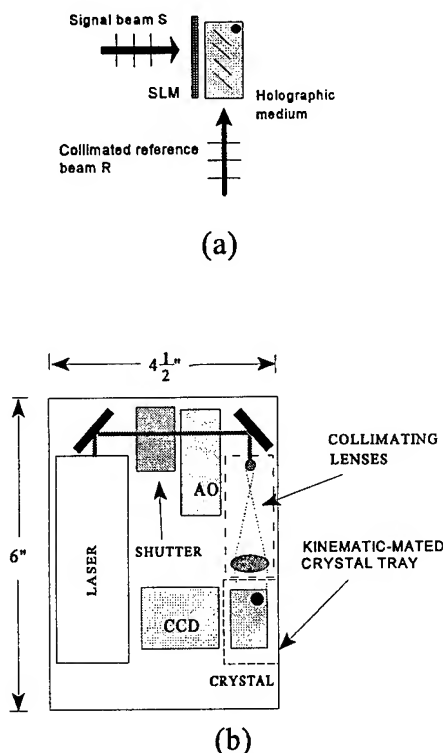


Figure 3. Schematic of a ROM.

angle of the read beam can be altered by the A-O cell to access different data pages. The 90 degree geometry is chosen in this case because it allows almost direct contact between the CCD and "optical cube" to achieve more compact packages and higher diffraction-limited resolution.

Figure 4 shows the layout of a simplified WORM based on the LPCH approach. Wavelength-multiplexing is used for the WORM. During the "write" cycle, shutter G1 is turned on and G2 is turned off, and the holographic data are written in the recording material by interfering the signal beam S with reference beam R . Multiple pages of

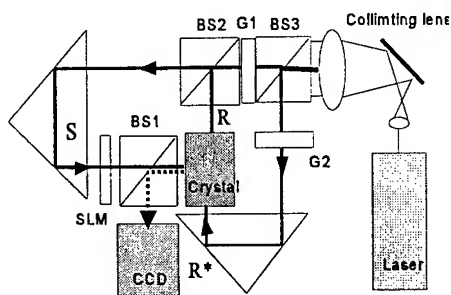


Figure 4. Schematic of a WORM.

data can be written by varying the recording wavelength. During the "read" cycle, shutter G1 is turned off and G2 is switched on, letting a collimated plane wave at the opposite direction (phase-conjugate reference wave R^*) recall the stored data. The beam splitter BS1 is used to "image" the reconstructed S^* onto the CCD detector. Thus, by using a simple optical element, i.e., beamsplitter, a read-write optical memory based on the LPCH can also be implemented.

In summary, we have proposed a system architecture based on the phase-conjugation property of volume holograms. The novel lensless scheme offers tremendous advantages over conventional holographic systems, making the LPCH an attractive approach for practical holographic data storage applications.

REFERENCES:

- [1] F. Zhao and K. Sayano, "Compact, high resolution holographic storage," paper CWF11, Conf. of Lasers and Electro-Optics (CLEO'96), Anaheim, CA (1996).
- [2] F. Zhao and K. Sayano, "Compact read-only memory based on lensless phase-conjugate holograms," submitted to *Opt. Lett.*, (1996).
- [3] J. W. Goodman, *Introduction to Fourier Optics*, (McGraw-Hill, San Francisco, 1968), chap. 8, p.252, and chap. 6, p.130.

Spectral-hole-and-angle multiplexed volume holographic memory

Xianmin Yi, Changxi Yang, Shiuan-Hui Lin and Pochi Yeh

Electrical and Computer Engineering, University of California, Santa Barbara, California 93106
Santa Barbara, California 93106

Claire Gu

Electrical Engineering, Pennsylvania State University, University Park, PA 16802

Volume holographic data storage is an exciting research area due to the prospect of large storage density and fast access rate. In recent years, a new kind of storage media, the spectral hole burning material, has been proposed and investigated¹⁻³. The storage of 2,000 high-resolution holograms in a single sample has been demonstrated by Kohler et. al. via spectral hole multiplexing swept frequency recording scheme.³ Spectral hole multiplexing is fundamentally different from angle multiplexing and wavelength multiplexing with conventional holographic materials where Bragg matching is the only method to select a particular hologram from all the holograms recorded in a common volume.⁴⁻⁶ In this paper, we demonstrate theoretically that spectral-hole multiplexing and Bragg-angle multiplexing can be used together for spectral hole burning materials. We find that the cross-talk-limited storage density can be significantly increased.

Consider a Fourier plane holographic storage system using spectral hole burning material as the storage medium (See the configuration in Ref.[4]). N spectral holes are burned at different wavelengths, labeled as $n=1, 2, \dots, N$. There are $2M+1$ angle-multiplexed holograms in each spectral hole, labeled as $m=-M, -(M-1), \dots, M$. Each hologram is recorded using swept frequency recording technique. With the presence of the $N(2M+1)$ holograms, the modulation of the dielectric constant of the medium can be written as

$$\Delta\epsilon(\vec{r}, \omega) \propto \sum_{n=1}^N \sum_{m=-M}^M \int_{\omega_n - \Delta\omega/2}^{\omega_n + \Delta\omega/2} R_{nm}^*(\vec{r}, \omega_b) S_{nm}(\vec{r}, \omega_b) \frac{\exp[i\varphi(\omega_b)]}{(\omega_b - \omega) - i(\Gamma/2)} d\omega_b \quad (1)$$

where $R_{nm}(\vec{r}, \omega_b)$ is the reference beam, $S_{nm}(\vec{r}, \omega_b)$ is the signal beam, ω_n is the center frequency of the n th spectral hole, $\Delta\omega$ is the frequency sweeping range in recording each hologram, Γ is the hole width, and $\varphi(\omega_b) = 2\pi(\omega_b - \omega)/\Delta\omega$ is the phase difference between

the reference beam and the object beam. The expressions for the reference beam and the signal beam can be found in Refs. [4] and [5].

During the readout, a plane wave with wave vector \vec{k}_p is incident upon the volume holograms. The dielectric constant modulated with hologram information will cause scattering of the incident plane wave. Using the scalar diffraction theory and following a similar procedure as in Refs. [4]-[5], we can obtain the electric field of the diffracted beam at the output plane explicitly. The electric field at the output plane consists of both the signal and the noise. After several steps of algebraic derivation, the signal-to-noise ratio of the cross-talk noise can be written

$$\text{NSR} = \sum_{\substack{m=-M \\ m \neq p}}^M \text{sinc}^2 \left[\frac{t}{2\pi} \left(\Delta k_{nmpz} + \frac{1}{F} \Delta k_{nmpy} y_2 + \frac{c}{2\omega_p} \Delta k_{nmpy}^2 \right) \right] + \frac{1}{|\gamma|^2} \sum_{\substack{n=1 \\ n \neq p}}^N \left| \int_{\omega_n - \Delta\omega/2}^{\omega_n + \Delta\omega/2} \frac{\exp[i\varphi(\omega_b)]}{(\omega_b - \omega_p) - i(\Gamma/2)} d\omega_b \right|^2 \quad (2)$$

where $\gamma = \int_{-\Delta\omega/2}^{\Delta\omega/2} \exp(i2\pi\omega/\Delta\omega) / [\omega - i\Gamma/2] d\omega$ is the signal amplitude. The first term in Eq.(2) represents the cross-talk noise from other holograms in the same spectral hole as the readout hologram, while the second term represents the cross-talk noise from all the holograms in other spectral holes. According to Eq.(2), although a large number of holograms are angularly multiplexed in each spectral hole, the cross talk between two spectral holes are the same as if only one hologram is recorded in each spectral hole.

Numerical simulation shows that the cross-talk noise from a spectral hole decreases rapidly as $(\omega_n - \omega_b)^{-4}$.^{3,4} Thus a small frequency separation between adjacent spectral holes is often adequate to reduce the inter-hole cross-talk noise significantly. Let $\Delta\omega_t$ be the total frequency range and $\Delta\omega_s$ is the frequency separation between adjacent spectral holes, then the number of spectral holes that can be burned will be $\Delta\omega_t/\Delta\omega_s$. The first term of Eq.(2) represents the cross-talk noise from other holograms within the same spectral hole as the readout hologram. It is the same as that of angle-multiplexed holographic storage with conventional holographic materials. When the holograms in the same spectral hole are separated by one sinc lobe, the storage density per spectral hole will be $\rho = \alpha / (\text{SNR} \cdot \lambda^3)$.⁶ Thus the total storage density including all the spectral holes will be

$$\rho = \frac{\alpha}{SNR} \frac{1}{\lambda^3} \frac{\Delta\omega_t}{\Delta\omega_s} \quad (3)$$

where SNR is the signal-to-noise ratio required to achieve a certain bit error rate.

Now, let us look at some typical values. In Kohler et. al.'s demonstration,⁴ the spectral hole width Γ is 0.5GHz, the frequency sweeping range $\Delta\omega$ is 1.0GHz, the frequency separation between adjacent spectral holes $\Delta\omega_s$ is 2.5GHz, the total frequency range $\Delta\omega_t$ is 625GHz, and 250 spectral holes are burned at the same applied electric field. So the storage density of spectral hole burning materials can be orders of magnitude larger than that of the conventional holographic materials. Kohler et. al. also multiplexed spectral holes in the electric field domain. Eight equally spaced voltages are applied in the range of -150KV to 150KV in a sample of 65 μ m thick. This leads to a total of 2000 spectral holes. Thus, we can see that spectral hole burning materials offers an additional dimension to increase the cross-talk-limited storage density.

In conclusion, we have investigated theoretically a 4-D spectral-hole-and-angle-multiplexed volume holographic storage system with spectral hole burning materials. It is found that the cross-talk-limited storage density in each spectral hole is the same as that with conventional holographic materials and that total storage density is increased by a factor equal to the number of spectral holes.

References

1. A. J. Meixner, A. Renn, and U. P. Wild, J. Chem. Phys. **91**, 6278 (1989).
2. S. Bernet, B. Kohler, A. Rebane, A. Renn, and U. P. Wild, J. Opt. Soc. Am. B **9**, 987 (1992).
3. B. Kohler, S. Bernet, A. Renn, and U. P. Wild, Opt. Lett. **18**, 2144 (1993).
4. C. Gu, J. Hong, I. McMicheal, R. Sexena, and F. H. Mok, J. Opt. Soc. Am. A **9**, 1978 (1992)
5. K. Curtis, C. Gu, and D. Psaltis, Opt. Lett. **18**, 1001 (1993).
6. X. Yi, P. Yeh, and C. Gu, Opt. Lett. **19**, 1580 (1994).

Tuesday, July 9, 1996

Joint Poster Session

JTuD 8:30 pm-10:30 pm
South Pacific Ballroom

NOVEL AZO-DYE DOPED PMMA FILMS AS OPTICAL DATA STORAGE MEDIA

V. P. Pham, A. Granger, T. Galstyan and R. A. Lessard

Center for Optics, Photonics and Laser (COPL)

Department of Physics - Pavillon Alexandre-Vachon

University Laval

Quebec, Qc. G1K 7P4

Canada

Optical information was holographically stored, retrieved, erased and overwritten on new azo-dye doped PMMA guest-host films. The information is stored in the form of highly localized dichroism and birefringence of the polymer films, induced by spatially modulated polarization and intensity of writing light. In this paper, we are presenting new data concerning the dynamic behaviour of these films. We have also investigated the effect of the intensity of the reading beam on the storage time of these polymeric systems.

Off-Bragg Analysis of Diffraction Efficiency of Photorefractive Holograms

Koutarou Nonaka

NTT Interdisciplinary Research Laboratories

3 - 9 - 11 Midori-cho, Musashino-shi, Tokyo, 180 Japan

Phone: +81 422 59 2538 Fax: +81 422 59 2340

I. INTRODUCTION

A photorefractive medium is widely used for multiplexed holographic recording¹. Although the diffraction properties for off-Bragg conditions are important in evaluating cross-talk noise and wavelength and angular sensitivities for multiplexed holographic recording, most previous analyses have focused on the on-Bragg readout conditions. In a photorefractive medium, a photorefractive phase shift and fringe bending effect² appear within the medium. These phenomena make off-Bragg analysis for photorefractive hologram gratings very difficult. Consequently, off-Bragg analysis has been reported only for special cases³. A numerical calculation for the off-Bragg condition has also been reported⁴, but an analytical formula for calculating the diffraction efficiency for the off-Bragg condition is essential in order to easily evaluate the cross-talk noise and wavelength and angular sensitivities for the multiplexed holographic recording.

This paper derives an analytical formula for calculating the diffraction efficiency of a transmission photorefractive hologram. Optimum medium parameters and the diffraction properties for the off-Bragg conditions are discussed using the derived formula.

II. ANALYSIS

The analysis model is shown in Fig. 1. The grating slant angle ϕ is the angle between grating vector \mathbf{K} (magnitude: $2\pi/\Lambda$, where Λ : grating period) and the z -axis. The coupled-wave equations for the photorefractive medium are:

$$c_r \frac{dR}{dz} + \alpha' R = i e^{i\phi_g} \Gamma m(z) e^{i\phi(z)} e^{-i\Delta k_z z} S, \quad (1a)$$

$$c_s \frac{dS}{dz} + \alpha' S = i e^{-i\phi_g} \Gamma m(z) e^{-i\phi(z)} e^{i\Delta k_z z} R, \quad (1b)$$

where $c_r (= \cos \theta)$ and $c_s (= \cos \theta - 2 \cos(\phi - \theta) \cos \phi)$ are the obliquity factors, $\alpha' (= \alpha / 2)$ is the absorption coefficient of the medium for the amplitude of the light beam, ϕ_g is the phase difference between the optical intensity grating and the induced index grating, Γ is the coupling constant, and Δk_z is the z component of the wave-vector mismatch. These are given by

$$\Gamma = \pi \Delta n_L / \lambda, \quad \Delta k_z = K [\cos(\phi + \Delta\theta) - \cos \phi]. \quad (2)$$

Δk_z gives the mismatch from the Bragg condition when $\Delta\theta$ represents the angle mismatch from the Bragg angle θ_0 , Δn_L is the modulation depth (amplitude) of the refractive index during reconstruction, and λ is the wavelength of the light beams.

The index modulation depth $m(z)$ and phase difference between the reference and object beams $\phi(z)$ are⁵

$$m(z) = \frac{2}{\sqrt{r} e^{-\gamma z/2} + e^{\gamma z/2} / \sqrt{r}}, \quad \phi(z) = \cot \phi_g \times \ln \frac{\sqrt{r} + 1 / \sqrt{r}}{\sqrt{r} e^{-\gamma z/2} + e^{\gamma z/2} / \sqrt{r}}, \quad (3)$$

where r and γ are given by

$$r = \frac{R_{wo}}{S_{wo}}, \quad \gamma = \frac{2 \pi \Delta n_S}{\lambda \cos \theta_0} \sin \varphi_g, \quad (4)$$

where r is the recording beam intensity ratio, Δn_S is the modulation depth (amplitude) of refractive index during recording, and $\varphi(z)$ represents the fringe bending effect.

The general solution of Eqs. (1) is derived as follows⁶:

$$S = \left(\frac{t}{1-t} \right)^{h_s} [C_1 \times {}_2F_1(v_S, v'_S, w_S, t) + C_2 \times t^{1-w_S} {}_2F_1(u_S + \sqrt{D}, u_S - \sqrt{D}, 2 - w_S, t)],$$

where

$$\begin{aligned} u_S &= \frac{1}{2} - h_s + h_r - i\Delta, & w_S &= \frac{1}{2} + h_s - h_r + i \left(\frac{1}{2} \cot \varphi_g + \Delta \right), \\ v_S &= i \frac{1}{2} \cot \varphi_g + \sqrt{D}, & v'_S &= i \frac{1}{2} \cot \varphi_g - \sqrt{D}, & D &= \frac{4\Gamma^2}{c_r c_s \gamma^2} - \frac{1}{4} \cot^2 \varphi_g, \\ h_r &= \frac{\alpha'}{c_r \gamma}, & h_s &= \frac{\alpha'}{c_s \gamma}, & \Delta &= \frac{\Delta k_z}{\gamma}, & t &= \frac{1}{1 + e^{\gamma z / r}}, \end{aligned} \quad (6)$$

${}_2F_1(\)$ is the hypergeometric function, and C_1 and C_2 are constants. The constants are determined by the boundary conditions $R(0) = 1$, $S(0) = 0$, and Eqs. (1).

The diffraction efficiency η is given by

$$\eta = (|c_s|/c_r) S(T) S^\dagger(T), \quad (7)$$

Where the dagger indicates the complex conjugate.

III. RESULTS OF THE ANALYSIS

Signal and reference wave propagation within the photorefractive medium are shown in Fig. 2. The signal beam intensity I_S and the reference beam intensity I_R within the medium are plotted against distance into the medium z for $T = 5\text{mm}$. I_S versus z corresponds to η versus T . Therefore, Fig.2 also shows the diffraction efficiency η as a function of medium thickness T . The photorefractive phase shift φ_g is taken as a parameter. The beam intensities show damped oscillation with z . This is caused by energy transfer between the signal and reference beams and light absorption within the medium. From Fig.2, we obtain an optimum medium thickness of 2.0 to 2.5mm for high diffraction efficiency.

It is known that angle mismatch from the Bragg condition strongly affects the diffraction efficiency. Here, we show the signal and the reference beam intensity distribution within the medium for the off-Bragg condition. Figure 3 shows the distribution for $\Delta\theta = 0.05^\circ$. Calculation conditions are the same as those in Fig.2 except for $\Delta\theta$. The signal beam intensity I_S is smaller and the reference beam intensity I_R is larger than in Fig.2 which is for the on-Bragg condition of $\Delta\theta = 0^\circ$. The behavior of the curves is more complex than in Fig.2. This occurs because the energy transfer between the signal beam and the reference beam becomes weak due to the Bragg mismatch.

The diffraction efficiency η is plotted against angle mismatch $\Delta\theta$ in Fig. 4 for various values of φ_g . A deviation from the Bragg angle causes a change in diffraction efficiency. The behavior of the mismatch curves is very complex; one sees asymmetric curves and broadening of the peaks. Experimental measurements by Vré et al.² gave similar results, but, when $\varphi_g = 90^\circ$, the mismatch curve was symmetric with respect to $\Delta\theta = 0$.

IV. CONCLUSION

An analytical formula was derived for calculating the diffraction efficiency of transmission photorefractive hologram gratings in the off-Bragg condition. The photorefractive phase shift and the fringe bending effect were taken into account in this analysis. Using this formula, it is possible to evaluate the optimum medium parameters. The angular sensitivity for the off-Bragg condition was also quantified by the derived formula. These results will play an important role in evaluating crosstalk of multiplexed hologram recording and properties of photorefractive media.

REFERENCES

- ¹P. Günter and J.-P. Huignard (Ed.), *Photorefractive Materials and Their Applications* (Springer-Verlag, Berlin, 1989), Vol.II, Chap. 6.
- ²R. De Vr , M. Jeganathan, J.P. Wilde, and L. Hesselink, *Opt. Lett.*, **19**, 910(1994).
- ³R. Hofmeister, A. Yariv, and S. Yagi, *J. Opt. Soc. Am. A*, **11**, 1342 (1994).
- ⁴C. Gu, J. Hong, and P. Yeh, *J. Opt. Soc. Am. B*, **9**, 1473 (1992).
- ⁵P. Yeh, *IEEE J. Quantum Electron.*, **25**, 484(1989).
- ⁶K. Nonaka, *J. Appl. Phys.*, **78**, 4345 (1995).

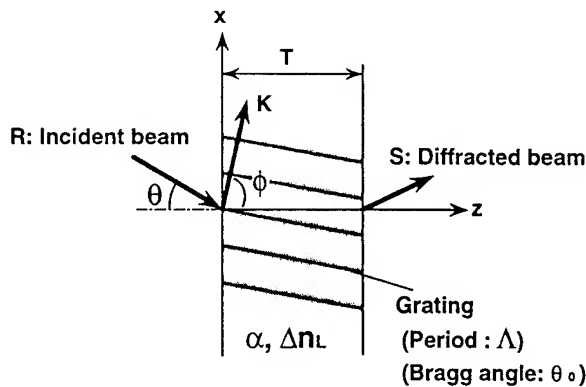


FIG. 1. Model of a hologram grating during reconstruction.

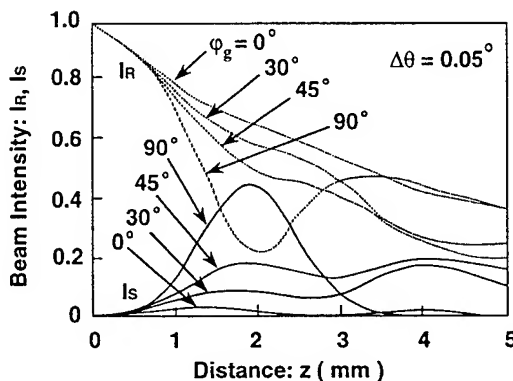


FIG. 3. Signal and reference beam intensity for off-Bragg condition $\Delta\theta=0.05^\circ$. Parameters used in the analysis are the same as those in Fig. 2 except for $\Delta\theta$.

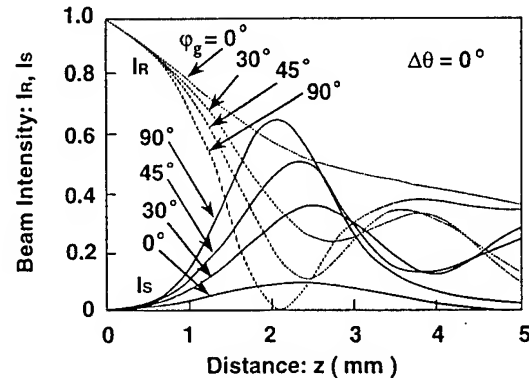


FIG. 2. Signal beam intensity I_S and reference beam intensity I_R within the medium for various values of ϕ_g with $r = 100$ and $T=5$ mm. Calculation conditions are: $\Delta n=200 \times 10^{-6}$ ($=\Delta n_S = \Delta n_L$), $\alpha=200\text{m}^{-1}$, $\Lambda=5 \mu\text{m}$, $\phi=90^\circ$, $\theta_0=3.05^\circ$, $\lambda=0.532 \mu\text{m}$, and $\Delta\theta=0$.

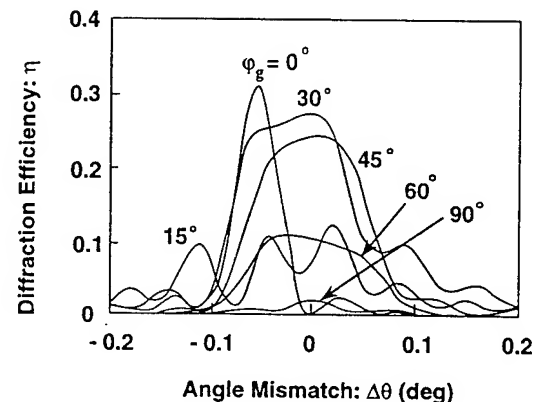


FIG. 4. Diffraction efficiency η as a function of angle mismatch $\Delta\theta$ from the Bragg angle θ_0 for various values of ϕ_g . Parameters used in the analysis are the same as those in Fig. 2 except for $\Delta\theta$.

Theory of Two-Species Transport in Photorefractive Crystals Using Two Wavelengths for Nondestructive Readout

A. Y. Liu, M. C. Bashaw, L. Paraschis*, L. Hesselink

Department of Electrical Engineering, Stanford University, Stanford, CA 94305

*Department of Applied Physics, Stanford University, Stanford, CA 94305

Ph: 415-725-3294, Fax: 415-723-3377

Holographic storage offers many advantages over conventional storage methods, however, readout of information cannot be made non-destructive without special fixing procedures, such as thermal and electrical fixing. Several other techniques enabling non-destructive readout of information have been investigated, including two-photon recording in single species crystals[1], and sensitizing with a short wavelength and recording and reading with a long wavelength with two species[2,3]. The last method has the advantage of allowing each species to be chosen, so that the photorefractive properties can be optimized while retaining the information during readout.

Although various aspects of two-species model have been examined, including the theory of photorefractive effect in the steady state limit under single wavelength illumination with one deep and one shallow species[4], and dark decay of gratings in crystals of two species[5], modeling of holographic recording using two photorefractive species and two wavelengths to achieve nondestructive readout remains to be studied. We present here the electron transport analysis for preillumination, writing, and reading cycles using two wavelengths in a crystal with a shallow and deep level.

Figure 1 shows the energy level diagram that the model is based on. First, the crystal is illuminated with a uniform beam of wavelength λ_1 with enough energy to excite the electrons in the deep level to the shallower level, then a longer wavelength λ_2 having enough energy to excite only the electrons in the shallower level is used to write a grating. This process allows a grating to form in the shallower level, and another grating to form in the deeper level due to electrons from the shallower level recombining with the empty donors in the deep level. Upon readout, the grating in the shallower level is erased, while the grating built up in the deep level remains unaffected.

The equations that govern the model are the rate equations for the empty deep donor density N and filled shallower donor density M , the continuity equation, the current density equation, and Poisson's equation. During preillumination, a uniform beam of wavelength λ_1 excites electrons from the deep level to the conduction band; they subsequently relax in the shallower level. For the case of the total deep donor density much larger than that of the shallower donor density, an approximate expression for the filling rate of electrons in the shallower level can be found as

$$\Gamma_{fill} = s_D(\lambda_1)I_0 \frac{\gamma_D N_{DA}}{\gamma_T M_T + \gamma_D N_A}$$

where s_D is the photoexcitation coefficient for the donor level, I_0 is the preillumination intensity, $\gamma_{D,T}$ are the electron recombination coefficient for the deep and the shallower levels, respectively, M_T is the total number of available shallower empty donors, N_A is the number of inactive traps, and N_{DA} is the total number of filled donors before preillumination. Figure 2(a) shows the behavior of the empty deep donor and filled shallower donor densities for such a case during preillumination.

After a substantial number of electrons are transferred to the shallow level, a second laser beam of energy much smaller than that sufficient to excite electrons in the deep donor level can be used to write gratings. In this step $s_D(\lambda_2)$ should be significantly smaller than before to ensure nondestructive readout with the same wavelength. The prefilled electrons (zeroth order quantity) in the shallower species redistribute themselves to reach a new equilibrium under this new condition. The equilibrium for the zeroth order quantity decreases as s_D decreases until it eventually vanishes for the case of $s_D=0$, as shown in figure 2(b), since all electrons eventually

recombine with the empty donors in the deep level. In this case the zeroth order quantity decay rate at large time is given by

$$\Gamma_{ilarg e}^0 = \frac{s_T(\lambda_2)I_0 + \beta}{1 + \frac{\gamma_T M_T}{\gamma_D N_A}}$$

where β is the thermal excitation coefficient for the shallower level. In addition to the zeroth order change, charge gratings in both the shallower level and the deep level (first order quantities) start building up. The build up of gratings in the shallower and deep levels is illustrated in figure 3(a) for $s_D = 0$. The initial build up of the grating in shallower level is not affected by the deep level; it then decays due to the decrease in the zeroth order quantities, and the rate follows the decay rate of the zeroth order quantity. In the deep level a complementary grating builds up from recombining electrons excited; it then decays as the zeroth order quantity decreases, and eventually reaches a nonzero steady state. The total electric field goes through a change of phase, as shown in figure 4, however, it can be made either in or out of phase depending on the chosen rate parameters. If s_D is small but nonzero, there is also an in phase grating that builds up slowly, making the total steady state grating in phase with the shallow level grating.

The grating behaviors during readout are then examined. The remaining gratings decay exponentially if sufficiently long writing time is allowed so that the zeroth order quantities are small compared to the total numbers of available deep and shallower donors. The decay for gratings in both the shallower and deep levels are plotted in figure 3(b). The decay rate for both gratings is given by

$$\Gamma_{read}^1 = \frac{K^2 + K_D^2}{K^2 + K_0^2} \Gamma_{IM},$$

where K is the grating vector, K_D^{-1} is the average distance an electron travels before recombining with an empty deep donor, K_0^{-1} is the average distance an electron travels before recombining with either a empty deep or shallower donor, and Γ_{IM} is the total electron ionization rate in the shallower level. The grating in the shallower level eventually decays to zero, and the grating in the deep level decays to a constant level of

$$N_{lss} = N_1(t_{read} = 0) - \frac{M_1(t_{read} = 0)}{1 + \frac{K^2}{K_D^2}}$$

This remaining grating is insensitive to the reading beam, since this wavelength is not enough to reexcite electrons out of the deep donor levels. Thus nondestructive readout can be achieved. Figure 5 shows the normalized total grating decay for several s_D values ranging from 0.1 to 0. It can be seen that the decay rate upon readout decreases steadily as the photoexcitation coefficient approaches the limiting case of $s_D=0$.

In summary, we have solved the dynamics of the entire sequence of preillumination with a shorter wavelength, writing and nondestructive reading with a longer wavelength in a crystal having a deep and a shallower donor level. We have derived expressions for cases of interest. This model offers the formalism of optimizing the writing wavelength, the impurity levels, and the preillumination and writing times, so that both high diffraction efficiency and non-destructive readout can be achieved. This work is supported in part by ARPA/NSIC PRISM Consortium.

- [1]. D. von der Linde, A. M. Glass, and K. G. Rodgers, *J. Appl. Phys.* **47**, 217 (1976).
- [2]. Staebler and W. Phillips, *Appl. Phys. Lett.* **24**, 268-270 (1974).
- [3]. K. Buse et al. and E. Krätzig, *Optical Materials* **4**, 237-240 (1995).
- [4]. M. C. Bashaw, M. Jeganathan, and L. Hesselink, *J. Opt. Soc. Am B* **11**, 1743-175 (1994).
- [5]. P. Tayebati and D. Mahgerefteh, *J. Opt. Soc. Am. B* **8**, 1053-1064 (1991).

Figures

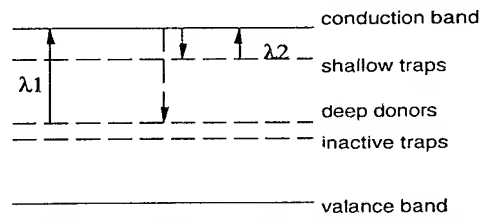


Figure 1: Energy Level Diagram for a crystal with a shallow and a deep level.

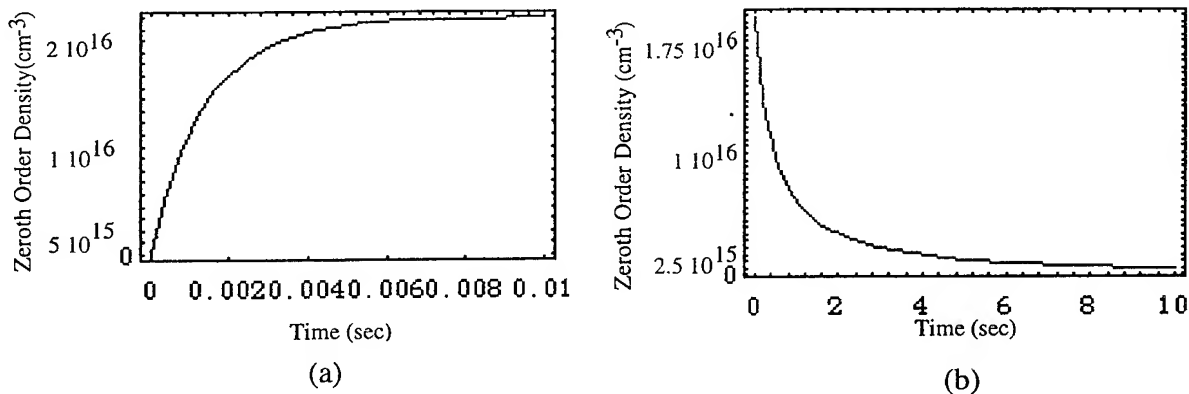


Figure 2: Zeroth Order (M_0, N_0) During Preillumination (a) and Writing (b)

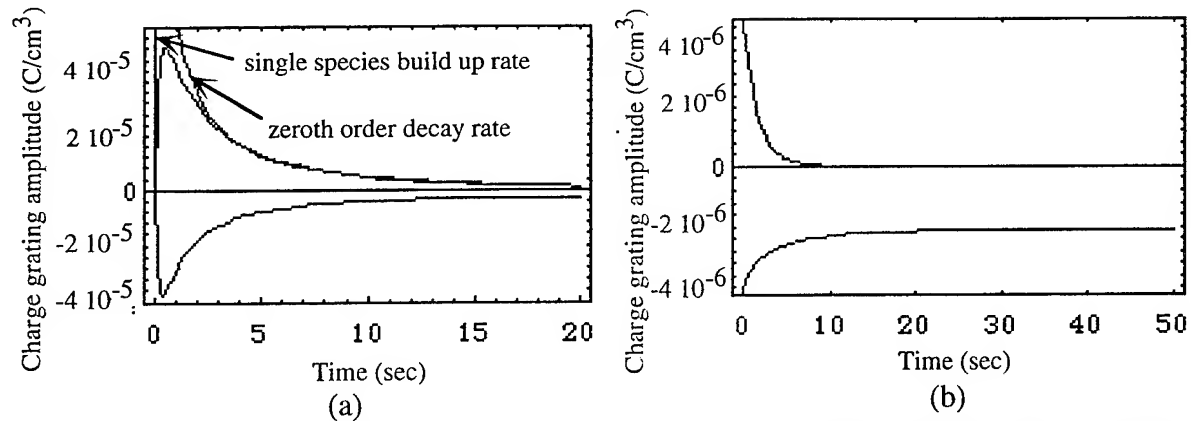


Figure 3: Positive charge grating in shallower level and negative charge grating in deep level build up after 0.01 seconds of preillumination (a) and decay after 10s write time (b)

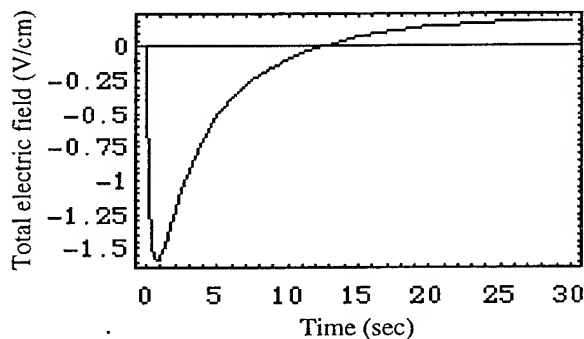


Fig.4: Total E-field during writing.

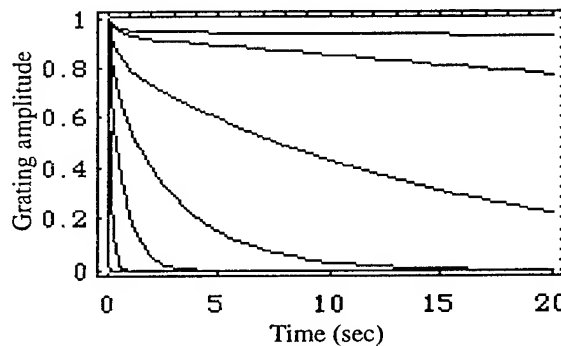


Fig.5: Erasure rates for total grating at $s_D=0, 10^{-1}, -2, -3, -4, -5, -6, -7$.

Properties of Resonant Two-Photon Processes in Photorefractive Media

L. Paraschis[†], M. C. Bashaw*, A. Liu*, and L. Hesselink*

Departments of Applied Physics[†] and Electrical Engineering*,
Stanford University, Stanford, CA 94305

[†]Tel. 415 723-4940

FAX 415 725-3377

[†]Email: loukas@kaos.stanford.edu

Holographic data storage systems [1] require sensitive optical materials that provide some means of nondestructive readout [2]. Among the number of techniques for nonvolatile readout available [2], the sensitization of a photorefractive medium by illumination at one wavelength, called gating, for writing at a second using a resonant two-photon process, constitutes the most versatile all-optical nondestructive method. Typically, this process consists of absorption of a photon at frequency ω_1 to generate an intermediate excited state, followed by absorption of a second at ω_2 to generate a free carrier [3, 4, 5]. Gating occurs for absorption of two photons at two different wavelengths. In the present work, we identify the critical physical characteristics of the processes that provide the simultaneous realization of true gating and writing sensitivity at a variety of frequencies, evaluate the refractive index perturbation and the response rate, and investigate the significance of the intermediate state occupancy and the arising nonlinear photorefractive behavior at its saturation regime.

We distinguish the different cases of photoelectron production with respect to the relative frequencies of the two photons involved in each process. These are shown in Fig.1. True gating requires $\omega_1 < \omega_2$ (i.e. higher frequency ionization). The gratings may then be probed nondestructively using only the writing wavelength, while they may be erased using the writing and gating wavelengths simultaneously, as shown in Fig.2. We identify the two principal cases of interest for nonvolatile readout, which correspond to the *higher-frequency ionization gating* (HIG) case, in which the signal and reference beams write a grating at frequency ω_1 , and gating occurs at frequency ω_2 to complete photogeneration of free carriers, and the complementary *lower-frequency excitation gating* (LEG) case, in which gating occurs at frequency ω_1 and the signal and reference beams write a grating at frequency ω_2 . Because of the resonance involved, red or even infrared frequency sensitivity may be realized.

We develop a charge transport model that describes the resonant two-photon processes, by modifying the established single photon formalism [6], to account that a filled impurity center initially undergoes an excitation from its ground state to the impurity excited state and subsequently ionizes to the conduction band by absorbing a second photon. All the possible transition rates (r_{ij}) are indicated in Fig.3. It should be noted that in the relaxation rate r_{10} , both the spontaneous and stimulated emission are taken into account. Nonuniform illumination results in nonuniform distribution of filled and empty states thus allowing interfering waves to record a holographic grating.

In the quasi-steady-state approximation, in which the zero order quantities reach steady-state on a time scale faster than the photorefractive time scale, we obtain solutions for the photorefractive behavior under continuous-wave small modulation depth illumination. For the higher frequency ionization, the amplitudes of the steady-state index perturbation obey

where E_i^{sc} is the steady-state space-charge field, and E_0 , E_D and E_q are the externally applied, diffusion and limiting fields respectively. The subscript i distinguishes between the HIG and LEG cases, where the ratio of modified modulation depths m_i^{eff} are equal for low gating intensities (far from the saturation regime). For the response rate, we obtain a simple exponential behavior, as expected for single-impurity, where:

$$\Gamma_{HIG} = \Gamma_{LEG} = f(K)\Gamma_{die} = \left[f(k) \frac{\sigma_{1c} I_{02}}{\gamma_{rec}} \frac{N_0^*}{N_0^o} \right] \left(\frac{N_e^*}{N_0^*} \right) \quad (2)$$

with $f(k)$ a factor depending on the details of the charge transport (but not on intensity), γ_{rec} the total recombination rate, I_{02} the ionization intensity amplitude, σ_{1c} the ionization cross-section, N_0^o the unfilled impurity concentrations. The occupancy of excited stated concentration (N_e^*) of filled impurities (N_0^*) due to excitation illumination I_1 , in a three-level system (Fig.3), is:

$$\frac{N_e^*}{N_0^*} = \left[\frac{\tau_{exc} \sigma_{01} I_{01}}{1 + 2\tau_{exc} \sigma_{01} I_{01} + \tau_{exc} \sigma_{1c} I_{02} (1 - \alpha)} \right] \quad (3)$$

and is proportional to the excited state lifetime τ_{exc} (where α the ratio of the recombination rates to the excited and ground states, and all additional coefficients are obtained by direct extension); the factor of 2 occurs because of stimulated emission.

The filled impurity excited state occupancy as function of gating intensity (LEG case) is shown in Fig.4, for typical parameters of a transition metal doped photorefractive crystal. For low intensity, we obtain the established linear behavior [3, 4]. At higher intensities, the response rate saturates. As the above analysis establishes, this occurs at the excitation intensity levels needed to saturate the concentration of excited impurity states and is attributed to the strong stimulated emission effect in the saturation regime. The ionization intensity, on the other hand, contributes to desaturation as it grows (for $I_{02} \gg I_{01}$), due to the corresponding high rate of free carrier generation.

We conclude that the photorefractive quantities depend on the intermediate state occupancy which gives rise to nonlinear behavior at the high-intensity saturation regime, that is consistent with experimental observations [4]. Also, the nonlinear photorefractive sensitivity depends on the product of the intermediate-state lifetime and the excitation and ionization cross-section. The corresponding parameters for the four-level systems distinguishes further the resonant two-photon processes, and allow comparison between transition metal and rare-earth impurity species. Evaluation of all these characteristics is crucial for the complete characterization of resonant two-photon processes in photorefractive media and will be discussed in detail.

- [1] J. F. Heanue, M. C. Bashaw, and L. Hesselink, *Science* **265**,749 (1994).
- [2] L. Hesselink and M. C. Bashaw, *Opt. and Quantum Electron.* **25**,S611-S661 (1993).
- [3] D. von der Linde and A. M. Glass, *Appl. Phys.* **8**,85 (1975).
- [4] D. von der Linde, A. M. Glass, and K. F. Rodgers, *J. Appl. Phys.* **47**,217 (1976).
- [5] H. Vormann and E. Krätzig, *Solid State Commun.* **49**,843-847 (1984).
- [6] N.V. Kukhtarev, *Pis'ma Zh. Tekh. Fiz.* **2**,1114 (1976). [English Transl.: *Sov. Tech. Phys. Lett.* **2**, 438 (1976).]

This research work has been supported in part by the ARPA/NSIC.

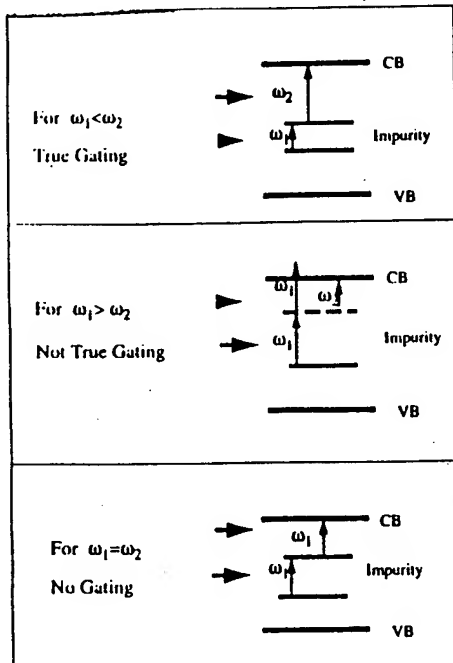


Figure 1. Resonant two-photon free-electron production mechanism in a photorefractive medium with a single impurity species.

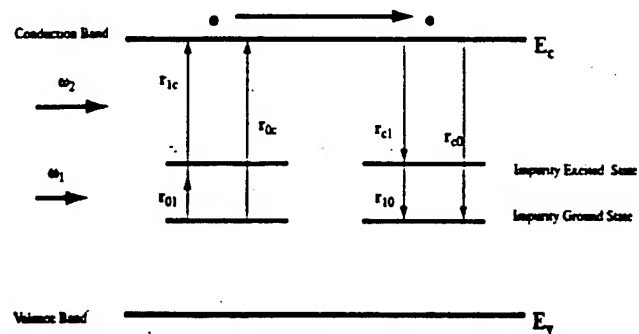


Figure 3. Resonant two-photon excitation, ionization and recombination band transport model for a three-level system.

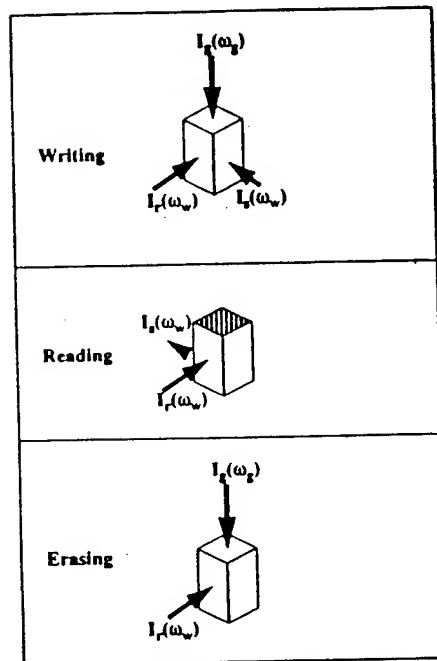


Figure 2. Two-photon holography, where the signal $I_s(\omega_s)$ and the reference $I_r(\omega_r)$ beams create the grating in the presence of the uniform gating $I_g(\omega_g)$ illumination.

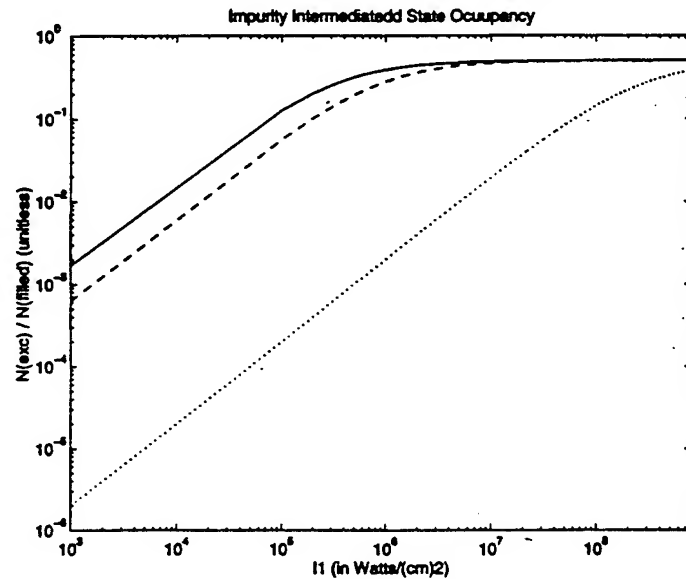


Figure 4: Filled impurity intermediate state occupancy dependence on excitation illumination for typical parameters of a transition metal doped photorefractive crystal, where $\sigma_{01} = 10^{-18} \text{ cm}^2$, $\sigma_{1c} = 10^{-17} \text{ cm}^2$ and $\tau_{rec} = 500 \text{ ns}$. At high intensities saturation occurs. The three different curves correspond to the three different regimes of ionization intensity I_0 ; i.e. for $I_0 < I_{01}$ [solid line] (here specifically $I_{01} = (500)^{-1} I_0$), for $I_0 \approx I_{01}$ [dashed line] (here $I_{01} = I_0$), and for $I_0 > I_{01}$ [dotted line] (here $I_{01} = (500) I_0$).

Optical implementation of composite filters as volume holograms in LiNbO_3 for pattern recognition

Tracy D. Hudson, Amy S. Kransteuber, and Deanna K. McMillen

U. S. Army Missile Command
AMSMI-RD-WS-PO
Redstone Arsenal, Alabama 35898-5248
(205) 876-6242
(205) 876-7360 fax

Francis T. S. Yu and Shizhuo Yin

Pennsylvania State University
Department of Electrical Engineering
University Park, PA 16802-2706
(814) 863-4256
(814) 865-7065 fax

The optical correlator originally proposed by Vander Lugt [1] has been extensively investigated as a laboratory novelty but not widely employed in application-specific pattern recognition systems. This result is due in part to the classical matched filter being sensitive to rotation and scale variations of the imagery. Two major avenues of approaching this image distortion limitation are currently being pursued.

First, filter designs are being investigated to incorporate information of multiple images to recognize an object over a range of distortions in a singular composite filter [2]. These filter designs are usually intended for implementation on spatial light modulators (SLMs) located in the Fourier plane of the optical processor. The filters must be serially processed which can present a processing bottleneck if a filter bank for object detection is large enough to detect a practical number of objects.

Second, volume holographic memories are being investigated to multiplex numerous holograms in optical processors [3][4]. These holograms are usually of images or Vander Lugt filters which may be addressed in parallel by an input scene. These multiplexed holograms may be recorded in a variety of volume holographic materials. For this research, LiNbO_3 is being used as the recording material because of its insensitivity to environmental factors, relatively long storage lifetime among photorefractives, and availability of thick crystals which allows dense packing of holograms[5][6]. However, it is well known that the diffraction efficiency of a hologram stored in a photorefractive crystal decreases by $1/N^2$ as the total number of multiplexed holograms, N , in the crystal increases.

A combination of the two approaches, composite filters and multiplexed holograms, for fast optical pattern recognition is proposed in this summary. The design of composite filters which may be optically implemented as multiplexed holograms in a lithium niobate crystal is discussed. It is believed that a much broader range of objects and their distortions may be detected and classified with this scheme than ever achieved before.

The bipolar composite filters (BCF) in this investigation is a variant of the synthetic discriminant function (SDF) filter in that the filter is composed of a linear combination of filters for each training image. Unlike most SDF filters which are designed to be implemented as complex frequency filters, the BCF is designed to operate as a phase-only filter. The BCF

elements take on the values of +1 or -1 which correspond to 0 or π radians phase shift of the filter's transmittance function.

An optimum BCF was designed to recognize a M60 tank through 60° of out-of-plane rotation with the suppression of any correlation from a similar object - a T72 tank. Figure 1 shows one of these two sets of training images - 13 images of an M60 tank with 5° increments of out-of-plane rotation between each successive image. The other set consisted of similar perspective views of the T72. Each of the images is a 128×128 pixelated array with 256 possible gray levels.

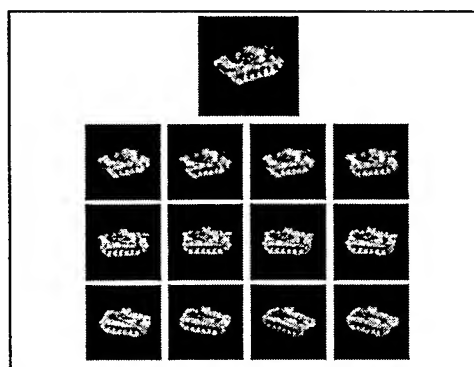


Figure 1. The target training set.

The BCF template, shown in Figure 2, was designed for use in the input plane of an optical correlator. This BCF template is composed of 128×128 pixels where each data element assumes the value of -1 or +1. These values are represented as black or white in the figure.

The correlation response of the designed filter was simulated against a full 360° range of out-of-plane rotations at 5° increments for each of the two tank types. Figure 3 is a plot of the correlation intensities as a function of the out-of-plane rotation. There is more than a factor of three difference between the peak cross-correlation intensities of the target and anti-target images over the designed 60° rotation range ($60 - 120^\circ$ in the figure). There is negligible difference between the cross correlations of the BCF with the M60 and T72 images outside of the designed rotation range.

A photorefractive correlator, schematically shown in Figure 4, was constructed to demonstrate proof-of-concept in implementing the above BCF template design. The input SLM was a transmissive liquid crystal display. The Fourier transform of the central diffraction order from the input SLM was interfered with a reference plane wave in an Fe:LiNbO₃ crystal. For the demonstration, two BCF templates were implemented as wavelength-multiplexed holograms with $\lambda = 488$ and 514 nm. These templates may also be implemented as angle-multiplexed holograms. A CCD camera was located at the correlation plane. Figure 5 photographically depicts the optical cross-correlation of the each tank against a filter designed to recognize the M60.

To record holographic BCF, the BCF's template is displayed on a phase-modulated SLM. Vertically polarized light is incident on the SLM. The light transmitted by the SLM has the polarization rotated between the "full on" and "full off" states according to the filter displayed. In order to get the phase information from these states, an analyzer polarizer is used with its orientation perpendicular to the bisector of the "full on" and "full off" polarization states. A retarder is then used to rotate the transmitted light's polarization vertically before it reaches the photorefractive crystal located in the Fourier plane. The resultant central diffraction order from the SLM is Fourier transformed and interfered with a reference plane wave. The second BCF was recorded by tuning the wavelength of the argon laser source.

To address the holographically stored BCFs, the input SLM is operated in an amplitude modulation mode. The

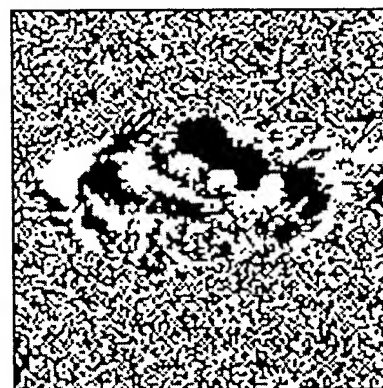


Figure 2. The BCF template.

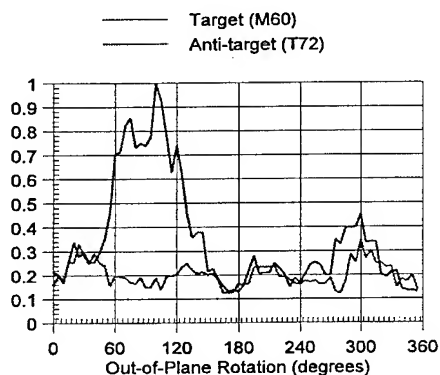


Figure 3. Simulated Response of BCF to M60 and T72.

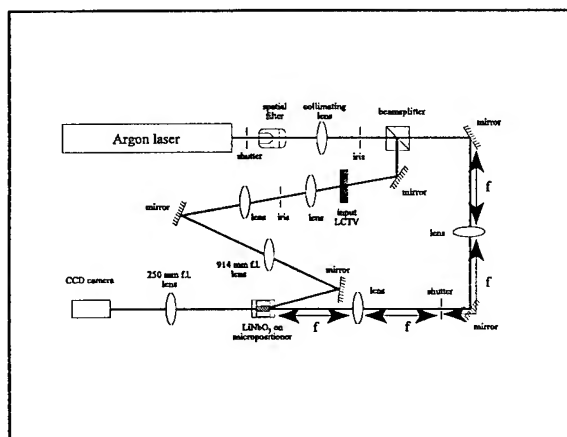


Figure 4. The photorefractive correlator.

director of the output analyzer is aligned parallel with the input polarization direction. The reference beam is blocked by a shutter. If the image displayed on the input SLM is matched to any of the previously recorded frequency domain BCFs and satisfies the Bragg conditions, the conjugate of the reference beam is reconstructed along the direction of the original reference beam used to record the filter. A lens is then used to focus this reconstructed beam as a bright spot, correlation peak, on the CCD camera. The detection of the correlation peak on the CCD may be synced with the wavelength tuning range of the laser source to effectively determine which filter is successfully correlated against the candidate input scene.

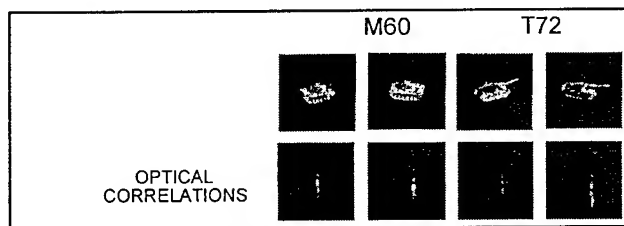


Figure 5. Optical cross-correlation results.

References:

1. A. Vander Lugt, "Signal Detection by Complex Spatial Filtering," *IEEE Trans. on Info. Theory*, 139-145 (1964).
2. B. V. K. Vijaya Kumar, "Minimum-variance synthetic discriminant functions," *J. Opt. Soc. Am. A* **3** (10), 1579-1584 (1986).
3. C. Halvorson, B. Kraabel, A. J. Heeger, B. L. Volodin, K. Meerholz, Sandaplhon, and N. Peyghambarian, "Optical computing by use of photorefractive polymers," *Optics Letters* **20** (1), 76-78 (1995).
4. Stanislaw Bartkiewicz and Andrzej Miniewicz, "Methylene blue sensitized poly(methyl methacrylate) matrix: a novel holographic material," *Applied Optics* **34** (23), 5175-5178 (1995).
5. F. H. Mok, "Angle-multiplexed storage of 5000 holograms in lithium niobate," *Optics Letters* **18** (11), 915-917 (1993).
6. F. T. S. Yu and Shizhuo Yin, "Bragg diffraction-limited photorefractive crystal-based correlators," *Optical Engineering* **34** (8), 2224-2231 (1995).

Switchable Diffractive Elements and Applications to Holographic and Multi-layer Optical Storage

Lawrence H. Domash and Badri N. Gomatam
Foster-Miller, Inc.
195 Bear Hill Road, Waltham MA 02154
tel 617+290+0992 fax +0693

James Leger and Gregg Kilby
Department of Electrical Engineering
University of Minnesota
Minneapolis, MN 55455

1. Electrically switchable holograms in polymer dispersed liquid crystal

Electrically switchable holograms or diffractive optical elements have recently been demonstrated in a fine-grained polymer dispersed liquid crystal material, giving a basis for a new family of compact, nonmechanical wavefront control devices well suited for applications in optical data storage. Examples of potential applications for both holographic volume storage and multilayer disk storage systems will be presented, and current experimental status summarized.

Polymer dispersed liquid crystals (PDLCs) are composites of LC droplets in a transparent polymer host whose index falls within the LC birefringent index range. For display purposes, PDLCs contain LC droplets on the scale of 2-5 μm optimized for modulation of scattering. Recently Sutherland et al developed a variant formulation of PDLCs with much finer scale LC droplets, about 0.1 μm , and recorded electrically switchable volume holograms [1]. Holographic gratings of high diffraction efficiency are formed through optical recording or mask-contact printing and subsequent polymerization into fringe structures of alternating LC rich and LC lean regions. By applying an electric field on the order of 5 V/ μm to modulate the index match, the volume holographic diffraction efficiency may be switched from $\approx 90\%$ to 0.3% on a time scale of 10-50 μs . Scattering is less than 0.5 db insertion loss per film by control of LC microdroplet dimensions.

In our laboratory, stacks of up to four series elements have been constructed and a variety of devices demonstrated based on switchable transmission Bragg holograms [2,3]. The simplest application is diversion of a laser beam through a fixed (possibly large) angle with no moving parts. Switchable focus lenses, fiber optic switches, and programmable beamlet arrays have been shown. Figure 1 illustrates the general concept of a programmable stack of spatial arrays composed of individual, pre-recorded transmission holograms. Each element may have an aperture < 1 mm. By switching the diffractive power of individual elements and utilizing multiple diffractions, a new family of optical interconnect devices can be realized. A structure of M layers of $n \times n = N$ elements per layer may have from NM up to 2^{NM} diffractive states, depending on what degree of multiple diffraction can be utilized in a design.

2. Device applications for optical data storage

Switchable diffractive elements are adaptable to miniaturization and integration into dense multidiffractive structures. The use of stratified volume holographic optical element designs [4] opens a rich set of functional interconnect possibilities.

2.1 Example 1: Interconnects for holographic data storage.

An ideal multiplexing scheme for very compact holographic storage would avoid both tunable lasers and moving parts. Switchable diffractive structures can be used for either angle or phase multiplexing [5]. Figure 2 shows schematically how series diffraction in stacks of submillimeter elements can yield a large number of discrete beam directions. For example, eight layers of 8X8 arrays will provide a minimum of 512 beam directions (arbitrary angles) within an integrated device less than 0.5 cm^3 in total volume.

2.2 Example 2: Holographic ROM

Whereas the previous example envisions switchable diffractive elements as the multiplexing or beam steering interface to complement an erasable volume holographic storage medium, an alternative approach is to use the switchable elements as an optical ROM medium directly, by prerecording a computer encoded diffractive pattern in each element. The data states are limited to one per switchable element, but a variety of stratified volumeschemes for distributing data among layers may be utilized for spatial compression. Figure 3 shows a conceptual sketch of a miniature ROM with no moving parts, 20 μs access times, and capacity for 100-1000 stored pages, each with 1-10 Mbyte data, useful for example as a map database in a laptop computer.

2.3 Example 3: Switchable aberration correction for multilayer disk storage

Switchable diffractives may also be applied to solve disk storage problems such as maintenance of optical performance in lenses required to focus through transparent layers of various depths. Although in principle all optical power could be designed into switchable focus diffractive lenses for electrically actuated focus, design models show that it is difficult to correct MTF for such systems. On the other hand, switchable multidepth aberration correction added to conventional, mechanically translated lenses appears feasible. Figure 4 shows a model calculation of geometric spot size as a function of focal depth based on a series stack of four optimized holographic correction plates.

3. References

1. R.L. Sutherland, L.V. Natarajan, V.P. Tondiglia, T.J. Bunning, Bragg Gratings in an Acrylate Polymer Consisting of Periodic Polymer-Dispersed Liquid-Crystal Planes, *Chem. of Materials*, 1993, 5, 1533-38
2. L. Domash, C. Gozewski, A. Nelson, J. Schwartz, Programmable beamlet generator, dynamic lens, and optical memory using electrically switched holographic devices, *Proc. SPIE Vol. 2026c, Very Large Optical Memories*, Ed. S. Kowel, 1993.
3. L. Domash et al, Switchable-focus lenses in holographic polymer dispersed liquid crystal *Proc. SPIE Vol. 2689, Diffractive and Holographic Optics Technology III*, Paper 26.
4. Nordin, Johnson and Tanguay, Diffraction properties of stratified volume holographic optical elements, *J.O.S.A.*, Vol. A9, p. 2206, 1992.
5. Lawrence Domash, Yong-Ming Chen, Michael Snowbell, and Conrad Gozewski, Switchable holograms and approaches to storage multiplexing, *Proc. SPIE Vol. 2297, Photonics for Processors, Neural Networks and Memories II*, 1994.

Figure 1. 3D stacks of arrays of individually prerecorded switchable holographic cells offer a new class of programmable diffractive system.

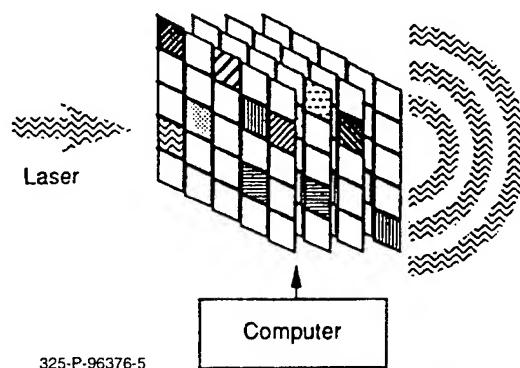


Figure 2. Multiplexed integrated stacks can be applied for discrete beam steering. If H = the total number of holograms, the number of beam directions can be from H up to 2^H for a fully multiple-diffractive structure.

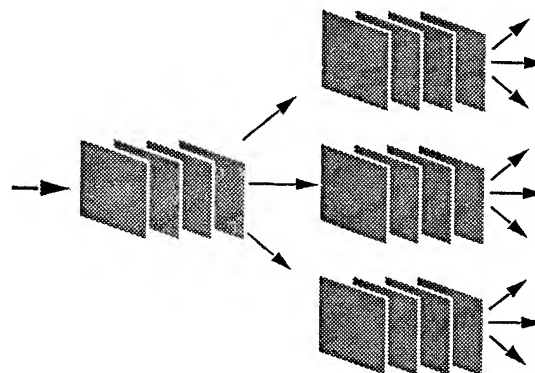


Figure 3. Compact optical ROM is structured similarly, except that data is encoded into each prerecorded diffractive element.

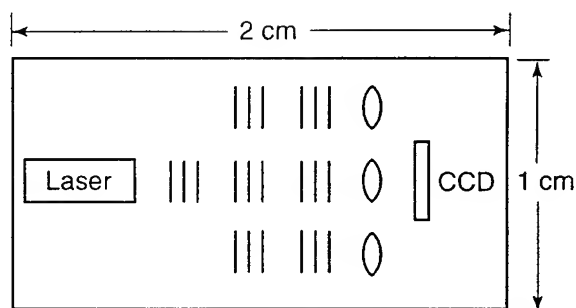
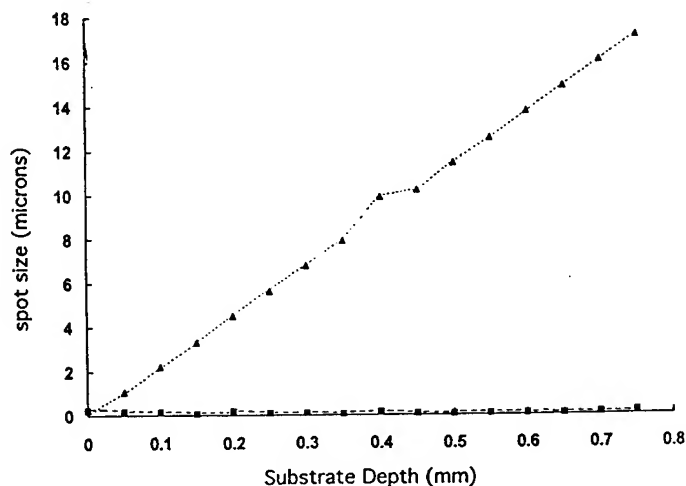


Figure 4. An optical design model shows that spot size versus depth through a transparent medium of a mechanically translated lens (triangles) can be improved by incorporating four switchable diffractive aberration correctors (squares).



Mobile Ion Compensation in Photorefractive Media for Multiplex Holography

M. C. Bashaw*, J. F. Heanue[†], and L. Hesselink*

*Department of Electrical Engineering, Stanford University, Stanford, CA 94305-4035

[†]Department of Applied Physics, Stanford University, Stanford, CA 94305-4035

TEL 415 723-2166; FAX 415 725-3377

Volume holography is an important candidate for data storage and data processing applications. Its advantages lie in the inherent high capacity of volume memory, fast access due to optical addressing, and fast transfer rates due to the parallel nature of holography [1]. Multiple holograms, or data pages, may be stored using angular multiplexing, wavelength multiplexing, and related techniques. Capacity is determined by the angular bandwidth of the signal, the number of holographic pages, and the acceptable level of noise due to crosstalk and other sources present in the system. Volume holography is also an important candidate for optical interconnects and wavelength division multiplexing in communications and computing systems. Frequently, the same criteria required for data storage coincide with those required for other applications.

An important property is the lifetime of holograms under normal use in a system. Hologram formation in photorefractive media is a result of the photoexcitation and redistribution of electrons, so that without further processing then media remain susceptible to erasure on readout of stored holograms. Among several techniques proposed to provide nondestructive readout of recorded data [2], thermally activated mobile ion compensation holds considerable promise [3]. Using this technique, a medium in which an electronic grating has been recorded is heated to a higher temperature, at which an ionic species becomes mobile and partially screens the electronic gratings. At this point the electronic and ionic systems represent two complementary constituent gratings that are out of phase. On cooling to room temperature, the ionic mobility is substantially reduced, so that the ionic grating decays on a time scale significantly longer than the electronic grating. During data readout, illumination affects the electronic grating, so that the electrons now redistribute to screen the ionic grating. The final strength depends on the initial electronic grating, the compensating ionic grating, and the residual electronic screening. When the screening is partial, the screened ionic grating results in a measure diffraction with a lifetime longer than an electronic grating.

In a variation of this technique, electronic gratings are recorded at the higher temperature. The ionic and electronic gratings are mutually screened, resulting in an ambipolar diffusion process that enhances the strength of the constituent gratings without increase in the net grating. On cooling to room temperature, electron screening upon illumination follows the same process, so that a stronger constituent ionic grating results in stronger net gratings.

From the perspective of physical optics, however, holograms recorded at high temperature undergo a change in character on cooling to room temperature due to temperature dependence in the index of refraction and anisotropic thermal expansion. In a volume Fourier holographic arrangement frequently used in holographic data storage, these effects result in the inability to reconstruct the entire field of view of an image due to the inability to match the reference beam to the entire continuum of grating vectors representing the hologram [4]. A critical issue, therefore, is to what extent the ambipolar diffusion results in stronger holograms, and, consequently, when the diffraction strengths of holograms recorded at low temperature and compensated at high temperature are comparable to holograms recorded at high temperatures.

In a photorefractive medium dominated by diffusion, the electronic transport is charac-

terized by the Debye number k_D [5]:

$$k_D = (e^2 N_R / \epsilon \epsilon_0 k_B T)^{1/2} \quad (1)$$

in which e is the charge of the electron, k_B is the Boltzmann constant, ϵ_0 is the permittivity of free space, T is the ambient temperature. The parameters of the material are dielectric constant ϵ , the density of photorefractive impurities, N , the density of oxidized impurities N° , and the density of reduced impurities $N^\bullet = (N - N^\circ)$, for which we identify an effective impurity density $N_R = N^\circ N^\bullet / N$. Grating wave numbers above the Debye number result in holograms limited in strength by the effective impurity density, and grating wave numbers below the Debye number result in holograms limited by diffusion. The strength of the hologram is greatest at the Debye number. Higher impurity concentrations result in higher Debye numbers and stronger index perturbations above the Debye number, but do not significantly increase the index perturbations at the current Debye number. It is therefore critical to affect the impurity properties so that the Debye number corresponds to the grating numbers used in data storage and optical communication applications. In perpendicular and reflection geometries used for these applications, respectively, the grating periods in high refractory oxide ferroelectrics are on the order of $0.1 \mu\text{m}$ at visible wavelengths. In high Curie temperature materials such as lithium niobate, this corresponds to an effective impurity concentration of 10^{17} cm^{-3} , but in low Curie temperature materials such as barium titanate this corresponds to an effective impurity concentration of 10^{19} cm^{-3} due to the higher dielectric screening.

Using techniques established in earlier work [6,7,8], we evaluate the performance of mobile ion compensation within the context of the Debye number. We first consider simultaneous writing and compensation at high temperature. Figure 1 shows the revealed, yet partially screened, ionic grating at room temperature. The spatial frequency is normalized to the Debye number. The results show that when the ion concentration is significantly greater than the effective impurity concentration, the revealed grating approaches the strength corresponding to a grating written by electron transport only. At the Debye number, when the ion concentration is comparable to the effective impurity concentration, the strength of the revealed grating is comparable. Recording at low temperature and subsequent compensation at high temperature results in somewhat different behavior. When the ion concentration is significantly high, the revealed grating approaches the strength of the initial electronic grating. At the Debye number, when the ion concentration is comparable to the effective impurity concentration, the strength of the revealed grating is again comparable, but somewhat lower than that for simultaneous writing. A direct comparison of the two cases (Figure 3) illustrates that at significantly high grating wave numbers the two techniques give comparable results. A final important consideration is the lifetime of revealed ionic holograms at room temperature [8]. The ionic decay rate is roughly proportional to the ionic concentration, so that wide variations in ionic response rate in otherwise untreated materials will be determined by evaluating optimizing a materials Debye number and ionic concentration. The transition point is when the concentrations are comparable at a Debye number equal to the grating number, suggesting this as a preferred operating point.

This research has been supported in part by the ARPA-Industry-University Photorefractive Information Storage Materials (PRISM) Consortium (MDA972-94-2-0008).

1. J. F. Heanue, M. C. Bashaw, and L. Hesselink, *Science* 265, 749 (1994).
2. L. Hesselink and M. C. Bashaw, *Opt. and Quantum Electron.* 25, S611 (1993).
3. D. L. Staebler, W. J. Burke, W. Phillips, and J. J. Amodei, *Appl. Phys. Lett.* 26, 182 (1994).
4. J. F. Heanue, K. Gürkan, M. C. Bashaw, R. De Vré, and L. Hesselink, "Thermal Fixing in Digital Holographic Data Storage," 1996 OSA Annual Meeting, Portland, Oregon (September 1996).
5. N. V. Kukhtarev, *Sov. Tech. Phys. Lett.* 2, 438 (1976).
6. M. Carrascosca and F. Agulló-López, *J. Opt. Soc. Am. B* 7, 2317 (1990).
7. G. Montemezzani, M. Zgonik, and P. Günter, *J. Opt. Soc. Am. B* 10, 171 (1993).
8. A. Yariv, S. Orlov, G. Rakuljic and V. Leyva, *Opt. Lett.* 20, 1334 (1995).

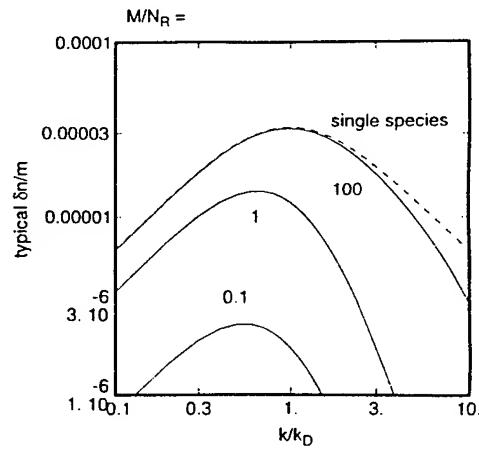


Figure 1: Revealed normalized index perturbation $\delta n/m$ at room temperature, for modulation depth m , after simultaneous writing and compensation at elevated temperatures.

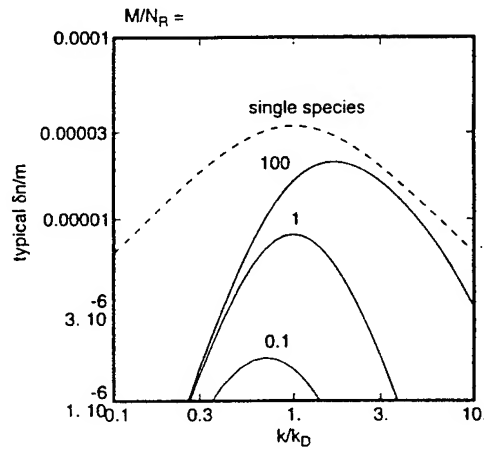


Figure 2: Revealed normalized index perturbation $\delta n/m$ at room temperature, for modulation depth m , after writing at low temperature and compensation at elevated temperatures.

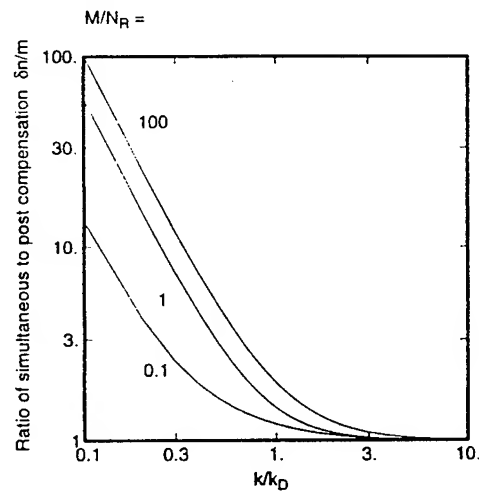


Figure 3: Ratio of revealed index perturbation for simultaneous compensation to revealed index perturbation for subsequent compensation.

Phase-conditioning techniques for leveling of the reference beam intensity in orthogonal phase-encoded multiplexing for holographic data storage.

Peter B. Catrysse*, Matthew C. Bashaw*, John F. Heanue†, Lambertus Hesselink*

* Department of Electrical Engineering, Stanford University, Stanford, CA 94305-4035

† Department of Applied Physics, Stanford University, CA 94305-4090

Phone: (415) 723-9127

Fax: (415) 725-3377

Volume holographic data storage is a promising alternative to current surface storage technologies, since it can provide simultaneously large digital storage capacity, fast data transfer rates, and short access times [1]. This is achieved by storing multiple holographic data pages in a common recording volume, while retaining the ability to retrieve any individual page. Multiplexing of data pages can be performed either at one wavelength, using angular or phase-encoded multiplexing, or at different wavelengths, using wavelength multiplexing. This investigation focuses on phase-encoded multiplexing, which for example allows direct binary arithmetic operations on recorded pages and enables data encryption [2].

Previous phase-encoded multiplexing work primarily addressed the issue of phase noise and its implications on system performance [3]. In this investigation we will study the spatial uniformity of the reference beam intensity, which is equally important. Non-uniformity results from intra-beam interference between the constituent waves and leads to spatial structure in the intensity pattern inside the recording medium. This can give rise to a loss of diffraction efficiency, because no optimal intensity match between the signal and reference beam is possible anymore. This in turn can lead to a loss of storage capacity. We present here a technique, that we will refer to as phase-conditioning, allowing us to obtain a more uniform reference beam intensity pattern, and to alleviate to some degree the possible loss of capacity in phase-encoded multiplexing systems.

In phase-encoded multiplexing M orthogonally phase-coded reference beams are used to store M different data pages. Each reference beam consists of a set of M monochromatic plane waves carrying a specific phase. The beam is generated using a phase spatial light modulator (PSLM) and a lens. The horizontally displaced pixels of the PSLM, described by the position vectors r_l , are thus transformed into a set of plane waves, denoted by the corresponding wave vectors k_l . The M pixels are modeled as point-sources, but a more realistic rectangular pixel shape may be considered. The i -th reference beam $R_i(\mathbf{r})$, carrying the i -th code, is given by

$$R_i(\mathbf{r}) = |R_0| \sum_{l=1}^M r_{il} \delta(\mathbf{r} - \mathbf{r}_l) \xrightarrow[\text{by lens}]{\text{Transform performed}} R_i(\mathbf{r}) = |R_0| \sum_{l=1}^M r_{il} e^{ik_l \cdot \mathbf{r}} \quad \text{with} \quad r_{il} = \frac{e^{i\phi_{il}}}{\sqrt{M}}$$

where r_{il} is the normalized amplitude of the l -th pixel of the i -th code (Figure 1) and $|R_0|^2$ the average intensity. We are investigating here one type of orthogonal phase codes, namely binary Walsh-Hadamard (WH) codes for which all M phases ϕ_{il} are either 0 or π , where M is a power of two. These codes have been successfully applied for phase-encoded multiplexing [4]. Their spatial spectrum after transformation, however, exhibits a large dynamic range. We define dynamic range as the root-mean-square (RMS) intensity value of the spectrum and denote that a perfect uniformity is characterized by a dynamic range equal to one. The large dynamic range yields pronounced spatial intensity structure, inside the recording medium, as shown in Figure 2a for a typical WH code with respectively $M = 2, 4, 16$, and 256 elements. Our goal is to achieve

more efficient spatial intersection of signal and reference beam, as characterized by a low intensity RMS value inside the recording medium, thus yielding a reduction in the loss of capacity. This is realized by maximizing the spatial uniformity of the reference beam intensity by means of an intensity leveling step, that we will call phase-conditioning. Phase-conditioning is performed by adding an additional phase ϕ_l to each pixel. To retain orthogonality, this additive phase must be the same for every code. Rewriting the code vectors $R_i(\mathbf{r})$ in a more convenient notation $|R_i\rangle$, and describing the method using a matrix operator \hat{U} yields [2],

$$|R_i\rangle = |R_o\rangle \left| \sum_{l=1}^M r_{il} e^{ik_l \cdot \mathbf{r}} \right\rangle \quad \Rightarrow \quad \hat{U}|R_i\rangle = |R_o\rangle \left| \sum_{l=1}^M r_{il} \hat{U}_{il} e^{ik_l \cdot \mathbf{r}} \right\rangle$$

For unconditioned codes we have orthogonality, $\langle R_i | R_j \rangle = \delta_{ij}$, and after phase-conditioning we should retain this essential property, $\langle R_i | \hat{U}^\dagger \hat{U} | R_j \rangle = \delta_{ij}$. This puts a constraint on the matrix operator \hat{U} requiring it to be unitary.

Two types of phase-conditioning are possible. The first is random phase-conditioning, using random phases. This method has been applied for data encryption purposes [2] and is used here for intensity leveling. The second method is deterministic phase-conditioning, in which a deterministic phase sequence is applied. We show that generalized, object independent Schroeder codes $\phi_l = \pi l^2 / M$, derived from the original Schroeder codes [5], as developed for radar applications and implemented earlier for spectral leveling of the signal beam [6,7], can be used for our purpose. The improved uniformity for the spectrum of typical WH codes, using deterministic phase-conditioning can be seen in Figure 2b. Finally we show in figure 3 the leveling capabilities of both phase-conditioning techniques as a function of the number of pixels M on the PSLM. We obtain increasing leveling with increasing M , yielding a improvement of the dynamic range by an order of magnitude for a realistic number of 256 pixels on the PSLM. A quantitative evaluation of regained storage capacity due to phase-conditioning, however, involves a more detailed analysis of several other systems parameters and merits further investigation.

In conclusion, we present phase-conditioning techniques allowing substantial increase in spatial uniformity of the intensity of phase-encoded reference beams, positively affecting storage capacity for a phase-encoded multiplexing system. Other deterministic phase-conditioning codes are under investigation as well as other strategies for improving the uniformity of the reference beam.

This research has been supported in part by the Advanced Research Project Agency/ National Storage Industry Consortium through the Holographic Data Storage System Project.

References:

1. J.F. Heanue, M.C. Bashaw, and L. Hesselink, *Science* **265**, 749-752 (1994)
2. J.F. Heanue, M.C. Bashaw, and L. Hesselink, *Appl. Opt.* **34**, 6012-6015 (1995)
3. M.C. Bashaw, J.F. Heanue, A. Aharoni, J.F. Walkup, and L. Hesselink, *J. Opt. Soc. Am. B* **11**, 1820-1836 (1994)
4. C. Denz, G. Pauliat, G. Roosen, and T. Tschudi, *Opt. Commun.* **85**, 171-176 (1991)
5. M.R. Schroeder, *IEEE Trans. Inf. Theory* **IT-16**, 85 (1970)
6. David C. Chu and J.W. Goodman, *Appl. Opt.* **11**, 1716-1724 (1972)
7. H. Akahori, *Appl. Opt.* **12**, 2336-2343 (1973)

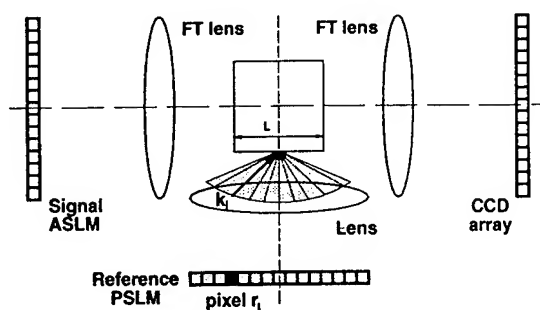


Figure 1: Phase-encoded multiplexing setup.

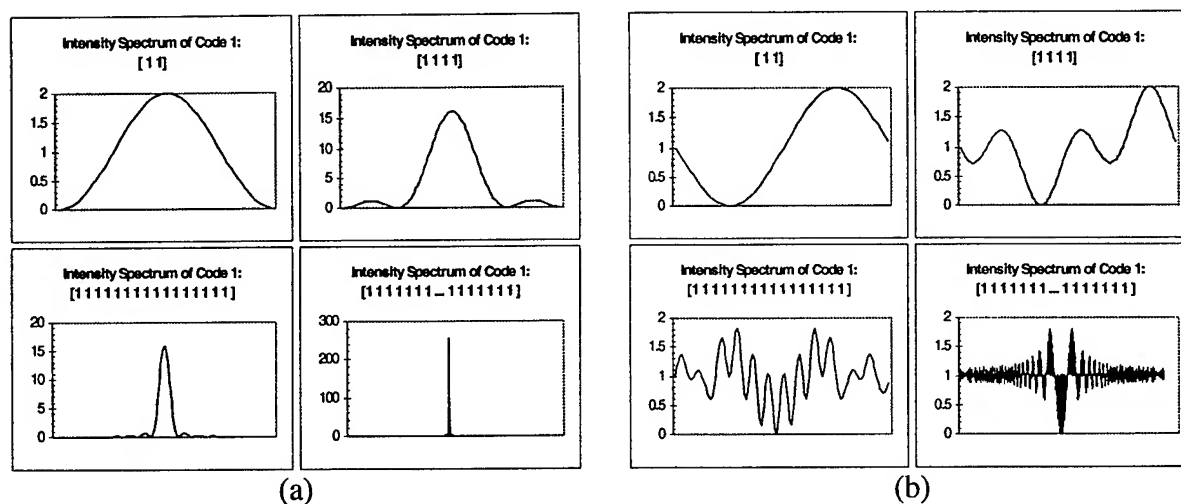
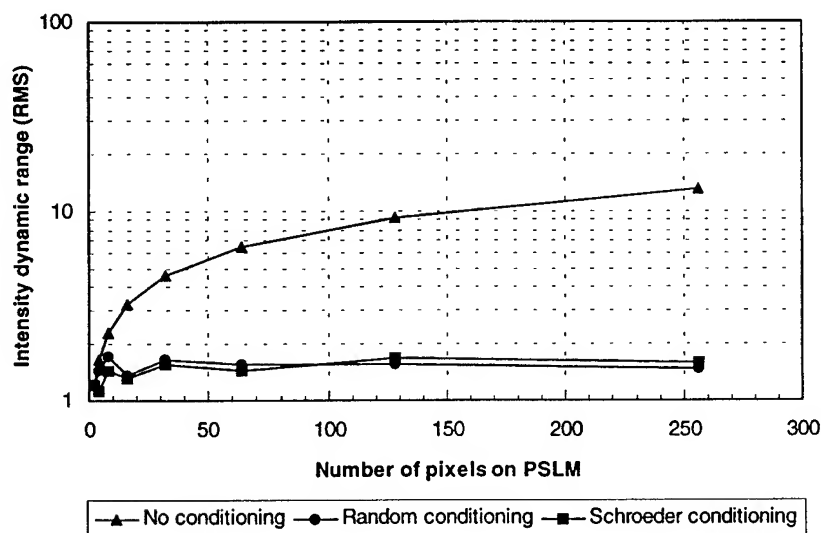
Figure 2: WH-code intensity pattern (a.u.) versus width L of the recording medium for $M = 2, 4, 16, 256$: (a) without and, (b) with Schroeder deterministic phase-conditioning.

Figure 3: Intensity dynamic range (RMS) with and without phase-conditioning versus number of pixels on phase spatial light modulator (PSLM).

Digital Quasi-Phasematched Two-Color Nonvolatile Holographic Storage

E.S. Bjornson

Department of Physics Stanford University
Durand Bldg 003, Stanford University, Stanford, CA 94305
Phone: (415)497-4855 Fax: 415 725-3377

M.Bashaw and L.Hesselink

Department of Electrical Engineering Stanford University
Durand Bldg 353, Stanford University, Stanford, CA 94305
Phone: (415) 723-0470 Fax: 415 725-3377

1. INTRODUCTION

One difficulty for the successful implementation of holographic data storage is having the ability to read data without affecting the data. Thermal fixing[1] as well as two-photon techniques[2] have been investigated as possible solutions. Reading data with a wavelength other than that which the data had been written is another viable alternative. Furthermore, choosing a reading wavelength that corresponds to a laser of a more favorable size, price, or ease of use could also be a benefit of such a system. Kùlich has previously investigated how to minimize the error induced due to reading and writing using different wavelengths by reading data with a spherical beam[3]. Psaltis et al. later introduced a formatting technique to allow a page to be read with a different wavelength by writing the page of data in pieces using several reference angles[4]. For digital data to be accurately read with an acceptable amount of mismatch, a three-dimensional mapping of the data must be applied to a system using this formatting technique. Optimization of such a system then requires the investigation of mismatch as a parameter effecting the diffraction efficiency.

2. MAPPING BETWEEN TWO COLORS

Although two-color setups may be used for many data storage systems, this paper will discuss angular multiplexing where the rotation axis of the reference beams is defined to be \hat{x} . It is assumed that digital data is desired to be read from a rectangular grid by the use of a camera. Throughout this paper, subscripts of R , W , σ , and ρ will be used to indicate reading, writing, signal beam and reference beam respectively. For writing to form a grating that can be read without mismatch, Bragg matching is needed as shown in Fig. 1 where k is a wave vector and K is the grating vector (i.e. $k_{\sigma W}$ is the wave-vector for the writing signal beam). Due to the angular separation between the reading and writing signal beams, the ideal configuration of the system is to have the surface where the writing beam enters the crystal and the surface where the reading beam exits the crystal being non-parallel. This paper will use such a system as shown in Fig. 2 with lenses being used for the Fourier transforming of the signals.

In three dimensions, equating the grating needed for the reading to the grating formed from the writing gives a vector equation allowing the solution of the writing signal and reference beams to be determined. The resulting relationship of reading and writing angles when limited to two-dimensions has been previously determined [5] and is illustrated in Fig. 3. From this it can be seen that the mapping from reading to writing is linear for small angles. A page of data is defined to be the data written by the signal beam at a single reference angle and may be viewed as the composition of many plane-waves. Thus Fig. 3 also shows that a single reading page may correspond to an entire range of writing reference angles and therefore cannot be written within a single page. With P representing the number of pages an approximate linear relationship can be found to be

$$P_W = N + R(P_R - 1) \quad (1)$$

where N is the minimum number of writing pages and R is the ratio of writing pages to reading pages. Because the precise reference angle correspondence for each data point will need to be approximated to the nearest writing page, strict Bragg matching cannot be achieved. Since the number of writing pages effects the diffraction efficiency, evaluation of this is an important factor of the system.

Each page of data to be read will contribute subsets of its data or "strips" to several writing pages, the width of which depends on the angular separation between reading pages and the separation between writing pages. Figure 4 shows a single writing page that has had contributions from 5 pages of data to be read. Similar to the mapping process between different wavelengths shown by J.Goodman[6], first order derivatives of the previously explained process can be used to approximate the magnification as being the ratio of reading wavelength to writing wavelength. Due to a varying angle between the intersection of the sphere of reading gratings and the

sphere of writing gratings, magnification within the grid may vary between the axes and within each strip. Non-linearity of the mapping process also introduces a curvature to the data needing to be written.

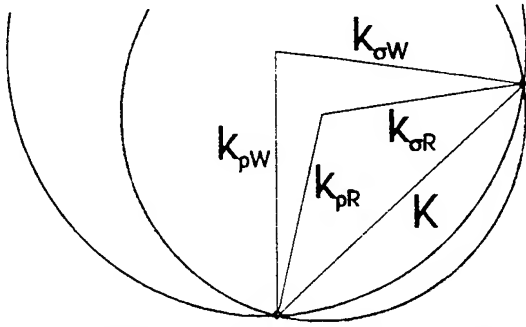


Fig 1. Matching a desired grating to be read with one color via a different writing color (2 dimensions)

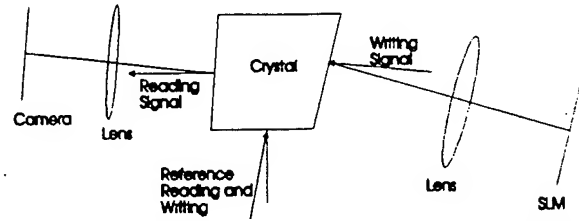


Fig 2. Example of a two-color holographic storage system

3. OPTIMIZING DIFFRACTION EFFICIENCY

Mismatch will result from not writing all of the points at exactly the reference angle calculated. Define $\Delta\theta$ as a point's variance from the ideal reference angle for that point. If only the point's reference angle were to vary from the ideal value, this would also result in an effect of the direction of the signal when read. Thus, the direction of the writing signal must also be modified so as to prevent such a change in reading position. When this is taken into account the resulting mismatch of the modified readout may be approximated as

$$\xi = \frac{\Delta\theta L k_W}{2 \cos(\theta_{pR})} \frac{(\hat{k}_{pW} \times \hat{k}_{\sigma W}) \cdot \hat{x}}{\hat{k}_{\sigma R} \cdot \hat{k}_{\sigma W}} \quad (2)$$

where L is the length of the sample, $k_W = 2\pi/\lambda_W$, and θ_{pR} is the angle between the reading reference beam and the normal to the crystal's surface. Thus mismatch is proportional to the difference in the actual reference angle used and that which would produce the ideal grating.

Because diffraction efficiency is inversely proportional to the square of the number of writing pages it is critical to decrease the number of writing pages. Define Δk_{pW} (Δk_{pR}) as the separation in the z-components of writing (reading) reference wave-vectors. The simplest method of decreasing the number of writing pages is increasing Δk_{pW} and thus writing more data on each page. Unfortunately, as Δk_{pW} increases, so does the range of mismatch, which itself decreases the diffraction efficiency. Thus there is an optimum value for Δk_{pW} that will now be evaluated.

Although the modification from the ideal writing reference angle will vary from point to point, no point will have a difference of more than half of the separation between adjacent writing pages. Thus when approximated for a 90° geometry, the diffraction efficiency of Eq. 2 will always be limited to

$$\xi \approx \Delta\theta k_W L/2 < \Delta k_{pW} L/4 \cos(\theta_{pW}) \quad (3)$$

With the diffraction efficiency obtainable with writing a single page being η_o , the diffraction efficiency of the point with the largest mismatch will be $\eta_{RW} = \eta_o \text{sinc}^2(\xi)/P_W^2$. For a given set of data we may write $P_W = NA_W/\Delta k_{pW}$ where NA_W is the numerical aperture of the writing reference vectors required for the given set of data. Combining these with equation 3 gives

$$\eta_{RW} = \eta_o \Delta k_{pW}^2 \text{sinc}^2(\Delta k_{pW} L/4 \cos \theta_{pW}) / NA_W^2 \quad (4)$$

Since no point's diffraction efficiency should be allowed to be zero, the limit must be imposed of

$$\xi < \pi \quad \text{or equivalently} \quad \Delta k_{pW} < 4\pi \cos \theta_{pW} / (k_W L) \quad (5)$$

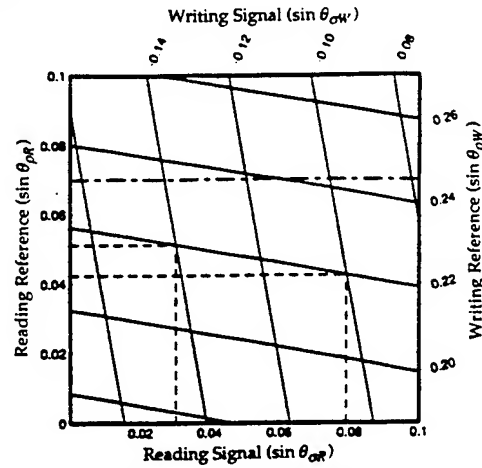


Fig 3. Mapping of signal and reference angles between reading and writing processes[5]

To maximize the diffraction efficiency the separation between writing pages should be chosen such that

$$\xi = \pi/2 \quad \text{or equivalently} \quad \Delta k_{\rho W} = 2\pi \cos \theta_{\rho W} / (k_W L) \quad (6)$$

Thus points whose writing reference angle corresponded exactly to a writing page would have no mismatch, while points with writing reference angles in-between writing pages would have mismatches as large as $\pi/2$. The separation between writing pages within a two-color system therefore has both an upper limit and a specific value for optimizing the system's diffraction efficiency.

Such a large variance in mismatch will significantly impact the crosstalk. The separation between reading pages is usually chosen so that the contribution of one page's data to the reading of another page falls near to a minimum as shown in Fig 5. Thus if crosstalk were an important factor in being able to accurately read the data, variance in mismatch may need to be further restricted below the previously calculated value such that the mismatch between different pages lies closer to a minimum. Commonly crosstalk can be reduced by increasing the separation between adjacent reading pages. Since the separation of writing pages has a definite upper limit, it cannot be increased along with the separation between reading pages. Thus such increases would significantly decrease R .

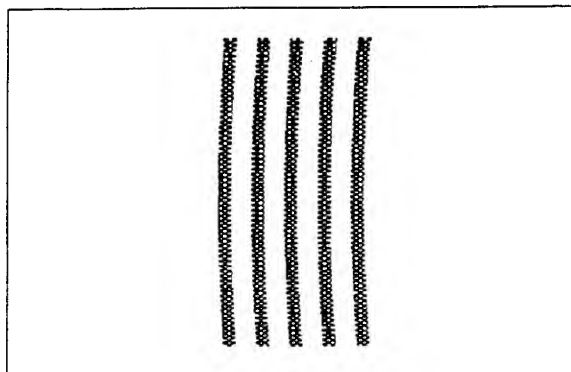


Fig 4. Example of a writing page resulting from 5 pages of data to be read ($\lambda_R=633\text{nm}$ and $\lambda_W=514\text{nm}$)

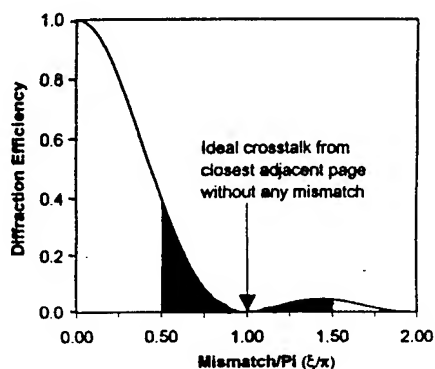


Fig 5. Crosstalk contribution between adjacent pages. Shaded range indicates mismatch present in optimized system.

4. CONCLUSION

Unwanted loss of data can be reduced by reading with a different wavelength than that which the data had been written. Such a system would require modification of the data before it is written so that the writing process will produce the gratings needing to be read. Each grating desiring to be read must be written not at the ideal writing reference angle, but rather at the nearest writing page. This causes each reading page to contribute data to multiple writing pages as well as inducing Bragg mismatch. This effect of mismatch was then used to optimize the diffraction efficiency of a two-color system. Further calculations are needed to understand the contributions to crosstalk from the mismatch as well as the possibility of canceling the effects of crosstalk by modifying the data being written.

REFERENCES

1. D.Staebler, W.Burke, W.Phillips, J.Amodei, "Multiple storage and erasure of fixed holograms in Fe-doped LiNbO_3 ," *Appl. Phys. Lett.* **26**, 182 (1975).
2. D.von der Linde, A.Glass, K.Rodgers, "Optical storage using refractive index changes induced by two-step excitation," *J. Appl. Phys.* **47**, 217 (1976).
3. H.Külich, "A new approach to read volume holograms at different wavelengths," *Optics Commun.* **64**, 5 (1987).
4. D. Psaltis, "Nonvolatile storage in photorefractive crystals," *Opt. Lett.* **19**, 210-212 (1994).
5. M.C. Bashaw, "Impact of materials properties on multiplex holographic data storage," *SPIE-proceedings*, Vol. 2176, pp. 132-143, 1994.
6. J.W. Goodman, *Introduction to Fourier Optics*, pp. 215-8. McGraw-Hill, Inc., San Francisco, CA, 1968.

Storage and readout of high resolution holographic images for optical data storage and security applications

Koichi Sayano and Feng Zhao
Accuwave Corporation
1651 19th St., Santa Monica, CA 90404
(310) 449-5540 (Ph)
(310) 449-5539 (FAX)

One of the major challenges with high density holographic data storage is readout of the data, which by necessity is comprised of high resolution features, onto the detector array.¹ With minimum feature size of $10\ \mu\text{m}$ or less being proposed for high data capacity, the optical system resolution requirement is approaching the diffraction limit of available optics. Low f-number, high line resolution, 1:1 magnification, wide field of view optics is extremely expensive, but necessary to image large, high resolution arrays of data from proposed holographic memory devices. Recently, we applied optical phase conjugation in the holographic recording process to correct for Fresnel diffraction and image aberration during readout, eliminating the need for the bulky and expensive optical imaging system.²

Figure 1(a) illustrates the recording process for volume holographic storage, where the object beam is modulated by a high resolution image, such as a high density spatial light modulator (SLM). Because of Fresnel diffraction, particularly for high spatial resolution features, the image diffracts as it propagates through free space, and this aberrated wavefront is recorded in the volume hologram. When the hologram is read out in the conventional form shown in Figure 1(b), the hologram represents a virtual object behind the crystal. Therefore, an imaging lens is needed to reconstruct the image onto the detector plane. For a high spatial resolution image, precise alignment of the lens (on all five axes) is necessary to avoid introducing additional aberrations and distortion.

To generate a real image of the recorded hologram without optics, the hologram is illuminated by the phase conjugate of the original reference wave so the readout is a phase conjugate reflection of the original object.³ The phase conjugate reflection exactly retraces the object beam, resulting in an exact reproduction at the detector plane, as shown in Figure 1(c).⁴ The real image is formed at the exact position of the original modulating object (during recording). Therefore, no lens is

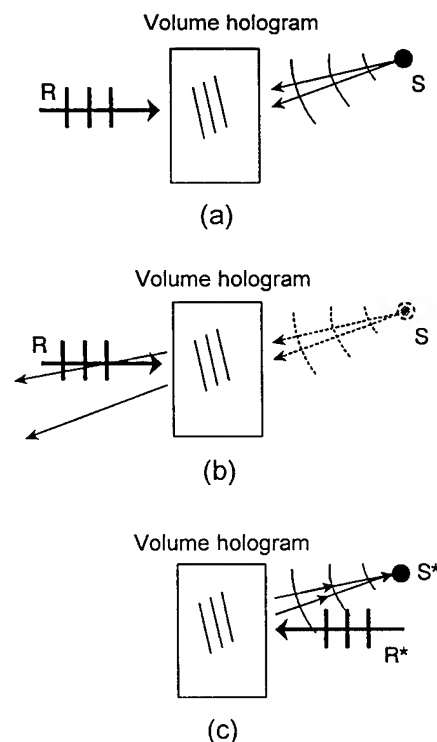


Figure 1

needed, which is a considerable savings in complexity and cost. Moreover, any Fresnel diffraction and phase aberration introduced during propagation of the optical signal between the object and the holographic element will be reversed during readout, with the necessary phase information stored in the hologram itself.

Figure 2 shows an image of a resolution chart that was recorded using the approach illustrated in Figure 1(a) and read out (as shown in Figure 1(c)) without the use of any optics. The hologram aperture was selected to have sufficient width to include the high resolution diffraction features. This image was one of 500 that were recorded in a 10 mm thick LiNbO_3 crystal using wavelength multiplexing. In the image shown in Figure 3, the image to detector distance was varied to show that the image is outside the near field approximation.

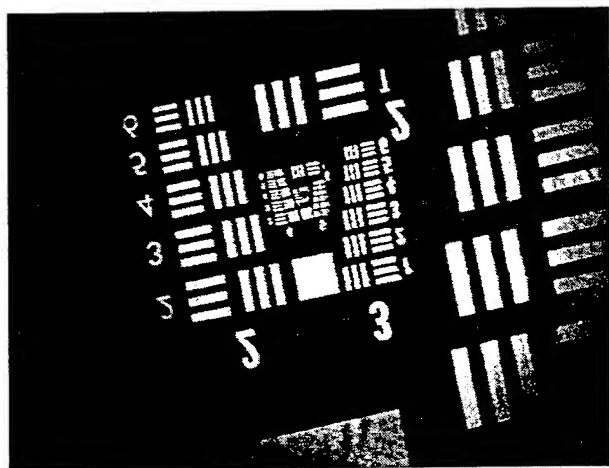


Figure 2

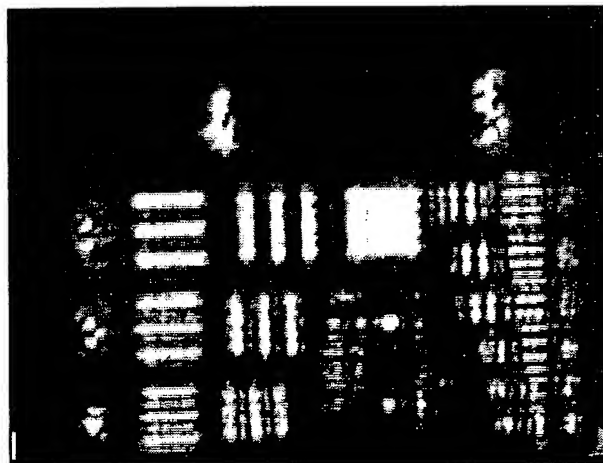


Figure 3

These results have significant impact on the potential for high capacity holographic memories, including: (1) significant cost savings from eliminating the need for the imaging lens for readout of the stored holograms; (2) simplified alignment by reduction of optical elements; (3) reduction in the effects of coherent noise and its impact on signal to noise ratio; and (4) smaller overall size of the memory system.

In addition to correcting for the distortion introduced by propagating through free space, phase conjugate storage can also be used in the presence of an external phase aberrator in the object beam path. Readout through the same phase distortion at the same position will exactly correct the aberrations and enable the image to be read, as shown in Figure 4. When no aberrator is used for readout, the image is undecipherable. Therefore, the phase aberrator becomes a necessary condition

for proper readout of the stored image. This presents significant opportunities in encrypted image storage, where the phase aberrator serves as an external decryption "key" that will be needed to decypher the image. This implementation also enjoys the advantage of not requiring imaging optics, unlike the phase code multiplexing approach that has been previously reported.

The results of this experiment, where an image was recorded using the phase conjugate holography scheme with a phase distortion intentionally inserted in the beam path, is shown in Figures 5 and 6. When the signal reverse propagates through the same phase distortion, the wavefront aberrations introduced by the aberrator are "reversed" and the original image is reconstructed, as shown in Figure 5. When the phase aberrator is removed, the aberrations introduced during recording are not corrected and the resulting image is scrambled. Figure 6 illustrates the scrambled readout image that was obtained using this plane wave for readout.

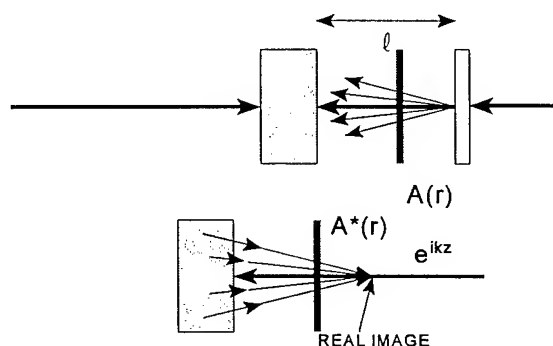


Figure 4

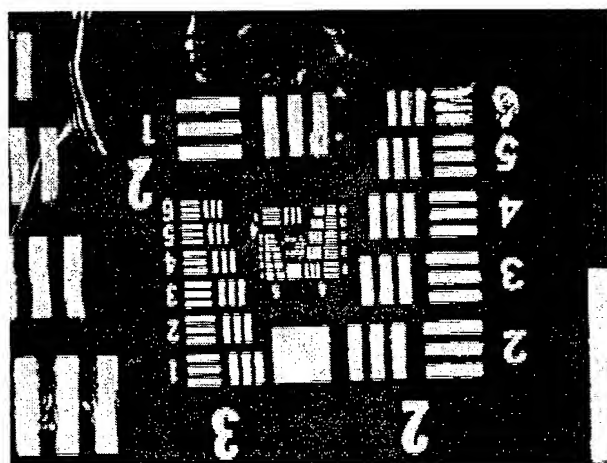


Figure 5



Figure 6

REFERENCES

1. L. Hesselink, J.F. Heanue, and M.C. Bashaw, paper MP-1, Optical Society of America Annual Meeting, Portland, OR (1995).
2. F. Zhao, and K. Sayano, paper CWF11, Conf. of Lasers and Electro-Optics, Anaheim, CA (1996).
3. J.W. Goodman, *Introduction to Fourier Optics* (New York, McGraw-Hill, 1968).
4. A. Yariv, *Opt. Commun.* vol. 21, p. 49 (1977).

Optical correlation of phase- and amplitude-encoded objects using wavelength-multiplexed holographic storage elements

Koichi Sayano and Feng Zhao
 Accuwave Corporation
 1651 19th St., Santa Monica, CA 90404
 (310) 449-5540 (Ph)
 (310) 449-5539 (FAX)

Optical image correlation has been demonstrated for recognition of patterns and images by comparing against stored reference filters corresponding to known images. Optical implementation of this operation is highly desirable because image correlation can be generated in an analog fashion using common optical elements, providing considerable speed advantages over digital computation. Spatial light modulators have been used as the filters in a VanderLugt correlator configuration, but low throughput and slow download times, particularly for a large number high resolution images, were major drawbacks. Using a wavelength multiplexed holographic element for storage of the reference image filters provides increased access speed, and the recent availability of visible wavelength, tunable external cavity semiconductor lasers, wavelength multiplexing becomes practical. In this paper, we report on an optical image correlation system using a holographic storage element for fast access speed and translation tolerance. Amplitude and phase encoded transparencies, as well as spatial light modulators, were used as the input image sources.

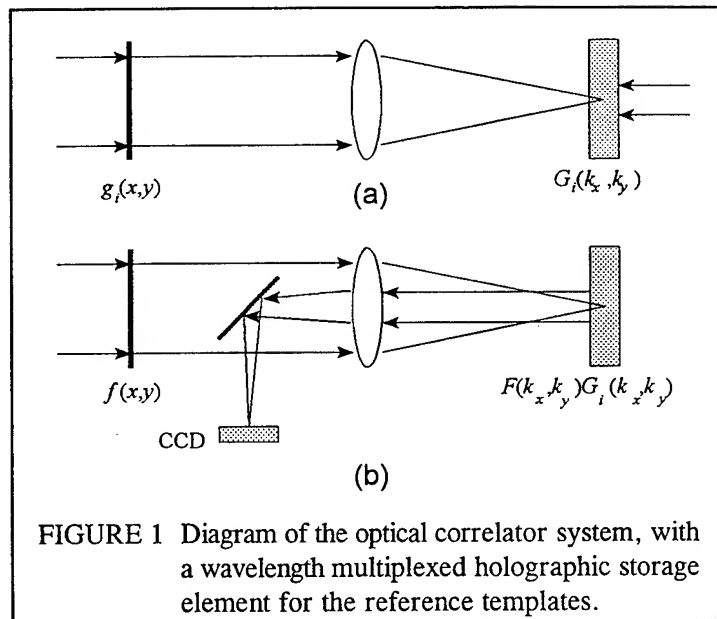


FIGURE 1 Diagram of the optical correlator system, with a wavelength multiplexed holographic storage element for the reference templates.

The optical image correlator demonstration is based on the standard $4f$ VanderLugt correlator, with a holographic element storing the reference templates and an SLM providing the input, as shown in Figure 1.^{1,2} Fourier transform holograms, recorded in a volume storage medium with a counter-propagating plane reference wave, serve as the stored image filters for generating the correlation with the input image. Two-dimensional Fourier transforms and inverse transforms are generated optically using a single lens. The readout signal falling on the detector is the correlation between the input test image and the stored image being addressed at that particular wavelength:

$$h_i(x,y) = \int_{-\infty}^{\infty} \int_{-\infty}^{\infty} F(k_x, k_y) G_i^*(k_x, k_y) dk_x dk_y \quad (1)$$

where F and G are the Fourier transforms of $f(x,y)$ and $g(x,y)$, respectively. A correlation experiment using

approach with amplitude modulated transparencies has been demonstrated.² As the next step towards a self-contained system, the correlator is being demonstrated with a ferroelectric spatial light modulator (SLM) as the input image source for readout, using the configuration illustrated in Figure 2. Since these SLM's are reflective, the polarizing beamsplitter cube with the rotating waveplate is used to reduce beamsplitter losses.

With any amplitude modulated image, a certain fraction of the available input light is being thrown away. This reduces the amount of optical power incident on the holographic element. For recording, longer exposure times will be required; during readout, the output signal to noise ratio will be lower. The latter is particularly an issue since total available power using a tunable semiconductor laser source is usually less than 5 mW. However, a phase-modulated object will have 100% transmission through the modulating object, resulting in increased optical throughput.

In a phase modulated transparency, the variation is in the phase of the wavefront, so the input image $f(x,y)$ is given by

$$f(x,y) = e^{[-i\varphi(x,y)]} \quad (2)$$

where $\varphi(x,y)$ is the phase modulation function. The correlation is obtained as described by Eqn. (1) and the Fourier transform of Eqn. (2). The holographic optical image correlator is particularly useful for use with phase modulated images because wavefront information is preserved in the volume hologram. SLM-based correlators, or pattern recognition systems relying on digital computation of the correlation integral, will not be able to preserve the phase modulation of the optical signal. This feature can be advantageously used in security verification and anti-counterfeiting applications, where the phase-encoded object can be used as a security emblem that is considerably more difficult to copy than visual devices.

Figure 3(a) and (b) illustrate an auto- and cross-correlation of a phase-encoded object using the holographic image correlator shown in Figure 1. A transparency with an embossed pattern of a fingerprint (so the thickness of the material is spatially varying) was used to record the reference filter. The same image generated the sharp peak shown in Figure 3(a), which is the auto-correlation. Figure 3(b) shows a cross-correlation, for which a plane wave input was used. With a dissimilar image (i.e. a different fingerprint pattern), the correlation intensity was even lower. The plane wave represents the worst case for cross-correlation because of the background dc component of the spatially modulated optical signal.

In a further variation of the phase encoded object theme, an image recorded in a volume hologram was used as the input image source for the optical correlator. Because of the high Bragg selectivity of volume holograms, copying of the encoded pattern becomes considerably more difficult. The auto- and cross-correlation results, shown in Figure 4(a) and (b), show even sharper signal to noise ratios. Figure 4(a) illustrates the auto-correlation, while Figure 4(b) shows the cross-correlation, again for a plane wave input.

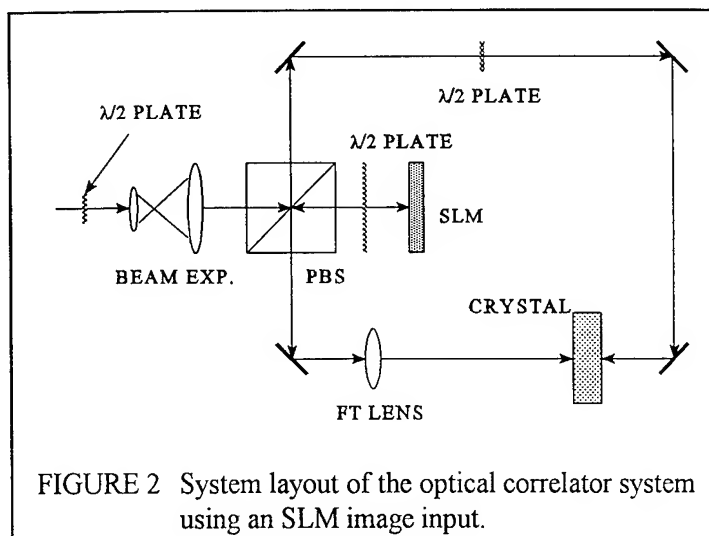
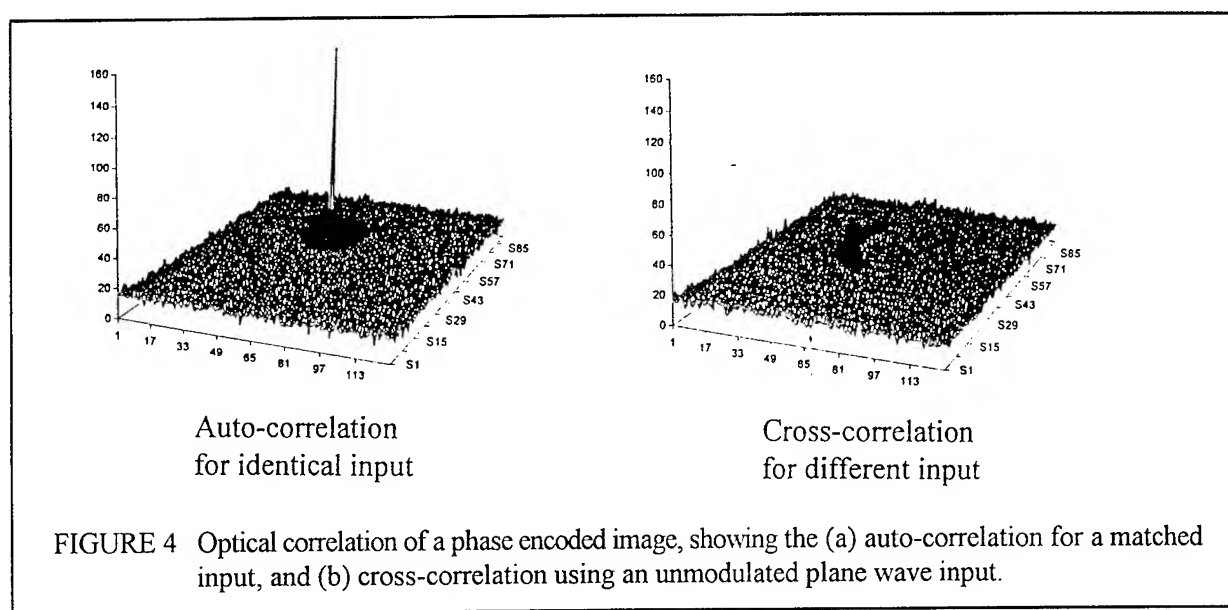
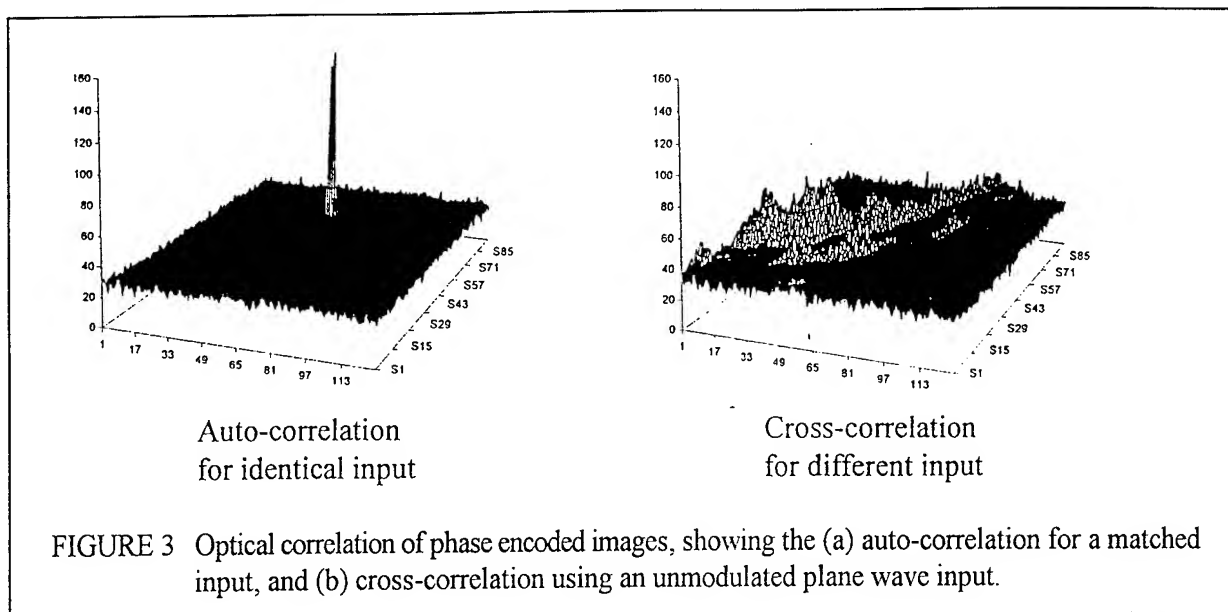


FIGURE 2 System layout of the optical correlator system using an SLM image input.



REFERENCES

1. A.B. VanderLugt, "Signal detection by complex spatial filtering," *IEEE Trans. Inf. Theory* IT-10, pp. 139-146 (1964).
2. K. Sayano, G.A. Rakuljic, and G. Brost, "Application of orthogonal data storage volume holography to optical image correlation," *Proc. SPIE* 2216, pp. 244-253 (1994).

Random Phase Diffuser Design for Holographic Storage

Deanna McMillen, Tracy D. Hudson, Amy S. Kransteuber

U.S. Army Missile Command
Redstone Arsenal, Alabama 35898-5248
(205)955-8154
(205)876-7360 fax

Don A. Gregory, Peter S. Erbach, and Cynthia G. Zabel

University of Alabama in Huntsville
Physics Department
Huntsville, Alabama 35899
(205)895-6276
(205)895-6873 fax

Diffusers have frequently been used in holography to overcome the problem of limited dynamic range in the recording material. The limited dynamic range is even more of a problem when recording the Fourier transform of an image as is done when making matched filters for Vander Lugt-type correlators. A diffuser designed to be used when holographically storing matched filters must spread the energy over the recording material, but not diffuse it so much that information is lost. The key is to design a diffuser whose parameters are dependent on the recording material and not so much on the input.

One solution to the diffuser design problem is a diffractive optical element consisting of an array of rectangles, each with a random phase delay ϕ , between 0 and 2π . The diffuser's transmittance can be described mathematically by

$$\text{rect}\left(\frac{x}{am}, \frac{y}{bn}\right) \exp\left[i \sum_{j=1}^m \sum_{k=1}^n \phi_{jk} \text{rect}\left(\frac{x}{a} - j + \frac{1+m}{2}\right) \text{rect}\left(\frac{y}{b} - k + \frac{1+n}{2}\right)\right] \quad (1)$$

The first rect function describes the external dimensions of the diffuser element am and bn . The terms in the exponential describe the $m \times n$ array of rectangles of dimension $a \times b$ that make up the diffuser. The indexes j and k identify each rectangle and associate it with a randomly assigned phase delay ϕ_{jk} . The diffuser is illustrated in Figure 1 with gray levels indicating various phase delays.

The diffuser is placed immediately after the input scene during recording. The Fourier

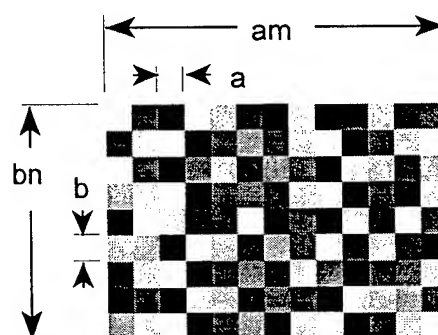


Figure 1 Random phase diffuser

transform lens immediately follows the diffuser. The field in the transform plane is proportional to

$$T = ab \mathcal{F}\{g(x,y)\} * \text{sinc}\left(\frac{ax_f}{\lambda f}, \frac{by_f}{\lambda f}\right) \sum_{j=1}^m \sum_{k=1}^n e^{i\phi_{jk}} \exp\left[-i\pi \frac{ax_f(2j-1-m) + by_f(2k-1-n)}{\lambda f}\right] \quad (2)$$

where $g(x,y)$ is the input scene. A significant parameter in Equation (2) is the sinc

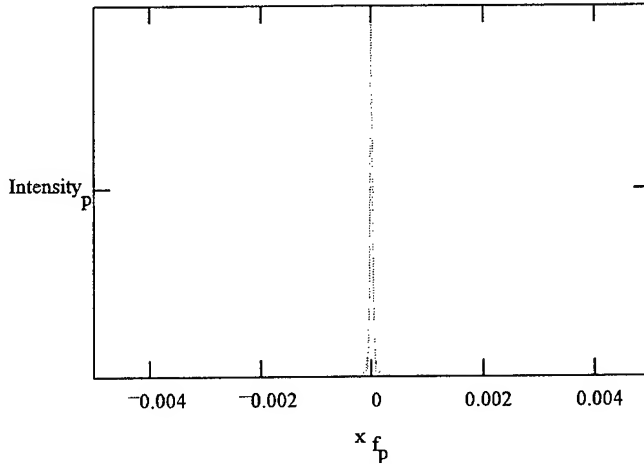


Figure 2 Normalized intensity profile of a rectangular aperture of dimension am

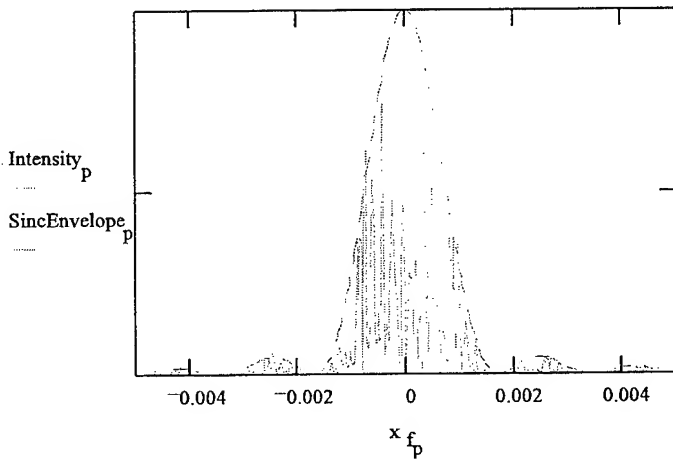


Figure 3 Normalized intensity profile of a rectangular aperture of dimension am with phase delay rectangle size $a = 300 \mu\text{m}$

perform pattern recognition while the diffused storage will effectively increase the capacity of the storage medium.

envelope. It determines the spread of energy. The sinc envelope is only dependent on the dimensions of the phase delay rectangles, a and b , the focal length of the transform lens f , and the wavelength λ . By varying these parameters, the amount of diffusion can be controlled and specified so the area the energy is spread over matches the area of the recording material.

Illustrating the simplest case of a plane wave object, Figure 2 shows the intensity profile for one dimension in the Fourier plane of a rectangular aperture with dimension $am \times bn$ corresponding to a single large phase delay rectangle. Figure 3 shows the one dimensional intensity profile for the same rectangular aperture, but with the phase delay rectangles reduced to $300 \mu\text{m}$ in size. The dotted line is the sinc envelope that appears in Equation (2). The vertical axis has been normalized in each of the figures.

This paper will show that an optical correlator utilizing angularly multiplexed holograms of diffused filters will retain the necessary scene information to

Pseudorandom Codes for Volume Holographic Storage Application

V. Morozov, K. Johnson, A. Lahrichi
University of Colorado at Boulder, OCSC, Boulder, CO, 80309

Motivation

The capacity of volume holographic storage depends largely on the number of holograms that can be multiplexed in a volume material and retrieved with minimum crosstalk and noise. There are different techniques under development for hologram multiplexing: spatial, angular, and wavelength multiplexing [1,2,3]. Spatial multiplexing is promising technology since it does not require any beam steering devices. The orthogonal codes were proposed as a solution to minimize hologram crosstalk noise [3]. It was found later that for minimum crosstalk noise, in addition to being orthogonal, the hologram address codes must be symmetric or antisymmetric around the midpoint [4]. In contrast to these investigations, instead of orthogonal codes, we propose to use pseudorandom codes for volume holographic storage applications such as: hologram spatial multiplexing, key words for associative memory, and memory based on image holography.

Pseudorandom Codes Properties.

Pseudorandom codes constitute a class of binary random codes with similar autocorrelation properties as those of purely random codes but with bounded crosscorrelation peaks [5,6,7]. In spread spectrum communications information is encoded with these codes so that they use the same bandwidth with minimum interference. It was estimated through computer simulation that the maximum amplitude of the cross-correlation function does not exceed $1.25 \sqrt{N}$, where N is the pseudorandom code length. It follows that the ratio of the crosscorrelation function maximum peak intensity to the autocorrelation function peak intensity (noise to signal ratio) is $\sim \frac{2.4}{N}$, and approaches a small value as code length increases. We verified numerically the correlation properties of pseudorandom sequences for the 2-D case. To generate pseudorandom sequences we select purely random sequence and then run it through a shift register algorithm to generate an infinite number of new sequences [5]. Then we select from this set two sequences which can be either the same or different and lay out one sequences over all the SLM rows and the other over all the SLM columns of a square SLM. By varying the one-dimensional sequence combinations we can construct an infinite set of two-dimensional pseudorandom codes. The results of numerical simulation are presented in Fig. 1 and Fig. 2. Fig.1 displays the autocorrelation functions for two different SLM masks consisting of 20x20 pixels and 2-D pseudorandom patterns are shown above each plot. Fig.3 shows the crosscorrelation of two different masks. Above each plot corresponding masks are shown. Notice the difference in scale for normalized intensity. We analyzed crosscorrelation properties of pure random codes and compared them with pseudorandom codes. The signal to noise ratio for a set of 2-D random codes varies from 1/4 to 1/30. As a result of this simulation we may conclude that purely random codes are not feasible for application in volume holographic storage since the intensity of the crosscorrelation function peaks may fluctuate significantly. Experimental results on the hologram spatial multiplexing in lithium niobate with purely random and pseudorandom codes confirmed theoretical predictions about superiority of correlation properties of pseudorandom sequences.

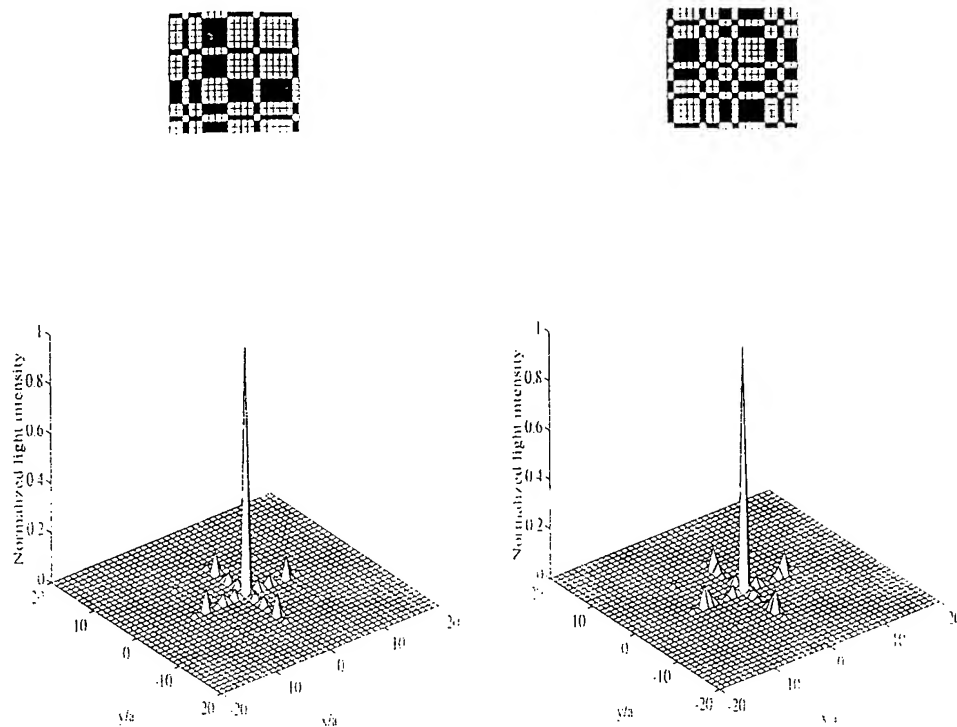


Fig. 2 Autocorrelation functions for the 2-D 20 elements pseudorandom code

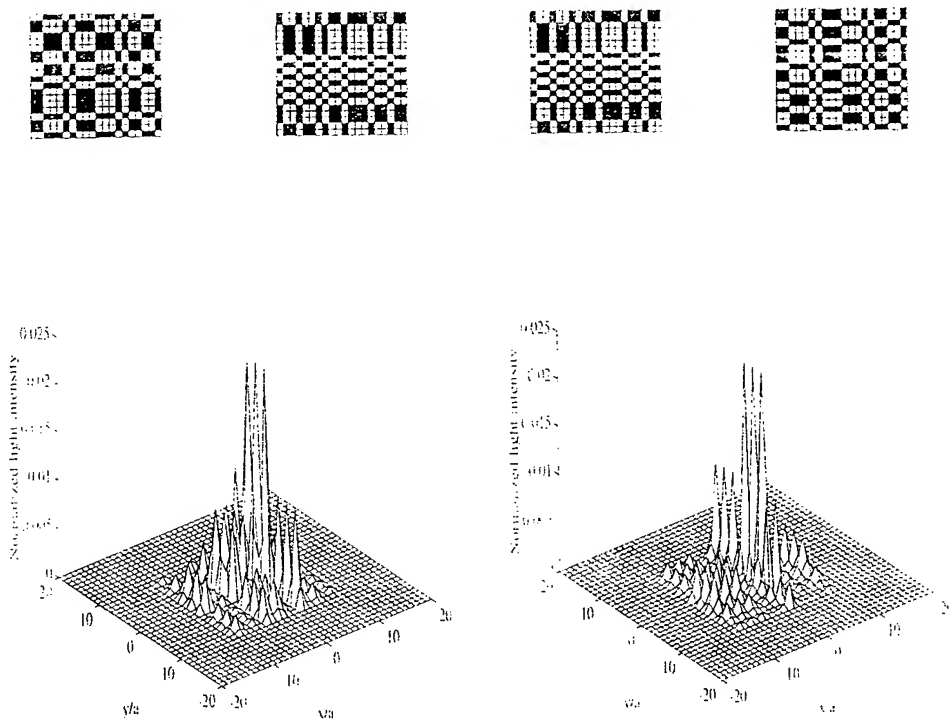


Fig. 3 Crosscorrelation functions for the 2-D elements pseudorandom codes

Pseudorandom codes as key words in associative memory

A good example of the usefulness of pseudorandom codes is an associative memory that utilizes pseudorandom sequences as key words. Associative memory based on an optical correlation method has been discussed already in literature[9,10] and an optical scheme is depicted in Fig. 3.

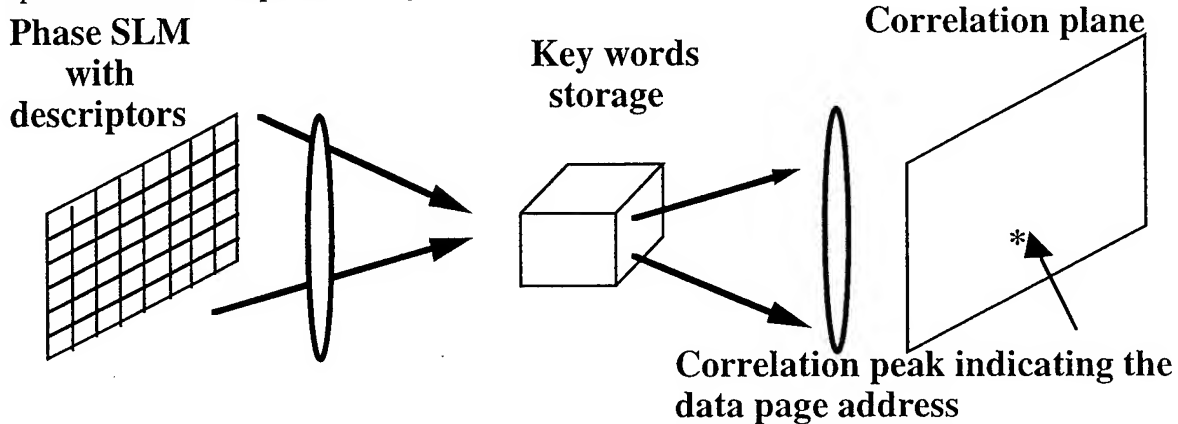


Fig. 3. Optical scheme of associative memory based on correlation search of key words.

The implementation of that idea suffered from the fact that the discrimination between the cross-correlation peaks representing noise and autocorrelation peak representing signal was a serious problem. Almost digital accuracy of the data address finding would be possible due to unique auto and cross-correlation properties of the pseudo-random codes.

Another aspect of pseudorandom codes utilization in volume storage will be discussed.

References.

1. F.Mok, "Angle-multiplexing of 5000 holograms in lithium Niobate", Opt. lett. 18, 915-917 (1993).
2. G. Rakuljic, V. Leyva, and A. Yariv, "Optical data storage by using orthogonal wavelength-multiplexed volume holograms", Opt. Lett. 17,20, 1471-1473 (1992).
3. C. Denz, G. Pauliat, G. Roosen, and T. Tschudi, "Potentialities and limitations of hologram multiplexing by using the phase-encoding technique," Appl. Opt. 31, 26, 5700-5705 (1992).
4. A. Hermanns, Department of Physics, University of Colorado, Boulder, CO, Ph.D. thesis 1994.
5. T. Lewis and W. Payne, "Generalized Feedback Shift Register Pseudorandom Number Algorithm," J. Assoc. Comput. Mach. 20,3,456-468 (1973).
6. A. Arvillas and D. Maritsas, "Partitoning the Period of a Class of m-sequences and Application to Pseudorandom Number Generation," J. Assoc. Comput. Mach.25,4,675-686 (1978).
7. V. Morozov, "Theory of holograms formed using a coded reference beam", Sov. J. Quantum Elect. 7,8, 961-964 (1977).
8. S. Park and K. Miller, "Random Number Generators: Good Ones are Hard to Find" J. Assoc. Comput. Mach. 31, 10, 1192-1201 (1988).
9. G. Knight, "Page-oriented associative holographic memory", Appl. Opt., V. 13, N.4, 904-912 (1974).
10. G. Knight, "Holographic associative memory and processor", Appl. Opt. V.14, N.5, 1088-1092 (1975).

"Holographic Digital Storage Beyond the Diffraction Limit. Is It Possible?"

Conceptual Analysis of Holographic Digital Storage with Synthetic Aperture"

Valentine Morozov

University of Colorado at Boulder

Boulder, CO, 80309-0525

phone 303-492-0478 fax 303-492-3674, morozov@boulder.colorado.edu

Motivation

Holographic digital storage is a promising technology for a Tbit memory with fast access time. Nevertheless, a competition with magnetic storage in terms of storage capacity remains strong due to continuing progress in magnetic storage development. New innovative ideas are needed to increase holographic storage capacity beyond the limits imposed by diffraction limits.

Synthetic-aperture radar in microwaves

One of the most successful applications of optical information processing technology has been in the formation of high-resolution maps from data collected by synthetic aperture radar. An aircraft carries a small, broad beam antenna that transmits radar pulses from a sequence of positions along the flight path (Fig.1). The phase and amplitude of radar returns are recorded along the flight path. The knowledge of phase and amplitude of the returns allows for a spatial resolution that is significantly better than the antenna beam resolution.

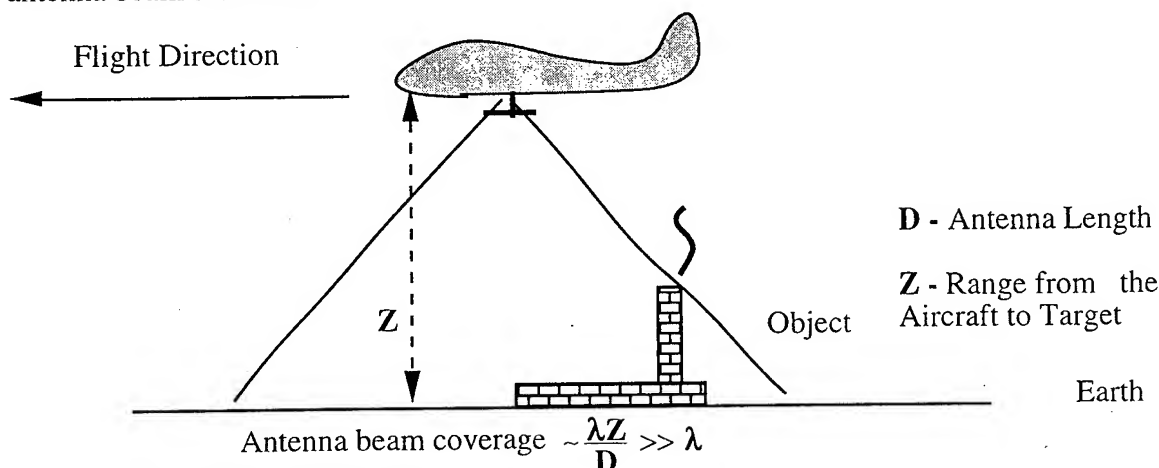


Fig. 1 A schematic of sidelooking radar geometry

Optical super resolution technique is actually an optical version of microwave synthetic aperture. Diffraction gratings are used to code the image and decode it optically with increased resolution.

Synthetic-aperture in the optical domain

Optical system with super resolution is presented in Fig.2. The object is imaged with an objective lens and an aperture stop is placed in front of the objective to simulate conditions of a microwave radar. The aperture stop diameter is significantly less than the lens diameter. Diffraction gratings are placed in object and image space. Due to diffraction on these gratings, a few super resolved identical images will appear at the image plane,

reducing the useful object field. Only one super resolved image of a point source is shown in Fig.2.

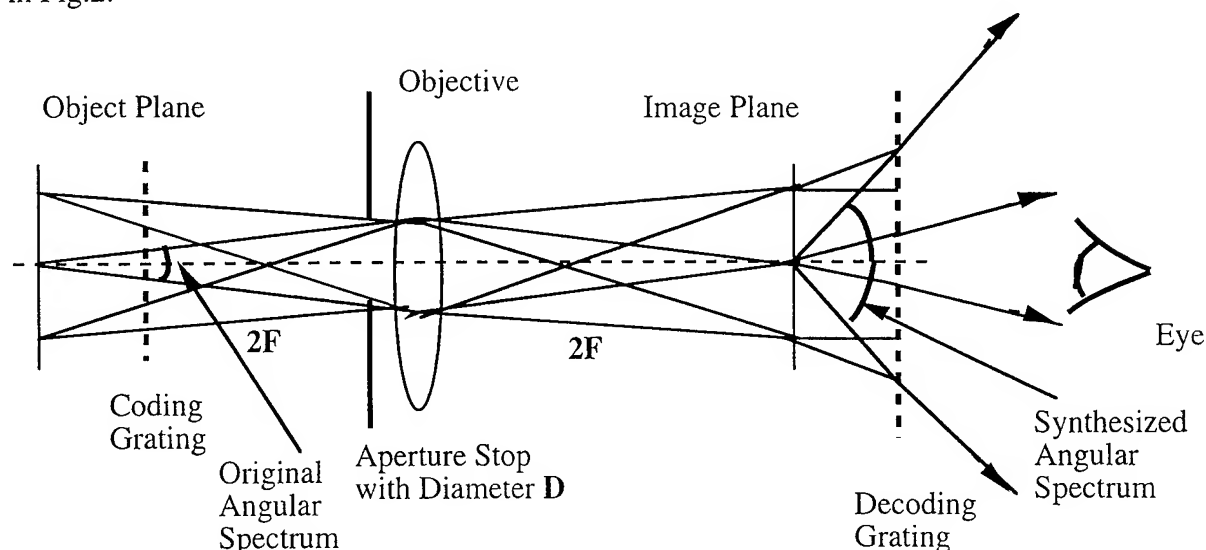


Fig.2. Optical super resolution scheme with diffraction gratings. Only one super resolved point source image is shown.

The optical scheme depicted in Fig.2 was analyzed theoretically and experimentally [1-6] in detail. It was found that gain in resolution is proportional to the number of diffraction orders. This is true until the diffraction spot size in the image plane approaches the light wavelength. The usable object field is reduced due to the multiple copies of the object created in the object plane by gratings (not shown in Fig.2). The essence of the super resolution technique is the redistribution of the degrees of freedom of the wavefield.

Holographic Digital Storage with Synthetic Aperture (HDSSA)

Holographic storage with synthetic aperture is essentially traditional holographic storage but modified by insertion of gratings at the recording and reconstruction stages [7]. Optical scheme for hologram recording with angular multiplexing is shown in Fig. 3. A diffraction grating is placed between the page composer and Fourier lens and multiple copies of data from the page composer are recorded on a 3-D storage medium.

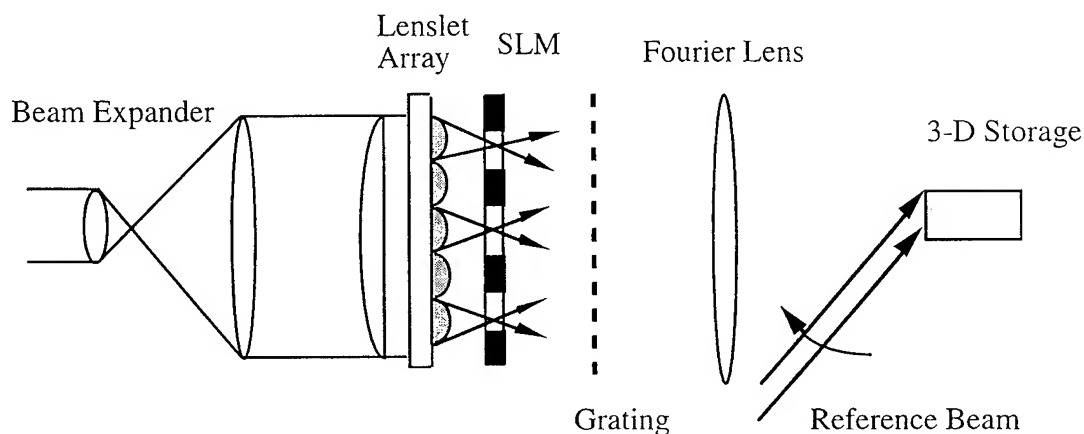


Fig. 3. Hologram recording in Holographic Digital Storage with Synthetic Aperture.

For hologram readout, the hologram is illuminated by a light beam at the same angle as it was recorded. A grating is placed between the Fourier lens and detector array. The function of this grating is a synthesis of data "points" at the image plane.

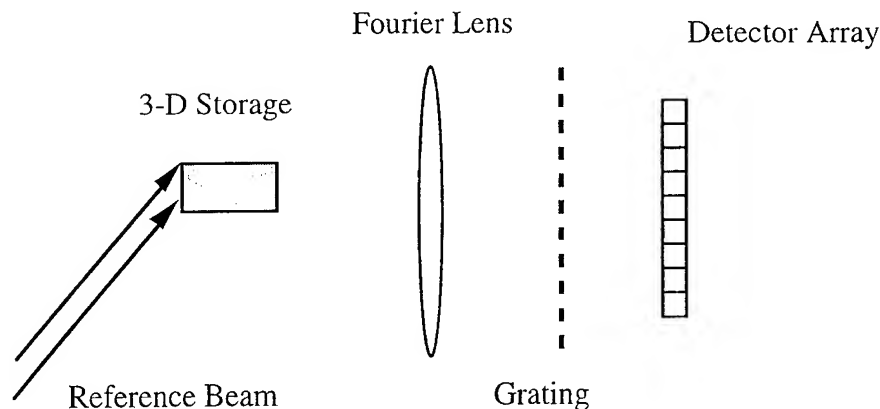


Fig.4. Hologram readout in Holographic Digital Storage with Synthetic Aperture.

The resolution in the image plane is now determined by the width of the grating auto-correlation function rather than by the diffraction of the hologram aperture. Super resolved image of a page composer will be reconstructed at the photo detector plane as a result of aperture synthesis by diffraction gratings.

There is one crucial circumstances for a HDSSA design. According to theory, the increase in resolution is achieved due to a reduction of the object field. This means that the image field is equally reduced. *A priori* knowledge of the data location at the page composer is needed to utilize holographic storage density above classical diffraction limit. Proper placement of the signals at the page composer allows to avoid cross-talk between different data "point" signals. It will be shown how synthetic aperture allows increasing holographic storage density by placing and retrieving a few signals within a light spot whose dimension is determined by the diffraction of the hologram aperture.

The price to pay for increased storage density and storage capacity is increased optical power needed to retrieve data. Multiple copies of the data page are reconstructed from the hologram and each copy consumes part of the optical power.

References

1. W. Lukosz, "Optical Systems with Resolving Power Exceeding the Classical Limit", JOSA, V. 56, N.11, pp. 1463-1472, 1966.
2. W. Lukosz, "Optical Systems with Resolving Power Exceeding the Classical Limit. II", JOSA, V. 57, N.7, pp. 932-941, 1967.
3. A. Bachl and W. Lukosz, "Experiments on Superresolution Imaging of a Reduced Object Field", JOSA, V. 57, N. 2, pp. 163- 169, 1967.
4. A. Malov, V. Morozov, I. Kompanets, and Yu. Popov, "Enhancement of the Resolving Power of Coherent Optical Systems by Aperture Synthesis Method", Sov. J. Quantum Electronics, V. 7, N 7, pp. 918-919, 1977.
5. A. Malov, V. Morozov, I. Kompanets, and Yu. Popov, "Formation of an Image in a Coherent Synthesized-Aperture System", Sov. J. Quantum Electronics, V. 7, N.9, pp. 1125-1130, 1977.
6. A. Malov, V. Morozov, I. Kompanets, and Yu. Popov, "Recording of Fourier Holograms in an Optical System with a Synthetic Aperture", Sov. J. Quantum Electronics, V. 10, N.2, pp. 162-166, 1980.
7. V. Morozov and Yu. Popov, "High-Capacity Holographic Memories with Synthesized Aperture", Sov. J. Quantum Electronics, V. 6, N.11, pp. 1265-1271, 1976.

Tuesday, July 9, 1996

NLO Poster Session: 2

NTuA 8:30 pm-10:30 pm
South Pacific Ballroom

Multiwavelength Optical Computing Using Optical Wave Mixing in Photorefractive Media

Weishu Wu and Pochi Yeh

Department of Electrical and Computer Engineering
University of California, Santa Barbara, CA 93106

Digital optical computing has been proposed for many years. However, much attention has only been focused on the spatial parallelism optics offers. The broad bandwidth of optical waves and optical media has been neglected for quite a long time. In multiwavelength optical computing, the broad bandwidth of optical waves and optics is utilized to increase the throughput of optical computing by using wavelength as an additional dimension.

Our first device for multiwavelength optical computing was a half adder [1]. A half adder consists of two operational units: an AND gate for CARRY operation and an XOR gate for SUM operation. In multiwavelength information processing including the multiwavelength half adder, each bit of a binary number was represented by a given wavelength. Binary number 1 was represented by the presence of the wavelength and binary number 0 represented by the absence of the wavelength. Different binary words were obtained by different combinations of wavelengths. The AND gate was implemented by phase-matched multiwavelength four-wave mixing in a photorefractive crystal. Using holographic interferometry, the XOR gate was implemented by a Mach-Zehnder interferometer in conjunction with a photorefractive crystal. The output from the XOR gate was then obtained by reading out the gratings using a multiwavelength beam [1].

Arithmetic addition using half adders is not an efficient operation. To obtain the final result, one has to repeat the operations until the outputs from the AND gate are zeros for all bits. One approach to avoid repeated operations is to use a full adder architecture. However, the conventional ripple-carry full adder is not suitable for multiwavelength optical computing due to its sequential bit-by-bit operation [2]. In order to implement a full adder, while still taking advantage of spectral parallelism, a carry lookahead device is necessary. To achieve this, we have proposed and implemented a carry lookahead device for a multiwavelength full adder [3]. By using a novel four-wave mixing scheme, all the carries could be calculated in advance without calculating both SUM and CARRY bit by bit. After all the carries were obtained, spectrally parallel SUM operation can be performed simultaneously. A schematic of a multiwavelength XOR gate with polarization encoding scheme [3] performing spectrally parallel SUM operations is illustrated in Fig. 2.

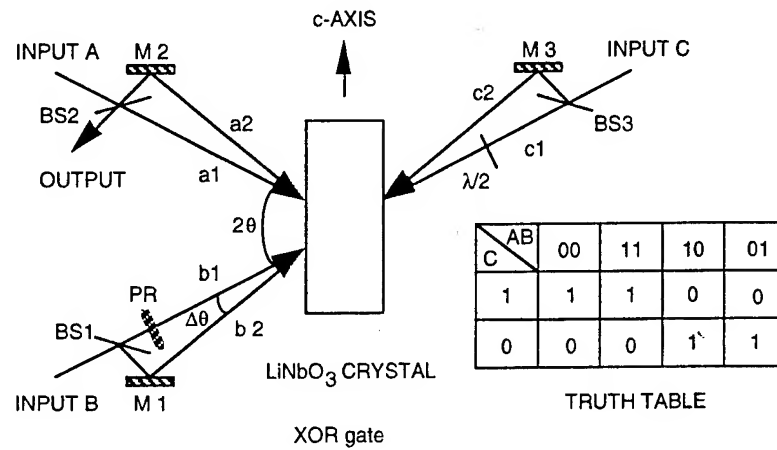


Fig. 1 An XOR gate used to calculate the SUM for a multiwavelength full adder.

Multiwavelength optical computing is also useful in fuzzy logic processing. Fuzzy logic can be in general regarded as an extension of binary logic. The major difference between binary logic and fuzzy logic is that the value of a fuzzy variable can be anywhere between 0 and 1, in contrast to two discrete values (0 or 1) for binary logic. Fuzzy logic and fuzzy set reasoning has potential application in fields such as pattern recognition and process control. According to fuzzy set theory, any control action described by a fuzzy clause [4] can be expressed by some fuzzy reasoning in forms of fuzzy complement, union, intersection and inference. A fuzzy relation R from $U=\{x\}$ and $V=\{y\}$ is defined as a fuzzy set on the Cartesian product $U \times V$, which is characterized by a characteristic function (a fuzzy matrix) $\mu_R(x, y)$. Given this relation R from U and V and a fuzzy subset A of U , a fuzzy subset B of V can be inferred by the compositional rule of inference:

$$\mu_B(y) = \max_x \{ \min \{ \mu_R(x, y), \mu_A(x) \} \}, \quad (1)$$

where $\mu_A(x)$, $\mu_R(x, y)$ are the bit-vector representation of fuzzy set A and fuzzy relation R , and \max and \min stand for fuzzy union and intersection operations. Thus, implementation of fuzzy logic inference described by Eq.(1) constitutes the basis of synthesis of fuzzy controllers.

To implement a multiwavelength fuzzy controller in photorefractive crystals, the fuzzy value is first 'digitized'. The fuzzy value of 1 (corresponding to full membership of an element to a given fuzzy set) is represented by a certain number of wavelengths (see Fig. 2). Accordingly, the degree of membership of an element is represented by the number of wavelengths present in the element. Fig. 3 shows a schematic diagram that describes the principle of operation of the photorefractive fuzzy controller. A fuzzy matrix (representing the fuzzy relation R between two fuzzy sets $U \subseteq X$ and $V \subseteq Y$) and a fuzzy vector (representing a fuzzy subset of U) are encoded as described above and placed at the front focal plane of lens L_1 . When the light beams from these two patterns intersect in a photorefractive crystal, which is placed at the rear focal plane of

lens L_1 , multiple gratings will be recorded inside the crystal. The number of gratings which can be recorded for a given pair, say A_i and R_{i1} , is determined by the smaller number of wavelengths present in the two elements. In this way, the fuzzy intersection operation (min) is achieved. Upon readout, the recorded gratings will be read out simultaneously by a read beam set containing all wavelengths. The read beams are from a spot located at the front focal plane of lens L_2 with the same focal length as L_1 . Due to the grating degeneracy (grating vectors are the same for different i), each wavelength will read all degenerate gratings. The number of wavelengths contained in the diffraction spot is hence equal to the maximum number of gratings recorded by all the element pairs. In this way, the fuzzy union operation (max) is achieved. The experimental results show that the fuzzy controller has a high accuracy and immunity to intensity fluctuation.

In summary, we have proposed and implemented several novel devices for multiwavelength information processing. For the first time, a multiwavelength fuzzy controller has also been analyzed and demonstrated in a photorefractive crystal. By virtue of the spectral parallelism, these novel devices, including the fuzzy controller, can significantly increase the capacity and information throughput.

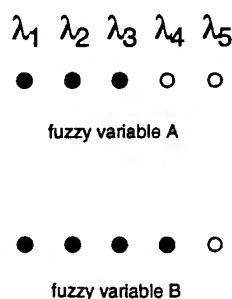


Fig. 2 Encoded fuzzy elements using wavelength encoding scheme for $\mu_A=0.6$ and $\mu_B=0.8$. O represents absence of a wavelength.

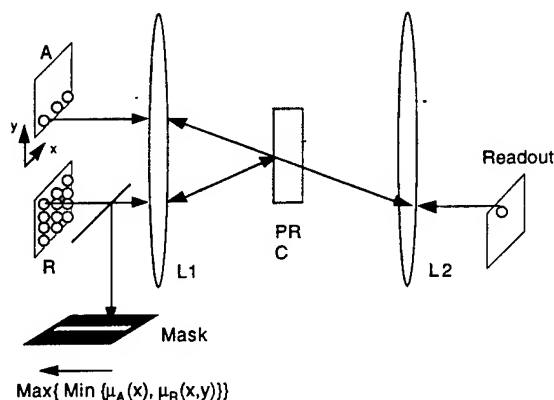


Fig. 3 Schematic diagram of a photorefractive fuzzy controller. Each element of the inputs is represented by several wavelengths according to its fuzzy value. The encoded inputs are placed at the front focal plane of the lens L_1 .

References:

1. P. Yeh, S. Campbell, and S. Zhou, Opt. Lett., 18, 903-905 (1993).
2. W. Wu, S. Campbell, S. Zhou, and P. Yeh, Opt. Lett. 19, 646-648 (1994).
3. W. Wu, S. Campbell, S. Zhou, and P. Yeh, Opt. Lett., vol. 18, pp. 1742-1744, 1993.
4. M. M. Gupta, Fuzzy Automata and Decision Processes, (Elsevier North-Holland, New York, 1977) Chaps. 5-7, pp. 77-131.

Dye-doped liquid crystal films for potential wave-mixing, limiting, and photorefractive applications at 1320nm.

Peter G. LoPresti and Daniel Hemphill
 Department of Electrical Engineering
 The University of Tulsa
 600 South College Avenue
 Tulsa, OK 74104-3189
 ph: (918)-631-3274
 fax: (918)-631-3344

It has been demonstrated that the nonlinear response of liquid crystalline materials can be beneficially modified through the introduction of a variety of dopant materials^{1,2,3}. Novel wave-mixing phenomena, reduced energy density thresholds for limiting applications, and recently permanent holographic gratings^{2,3} have been observed for visible wavelength inputs. In this paper, we report the results of a series of experiments conducted on liquid crystal samples appropriately doped to respond to infrared wavelengths (specifically 1320nm), where initial measurements show promise for a variety of applications in infrared processing and communications systems.

Thin film, homeotropically-aligned samples are constructed by sandwiching the doped nematic liquid crystal PCB between glass substrates, which for selected samples were ITO coated. Mylar spacers are used to control film thickness between 25 and 70 μm . Each sample is doped with a small amount of the laser dye IR-5, typically less than 2 percent by weight. The dye material improves the sample absorption at the wavelength of interest to 15cm⁻¹ and possesses a permanent dipole within its molecular structure.

Figure 1 shows the experimental setup used to evaluate the self-limiting effect in each sample. The shuttered output from a Nd:YAG laser operating at $\lambda = 1320\text{nm}$ is focused onto the liquid crystal film, and a HeNe laser is focused to the same point to provide a visual record of the limiting behavior. Both lasers are linearly polarized perpendicular to the nematic director when the sample is untilted, and the central intensity of each output is monitored as the laser power and sample tilt angle are varied. Similar behaviors are observed for all sample thicknesses investigated, though only those results obtained for 40 μm samples are presented here.

Significant self-limiting is observed in the ITO-coated, dye-doped samples even under normal incidence conditions. To identify the primary source of this self-limiting, the ambient temperature is maintained at a value (15.6 C) far below the nominal nematic-isotropic transition temperature of 35.3 C, and temporal decay of the effect after shutter closure is monitored. The absence of appreciable thermal contributions except at very long exposure times, and measured decay times on the order of several hundred milliseconds both indicate director re-orientation as the source of the observed self-limiting⁴. Theoretical modeling of the experiment using the measured absorption coefficient reinforces this conclusion. For sample tilt angles other than normal incidence, the threshold energy expectedly decreases, as is shown in the plots of Figure 2. Using an approximated infrared laser spot size of 150 μm , and correcting for reflections at the lens and the substrate, the self-limiting under the existing conditions is found to have a threshold power density of 14 W/cm².

An interesting result is obtained when the experiments are performed again on dye-doped samples constructed upon non-conducting substrates. Under the same conditions as described above, no self-limiting or other nonlinear optical response of any kind is observed. Thermal lensing is observed only for ambient temperatures near the phase transition temperature, and no reorientation-based phenomena are observed under any of the conditions attempted in the laboratory. A comparison of two samples of equal thickness and dopant levels under identical infrared radiation levels which demonstrates this result is presented in Figure 3. The output intensity level of the HeNe is unchanged regardless of tilt angle for the non-ITO-coated sample, while the sample made with conducting substrates shows significant self-limiting for the more oblique incidence conditions. Similar experiments conducted on samples constructed with one conducting and one non-conducting substrate still demonstrate self-limiting behavior, but to a lesser degree. It is our belief that the behavior observed arises from the interaction between the permanent dipole present in the dye material and the conducting surfaces of the substrates. It has been documented previously that liquid crystal dopants which enhance the value and anisotropy of the conductivity of the combined material can lead to the presence of galvanic effects and possibly the creation of a space-charge field³, both of which are subsequently responsible for altering the director orientation from that imposed by chemical treatment of the substrate surfaces. If such is the case, the possibility exists that permanent or near-permanent holographic gratings could be written in these dye-doped materials, opening up many interesting applications in optical processing and transmission systems. Experiments are currently underway to test this hypothesis and to document more fully the observed phenomenon.

1. T. Kosa, I. Janossy, Opt. Lett., **20**, 1230, (1995).
2. A. G.-S. Chen, D. J. Brady, Opt. Lett., **17**, 1231, (1992).
3. I. C. Khoo, Opt. Lett., **20**, 2137, (1995).

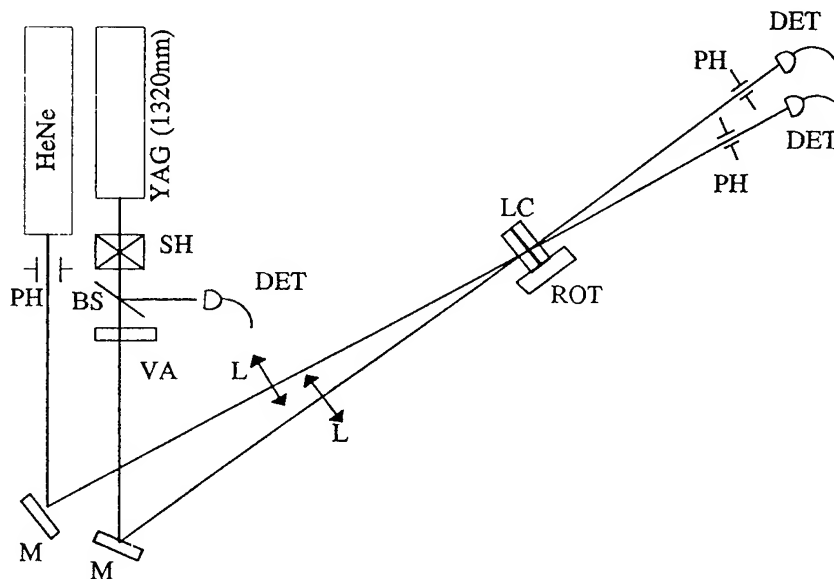


Figure 1: Experimental set-up for evaluating self-limiting effects. PH = pinhole, SH = shutter, VA = variable attenuator, BS = beamsplitter, L = lens, M = mirror, DET = detector, ROT = rotational stage for changing sample angle with respect to laser propagation direction.

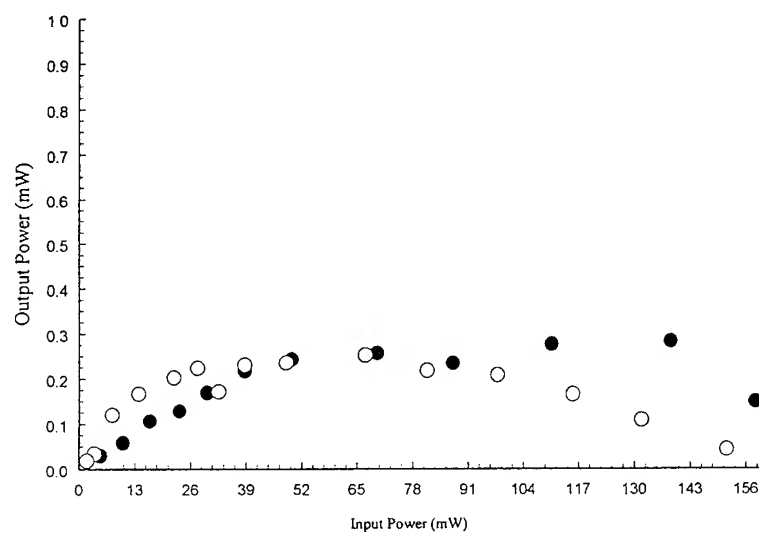


Figure 2: Power limiting curves for YAG laser at two different tilt angles. Open circles: 45 degrees, Solid circles: 0 degrees (normal incidence). Samples were dye-doped, 70 μ m thick, homeotropically aligned, and had ITO-coated substrates.

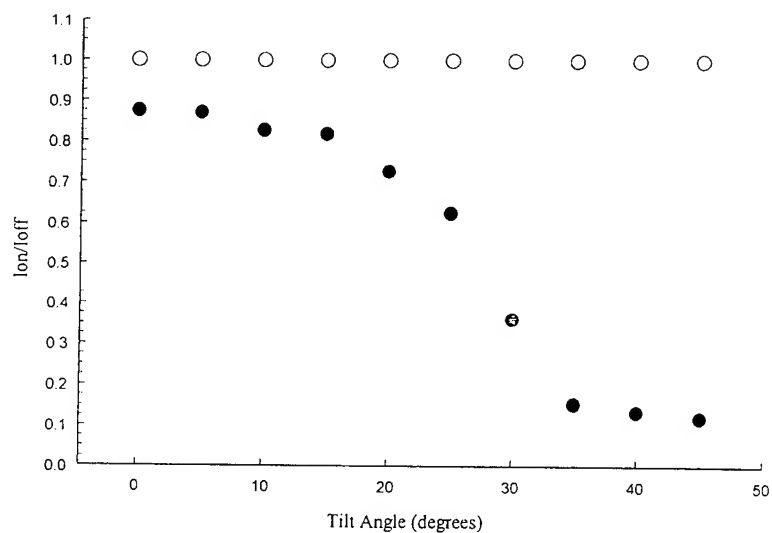


Figure 3: Response of the HeNe probe laser as a function of the tilt angle for ITO coated (solid circles) and non-ITO coated (open circles) samples of dye-doped PCB of 40 μ m thickness, homeotropically aligned, with an input YAG power of 190mW.

DIELECTRIC PHOTOREFRACTIVE GRATINGS IN KLTN AT THE PARAELECTRIC PHASE

Aharon J. Agranat, Meir Razvag and Michal Balberg

Department of Applied Physics

The Hebrew University of Jerusalem

Jerusalem 91904, ISRAEL.

Agranat@shum.huji.ac.il ; TL. 972-2-6584710; Fax 972-2-663878;

We present experimental evidence indicating that in the paraelectric phase, slightly above the phase transition, photorefractive (PR) gratings are formed by spatial modulation in the low frequency dielectric constant. The PR effect is normally attributed to the formation of spatially modulated space charge, which induces a correlated modulation in the birefringence through the electrooptic effect. In the paraelectric phase the electrooptic effect is quadratic and is given by

$$\Delta n = \frac{1}{2} n_o^3 g P^2 \quad [1]$$

where Δn is the birefringence, n_o is the refractive index, g is the quadratic electrooptic coefficient, and P is the polarization. Therefore, a spatial modulation in the birefringence induced by a modulation of the polarization is given by

$$\delta(\Delta n)_{(X)} = n_o^3 g P \delta P_{(X)} \quad [2]$$

Assume that P is in the linear region, i. e. $P = \epsilon E$; where ϵ is the dielectric constant and E is the electric field in the crystal. Then, if $E_{sc}(x)$ is the space charge formed in the PR process, the modulation of the birefringence is given by

$$\delta(\Delta n)_{(X)}^{sc} = n_o^3 g \epsilon^2 E_o E_{sc(X)} \quad [3]$$

where E_o is the electric field in the crystal. This is the so called voltage controlled PR effect (1,2). Considering equ. [2] it can be seen that if a modulation in ϵ is formed, it will induce a modulation in the birefringence given by

$$\delta(\Delta n)_{(X)}^D = n_o^3 g \epsilon \delta \epsilon_{(X)} E_o^2 \quad [4]$$

We have observed that slightly above the phase transition such a dielectric grating was formed in potassium lithium tantalate niobate (KLTN) doped with copper and vanadium. The experiments were conducted in a KLTN sample with a ferroelectric phase transition at $T_c=170K$. Prior to the experiment the crystal was cooled slowly from 200K to 160K at 0.5K/minute under a field to 1.8kV/cm, and was then warmed slowly to the experiment temperature.

A photorefractive grating was formed at 174K by two 514 nm Ar laser beams of 40mW each, incident at $\pm 9.5^\circ$ with respect to the normal of the crystal input plane. The light was polarized orthogonal to the incidence plane. An electric field of 1.8kV/cm was applied in the plane of incidence, orthogonal to the bisector of the writing beam directions of propagation. The exposure time was 7 seconds. A weak He-Ne beam polarized in the plane of incidence and Bragg matched with the formed grating, was used to monitor the diffracted intensity.

The diffraction efficiency vs. the applied field was measured immediately after the writing. The results are shown in Figure 1a. As can be seen, the results are in accord with eq. [2]. Note that the diffraction efficiency η dependence on δn is given by

$$\eta \propto \sin^2 \left(\frac{2\pi \delta n d}{\lambda_R \cos \theta} \right) \quad [5]$$

where d is the thickness of the crystal, θ is the probe angle of incidence, and λ_R is the probe wavelength in the material. Therefore, the diffraction efficiency is expected to be quadratic with the applied field. The shift of the minimum in η from $E_0=0$ is attributed to the formation of a metastable polarization during the poling process. Consequently, the electric field inside the crystal is actually $E = E_0 - P_0/\epsilon$. After the writing stage the crystal was left to dwell in the dark for 20 minutes under a field of 1.8kV/cm. During the dwell period the diffraction efficiency was monitored and was observed to be decreasing. Results of the diffraction efficiency dependence on the applied field at the end of the dwell period are shown in Figure 1b. As can be seen the minimum point remained shifted (at $E_0=0.75$ kV/cm), however, the curve is no longer symmetrical around the minimum point.

After the dwell period the diffraction was monitored while the crystal was subjected to a 514 nm erasure beam incident perpendicular to the input plane of the crystal. The diffraction first increased significantly and then decayed slowly. This result indicates that after the dwell period two compensating gratings exist in the crystal although they can be formed by two compensating space charges.

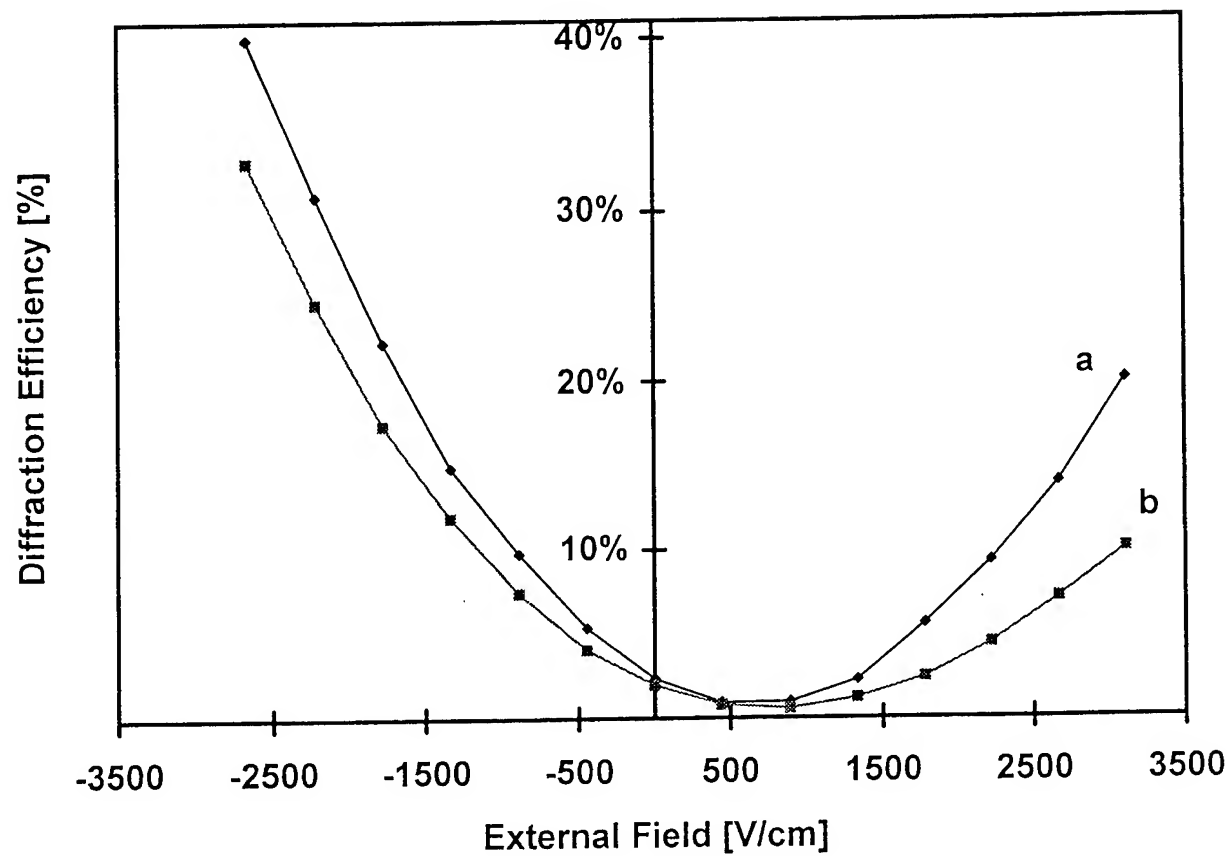
However, the deviation of $\eta(E)$ from symmetry after the dwell, cannot be explained by a PR effect which originates purely from the formation of a space charge. It must be assumed that both δn^{sc} and δn^{D} exist together so that the diffraction efficiency contains a cubic dependence on E_0 . We attribute this phenomena to the formation of a compensating dipolar grating around the photorefractive centers (Cu^+ and Cu^{++}). The dipolar grating is created by the deviation of the small Li ions from the center of inversion of the large K sites in which they are situated. The dipolar grating induces changes in T_c which results in changes of the dielectric constant through the Curie Weiss law. Such changes become large close to the phase transition temperature where $\delta \epsilon \propto \delta T_c / (T - T_c)$.

Finally it should be added that in similar experiments that were carried out 20K above the transition the dwell period had no effect on the formed PR grating, and the behavior was completely consistent with the voltage controlled PR effect.

References:

1. A. J. Agranat, V. Leyva, and A. Yariv, Opt. Lett. **14**, 1017 (1989).
2. A. J. Agranat, R. Hofmeister and A. Yariv, Optics Letters **17**, 713 (1992).

Figure 1. The diffraction efficiency vs. the applied electric field. (a) Immediately after the writing; (b) After the dwell period.



Optimization of Rhodium-Doped BaTiO₃ for High-Power Photorefractive Applications in the Near Infrared

B.A. Wechsler, G.D. Bacher, C.C. Nelson, M.B. Klein

Hughes Research Laboratories

3011 Malibu Canyon Road

Malibu, CA 90265

Tel: (310) 317-5639

Fax: (310) 317-5483

S. MacCormack and J. Feinberg

University of Southern California

Department of Physics

Los Angeles, CA 90089-0484

Phase conjugation and two-wave mixing in photorefractive crystals are used for frequency locking, power combining and beam cleanup of laser diodes. One requirement for these processes is a high gain or coupling coefficient, which implies a high trap density. For use at high power levels, another important requirement is low absorption, to minimize insertion loss and heating of the crystal. In order to increase the trap density, researchers have doped crystals to higher and higher concentrations.^{1,2} Unfortunately, this almost always leads to an undesirable increase in absorption coefficient. In this presentation we describe the use of Rh doping^{3,4} followed by post-growth annealing to produce BaTiO₃ crystals with both high trap density and low absorption at 860 nm.

In photorefractive crystals, the trap density N_E and the absorption are intimately related. In the simplest case of a single active dopant (with two possible charge states):

$$N_E = \frac{N_{full} N_{empty}}{N_{total}}.$$

For a fixed number of dopants $N_{total} = N_{full} + N_{empty}$, N_E is maximized when the number of full sites N_{full} equals the number of empty sites N_{empty} .

In this case, $N_E = \frac{1}{4} N_{total}$. We dope crystals to increase the total number of trap sites N_{total} and then anneal the crystals in a controlled atmosphere to set the ratio of full and empty sites. In addition to altering the trap density, the annealing treatment also changes the absorption of the crystal because a full trap site has a different optical cross section than an empty site. This can be seen clearly in Figure 1, where we plot the calculated effective trap density as a function of the absorption coefficient, assuming a given dopant concentration, and assuming that all the absorption comes from filled traps.

We have used a combination of doping and annealing in BaTiO₃ to optimize crystals for use in the near infrared spectral region. Our target values are a trap density $N_E = 4 \times 10^{16} \text{ cm}^{-3}$ and an absorption coefficient below 0.15 cm^{-1} at 860 nm. Usually, adding enough Rh to meet the trap density requirement raises the absorption coefficient of the crystals above 0.5 cm^{-1} . Such high coefficients yield unacceptable amounts of insertion loss and crystal heating. We grew crystals using two different Rh concentrations and then performed a series of annealing runs to reduce the absorption coefficient while maintaining the required value of trap density. The results are summarized in Fig. 2. It is clear that the use of doping and annealing has allowed us to achieve the required values of trap density and absorption coefficient. The measured values could not be obtained without the combination of moderately heavy doping and annealing. In our presentation we will provide details of our experiments and discuss specific device performance.

This work was funded by Air Force Phillips Laboratory, Kirtland AFB, New Mexico.

References

1. M.D. Ewbank, R.A. Vazquez, R.R. Neurgaonkar, and F. Vachss, J. Opt. Soc. Amer. B12, 87, 1995.
2. J.Y. Chang, M.H. Garrett, P. Tayebati, H.P. Jenssen, and C. Warde, J. Opt. Soc. Amer. B12, 248, 1995.
3. B.A. Wechsler, M.B. Klein, C.C. Nelson, and R.N. Schwartz, Opt. Lett. 19, 536, 1994.
4. T.W. McNamara, S.G. Conahan, I. Mnushkina, M.H. Garrett, H.P. Jenssen and C. Warde, SPIE Critical Review Proceedings CR-48, P. Yeh and C. Gu, Ed., 100 (1994).

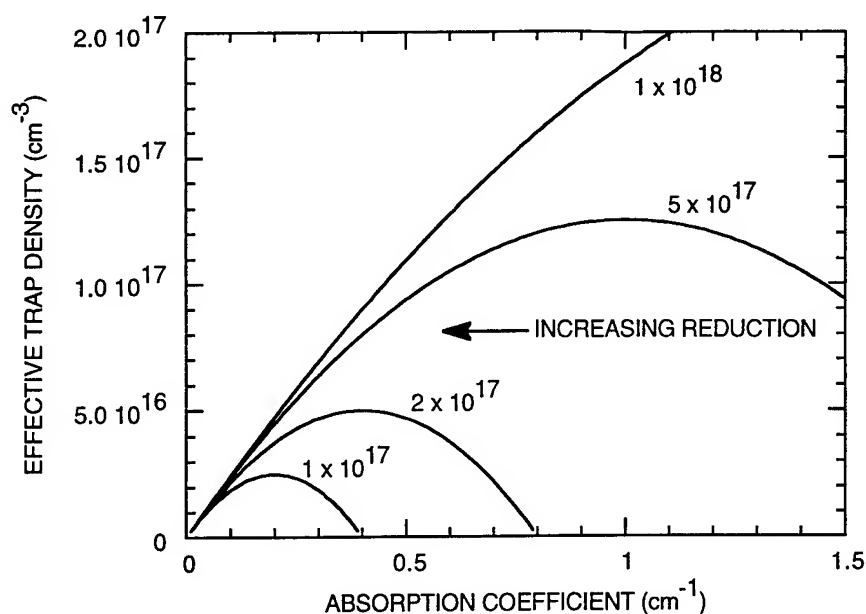


Fig. 1. Calculated trap density and absorption coefficient for various total dopant concentrations (cm^{-3}) in the crystal. Each curve represents one particular value of the total dopant concentration. The charge state of the dopant can be adjusted by oxidizing or reducing the sample. More reducing conditions move the trap density and absorption along each line toward the left. A fixed absorption cross section $\sigma = 4 \times 10^{-18} \text{ cm}^2$ has been assumed for the filled traps.

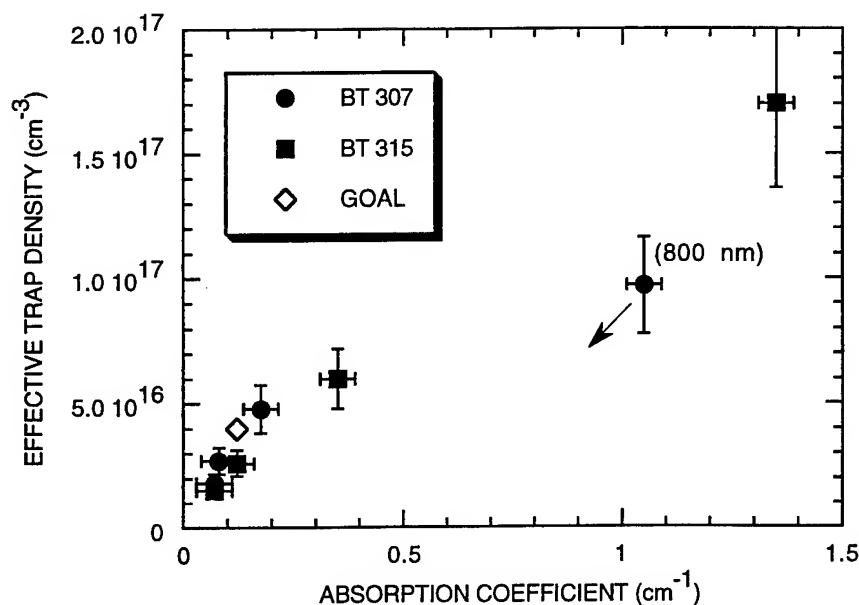


Fig. 2. Measured trap density and absorption coefficient for two different Rh-doped BaTiO_3 crystals (BT307 and BT315). The device goal is also shown. All measurements were carried out at a wavelength of 860 nm, except in one case, where 800 nm was used. For this point, an arrow indicates the direction in which the values would be expected to change as the wavelength is increased toward 860 nm.

Measurement of Photorefractive Dynamics Using Time Autocorrelation Function

David Statman and Traci L. Rendulic
Department of Physics
Allegheny College
Meadville, PA 16335
Ph. 814-332-2799 FAX. 814-332-2789

Photorefractive dynamics are typically described by the material equations referred to as the Kukhtarev Equations. In dimensionless form these equations are given by

$$(1) \quad \frac{\partial(n - N)}{\partial t} = -n(n - N + 1) - E \nabla n + l_D^2 \nabla^2 n$$

$$(2) \quad \frac{\partial N}{\partial t} = f(N_D - N) - \gamma n N$$

where time is scaled to $\tau = \epsilon / e \mu N_A$, length to $\lambda / (4\pi n \sin \theta / 2)$, and density to N_A . n is the carrier density, N is the ionized donor density, N_D is the donor density, E is the electric field, l_D is the Debye screening length, f is the excitation rate, and γ is the recombination coefficient. The space charge field responsible for the photorefractive grating is given by

$$(3) \quad \nabla \cdot E = n - N + 1$$

These equations are inherently nonlinear, and cannot, in general, be integrated analytically. In order to do so, the equations are linearized with the anticipation that higher order terms are not significant. Recent work, however, has demonstrated that under certain conditions, typical of many experiments, the linearization of these equations is not appropriate. For those cases, any connection between model and experiment becomes quite difficult.

One possible way to get around this dilemma is to measure the time auto-correlation function of light scattered from a photorefractive grating while at steady state. According to linear response theory, if there is a disturbance to the photorefractive grating, either in n or N hence the space charge field E , the dynamics of that disturbance is described by Eqs. 1 and 2 can be expanded around the steady state values;

$$(4) \quad \frac{\partial(\delta n - \delta N)}{\partial t} = - (n_{ss} - E_{ss} \cdot \nabla + l_D^2 \nabla^2) \delta n + n_{ss} \delta N - \delta E \cdot \nabla n_{ss}$$

$$(5) \quad \frac{\partial \delta N}{\partial t} = - (f + \gamma n_{ss}) \delta N - \gamma N_{ss} \delta n$$

These equations are integrable for simple cases such as when the incident intensity in the photorefractive crystal is represented by a cosine function, as in a simple hologram. Eqs. 4 and 5 can be expanded as a Fourier series. The result is a multiexponential decay to the steady state.

The time autocorrelation function of the space charge field $\langle \delta E(t+\tau) \delta E(t) \rangle$ is calculated from the solutions to Eqs. 4 and 5, given by the same multiexponential decay, but to zero. This suggests that if the time autocorrelation function of the light scattered from a photorefractive grating can be accurately measured, the time dependent nonlinearities in the Kukhtarev equations can be avoided. Analysis of experimental results would be unambiguous. The dynamics of photorefractive materials would then be well characterized under those conditions where nonlinearities exist.

The experiment is shown in Fig. 1. Two beam coupling in photorefractive barium titanate is achieved for interaction angle θ . Light scattered over a small scattering volume is interrogated for scattering vector \mathbf{k} , corresponding to the photorefractive grating. This is achieved with pinholes and lenses. With a small scattering volume, the temporal noise due to fluctuations in the space charge field become significant enough to measure. During the measurement, the mean intensity of the scattered light at steady state is subtracted from instantaneous intensity, and the correlation function is calculated in real time on a pc.

In some instances the autocorrelation function has been seen to oscillate. It is currently believed that these oscillations cannot be explained by fluctuation dissipation theory. Rather they are the result of some other longer term dynamics in the material. However, we have developed a technique to suppress these oscillations. A typical time autocorrelation function is shown in Fig.2.

We will present the results of autocorrelation measurements for several interaction angles, comparing p and n doped barium titanate. In addition, these results will be used to explain rise time and decay behavior of two beam coupling in barium titanate.

References:

- D. Statman, J. Opt. Soc. Am., B, **9**, 849 (1992)
- C. Xu, D. Statman, and J.K. McIver, J. Opt. Soc. Am., B, **9**, 1825 (1992)
- B. Chu, "Laser Light Scattering, " Second Edition, Academic Press, New York (1988).

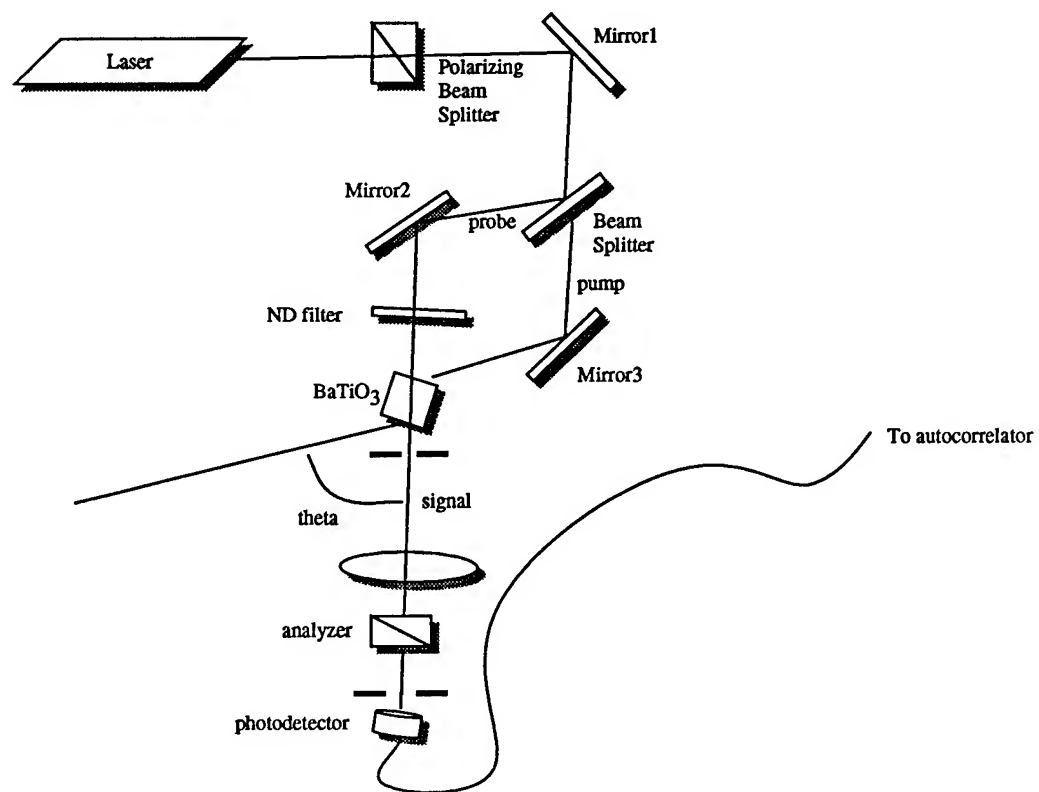


Fig. 1. Experimental setup for measurement of time autocorrelation function in two beam coupling.

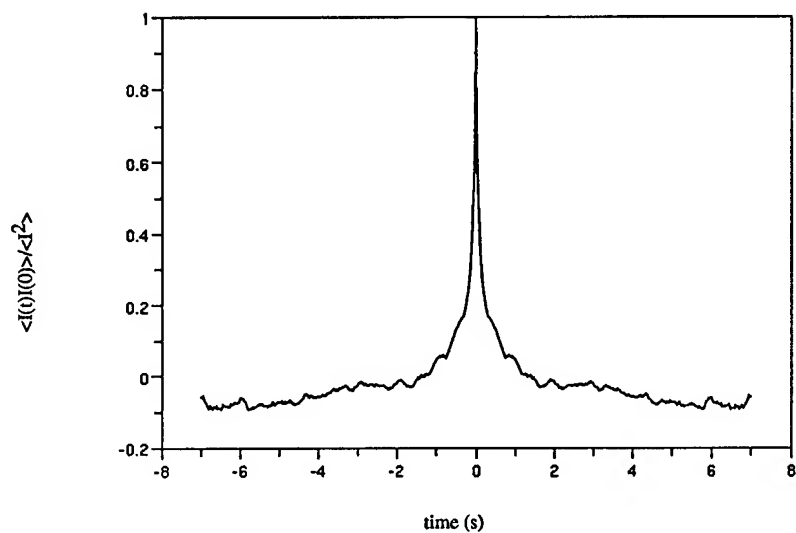


Fig. 2 Example of a time autocorrelation function from two beam coupling in barium titanate.

Self Phase Conjugation and Hexagonal Pattern Formation in Photorefractive Potassium Niobate

P.P. Banerjee

Dept. of ECE, Univ. Alabama in Huntsville, Huntsville AL 35899
ph.: (205) 895 6215 x 416; fax: (205) 895 6803

N.V. Kukhtarev and H.J. Caulfield

Physics Dept., Alabama A&M Univ., Normal AL 35762
ph.: (205) 851 5305; fax: (205) 851 5622

J.O. Dimmock

Center for Applied Optics, Univ. Alabama in Huntsville, Huntsville AL 35899
ph.: (205) 895 6030 x 400; fax: (205) 895 6618

T. Honda

Natl. Research Lab of Metrology, 1-1-4 Umezono, Tsukuba, Ibaraki 305 JAPAN
ph.: +81-298-54-4046; fax: +81-298-54-4135

Self phase conjugation is an interesting new phenomenon discovered in photorefractive (PR) crystals [1]. It gives a simple method for generation of a phase conjugate beam that can be used for image processing [2].

Another new nonlinear phenomenon, the spontaneous breakup of a laser beam in hexagonal patterns during interaction with PR crystals was discovered recently [3-6].

In this paper, we describe observation of both these phenomena viz., self phase conjugation and pattern formation (Fabry-Perot modes and hexagons) simultaneously in $\text{KNbO}_3\text{:Fe}$, and suggest a dynamic model employing six interacting waves to explain these phenomena as a manifestation of self-organization in a nonlinear system. In our model, we include the effect(s) of reflection gratings since it was found from independent experiments in a similar crystal that the coupling strength of reflection gratings is much greater than that of transmission gratings [7]. A simplified computer simulation based on the nonlinear model is also used to numerically demonstrate hexagon generation and rotation.

This type of six wave mixing resulting in phase conjugation was first observed in PR SBN [1], and explained as self-organization of scattering due to recording of transmission gratings.

Consider a 6 wave mixing geometry as shown in Fig. 1. Assuming predominantly reflection gratings for now, we can derive, starting from Maxwell's equations, the following set of coupled equations describing the spatial evolution of complex amplitudes C_m :

$$\begin{aligned} L_1 C_1 &= (n_{12} C_2 + n_{13} C_3 + n_{16} C_6) + (n_{46} C_3 + n_{56} C_2), \\ L_2 C_2 &= (n_{21} C_1 + n_{24} C_4 + n_{25} C_5) + (n_{65} C_1 + n_{35} C_4), \\ L_3 C_3 &= (n_{31} C_1 + n_{34} C_4 + n_{35} C_5) + (n_{64} C_1 + n_{24} C_5), \\ L_4 C_4 &= (n_{42} C_2 + n_{43} C_3 + n_{46} C_6) + (n_{53} C_2 + n_{13} C_6), \\ L_5 C_5 &= (n_{52} C_2 + n_{53} C_3 + n_{56} C_6) + (n_{12} C_6 + n_{42} C_3), \\ L_6 C_6 &= (n_{61} C_1 + n_{64} C_4 + n_{65} C_5) + (n_{21} C_5 + n_{31} C_4), \end{aligned} \quad (1)$$

where

$$L_m = (\nabla_T^2 + 2ik_{mz} \partial/\partial z)/k_0^2; \quad k_0 = 2\pi/\lambda \quad (2)$$

In (1), n_{sm} represents the induced reflection grating formed from waves C_s, C_m , whose time evolution can be found from the material equations. In a standard PR band transport model, this reads

$$\tau_{sm} \partial n_{sm} / \partial t = \gamma_{sm} C_s C_m^* - \beta_{sm} n_{sm}, \quad (3)$$

where τ is the Maxwell relaxation time, and γ and β are functions of the diffusion field E_D , the limiting space charge field E_q and the drift field E_μ . The parameter γ also depends on the crystal symmetry through the pertinent electrooptic tensor. In (2), ∇_T^2 denotes the transverse Laplacian, k_{mz} s refer to the z-component of the propagation constant for wave C_m and λ is the wavelength in the material. Note that the Eqs (1) are general in the sense that they can individually model both interacting plane waves or beams.

The nonlinear contributions to the evolution of the six waves as modelled in (1) can be better understood by means of scattering diagrams in the presence of reflection gratings, similar to those drawn in Ref. [6]. Of the five terms on the RHS of each equation in (1), the first three represent self-diffraction, while the last two are parametric diffraction terms.

In a typical experimental setup involving $\text{KNbO}_3:\text{Fe}$, an incident wave C_1 incident at about 10 degrees to the normal to the crystal surface is reflected from the crystal, producing C_2 . Due to scattering additional waves C_3 and C_4 develop, which propagate almost normal to the crystal surface. These represent concentric Fresnel rings, analogous to Fabry-Perot modes in a resonator. With time, the inner ring may decompose into a hexagonal pattern.

Furthermore, interaction of the four waves C_1 - C_4 gives rise to additional waves C_5 (counterpropagating to C_2) and C_6 (counterpropagating to C_1 and the phase conjugate of C_1).

A variation of the above experiment is interactions initiated by two beams C_1 and C_4 , and supported by reflections C_2 and C_3 , to eventually produce C_5 and C_6 .

In a linear system with a Fabry-Perot cavity, an incident (say, Gaussian) beam nominally normal to the interface, can give rise to a far-field intensity profile modified by a shaping function $S(\theta)$ which, to a first approximation, can be written as

$$S(\theta) \propto [1 + F(\theta) \sin^2 k_0 \theta^2 L/2]^{-1} \quad (4)$$

where F is the cavity finesse and L is the length of the cavity. From this the semi-angle of the first ring can be calculated as being approximately 0.4 degrees, which is close to our observed value.

In a nonlinear system where the incident beam may originate from light scattering, and the coupling between forward and backward traveling waves is provided through reflection gratings, the scattering angle may be shown to be nonlinearly modified, and depends on the strength of the reflection grating. An analogous result has also been found starting from Eqs. (1)-(3) in the steady state using six interacting plane waves with dominant pumps propagating normal

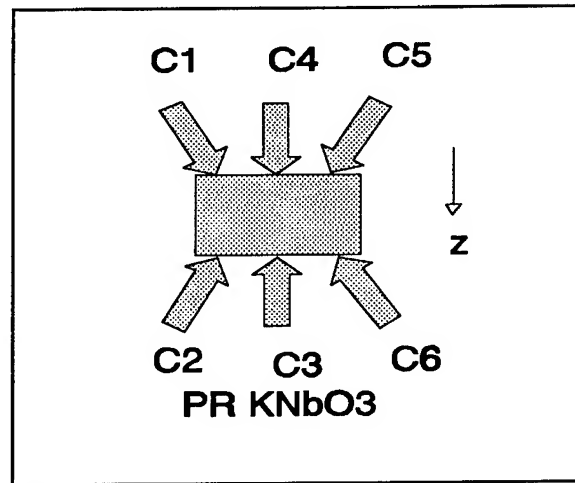


Fig. 1 Geometry of 6-wave mixing

to the interface and two pairs of weaker symmetric spatial sidebands, and the threshold conditions for the onset of spatial instabilities has been determined [7].

In the steady state the phase conjugate intensities I_5 and I_6 can be found from Eqs. (1)-(3), assuming that the last terms on the RHS of L_5C_5 and L_6C_6 are dominant:

$$I_6 \propto TR I_{1inc} I_{4inc}^2 / (1+R)^2 (I_{1inc} + I_{4inc})^2; \quad I_5 \propto R I_6, \quad (5)$$

where I_{1inc} , I_{4inc} are the input intensities of the waves 1 and 4; T and R represent the transmittivity and reflectivity of the interface. The time dynamics of I_5 and I_6 depend on τ_{42} and τ_{31} and the corresponding parameters for γ and β , and can be explicitly derived.

A two-transverse dimensional extension of (1), which can model the evolution of each of the seven forward and backward traveling (plane) waves forming the central spot and the hexagon in the far field, can be readily performed. Upon assuming a thin PR sample and isotropy of the nonlinear optical coefficients, time evolution of a stable hexagon from the first Fresnel zone has been observed through a winner-take-all competition for beam energy. When the crystallographic anisotropy of the nonlinear optical coefficients is incorporated, the computer model shows a continuous rotation of the hexagonal pattern, in accordance with experimental observations.

In conclusion, we have observed simultaneous self phase conjugation and pattern formation, and developed a model based on reflection gratings to explain these effects. Observed Fabry-Perot modes have been explained, and the angle of scattering of the rings has been determined. Based on an extension of the model, we have devised a computer simulation of hexagon formation and rotation. It was recently seen that our crystal has a significant photogalvanic current, prompting us to believe that our model may need to be further generalized by incorporating both local and nonlocal effects, and transmission and reflection gratings.

The authors wish to acknowledge Drs. M. Noginov and N. Noginova of Alabama A&M University for their assistance in measuring the photogalvanic current in the sample.

References

1. N. Bogodaev, Y. Kuz'minov, N. Kukhtarev and N. Polozkov, *Sov. Tech. Phys. Lett.* **12** 608 (1987).
2. P.P. Banerjee, H-L. Yu, D.A. Gregory and N. Kukhtarev, "Phase conjugation, edge detection and image broadcasting using two-beam coupling configurations in photorefractive KNbO_3 ", to appear in *Opt. and Photon. Lett.* (1996).
3. T. Honda, *Opt. Lett.* **18** 598 (1993).
4. P.P. Banerjee, H-L. Yu, D.A. Gregory, N. Kukhtarev and H.J. Caulfield, *Opt. Lett.* **20** 10 (1995).
5. T. Honda, *Opt. Lett.* **20** 851 (1995).
6. N.V. Kukhtarev, T. Kukhtareva, H.J. Caulfield, P.P. Banerjee, H-L Yu and L. Hesselink, *Opt. Engr.* **34** 2261 (1995).
7. T. Honda and P.P. Banerjee, "Threshold for spontaneous pattern formation in reflection grating dominated photorefractive media with mirror feedback", submitted to *Opt. Lett.* (1996).

Two-color Photorefractivity in LiNbO₃ Waveguides

D. Eger, M. A. Arbore and M. M. Fejer

Ginzton Laboratory, Stanford University, Stanford, CA 94305-4085

Phone: 415-725-8970; Fax: 415-723-2666

and M. L. Bortz

New Focus Inc. 2630 Walsh Ave., Santa Clara, CA 95051-0905

Phone: 408-980-8989 X 124, Fax, 408-980-8883

Short wavelength coherent light sources are required for applications such as process monitors and fluorescence based instruments. QPM waveguides can be used to frequency double GaAlAs diode laser output for this purpose. However the efficiency of chemically poled waveguides of different ferroelectric crystals such as LiNbO₃, LiTaO₃ and KTiOPO₄ degrade as the generated wavelength approaches the UV spectral range. The degradation is characterized by a decrease in the peak doubling efficiency, broadening of the QPM curve and reduction in the IR transmissivity of the waveguide. The damage increases with the intensity of the SH wave, limiting the power which can be generated by these waveguides. There is limited information in the literature on the degradation mechanism. The presence of the two waves in the waveguides and the strong variation of the SH power along the waveguide give rise to complex dependence of the output power with time, input IR power and wavelength that is difficult to characterize with SHG measurements alone.

In this work, we use a pump-probe method to measure the photoinduced refractive index changes in annealed-proton-exchanged (APE) waveguides of Ti or electric-field-periodically-poled LiNbO₃. In this method we couple different visible and IR pump beams into the waveguides and monitor, in real time, their effect on the QPM tuning curve generated by a low power frequency modulated IR probe beam. These changes are related to index changes in the waveguide. The experimental setup is shown in Fig. 1. The probe is a commercial 780 nm external cavity tunable diode laser (ECDL). Its frequency can be modulated continuously over 60 GHz. Using a linear ramp the entire QPM curve (typical peak width of 20 GHz) can be displayed in real time on an oscilloscope. The non-phased-matched IR pump was a 100 mW single-mode diode laser emitting at 790nm. For the visible light pump we used a 488 nm or 457 nm Ar-ion laser line. The different pump beams and the fundamental probe were simultaneously launched into the waveguide with a beamsplitter and a dichroic mirror and were filtered out after the waveguide so that the SHG intensity $I_{2\omega}$, generated by the probe could be detected using a Si detector or a photomultiplier tube.

The frequency shift of the peak of the QPM curve as a function of the IR beam power for different visible light powers in a Ti-poled waveguide is shown in Fig. 2. As seen, the frequency shift Δf increases with the IR power and is strongly enhanced by the visible light power coupled into the waveguide. For example 1.2 mW of the IR pump power induced a frequency shift of 6 GHz. With the addition of only 50 μ W blue light Δf increased to 12 GHz. Yet when coupling the same amount of blue light without the IR pump the shift was barely resolvable indicating that the contributions of the two pumps to Δf are not simply additive. Similar measurements on APE waveguides formed in electric-field poled substrates did not show any resolvable frequency shifts, indicating that Ti is involved in the photorefractive sensitivity problem.

The response time of frequency shift was measured by fixing the probe frequency at the QPM peak and launching into the waveguide low-repetition-rate low-duty-factor pulses from one of the pumps, using an acousto-optic modulator. The results for the initial decay time $\tau \equiv -I_{2\omega}/(dI_{2\omega}/dt)$ as function of the beam power are shown in Fig 3. When only the IR pump is coupled into the waveguide the response is slow at low power. τ decreases rapidly as the IR power is increased in the range of 0 to 1 mW, though not with the simple inverse proportionality expected for linear photoconductive and photogalvanic response. As seen in the figure, the response to the Ar pump pulse is between 20 to 80 times faster than to the IR beam.

Results of blue light pump transmissivity of a Ti-poled waveguide are shown in Fig. 4. As the IR light is coupled into the waveguide we observed a rapid drop in the transmissivity, followed in some cases by an additional slow decay. The results shown in Fig. 4 are only for the fast component of the transmissivity change. Observation of the waveguide showed that most of the loss is caused by forward scattering. Similar results were found for IR radiation scattering out of the waveguide induced by the Ar pump; again no measurable scattering occurred in electric-field poled waveguides.

From the data we conclude that the changes in SHG efficiency for Ti-poled APE LiNbO₃ waveguides are due to a photorefractive effect whose magnitude is much larger when both IR and short wavelength radiation are present in the waveguide than when either wavelength is present alone. The effect is not observed in electric-field poled waveguides. Further studies are necessary to more quantitatively characterize the wavelength and intensity dependence of the two-color photorefractivity and to identify the underlying mechanism.

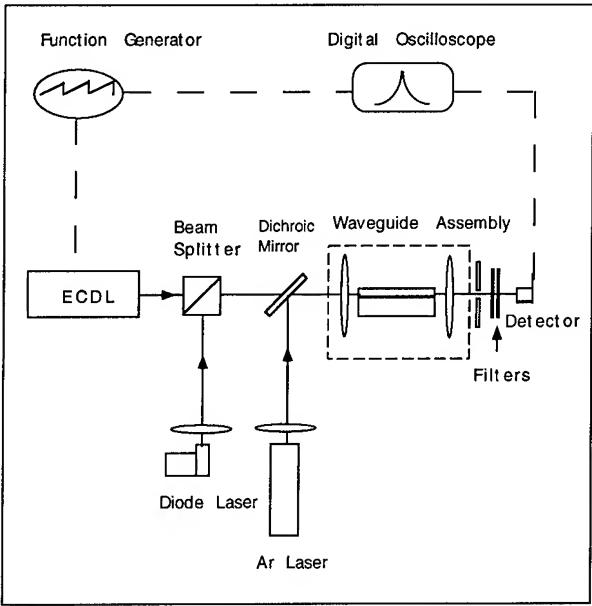


Fig.1. Experimental setup for pump-probe measurements.

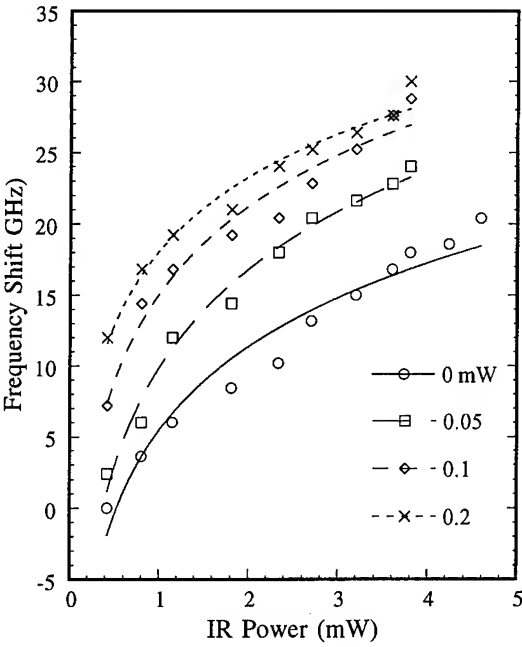


Fig. 2. QPM frequency shift as a function of IR power for different blue pump powers.

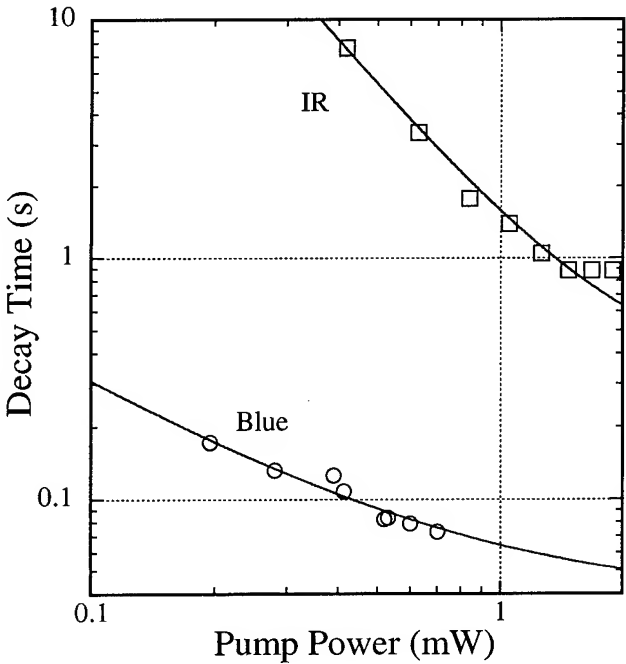


Fig. 3. SH intensity decay time vs. pump power.

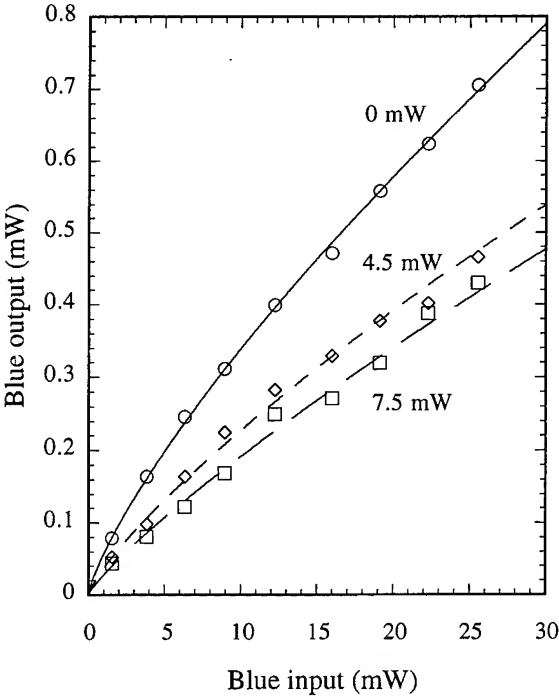


Fig. 4. Blue light transmission for different IR powers.

Exact Nonlinear Full-field Anisotropic Analysis of Higher-order Diffraction in Photorefractive Barium Titanate

J.M. Jarem and P.P. Banerjee

Dept. of ECE, U. Alabama in Huntsville, Huntsville AL 35899

Tels: (205) 895 6463; (205) 895 6215 x 416; fax: (205) 895 6803

Two-beam coupling in photorefractive (PR) materials has been extensively studied in the literature [1]. Theoretical analyses are based on linearized time dependent models [1], empirical predictions and nonlinear steady state albeit approximate theories. The difficulty in providing an analytical nonlinear time dependent theory is due to the inability to exactly decouple the Kukhtarev equations [1], and the fact that in a typical two-beam coupling setup, the PR crystal is finite and has a large linear refractive index mismatch with the surrounding medium if no matching liquid is used, prompting reflections from boundaries.

The purpose of this paper is to report our progress using rigorous coupled wave theory (RCWT) and the exact nonlinear Kukhtarev equations to study multiple wave mixing in a PR crystal [2-5]. In particular, we will report on conditions for higher order generation in PR BaTiO₃ in a two-beam coupling geometry. The time evolution of energy exchange resulting from the nonlinear dynamics is also shown. Also, the dependence of higher order generation on sample length, initial two-beam intensity ratio and boundary mismatch is investigated. While the above analysis assumes transmission gratings, we will provide an example of the use of RCWT to analyze reflection gratings in PR crystals.

For the first time to the best of our knowledge, the exact time dependent nonlinear Kukhtarev equations, taking both transverse and longitudinal electrostatic field components into account, are used, after reducing them to a set of coupled equations without any approximations. Furthermore, for numerical modeling, a RCWT algorithm [6] is employed to analyze optical propagation through the PR crystal. Thus our technique yields not only results for all the transmitted orders, but the reflected orders as well, and is well suited to analyze the multi-wave mixing problem in a PR material in the presence of induced transmission and reflection gratings.

The Kukhtarev equations comprise a set of four equations which may be used to model a diffusion dominated photorefractive material [1]. These comprise the continuity equation, the rate equation, the current equation and Poisson's equation. We use the Kukhtarev equations as given in Ref. [1], taking care to modify the second equation in order to include the contribution of the thermal excitation rate of charge carriers. Using the continuity equation, the current equation and Poisson's equation, it can be shown that the evolution of the transverse and longitudinal components of the space charge field $E_s(x,y,t)$, call them $E_{sx,y}(x,y,t)$, respectively, satisfy the following normalized partial differential equations [5]

$$\partial \Delta \epsilon_x / \partial \bar{t} + \Gamma_1 \bar{n} \Delta \epsilon_x = -\Gamma_2 \partial \bar{n} / \partial \bar{x}; \quad \partial \Delta \epsilon_y / \partial \bar{t} + \Gamma_1 \bar{n} \Delta \epsilon_y = -\Gamma_2 \partial \bar{n} / \partial \bar{y}, \quad (1)$$

$$\begin{aligned} \Delta \epsilon_x &= n_o^2 n_e^2 r_{42} E_{sx}, \quad \Delta \epsilon_y = n_o^2 n_e^2 r_{42} E_{sy}; \\ \bar{x} &= k_0 x, \quad \bar{y} = k_0 y, \quad \bar{n} = n/N_A, \quad \bar{t} = \beta t, \quad C = \beta/s \end{aligned} \quad (2)$$

$$\Gamma_1 = \mu e N_A / \beta \epsilon_s; \Gamma_2 = e k_0 N_A D_s n_o^2 n_e^2 r_{42} / \beta \epsilon_s \quad (3)$$

In the above equations e is the electronic charge, D_s is the diffusion constant, μ is the mobility, ϵ_s is the effective static permittivity [1], and $n(x,y,t)$ is the electron concentration. In the above derivation, we have assumed that nominal direction of propagation is along the y direction, x is a transverse coordinate, and t denotes time. Also, $n_{o,e}$ denote the ordinary and extraordinary refractive indices, respectively, N_A is the acceptor concentration, k_0 is the propagation constant of light in air, β is the thermal excitation rate (proportional to the dark current), s is the ionization cross-section and r_{42} is a (nonzero) electrooptic coefficient in BaTiO₃. Furthermore, using the rate equation and manipulating in a fashion similar to that presented in Ref. [4] we get, after considerable algebra,

$$\begin{aligned} \Gamma_2 \partial^2 \bar{n} / \partial \bar{x}^2 + \Gamma_1 \Delta \epsilon_x \partial \bar{n} / \partial \bar{x} + [-\Gamma_3(1+I/C) + (\Gamma_1 - \Gamma_4)(\partial \Delta \epsilon_x / \partial \bar{x} + \partial \Delta \epsilon_y / \partial \bar{y}) - \Gamma_3 \Gamma_4(1+\bar{n})] \bar{n} \\ = \Gamma_3 [\partial \bar{n} / \partial \bar{t} - (1+I/C)(N_D/N_A - 1 - (1/\Gamma_3)(\partial \Delta \epsilon_x / \partial \bar{x} + \partial \Delta \epsilon_y / \partial \bar{y}))] - \Gamma_2 \partial^2 \bar{n} / \partial \bar{y}^2 - \Gamma_1 \Delta \epsilon_y \partial \bar{n} / \partial \bar{y} \end{aligned} \quad (4)$$

$$\Gamma_3 = e N_A n_o^2 n_e^2 r_{42} / \epsilon_s k_0, \Gamma_4 = \gamma_R N_A / \beta \quad (5)$$

In Eq. (4), $I = I(x,y,t)$ represents the optical intensity profile and N_D is the donor concentration.

Eqs. (1-5) represent three coupled nonlinear equations for the electron density \bar{n} and the dielectric modulation functions $\Delta \epsilon_x$ and $\Delta \epsilon_y$. The form of these equations at any given time and at any given point in space in the photorefractive medium depends on the value of the optical intensity I at that point in space and time. The value of I itself in the photorefractive medium depends on the incident optical field and depends on the optical energy transmitted reflected and diffracted by the dielectric modulation functions which exist in the photorefractive medium at a given time. These transmitted, reflected and diffracted fields may be found through the RCWT algorithm which is briefly summarized below.

The solutions of Maxwell's equations in a diffraction grating is carried out by (1) expanding the unknown electric and magnetic fields \mathbf{E} and \mathbf{H} in this region in an infinite series of forward and backward traveling plane waves (Floquet harmonics) whose exponentials are multiplied by a set of spatially varying amplitudes whose value and form is unknown and are to be determined, (2) expanding the dielectric tensor elements ($\epsilon_{xx}, \epsilon_{xy}, \dots$) of the diffraction grating in a Fourier series, (3) substituting the plane wave expansion of \mathbf{E} and \mathbf{H} and the Fourier expansion of ϵ into Maxwell's equations and (4) from these substitutions, determining a set of coupled amplitude equations whose solutions determine the set of unknown plane wave amplitudes which were introduced in Step (1). The dielectric tensor elements for BaTiO₃, which comprise an intrinsic part and an induced part proportional to $\Delta \epsilon_x$ and $\Delta \epsilon_y$, have been extensively derived in Refs. [2-5].

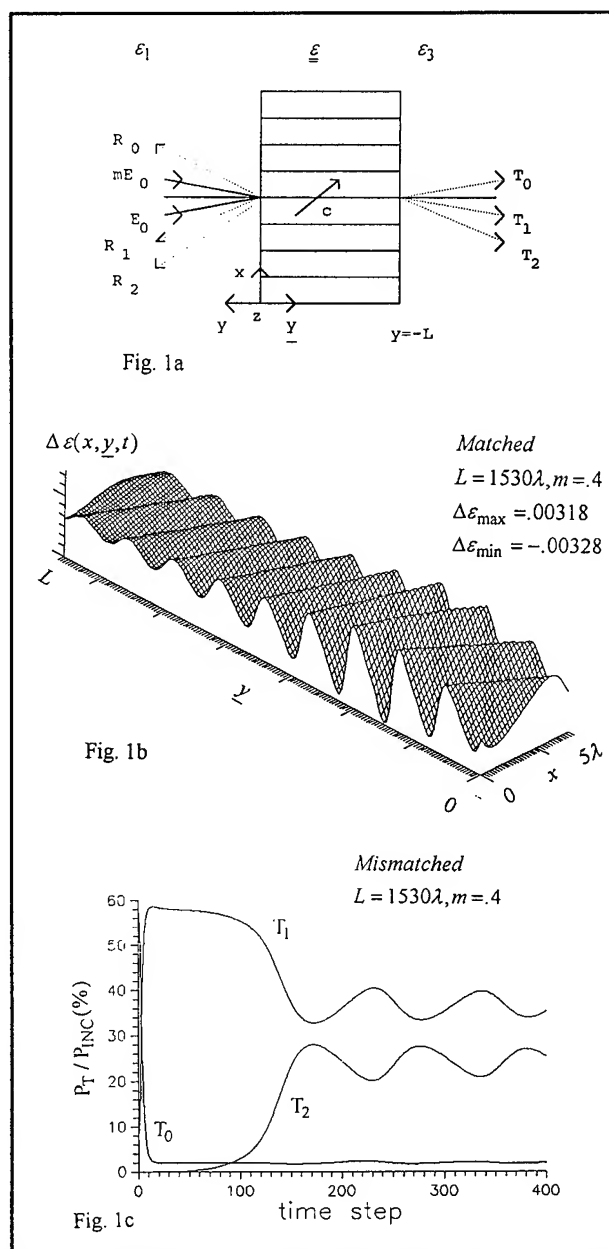
Numerical simulations were performed for the geometry shown in Fig. 1a. A finite-difference algorithm (incorporating periodic boundary conditions in x , see Fig. 1a) was used to solve the reduced Kukhtarev equations at each time step [2-5]. Fig. 1b shows a typical plot of $\Delta \epsilon = \Delta \epsilon_x$ ($\Delta \epsilon_y$ has been assumed to be zero) in the steady state for the matched case for $L=1530\lambda$, grating spacing $\Lambda=5\lambda$ ($\lambda=633\text{nm}$) and with m (the initial optical field ratio)=0.4, as an example of our numerical simulations. The period along y arises due to the difference in the y -

components of the propagation vectors in the crystal. Generation of higher order diffraction occurs only in the mismatched case, e.g., regions 1 and 3 are air, and depends critically on the crystal length. In this simulation we have not considered the effect of reflection gratings. As shown in Fig. 1c, for $L=1530\lambda$, one achieves the highest power conversion into second order and the zero order is completely depleted very rapidly. Second order diffraction was observed for power ratios $m=0.4$ and 1 and not observed for low values of $m(=0.1)$. Similar results were observed with the longitudinal field component (nonzero $\Delta\epsilon_y$) present in the calculations.

Reflection gratings, not included in the above analysis, can be incorporated by using a two-dimensional coupled mode approach which includes diffraction grating variation in the longitudinal ($\lambda/2$ gratings) as well as grating variation in the transverse direction which has already been considered.

References

1. P. Yeh, Introduction to Photorefractive Nonlinear Optics. Wiley: NY (1993).
2. P.P. Banerjee and J.M. Jarem, "Transient wave mixing and recording kinetics in photorefractive barium titanate: a nonlinear coupled-mode approach", Opt. Engr. **34** pp. 2254-2260 (1995).
3. J. Jarem and P.P. Banerjee, "A nonlinear transient analysis of two- and multi-wave mixing in a photorefractive material using rigorous coupled mode diffraction theory", to appear in Opt. Comm. (Feb 1, 1996).
4. J. M. Jarem and P.P. Banerjee, "An exact, dynamical analysis of the Kukhtarev equations in photorefractive barium titanate using rigorous coupled wave diffraction theory", accepted for publication in J. Opt. Soc. Amer. A (Apr. 1996).
5. P.P. Banerjee and J.M. Jarem, "The effect of induced longitudinal electrostatic field components during two and multi-wave mixing in barium titanate", submitted to J. Opt. Soc. Amer. B (1996).
6. E.N. Glytsis and T.K. Gaylord, "Rigorous three-dimensional coupled wave diffraction analysis of single, cascaded anisotropic gratings", J. Opt. Soc. Amer. B **4** pp. 2061-2080 (1987).



Wednesday, July 10, 1996

Coherent Effects in Semiconductor Structures

NWA 8:00 am-9:35 am
Maile Room

Ravi Jain, *Presider*
University of New Mexico

Nonlinear Optics of Semiconductor Microcavities

Hyatt M. Gibbs, Ove Lyngnes, Jill D. Berger, John Prineas, Sahnggi Park,
and Galina Khitrova

Optical Sciences Center, University of Arizona, Tucson, AZ 85721, USA

When the cavity mode of a high-finesse semiconductor microcavity is tuned toward a sharp quantum-well exciton absorption line, the dipole coupling between these two oscillators results in a normal-mode coupling (NMC) anticrossing curve [1]. When the two oscillators have the same frequency there are two transmission peaks (see Fig. 1 inset) and two reflection dips corresponding to two new eigenfrequencies of the coupled system. The nonlinear transmission and reflection of 150-fs modelocked pulses incident on an NMC microcavity are reported.

The measurements were performed on an MBE-grown microcavity with 14-period top and 16.5-period bottom GaAs/AlAs $\lambda/4$ mirrors with a $3\lambda/2$ spacer having two 80 Å $\text{In}_{0.03}\text{GaAs}$ quantum wells (each with $\alpha l \approx 0.1$ and 1 meV FWHM) placed at the antinodes of the cavity. The sample was excited at normal incidence by 150-fs pulses from a Ti:Sapphire laser with an 82-MHz repetition rate. An optical upconversion setup using a BBO crystal was used to measure the time-dependent intensity of the reflected light from the sample collected at normal incidence. A spectrometer with an optical multichannel array was used to simultaneously record the spectrum of the reflected light.

The narrow inhomogeneous linewidth of the quantum wells yields record splitting-to-linewidth ratios, Fig. 1 inset, and time-resolved depth of modulation of vacuum-field Rabi oscillations, Fig. 1. When the time-resolved reflectivity oscillations are observed in a magnetic field of 11.25 Tesla, the NMC oscillation frequency increases by about 1.24 close to that expected from the square root of the 1.64 measured increase in oscillator strength.

The reflectivity spectra of 150-fs pulses tuned in resonance with the NMC twin peaks are shown in Fig. 2 as a function of incident pulse fluence. Note that the reflectivity dips disappear with increased fluence with no change in splitting. This new [2,3] nonlinear NMC behavior is also seen with cw pumping above the mirror stopband or into either of the peaks. These nonlinear measurements agree with a transfer matrix simulation containing the separately measured nonlinear optical susceptibility in which the main effect is exciton broadening which increases the absorption at both NMC peaks. Agreement with a semiclassical description implies that these nonlinear experiments are not in the QED regime of strong coupling in which NMC of a single "atom" could be seen. That present-day microcavities are orders of magnitude away from that regime is also indicated by the need for $10^5 \hbar\omega$ excitations for the observed nonlinear behavior.

Fig. 3 shows the time-resolved reflection from the sample at 6K and zero detuning for different pump intensities. The oscillation period of the signal is about 0.9 ps in good agreement with the observed splitting of 2.8 nm in the reflection spectrum shown in Fig. 2. The signals show a much stronger modulation (limited by the 150-fs reference pulse width) than reported earlier[4,5], consistent with the excellent reflectivity splitting to linewidth ratio (~ 7) of our samples. Both the period of oscillations shown in Fig. 3 and the splitting between the reflection dips shown in Fig. 2 show very little dependence on pump intensity

before they are damped out. This is different from previously reported time-resolved measurements of NMC splitting [3] showing a strong change in splitting with time after excitation by a femtosecond pulse. The difference in the measurements is the large splitting to linewidth ratio of our sample, making the increase in decay rate the main effect of increasing the excitation density. The strong dependence of the decay rate of the NMC

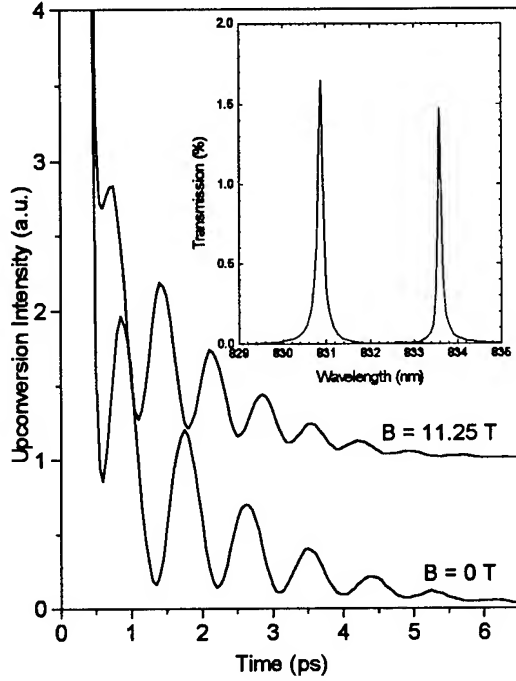


Figure 1: Time resolved vacuum-field Rabi oscillations at $B = 0$ T (lower curve) and $B = 11.25$ T (upper curve). The data are normalized to the reflected pump peak intensity at time zero and magnified by 1000. The inset shows the transmission of 150 fs pulses through a $3\lambda/2$ microcavity similar to that in the text except with 19/21.5 period mirrors.

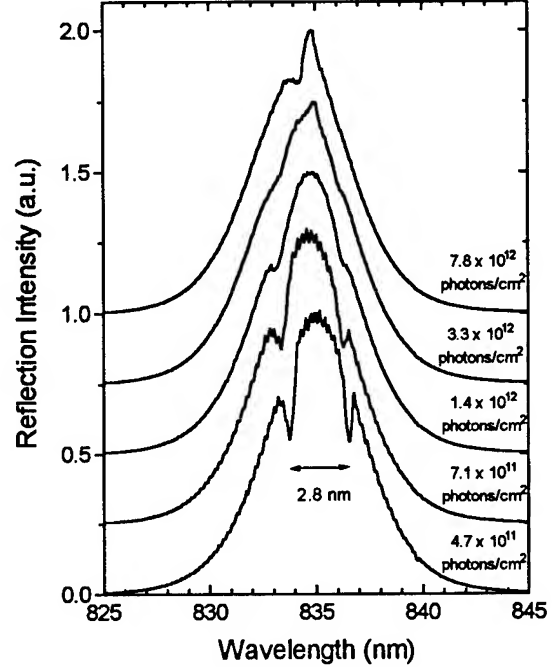


Figure 2: Reflected pump spectra for different pump fluences showing the NMC reflection dips washing out and the occurrence of a PL peak approximately halfway in between the reflection dips at high excitation densities. The maxima of the curves have been normalized to 1 and then offset by 0.25 with respect to each other.

oscillation envelope on the optical fluence of the pump pulse onto the sample is shown in Fig. 3. The decay rate of the intensity is given by $\kappa + \gamma$, where κ is the empty cavity damping rate and γ accounts for all other losses including the exciton dephasing rate. $1/\kappa$ was measured by detuning the cavity far away from the exciton resonance and found to be 1.3 ps. γ calculated from the measured total decay time is also plotted in Fig. 4. We conclude that the main effect of increasing the carrier density is an increase in the decay rate of the NMC oscillations. This increase in the decay rate damps out the NMC oscillations and reflection dips before an increase in oscillation period / decrease in splitting is observed. Further analysis will be needed to determine whether this increase in decay rate results from dephasing exciton collisions as in the cw nonlinear experiments.

We acknowledge support from NSF Physics and Lightwave Technology, ARPA/ARO, JSOP, and COEDIP.

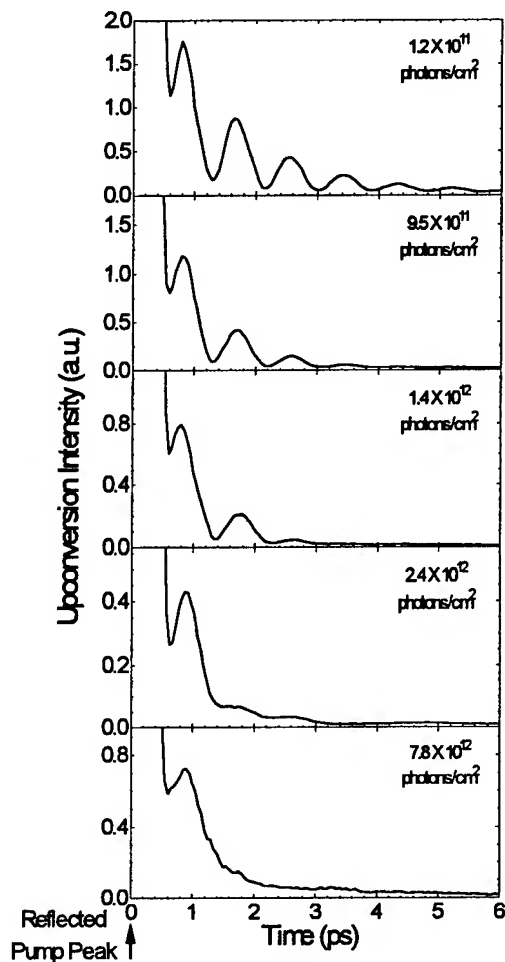


Figure 3: Reflected signal from the microcavity sample as function of time after excitation by a 150-fs laser pulse, measured using upconversion, for different pump intensities. All of the curves are normalized to 1000 at $t = 0$ ps. The pump fluence onto the sample is shown for each curve.

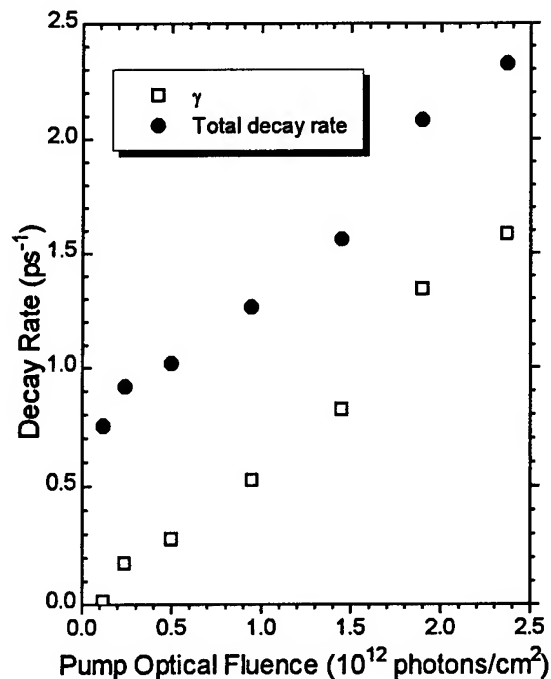


Figure 4: Total $1/e$ decay rate of the oscillation envelope of the reflected signal (solid circles) as function of pump intensity and the calculated γ (open squares) calculated as the total decay rate minus $(1.3 \text{ ps})^{-1}$.

References:

- [1] Weisbuch, C., Nishioka, M., Ishikawa, A., and Arakawa, Y., Phys. Rev. Lett. **69**, 3314 (1992).
- [2] Houdré, R., Gibernon, J. L., Pellandini, P., Stanley, R. P., Oesterle, U., Weisbuch, C., O'Garman, J., Roycroft, B., and Ilegems, M., Phys. Rev. B **52**, 7810 (1995).
- [3] Rhee, J.-K., Lai, R., Norris, T. B., Arakawa, Y., and Nishioka, M., QThI3 QELS '95.
- [4] Norris, T., Rhee J. K., Sung, C. Y., Arakawa, Y., Nishioka, M., and Weisbuch, C. (1994) Phys. Rev. B **50**, 14663.
- [5] Jacobsen, J., Pau, S., Cao, H., Björk, G., and Yamamoto, Y. (1995) Phys. Rev. A **51**, 2542.

Ultrafast Time-Resolved Ellipsometry of Four-Wave-Mixing Signals: Measurement of Coherent Nonlinear Processes in Semiconductors

Arthur L. Smirl, A. E. Paul and J. A. Bolger

*Laboratory for Photonics & Quantum Electronics, 100 IATL, University of Iowa,
Iowa City, IA 52242 Phone: (319)335-3460 Fax: (319)335-3462*

Temporally and spectrally-resolved degenerate four-wave-mixing (FWM) techniques have been enormously successful in providing new information about fundamental nonlinear and coherent optical processes in atomic, molecular and solid state systems. Typically, in such studies, the time-integrated or time-resolved magnitude of the FWM emission (or its spectrum) is studied as a function of the input parameters (such as the fluence, time delays or the polarization states of the incident pulses), but the polarization state of the FWM signal itself has been largely ignored. Moreover, the few attempts that have been made to determine the polarization state of the FWM emission have been restricted to measuring the direction of polarization, but they have left the ellipticity and the degree to which the signal is unpolarized unspecified.

Here, we describe a novel technique that combines standard ellipsometric and time-resolved pump-probe techniques to *completely* determine the polarization state of both the time-integrated (TI-FWM) and the time-resolved four-wave-mixing (TR-FWM) emission. We demonstrate the potential of this technique by examining the rich structure exhibited by both the time-averaged and time-resolved polarization state of the FWM signal from a GaAs/AlGaAs multiple quantum well (MQW). For example, we show that the time-averaged polarization state associated with the TI-FWM signal has a significant unpolarized component and that the polarized portion is highly elliptically polarized. In addition, we show that the TR-FWM signal is completely polarized at each instant of time, but that both the ellipticity and the orientation of the polarization ellipse vary dramatically and continuously with time during the emission. Moreover, the ellipticity and the orientation of the polarization ellipse are each strongly dependent on the carrier density, the incident polarizations and on whether the time delay between the incident pulses is negative or positive. By numerically integrating the time-resolved Stokes parameters, we also show that the TR-FWM polarization measurements are consistent with the TI-FWM polarization measurements. Most importantly, we demonstrate that the time-resolved dynamics of the polarization of the FWM signal exhibit novel qualitative features that place new constraints on models describing FWM in MQW's.

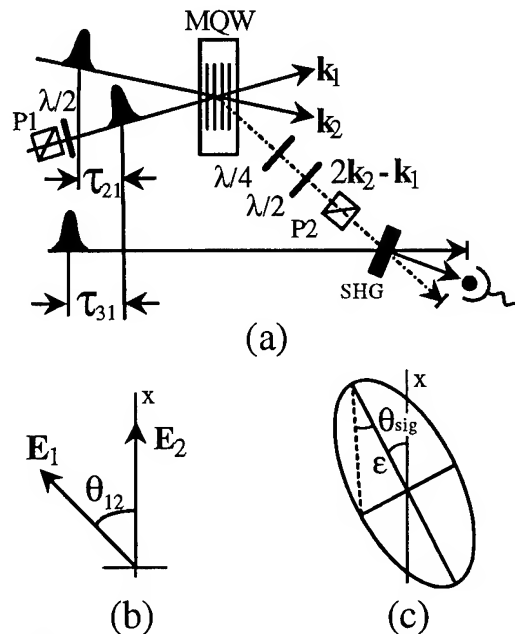


FIG. 1. (a) Geometry for time-resolving the polarization state of the FWM signal (b) the orientations of the input polarizations, and (c) the polarization ellipse showing the azimuthal angle θ_{sig} and the ellipticity angle ϵ of the FWM signal.

The TR-FWM measurements were performed using 160 fs pulses from a tunable mode-locked Ti:sapphire laser and the conventional two-pulse geometry shown in Fig. 1(a). The complete polarization state of the FWM emission in the direction $2\mathbf{k}_2 - \mathbf{k}_1$ was measured using a quarter-wave ($\lambda/4$) plate, a half-wave ($\lambda/2$) plate and an analyzing polarizer (P2). Measurements were performed with and without the quarter waveplate present. When present, the quarter wave plate was stationary and was oriented with its fast axis along the x-direction (parallel to the incident s-polarized \mathbf{E}_2 field). For all measurements, the analyzer was present, was stationary and was oriented to pass s-polarized light. The half-wave plate was also present for all measurements, but for each fixed incident polarization state \mathbf{E}_1 , it was rotated through angles ranging from 0° to 90° . One can readily show that all four Stokes parameters can be determined from measurements of the FWM signal for four orientations of the half-wave plate [e.g., at 0° , 22.5° and 45° without the $\lambda/4$ plate and 0° with the $\lambda/4$ plate]. To check internal consistency, however, six measurements were made for each set of experimental conditions.

For each incident polarization and for each orientation of the half-wave plate, the TR-FWM signal transmitted by these components was measured by cross correlating it with a reference pulse in a second harmonic generation (SHG) crystal. In addition, the TI-FWM signal passed by these components was measured by removing the SHG crystal and collecting the transmitted signal on a photomultiplier. The fraction P of the light that was polarized ($P=1$ denotes completely polarized light) and the ellipticity angle ϵ and the azimuthal angle θ_{sig} for the polarization ellipse associated with the polarized portion (see Fig. 1(c)) were then extracted from the Stokes parameters. In this way, the complete polarization states of the TI-FWM and the TR-FWM signals were measured as a function of the angle θ_{12} between the two linear input polarizations \mathbf{E}_1 and \mathbf{E}_2 (see Fig. 1(b)).

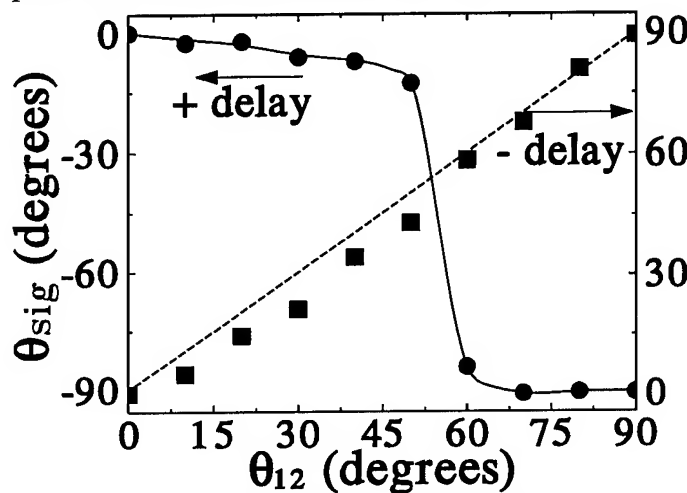


Fig. 2. Time-averaged measurements of the azimuthal angle θ_{sig} as a function of the angle θ_{12} between the two input polarizations for delays of $\tau_{21} = -300$ fs and $\tau_{21} = +300$ fs.

Monitoring the polarization state in this way during the FWM emission process provides one with an additional very powerful probe of the processes that contribute to the nonlinear response. As an example, the time-averaged and time-resolved polarization state of the FWM signal from a homogeneous broadened GaAs/AlGaAs MQW at 80 K is shown in Fig. 2 and Fig. 3 as the input polarization \mathbf{E}_1 is rotated counter clockwise. Results are shown for a positive delay $\tau_{21} = +300$ fs (i.e. \mathbf{E}_1 arrives first) and an equal negative delay $\tau_{21} = -300$ fs (\mathbf{E}_2 arrives before \mathbf{E}_1). Notice that the functional dependencies of the FWM polarization state on input polarization and time are very different for the two

delays. For the positive delay, the time-averaged orientation of the polarization ellipse rotates clockwise (toward more negative angles) as the input polarization rotates counterclockwise (see Fig. (2)). As shown in Fig. 3(a) and 3(b), the polarization state also changes dramatically and continuously during emission, and several features are worth noting. Most importantly, there is a

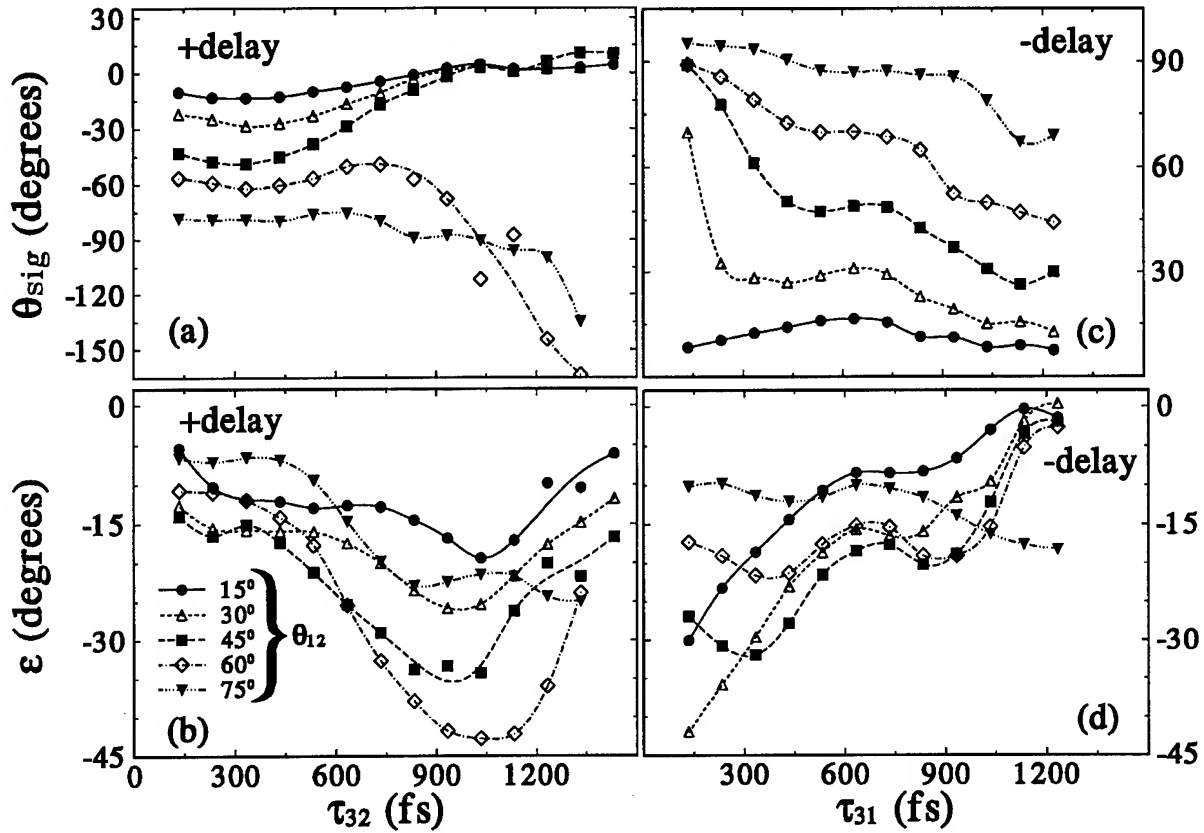


Fig. 3. Time-resolved measurements of the azimuthal angle θ_{sig} and the ellipticity angle ϵ as a function of time for selected angles θ_{12} between the two input polarizations and for delays of $\tau_{21} = +300$ fs and $\tau_{21} = -300$ fs.

distinct bifurcation in the temporal evolution of the azimuthal angle (see Fig. 3(a)). Specifically, for small angles, the ellipse rotates counterclockwise with increasing time. By contrast, for larger angles, the ellipse rotates clockwise. Also notice that the FWM signal is elliptically polarized (Fig. 3(b)) and that the ellipticity ϵ tends to increase then decrease with time (for a fixed θ_{12} between the two input polarizations) and that ϵ tends to increase then decrease with increasing θ_{12} (at a fixed time).

By contrast, for the negative delay, the time-averaged polarization (Fig. 2) rotates counterclockwise as the input polarization is rotated counterclockwise (i.e., $\theta_{\text{sig}} \sim +\theta_{12}$), opposite to the direction that it rotates at positive delays. Moreover, the ellipse always rotates clockwise in time, and no bifurcation is seen (Figs. 3(c) and 3(d)).

Such novel features in the time-resolved dynamics of the polarization state of the FWM signal place new constraints on models describing FWM in MQW's. We will demonstrate these constraints by comparing our results to a model based on the optical Bloch equations with local field corrections, excitation-induced dephasing and biexciton formation included phenomenologically. Based on qualitative behavior (which is insensitive to fit parameters), we show that the gross features in our data over a wide range of experimental conditions can be reproduced if we include all three processes.

Coherent Phonons as an Ultrafast Probe of Optical Nonlinearities in Semiconductors

H. Kurz¹⁾, G.C. Cho¹⁾, T. Dekorsy¹⁾, S. Hunsche²⁾, H.J. Bakker²⁾

¹⁾ Institute of Semiconductor Electronics, RWTH Aachen, Sommerfeldstr. 24, D-52056 Aachen, Germany, Tel. +49-241-807890, FAX +49-241-8888246

²⁾ FOM Institute for Atomic and Molecular Physics, Kruislan 407, 1098 SJ Amsterdam, Netherlands

Since the first time-resolved observation of coherent phonons in semiconductors [1], the excitation of coherent lattice vibrations in solid states has attracted considerable interest due to the information, which can be obtained from these kind of experiments not accessible by other experimental techniques. We discuss two recent achievements on the observation of the nonlinear dynamics of the coupled phonon-carrier system by pump-probe reflectivity spectroscopy using femtosecond laser pulses.

Detection of coherent plasmon-phonon coupled modes via the Franz-Keldysh effect in GaAs

The detection of coherent LO phonons in GaAs - up to now - has been based on the detection of electro-optic reflectivity changes via the Pockels effect ($\chi^{(2)}$) associated with the macroscopic polarization of the coherent mode [1]. The reflectivity changes due to resonant electromodulation in the vicinity of critical points of the band structure can be described by a $\chi^{(3)}$ nonlinear optical susceptibility at low-fields [2]. The advent of the Ti:sapphire laser allows now to study the optical response of coherent phonons close to the fundamental band gap. We investigate the dynamics of coherent plasmon-phonon coupled modes in GaAs with 50 fs laser pulses. For excitation energies close to the band gap of GaAs (1.42 eV) at room temperature, the contribution of the isotropic reflectivity change based on $\chi^{(3)}$ is compared to the anisotropic changes induced by the Pockels effect. Figure 1 depicts the dominant $\chi^{(3)}$ contribution of the coherent plasmon-phonon amplitude to the nonlinear optical change at 1.47 eV. The large isotropic contribution $\chi^{(3)}$ at this photon energy is resonantly enhanced [3]. The difference of the amplitude in the reflectivity between [011] and [01-1] oriented polarization of the probe pulse corresponds to the refraction change due to the Pockels effect. The frequency of 7.6 THz is assigned to coherent coupled plasmon-phonon modes at an excitation density larger than 10^{18} cm^{-3} . The coherent coupled modes dephase much slower than bare plasmon oscillations in the THz range at low lattice temperatures [4]. The observed relatively slow dephasing indicates that the oscillations are mainly dominated by the lattice like part. The resonant detection scheme based on the Franz-Keldysh effect provides one order of magnitude increased reflectivity changes compared to the non-resonant Pockels detection, thus allowing a detailed study of coherent plasmon-phonon interaction in the time domain.

Monitoring the pathway towards non-thermal melting via coherent phonons in tellurium

At sufficiently high excitation densities it is expected that the lattice of a semiconductor is destabilized due to the excitation from bonding to anti-bonding states. Theoretical calculations predict that a complete instability occurs at an inversion rate of approximately 9% [5]. Time-resolved studies of irradiation induced phase transitions have been performed in second-harmonic generation experiments in GaAs and Si [6]. In these experiments the loss of crystal symmetry provides information whether the phase transition has occurred or not. We investigate the lattice instability via the impulsive mode softening of coherent phonons in single crystal tellurium. We generate 100 fs pump pulses of up to 1.2 μJ pulse energy with a Ti:sapphire laser amplified in a 6-pass dye amplifier pumped by a copper-vapor laser. Figure 2 shows the Fourier transforms of the time-resolved reflectivity changes, which are dominated by the modulation due to the coherently excited A_1 mode [7]. The highest fluence corresponds to carrier densities of $1.1 \times 10^{21} \text{ cm}^{-3}$, corresponding to 2% of all valence electrons. With increasing fluence, the phonon frequency shifts from the unperturbed value of 3.6 THz below 3 THz involving frequency components below 1 THz. The phonon frequency shows a linear dependence on the fluence. From additional double-pump-pulse experiments we conclude that the observed mode softening is only due to the excitation density and not affected by transient lattice heating effects [8]. Therefore, the coherent phonon-mode softening is due to a non-thermal melting of the tellurium crystal. The application of this technique to other materials such as GaAs or Si requires shorter amplified pulses, which have become available recently.

- [1] G.C. Cho, W. Kütt, and H. Kurz, Phys. Rev. Lett. **65**, 764 (1990).
- [2] D.E. Aspnes, Surf. Sci. **37**, 418 (1973).
- [3] G.C. Cho, et al, Phys. Rev. B **53**, (1996) in press.
- [4] W. Sha, A. Smirl, W.F. Tseng, Phys. Rev. Lett. **74**, 4273 (1995).
- [5] P. Stampfli and K.H. Bennemann, Phys. Rev. B **49**, 7299 (1994).
- [6] P.N. Saeta, et al, Phys. Rev. Lett. **67**, 1023 (1991).
- [7] T.K. Cheng, et al. Appl. Phys. Lett. **57**, 1004 (1990); *ibid.* **59**, 1923 (1992).
- [8] S. Hunsche, et al., Phys. Rev. Lett. **75**, 1815 (1995).

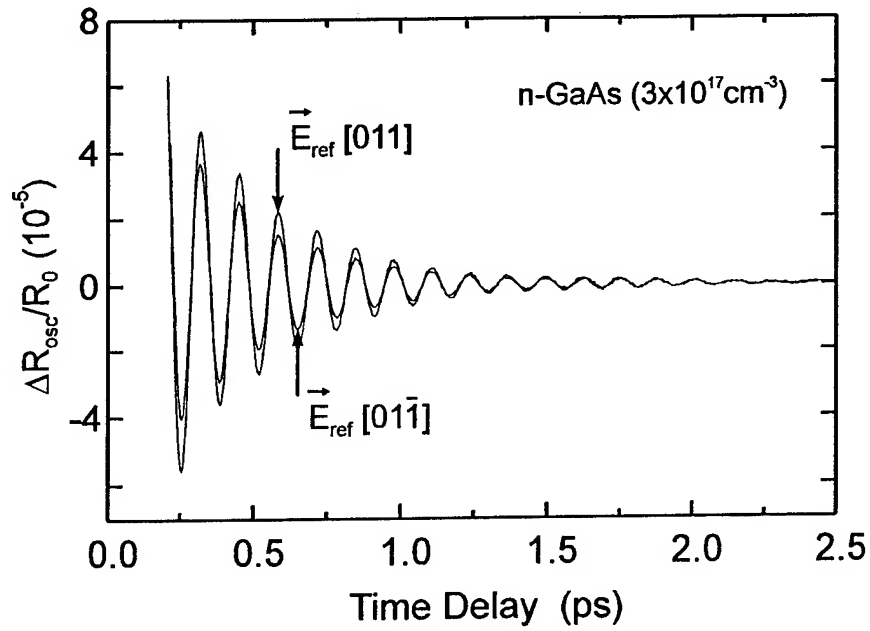


Fig.1 : Oscillatory signal extracted from reflectivity change as a function of time delay between the pump and the probe pulse in GaAs. The polarization of the reflected probe is along the [011] and [01-1] crystal axes.

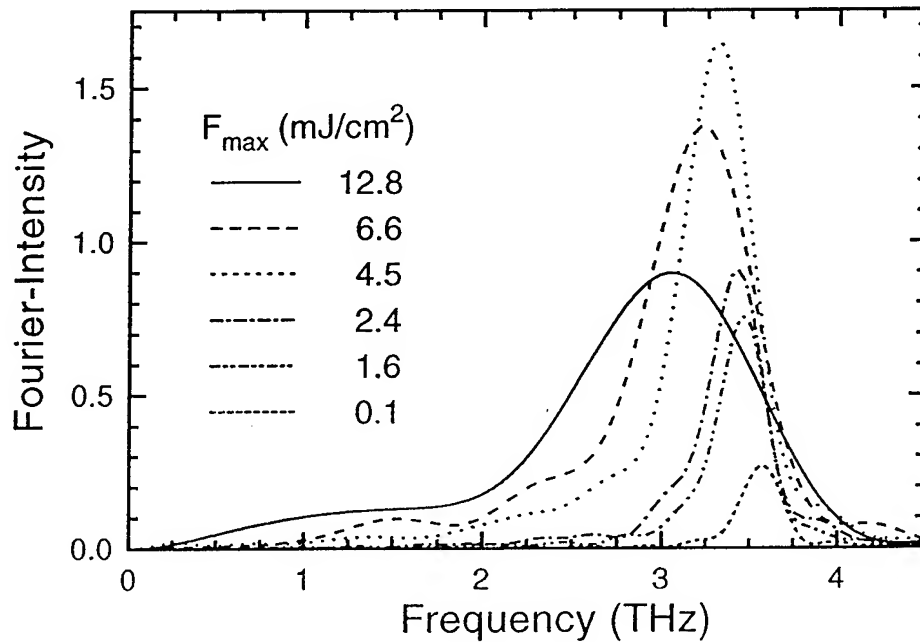


Fig.2 : Fourier spectra of time-resolved reflectivity changes in Te for different laser fluences of the pump pulse as defined in the figure.

Coherent-transient studies of ZnSe/ZnCdSe multiple-quantum-wells

I J Blewett, A Tookey, A K Kar, I Galbraith,

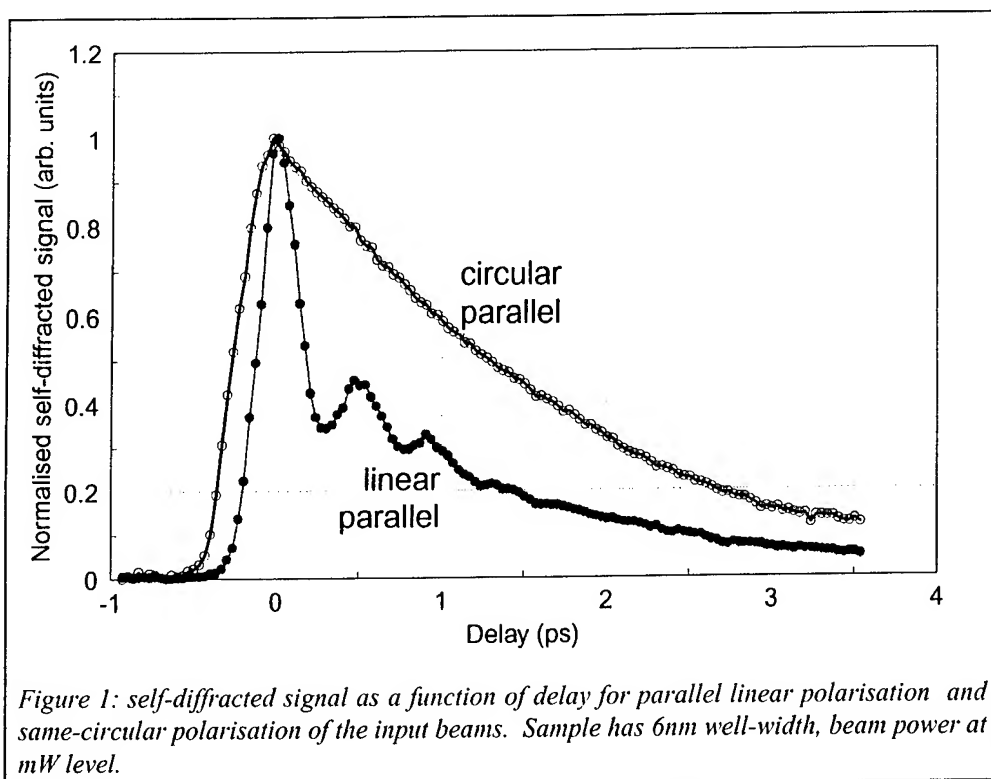
G Horsburgh, T A Steele, K A Prior, B S Wherrett

Physics Department, Heriot-Watt University, Riccarton, Edinburgh, UK EH14 4AS

phone: 0131-451-3049 fax: 0131-451-3136 e-mail: A.K.Kar@hw.ac.uk

A sequence of molecular-beam epitaxially-grown multiple-quantum-well samples with varying well-width have been investigated using the two-beam self-diffracted coherent-transient arrangement¹. The four samples were grown sequentially to provide a consistent sample set, each with identical substrate, buffer and cap layers. The cadmium concentration and number of quantum-wells were maintained at 20% and fifty respectively and the well-widths were varied from 1nm to 6nm.

Experiments were carried out in a cryostat (at around 4K) to reduce phonon activity, and the samples were etched to allow a transmission geometry to be used. For each sample, the quantum-well heavy-hole was resonantly excited using a frequency-doubled Ti:sapphire laser providing 150fs pulses. A second beam derived from the pump-beam then probed the polarisation coherence remaining after a particular delay. The self-diffracted signal produced from the interaction of the second (probe) beam and the remaining material polarisation is plotted as a function of probe delay in the conventional manner. Typical results are shown in figure 1. The coherence loss timescale is found to be around 4ps, decreasing if either the temperature or the pump-power is increased, in line with expectations of increased dephasing due to extra exciton-phonon and exciton-exciton interaction. No clear pattern of coherence-loss timescale with well-width has been observed, contrary to expectations arising from the greater influence of well-width fluctuations for narrower-well samples.

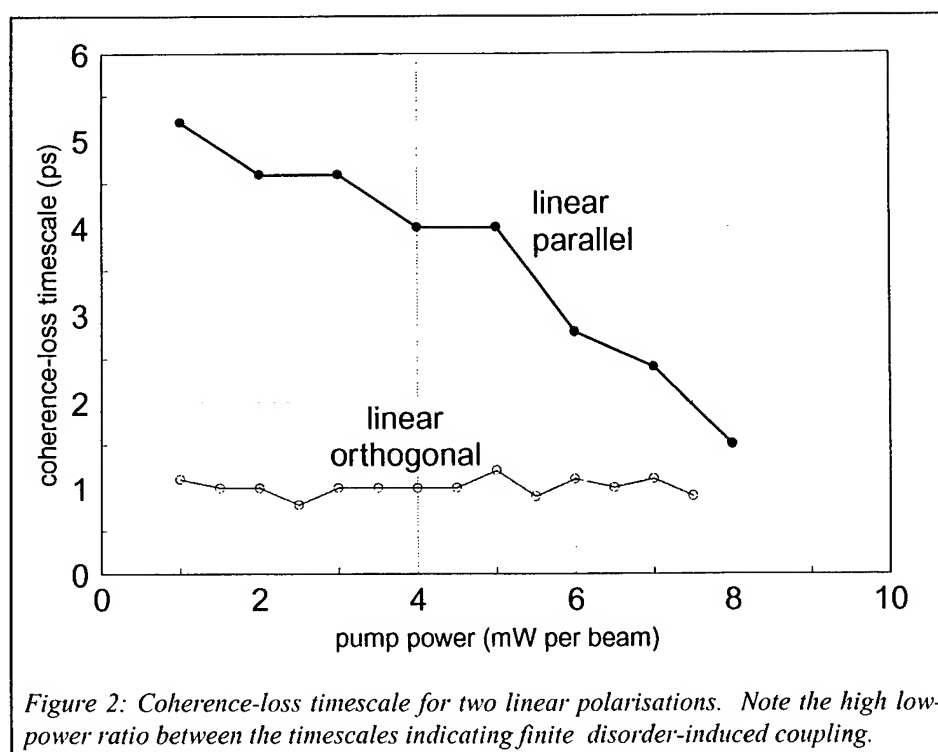


The pronounced, yet decaying, beating in the signal due to linear parallel input beams corresponds to an energy separation of around 10meV. At low temperature, the heavy-hole-light-hole separation is much greater than this (30 - 70meV), and the linear absorption spectrum of the samples show no possible assignment for this energy separation. The conclusion must be that the beating is due to a species not present in the unexcited material.

One candidate for the appropriate excited species is the bi-exciton², formed from the absorption of a photon following previous resonant excitation of an exciton (analogous to a two-photon absorption process from the ground-state). The excited, four-particle body has been shown to possess a renormalised energy, displaced from the exciton binding energy by an amount ΔE^{BiX} , thus enabling beating to occur^{1,3}. An experimental test for this relies on the bi-excitonic property of zero angular momentum. An exciton excited via a circular polarisation possesses a finite angular-momentum and cannot therefore form a bi-exciton through the subsequent absorption of same-circular polarised light. This is confirmed by the second trace of figure 1. However, the assignment of the bi-exciton to the observed beating does not correspond with the property that the ΔE^{BiX} is conventionally thought to be around ten-

percent of the exciton-binding energy (ie; $\Delta E^{\text{BiX}} \approx 3\text{meV}$). Nevertheless, renormalisations based around a more complex species⁴, the bi-polariton (involving two electrons, two holes and a photon) indicate that ΔE^{BiX} as high as 8 - 12meV may be possible.

It has been suggested¹ that sample quality may affect the signals obtained from differing input polarisations. Disorder-induced coupling between excitonic levels predicts that linear orthogonal polarised input should produce an excitation with a coherence-loss timescale unaffected by increased excitation density whereas the linear-parallel configuration has a timescale shortened by excess excitation. Our experiments demonstrate this phenomenon (see figure 2), with a $T_2^{\text{PARALLEL}} / T_2^{\text{ORTHOGONAL}}$ ratio of at least five, suggesting a finite disordering within the material.



¹ J Kuhl, EJ Mayer, G Smith, R Ecclestone, D Bennhardt, P Thomas, K Bott, O Heller, *Optical dephasing of excitons in III-V semiconductors*, NATO ASI B 330 1-32 (1994)

² A L Ivanov, H Haug, *Self-consistent theory of the biexciton optical nonlinearity*, Phys Rev B 48 1490-1504 (1993)

³ H Nickolaus, F Henneberger, A Schulgen, *Coherent exciton-exciton interaction in bulk ZnSe and ZnSe-based quantum-wells*, 7TH INT CONF II-VI COMPOUNDS AND DEVICES, Edinburgh (1995)

⁴ A L Ivanov, H Haug, *Radiative renormalisations for excitonic molecules*, Rhys Rev Lett, 74 438-441 (1995)

Exciton Polariton Boser

Y. Yamamoto, S. Pau, H. Cao and G. Björk
ERATO Quantum Fluctuation Project, E. L. Ginzton Laboratory,
Stanford University, Stanford, CA 94305

Wannier excitons in a GaAs quantum well planar microcavity strongly couple with a single-mode photon field and form "microcavity exciton-polaritons". This quasi-particle has a bosonic character when the inter-particle scattering is negligible. Compared to GaAs bare excitons, exciton-polaritons have much lighter mass (by four orders of magnitude) and thus the thermal de Broglie wavelength of GaAs exciton-polaritons is 100 times longer than that of GaAs bare excitons at the same temperature. Therefore, the quantum statistical effect should emerge at a relatively low density.

We have studied the microcavity exciton-polariton emission under non-resonant optical excitation. When the pump laser is tuned a single longitudinal optical (LO) phonon energy above the $k_{\parallel}=0$ microcavity exciton-polaritons, the microcavity exciton-polariton emissions are resonantly enhanced. If the pump laser intensity passes through a certain threshold, the emission intensity nonlinearly increases and the emission spectral linewidth is abruptly decreased. This lasing behavior is explained by the exciton-polariton boser model, in which the LO phonon emission rate is enhanced by the final-state stimulation due to the finite population of bosonic quasi-particles, "exciton-polaritons".

Wednesday, July 10, 1996

Wavemixing in Semiconductors

NWB 10:00 am-11:20 am
Maile Room

Arthur Smirl, *Presider*
University of Iowa

Engineering the Second-order Optical Nonlinearity in Semiconductors

S. Janz

Institute for Microstructural Sciences, National Research Council, Ottawa, Ontario
Canada, K1A 0R6; Telephone: (613)-990-0926, FAX: (613)-952-8701
E-mail: janz@nrcphy1.phy.nrc.ca

Quasi-phase matching techniques have revolutionized the field of nonlinear optical frequency mixing. Nonlinear crystals for conventional second-harmonic (SH) generation require anisotropic linear optical properties to permit the phase matching of the pump and SH beams. This requirement severely limits useable materials and geometries. The mismatch between pump and SH beams can be compensated by periodically modulating the optical properties of a material, resulting in a quasi-phase matched (QPM) geometry with efficiencies approaching that of conventional phase matched geometries. Although the concept of QPM has been known for more than thirty years, only in the last decade has QPM been widely implemented for a variety of applications¹. For example, QPM SH generation with very high efficiencies has been achieved in LiNbO₃ and KTP waveguides¹, and optical parametric oscillators (OPO) employing QPM structures have been demonstrated². The advent of QPM has important implications for optical materials science. Virtually any material with a non-zero second-order susceptibility, $\chi^{(2)}$, may be useful for nonlinear devices, and so it has become increasingly important to understand and learn how to control the optical nonlinearities in a wide variety of materials.

Semiconductors such as Al_xGa_{1-x}As are particularly interesting because they can have very large second order nonlinearities. For example, $\chi^{(2)}$ in GaAs is an order of magnitude larger than in LiNbO₃. Equally important, however, is the advanced state of semiconductor growth and processing technology, which allows the fabrication of a wide variety of monolithically integrated waveguide structures, optical components, and semiconductor lasers. The optimization of QPM semiconductor devices depends on the ability to spatially modulate $\chi^{(2)}$. Within the Al_xGa_{1-x}As system, a number of approaches have been explored, the simplest of which is to vary the Al concentration. Measurements³ have shown that in the near-infrared $\chi^{(2)}$ decreases by an order of magnitude as x increases from 0 to 1. This variation in $\chi^{(2)}$ with increasing x can be attributed to the increase in the E₀, E₁, and E₂ critical point transition energies of the Al_xGa_{1-x}As band structure⁴. QPM surface emitting waveguides using alternating

layers of high and low Al concentrations can have SH conversion efficiencies several orders of magnitude higher than similar homogeneous GaAs waveguides. Although the absolute SH conversion efficiency is smaller than for other QPM geometries, the surface emitting waveguide configuration has numerous applications involving nonlinear optical signal processing⁵. To achieve SH conversion efficiencies of several per cent or higher, geometries in which the SH and pump beams copropagate over lengths of a few millimeters are necessary. Fabricating suitable QPM waveguides for the copropagating geometry by modulating the Al concentration would require the use of problematic epitaxial overgrowth techniques.

An alternative approach is to use asymmetric quantum wells (AQWs) or biased symmetric quantum wells to modify $\chi^{(2)}$ in a semiconductor device. Since AQWs do not have inversion symmetry, the confined electronic states have a $\chi^{(2)}$ associated with them. For example, a typical AQW will introduce new tensor components $\chi_{zzz}^{(2)}$, $\chi_{xzx}^{(2)}$, $\chi_{zxx}^{(2)}$, $\chi_{zxy}^{(2)}$, and $\chi_{xyz}^{(2)}$ (z is the growth direction, and x and y are interchangeable). For frequency mixing experiments in the infrared, the $\chi^{(2)}$ associated with AQWs can be huge, since double resonances between three subband levels can be utilized, and the dipole matrix elements are large⁶. Unfortunately, only singly resonant interband transitions can be utilized for frequency conversion processes in the near-infrared and visible. Furthermore, at these wavelengths the smaller dipole matrix elements and a cancellation of terms in the expression for the interband $\chi^{(2)}$ conspire to make the $\chi^{(2)}$ in AQWs approximately an order of magnitude smaller than that of bulk GaAs⁷. Both theoretical⁷ and experimental⁸⁻¹⁰ investigations of AQWs and biased quantum wells have determined values of $\chi^{(2)}$ in the near-infrared to be in the vicinity of $\chi^{(2)} = 10^{-11} \text{ mV}^{-1}$. Note, however, that the near-infrared AQW susceptibilities remain comparable to those of commonly used metal-oxide nonlinear crystals. In addition, recent theoretical calculations suggest that AQWs may be more promising for certain applications than originally thought, since the $\chi^{(2)}$ of an AQW near the exciton resonance may be an order of magnitude larger than that of bulk GaAs¹¹. In this presentation, recent experimental evidence to support this prediction, from both this laboratory and others, will be discussed.

The primary attraction of asymmetric or biased quantum wells is that $\chi^{(2)}$ can be modulated. For example, in a surface emitting waveguide heterostructure, QPM is achieved by periodically reversing the orientation of the AQWs to produce alternating regions of positive and negative $\chi^{(2)}$. There has been much recent research on the use of quantum well intermixing to modify the optical properties of quantum wells, using

techniques such as ion implantation or annealing. These post-growth techniques are suitable for creating QPM waveguides where the pump and sum (or difference) frequency beams are copropagating. Once appropriate techniques have been investigated and refined, QPM semiconductor devices with efficiencies comparable to those of state of the art dielectric waveguides may be achievable. This would permit the fabrication of efficient semiconductor frequency converters for use in WDM frequency shifting devices, and perhaps waveguide OPOs.

Finally, centrosymmetric semiconductor systems such as $\text{Si}_{1-x}\text{Ge}_x$ have no bulk $\chi^{(2)}$. The applications of $\chi^{(2)}$ in $\text{Si}_{1-x}\text{Ge}_x$ extend beyond frequency mixing, since a $\chi^{(2)}$ nonlinearity can also be used to implement high speed electro-optic modulators, a fundamental component in a Si based optoelectronic system. Schemes for producing $\chi^{(2)}$ in $\text{Si}_{1-x}\text{Ge}_x$ using odd period superlattices¹² and ordered SiGe alloys¹³ have been proposed, but the required growth technology is not yet available. Therefore the most promising technique for creating $\chi^{(2)}$ in an Si based material may be through the use of $\text{Si}_x\text{Ge}_{1-x}$ AQW superlattices.

References

1. M.M. Fejer, G.A. Magel, D.H. Jundt, and R.L. Byer, IEEE J. Quantum Electron. **28**, 2631 (1992), and references therein.
2. M.L. Bortz, M.A. Arbore, and M.M. Fejer, Opt. Lett. **20**, 49 (1995).
3. S. Janz, F. Chatenoud, H. Dai, E. Vilks, M. Buchanan, R. Normandin, and A.J. Springthorpe, Mat. Res. Soc. Symp. Proc. Vol. 281, 301 (1993).
4. D.J. Moss, J.E. Sipe, and H.M. van Driel, Phys. Rev. B **36**, 9708 (1987).
5. Y. Beaulieu, S. Janz, H. Dai, E. Frlan, C. Fernando, A. Délage, P. van der Meer, M. Dion, and R. Normandin, J. Nonlinear Opt. Phys. and Mat. **4**, 893 (1995).
6. E. Rosencher, A. Fiore, B. Vinter, V. Berger, Ph. Bois, and J. Nagle, Science **271**, 168 (1996).
7. J. Khurgin, Phys. Rev. B **38**, 4056 (1988).
8. S. Janz, F. Chatenoud, and R. Normandin, Opt. Lett. **19**, 622 (1994).
9. X.H. Qu, H. Ruda, S. Janz, and A.J. Springthorpe, Appl. Phys. Lett. **65**, 3176 (1994).
10. A. Fiore, E. Rosencher, V. Berger, and J. Nagle, Appl. Phys. Lett. **67**, 3765 (1995).
11. R. Atanasov, F. Bassani, and V.M. Agranovich, Phys. Rev. B **50**, 7809 (1994).
12. E. Ghahramani, D.J. Moss, and J.E. Sipe, Phys. Rev. Lett. **64**, 2815 (1990).
13. R.A. Soref, J. Appl. Phys. **72**, 826 (1992).

Current Induced Second Harmonic Generation in Semiconductors

Jacob B. Khurgin

Department of Electrical and Computer Engineering
The Johns Hopkins University, Baltimore MD 21218

Second order nonlinear optical effects have been thoroughly studied and used ever since the very first experiment in the early 1960's. It is also well known that only materials lacking the center of inversion symmetry possess the second order susceptibility $\chi^{(2)}$ [1]. At the same time, externally applied fields can break the symmetry and cause the so-called field induced second order susceptibility. For example, this effect is believed to be behind the "seeded" second harmonic generation (SHG) in glass fibers where external field is produced by space charge [2]. In insulating materials it is not difficult to apply external fields high enough to produce appreciable $\chi^{(2)}$. One can then envision that this DC-induced SHG can be used to probe and map the distribution of the electric field. But what about the metals and semiconductors, where the electric fields are small while the currents can be quite strong? Here, using simple two-band model, we show that in the presence of a direct current a second order nonlinear susceptibility, proportional to the current exists.

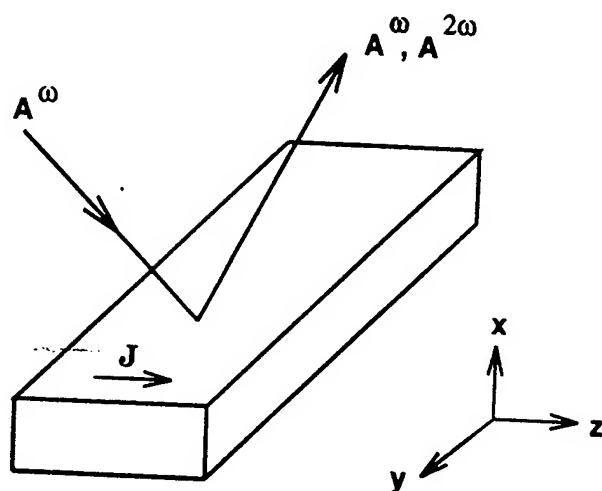
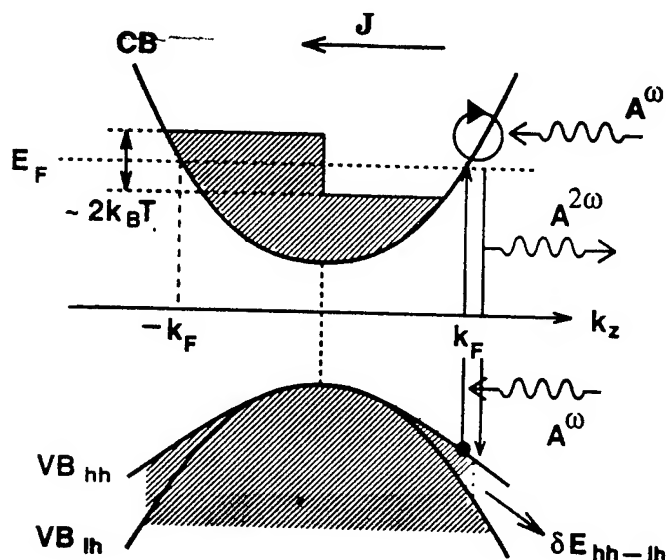


Fig.1 Band diagram of the states involved in the SHG. Fig.2 Geometry of the current-induced SHG

Consider an n-doped direct bandgap semiconductor with Fermi level E_F in the conduction band (CB) (Fig.1). As a result of the applied field E the distribution of the electrons in the CB is described by the Fermi function $f(\mathbf{k}) = f_e(\mathbf{k} - \mathbf{k}_E)$, shifted from the equilibrium one, by the amount $\mathbf{k}_E = -e\tau E/\hbar$ in \mathbf{k} -space. Assuming the field to be directed along z , the electrons with wave vectors $k_z \approx -k_F$ are not balanced by the electrons with $k_z \approx k_F$ and the current,

$$\mathbf{J} = - \sum_{\mathbf{k}} e \mathbf{v}(\mathbf{k}) f(\mathbf{k}) = - \frac{e\hbar}{m_c} \sum_{\mathbf{k}} \mathbf{k} f(\mathbf{k}) \quad (1)$$

flows in the sample.

Consider now interaction of this material with the coherent electro-magnetic wave (Fig.2)

$$\mathbf{A}(t) = \frac{1}{2} \mathbf{A}^\omega e^{-i\omega t} + \frac{1}{2} \mathbf{A}^\omega e^{i\omega t} \quad (2)$$

A pair of states in VB and CB with the same wave-vector \mathbf{k} involved in the nonlinear process is described by a density matrix

$$\hat{\rho}_{\mathbf{k}} = \begin{vmatrix} \rho_{vv,\mathbf{k}} & \rho_{vc,\mathbf{k}} \\ \rho_{cv,\mathbf{k}} & \rho_{cc,\mathbf{k}} \end{vmatrix} \quad (3)$$

and Hamiltonian

$$\hat{H}_{\mathbf{k}} = \hat{H}_{0\mathbf{k}} - \frac{e}{m_0} \hat{\mathbf{p}} \cdot \mathbf{A} = \begin{vmatrix} \frac{1}{2} \hbar \omega_{0,\mathbf{k}} + \frac{e}{m_v} \hbar \mathbf{k} \cdot \mathbf{A} & -\frac{e}{m_0} \mathbf{P}_{vc,\mathbf{k}} \cdot \mathbf{A} \\ -\frac{e}{m_0} \mathbf{P}_{cv,\mathbf{k}} \cdot \mathbf{A} & -\frac{1}{2} \hbar \omega_{0,\mathbf{k}} - \frac{e}{m_c} \hbar \mathbf{k} \cdot \mathbf{A} \end{vmatrix} \quad (4)$$

where $\hbar \omega_{0,\mathbf{k}} = E_g + \frac{\hbar^2 k^2}{2\mu}$, m_c and m_v are the effective masses, μ is a reduced mass, and $\mathbf{P}_{cv,\mathbf{k}}$ is a matrix element of the dipole transition. Solving the equation of motion in the second order, Keeping only the terms having the time dependence $e^{2i\omega t}$ and are nearly resonant, one obtains the results for the component of nonlinear current at frequency 2ω

$$\mathbf{J}^{[2\omega]} = -\frac{e^3}{4\hbar m_0^2 \mu} \sum_{\mathbf{k}} \left[\frac{\mathbf{P}_{vc,\mathbf{k}}(\mathbf{k} \cdot \mathbf{A}^\omega)(\mathbf{P}_{cv,\mathbf{k}} \cdot \mathbf{A}^\omega)(1-f(\mathbf{k}))}{(\omega_{0,\mathbf{k}} - 2\omega - \frac{i}{T_2})(\omega_{0,\mathbf{k}} - \omega - \frac{i}{T_2})} \right] \quad (5)$$

It is clear that when summation over \mathbf{k} takes place, due to the symmetry contribution of states with \mathbf{k} will be canceled by the states with $-\mathbf{k}$ and in fact only the states within $k_B T$ of the Fermi surface will contribute to SHG. Of course, they are the same states that are responsible for the DC current \mathbf{J} (Eq. 1). Then, one can approximate the detuning $\omega_{0,\mathbf{k}} - 2\omega$ as roughly $k_B T$.

Making transition from vector potential to electric field one can obtain the following expression for the current-dependent $\chi^{(2)}$

$$\chi_{\mathbf{J}}^{(2)}(2\omega; \omega, \omega) = \frac{e^3}{4\epsilon_0 m_0^2 \mu \omega^4 (k_B T + i\hbar T_2^{-1})} \sum_{\mathbf{k}} \mathbf{P}_{vc,\mathbf{k}}(\mathbf{k} \cdot \hat{\mathbf{e}})(\mathbf{P}_{cv,\mathbf{k}} \cdot \hat{\mathbf{e}}) f(\mathbf{k}) \quad (6)$$

where $\hat{\mathbf{e}}$ is a unit vector of the light polarization.

Clearly, expression (6) for the $\chi^{(2)}$ contains a sum very similar to the one in the expression for the DC current (1), and the nonlinear susceptibility must be proportional to the DC current. In order to find the exact degree of proportionality we must take into account the angular dependence of the $\mathbf{P}_{cv,\mathbf{k}}$, i.e we must consider specific band-structure, such as, for instance, zinc-blende. After some algebra [3], one arrives at the following expression for the $\chi^{(2)}$ tensor

$$\begin{aligned} \chi_{ijk}^{(2)}(2\omega; \omega, \omega, \mathbf{J}) &= \frac{3e^2}{4\epsilon_0 \mu (k_B T + i\hbar T_2^{-1}) \omega^3} \sum_l S_{ijkl}^{hh} J_l \\ &+ \frac{3e^2}{4\epsilon_0 \mu (k_B T + \delta E_{lh-hh} + i\hbar T_2^{-1}) \omega^3} \sum_l S_{ijkl}^{lh} J_l \end{aligned} \quad (7)$$

where the summation is over heavy and light holes, δE_{lh-hh} is a heavy-hole -light hole splitting, and the tensor S^v is simply a result of averaging over the angle and has only three distinct non-zero components for each band:

$$S_{iiii}^{hh} = 1/15; S_{iijj}^{hh} = S_{ijji}^{hh} = 1/30; S_{ijij}^{hh} = 2/15; \quad (8)$$

$$S_{iiii}^{lh} = 7/45; S_{iijj}^{lh} = S_{ijji}^{lh} = -1/30; S_{ijij}^{lh} = 4/45; \quad (9)$$

which, of course are the same non-zero components as in $\chi^{(3)}$ tensor of cubic crystal. Indeed, current induced $\chi^{(2)}$ is a process reverse to the coherent photo-galvanic effect [4] and must have the same symmetry, although not necessarily same magnitude. Thus, for the current flowing in z direction, these components of current-induced $\chi^{(2)}$ are not zero: $\chi_{zzz}^{(2)}$, $\chi_{xxz}^{(2)}$, $\chi_{zxx}^{(2)}$, and $\chi_{xxx}^{(2)}$. For the diagonal component, using GaAs as a typical material

$$|\chi_{zzz}^{(2)}| \approx \frac{\alpha \hbar \lambda^3}{40\pi^2 m_0 c^2 (k_B^2 T^2 + \hbar^2/T_2^2)^{1/2}} \frac{m_0}{\mu} J_z = 1.21 \times 10^{-6} \left(\frac{pm}{V} \frac{cm^2}{A} \right) \times J_z, \quad (10)$$

where α is a fine structure constant.

Therefore, for the current densities of $10^4 A/cm^2$, that are available in both bipolar and unipolar devices and do not lead to the current crowding and breakdown [5], one can expect a susceptibility of $0.01 pm/V$. Although much smaller than natural $\chi^{(2)}$ of GaAs, current-induced $\chi^{(2)}$ has different symmetry and thus can be observed.

One can also estimate the amount of SH power produced by nonlinear interaction in, for example a channel of the FET.

$$P^{2\omega} \approx \left[\frac{\alpha \hbar \lambda^2}{10\pi m_0 c^2 (k_B^2 T^2 + \hbar^2/T_2^2)^{1/2}} \right]^2 \left(\frac{m_0}{\mu} \right)^2 \eta_0 \frac{[J_l P^\omega]^2}{a^2} \approx 3 \times 10^{-19} \left(\frac{cm^4}{W \cdot A^2} \right) \times \frac{[J_l P^\omega]^2}{a^2} \quad (11)$$

where a^2 is the area on which the light impinges, and J_l is the linear current density (per unit length on the surface), and $\eta_0 = 377\Omega$. Consider the case of 100 ps, $0.1\mu J$ Q-switched or mode-locked laser pulse focused into $10\mu m^2$ of the FET with $J_l = 1 A/cm$. Output of $2 \times 10^{-10} \mu J$ or about 10^3 photons per pulse is expected. This is a better result than one obtained in typical surface SHG experiments, [6] and can be measured by sensitive detector. Therefore, one can envision current probing using the described technique. The advantage of these non-contact current sensing lies in its speed and possibility of measuring both direction and magnitude of current.

In conclusion, we have pointed out a novel phenomenon - current-induced SHG nonlinear optical effects and estimated its magnitude in zinc-blende semiconductors. We have shown that this effect can be used in ultrafast probing of current in semiconductor devices.

References

- [1] Y. R. Shen, "The Principles of Nonlinear Optics", J. Wiley @ Sons, New York, 1984 pp. 27-28
- [2] Y. Sasaki and Y. Ohmori, *Appl. Phys. Lett.* **39**, 466 (1981)
- [3] J. B. Khurgin, *J. Opt. Soc. Am.*, **11** (1994)
- [4] E. Dupont, P. B. Corcum, H. C. Liu, Z. R. Wasiliewski, M. Buchanan, in "7-th International Conference on Superlattices, Microstructures and Microdevices", Banff, Alberta, Canada, 1994, p. 496
- [5] S. M. Sze, "Physics of Semiconductor Devices", J. Wiley @ Sons, New York, 1981 pp. 147, 480
- [6] C. K. Chen, T. F. Heintz, D. Ricard and Y. R. Shen, *Phys. Rev. Lett.*, **46**1010 (1962)

Generation of terahertz radiation by difference-frequency mixing of femtosecond pulses in InSb and InAs

S. C. Howells and L. A. Schlie

Laser and Imaging Directorate (PL/LIDD), Phillips Laboratory, 3550 Aberdeen Ave SE,
Kirtland AFB, NM 87117 ph. (505) 846-4602 fax. (505) 846-5041

The role of nonlinear optical phenomena in the generation of terahertz radiation via nonlinear mixing of ultrashort infrared laser pulses at semiconductor surfaces is described. Several mechanisms lead to the generation of terahertz radiation from semiconductor surfaces, including depletion-field driven current (current surge),¹ bulk difference-frequency mixing (DFM),² and electric-field-induced optical rectification.³ Previous studies reported that when InSb is illuminated with unfocused above-gap ultrashort optical pulses, the spectrum of the emitted radiation, which is due to the current surge mechanism, shifted to lower frequency as the sample temperature decreased.^{1,4} This unique feature has led us to study the temperature dependence of difference-frequency mixing from InSb crystals illuminated with focused laser pulses. Increasing the intensity of the 100 fs laser pump beam leads to measurable amounts of terahertz radiation by nonlinear mixing of the spectral components of the pump pulse, as well as a decrease in the current-surge-induced terahertz radiation.² By rotating an undoped (111) InSb sample about its surface normal, we were able to separate the contribution of the azimuthally-dependent DFM signal from the total terahertz waveform. Contrary to the current surge pulses emitted from (111) InSb, the DFM pulses did not show any frequency shift with temperature. However, there was a pronounced temperature dependence of the DFM pulse amplitude that closely followed that seen from the current surge pulses. Finally, analysis of the angular dependence of terahertz radiation emitted from (100) InAs shows that the dominant nonlinear mixing term is bulk optical rectification.

The experimental set-up was a time-resolved, optoelectronic, coherent detection system using photoconductive antennas.⁴ The antennas were oriented either vertically or horizontally to detect TM- or TE-polarized terahertz radiation, respectively. The InSb samples were placed in a compact cryostat (80-400 K) and mounted to a rotation stage that allowed the samples to be rotated azimuthally. After cooling, the samples were illuminated with 1.4 μm , 120 fs pulses from a Ti:sapphire laser at an incident angle of 45°. Throughout these experiments, the focused pump irradiance remained approximately 60 MW/cm² and the samples used were undoped ($n \approx 1.5 \times 10^{14} \text{ cm}^{-3}$) (111) InSb and undoped (100) InAs.

The far-infrared radiation (FIR) due to bulk rectification is proportional to the second order polarization, $P_i^{(2)}(\Omega = \omega_1 - \omega_2) = 2\epsilon_0 \chi_{ijk} E_j(\omega_1) E_k(\omega_2)$. The second order susceptibility tensor, χ_{ijk} , is non-zero for zincblende crystals only for $i \neq j \neq k$ where i, j, k are the principal axes. Also, all of the non-

zero elements are equal, $\chi_{xyz} = \chi_{yxz} = \dots = \chi$. The azimuthal dependence of the TE-polarized DFM signal emitted from (100) zincblende crystals for TM- and TE-polarized incident pumps is given by, respectively,

$$TE_{TM-pump} = -E^2 \chi \cos(\alpha) \sin(\alpha) \sin(2\phi), \quad (1)$$

$$TE_{TE-pump} = 0 \quad (2),$$

where α is the internal propagation angle of the terahertz pulse. Figure 1a shows the azimuthal dependence of terahertz radiation from (100) InAs, in agreement with Eqns. 1 and 2. This unambiguously verifies that bulk rectification is a dominant mechanism of nonlinear difference frequency mixing in InAs, since electric-field-induced DFM predicts no azimuthal dependence of the terahertz radiation emitted from (100) surfaces. The DC offset of the signals in Fig. 1a is due to the the current surge mechanism.

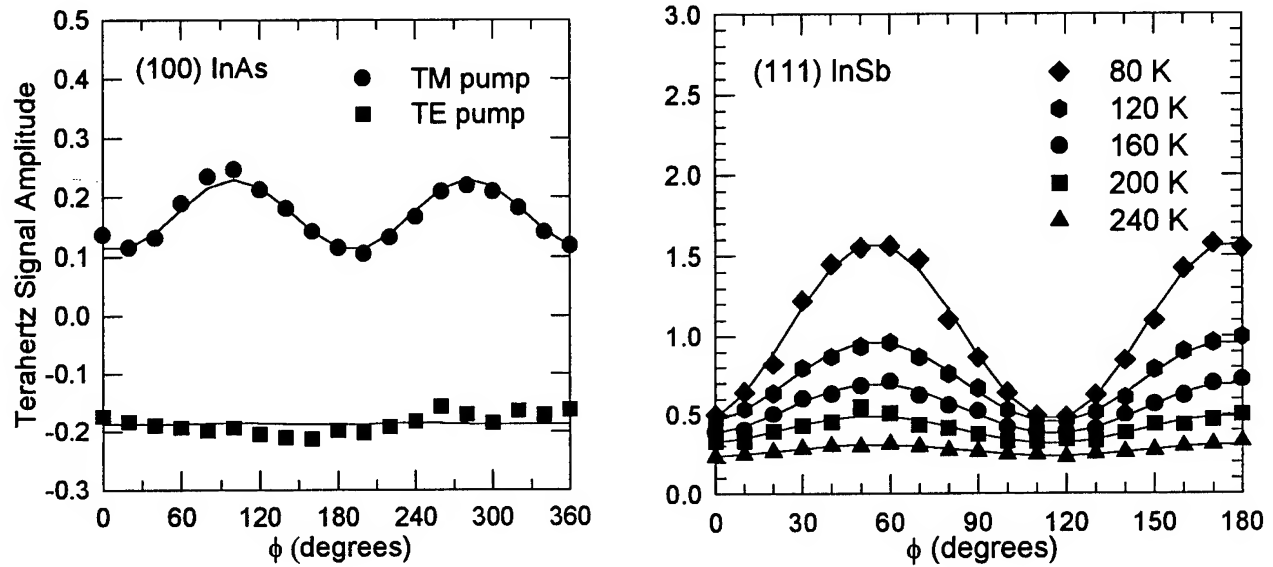


Fig1. a) Azimuthal dependence of terahertz radiation emitted from (100) InAs. The angular dependence confirms that the nonlinear mixing is due to bulk difference-frequency mixing. b) Azimuthal dependence of terahertz radiation emitted from (111) InSb showing the expected 3ϕ dependence and a temperature dependence of the emitted DFM signal.

Turning next to the (111) surface, the azimuthal dependence of the TM-polarized DFM signal emitted from a (111) zincblende crystal for a TM-polarized incident pump is given by

$$TM_{TM-pump} = 0.75 E^2 \chi \cos^2(\alpha) \cos^3(\theta) \cos(3\phi), \text{ where } \theta = 35.3^\circ. \text{ Figure 1b shows the azimuthal}$$

dependence of the terahertz pulse amplitude emitted from (111) InSb at a number of temperatures with the expected 3ϕ dependence. Note that the amount of modulation, and therefore the DFM signal emitted from (111) InSb, decreases with increasing temperature. It was also found that, unlike the current surge induced radiation, the DFM pulse shape does not vary with temperature.

Lastly, Fig. 2 shows a detailed comparison of the temperature dependence of the current surge and DFM signals emitted from (111) InSb. For the current surge signal, this was done by simply measuring the terahertz pulse amplitude generated by the unfocused pump. The DFM amplitude was obtained by subtracting the terahertz waveform obtained at azimuthal angle of 0° from the waveform obtained at 60° and measuring the amplitude. Figure 2 shows a strong similarity between the current surge and DFM signals, as they decrease in tandem by an order of magnitude between 100-260 K. There is some difference above 200 K, with the DFM signal decreasing faster than the current surge signal. From the decrease of the terahertz signals, one can relate the diminution of the current surge signal, which is predominantly a function of the transient mobility, to the diminution of the DFM signal, which is directly related to $\chi^{(2)}(\Omega, \omega_1, \omega_2)$. The pronounced temperature dependence of terahertz radiation due to nonlinear mixing was previously predicted by Chuang, et al.³ It is not surprising that the temperature dependent curves are similar, since the scattering mechanisms that affect the mobility will also cause dephasing of the nonlinear polarization.

In conclusion, we measured the terahertz radiation emitted from (100) InAs and (111) InSb illuminated at 45° . Analysis of the angular dependence of radiation emitted from (100) InAs shows that the dominant nonlinear mixing term is bulk optical rectification. Furthermore, there was a pronounced temperature dependence of the DFM pulse amplitude that closely followed that seen from the current surge pulses emitted from (111) InSb. Finally, we were not able to detect any frequency shift of the DFM signal as a function of temperature as was previously seen with the current surge mechanism in undoped InSb.

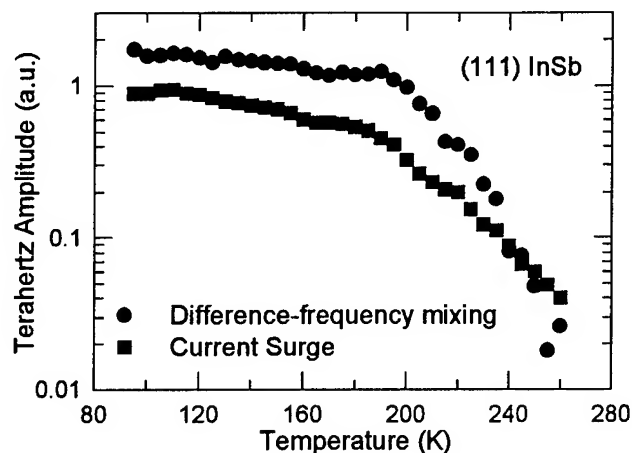


Figure 2. Temperature dependence of terahertz radiation amplitude emitted from (111) InSb due to current surge and difference-frequency mixing.

¹ B. B. Hu, X. C. Zhang, and D. H. Auston, *Appl. Phys. Lett.* **57**, 2629 (1990).

² P. N. Saeta, B. I. Greene, and S. L. Chuang, *Appl. Phys. Lett.* **63**, 102 (1992).

³ S. L. Chuang, S. Schmitt-Rink, B. I. Greene, P. N. Saeta, A. F. J. Levi, *Phys. Rev. Lett.* **68**, 102 (1992).

⁴ S. C. Howells, S. D. Herrera, and L. A. Schlie, *Appl. Phys. Lett.* **65**, 2948 (1994).

Design of Quantum Well Intersubband Transitions for Non-linear Difference Frequency Mixing

J.S. Harris, Jr.

Center for Nonlinear Optical Materials
Stanford University, Stanford, CA 94305

Abstract: The use of intersubband transitions in quantum wells is discussed, particularly with application to Difference Frequency Generation. The use of quasi-bound states is also explored.

Nonlinear optical techniques are often used to extend the wavelength range of common light sources. For example, Nd:YAG lasers at 1064 nm can have their frequencies doubled to produce blue light 532 nm. Another possibility with nonlinear materials is Difference Frequency Generation (DFG). Here, one frequency of light is subtracted from another to produce a low frequency, long wavelength output. There are a number of applications for an intense, mid-IR light source, however, lasers in this region of the spectrum are scarce, or prohibitively difficult to operate. Utilizing a suitable nonlinear material, two diode lasers in the near IR can be mixed to produce an output ranging from the mid to far IR. Diode lasers are compact, efficient, and can be easily integrated with other materials. The necessary nonlinear material would need to possess a large nonlinear coefficient in the near to mid IR, would need to be phasematchable, and be integrable with diode lasers.

Although semiconductor materials usually possess large nonlinear coefficients ($\chi^{(2)} \sim 180$ pm/V for bulk GaAs), these materials have not been widely used for nonlinear optics applications. This is due in large part to the lack of birefringence, and hence phasematching, in these materials. One possible phasematching technique utilizing bulk $\chi^{(2)}$ involves using specially patterned substrates that rotate the semiconductor lattice, and hence $\chi^{(2)}$, periodically.

Quantum well intersubband transitions (ISBTs) can fulfill the necessary requirements for efficient nonlinear DFG. Values of $\chi^{(2)}$ for ISBTs can be as large as 100,000 pm/V, in contrast to 180 pm/V for bulk GaAs. In addition, quasi-phasematching can be achieved by proton bombardment, creating traps in the material to effectively reduce the intersubband population to zero. In addition, ISBTs can be easily tailored for conversion at the wavelength of interest.

One common material system for creating quantum wells is the GaAs/AlAs system, with GaAs being used for the wells and AlGaAs for the barriers. Since these two materials are lattice matched, they (and any alloy of the two) can be grown epitaxially on top of one another, while maintaining the crystal structure of the substrate. Another possibility is to use an InGaAs alloy for the well material. This results in greater confinement, since InAs has a smaller bandgap than GaAs. InAs, however, is not latticematched to GaAs. One possibility is to grow thin layers, thinner than the critical thickness at which dislocations occur. Another possibility is to use a graded buffer layer. By gradually increasing the indium content, a layer is formed which acts as a

experiments of bound to quasi-bound optical absorption have shown clear confinement of the resonant state above the barrier [2]. Spatial confinement using Bragg reflectors was considered for creating population inversion between two above-barrier states [3] and used for improving threshold current in recently invented quantum cascade lasers [4]. Above-barrier states can also be used for intersubband transitions, nonlinear optics and detectors at short wavelengths less than $2\text{ }\mu\text{m}$ when incorporated in deep quantum wells.

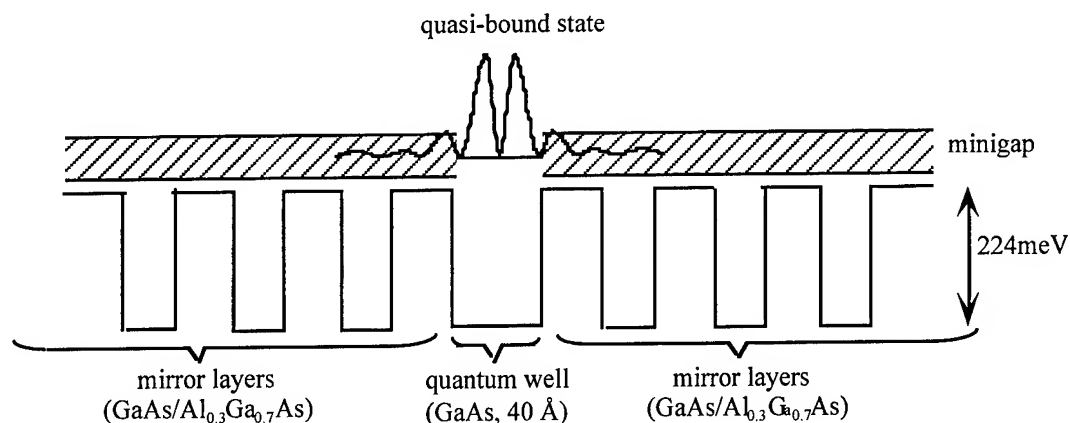


Figure 1. Conduction band diagram of the quantum well and mirror layers. A quasi-bound state forms around the middle of the minigap due to the reflection off the mirrors and boundary conditions across the quantum well.

Because of the flexibility of ISBTs, they can be designed to cover a broad wavelength range. This, coupled with their ability to be quasi-phasematched and easily integrated with diodes, make ISBT devices ideal for many applications requiring intense, coherent, mid to far IR light sources. Possible applications include eye-safe infra-red radar, sensors for many gases and molecules (i.e. glucose) and airborne countermeasure devices. Progress to date has included successful DFG experiments. In addition, the use of quasi-bound states should increase the wavelength range of ISBTs in the near future.

References:

- [1] H. C. Chui, G. L. Woods, M. M. Fejer, E. L. Martinet, and J. S. Harris, Jr, Appl. Phys. Lett. 66, 265 (1995)
- [2] C. Sirtori, F. Capasso, J. Faist, D. L. Sivco, S. N. G. Chu, and A. Y. Cho, Appl. Phys. Lett. 61, 898 (1992)
- [3] G. N. Henderson, L. C. West, T. K. Gaylord, C. W. Roberts, E. N. Glytsis, and M. T. Asom, Appl. Phys. Lett. 62, 1432 (1993)
- [4] J. Faist, F. Capasso, C. Sirtori, D. L. Sivco, A. L. Hutchinson, and A. Y. Cho, Appl. Phys. Lett. 66, 538 (1995)

new substrate, with a lattice constant intermediate between the AlGaAs barrier and the InGaAs well. This increases the critical thickness to a usable amount (i.e. from 40 Å to 100 Å).

The nonlinear coefficient $\chi^{(2)}$ of an intersubband transition for DFG is given by:

$$\chi^{(2)}(\omega = \omega_1 - \omega_2) \equiv \frac{e^3 N_{\text{eff}}}{\epsilon_o} \frac{z_{12} z_{23} z_{31}}{(\hbar\omega - E_{21} - i\Gamma_{21})(\hbar\omega_1 - E_{31} - i\Gamma_{31})}$$

It can be seen that this term will be maximized when both terms in the denominator are resonant. This condition can be achieved through careful design of the quantum well structure. Typically, a coupled-well structure is used. This is two thin quantum wells (of differing thickness) separated by a thin barrier. By changing the thickness of the barrier and wells, conditions of either single or double resonance can be achieved. In order for the z_{31} dipole moment to be non-zero, the coupled-well must be asymmetrical. As mentioned earlier, proton bombardment reduces N_{eff} (intersubband population) to zero, thus eliminating $\chi^{(2)}$ and providing a means of quasi-phasing the sample.

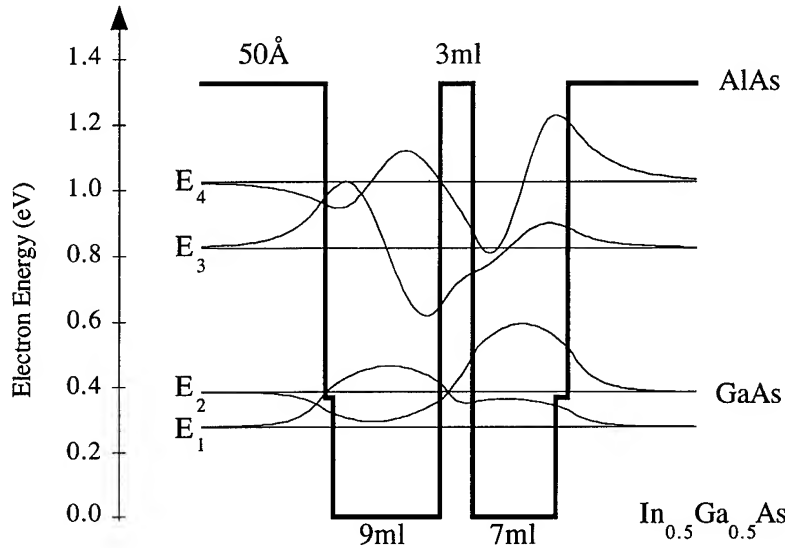


FIG 1. Band diagram of coupled QW sample for DFG experiment

One difficulty that has been encountered has been creating quantum wells with large enough transition energies that they may effectively be pumped by short wavelength lasers. One approach utilized use high-indium content quantum wells on top of strained buffer layers. Using this technique, Chui et al. demonstrated DFG using the quantum well intersubband nonlinearity. Two outputs from a Nd: YAG pumped OPO, at $\sim 1.9 \mu\text{m}$ and $\sim 2.4 \mu\text{m}$, were differenced to produce an output ranging from $8.66 \mu\text{m}$ to $11.34 \mu\text{m}$ [1].

Another possibility to increase the effective well depth is to use above-band states. Contrary to the conventional method of confining carriers in a potential well, carriers can be confined above a barrier using the optical analogy of Bragg reflectors. Recent

Wednesday, July 10, 1996

Nonlinear Probes of Materials and Devices

NWC 1:30 pm-2:40 pm
Maile Room

George Stegeman, *Presider*
University of Central Florida

**Second Harmonic Spectroscopy of Buried Si(001)/SiO₂ Interfaces
and Si(001) Epitaxial Growth Surfaces**

Michael Downer
University of Texas

Summary not available.

Application of nonlinear optics for probing of silicon-based circuits

H. Kurz, C. Ohlhoff, C. Meyer, G. Lüpke, T. Löffler, T. Pfeifer, and H.G. Roskos

*Institute of Semiconductor Electronics II, Rheinisch-Westfälische Technische Hochschule,
D-52056 Aachen, Germany*

Rapid progress in the development of silicon monolithic millimeter-wave integrated circuits (MMIC) operating at frequencies up to 100 GHz demands for new test techniques with high temporal and spatial resolution.[1] Nonlinear optical methods based on the internal Pockels effect have been used effectively to noninvasively probe both analog and digital signals in GaAs MMIC's. While this approach is adequate for measuring voltage waveforms in III/V-based circuits it is not applicable to silicon integrated circuits. Silicon exhibits no bulk second-order nonlinearities, because of its centrosymmetric crystal structure. To overcome this limitation and simultaneously retain the noninvasiveness of direct electro-optical probing, we apply electric field-induced second-harmonic generation (EFISHG) to monitor the internal electric field distribution in silicon MMIC's. We present the first results of a picosecond EFISHG study showing a free-running microwave signal on a photoconductive dipole antenna fabricated on a radiation-damaged silicon-on-sapphire substrate.[2]

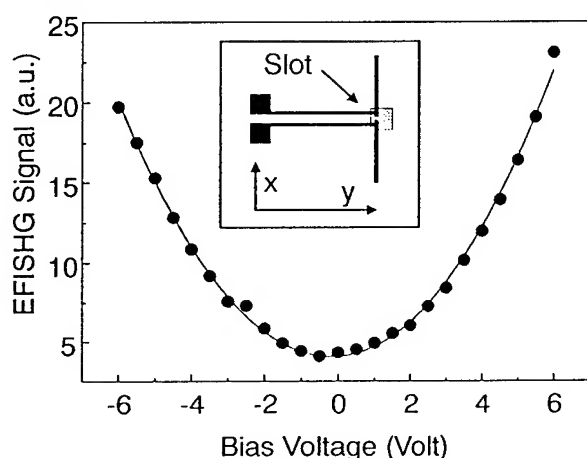


Fig. 1: Dependence of $I_{x,x}^{(2\omega)}$ on the applied dc voltage bias in the slot of a photoconductive antenna. The solid curve represents the parabolic relationship. The inset displays the antenna configuration (black: Au metalization, dotted area: silicon mesa).

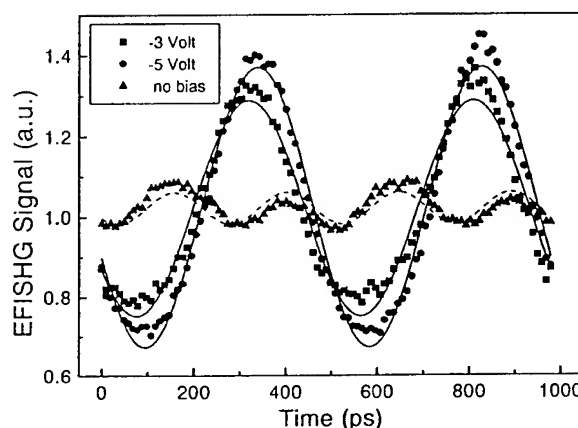


Fig. 2: A freely running 2.0/3 GHz signal on a photoconductive antenna for different applied bias U_{dc} sampled with a time resolution of 10 ps. The solid (dashed) lines represent fits to a pure sinusoidal wave with frequency f_s ($2f_s$) and are adjusted to the signal offset.

The antenna consists of 4 mm long and 10 μm wide dipole arms oriented along the x direction and electrically contacted by ~ 6 mm long coplanar strips ending in contact pads as shown in the inset of Fig. 1. The silicon is ion-implanted to achieve sub-picosecond carrier lifetime. For EFISHG we use a mode-locked Ti:Sapphire laser operating at a wavelength of 744 nm, generating a train of 100 fs pulses at a repetition rate of 75.6 MHz. The laser beam attenuated to an average power of 40 to 60 mW is focused on the 5 μm wide slot of the photoconductive

antenna to a spot diameter of 10 μm at a 45° angle of incidence. The reflected x polarized second-harmonic response $I_{x,x}^{(2\omega)}$ generated by a x polarized fundamental field $E_x^{(\omega)}$, where x denotes the direction normal to the plane of incidence is given by:

$$I_{x,x}^{(2\omega)} \propto [\chi_{xxx}^{(2)} + \chi_{xxxx}^{(3)} \mathcal{E}_x(\omega_{RF})]^2 I_x^{(\omega)^2} \quad (1)$$

containing two nonlinear susceptibility tensor elements, $\chi_{xxx}^{(2)}$ and $\chi_{xxxx}^{(3)}$. $\mathcal{E}_x(\omega_{RF})$ denotes the x component of the electric field across the gap to which the signal is exclusively sensitive in the chosen polarization combination. Since in electric dipole approximation the second-order susceptibility $\chi^{(2)}$ vanishes in the bulk of centrosymmetric media like silicon, the field-independent $\chi^{(2)}$ contributes to $I_{x,x}^{2\omega}$ only at the interface between the Au metallization of the antenna and the silicon substrate in the slot, where the inversion symmetry with respect to the x axis is broken.[3] The ion implantation partly amorphizes the silicon substrate and thus the contribution of the anisotropic bulk electric-quadrupolar component ζ is diminished and can be neglected.

To obtain the relationship between the detected EFISHG signal and the probed voltage the source term has to be integrated over the generating volume. Since the escape depth d_{ED} of the second-harmonic signal is less than 50 nm in our experiments absorption of the fundamental radiation is negligible and walk off is of no importance. Further we assume the fundamental field to be constant across the slot. The voltage-induced contribution $E^{(2\omega)}(U)$ to the harmonic signal is therefore given by:

$$\begin{aligned} E_x^{(2\omega)}(U) &\propto \int_{slot} dx \int_{ED} dz \chi_{xxxx}^{(3)} E_x^{(\omega)} E_x^{(\omega)} \mathcal{E}_x^{(\omega_{RF})} \\ &\propto d_{ED} \cdot \chi_{xxxx}^{(3)} \int_{slot} dx \mathcal{E}_x^{(\omega_{RF})} \\ &\propto (U - U_{FB}), \end{aligned} \quad (2)$$

where U_{FB} is the flatband potential and U denotes the applied voltage. If $I_{x,x}^{(2\omega)}$ is dominated by the cubic nonlinearity term (second term in Eq. 1), the observed potential dependence should be parabolic with a minimum near the flatband potential.[4] Under conditions, where the surface and/or bulk quadratic nonlinearities (first term in Eq. 1) are of comparable magnitude, a parabolic potential dependence with a minimum shifted from flatband would be observed. Figure 1 displays the observed EFISHG signal as a function of applied dc bias voltage U and the data clearly confirm the expected parabolic dependence with a minimum at $U_{min} = -170$ mV shifted from flatband (~ -10 mV). From the results shown in Fig. 1 we estimate a sensitivity of the EFISHG method of several 100 mV at 0 V dc bias and a fluence level of 400 $\mu\text{J}/\text{cm}^2$ on the silicon substrate. The sensitivity which increases further with higher applied voltage depends critically on the doping concentration of the Si substrate, i.e. the voltage decay over the probe volume.[3]

Next we demonstrate the application of the EFISHG technique for sampling amplitude and phase of a free-running microwave. A sinusoidal signal at a frequency of 2.043 GHz generated

by a microwave synthesizer (Rhode & Schwarz SMP03) is transmitted to the photoconductive antenna via a SMA coaxial cable and non-impedance-adjusted wire bonds. An additional dc-voltage bias can be applied to the antenna via an interconnected T-base. To achieve a time resolution of a few picoseconds without any synchronization between the free-running oscillator and the laser, the frequency f_s of the microwave signal is mixed with the n -th harmonic ($n=27$) of the laser repetition frequency f_l . In this way an exact replica of the microwave signal at an intermediate frequency $f_i = f_s - n \cdot f_l$ is obtained.[5] In our experiments, a trigger signal at $f_i \sim 500$ Hz is used for gating a multichannel data processing unit which sequentially samples the EFISHG signal. To enhance the time resolution to better than 10 ps timing jitter has to be limited. We have accomplished this by phaselocking the Ti:sapphire laser to a master oscillator crystal at a frequency f_l of 76.5 MHz by using a commercial timing stabilizer (Lightwave S1000) which controls f_l via the cavity length.[5] This is achieved by moving the output coupler with a piezo-electric transducer.

The EFISHG data presented in Fig. 2 show the microwave signal with a time resolution of approximately 10 ps for three different applied bias U_{dc} : -5 V (●), -3 V (■), and 0 V (▲). The data clearly reveal the combined effect of the applied bias and the microwave signal, $U_{RF} \sin(f_s t)$. Without any bias, (▲), the EFISHG signal exhibits a small modulation $\propto U_{RF}^2 \sin(2f_s t)$ at twice the frequency of the microwave signal due to the quadratic EFISHG to voltage characteristic shown in Fig. 1. In this case the EFISHG response is not sensitive to the RF field polarity. The observed deviation from a perfect $\sin(2f_s t)$ waveform (dashed line) can be attributed to an additional contribution $\propto 2U_{RF}U_{min} \sin(f_s t)$ due to the voltage offset U_{min} . Applying a bias of -3 V (■) yields a slightly distorted replica of the microwave signal generated by the dominant EFISHG contribution $\propto 2U_{dc}U_{RF} \sin(f_s t)$. The deviation from a pure sinusoidal wave (solid line) is now caused by the term $\propto U_{RF}^2 \sin(f_s t)^2$ indicating that $U_{dc} > U_{RF}$. Finally for a bias which is much larger than the RF signal, e.g. -5 V (●), the enhanced modulation in the EFISHG response becomes almost linear with respect to the probed microwave signal, $U_{RF} \sin(f_s t)$, allowing $U_{RF} = 1.0 \pm 0.2$ V and the phase of the RF signal to be determined accurately.

- [1] J.-F. Luy and P. Russer, *Silicon-based millimeter-wave devices*, volume 32 of *Springer Series in Electronics and Photonics*, Springer Berlin Heidelberg New York, 1994.
- [2] C. Ohlhoff, C. Meyer, G. Lüpke, T. Löffler, T. Pfeifer, H.G. Roskos, and H. Kurz, to be published in APL.
- [3] G. Lüpke, C. Meyer, C. Ohlhoff, H. Kurz, S. Lehmann, and G. Marowsky, *Opt. Lett.* **20**, 1997 (1995).
- [4] O. A. Aktsipetrov, A. A. Fedyanin, V. N. Golovkina, and T. V. Murzina, *Opt. Lett.* **19**, 1450 (1994).
- [5] T. Löffler, T. Pfeifer, H. G. Roskos, and H. Kurz, *IEEE Photon. Technol. Lett.* **7**, 1189 (1995).

Functional imaging of neurons with two-photon confocal microscopy using a Saturable-Bragg Reflector-modelocked compact solid state laser

W.H. Knox and S. Tsuda, Bell Laboratories Lucent Technologies, Holmdel, NJ 07733

K. Svoboda and W. Denk, Bell Laboratories Lucent Technologies, Murray Hill, NJ 07974

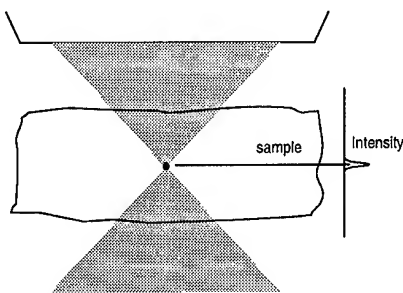


Figure 1. Two photon absorption causes extremely localized excitation in 3D

Two-photon excitation laser scanning microscopy (TPLSM) allows high resolution fluorescence imaging with minimal photodamage and photobleaching (for a review see [1]). TPLSM has recently been used to study, for example, information processing in dendritic spines, cell division in developing embryos, and calcium dynamics in auditory hair cells. TPLSM yields intrinsic submicron three-dimensional resolution (Fig. 1) and optical sectioning equivalent to one-photon confocal

microscopy simply by spatial confinement of excitation. This eliminates counterproductive absorption outside the focal slice. In highly scattering samples, such as nervous tissue, the red or near-infrared light used for illumination in TPLSM leads to a much improved penetration depth and the absence of a detector pinhole permits ballistic and diffuse photons to contribute to the signal [1]. Because two-photon absorption

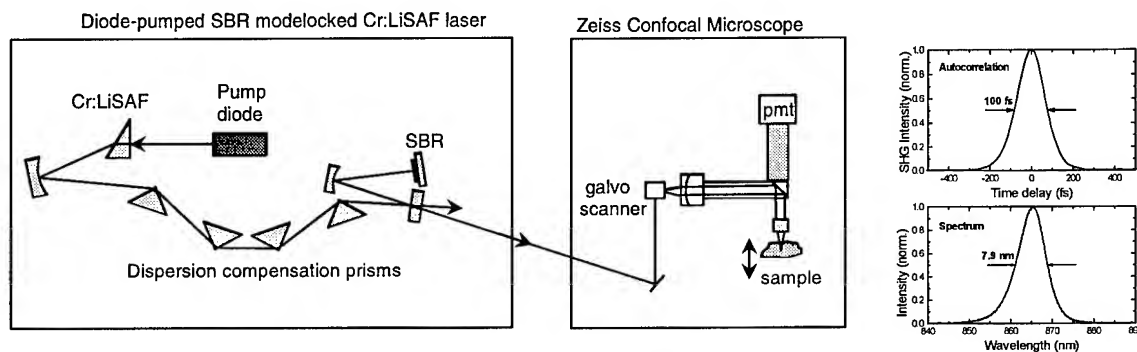


Figure 2. A diode-pumped Cr:LiSAF laser produces 90-100 fs pulses at 88 mw power at 860 nm. This source is used for two-photon laser scanning microscopy. Autocorrelation/spectrum are shown.

depends on the square on the instantaneous light intensity, ultrashort pulses are essential for TPLSM to achieve efficient excitation while using low average power. The main impediment to a more widespread use of TPLSM have been the cost, utility, and space requirements for femtosecond modelocked lasers that are based on large-frame argon-ion pump sources. The use of passive modelocking schemes that directly produce pulses of < 100 fs duration is desirable to reduce overall complexity and optimize performance.

Recently an all solid-state, diode-pumped, passively self-starting laser that is mode-locked with a saturable bragg reflector (SBR) was demonstrated [2]. Using a 500 mW, 670 nm diffraction-limited laser diode pump we obtain an output power of 88 mW at a 150 MHz repetition rate. When focused by a high aperture objective lens these parameters allow two-photon absorption close to saturating rates for typical fluorophores [1]. To test the performance of this arrangement we imaged living neurons deeply imbedded in slices of highly scattering cortical tissue. Brain slices (250 to 300 μm thick)

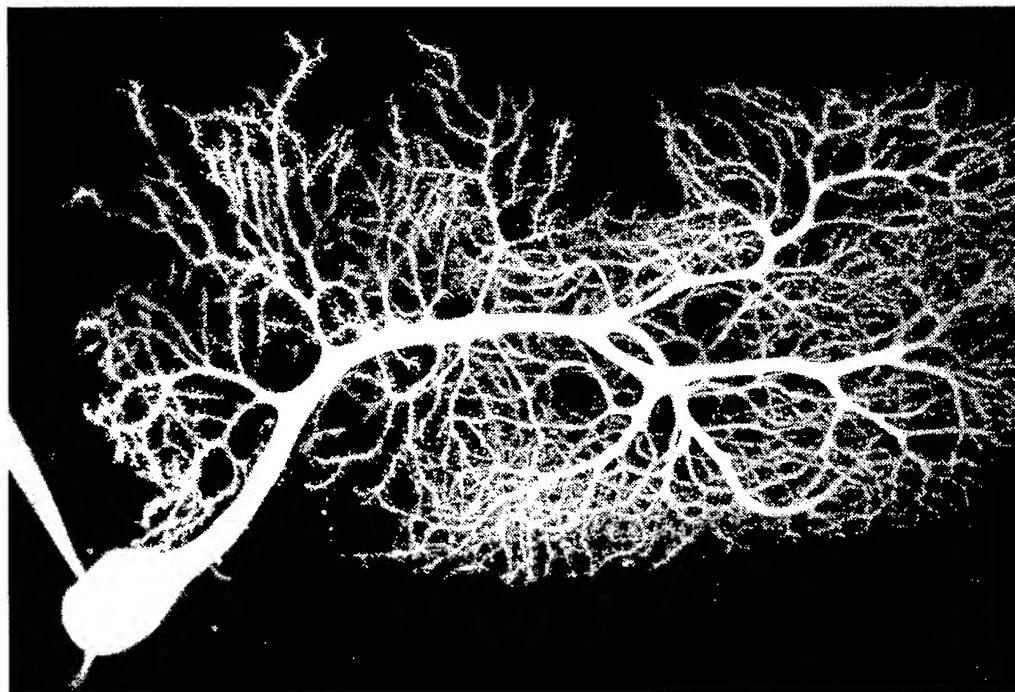


Figure 2. Two-photon excitation scanning image of living cerebellar Purkinje cell in a brain slice. Picture scale is 201 microns wide.

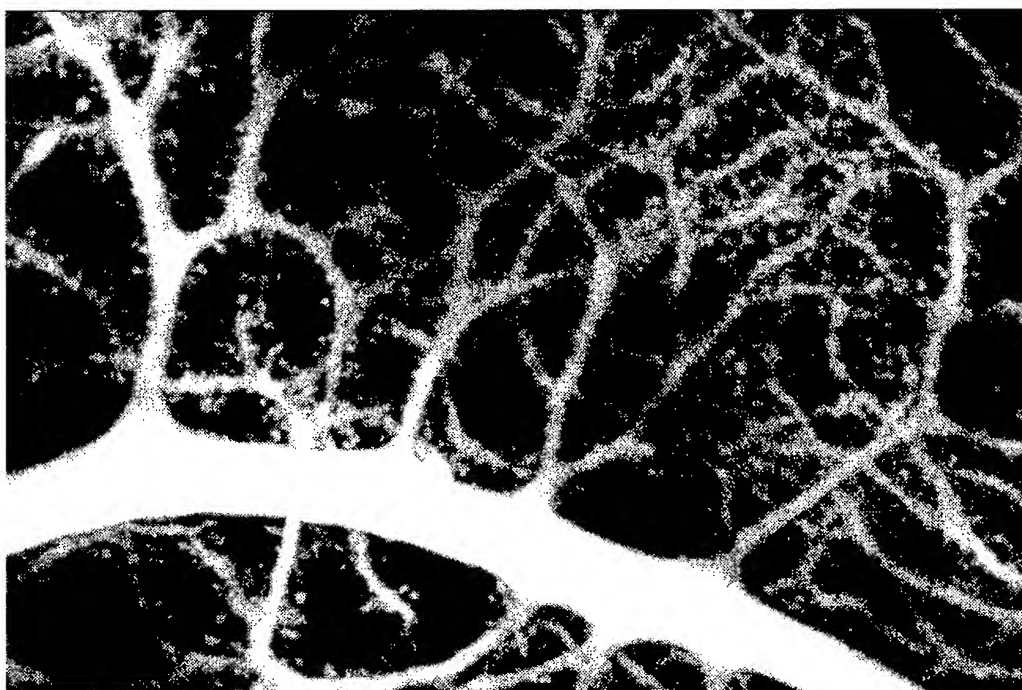


Figure 3. Higher resolution picture of synapses of Purkinje cell. 61 microns wide.

were prepared using standard techniques. For anatomical imaging, cells located 50-100 μm below the slice surface were filled by diffusion out of whole-cell patch electrodes containing 400 μM fluorescein dextran (MW=3 kD, Molecular Probes). A TPLSM image (Fig. 2; maximum projection of a focal stack) shows the typical dendritic arbor of a Purkinje cell, densely packed with clearly resolved dendritic spines. A close-up view of a number of these spines, which are the sites of synaptic input and constitute the smallest neuronal compartments, is shown in Fig. 3.

To demonstrate functional imaging we measured changes in the concentration of calcium ions $[\text{Ca}^{2+}]_i$ inside neocortical pyramidal neurons that were loaded with the fluorescent calcium indicator Ca-green-1 (300 mM, Molecular Probes) by diffusion from patch pipettes. We imaged fluorescence intensity changes, which reflect changes in $[\text{Ca}^{2+}]_i$ because the indicator increases its fluorescence quantum yield about 5-fold upon Ca^{++} binding, with high time resolution (on the scale of physiological processes) by repeatedly scanning a single line across the main apical dendrite. Action potentials were triggered by injecting pulses of current into the cell via the recording electrode. Changes of $[\text{Ca}^{2+}]_i$ evoked in the dendrite by single action potentials could easily be detected as is shown in Fig. 4. These measurements were repeatable tens of times without signs of photodamage.

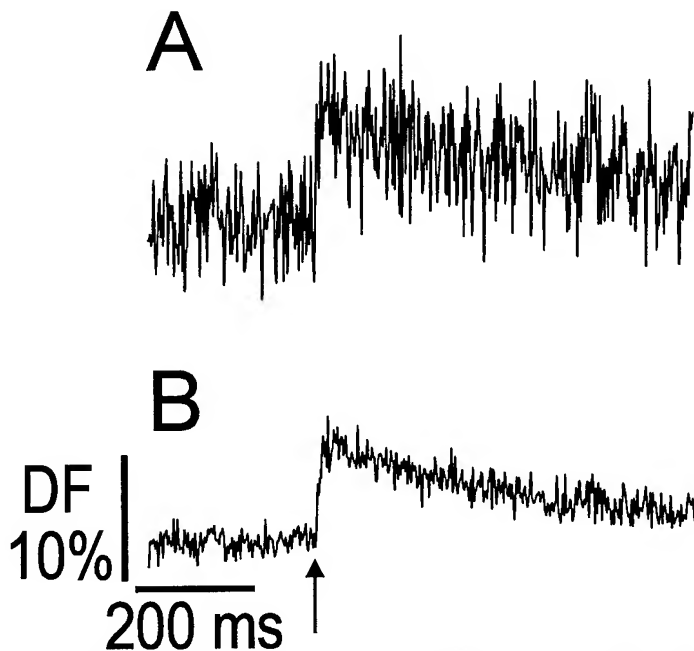


Figure 4. Changes of two-photon excited fluorescence (DF) in the apical dendrite of a pyramidal cell reflecting $[\text{Ca}^{2+}]_i$ changes evoked by single action potentials (arrow). Data were acquired by repeatedly scanning a single line across the dendrite at 2 ms intervals. *a)* Single response. *b)* Averaged ten times.

[1] W. Denk et. al., Journal of Neuroscience Methods, **54**, 151 (1994).

[2] S. Tsuda, W.H. Knox, E.A. de Souza, W.Y. Jan and J.E. Cunningham, Opt. Lett. **20**, 1406 (1995).

Observation of surface oxide properties by the second harmonic magneto-optic Kerr effect in $\text{Ni}_{81}\text{Fe}_{19}$ films

T. J. Silva

NIST, 325 Broadway, Boulder, Colorado 80303

phone: (303) 497-7826

fax: (303) 497-5869

T. M. Crawford and C. T. Rogers

Condensed Matter Laboratory, Department of Physics, University of Colorado

at Boulder, Boulder, Colorado 80309-0390

phone: (303) 492-4476

fax: (303) 492-2998

Y. K. Kim

Quantum Peripherals Colorado, Inc., Louisville, Colorado 80028-8188

phone: (303) 604-4375

fax: (303) 604-5070

The surface properties of air-exposed magnetic thin films are attracting increased interest as the magnetic disk drive industry moves toward higher storage densities, requiring ever smaller read sensor dimensions [1, 2]. A rapid increase in the magnitude of magnetostriction in NiFe films with thickness below 5-6 nm is attributed to the surface properties of the films, which begin to dominate as the surface layer becomes a larger percentage of the total film volume [1, 2]. NiFe films are of particular interest in this regard, owing to the material's extensive use in magnetic data storage devices.

The second-harmonic magneto-optic Kerr effect (SH-MOKE) has potential as a tool for the investigation of surface and interfacial properties of magnetic films and heterostructures. SH-MOKE combines the interfacial specificity of second harmonic generation in centro-symmetric materials with enhanced sensitivity to magneto-optic phenomena [3, 4].

We will present the results of an investigation into the effects of air-annealing upon the SH-MOKE properties of NiFe films. Large SH-MOKE signals have been recently observed in these films [4]. Previous studies of SH-MOKE with pure Fe films under UHV conditions have found a rapid decrease in

the SH-MOKE signal upon surface oxidation [5]. The films used in the present study form a self-passivating oxide surface layer of approximately 1-2 nm which greatly reduces further oxidation and corrosion rates [6]. Annealing of NiFe films in O_2 at modest temperatures between 150° and 250°C has been shown to result in stable growth of the surface oxide layer [6]. Thus, annealing may be used to study the effects of surface oxide formation upon SH-MOKE measurements.

Polycrystalline NiFe films were prepared by rf diode sputtering on 7.6 cm (001) Si substrates without any intentional substrate heating. The substrates were first coated with 200 nm of alumina to minimize substrate orientation effects. SH-MOKE data was taken in the transverse p-orientation: The incident fundamental light was p-polarized (TM incidence), with the applied magnetic field axis perpendicular to the plane of incidence. A Ti:sapphire pulsed-laser source is used, with a focused spot size of $\sim 90 \mu\text{m}$. Details of the experimental configuration have been previously reported [4]. Upon reversal of the magnetization orientation by an applied field, the intensity of the second harmonic signal changes, in some cases by as much as 60%. This is approximately $10^3\times$ greater than the analogous

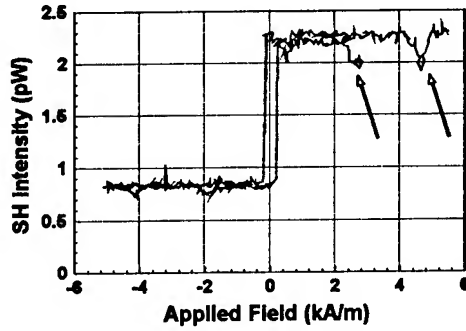


Figure 1 – Hysteresis loop obtained with SH-MOKE for 100 nm thick NiFe film. Reproducible dip structures are indicated with arrow.

linear transverse magneto-optic Kerr effect.

Samples of 100-nm-thick NiFe films were used for a study of annealing effects. Portions of the same wafer were annealed in air at a temperature of 230°C for times varying from 10 to 40 minutes. The macroscopic, in-plane magnetization of annealed and unannealed samples were measured with a vibrating sample magnetometer. It was found that the annealing had negligible effect upon the saturation magnetization of the samples. The coercivity and squareness of the samples were affected by the annealing process, most likely due to the loss of an anisotropy axis in the absence of an applied magnetic field during annealing.

A hysteresis loop obtained by SH-MOKE for a 100 nm thick NiFe film is shown in Fig. 1. The loop exhibits high squareness and low coercive fields, typical for high-quality NiFe films. On the other hand, two small dips were observed in the upper portion of the loop that were all approximately 900 A/m (11 Oe) wide. These dips were found to be reproducible over multiple magnetic field sweeps. However, the number of dips and the field required to cause them appeared to vary as a function of position on the sample.

In Fig. 2, we plot the average SH powers, $P_+(2\omega)$ and $P_-(2\omega)$, versus the annealing time of the samples for "up" and "down" saturated-magnetization orientations, respectively. In Fig. 3, we replot the data of Fig. 2 in terms of even and odd SH conversion efficiencies, $\alpha^{even} = [I_+(2\omega) + I_-(2\omega)]/2I^2(\omega)$ and $\alpha^{odd} = [(I_+(2\omega) - I_-(2\omega))]/2I^2(\omega)$, where I is the peak intensity, and α^{even} (α^{odd}) represents those portions

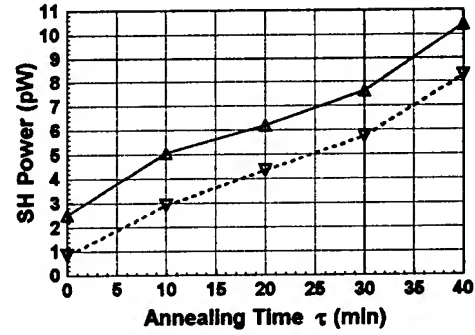


Figure 2 – Average optical power of second harmonic generation from NiFe film surface for oppositely-saturated magnetization directions in the p-incidence, transverse geometry.

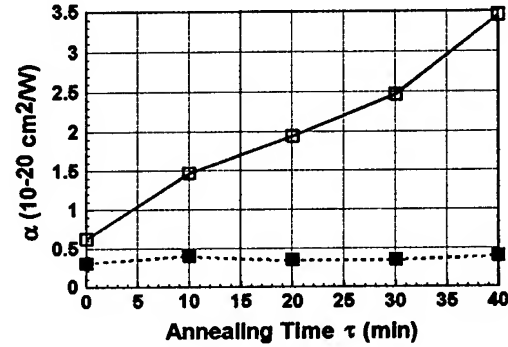


Figure 3 – Even and odd SH conversion efficiencies, α^{even} and α^{odd} . The empty squares are for α^{even} and the filled squares are for α^{odd} .

of the second harmonic conversion efficiency that exhibit even (odd) symmetry with regard to magnetization.

It is clear from Fig. 3 that α^{even} is strongly affected by annealing, while α^{odd} exhibits little change. The increase in α^{even} might be due to an increase in the non-magnetic contribution to SH relative to a nearly unchanged magnetic component. However, one must be cautious when appraising the origins of such phenomena, because interference effects can also result in changes of α^{odd} and α^{even} [4]: A clearer determination as to the physical origins of the effect in terms of second-order susceptibility components awaits the results of s-incidence, longitudinal SH-MOKE measurements, which are in

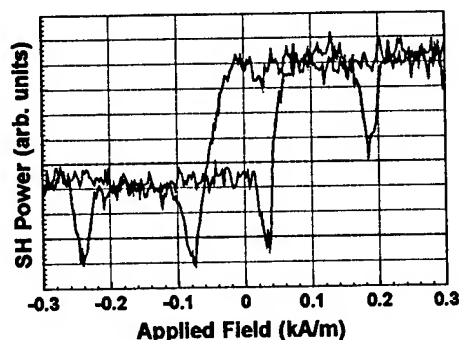


Figure 4 – Hysteresis loop measured by SH-MOKE for 100 nm NiFe film after 60 minutes annealing at 230° C. The four dip structures in the data were reproducible over multiple magnetic field sweeps.

progress.

An example of a hysteresis loop obtained by SH-MOKE from an annealed sample is presented in Fig. 4. This particular sample was annealed for 60 minutes at 230° C. Dips in the intensity as a function of applied field are seen, as is the case for Fig. 1, however the dips are much larger relative to the net change in SH intensity attributable to ferromagnetic switching in the sample. The dips were reproducible over several sweeps of the magnetic field. We have observed that the magnitude of the dips tends to scale with α^{even} .

Oxide formation in NiFe films has been extensively studied by both Auger spectroscopy and XPS [1, 6, 7, 8]. The oxide layer is rich in Fe^{3+} , which is most likely a component of $\alpha\text{-Fe}_2\text{O}_3$, an antiferromagnet [1, 8]. Annealing of NiFe films in O_2 increases the thickness of the oxide layer in proportion to the square of the annealing times, indicating diffusion-controlled oxide formation [6]. Lee and co-workers found that the diffusion growth rate, k_g , of the oxide layer obeyed the following rate equation: $k_g = \nu \exp(-E_a/k_bT)$, where E_a is the diffusion activation energy and ν is the asymptotic growth rate, with $E_a = 0.5$ eV and $\nu = 1.23 \mu\text{m}^2/\text{hour}$. The thickness of the oxide layer, d , is given by $d = \sqrt{k_g \tau}$, where τ is the annealing time: 3 nm of oxide is expected to form in 40 minutes at 230° C. If the SH electric field produced by the oxide layer is linearly proportional to d , then we would expect to find that the contribution of the oxide layer to the average SH intensity (α^{even}) scales linearly with τ , as seems to be apparent from Fig. 3.

The origin of the field-induced dips observed in Figs. 1 and 4 remains a subject of investigation. Possible causes include domain wall motion within the NiFe film, i.e. Barkhausen jumps, or magnetization reversal processes within the oxide surface layer. The fact that the dips in the SH response observed in Figs. 1 and 3 appear to scale with α^{even} suggests that the dips may be caused by some magnetic reordering taking place in the oxide layer, though a more conclusive study remains to be made. It is possible that the dips result from the reorientation of antiferromagnetic domains in $\alpha\text{-Fe}_2\text{O}_3$. Strong circular dichroism has been observed in SHG experiments with Cr_2O_3 , which was then used to image antiferromagnetic domains [9]. It is noteworthy that $\alpha\text{-Fe}_2\text{O}_3$ has the same rhombohedral crystalline structure as Cr_2O_3 and would therefore exhibit similar symmetry properties with regard to the second-order susceptibility tensor [10].

REFERENCES

- [1] K. Ounadjela, H. Lefakis, V. S. Speriousu, C. Hwang, and P. S. Alexopoulos, *J. Appl. Phys.* **65** (1989) 1230.
- [2] Y. K. Kim and T. J. Silva, *Appl. Phys. Lett.*, in press.
- [3] Bert Koopmans, Marcel Groot Koerkamp, Theo Rasing, and Hugo van den Berg, *Phys. Rev. Lett.* **74** (1995) 3692.
- [4] T. M. Crawford, C. T. Rogers, T. J. Silva, and Y. K. Kim, *Appl. Phys. Lett.* **68** (1996) 1573.
- [5] J. Reif, J. C. Zink, C.-M. Schneider, and J. Kirschner, *Phys. Rev. Lett.* **67** (1991) 2878.
- [6] W.-Y. Lee, G. Scherer and C. R. Guarnieri, *J. Electrochem. Soc.* **126** (1979) 1533.
- [7] R. A. Pollak and C. H. Bajorek, *J. Appl. Phys.* **46** (1975) 1382.
- [8] C. R. Brundle, E. Silverman and R. J. Madix, *J. Vac. Sci. Technol.* **16** (1979) 474.
- [9] M. Freibig, D. Froehlich, and G. Sluyterman v. L., R. V. Pisarev, *Appl. Phys. Lett.* **66** (1995) 2906.
- [10] S. Chikazumi, *Physics of Magnetism* (John Wiley, 1964), p. 86.

Wednesday, July 10, 1996

Organic Nonlinear Optical Materials and Polymers

NWD 3:00 pm-4:20 pm
Maile Room

Robert Twieg, *Presider*
IBM Almaden Research Center

Theory of the Third-Order Nonlinear Optical Response of Organic Materials

Shuji Abe^{*} and V. A. Shakin

Electrotechnical Laboratory
1-1-4 Umezono, Tsukuba, Ibaraki 305, Japan

Optical nonlinearity of organic materials has been studied for a long time. In mid 1970's it was recognized that delocalization of electrons in long conjugated polymers is an important enhancement factor for the third-order nonlinear susceptibility. Since then many experimental and theoretical studies have been conducted on the nonlinear optical properties of conjugated polymers.

Although the initial theoretical studies were rather limited to models of non-interacting electrons, it has also been pointed out that Coulomb interactions play important roles in conjugated polymers. In recent years there have been much progress in theoretical understanding of the electronic excited states of conjugated polymers, especially with respect to the influence of Coulomb interaction and correlation.

In this paper we focus on the Pariser-Parr-Pople (PPP) model of conjugated polymers. It is a tight-binding model for π electrons, in which electron-electron repulsion is taken into account in addition to one-electron transfer energies. To calculate excited states we employ the approach of configuration interaction (CI) either among single excitations ("single-CI") or among single and double excitations ("double-CI").

An important conclusion obtained at the single-CI level is that the dominant optical excitations are excitons rather than interband electron-hole excitations [1-3]. The exciton of the lowest energy has extremely large oscillator strength due to its one-dimensional nature. The band-to-band transitions are located much higher in energy than the exciton, and they exhibit unique features in nonlinear spectra of, e.g., two-photon absorption, electroabsorption, and third-harmonic generation.

When the incident photon energy becomes close to the exciton energy, the creation of two excitons becomes feasible. The theoretical description of such a situation requires the double-CI approach. The results of double-CI calculations [4] indicate that a bound state of two excitons, viz., a biexciton state, becomes relevant in the two-photon absorption spectrum just below the one-photon resonance energy.

These results are obtained by use of the standard Orr-Ward formula of the third-order nonlinear susceptibility [5]. Now we would like to discuss the most interesting region of resonant nonlinearity just at the exciton absorption peak. In this case the Orr-Ward approach is not appropriate, and we should use a formula obtained with a density matrix approach [6],

^{*} E-mail: abe@etl.go.jp, Tel. +81(298)58-5370, Fax: +81(298)58-5375

where diagonal as well as off-diagonal damping rates are incorporated. We have carried out such calculations with the double-CI description of the PPP model [7].

Figure 1(a) displays the calculated degenerate four wave mixing signal (the absolute value of $\chi^{(3)}(-\omega; \omega, -\omega, \omega)$) together with the linear absorption (the imaginary part of $\chi^{(1)}(\omega)$). Here t is the average intersite transfer energy, and $\chi_0^{(3)}$ and $\chi_0^{(1)}$ are normalization factors [4,7]. We would like to discuss the relationship between the two quantities, because there have been an experimental report [8] on a "scaling" relation between them. In Fig.1(b), we plot the relationship of the two quantities both on logarithmic scales. The solid line corresponds to the low energy side of the absorption peak, while the broken curve to the high energy side. Clearly there is a power law dependence:

$$|\chi^{(3)}(-\omega; \omega, -\omega, \omega)| \approx c \left\{ \text{Im}[\chi^{(1)}(\omega)] \right\}^p.$$

The power p is about 1.2 on the low energy side and about 1.8 on the high energy side. The low-energy power is close to the empirical value $p \sim 1$ obtained by Bubeck *et al.* [8]. Thus we can explain the experimental scaling law without assuming inhomogeneous broadening.

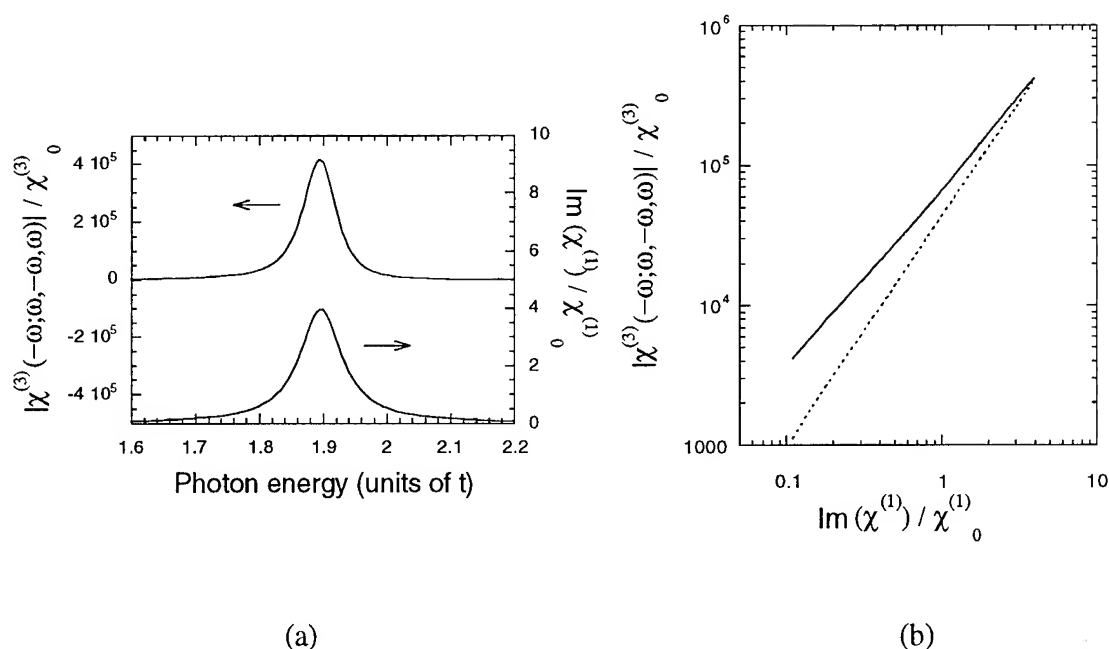


Fig. 1 (a) An example of calculated dispersion of the third-order nonlinear susceptibility (upper curve) and linear absorption (lower curve) around the exciton resonance, and (b) the scaling relationship between the two quantities in logarithmic scales, with solid and broken curves corresponding to the low and high energy side of the absorption peak.

Another interesting result obtained in this study is the dephasing-induced extra resonance [7]. In the two-photon absorption region of $\chi^{(3)}$ spectra, the calculated spectrum exhibits quite a few additional peaks, for which the doubled peak energy does not correspond to an energy of two-photon allowed state. The photon energy of an extra resonance corresponds to an energy difference between two excited states. The height of an extra peak grows with Γ_2/Γ_1 , where Γ_1 and Γ_2 are longitudinal and transverse relaxation rates, respectively. The effect is similar to the extra resonance discussed by Bloembergen *et al.* in a slightly different context [9]. An important point in the present case is that the extra resonance is not a weak effect. An extra peak can become higher than ordinary two-photon absorption peaks. This theoretical result is relevant for experiments, because the ratio Γ_2/Γ_1 in real conjugated polymers are usually very large.

References

- [1] S. Abe, M. Schreiber, W.P. Su and J. Yu, Phys. Rev. **B45**, 9432 (1992).
- [2] S. Abe, in *Relaxation in Polymers* edited by T. Kobayashi (World Scientific, Singapore, 1993) pp.215.
- [3] S. Abe, Y. Shimoi, V. A. Shakin, and K. Harigaya, Mol. Cryst. Liq. Cryst. **256**, 97 (1994).
- [4] V. A. Shakin and S. Abe, Phys.Rev. **B50**, 4306 (1994).
- [5] B.J. Orr and J.F. Ward, Mol. Phys. **20**, 513 (1971).
- [6] R.W. Boyd, *Nonlinear optics* (Academic, London, 1992), Chap.3.
- [7] V. A. Shakin, S. Abe, and T. Kobayashi, Phys. Rev. **B53** (1996), in print.
- [8] C. Bubeck, A. Kaltbeitzel, A. Grund and M. LeClerc, Chem. Phys. **154**, 343 (1991).
- [9] N. Bloembergen, H. Lotem, and R. T. Lynch, Indian J. Pure Appl. Phys. **16**, 151 (1978).

Novel High Nonlinearity Organic Crystals

Peter Guenter
Nonlinear Optics Laboratory

We will present the most recent results on the growth and characterization of novel high quality molecular crystals for nonlinear optics. These crystals are based on ionic or hydrogen bonding of new and known chromophores with large second-order hyperpolarizabilities. Detailed results of optical, electro-optical and nonlinear-optical properties of high quality and large size DAST crystals, of hydrazone derivatives and new co-crystals will be presented. It will be shown that optimized parallel alignment of chromophores as well as optimum structures for phase-matched frequency mixing have been realized. In addition, we report on the measurement of the highest known phase-matchable nonlinear susceptibility coefficient of 200 pm/v determined recently in our laboratory.

Nonlinear Optical Waveguide Spectroscopy of Poly(p-Phenylenevinylene)

K. Ueberhofen, R.O. Garay[†], K. Müllen, C. Bubeck

Max-Planck-Institute for Polymer Research, Postfach 3148, D-55021 Mainz, Germany

[†] present address: Univ. Nacional del Sur, Av. Alem 1253, 8000 Bahia Blanca, Argentina

Poly(p-phenylenevinylene) (PPV) is a typical representative of conjugated polymers, which have a highly delocalized, one-dimensional conjugated π -electron system. These polymers have found much interest, because most of them can be processed rather easily to thin film waveguides and because of their large third-order nonlinearities [1-3]. Thin films of PPV are prepared by spin-coating of a soluble precursor polymer on fused silica substrates and thermal annealing under vacuum as described recently [4]. We have used thin films of PPV to develop and demonstrate a sensitive characterization method of the intensity dependent refractive index $n = n_0 + n_2 I$ and absorption coefficient $\alpha = \alpha_0 + \alpha_2 I$. The utility of any material for applications in photonics depends primarily on these quantities.

Prism coupling of waveguide modes is a well known and very accurate technique to measure the refractive index of thin films [5]. We have used the intensity dependence of the coupling angles to study n_2 and α_2 . Our experimental setup is shown schematically in Fig. 1. Picosecond light pulses from a Nd:YAG laser are used to pump an optical parametric generator/amplifier configuration (OPA). Using LiIO_3 crystals we can tune the laser wavelength λ_L in the range between 700 nm and approximately 1600 nm.

Fig. 2 shows a typical measurement of the TE₀ mode of a PPV film. The evaluation method of prism coupling [6,7] was developed further and allows us to derive the sign and absolute magnitude of n_2 . The nonlinear absorption α_2 , however, can be evaluated only in relative units so far.

The spectral dependencies of α_0 , α_2 and n_2 are shown in Fig. 3 for comparison. We can identify two-photon absorption states I and II with $\alpha_2 > 0$ at 3.1 eV and 2.8 eV, which are located energetically above the onset of the linear absorption spectrum. The characteristic correlated spectra of α_2 and n_2 can be seen most clearly at resonance I. The resonance III with $\alpha_2 < 0$ is assigned to a saturable absorption at 1.3 eV.

Our data show (see the data points at $\lambda_L = 925$ nm) that it is possible to achieve large resonantly enhanced values of n_2 and still small nonlinear losses with α_2 close to zero. This unexpected situation can result from a suitable combination of two-photon absorption and saturable absorption, which leads to a compensation of their losses.

References

- [1] C. Sauteret, J.-P. Hermann, R. Frey, F. Pradère, J. Ducuing, R.H. Baughman, R.R. Chance, Phys. Rev. Lett. 36 (1976) 956.
- [2] D.S. Chemla, J. Zyss (Eds.), Nonlinear Optical Properties of Organic Molecules and Crystals, Vol. I and II, Academic Press, Orlando, 1987.
- [3] F. Kajzar, J.D. Swalen (Eds.), Science and Technology of Organic Thin Films for Waveguiding Nonlinear Optics, Gordon & Breach Sci. Publ., in press.
- [4] A. Mathy, K. Ueberhofen, R. Schenk, H. Gregorius, R. Garay, K. Müllen, C. Bubeck, Phys. Rev. B 53 (1996) 1.
- [5] P.K. Tien, R. Ulrich, J. Opt. Soc. Am. 60 (1970) 1325.
- [6] R. Ulrich, J. Opt. Soc. Am. 60 (1970) 1337.
- [7] G. Assanto, R.M. Fortenberry, C.T. Seaton, G.I. Stegeman, J. Opt. Soc. Am. B 5 (1988) 432.

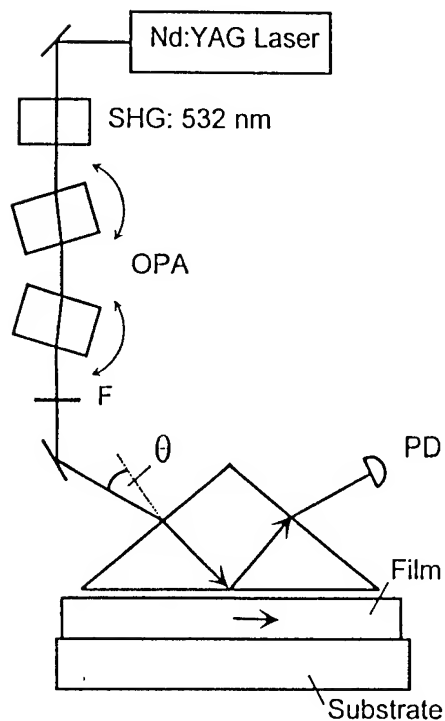


Fig. 1: Experimental setup for intensity dependent prism coupling; F: filter, PD: photodiode.

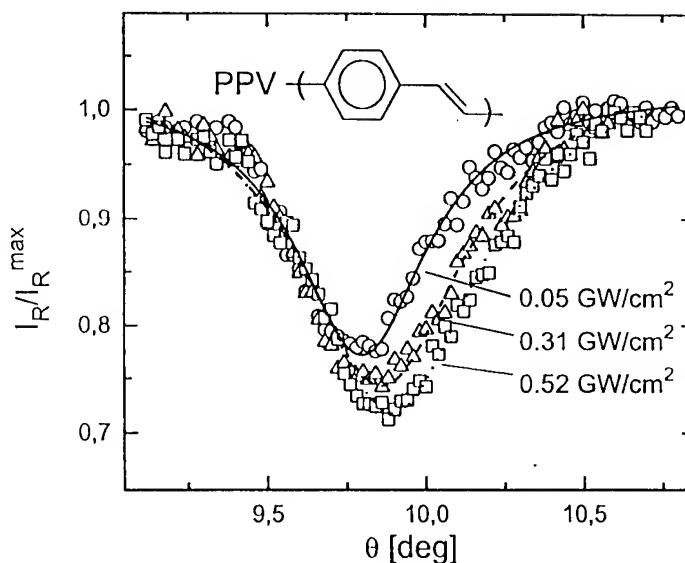


Fig. 2: Angular dependence of the reflected intensities at the photodiode (see Fig. 1). The minimum occurs due to the excitation of the TE₀ mode. It shifts, if the laser intensity increases (numbers refer to a position in front of the rutile prism, $\lambda_L = 896$ nm).

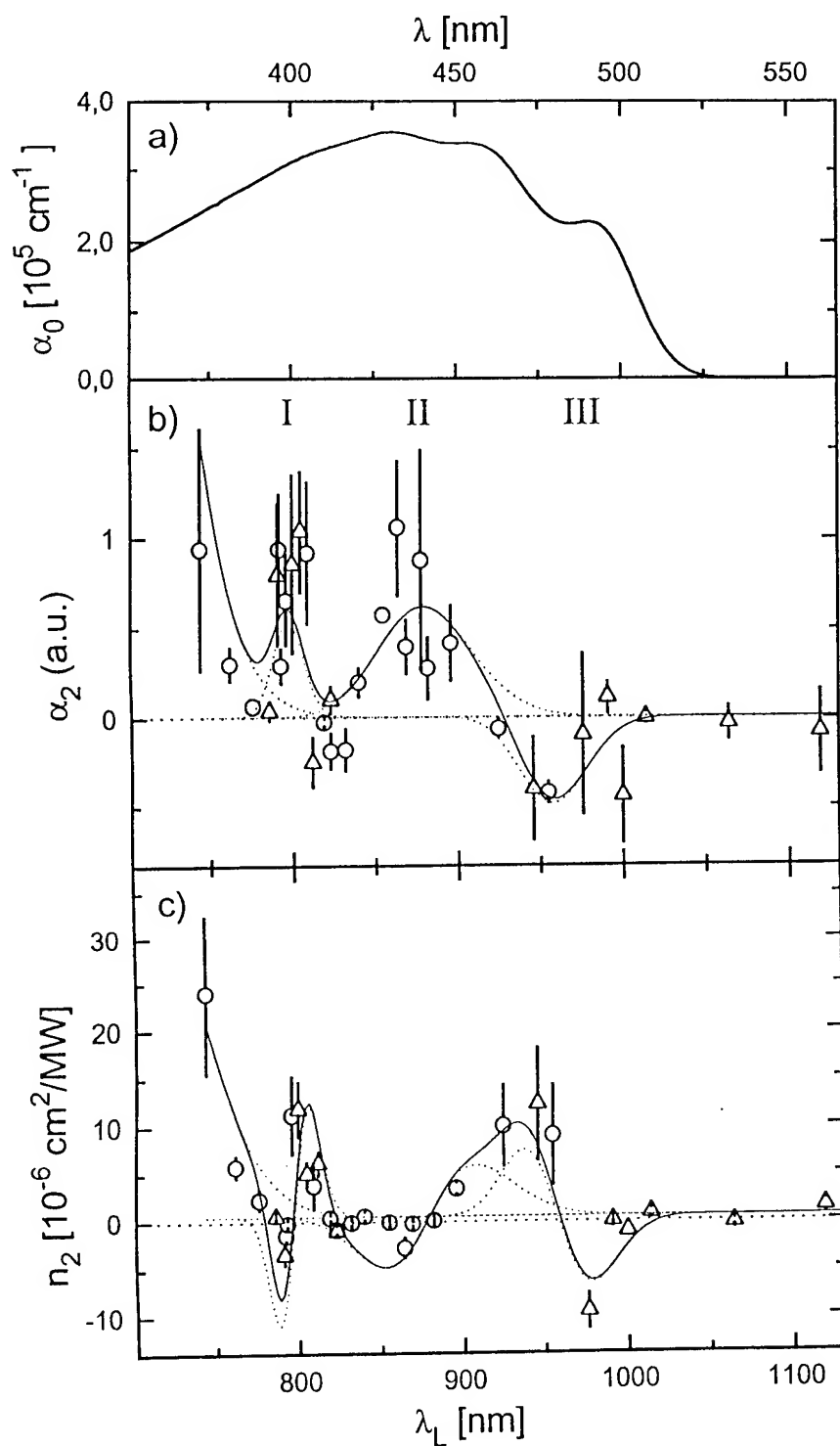


Fig. 3: Linear absorption spectrum $\alpha_0(\lambda)$ of PPV in comparison with nonlinear optical data (b and c) which are measured at the laser wavelengths λ_L . The lines in parts b) and c) are a first attempt to model the measured data points by two-photon absorptions I, II and a saturable absorption III.

Magnitude and Sign of the Third Order Optical Nonlinearity in Polydibutylstannane

Ardie. D. Walser, Richard Priestley, Roger Dorsinville

W. K. Zou¹, D.Y. Xu¹, and Nan-Loh Yang¹

Dept. of Electrical Engineering, The City College of CUNY, 140th St. & Convent Ave.
New York, N.Y. 10031, (212) 650-6619, (212), 650-8249: fax

¹Dept. of Chemistry, College of Staten Island of CUNY, Staten Island, N.Y. 10314

INTRODUCTION

The field of nonlinear optics plays a major role in the implementation and development of many photonic technologies useful in processing optical information at enhanced speeds. Materials with large optical nonlinearities and fast responses are crucial for the development of these technologies. Recently, silicon based polysilane and polygermane polymers have attracted great interest. As σ electron systems, these polymers are unique in that the σ electron-delocalization along the backbone chromophore renders the polymers transparent through the visible to the infrared in contrast to the π -conjugated polymers which normally absorb strongly in the visible. In this letter we wish to report the first measurements of the third-order nonlinearity of the tin based polymer polydibutylstannane. Due to the large atomic size of tin, the electron polarizability is expected to be high, which allows for the possibility of a large χ^3 .

SYNTHESIS

The preparation of organo oligostannanes has been demonstrated through Wurtz coupling of dichlorotin compounds [1]. The synthesis of high molecular weight polydibutylstannane was conducted through rigorous control of stoichiometry and purity of the chemicals involved [2]. The structure of polydibutylstannane is shown in Fig. 1.

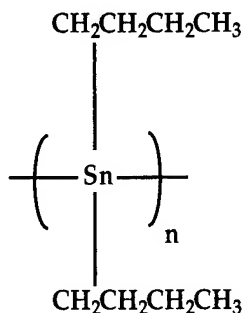


Fig. 1. Polydibutylstannane structure

EXPERIMENT

The two nonlinear experimental techniques used in this study were the degenerate four-wave mixing (DFWM) in the folded boxcar geometry [3] and the single beam Z-scan technique [4]. A passively/actively mode-locked Nd:YAG laser provided 1.06 μm pulses at 20Hz with a pulse duration of about 35psec. A maximum of 30mJ/pulse at 532nm is

generated by frequency doubling in a KTP crystal. Various solutions of polydibutylstannane dissolved in chloroform were placed in a 2mm quartz cells. A second 2mm cell containing CS₂ was used as a reference under the same excitation conditions. The nonlinear signal generated was detected using a silicon PIN diode. The three input beams at the sample site were approximately 100μm in diameters with a total incident energy of approximately 24μJ. The relative arrival times of the pulses at the sample were individually controlled with submicron resolution. The schematic diagram for the Z-scan technique has been described elsewhere [5]. With information obtained from the two techniques, we were able to characterize the third-order nonlinear susceptibility of polydibutylstannane.

RESULTS AND DISCUSSION

The values of χ^3 for the samples were obtained by using CS₂ in a 2mm quartz cell as a reference under the same excitation conditions and eq. (1)

$$\chi_s^3 = \chi_{CS2}^3 \left(\frac{I_s}{I_{CS2}} \right)^{1/2} \frac{n_s l_{CS2}}{n_{CS2} l_s} \exp(-\alpha_s l_s), \quad (1)$$

where s stands for sample, I is the FWM signal, n is the index of refraction, l is the sample length, and α is the absorption coefficient. The absolute value of the third order nonlinear coefficient is obtained from the DFWM measurement. All the FWM measurements for the various concentrations were taken using the xxxx configuration where all the polarizations are parallel to each other. The time response of the samples were limited by our experimental setup (<35 psec) and no slow component was observed. The χ^3 values for the various concentrations are shown in Table 1.

Concentration (mol/L)	χ^3 (esu)
4.56*10 ⁻²	5.52*10 ⁻¹²
3.06*10 ⁻²	3.24*10 ⁻¹²
1.36*10 ⁻²	2.64*10 ⁻¹²

Table 1.

The molecular weight for each repeat unit associated with one tin atom is 232 g/mol. The χ^3 values obtained for polydibutylstannane, at concentrations of 1X10⁻² to 5X10⁻² M/L used in these measurements, were two to four times larger than those measured for polysilane with a concentration of 0.5 M/L [5]. We extrapolated the χ^3 value of polydibutylstannane to a solid film by assuming a density of about 1g/cm³. This was done using eqn. (2).

$$\chi_{\text{Thin Film}}^3 = \frac{N}{N_{\text{Solution}}} \chi_{\text{Solution}}^3, \quad (2)$$

where N is the assumed density of the polydibutylstannane solid. The extrapolated value in solid film was found to be about 5.0 X10⁻¹⁰ esu. This value is two orders of magnitude

larger than the χ^3 value for solid polysilane. This along with its fast response and transparency in the visible region suggests that this material could be a good candidate for use in future optical applications.

We determined the sign of χ^3 in polydibutylstannane using the single-beam Z-scan technique at 532 nm. The transmittance through the far field aperture as a function of sample position 'z' for the polydibutylstannane solution with a concentration of 4.56×10^{-2} M/L is shown in Fig. 2. The peak-valley configuration as the sample is moved from -z to +z for polydibutylstannane indicates that it has a negative nonlinearity ($n_2 < 0$) at 532nm. This could be an indication of two photon absorption enhancement at 532nm as in the case of polysilane [5]. However, two photon absorption measurements using the open aperture Z-scan technique showed negligible absorption losses within our intensity range.

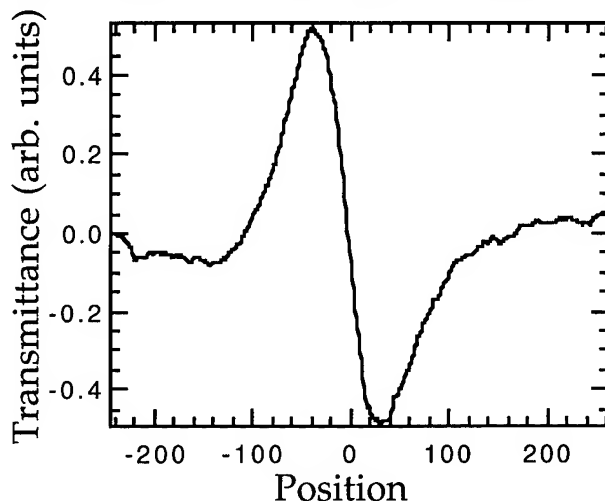


Fig. 2. Transmittance through a far field aperture at 532nm.

CONCLUSION

We have used DFWM and Z-scan measurements at 532nm to characterize the third-order nonlinear response of polydibutylstannane. Our results show that this tin based polymer has one of the largest known nonresonant nonlinear optical coefficient in the visible ($\chi^3 > 10^{-10}$ esu) with a response time possibly in the subpicosecond range. Like polysilane the sign of the third-order susceptibility of polydibutylstannane has been shown to be negative at 532nm.

REFERENCES

- [1] A. G. Daves and P. J. Smith, in *Comprehensive Organometallic Chemistry*, Ed. by G. Wickins, 1988, Vol. 2, p. 545.
- [2] W. K. Zou and N.-L. Yang, *Polym. Prepr. (Am. Chem. Soc. Div. Polym, Chem.)* 33 (1992) 188.
- [3] L. Yang, Q.Z. Wang, P.P. Ho, R. Dorsinville and R.R. Alfano, *Appl. Phys. Lett.* 53 (1988) 1245.
- [4] M. Sheik-bahae, A.A. Said and E.W. Van Stryland, *IEEE J. Quantum Electron.* 26 (1990) 760.
- [5] L. Yang, R. Dorsinville, R.R. Alfano, *Opt. Lett.* (1991) 758.

Thursday, July 11, 1996

Photorefractive Nonlinear Optics

NThA 8:00 am-9:30 am
Maile Room

Gary L. Wood, *Presider*
U.S. Army Research Laboratory

A powerful, diffraction-limited semiconductor laser using photorefractive beam coupling

Stuart MacCormack and Jack Feinberg

Department of Physics, University of Southern California

Los Angeles, CA 90089-0484

Tel: (213) 740 0046, Fax: (213) 740 6653, e-mail: mcmack@usc.edu

Steve O'Brien and Robert J. Lang

SDL, 80 Rose Orchard Way,

San Jose, CA 95134

Marvin B. Klein and Barry A. Wechsler

Hughes Research Laboratories,

3011 Malibu Canyon Road, Malibu, CA 90265

Semiconductor flared amplifiers now routinely emit ~1 watt of light in a diffraction-limited, single-frequency beam when driven at currents of a few amps.¹ However, if driven at higher currents, the output beam breaks into filaments that spread light into higher-order modes.² Here we present a simple method for extracting a diffraction-limited beam from the highly-filamented output of a semiconductor amplifier. With this method we can now operate the amplifiers at currents 3 - 4 times their diffraction-limited range and still obtain a diffraction-limited beam. By combining the outputs of multiple amplifiers, this method should produce very high power diffraction-limited beams from semiconductor lasers.

Figure 1 shows a 500 mW tunable laser diode (SDL 8630) at $\lambda = 860$ nm which we used as our single-mode master laser. A beam splitter equally divided the laser's output into signal and pump beams. We directed the signal beam into a Rh:BaTiO₃ crystal³ so that it traveled exactly along the crystal c-axis to eliminate beam fanning. We focused the pump beam into a flared amplifier, first attenuating the pump to 40 mW to avoid damaging the amplifier's entrance face. The amplifier was 3.1 mm long; its dimensions flared from 200 μm x 1 μm at its entrance face to 2500 μm x 1 μm at its exit face. At a current of 8A and with 40 mW of injected light this amplifier generated 2.2 W of aberrated light. A lens having a high numerical aperture

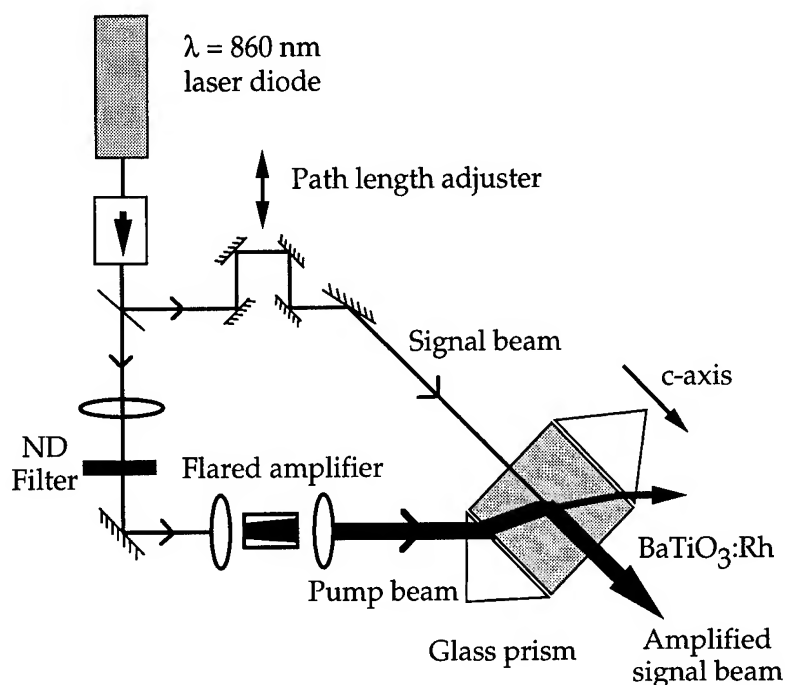


Figure 1. The semiconductor laser plus tapered amplifier pumps a photorefractive beam amplifier to produce a diffraction-limited output beam.

collected this aberrated pump beam from the amplifier and directed it (with a coupling prism) into the BaTiO_3 crystal. The pump beam intersected the signal beam at an internal full angle of 68° . By two-beam coupling the photorefractive crystal transferred optical power from the aberrated pump beam into the spatially clean signal beam.

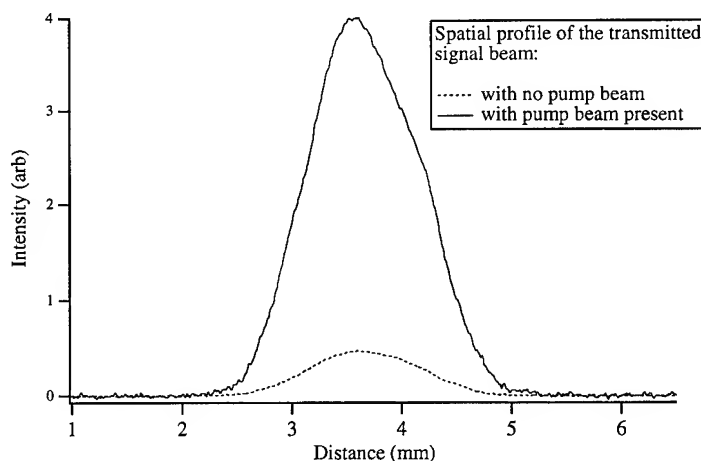


Figure 2. A slice through the collimated signal beam after it exited the Rh:BaTiO_3 crystal. The slight asymmetry in the amplified beam is caused by beam depletion of the pump beam. Note that the signal beam preserves its spatial quality even when amplified by an aberrated pump beam.

Fig. 2 shows the transmitted signal beam with and without the pump beam present; there is very little change in its spatial profile. From a pump power of 2.2 W and a signal power of 0.22 W incident on the crystal we obtained 1.11 W in the amplified output, (We estimate that coating the crystal to eliminate the $\sim 17\%$ reflections at each crystal face would have increased the output beam to 1.52 W).

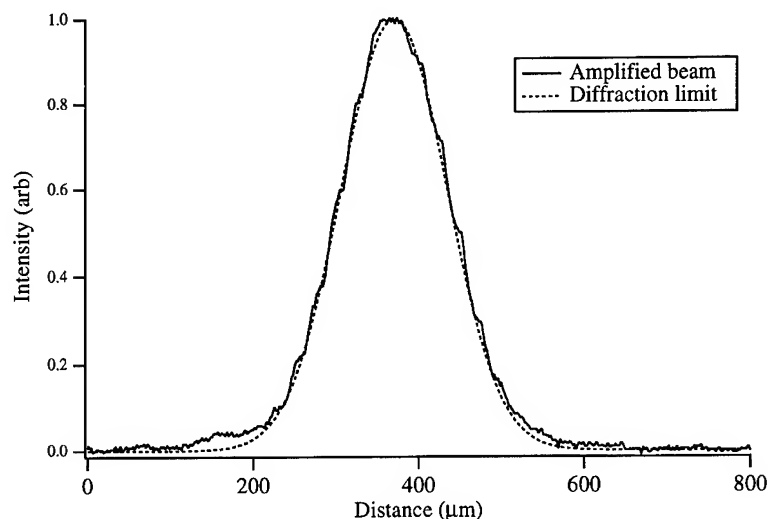


Figure 3. A slice through the signal beam waist after focusing by an $f = 500$ mm lens. The "steps" on the beam profile are an artifact caused by the finite pixel size of our photodiode array.

As an additional check on the spatial quality of the amplified signal beam, we focused the signal beam with an $f = 500$ mm lens to obtain the profile shown in Fig. 3. We measured $1/e^2$ waist radii of $139 \mu\text{m}$ and $138 \mu\text{m}$ for the amplified and un-amplified signal beams respectively. These values correspond to 1.04 and 1.01 times the diffraction limit, respectively, and demonstrate that photorefractive amplification maintains the spatial quality of the signal beam.

This work was funded by Air Force Phillips Laboratory, Kirtland AFB, New Mexico.

References

- 1) L. Goldberg, D. Mehuys, M. R. Surette, and D. C. Hall, IEEE J. Quantum. Elect. **QE-29**, 2028 (1993).
- 2) R. J. Lang, A. Hardy, R. Parke, D. Mehuys, S. O'Brien, J. Major, and D. Welch, IEEE J. Quantum. Elect. **QE-29**, 2044 (1993).
- 3) B. A. Wechsler, M. B. Klein, C. C. Nelson, and R. N. Schwartz, Opt. Lett. **19**, 536 (1994).

Two- wave mixing with partially coherent waves in photorefractive crystals

Xianmin Yi, Changxi Yang and Pochi Yeh

Electrical and Computer Engineering, University of California, Santa Barbara, CA 93106

Two-wave mixing in photorefractive crystals in various configurations has been investigated extensively. Most of the previous works in this area are on wave mixing with mutually coherent waves.¹ It is known that partial temporal coherence may affect the strength of the grating and the coupling.² Two-wave mixing with partially coherent waves has been studied recently for the case of transmission grating interaction^{4,5}. In this paper, we present the results of our theoretical and experimental investigation for the case of reflection grating interaction.

As is shown in Fig.1, two counterpropagating partially coherent waves $E_1(z,t)\exp(-i\omega_0 t + i\mathbf{k}_0 z)$ and $E_2(z,t)\exp(-i\omega_0 t - i\mathbf{k}_0 z)$ interact in a photorefractive medium. Reflecting the partial coherence, $E_1(z,t)$ and $E_2(z,t)$ are stationary random variables representing the random fluctuation of the optical wave amplitudes. Let $E_{11}(z,\omega)$ and $E_{22}(z,\omega)$ denote the self spectral density functions of $E_1(z,t)$ and $E_2(z,t)$ respectively and $E_{12}(z_1, z_2, \omega)$ be the cross spectral density function between $E_1(z_1, t)$ and $E_2(z_2, t)$. Then the intensities of the two waves can be expressed as $I_1(z) = \int E_{11}(z, \omega) d\omega$ and $I_2(z) = \int E_{22}(z, \omega) d\omega$, and the mutual coherence as $Q(z) \equiv \langle E_1(z, t) E_2^*(z, t) \rangle = \int E_{12}(z, z, \omega) d\omega$. As a result of the partial coherence of the two waves and the photorefractive response, a nearly stationary holographic grating is recorded in the medium. The index grating can be written as $\delta n(z) = -i\Gamma c / (2\omega_0) \{ Q(z) / [I_1(z) + I_2(z)] \exp(2i\mathbf{k}_0 z) + \text{c.c.} \}$, where Γ is the intensity coupling coefficient.

Given an arbitrary function $Q(z) / [I_1(z) + I_2(z)]$, we can specify an index grating $\delta n(z)$. The scattering of partially coherent optical waves by a stationary index grating is a linear process. Thus the index grating can be thought of as a linear system. Both faces of the photorefractive medium ($z=0$ and $z=L$ planes) can be taken as the input planes with $E_1(z=0, t)$ and $E_2(z=L, t)$ being the corresponding input signals. An arbitrary plane in between can be taken as the output plane with $E_1(z, t)$ and $E_2(z, t)$ being the output signals. Propagation of monochromatic waves through the index grating can be modeled by standard coupled-mode theory. By solving the coupled-mode equations, we can obtain the frequency transfer functions of the linear system. They are denoted as $H_{11}(z, \omega)$, $H_{12}(z, \omega)$, $H_{21}(z, \omega)$ and $H_{22}(z, \omega)$ respectively as is shown in Fig.1. With these frequency transfer functions, the spectral density functions of the two outputs, i.e. $E_{11}(z, \omega)$, $E_{22}(z, \omega)$ and $E_{12}(z, z, \omega)$, can be expressed as a linear combination of the spectral density functions of the two inputs, i.e. $E_{11}(z=0, \omega)$ and $E_{22}(z=L, \omega)$ and $E_{12}(z=0, z=L, \omega)$.⁵ Note that the spectral density functions of the two inputs are given through the boundary conditions.

With the spectral density functions $E_{11}(z, \omega)$, $E_{22}(z, \omega)$ and $E_{12}(z, z, \omega)$ thus obtained from an arbitrary initial function $Q(z)/[I_1(z) + I_2(z)]$, we can obtain a new version of the function $Q(z)/[I_1(z) + I_2(z)]$ by using the relationships in paragraph two. After several iterations, the function $Q(z)/[I_1(z) + I_2(z)]$ will converge. The solution is found because a steady state of two-wave mixing in the photorefractive medium is reached when the two optical waves coupled via the photorefractive grating can exactly sustain the same photorefractive grating.

The general formulation described above to model contradirectional two-wave mixing in photorefractive crystals can be implemented numerically. Let us consider a typical case in which the coherence length of the source laser wave is finite but much longer than the thickness of the photorefractive medium. Using the following parameters $\Gamma = 4.0 \text{ cm}^{-1}$, $\alpha = 1.0 \text{ cm}^{-1}$, $L = 0.72 \text{ cm}$, $\Delta\omega = 1.83 \text{ GHz}$, we obtain the signal intensity gain and the mutual coherence between the signal wave and the pump wave at pump wave entrance plane. These results are shown in Figs. 2(a) and 2(b) as functions of the optical path difference between the two waves at the signal wave entrance plane for various intensity ratios β between the signal wave and the pump wave. The signal intensity gain and the normalized mutual coherence of the two waves at the pump wave entrance plane decrease as the optical path difference and the intensity ratio of the two waves increase. The normalized mutual coherence of the two waves at the pump wave entrance plane is enhanced by the two-wave mixing process.

We used an argon laser (wavelength $\lambda = 0.514 \mu\text{m}$ and linewidth $\Delta\omega = 1.83 \text{ GHz}$) and a $\text{KNbO}_3\text{:Co}$ crystal ($\Gamma = 3.43 \text{ cm}^{-1}$, $\alpha = 1.0 \text{ cm}^{-1}$, $L = 0.72 \text{ cm}$) in our experimental study. The intensity ratio of the two waves was chosen to be $\beta = 10^{-3}$. We measured the signal intensity gain as a function of the optical path difference of the two waves at the signal wave entrance plane. We also performed the numerical simulation with the same set of parameters. The results are shown in Fig. 3. The experimental results are in excellent agreement with the theoretical predictions.

In conclusion, we have investigated theoretically and experimentally contradirectional two-wave mixing with partially coherence waves in KNbO_3 photorefractive crystals. A general formulation based on the statistical theory of linear systems is presented. Results of numerical simulation and experimental measurement are provided.

References:

1. See, for example, P. Yeh, *Introduction to photorefractive nonlinear optics*, (Wiley, New York, 1993).
2. B. Fischer, S. Sternklar, and S. Weiss, *IEEE J. Quantum Electron.* **25**, 550 (1989).
3. N. V. Bogodaev, L. I. Ivleva, A. S. Korshunov, N. M. Polozkov, and V. V. Shkunov, *J. Opt. Soc. Am. B* **10**, 2287 (1993).
4. H. Z. Kong, C. K. Wu, and M. Cronin-Golomb, *Opt. Letts.* **16**, 1183 (1991).
5. See, for example, J. W. Goodman, *Statistical Optics*, ch. 3 (Wiley, New York, 1985).

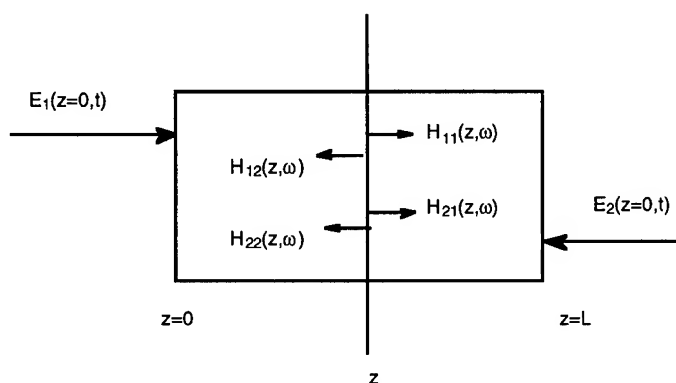


Fig. 1. Two-wave mixing with partially coherent waves in photorefractive crystals modeled as a linear system.

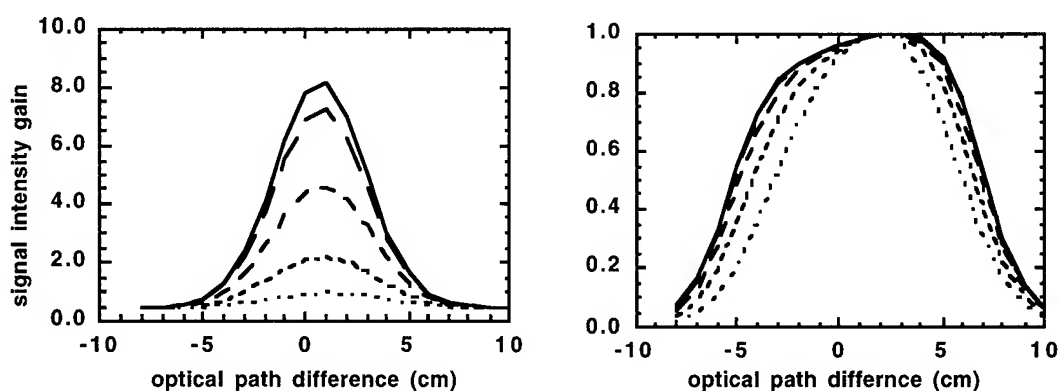


Fig. 2. (a) Signal intensity gain and (b) mutual coherence of the two waves at the pump wave entrance plane as functions of the optical path difference at the signal wave entrance plane. The values of β from the solid curve to the increasingly dashed curves are 1.0×10^{-4} , 1.0×10^{-2} , 6.25×10^{-2} , 2.5×10^{-1} and 1.0 respectively.

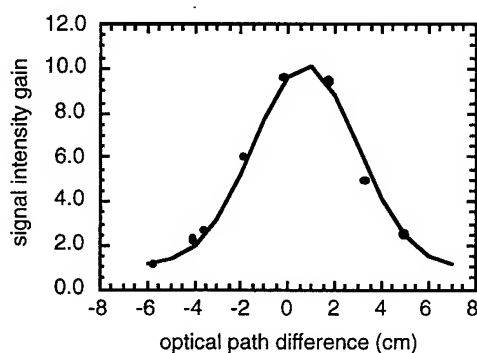


Fig.3 Signal intensity gain as a function of the optical path difference of the two waves at the signal wave entrance plane obtained from experimental measurement (dots) and numerical simulation (curve).

Amplification of Optical Signals in $\text{Bi}_{12}\text{TiO}_{20}$ Crystal by the Fanned Beam

Anatoli V. Khomenko and Alfonso García-Weidner

Centro de Investigación Científica y de Educación Superior de Ensenada,
Carretera Tijuana-Ensenada km. 107, Aportado Postal 2732, Ensenada, B.C.,
México

tel. + 52-617-44501 ext.2236, fax. + 52-617-45155, e-mail: akhom@cicese.mx

Alexei A. Kamshilin

University of Joensuu, Department of Physics, Vaisala Laboratory, Department of
Physics, P.O. Box 111
SF-80101, Joensuu, Finland

tel. + 358-73-1513235, fax. + 358-73-1513290, e-mail: kamshil@cc.joensuu.fi

The photorefractive sillenite crystals ($\text{Bi}_{12}\text{TiO}_{20}$, $\text{Bi}_{12}\text{SiO}_{20}$, and $\text{Bi}_{12}\text{GeO}_{20}$) been possess the high sensitivity, but the experimentally achieved gain for optical signals amplification by two-beam coupling does not exceed 1,500.^{1,2} This value is more than one order of magnitude less than the gain recently measured with BaTiO_3 crystals.^{3,4} The main limitation for the gain in sillenites is introduced by the beam fanning.

In this paper we propose to use the fanned beam as the energy source for the signal beam amplification. We show that with the long $\text{Bi}_{12}\text{TiO}_{20}$ crystal up to 95% of the energy can be transferred from the pump beam to the fanned beam. Than the coupling between the signal beam and fanned beam leads to signal beam amplification. This technique solves the problem of the pump beam depletion due to fanning and allows a high-gain low-noise amplification of ultraweak signals in sillenites.

We carried out our experiments on a photorefractive $\text{Bi}_{12}\text{TiO}_{20}$ crystal, which size was 0.8 mm x 3.0 mm x 20.0 mm. The sample was cut out of a bulk crystal along the $\langle 110 \rangle$ crystallographic axis. The side faces of the sample were covered by a conducting silver paste to apply an external electric field. The interacting optical beams propagate

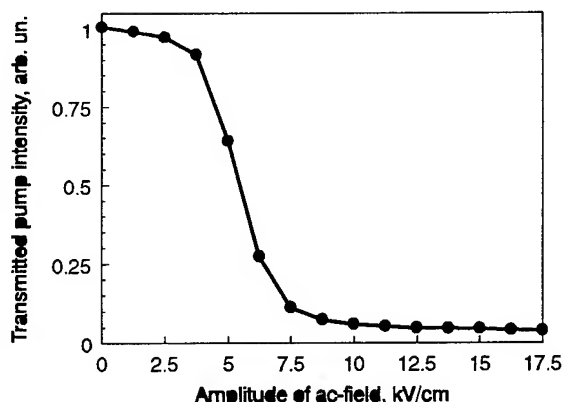


Fig. 1. Transmitted pump beam intensity as a function of the ac electric field amplitude.

under small angles respect to the $\langle 110 \rangle$ axis and the applied electric field is parallel to the $\langle 1\bar{1}1 \rangle$ axis. We applied to the crystal an alternating bipolar electric field of square-wave form, which allows to get the highest gain factor for sillenite crystals.⁵ The crystal was illuminated by a 1-mm-diameter pump beam and a 1-mm-diameter signal beam, both originating from the 15 mW He-Ne laser ($\lambda = 632.8$ nm).

Fig.1 shows the depletion of the pump beam due to fanning. One can see that up to 95% of pump beam energy

transferees to the fanned light. Fig. 1 shows the difference between the long photorefractive crystal, where the beams suffer the internal reflections, and a short bulk photorefractive crystal. It has been shown that in crystal without internal reflections of the beams the transmitted pump beam approaches zero-intensity when a photorefractive coupling constant increases.⁶ In contrast, as it follows from our experiments (Fig. 1), the transmitted pump beam intensity approaches non-zero near-to-constant value while the ac field amplitude grows up increasing the coupling coefficient. Here the pump beam losses its intensity to amplify the fanned beam directed toward the crystal surface. At the same time, the fanned beam reflected on the surface amplifies the pump beam. This process leads to a stable transmitted pump intensity when ac field amplitude is higher than 12 kV/cm.

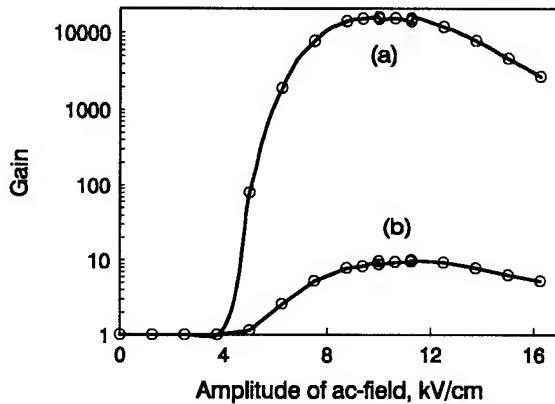


Fig. 2. The gain of the signal beam (a), and the scattered light (b) as a function of the electric field amplitude.

Using the experimental setup with a spatial filtering of the fanned beam we have shown that main source of a seed wave for the fanned beam is situated near the corner of the input surface of our crystal samples. This result indicates that the pump beam diffraction off the crystal edge gives the origin for a seed wave in our samples in contrast to usually supposed surface or bulk scattering in the photorefractive crystal. Our numerical calculations based on the beam propagation method support this experimental result.

The gain as a function of the external field amplitude is shown in Fig.2 by curve (a). We calculate the gain as the ratio

$$G(E) = \frac{I(E)}{I}, \quad (1)$$

where $I(E)$ is the intensity of the transmitted signal beam when the amplitude of the ac-field is equal to E , and I is the intensity of the signal beam when $E = 0$ and the pump beam is blocked. The signal and pump beams are linearly polarized along the $\langle 1\bar{1}1 \rangle$ crystal axis and have 7.6×10^{-7} intensity ratio. As one can see, the signal beam amplification is near unity until the external field amplitude $E < 3.5$ kV/cm. After that, the gain abruptly grows up reaching the peak value of 16,000. A sharp increasing of the gain coincides with the fanned light appearance. To

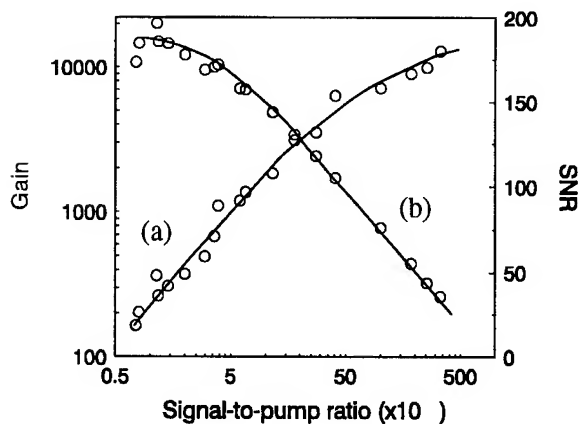


Fig. 3. Dependencies on the input signal-to-pump intensity ratio: (a), the experimental points for the SNR; (b), the experimental points for the signal gain.

illustrate this we show in Fig.2 by curve (b) the dependence of the fanned beam enhancement on the applied voltage. This has been measured as a ratio between the intensity of the light scattered at the vicinity of the signal beam from the crystal with applied electric field and that without electric field. It is worth noting that the scattered light traveling almost in the same direction as the signal beam gets 1500 times lower enhancement. Both the signal and fanning light amplification are diminishing for higher amplitude of the external field.

A signal-to-noise ratio (SNR) is one of the most important characteristics of an amplifier. In our case, we define it as a ratio of the output signal beam intensity to the average intensity of the fanned light measured in far field at a vicinity of the signal beam. The experimentally measured output SNR dependence on the input signal-to-pump ratio is shown in Fig.3 by curve (a). Even for very low signal beams, the output SNR exceeds 20. It should be underlined that for $\beta = 10^{-6}$ the intensity of a signal beam transmitted through the crystal without external electric field, when the signal gain is negligible, is 50 times smaller than an average intensity of the scattered light from the pump. If the ac voltage is applied to the crystal, both the scattered light and the signal beam are amplified. The signal gain is three orders of magnitude higher than the scattered light gain, thus resulting in a high output SNR. Our numerical simulation of the beams propagation in the long photorefractive crystal also shows the lower gain for a noise-like scattered wave as compared with the gain for a plane wave.

To conclude, we have proposed and experimentally demonstrated a novel configuration of the photorefractive coherent amplifier, which effectively exploits the fanned beam in the $Bi_{12}TiO_{20}$ crystal. In such a configuration the light is confined near the long photorefractive crystal due to internal reflections, thus providing an increased light power density for a long interaction length. The proposed scheme has potentially high speed of operation and solves the problems associated with the fanned light, namely, the pump beam depletion and the output signal corruption by a background noise. We have demonstrated experimentally that our configuration with the $Bi_{12}TiO_{20}$ crystal allows a high gain value of 16,000 of a weak signal with output SNR > 20.

REFERENCES

1. P. Refregier, L. Solymar, H. Rajbenbach, and J. P. Huignard, J. Appl. Phys. **58**, 45 (1985).
2. P. B. Mathey, G. Pauliat, J. Launay, and G. Roosen, Opt. Commun. **82**, 101 (1991).
3. A. Brignon, S. Breugnot, and J.-P. Huignard, Opt. Lett. **20**, 1689 (1995).
4. M. Kaczmarek and R. W. Eason, Opt. Lett. **20**, 1850 (1995).
5. S. L. Sochava, E. V. Mokrushina, V. V. Prokofiev, and S. I. Stepanov, J. Opt. Soc. Am. **B10**, 1600 (1993).
6. Q. B. He, P. Yeh, Appl. Opt. **33**, 283 (1994).

Demonstration of 3-D Image Reconstruction Using a Photorefractive Storage Media

by

Richard J. Anderson

National Science Foundation, Arlington, Virginia 22230

Phone: (703) 306-1683 Fax: (703) 306-0456

Brian P. Ketchel and Gary L. Wood

U.S. Army Research Laboratory,

10235 Burbeck Road, Suite 110

Fort Belvoir, Virginia 22060-5838

Phone: (703) 703-3667 Fax: (703) 704-2033

Gregory J. Salamo

Department of Physics, University of Arkansas

Fayetteville, Arkansas 72701

Phone: (501) 575-5931 Fax: (501) 575-4580

Photorefractive crystals have been used for a long time for holographic storage of two dimensional (2-D) images. In this paper we report the use of strontium barium niobate (SBN) crystal to store and project three dimensional (3-D) images.

The experimental setup which was used for 3-D storage and projection is shown in Figure 1. The output of an argon-ion laser, operating at $\lambda = 488$ nm and polarized horizontally with respect to the optical bench, was divided into three beams. Beam E_1 was used as the reference beam and directed into a 1 mm thick, 5 x 10 mm area Ce-doped SBN:60 storage photorefractive crystal. Beam E_2 was incident on the object and the laser light scattered from the object was also allowed to fall onto the storage crystal. The c-axis of the crystal was oriented parallel to the surface of the optical bench and the normal to the crystal surface bisected beams E_1 and E_2 . Together, beam E_1 and the scattered light from the object wrote a hologram in the photorefractive storage crystal. The portion of the incident laser light (E_1) transmitted through the storage crystal was directed into a second 13.5 x 12.2 x 6 mm Ce-doped SBN:60 photorefractive crystal which acted as a double phase conjugate mirror. The double phase conjugate mirror was used to produce the conjugate of the reference beam, $E_3 = E_1^*$, and direct it into the storage crystal in a direction counter-propagating to beam E_1 . This conjugate beam, therefore, was used to read the hologram and insured that the projected 3-D image was of high quality. Images representing different perspectives of the object appeared at distances of 35 mm from the crystal in the image planes marked IP_1 and IP_2 on the diagram.

Before storage of the object, a small wire of 1mm diameter was set up vertically a distance of 10 mm in front of the object. The purpose of the wire was to make it possible to view the 3-D image from different perspectives and to use parallax between the wire and the object to distinguish different views of the 3-D image.

The projected image was viewed using the eye and a CCD camera. Using the eye, one could easily see the perspective of the image change as one's head is moved in a direction perpendicular to the viewing direction. Comparing the position of the wire relative to the object, one can easily see that the projected image is three dimensional. Figures 2 and 3 present four views imaged by an achromatic relay lens in combination with a TV zoom lens onto the CCD, corresponding to two different perspectives. In particular, Figures 2a and 2b show the vertical wire next to the bottom of the letters 'LIB' in the word 'LIBERTY' on a U.S. ten-cent coin (dime). Figures 3a and 3b represent an angular shift of approximately one degree and show that the wire is now barely hiding the tip of Roosevelt's nose. Also, in Fig. 3a, the camera lens is focused on the dime, whereas in Fig. 3b the wire was brought into focus for the photograph.

Future work is aimed at using larger storage crystals in order to increase the captured perspective and to use higher incident laser intensity so that the 3-D projected image could easily be seen using particulates in the air.

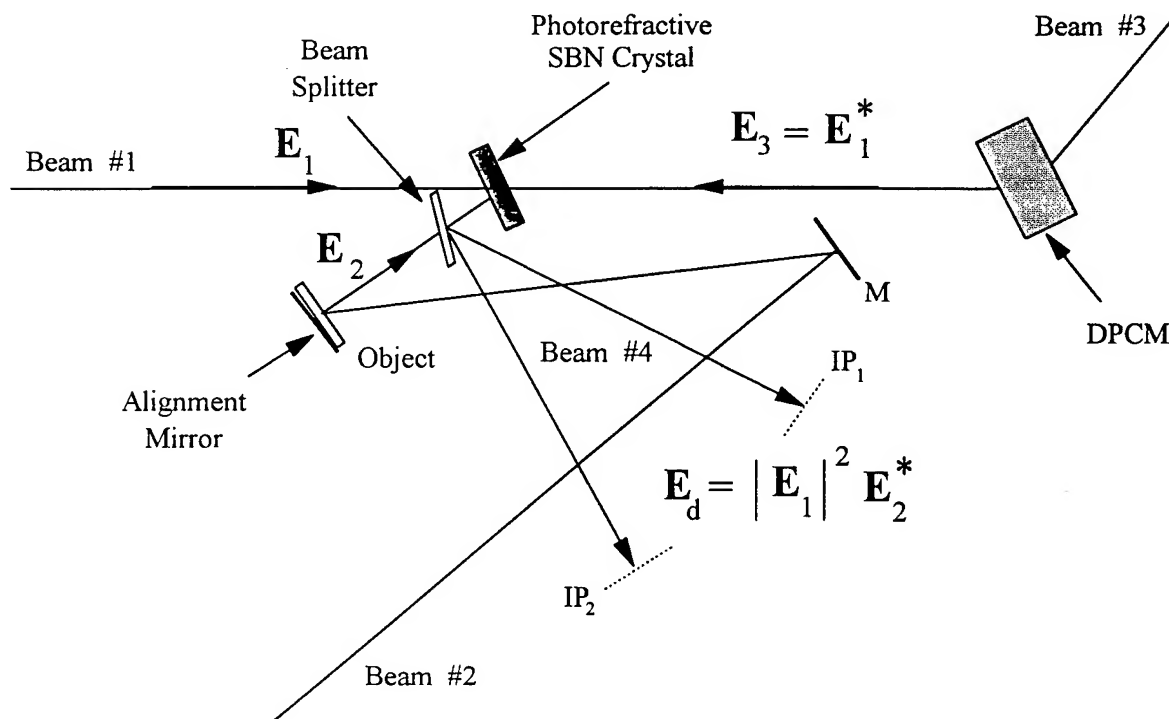
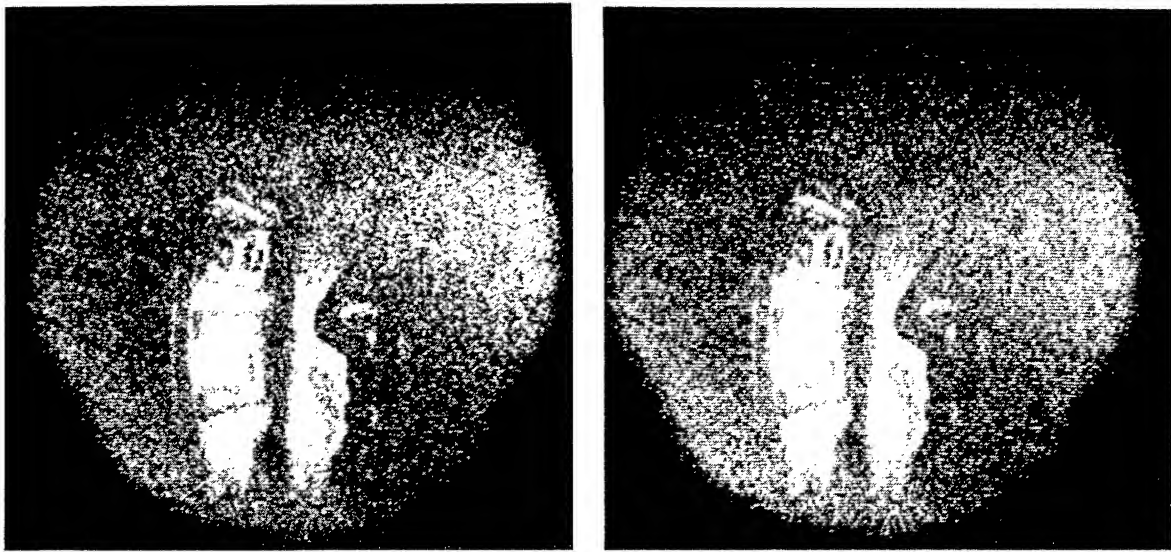
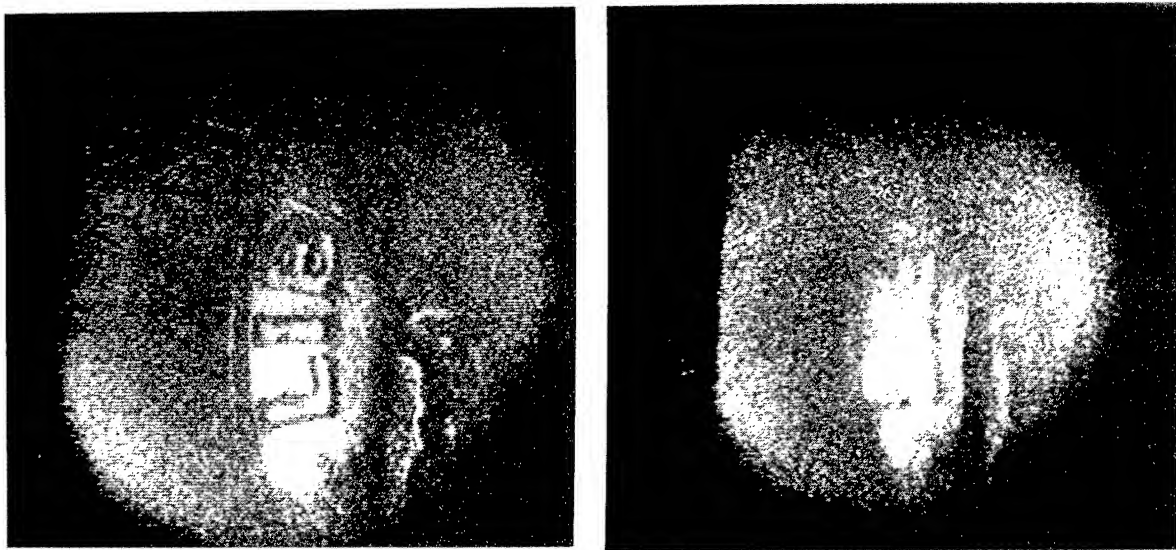


Figure 1. Schematic of experimental setup



Figures 2a and 2b. Image of 1 mm wire 10 mm in front of U.S. dime for two different exposures.



Figures 3a and 3b. Perspective of image shifted one degree from Fig. 2 with the dime in focus (Fig. 3a.) and the wire in focus (Fig. 3b.).

Self-Compensating Laser-Based Ultrasound Sensors Using Photo-Induced EMF Detection

**D.M. Pepper*, G.J. Dunning, P.V. Mitchell,
M.B. Klein, and T.R. O'Meara**

**Hughes Research Laboratories
3011 Malibu Canyon Road
Malibu, CA 90265 USA**

***Point-of-contact: 310/317-5125
310/317-5679 (FAX)
dpepper@msmail4.hac.com (e-mail)**

Laser ultrasonics [1] offers a technique for nondestructive, noncontact ultrasonic inspection, with the potential for in-factory closed-loop control and quality assurance of the manufacturing process. Progress has been made [1,2,3] which may enable this novel diagnostic to find its way into the manufacturing arena. However, the technology has yet to be cost-effective for most industrial end-users. In particular, the need to compensate for workpiece vibrations, relative platform motion, and optical distortions has driven up the system cost, including active stabilization and costly optics. Compensation techniques including optical phase conjugation [4,5], double-pumped phase conjugation [6,7,8], and two-wave mixing [9,10,11] can potentially enhance the performance of laser ultrasonic diagnostics. These schemes enable wavefront-matching of the beams for efficient coherent detection. However, in some cases, expensive electronic post-processing is required to track out residual mechanical vibrations.

We describe a novel technique which can result in a compact, high-bandwidth, low-cost laser-based ultrasonic receiver, with all-optical compensation, large field-of-view, minimal post-processing, and laser-diode compatibility. Our approach involves an adaptive photodetector using nonsteady-state photo-emf in a crystal of GaAs, first described by Petrov and Stepanov, et. al. [12,13]. The photodetector crystal generates a time-varying output current in response to a transient lateral motion of an optical pattern. The optical pattern is derived from the interference of a probe-beam, scattered by a workpiece undergoing inspection, with a coherent reference beam. An internal space-charge field is formed in the crystal by the time-averaged pattern. Transient photocurrents are generated when the pattern is perturbed about its time-averaged position, as long as the transients occur on a time-scale faster than the space-charge field formation time. In our case, the dynamic pattern changes are induced by the ultrasound which perturbs the surface of the workpiece under inspection. Slower changes in the pattern do not generate an output current, since the space-charge field can reconfigure itself in response to these perturbations. In this manner, the crystal can automatically compensate for adverse distortions in an industrial environment (e.g., mechanical vibrations, speckle, relative platform motion, thermal distortions, etc.) by tracking out these undesirable spatio-temporal noise components as new space-charge field patterns are generated.

We have constructed a laser-based ultrasonic inspection system to evaluate our sensor, as

shown in Figure 1, using either a 200 mW cw 2xNd:YAG laser as the probe in one case, or a 150 mW cw AlGaAs diode laser in another case. A 100 mJ Q-switched Nd:YAG laser was used to generate the ultrasound in a steel plate. The adaptive photodetector sensor consisted of a crystal of Cr:GaAs as the photo-emf element, and a transimpedance amplifier as the gain module. In some experiments, an optional time-delay interferometer was used to enable common-mode rejection of low-frequency, large-amplitude phase noise, as shown in Figure 2. The interferometer employed a 10 meter length of multimode fiber in one leg, resulting in a time delay of about 50 nsec, and, therefore, a compensated detection bandwidth in the range of 20 MHz.

Results of initial experiments are shown in Figure 3, where the photo-emf output, corresponding to a dynamic phase shift, or surface displacement, is shown as a function of time (called an "A-scan"), in response to a laser-induced ultrasonic transient in a steel plate. In Figure 3a, data using a reference-beam interferometer is presented, using a plane-wave reference beam. When combined with an optical-fiber-based time-delay interferometer (as shown in Figure 2), additional compensation capabilities are realized, since common-mode, low-frequency, dynamic distortions are passively compensated, whose time scales are greater than the pre-determined time delay. Figure 3b shows an A-scan using the time-delay interferometer geometry, in which case the leading and trailing edges of the ultrasonic signal appear as bipolar responses (the time delay was set to approximately that of the expected ultrasonic pulse width); note that the low-frequency components are canceled out. In both architectures, the arms of the interferometers were directed onto the surface of the photo-emf detector. The adaptive nature of the sensor compensates for speckle and vibration, while detecting the desired, high-frequency ultrasound. These results give us confidence that an adaptive photodetector can potentially replace cumbersome expensive sensors and post-tracking hardware, and may lead to a low-cost, compact, in-factory diagnostic, with noise immunity — all without compromising system performance.

References

1. C. Scruby and L. Drain, *Laser Ultrasonics: Techniques and Applications* (Hilgar Press, Bristol, 1990).
2. J.-P. Monchalín, IEEE UFFC **33**, 485 (1986);
ibid., Rev. Prog. Quant. NDE, Vol. 12 (Plenum, New York, 1993), pp. 495-506.
3. J.W. Wagner, "Optical Detection of Ultrasound," in *Physical Acoustics, Vol. XIX*, W.P. Mason, Ed. (Academic Press, New York, 1990), pp. 201-265.
4. M. Paul, B. Betz, and W. Arnold, Appl. Phys. Lett. **50**, 1569 (1987).
5. Y. Matsuda, H. Nakano, and S. Nagai, Jpn. J. Appl. Phys. **31**, L987 (1992).
6. D.M. Pepper, P.V. Mitchell, G.J. Dunning, S.W. McCahon, M.B. Klein, and T.R. O'Meara, 7th Int. Sym. on Nondestr. Char. of Mat., Prague, June, 1995.
7. P. Delaye, A. Blouin, D. Drolet, and J.-P. Monchalín, Rev. Prog. in Quant. NDE Conf., Seattle, WA, August 2, 1995; ibid., Appl. Phys. Lett. **67**, 3251 (1995).
8. H. Nakano, Y. Matsuda, S. Shin, and S. Nagai, Ultrasonics **33**, 261 (1995).
9. R.K. Ing and J.-P. Monchalín, Appl. Phys. Lett. **59**, 3233 (1991).
10. A. Blouin and J.-P. Monchalín, Appl. Phys. Lett. **65**, 932 (1994).
11. T. Honda, T. Yamashita, and H. Matsumoto, Jpn. J. Appl. Phys. **34**, 3737 (1995).
12. M.P. Petrov, S.I. Stepanov, and G.S. Trofimov, Sov. Tech. Phys. Lett. **12**, 379 (1986);
I.A. Sokolov and S.I. Stepanov, J. Opt. Soc. Am. **B10**, 1483 (1993).
13. S.I. Stepanov, Appl. Opt. **33**, 915 (1994).

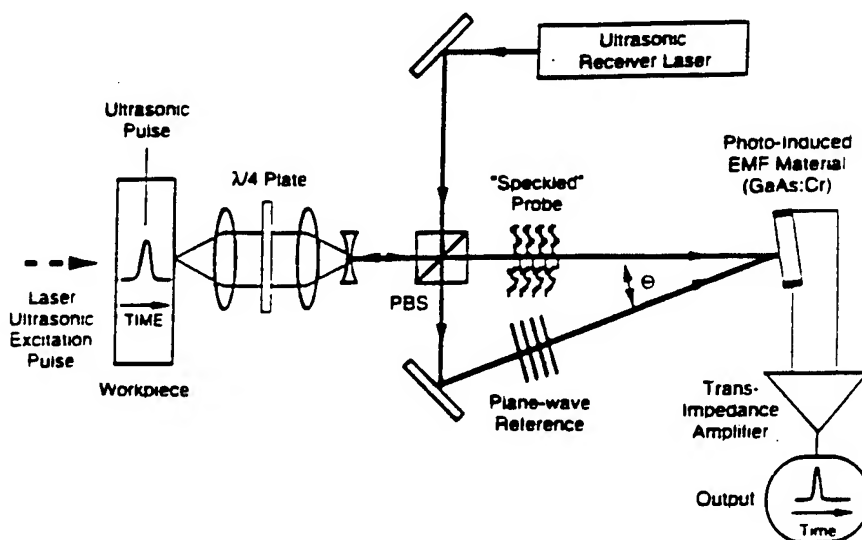


Figure 1. Laser-based ultrasound system employing a photo-emf-based detector using a reference beam interferometer, RBI, configuration.

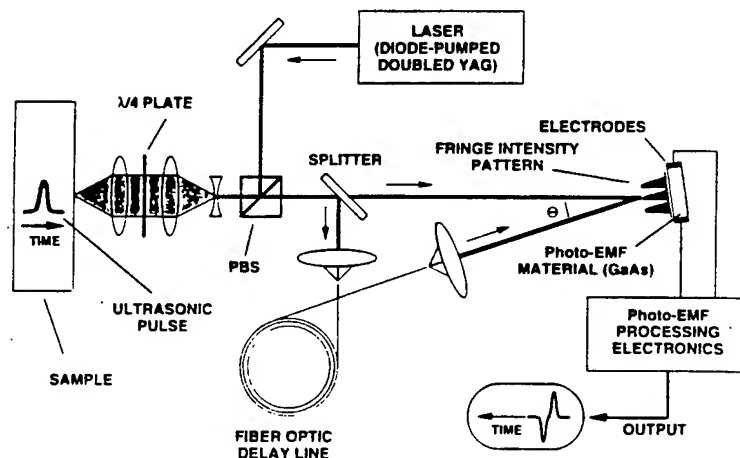


Figure 2. Laser-based ultrasound system employing a photo-emf-based detector using a time-delay interferometer, TDI, configuration.

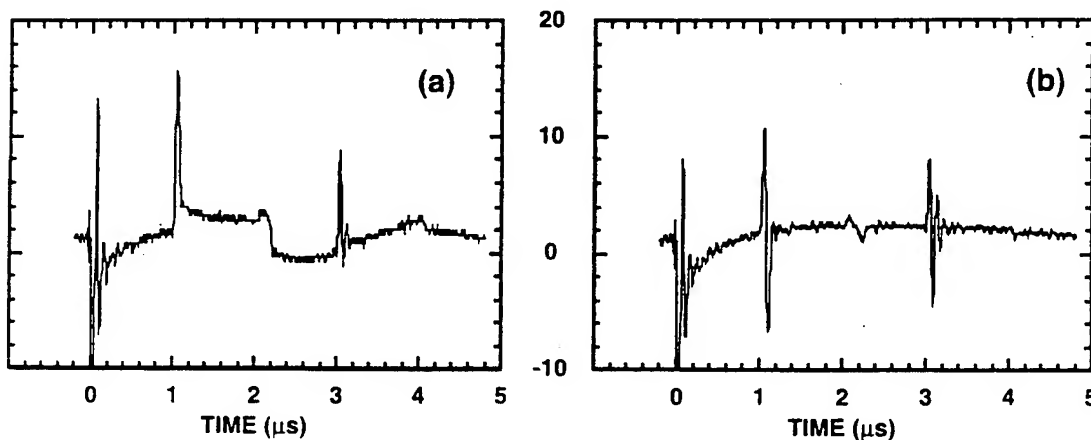


Figure 3. A-scan data using a photo-emf-based system, comparing a RBI architecture (left) with a TDI architecture (right). The system configurations are shown in Figures 1 and 2, respectively.

Competition of hexagonal and square patterns in a photorefractive feedback system

**Markus Sedlatschek, Torsten Rauch, Cornelia Denz,
Theo Tschudi**

Technische Hochschule Darmstadt, Institut für Angewandte
Physik, Licht- und Teilchenoptik, Hochschulstraße 6, D-64289
Darmstadt, Germany

Phone: +49 6151 / 16 3482 ; Fax: +49 6151 / 16 4123

Tokuyuki Honda

National Research Laboratory of Metrology, 1-1-4 Umezono,
Tsukuba, Ibaraki 305, Japan

Square and squeezed hexagonal patterns have been observed for the first time in an optical pattern formation experiment very recently by the authors of this presentation [1]. The experimental setup consists of a reflection-grating dominated photorefractive phase conjugator and a feedback path containing an ordinary mirror and a thin imaging lens at distance $2f$ from the photorefractive crystal and distance $2f + L$ from the mirror. The schematic of the setup is shown in fig. 1.

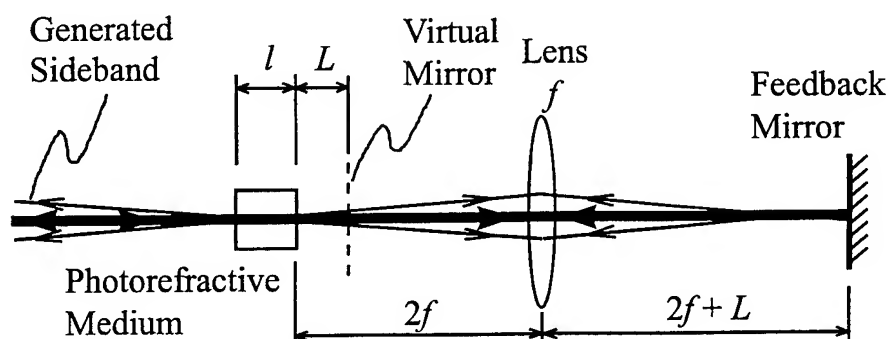


Fig. 1: Schematic of the experimental setup.

The imaging lens creates an image of the mirror at distance L from the back surface of the crystal. By translating the mirror, the value of L can be varied, and in particular, negative propagation lengths can be achieved, i.e., the image of the feedback mirror is inside the crystal. In this case, the crystal is divided into two regions by the image of the feedback mirror. In addition to regular hexagons which have been observed earlier in a related but simpler system [2, 3], squares and squeezed hexagons were observed when the image of the feedback mirror was inside the crystal. Square patterns have been predicted theoretically and numerically for optical feedback systems using Kerr nonlinearities [4, 5], but have not been experimentally verified prior to our observation. Fig. 2 shows examples of the observed patterns (next page).

Between the mirror positions for obtaining stable squares and hexagons, the two types of patterns appeared alternately in time in an irregular manner. This is an exciting phenomenon, because it is a competition of patterns with one length scale (hexagons) and two length scales (squares and squeezed hexagons).

In contrast to a manuscript of ours recently submitted to Phys. Rev. Lett., the presentation will concentrate on the dynamics of the competition of different patterns and the temporal behaviour of the spots in the far field. Furthermore, we will present an induced transition from squares or squeezed hexagons to regular hexagons by use of an aperture, placed in the feedback path.

References

- [1] T. Honda, H. Matsumoto, M. Sedlatschek, C. Denz, T. Tschudi, submitted to Phys. Rev. Lett.
- [2] T. Honda, Opt. Lett. 18, 598 (1993).
- [3] T. Honda and H. Matsumoto, Opt. Lett. 20, 1755 (1995).
- [4] J. B. Geddes, R. A. Indik, J. V. Moloney, and W. J. Firth, Phys. Rev. A 50, 3471 (1994).
- [5] R. Neubecker, G.-L. Oppo, B. Thüring, and T. Tschudi, Phys. Rev. A 52, 791 (1995).

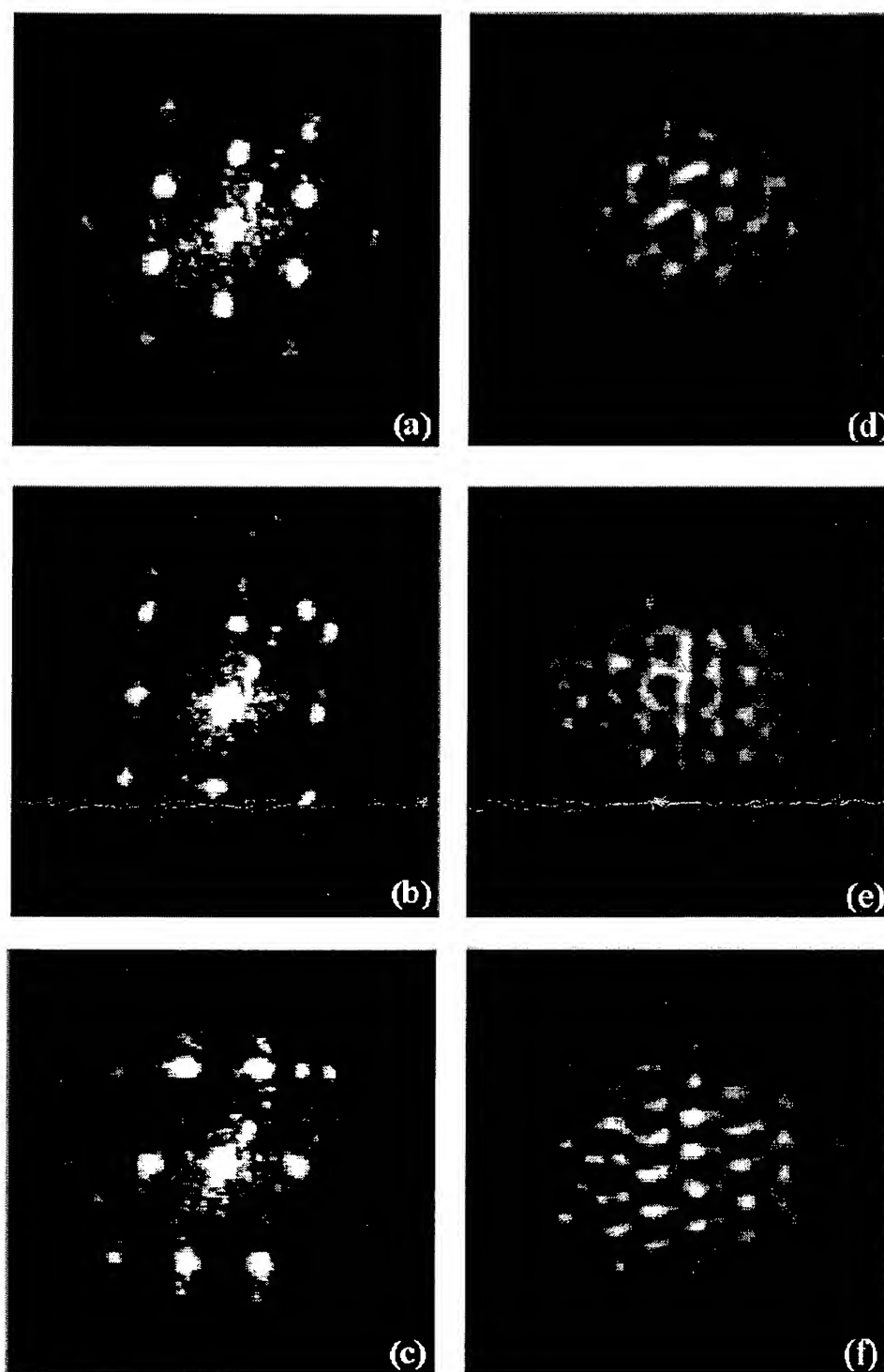


Fig. 2: Snapshots of experimentally observed far-field (a-c) and near-field (d-f) patterns.

Thursday, July 11, 1996

Thermal Nonlinear Optics and Mode Locking Mechanisms

NThB 10:00 am-11:30 am
Maile Room

John Ottusch, *Presider*
Hughes Research Laboratories

PHASE CONJUGATION BASED ON THERMAL NONLINEARITY

Alexander A. Betin

Optical Physics Laboratory
Hughes Research Laboratories
3011 Malibu Canyon Road
Malibu, CA 90265

Telephone: (310) 317-5028
Fax: (310) 317-5679
E-mail: abetin@msmail4.hac.com

The possibility of controlling the spatial structure of laser radiation, and in particular, of forming a diffraction limited beam is the key factor for the majority of laser applications. This problem can be successfully solved by means of a phase conjugation (PC) effect. In principle, PC mirrors allow us to cope with such problems as compensation for highly-inhomogeneous phase distortions, auto-guidance of laser radiation, and phase-locking of individual amplifying channels and segments of optical components. These capabilities are of particular importance for high-power laser systems with dynamically varying inhomogeneities and involving large-aperture optical elements. Accordingly, this report is a review of the history and recent achievements in the development of phase conjugation mirrors (PCM) based on the thermal nonlinear mechanism.

Any nonlinear process may be somewhat useful for applications, and yet have a negative effect in particular situations. But, thermal nonlinearity is mostly known as a parasitic effect that restricts performance of lasers and nonlinear optical devices (including PCM, for instance, based on SBS), and as well as causing problems in the propagation of laser radiation. However, recently there has been an increase of interest in employing this process for PC. Unlike SBS and photorefractive nonlinear mechanisms, thermal nonlinearity is able to work outside the visible and near-IR regions, and the possibility of thermal nonlinearity PC (TPC) has been demonstrated for 0.25 to 10.6 μm lasers [1-3]. The attractive features of TPC also include a large nonlinear constant, simple handling and the wide choice of available nonlinear media (primarily liquids and gases), plus suitability for short and long pulses, as well as for broad bandwidth radiation. Although similar to SBS it can produce a thermal stimulated backscattering (see, for example, at 1.06 μm [4], and at 10.6 μm [5]), however, a really practical approach for PC is possible only using a four-wave mixing (FWM) method or its excellent modification - FWM in a feedback loop scheme.

In the FWM method, as shown in Fig.1, signal beam E_3 , which we want to be conjugated, enters into a cell with a nonlinear medium and intersects two counterpropagating pump waves E_1 and E_2 at convergence angle Φ . The interference of the pump waves with signal waves creates spatially varying intensity, and consequently, via absorption, it produces temperature gratings in the nonlinear medium. The diffraction of the pump waves on these gratings causes the appearance of the reflected beam E_4 , conjugated to the initial signal beam E_3 . Using the simplest approximation, the reflectivity R of a FWM-mirror can be estimated as $R \approx [g \times (\alpha \ell) \times W]^2$.

Here g is a nonlinear constant, α and ℓ are the absorption coefficient and thickness of the nonlinear medium. W [J/cm^2] is the energy fluence of a pump pulse if the pulse duration t_p is less than the decay times τ of the temperature gratings, and $W \approx I \times \tau$, if $t_p > \tau$; where I [W/cm^2] is the intensity of the pump beam, and $\tau = \Lambda^2 / 4\pi^2 \chi$; χ is the thermal diffusivity and Λ is the period of the grating (for instance, the transmission grating has $\Lambda = \lambda / [2 n \sin(\Phi/2)]$). The nonlinear constant g ($g = 2\pi(dn/dT)_p / \lambda \rho C_p$) for a variety of liquids such as acetone, CCl_4 , etc. is about g [cm^2/J] $\approx 30 \lambda^{-1} [\mu\text{m}]$, and this means that the reflectivity may be close to one when the pump energy fluence equals the characteristic value W_{th} [J/cm^2] $\approx 0.1 \lambda [\mu\text{m}]$. This number shows the strength of the thermal

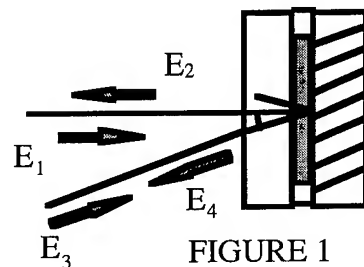


FIGURE 1

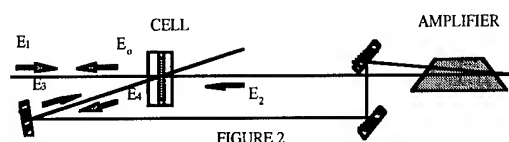
nonlinearity and allows us to make simple estimations. For a laser beam of diameter D , the required pump energy is $W_{th} \approx W_{th} D^2$, and for minimal possible $D \approx \lambda$: $W_{th} [nJ] \approx \lambda^3 [\mu m]$. The characteristic (minimum) value of pump power P_{th} required for effective FWM of long pulses ($t_p > \tau$) or CW can be estimated from $W_{th} \approx I \times \tau$, if we take the interaction angle Φ close to the diffraction limit θ_D , so $D \approx \lambda$ and for liquids: $P_{th} [mW] \approx 3 \lambda [\mu m]$. For PC of highly aberrated beams with divergence $\theta \gg \theta_D$, the convergence angle Φ should be more than θ , and the needed pump power is increased at least $(\theta/\theta_D)^2$ times. For most applications $\theta/\theta_D < 100$, and the required pump power $P_{th} [W] < 30 \lambda [\mu m]$.

These estimates show the great potential of TPC. However a big concern is that the process of phase conjugation is simultaneously accompanied by unwanted effects related to the general heating of the medium: these are thermal lensing (blooming), the frequency sweep of the interacting waves, and -for liquids - large scale heat-induced expansion of the medium, convection, and boiling [6]. Especially these effects cause troubles for long pulses. Fortunately, their influence can be eliminated or minimized by using a thin layer of the nonlinear medium and a proper design of the cell. If you decrease the layer thickness ℓ and make it close to a grating period Λ , the relaxation of the average heating of the medium, due to diffusion heat removal through the nonlinear medium boundaries, can proceed over practically the same time as the grating itself. In this case, a PC process occurs under effective limitations on the average heating, which consequently restricts all the parasitic effects. Using a thin nonlinear medium along with mirror cell geometry (Fig.1), when the pump wave E_2 is produced by 100% reflection off a good, thermal conducting mirror closely attached to that thin layer, gives you another advantage by providing a 16-fold increase in the reflectivity of the FWM.

The efficiency of TPC by FWM has been confirmed experimentally not only for short laser pulses but also for quasi-CW and CW radiation. The most detailed studies have been conducted for mid-IR lasers with organic solvents as nonlinear media [6-10]. For instance, for pulsed Er:YAG and CO₂ lasers, reflectivity was more than 3 at pump energy fluences of about 2 J/cm² and 7 J/cm², respectively. For quasi-CW and CW CO₂ lasers, reflectivity was close to one for a pump wave intensity of about 100 W/cm². PC fidelity was measured at more than 75%.

In our recent experiments [11] with a Nd:YAG laser, we got a reflectivity of about 20 in transient regime of FWM for 400W peak power of 1 ms pulses; and at steady state condition for 50-100W peak power pulses up to 20 ms length, reflectivity was more than one. PC fidelity was close to 100%. By employing different media, there are a lot of possibilities for changing or improving the FWM parameters. For example, compressed gases have smaller decay time and might be better for a pulsed regime [12]. Media with temperature dependant phase transitions permit a lower required laser power. Using nematic liquid crystals, a reflectivity of FWM of 500% for a CW CO₂ laser was achieved at a pump intensity only 20 W/cm² [13]. Very low power and energy FWM was also realized with a pulsed CO₂ laser utilizing a semiconductor-metal phase transition in a VO₂ film [14].

The drawback of the FWM method itself is that a high-power, high-quality pump beam that are an order or more intense than the signal or FWM-reflected beam is required. Important step in overcoming this drawback [15] was made in the suggestion of a ring optical scheme of FWM with an amplifier in a feedback loop (Fig.2). This loop PCM works as a self-PCM and is suitable with practically any kind of nonlinearity. A signal wave E_1



passes through a cell with a nonlinear medium, on through an amplifier, and then is returned by mirrors into the cell as a wave E_3 . There it intersects with the initial beam E_1 and they record a hologram in the medium, which serves as one of the mirrors in the ring resonator containing the amplifier. A beam E_2 , which starts from spontaneous noise, reflects from the hologram to become beam E_4 ; in turn, E_4 becomes the beam E_2 after passing the loop, and so we close the feedback. The lasing of output beam E_0 (which is passed through the cell part of E_2) starts if the reflection coefficient from the hologram R and the gain G inside the loop fulfill to the generation condition, $R \times G > 1$. Though the beam E_2 in the form of a conjugate wave to the initial signal E_1 (that is $E_2 \propto E_1^*$) is always close to a zero mode of the loop resonator, still certain measures must be taken to discriminate the nonconjugate waves [16-19]. For a Gaussian input beam it is enough that the signal wave passing through the optical path of the feedback loop be decreased in diameter; in this case the formed resonator is similar to an unstable one with high discrimination of modes. For a highly aberrated

input beam E_1 , besides narrowing, there is a need for either an additional spatial filter (a nonuniform phase plate inserted after the amplifier, which provides a divergence larger than the angle of view of the optical path to this plate), or utilization of an extended (or multilayer) nonlinear medium with a length largely exceeding the diffraction spread length of a field speckle.

At first glance, using a loop scheme as a PCM seems to be quite complicated (especially because the real scheme includes additional elements, which are not shown on Fig.2), but it allows considerable amplification of the conjugated beam, may be naturally incorporated in laser systems with amplifiers, and is, by itself, another promising way to build phase conjugate (or adaptive) lasers.

Loop PCM needs quite a high gain amplifier; usually for effective work the small signal round trip gain is about 100. There is a threshold for the input signal to initiate the lasing in the loop, and this threshold may be estimated as a fraction (one tenth or so) of W_{th} . Since the value W_{th} for liquids is not far from the saturation energy density W_{sat} of the active laser medium, there is a need to prevent gain saturation by the initial signal, and for this purpose nonreciprocal attenuators, decreasing the signal only, are used. As for usual lasers, the output of the loop PCM strongly depends on how effectively the loop resonator is built, including recording a holographic mirror, but in any case, it is finally determined by the amount of energy stored inside the active medium of the amplifier.

A loop scheme was first realized [20,21] and thoroughly studied for a CO_2 laser as an alternative to an SBS mirror, which was not feasible in the $10\mu m$ range. Different nonlinear media were used: liquids [20-22], saturable absorbed gases such as SF_6 [21,23], active CO_2 laser medium [24]. Pulse duration was from 100ns to 20 μs . For liquids, minimal threshold was about 10mJ, maximal reflectivity of the loop PCM was about 30, and an output energy per pulse of more than 10J was achieved. Diffraction limited generation was demonstrated despite strong inhomogeneities inside the loop resonator [25]. For an aberrated signal with $\theta/\theta_D \approx 20$, PC fidelity up to 40% was reported [26]. In a scheme with a power double-pass CO_2 amplifier this kind of PCM provided 1.6kJ output per pulse [27].

In the $1\mu m$ range, a loop scheme was first tried [28] for 30ns pulses with use of a Nd:YAG amplifier and thermal nonlinearity in liquids and then [29] for 300ns pulses train of total duration of 200 μs . For a Nd glass laser with Gaussian-like input beam, the threshold about 15mJ, reflectivity up to 25 and maximal output energy about 0.5J in 15ns long pulses were demonstrated along with good output beam quality [30].

In addition, we will also discuss our latest experiments performed at Hughes Research Laboratories, where we demonstrate good energy performance and the PC fidelity of a Nd:YAG loop PCM for short (30ns) and long (1ms) pulse format. We conclude that using thermal nonlinearity, especially in combination with a loop geometry, opens the entire area for the development of advanced phase conjugate mirrors for different lasers and different regimes of operation. It is also very promising for constructing phase conjugate lasers with scalable output energy and average power.

REFERENCES

1. R.G. Caro and M.C. Gower, "Amplified phase conjugate reflection of KrF laser radiation," *Appl. Phys. Lett.* 39, 855 (1981).
2. V.B. Gerasimov et al., "Influence of thermal self-interaction of optical beams on wavefront reversal in the free-running regime," *Sov. J. Quantum Electron.* 16, 223 (1986).
3. A.A. Betin, E.A. Zhukov, and O.V. Mitropol'skii, "Reflection of CO_2 laser radiation in the case of degenerate four-wave interaction in liquids," *Sov. J. Quant. Electron.* 15, 1248 (1985).
4. A.M. Berezinskaya, A.M. Dukhovny, and D.I. Stasel'ko, "Phase conjugation by stimulated thermal scattering in gas," *Optika i Spektroskopia*, 61, 1085, (1986).
5. V.I. Bespalov et al., "Self-phase-conjugation of middle infrared radiation by four-wave mixing and stimulated scattering," *SPIE Proceedings*, vol. 1841, 124 (1991).
6. O.L. Antipov et al., "Four-wave interaction of middle-infrared radiation in media with thermal nonlinearity," *Sov.J.Quant.Electron.*, 19, 1465 (1989).
7. A.A. Betin and O.V. Mitropol'sky, "Phase conjugation of pulsed CO_2 laser radiation by four-wave mixing in CCl_4 ," *Sov.J.Quant.Electron.* 18, 497 (1988).
8. S.I. Kliment'ev et al., "Optimization of conditions of four-wave interaction of cw radiation in an absorbing medium," *Sov. J. Quant. Electron.* 19, 387 (1989).
9. A.A. Betin, V.A. Kamensky and V.P. Novikov, "Investigation of phase conjugation as a result of four-wave interaction of YAG:Er laser radiation in organic solvents," *Sov.J.Quant.Electron.*, 21, 1354 (1991).
10. V.I. Kuprenyuk et al., "Phase conjugation of CW chemical laser radiation via four-wave mixing in

- absorbing liquid," Laser Optics'95 Conference, June 1995, St.Petersburg, Russia.
11. A.A. Betin, M.S. Mangir and D.A. Rockwell, "DFWM and phase conjugation in absorbing liquids at $1\mu\text{m}$ with 1 to 20 msec duration pulses," Proc.CLEO'95, p.4.
 12. A.M. Berezinskaya, A.M. Dukhovny, and D.I. Stasel'ko, "Efficient writing of thermal holograms in gases," Sov. Tech. Phys. Lett. 11, 374 (1985).
 13. L. Richard, J. Maurin and J.P. Huignard, "Phase conjugation with gain at CO_2 laser line $\lambda = 10.6\mu\text{m}$ from thermally induced gratings in nematic liquid crystals," Opt. Commun., 57, 365 (1986).
 14. N.K. Berger, E.A. Zhukov, and V.V. Novokhatskii, "Nonlinear interaction of infrared waves on a VO_2 surface at a semiconductor-metal phase transition," Sov. J. Quant. Electron. 14, 505 (1984).
 15. I.M. Bel'dyugin, M.G. Galushkin, and E.M. Zemskov, "Wavefront reversal of optical radiation using feedback in four-wave interaction," Sov. J. Quant. Electron. 14, (1984).
 16. A.A. Betin and N.Yu. Rusov, "On the formation of a conjugate wave in a scheme of four-wave mixing with feedback," Izv. Vyssh. Uchebn. Zaved., Radiofizika, 30, 676 (1987).
 17. A.A. Betin and N.Yu. Rusov, "Structure of lasing modes generated as a result of a four-wave interaction with feedback," Sov.J.Quant.Electron., 18, 657 (1988).
 18. V.I. Bespalov and A.A. Betin, "Spatial structure of radiation from lasers with controllable nonlinear mirrors," Bulletin of the Academy of Sciences of the USSR. Physical Series. 53, 52 (1989).
 19. A.A. Betin and A.V. Kirsanov, "Selection of a phase-conjugate wave in an oscillator based on a four-wave interaction with feedback in an extended nonlinear medium," Quantum Electronics, 24, 219 (1994).
 20. A.A. Betin, E.A. Zhukov and O.V. Mitropol'sky, "Large reflection coefficients in four-wave mixing of a CO_2 laser beam in liquids," Sov.Tech.Phys.Lett., 12, 435 (1986).
 21. A.A. Betin and O.V. Mitropol'sky, "Generation of radiation by four-wave interaction in a feedback system in the $\lambda=10\mu\text{m}$ range," Sov.J.Quant.Electron., 17, 636 (1987).
 22. V.I. Bespalov et al., "Phase conjugation of CO_2 laser radiation in a medium with thermal nonlinearity," IEEE Journal of Quantum Electronics, 25, 360 (1989).
 23. D.A. Goryachkin et al., "Experimental investigation of self-conjugation of CO_2 laser radiation," Sov. J. Quant. Electron. 20, 1259 (1984).
 24. A. A. Ageichik et al., "Self-phase conjugation of middle infrared radiation by four-wave mixing in active medium of CO_2 laser with feedback loop," Laser Optics'95 Conference, June 1995, St.Petersburg, Russia.
 25. A.A. Betin, K.V. Ergakov and O.V. Mitropol'sky, "Phase self-conjugation of a CO_2 laser beam in four-wave mixing," Sov.Tech.Phys.Lett. 14, 879 (1988).
 26. A.A. Betin, K.V. Ergakov and O.V. Mitropol'sky, "Reflection of speckle-inhomogeneous CO_2 laser radiation under four-wave interaction conditions with feedback," Quantum Electronics, 24, 59 (1994).
 27. I.K. Babaev et al., "High power amplifier with WFR-mirror," Proc. of the Int. Conference on Lasers'93, Lake Tahoe, NV, December 1993; STS Press 1994, p.748-750.
 28. A.S. Dement'ev and E.Ya. Murauskas, "Emission from a YAG:Nd laser with a four-wave thermal mirror in a ring resonator," Sov. J. Quant. Electron. 18(5), 631 (1988).
 29. M.S. Barashkov et al., "Strong reflection of a series of pulses from a four-wave mirror with thermal nonlinearity under parametric feedback conditions," Sov. J. Quantum Electron. 19, 518 (1989).
 30. A.A. Betin and A.V. Kirsanov, "Spatial structure of radiation from a neodymium glass four-wave feedback oscillator," Sov.J.Quant.Electron., 22, 715 (1992).

Study of Thermal Nonlinear Refraction in the Transient Regime

Pascale BROCHARD, Valérie GROLIER and Régis CABANEL

Thomson CSF Optronique, rue Guynemer, B.P.55, 78283 Guyancourt cedex, FRANCE

Tel : (33) 1 30 96 70 84 Fax : (33) 1 30 96 76 35

e-mail : pascale.brochard@thomson-csf.fr

Development of passive optical limiters for eye and sensor protection has led to the search for mechanisms that involve large optical nonlinearities in organic materials. Photo-induced thermal effects appear to be a major mechanism in defocusing optical limiters, based on nonlinear refraction ^{[1],[2]}. Until now, their efficiency has been demonstrated in the quasi steady-state regime, when pulse duration is larger than the thermal lens build-up time. In this paper, we demonstrate the influence of experimental parameters and material physical properties on the efficiency of thermal nonlinear effects in the nanosecond regime.

A single beam z-scan experiment, whose principle is described by Sheik-Bahae et al ^[3], is performed with dye solutions to show the influence of the system f-number on the rise-time of the nonlinearity. This experiment is completed with a two-color time resolved z-scan that shows the different mechanisms of the formation of the photo-induced thermal lens. We show experimentally that in the nanosecond regime, both acoustic wave, generated by the thermal impact in the solution, and heating of the solution, that relaxes with the thermal diffusion characteristic time, must be taken into account.

Along with the experiments, a theoretical analysis of the on-axis photo-induced index variation is developed, that considered both acoustic and diffusive contributions. It is based on the resolution of the linearized hydrodynamic equations ^[4], describing the interaction between the laser intensity and the dye solution. In our model, the spatial shape of the pulse intensity is assumed to be gaussian but it can be applied to any temporal shape of the pulse intensity. In the case of a gaussian temporal pulse, we show that the index variation can be expressed as function of two normalized parameters $u = t / \tau$ and $m = \tau_{ac} / \tau$, where t is the time parameter, τ is the 1/e pulse width and τ_{ac} is the acoustic time given by

$$\tau_{ac} = \frac{\omega \sqrt{\gamma}}{\nu_s}$$

w is the beam size, v_s is the sound velocity in the liquid, γ is the ratio between constant pressure and constant volume calorific capacities. Thus,

$$\Delta n(r, u, m) = \Delta n_{0ss} (f_{diff}(r, u) + f_{ac}(r, u, m))$$

where f_{diff} and f_{ac} are respectively the diffusive and acoustic contributions^[5], functions of the radial coordinate r , u and m . Δn_{0ss} , the on-axis index variation in the quasi steady-state approximation, is given by

$$\Delta n_{0ss} = \frac{\alpha_0}{C_p} F_0 \frac{dn}{dT}$$

dn/dT is the rate of change of the index with respect to temperature, F_0 is the on-axis incident fluence and α_0 is the linear absorption of the medium. Fig.1 shows an example of the calculation.

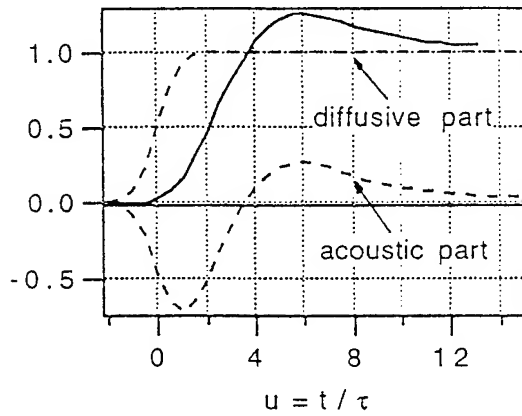


FIG.1 : Calculation of the acoustic part f_{ac} and the diffusive part f_{diff} (dashed line) and the sum of the two contributions (solid line) for $r = 0$, $m = 5.33$ ($\tau_{ac} = 16$ ns, $\tau = 3$ ns).

We note that f_{diff} rapidly tends to 1 and that f_{ac} oscillates before it tends to 0. It presents a valley followed by a peak at $u = m$. The sum of the two functions, proportionnal to Δn , shows an overshoot before reaching its quasi steady-state value Δn_{0ss} with a rise time related to m . The simulation is in good agreement with the experimental results of the pump/probe z-scan. The effective index variation during the pulse Δn_{0eff} is given by the averaged on-axis index variation during the pulse duration. Numerical calculation of the ratio $\Delta n_{0eff} / \langle \Delta n_{0ss} \rangle$ is displayed on Fig.2 for a temporally gaussian pulse. The calculated points can be fitted with an exponential curve that only depends on the m parameter and whose expression is given above :

$$\Delta n_{0eff}(m) = \langle \Delta n_{0ss} \rangle \exp\left[-\frac{m}{2.7}\right]$$

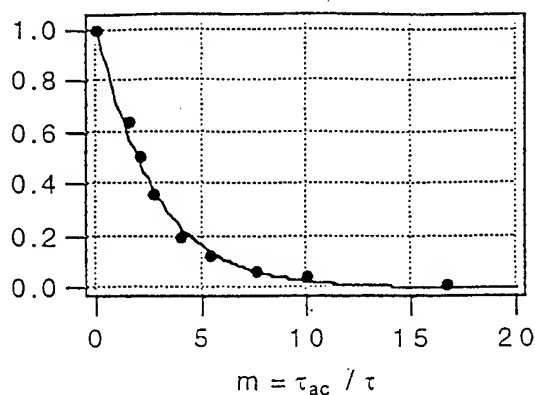


FIG.2 : Numerical calculation of $\Delta n_{eff} / \langle \Delta n_{0ss} \rangle$ in the hypothesis of a gaussian temporal pulse. Points are fitted with an exponential function (solid line).

We have used this model to calculate z-scans in dye solutions with different beam sizes. These curves have been compared to experimental results : it shows a good validity of the model, at least around the focus, when the spatial shape of the pulse is very close to a gaussian.

Thus, the estimation of the effective index variation permits a quantitative comparison of thermal nonlinear effects with faster nonlinearities as molecular reorientation in the nanosecond regime. We show that for a pulse duration bigger than a few nanoseconds, the thermal nonlinear index variation of a dye solution whose linear transmittance is 75%, is larger than the photo-induced index variation in pure carbon disulfide. However, for shorter pulses, it is necessary to consider both the nature of the solvent and the geometric configuration. It has led to define a dynamic figure of merit for thermal nonlinear refractive effects that takes into account the temporal shape of the incident pulse, the f-number of the geometric system as well as some intrinsic parameters of the solvent. Thus, in a given experimental configuration, it is possible to optimize the choice of the dye solution to optimize the thermal photo-induced index variation.

- [1] R.C.C.Leite, S.P.S.Porto, T.C.Damen
'The thermal lens effect as a power-limiting device'
Appl.Phys.Lett. 10, 100 (1967)
- [2] B.L.Justus, A.L.Huston, A.J.Campillo
'Broadband thermal optical limiter'
Appl.Phys.Lett. 63, 1483 (1993)
- [3] M.Sheik-Bahae, A.A.Said, T.H.Wei, D.J.Hagan, E.W.Van Stryland
'Sensitive measurements of optical nonlinearities using a single beam'
IEEE J.Quantum Electron. QE-26, 760 (1990)
- [4] S.R.J.Brueck, H.Kildal, L.J.Belanger
'Photoacoustic and photo-refractive detection of small absorptions in liquids'
Opt.Comm 34, 199 (1980)
- [5] P.Brochard
'Réfraction non linéaire d'origine thermique en solution : étude du régime transitoire'
Thèse, Université Paris XI Orsay, n°3738 (1995)

Critical Behavior of Femtosecond Nonlinearity of Metallic Indium on Melting

N.I.Zheludev, S.V.Popov, I.R.Shatwell

Department of Physics, University of Southampton, SO17 1BJ, UK

Tel : +44 01703 593566; Fax: +44 01703 593910; e-mail: <n.i.zheludev@soton.ac.uk>

V.E.Gusev

Laboratorium voor Akoestiek en Thermische Fysica

Katholieke Universiteit Leuven, Celestijnenlaan 200D, B-3001 Leuven, Belgium

We report on what is, to the best of our knowledge, the first observation of critical enhancement of optical nonlinearity in the vicinity of a phase transition. We studied the degenerate cubic optical

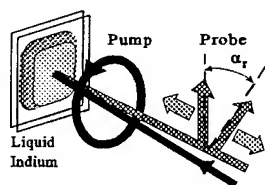


Fig.1. Pump-probe measurements of transient cubic nonlinearity in indium using the Specular Inverse Faraday Effect.

nonlinearity of metallic indium on melting. We found that in the vicinity of the melting point this nonlinearity changes dramatically with temperature. So far nonlinear optical properties of liquid metals, where mercury is an example [1], have been studied only by second harmonic generation technique. No data on cubic nonlinearity of liquid metals or metals undergoing the phase transition are available.

Recent observation of strong and very fast spin-flipping nonlinearity in bulk gold [2] stimulated us to investigate this nonlinearity in a liquid metal. The reflective, polarization-sensitive, time-resolved spectroscopic technique of the Specular Inverse Faraday Effect [3] was used in our experiments for the measurement of the cubic optical nonlinearity. In this technique a circularly polarized pump stimulates circular dichroism in the sample which is monitored by a weak linearly polarized probe on reflection (see fig.1). This results in the alteration of the polarization state of the reflected probe. The

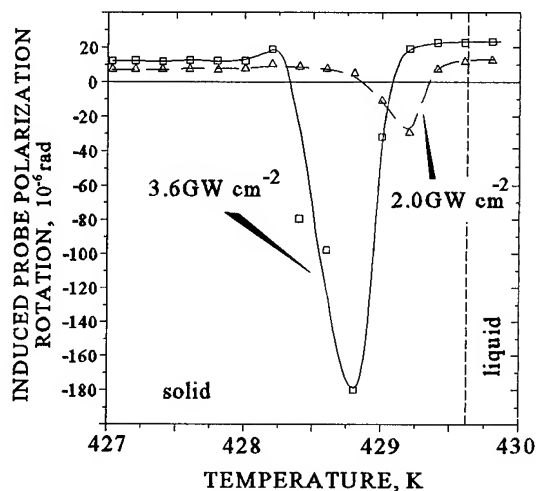


Fig.2 The magnitude of the nonlinear response as a function of temperature in the vicinity of the melting point in indium

value of the nonlinearity $\chi^{(3)}$ may be recovered from the observation of the reflected probe polarization azimuth rotation α_r :

$$\alpha_r = \frac{32 \pi I}{c |1 + n|^2} \text{Im} \left\{ \frac{\chi_{xyxy}^{(3)}(\omega, \omega, \omega, -\omega) - \chi_{xyyx}^{(3)}(\omega, \omega, \omega, -\omega)}{n(1 - n^2)} \right\} \quad (1)$$

where n is the complex dielectric constant of the medium, I is the pump intensity.

A sample of 99.999% pure indium was placed into a temperature-controlled glass optical cell. A femtosecond Cr:forsterite Kerr-mode-locked laser which generated 90fs pulses centered at wavelength 1260nm was used as the optical source for both pump and probe. The magnitude of the induced probe polarization azimuth rotation was measured across the melting point of indium ($T \sim 429.6\text{K}$). The sign of the induced rotation at temperatures well below and above the melting point was found to be the same (see fig. 2-3). The corresponding values of the nonlinearities as found from formula (1) are $|\chi_{xyxy}^{(3)}(\omega, \omega, \omega, -\omega) - \chi_{xyyx}^{(3)}(\omega, \omega, \omega, -\omega)| \sim 2 \cdot 10^{-8}$ esu for the liquid phase and $\sim 10^{-8}$ esu for the solid indium. However, in the vicinity of the melting point the rotation changes its sign and the magnitude increases dramatically to a corresponding value of $|\chi^{(3)}|$ in the peak reaching $\sim 10^{-7}$ esu.

We believe that the observed magnitude of the nonlinearity well above the phase transition may be explained within the free-electron spin-flipping model which accounts for conservation of the angular momentum when circularly polarized light is absorbed by free electrons in the metal [2]. The increase of the rotation in the liquid phase may be attributed to several factors. They include the possible relative increase of the spin relaxation time explainable by the change of the phonon spectrum and the increase of the free electron density due to the freeing of some bound electrons on liquefaction. The simple free-electron model [2] is not sufficient to explain the peculiarities of the effect in the vicinity of the phase transition. Although one can anticipate a critical enhancement of the susceptibility due to the spin exchange and correlation effects in the fluctuating environment of the phase transition, we believe that the account of the transitions involving the bound electrons is necessary for the explanation of the effect at the critical point.

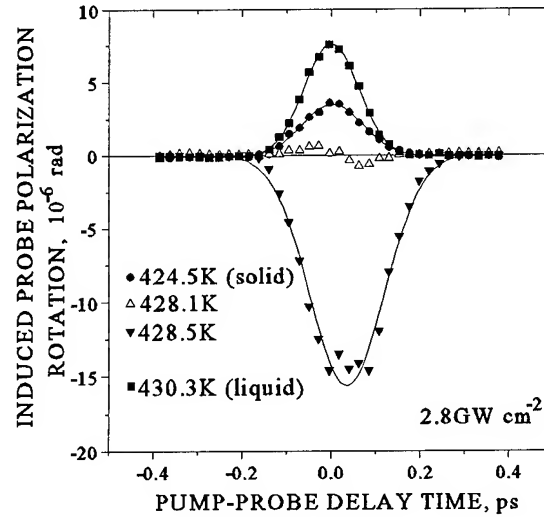


Fig.3 Induced reflected probe polarization rotation versus pump probe delay in indium at various temperatures. Note the zero off-shift of the cross-correlation function at negative peak (the bound electron contribution).

The increase of the bound electrons nonlinearity happens because of the modification of the binding potential in the proximity of the phase transition as sketched in fig 4. It is known that in indium some of the bound electrons become free on melting. With the temperature approaching the melting point the electron potential $U(r)$ becomes more and more non-parabolic and, the restoring force become more and more nonlinear. At some stage the nonlinear contribution of these weakly-bound electrons become comparable and even overcomes the spin-related nonlinearity of the free electrons (see fig. 2). The nonlinearity increases further up to some point below the melting temperature at which the electron becomes free losing its dipole nonlinearity and joining the ever present free electrons with the spin-flipping nonlinearity of opposite sign.

The critical behavior of the nonlinearity develops just below the melting temperature of the metal. As expected, we saw an indication of the local laser heating of the sample in the vicinity of the focal point. It manifests itself as a temperature down shift of the critical peak position as shown by the thermostat. This shift decreases with the drop of the pump average power (see fig.3). More importantly we observed that the increase of the bound electron nonlinearity is accumulated during the individual 90fs laser pulse. This manifests itself as an apparent delay of the induced rotation in respect to zero pump-probe delay. This may be seen in fig.3 for the negative peak which is due to the bound electrons. This indicates that laser-induced deformation of the electron binding potential in indium actually happens on a time scale comparable or faster than 10^{-14} s.

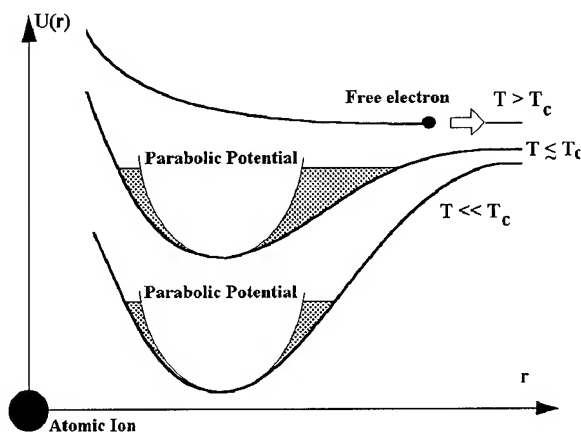


Fig.4 Sketch of the transformation of the bound electron potential in the proximity of the melting temperature. With increase of the temperature up to T_c , the potential more and more departs from the parabolic curve leading to the increase in the nonlinearity.

Finally for the first time we observed a new mechanism of critical enhancement of ultrafast cubic optical nonlinearity in metals.

1. E.D.Crozier, R.M.Ninnis, K.E.Rieckhoff. In: *The Properties of Liquid Metals*. Ed. S.Takeuchi. Taylor&Francis Ltd, 1973, p.239-243
2. N.I.Zheludev, P.J.Bennett, H.Loh, S.V.Popov, I.R.Shatwell, Y.P.Svirko, V.E. Gusev, V.Kamalov, E.V.Slobodchikov. *Opt.Lett.* 20, 1368 (1995)
3. S.V.Popov, N.I.Zheludev, Yu.P.Svirko. *Opt.Lett.* 19, 13 (1994)

Nonlinear Optical Processes in Laser Modelocking

Wilson Sibbett
University of St. Andrews, U.K.

Thursday, July 11, 1996

Fiber Nonlinear Optics

NThC 7:00 pm-8:00 pm
Maile Room

Wayne Knox, *Presider*
AT&T Bell Laboratories

Electrostrictive Intensity-Dependent Refractive Index of Silica Fibers

Eric L. Buckland and Robert W. Boyd
The Institute of Optics, University of Rochester, Rochester, NY 14627

Tel: (716) 275-5030 Fax: (716) 244-4936

Generally, it has been assumed that the non-resonant electronic response is the origin of the intensity-dependent refractive index in silica fibers. However, electrostriction has recently been shown to be the source of long range soliton interactions¹ through a time-dependent refractive index change. Additionally, recent experimental work has identified a discrepancy between cw cross-phase-modulation (XPM) measurements of the nonlinear refractive index and measurements made using self-phase-modulation (SPM) of 100 ps modelocked pulses². In the present work we identify electrostriction as the origin of this discrepancy and demonstrate that electrostriction makes a significant time-dependent contribution to nonlinear refraction in optical fibers.

The electrostrictive nonlinearity is due to a change in the linear susceptibility of the medium associated with an increased density in regions of high field strength. In the perturbation approximation, the refractive index change associated with electrostriction is

$$\Delta\tilde{n}(t) = \frac{\Delta\tilde{\epsilon}(t)}{2n} = \frac{1}{2n} \left(\frac{\partial\epsilon}{\partial\rho} \right) \Delta\tilde{\rho}(t) \quad (1)$$

where ϵ is the dielectric response at the signal frequency. In an optical fiber, we can calculate the time-dependent effective refractive index change by solving the acoustic wave equation for the density $\Delta\tilde{\rho}$ change across the fiber core. The appropriate wave equation is³

$$\frac{\partial^2 \Delta\tilde{\rho}}{\partial t^2} - \Gamma' \nabla^2 \frac{\partial \Delta\tilde{\rho}}{\partial t} - v^2 \nabla^2 \Delta\tilde{\rho} = -\frac{\gamma_e}{4\pi} \nabla_{\perp}^2 |\tilde{\mathbf{E}}|^2 \quad (2)$$

where the sound velocity is $v = 5.9 \times 10^5$ cm/s, Γ' is a damping parameter, $\rho_0 = 2.2$ g/cm³ is the density of the core and the pump intensity is $|\tilde{\mathbf{E}}|^2$. The magnitude of the response is determined by the electrostrictive coefficient $\gamma_e = \rho_0 (\partial\epsilon/\partial\rho)$, which we may estimate using the Lorentz-Lorenz local field result, that is,

$$\gamma_e = \frac{1}{3}(\epsilon_0 - 1)(\epsilon_0 + 2) = 1.5. \quad (3)$$

This result may be equivalently obtained using a mechanical model and the Pockel's coefficients⁴. The time-dependent change in the refractive index is then proportional to the convolution of the pump intensity with the acoustic impulse response, calculated equivalently by

$$\Delta\tilde{n}(t) = n_2^{str} I_0 \int_{-\infty}^{\infty} B(\Omega) H(\Omega) d(\Omega/2\pi) \quad (4)$$

where $B(\Omega)$ is the power spectrum of the driving field and $H(\Omega)$ is the acoustic frequency response function, normalized such that $H(0) = 1$. The coefficient of nonlinear refraction is a function of accessible physical parameters, and for a fiber with a gaussian transverse field profile is calculated to be

$$n_2^{str} = \frac{1}{8} \frac{1}{c \rho_0} \left(\frac{\gamma_e}{n v} \right)^2 = 0.57 \times 10^{-16} \text{ cm}^2/\text{W}. \quad (5)$$

The time scale of the electrostrictive response is given by the time it takes for sound to propagate across the beam waist in the fiber. Electrostrictive self-action is negligible for propagation of 100 ps pulses, as shown in Figure 1 for gaussian pulses, but becomes quite significant as the pulse duration approaches 1 ns. For the case of such long signals, the relative peak electrostrictive contribution, expressed as a fraction of the fast Kerr response is

$$\eta = \Delta n_{\max}(str) / [n_2 I_0] = 0.19.$$

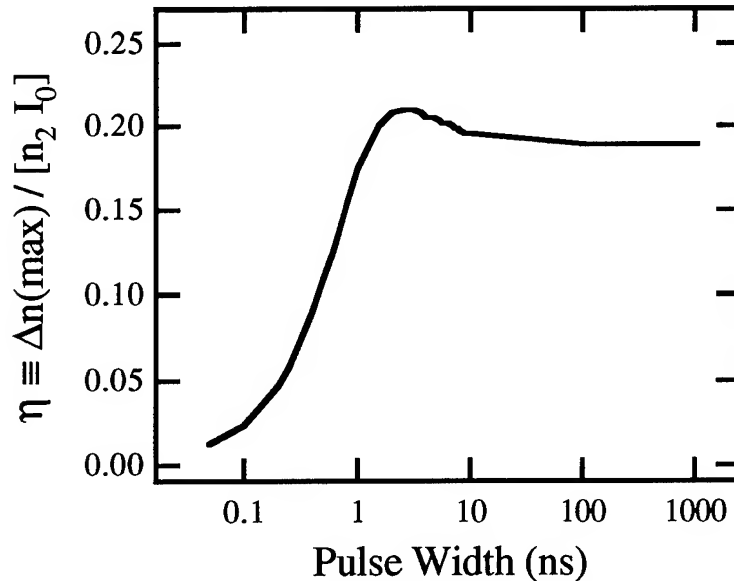


Figure 1. Magnitude of the peak electrostrictive nonlinearity Δn_{\max} relative to the fast non-resonant electronic contribution as a function of gaussian pulse width (FWHM), for a mode field radius $a = 4.5 \mu\text{m}$ and $n_2 = 2.96 \times 10^{-16} \text{ cm}^2/\text{W}$.

A new XPM measurement technique for measuring the nonlinear index, using an unpolarized, sinusoidally modulated pump, has recently been demonstrated². It is in these measurements that we notice an increased nonlinear response as compared to the modelocked pulse SPM measurements. Through consideration of the form of the electrostrictive nonlinearity in Eqn. 4, it can be shown that the strength of the time-varying part of the electrostrictive nonlinearity, in response to a harmonic signal, is proportional to the acoustic frequency response at the modulation frequency. Thus the measured nonlinear index will have a frequency dependence determined by the acoustic frequency response, as shown in Figure 2.

The 7 MHz modulation frequency of Ref. 2 is essentially cw. We can calculate the relative electrostrictive contribution to the nonlinear response in this experiment if we further recognize that (a), the electrostrictive response is polarization independent (radial acoustic modes dominate); (b), the appropriate weak-wave retardation factor for the electrostrictive response is unity; and (c), the polarization-corrected weak-wave retardation factor for the non-resonant electronic contribution to

the nonlinear response is 4/3. The relative electrostrictive contribution to the nonlinear refractive index in this experiment is then

$$\eta = \frac{4}{3} \left[\frac{n_2^{\parallel}(\text{reported})}{n_2^{\parallel}(\text{fast})} - 1 \right]. \quad (6)$$

The value of the linear-polarization intensity-dependent index reported from this experiment was $n_2^{\parallel}(\text{reported}) = 3.35 \times 10^{-16} \text{ cm}^2 / \text{W}$, while the typical value for similarly designed fibers⁵ is $n_2^{\parallel}(\text{fast}) = 2.96 \times 10^{-16} \text{ cm}^2 / \text{W}$. This indicates a relative electrostrictive contribution $\eta = 0.18$, or an electrostrictive nonlinear coefficient $n_2^{\text{str}} = \eta n_2^{\parallel}(\text{fast}) = 0.52 \times 10^{-16} \text{ cm}^2 / \text{W}$ for these germanium-doped silica optical fibers.

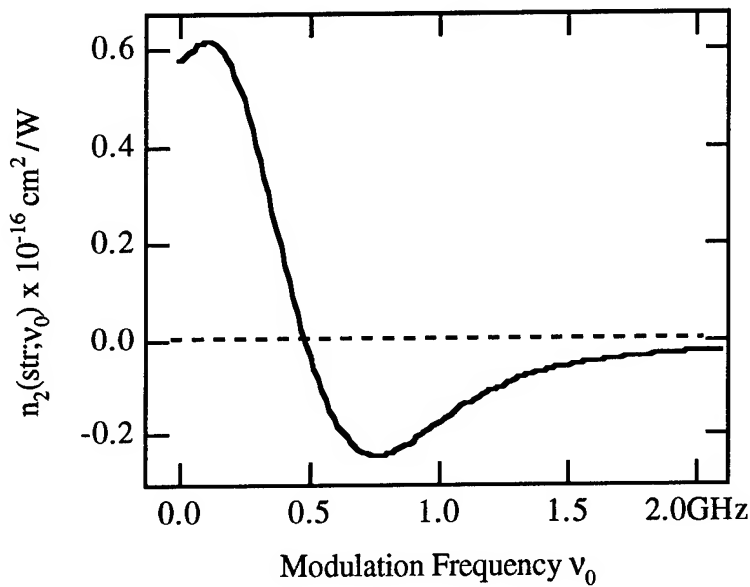


Figure 2. Time-varying part of the electrostrictive nonlinearity due to a harmonically modulated pump, for fibers with mode field radii $a = 3.0 \text{ } \mu\text{m}$.

REFERENCES:

1. E. Dianov, A. Luchnikov, A. Pilipetskii and A. Starodumov, *Opt. Lett.* **15**, 314 (1990).
2. T. Kato, Y. Suetsugu, M. Takagi, E. Sasaoka and M. Nishimura, *Opt. Lett.* **20** 988 (1995).
3. R. W. Boyd, *Nonlinear Optics* (Academic, San Diego, 1992).
4. D. Heiman, D. S. Hamilton and R.W. Hellwarth, *Phys. Rev. B* **19**, 6583 (1979).
5. K. Kim, R. Stolen, W. Reed and K. Quoi, *Opt. Lett.* **19**, 257 (1994).

Phase Mismatched Modulation Instability in Birefringent Fibres

S. G. Murdoch and J. D. Harvey
 Physics Department, University of Auckland
 Private Bag 92019
 Auckland
 New Zealand
 Ph +64-9-373-7599 Ext 8831
 Fax +64-9-373-7445

In the normal dispersion regime, two forms of modulation instability have been observed when birefringent single mode fibres are subjected to intense pump pulses. These instabilities are the cross phase or XPMI process [1,2] and the coherent or PMI process[3,4]. In both of these processes, the generated sidebands develop at the peak of the gain, which occurs corresponds to the phase matching condition between the pump and the sidebands corrected for the optical Kerr effect. In this work we report on the development of modulation instability in birefringent fibres, using fibre winding geometries in which phase mismatches are deliberately induced. The results are in accord with theoretical predictions.

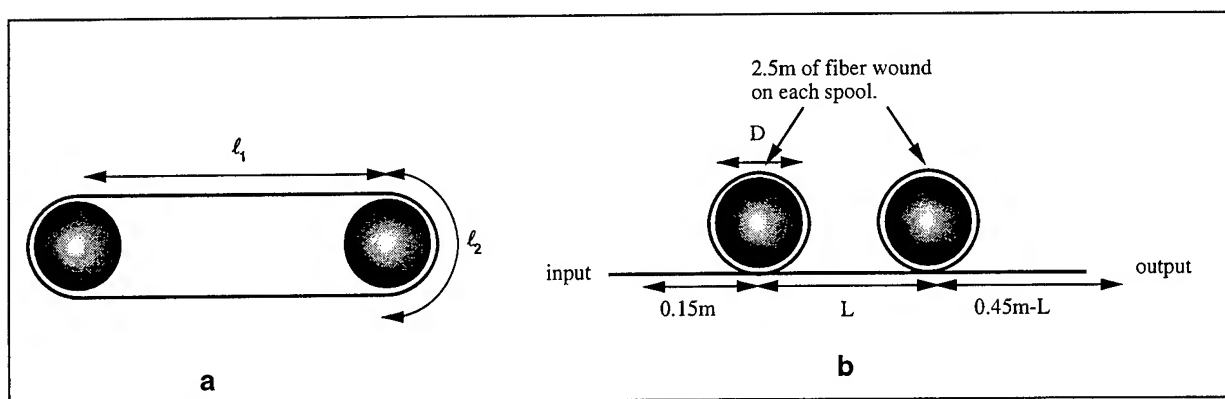


Figure 1 *Winding geometries*

In these experiments, the pump laser used was a mode locked cavity dumped Krypton ion laser, operating at 647nm, which can produce 60ps pulses with a peak power of in excess of 1kW at a repetition rate of 1.2MHz. The fibre used was standard low birefringence HeNe single mode fibre which was wound either in an oval configuration around two cylinders as shown in Figure 1a or with a straight section between the cylinders as shown in Figure 1b. The fibre thus has a weak induced birefringence in the semicircular (or circular) sections around the cylinders and no significant birefringence in the straight sections. The calculated PMI gain in each section is in very different frequency bands having no overlap, and yet Figure 2 shows the spectrum of the

light emerging from the end of a fibre wound as in Figure 1a, confirming the existence of PMI sidebands. This phenomenon can be explained by a "quasi phase matching" argument for the four wave mixing process involved, whereby the process is phase matched on average after traversing the straight and the curved sections. That is, it is assumed that the phase mismatch in the straight section is cancelled by the phase mismatch in the curved section. The calculated frequency of the sidebands is in accord with the data.

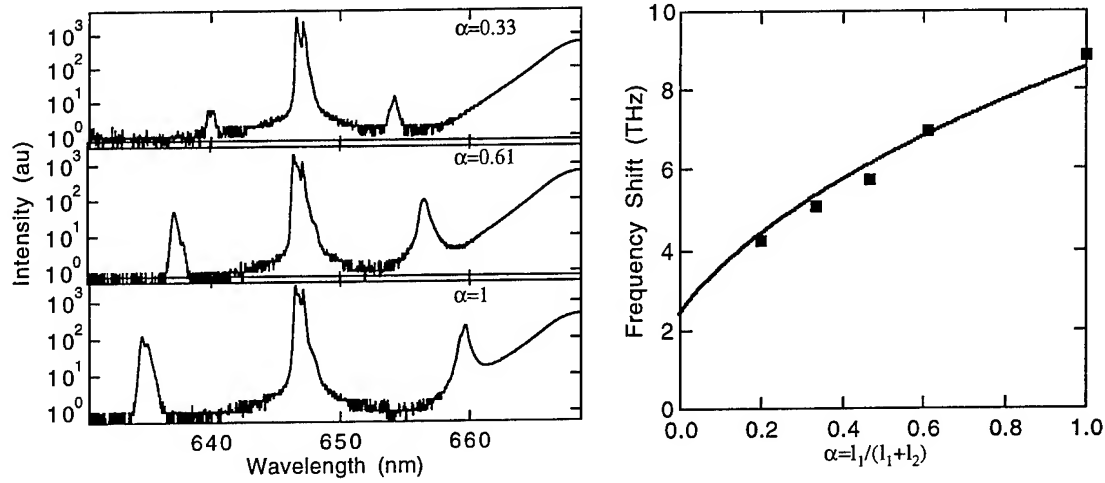


Figure 2 *Quasi Phase matched PMI*

For fibres wound as in Figure 1b, the section wound around the first cylinder generates PMI sidebands by the normal phasematched process, while the straight section between the cylinders generates a phase mismatch for the process. As has been shown for a general three wave mixing process[5], the gain depends sinusiodally on the phase of the process defined as:-

$$\phi(z) = \Delta kz + \phi_{\text{antistokes}}(z) + \phi_{\text{stokes}}(z) - 2\phi_{\text{pump}}(z)$$

where Δk , the wavevector mismatch is zero, and maximum gain corresponds to $\phi = \pi/2$ (this is the situation for the phasematched generation in the section around the first cylinder). The straight section generates a phase mismatch for the sidebands generated by the first cylinder, and so for the second cylinder, since the amplification is phase sensitive, power should flow from the pump to the sidebands, or from the sidebands back into the pump depending on the sign of $\sin(\phi)$.

Experimental results using the geometry of Figure 1b are shown in Figure 3. Low birefringence fiber (3M FSSN-3224) was wound onto two spools of diameter D which generated PMI

sidebands at frequency shift Ω_p with a short straight length L between them. The straight length generated a phase change of $(\beta_2 \Omega_p^2 - (2/3)RP)L$, and so depending on the phase change, the sidebands should either experience amplification or deamplification in the second spool. Figure 3a shows a plot of sideband power as a function of the length of the straight section L . The diameter of the spools was 2.5cm and the input power was 540W on the slow axis of the fiber. As expected an oscillation in sideband power is seen, and maximum sideband power occurs at $L=0$. The period of oscillation is 11.3cm. Changing the diameter of the spools D should alter the period of oscillation, and with $D=1.6$ cm, the observed period of oscillation here was 4.1cm (Figure 3b). Both of these results are in good agreement with the expected values calculated from the measured frequency of the shift.

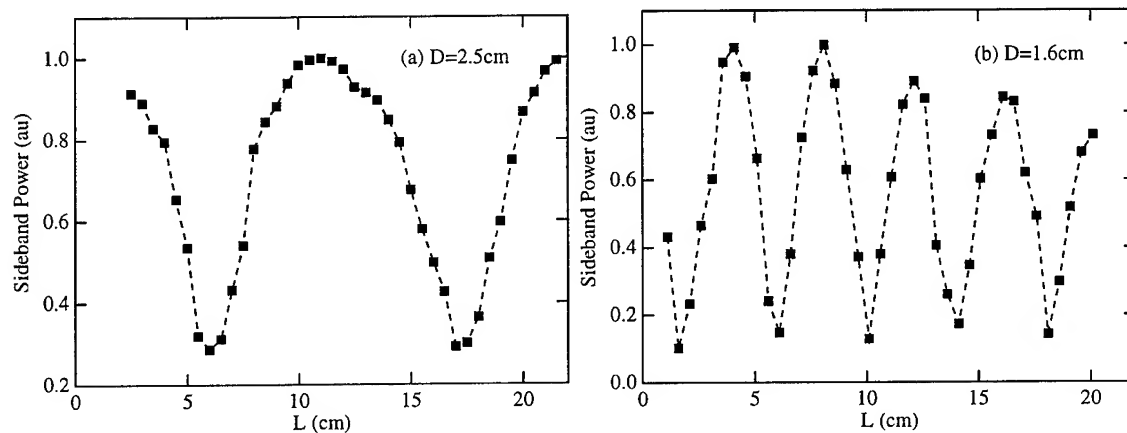


Figure 3 Sideband power as a function of length between spools for the geometry of Figure 1b

References.

1. P.Drummond, T.A.B.Kennedy, J.M.Dudley, R.Leonhardt, J.D.Harvey, Opt. Commun **78**, 137 (1990)
2. J.E.Rothenburg, Phys. Rev. A **42**, 682 (1990)
3. S.Wabnitz, Phys. Rev. A **38**, 2018 (1988)
4. S.G.Murdoch, R.Leonhardt and J.D.Harvey, Opt. Lett. **20**, 866 (1995)
5. G. Capellini and S.Trillo, J. Opt. Soc. Am. B **8** 824 (1991).

Nonlinear Liquid Crystal Optical Fiber Array

I. C. Khoo, M. Lee, K. Wang , M. Wood and B. D. Guenther

Department of Electrical Engineering
Pennsylvania State University
University Park, PA 16802
USA

Contact: I. C. Khoo
Tel:- 814-863-2299
Fax:- 814-865-7065
e-Mail: ick@ecl.psu.edu

Liquid crystals [LCs] in their various ordered and disordered phases have been shown to possess large optical and electro-optical nonlinearities over wide temporal [cw to picosecond] and spectral [visible to infrared] ranges [1]. Because of their unique physical properties, various novel liquid crystalline structures, such as thin films or pixels with, slab waveguides, LC cored fibers and fiber arrays, could be constructed that will provide superior performance in specific optical switching, imaging and processing applications. In particular, we have previously reported observation of low-threshold stimulated backscattering and optical limiting effects in an isotropic liquid crystal [ILC] cored fibers of centimeters in length [2].

In this paper, we present the results of a series of recent studies of a variety of isotropic liquid crystalline materials [single constituents, mixtures; doped or undoped] as fiber core material. These materials all exhibit unusually high optical nonlinearities that enable many of the previously observed nonlinear guided wave optical propagation to occur with very low threshold, and more importantly, in much shorter fiber length of a few mm. Consequently, compact fiber arrays of very high quality image transmission capability can be fabricated. The array function as very efficient sensor protection device against high power laser pulses.

Several nonlinear optical processes could occur when a laser pulse is incident on the liquid crystal array. In undoped LC fiber [2], the primary nonlinear optical processes are nonlinear absorption and subsequent temperature and density changes [2], nonlinear scattering, guided mode extinction within the fiber core; self-defocusing and bubble formation within the focused laser's confocal region at the entrance and exit planes could also contribute. These processes all act to limit the transmission above some intensity/fluence levels. In doped-LC cored fiber, the photo-absorption and the non-radiative inter- and intramolecular relaxations leading to temperature and density fluctuations will occur with even better efficiency. especially if the dopants themselves [such as Fullerene C₆₀] also exhibit nonlinear absorption [absorption increases with laser intensity] characteristics [3].

Figure 1 shows the measured output versus input energies curve of fibers with various LC core materials. ILC is a commercially available isotropic liquid crystal mixture [1, 2], whereas CCH -301, LC-X [4-4'bis(Heptyloxy)azoxybenzene] and LC-Y [a alkyl-tolane] are single constituent liquid crystals. The fiber length is 5 mm, with a core diameter of 30 μm . The pulsed laser used is the second harmonic [wavelength=0.53 μm] of a Nd: Yag laser, with a FWHM of 20 ns. The experimental set up used is similar to the one described in reference 2. These studies show that LC-Y or the C₆₀-doped ILC core material give the lowest optical limiting threshold [$<1 \mu\text{J}$] and clamped output level [$\sim 1 \mu\text{J}$]

The LC fiber array is made by filling the hollow cores of a glass capillary array (refractive index = 1.53) with an isotropic liquid crystal mixture (refractive index of 1.54) doped with 0.02% by weight of C-60. Figure 2 shows the image transmission

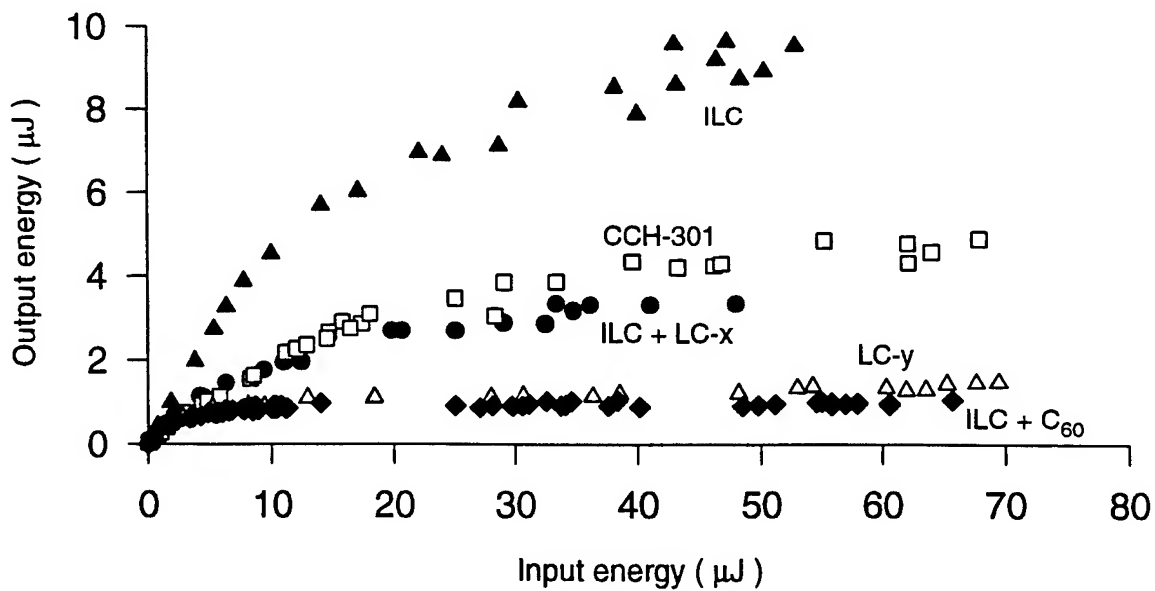


Fig. 1. Nanosecond laser pulse limiting for various liquid crystal fiber core materials.

capability of such array, when it is placed between two imaging lens. Because of the high transparency and short fiber array length [3mm -7mm range] very good quality color images can be transmitted through the array.

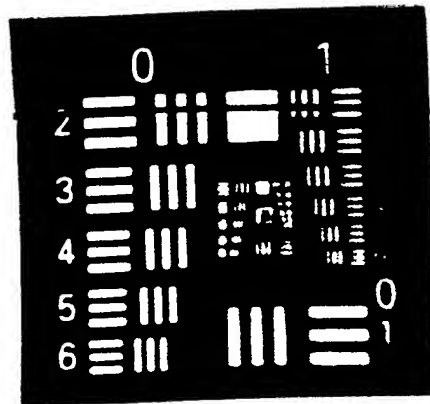


Fig. 2. Photograph of the resolution chart transmitted by the LC fiber array.

On the other hand, the high nonlinearity of the fiber array core material will limit the transmission of high energy laser pulses. Figure 3 shows a typical limiting performance of a 7.5 mm thick LC fiber array [core diameter= 25 μm].

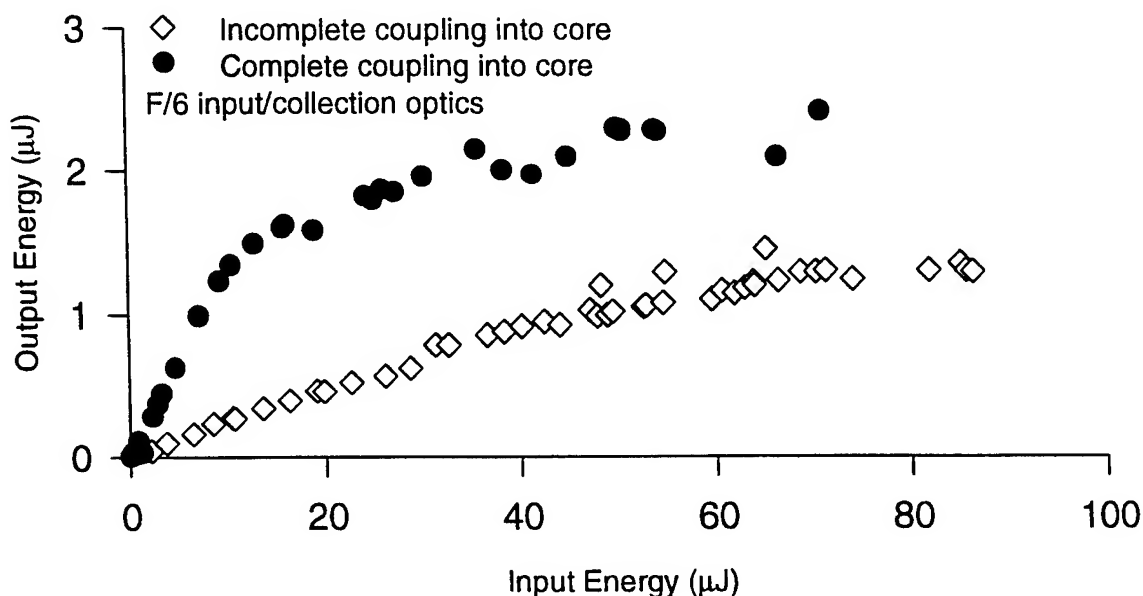


Fig. 3. Optical limiting action of the liquid crystalline fiber array

At very low input laser energy, the transmission begins to decrease from its initial value of around 60 %. The deviation from linear transmission becomes quite pronounced above an input laser energy of $\sim 1-2 \mu\text{J}$ [fluence of $\sim 0.15-0.3 \text{ J}/\text{cm}^2$ for a $30 \mu\text{m}$ core-diameter]. The output energy remains clamped at around $1-2 \mu\text{J}$ for input energies above $10 \mu\text{J}$ and beyond. With the use of optimized fiber arrays dimension and core dopant concentration, we expect at least an order of magnitude improvement in these limiting parameters. Experimental results for LC fiber arrays parameters and core materials along with a theoretical modeling of the fundamental nonlinear optical processes involved in the laser-material interactions and nonlinear waveguiding, will be presented at the meeting.

References

1. I. C. Khoo in "Liquid Crystals: Physical Properties and Nonlinear Optical Phenomena," [Wiley Interscience, NY 1994].
2. I. C. Khoo and H. Li, J. Appl. Phys. **B59**, 573 (1994); I. C. Khoo, H. Li, P. G. LoPresti and Y. Liang, Optics Letts. **19**, 530 (1994).
3. D. G. McLean, R. L. Sutherland, M. C. Brant, D. M. Brandelik, P. A. Fleitz and T. Pottenger, Optics Letters, **18**, 858 (1993). See also B. L. Justus, Z. H. Kafafi and A. L. Huston, Optics Letts. **18**, 1603 (1993).

Theory of Stretched Pulse Laser

S. Namiki, W. S. Wong, and H. A. Haus

Department of Electrical Engineering and Computer Science

and the Research Laboratory of Electronics

Massachusetts Institute of Technology

77 Massachusetts Avenue, 36-355, Cambridge, MA 02139, USA

Tel:+1-617-253-5481

Fax:+1-617-253-9611

(S. Namiki is also with Furukawa Electric Co.,Ltd., Tokyo, Japan)

Modelocked Erbium doped fiber ring lasers have been developed in many laboratories and commercial models are already available. The most common type is based on the soliton concept, a soliton-like pulse circulates around the ring. Modelocking is provided by a saturable absorber (e.g. quantum well)[1] or by Polarization-Additive-Pulse-Mode-locking(P-APM)[2]. Solitons can be driven unstable by periodic disturbance of gain and loss. For this reason, soliton fiber ring lasers tend to generate low average power.

The stretched pulse laser avoids soliton operation. The ring consists of fiber segments of positive and negative group velocity dispersion (GVD), the former being the gain segment, the latter a passive fiber segment. The pulse alternately expands and contracts, reaching minimum width twice in one roundtrip. The nonlinear action of the fiber is thereby greatly reduced compared with the soliton operation. The average power can be increased by more than an order of magnitude compared with a soliton fiber ring laser.

The experimental setup is shown in Fig. 1. The Erbium doped fiber is pumped by a master oscillator/power amplifier(MOPA) diode lasing at 980nm. The pumping is via a WDM coupler in the fiber ring. An isolator enforces unidirectional operation, waveplates adjust

the elliptic polarization to satisfy the conditions for P-APM. The polarization beam splitter in the cavity generates the P-APM which favors passage of higher intensities. The output of the laser is from the polarization beam splitter. A silicon prism pair provides group velocity dispersion. The performance of this kind of laser has already been reported [3,4]. Fig. 2 shows a typical spectrum of the output and autocorrelation traces of before and after the prism compression. An analytic theory of the stretched pulse laser has been published[5]. It predicts that pulse shapes are Gaussian over most of the temporal pulse profile, which has been confirmed by experiments[6].

In this paper, we develop a perturbation theory based on the analytic theory. We expand perturbations of the pulse in terms of the 3 lowest order Hermite Gaussians, from which six equations of motion are obtained. The six perturbations are amplitude, phase, timing, frequency, pulse width, and chirping. We also compare the results with computer simulations. It is expected that the pulse shifts the position of its minimum width with increasing pulse energy so as to avoid excessive nonlinearity. The analytic theory cannot predict this behavior, but computer simulations do. Similarly, computer simulation can predict the position of the output coupler for optimum energy and pulse-shape. Eventually, overdriving of the stretched pulse laser results in deterioration of the spectrum, the causes of which have not been identified at this time, but we hope, will be explained at the time of the conference.

It should be mentioned that the timing jitter of the stretched pulse laser can be made smaller than that of the soliton ring laser. Timing jitter in the soliton laser is caused by frequency fluctuations that are translated into timing fluctuations by GVD. The net dispersion in the stretched pulse laser can be made zero, thus eliminating this source of timing jitter. We have confirmed that the timing jitter of 4 PPM for the measurement time of 0.1 second is caused by spontaneous emission only, i.e. that it is quantum limited[4].

References

- [1] B.C. Barnett et al, Opt. Lett. **20**, 471-473(1995)
- [2] K. Tamura et al, Electron. Lett., **28**, 2226-2227(1992)
- [3] G. Lenz et al, Opt. Lett. **20**, 1289-1291(1995)
- [4] C.X. Yu et al, CLEO '96, OSA
- [5] H.A. Haus et al, IEEE J. of Quantum Electron., **31**, 591-598(1995)
- [6] K. Tamura et al, Appl. Phys. Lett., **64**, 149-151(1994)

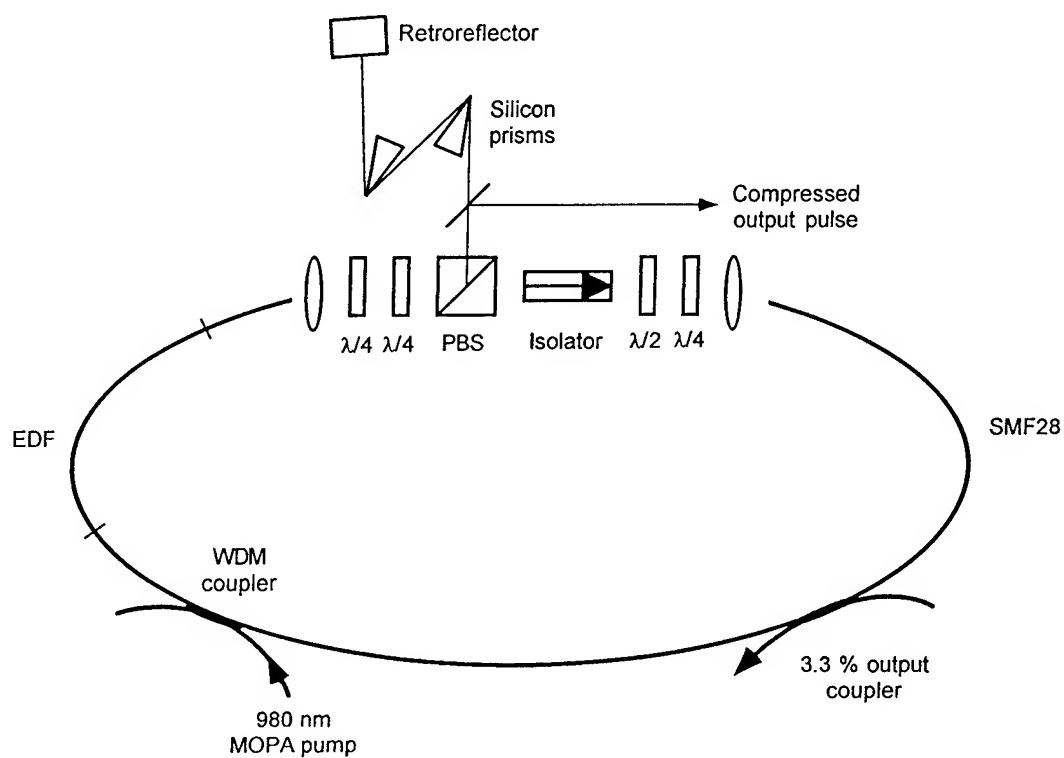


Fig. 1: Scheme of the stretched pulse laser. The cavity length is 5.7m corresponding to 36MHz repetition rate.

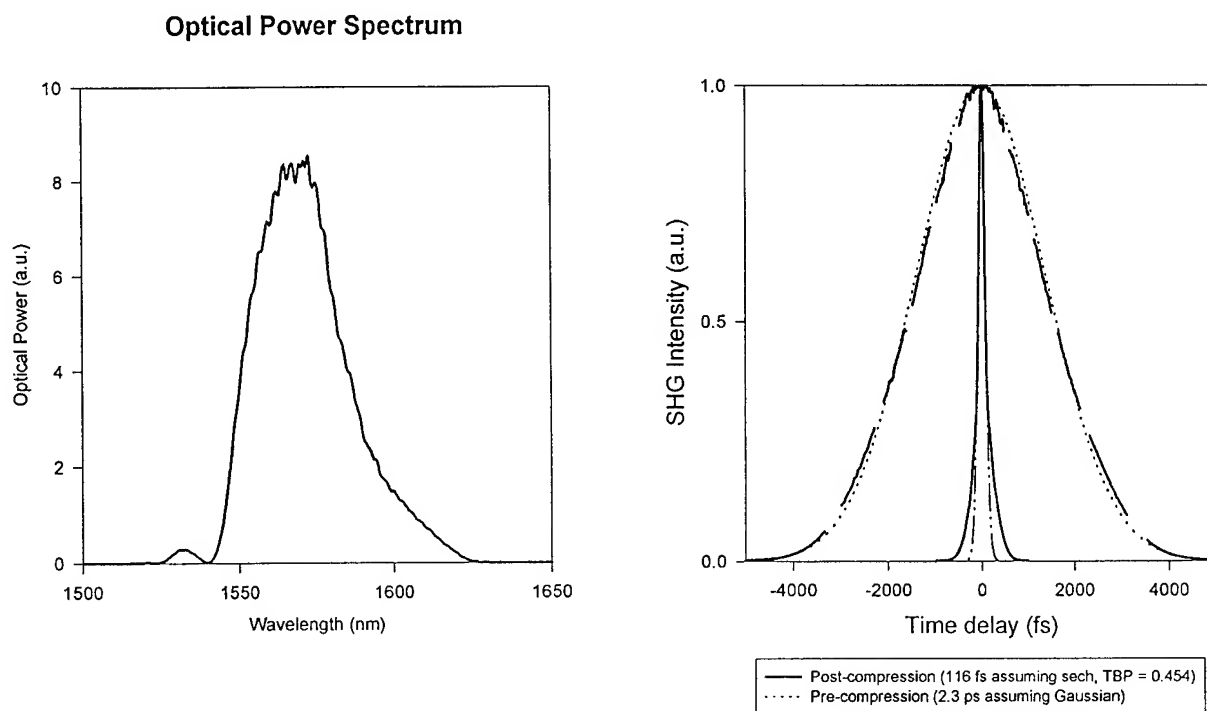


Fig. 2: Spectrum and autocorrelation trace of the output of the stretched pulse laser.

Thursday, July 11, 1996

Nonlinear Optics of Thin Films

NThD 8:00 pm-9:00 pm
Maile Room

Daniel Chemla, *Presider*
Lawrence Berkeley Laboratory

Phase-mismatched degenerate four-wave-mixing: measurement of the complex third-order nonlinear optical susceptibility in thin films

F. P. Strohkendl and L. R. Dalton

Department of Chemistry

University of Southern California, CA 90089-1062

Tel: (213) 740 4388, Fax: (213) 740 6653, e-mail : Strohken@mizar.usc.edu

R. W. Hellwarth

Department of Electrical Engineering

University of Southern California, CA 90089-0484

In degenerate four-wave mixing (DFWM), three beams of the same frequency ω overlap in a medium to generate a fourth, or more,¹ new beams, also of frequency ω . At low beam intensities, the power in each newly generated beam is proportional to the product of the powers of the three incident intensities, and the constant of proportionality has as a factor the absolute square of an element of a third-order susceptibility tensor, $\chi^{(3)}(-\omega, \omega, \omega, -\omega)$. As the beam frequency ω is increased to where it approaches or exceeds either (1) the lowest "one-photon" resonance frequency of the medium, or (2) half of the lowest "two-photon" resonance frequency of the medium, $\chi^{(3)}$ passes from being a positive real number to a complex number that varies in a complicated way with frequency ω . Knowledge of the phase of $\chi^{(3)}$, as well as of its magnitude, is relevant for the understanding of the electronic structure of materials as well as for the estimation of their device potential. We obtain this knowledge for a C₆₀ film by interference of its generated beam with that from the CaF₂ substrate.

In our method we employ the so-called forward-four-wave-mixing geometry where three "write" beams, 1, 2 and 3, propagate nearly along the z-direction and intersect at a small angle θ inside the sample, which consists of a thin film on a thick substrate. Fig. 1 shows the experimental geometry. The three write beams are arranged such that their points of intersection with a transverse "observation plane" define three corners of a square. The fourth corner of this square indicates the location of the phase-matched signal beam, 4, which emerges from the sample. DFWM experiments measure typically the strength of this phase-matched signal beam. The points of intersection of beams 1 through 4 with the observation plane define a "unit cell" as well as four "lattice points" of an extended lattice. Each point of this lattice indicates the location of a signal

beam generated inside the sample due to the nonlinear interaction of the three incident beams. Beams 4 through 12 are all generated by third order nonlinear interaction (possible contributions from higher order nonlinearities are assumed to be negligible).

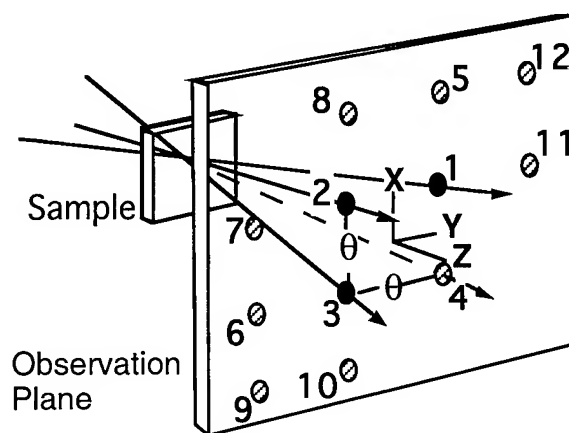


Figure 1. Degenerate four-wave-mixing beam geometry with phase-matched signal beam 4 and phase-mismatched signal beams 5 through 12.

In the following we deal only with signal beams 4, 5, and 6. The powers of these signal beams are all proportional to the product of the powers of beams 1, 2, and 3 and involve the same geometrical beam overlap. Their relative strengths are, therefore, directly comparable. Only beam 4 is strictly phase-matched and results from a coherent superposition of substrate and thin film signals. The nature of this superposition depends on the phase difference, ϕ , between the $\chi^{(3)}$ values of substrate and thin film and can vary continuously from constructive to destructive depending on the value of ϕ . The $\chi^{(3)}$ of the thin film can therefore not be determined from signal beam 4 alone, even if the signal strength from the pure substrate is known. Beams 5 and 6 occur in phase-mismatched directions. For sufficiently thick substrate and sufficiently thin film we find that the signal contributions from the substrate in the mismatched directions is negligible whereas the thin film signal is unattenuated. E. g., we find for a thin film sample, which consists of a polycrystalline 10 μm thick C_{60} film on a 1 mm thick CaF_2 substrate, with an external beam intersection angle, θ , of 2.8° that the substrate signal is attenuated by a factor 10^2 whereas the thin film signal is reduced by less than 0.1 percent.

As an example, Fig. 2 shows signals observed in the mentioned C_{60} sample. All beam polarizations are parallel. All signals can, therefore, be described in terms of χ_{1111} tensor components. We use 110 fs pulses at 768 nm and observe the signals 3, 4, and 5 as a function of the delay of one of the input beams. The phase-mismatched signals 4 and

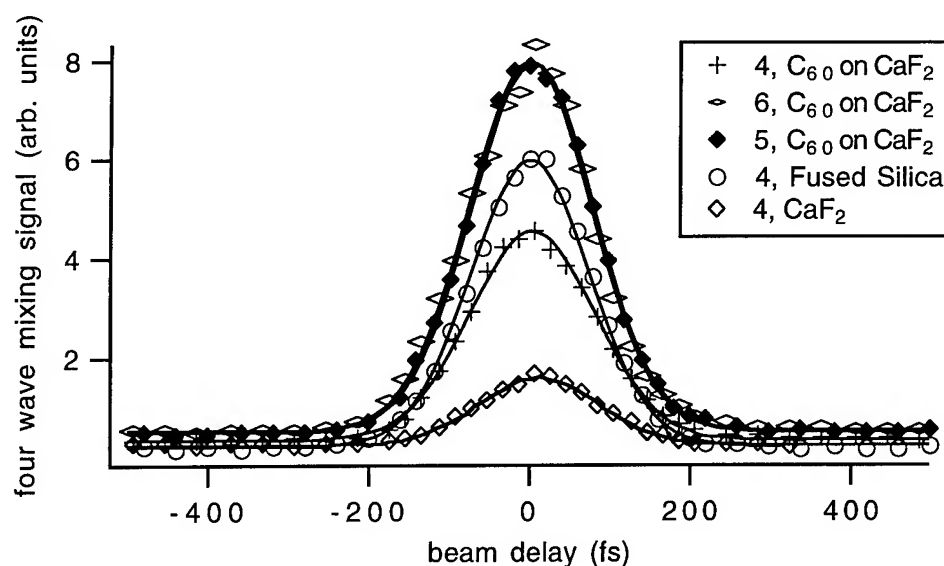


Figure 2. Various DFWM signals which were used to determine amplitude and phase of $\chi_{1111}(-\omega, \omega, \omega, -\omega)$ for a 10 μm thick C_{60} film.

5 have the same amplitude as expected in this polarization geometry. The amplitude of the phase-matched signal 4 is smaller than the amplitude of the phase-mismatched beams 5 and 6, i. e. it clearly exhibits some degree of destructive interference. The signal in beam 4 for the substrate alone is also shown. The corresponding signal from a 1 mm thick plate of fused silica is shown as a reference. From these signals, taking losses due to Fresnel reflections into account, we determine for the phase-angle difference between thin film and substrate $|\phi| = (142 \pm 5)^\circ$ and for the substrate-free thin-film nonlinearity a value of $|\chi_{1111}| = (1.42 \pm 0.03) \times 10^{-12}$ esu relative to that of fused silica ($\chi_{1111} = 4.0 \times 10^{-15}$ esu).

This work was supported by the National Science Foundation under grant number DMR-9528021 and by the Air Force Office of Scientific Research..

Reference

1. Xianmin Zhang, Xianfeng Ye, Kangshen Chen, Optics Commun. **113**, 519 (1995).

Measuring Weak Laser Pulses Using Frequency-Resolved Optical Gating

David N. Fittinghoff, Marco A. Krumbügel, John N. Sweetser, Rick Trebino
Sandia National Laboratories, MS-9051, Livermore, CA 94551-0969
 Tel: (510) 294-3690; Fax: (510) 294-2276
 email: dnfitti@sandia.gov

and

Thomas Tsang
 Brookhaven National Laboratory, Upton, NY 11973
 Tel: (516) 282-2225

Introduction

Frequency-Resolved Optical Gating [1] (FROG) measurements based on polarization gating [2] (PG FROG), self diffraction [3] (SD FROG), and second-harmonic generation [4] (SHG FROG) have been used successfully to measure ultrashort laser pulses with spatially uniform temporal pulse shape and phase with durations from 9 fs to 2 ps and with wavelengths from the ultraviolet to the near infrared. Temporal Analysis by Dispersing a Pair of Light E-fields [5] (TADPOLE), a combination of FROG and spectral interferometry, has been used to measure pulse trains with average pulse energies of 42 zeptojoules (42×10^{-21} J). None of these techniques, however, has proved capable of measuring the pulses from a Ti:sapphire laser without a temporal ambiguity or an amplified reference pulse. The difficulty lies in the fact that the pulses from such oscillators are too weak for PG or SD FROG, and SHG FROG has a time-reversal ambiguity due to the symmetry of the second-harmonic signal in time. TADPOLE, while capable of measuring extremely weak pulses, uses FROG to measure a reference pulse and thus has the same restrictions. Here we use surface third-harmonic generation (THG) to make an unambiguous measurement of the intensity and phase of pulses from a Ti:sapphire oscillator. In addition, we describe a new method for using TADPOLE for measuring ultrashort laser pulse fields that vary arbitrarily in time *and in space*.

THG FROG

THG is a third-order process with a signal field

$$E_{\text{THG}}(t, \tau) \propto E^2(t)E(t - \tau), \quad (1)$$

where $E(t)$ is the field of the pulse as a function of time. Thus FROG based on THG (THG FROG) does *not* have a time-reversal ambiguity. Although THG is dipole-allowed, the short coherence length of THG in a bulk material, however, results in low THG photon yield when using a femtosecond Ti:sapphire oscillator. In addition, the dispersion of the nonlinear material often distorts the measured FROG trace. Third-harmonic generation is enhanced at an interface[6], so we use surface THG to overcome these problems.

We measured the pulses from a self-mode locked Ti:sapphire laser that has an average output power of 300 mW, pulse durations on the order of 100 fs, and a repetition rate of 100 MHz. The center wavelength was 780 nm. The experimental arrangement is the same as for a multi-shot SHG FROG, where we use a standard background-free autocorrelation configuration. A 20x microscope objective focused the beams on the surface of a dielectric medium. The source of the THG is highly localized at the air-dielectric interface and disappears completely when the interface is traversed away from the beam focus. We note that this surface THG technique allows one to use dielectric materials (linear or nonlinear) that can be opaque to the harmonic by focusing the fundamental beams at the back surface of the material. In this experiment, we generated two THG signal beams at the back surface of a 160 μm thick cover glass. We then recollimated one of the two THG signal beams and measured its spectrum using a spectrometer equipped with a

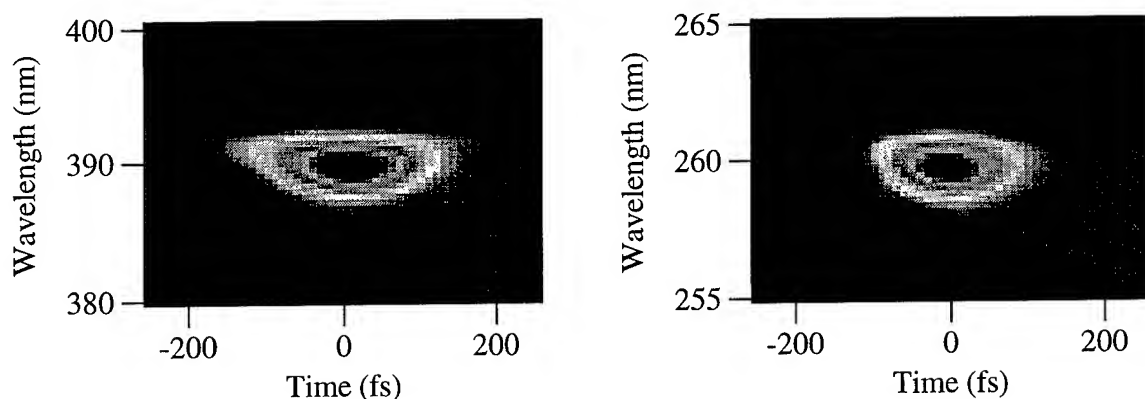


Figure 1 a) Experimental SHG FROG trace of pulse, and b) experimental THG FROG trace of pulses directly from a Ti:sapphire oscillator.

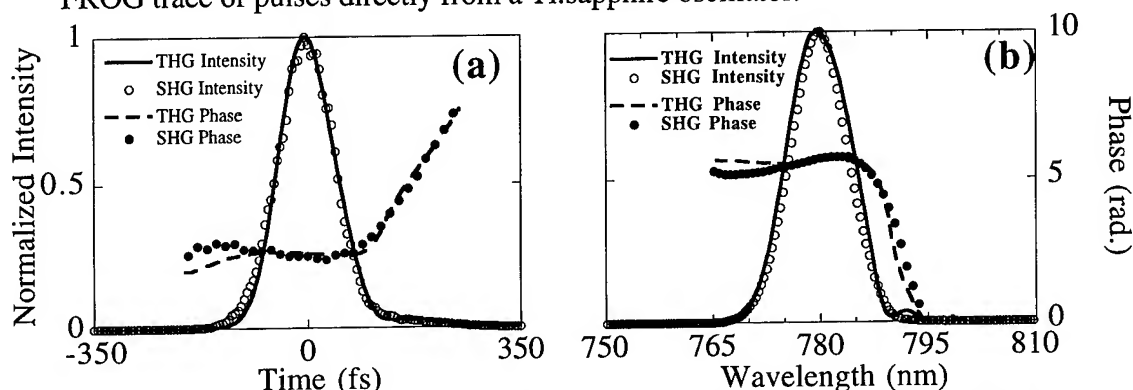


Figure 2 Comparison of the Ti:sapphire pulse intensity and phase retrieved from the SHG and THG FROG traces in the a) time domain and b) frequency domain. The agreement is quite good.

linear diode array detector. We generated the THG FROG traces by measuring the spectrum of the signal beam as a function of time delay. The delay stepsize was 10 fs. We also generated the corresponding SHG FROG trace for comparison.

Fig. 1 shows the measured SHG and THG FROG traces. The symmetry of the SHG trace in time shows the time-reversal ambiguity of SHG FROG. The THG trace, however, is asymmetric and shows the absence of a time-reversal ambiguity. Figure 2 shows the intensity and phase retrieved by the iterative FROG algorithm in both the time and frequency domains. The agreement between the two techniques is quite good and shows that THG FROG accurately measures the pulse.

The simplicity of the surface THG technique combined with its lack of a time-reversal ambiguity and minimal wavelength restriction will be useful for measuring pulses over a wide range of wavelengths. In particular, it may be useful for pulse widths below 10 fs where phase matching bandwidth and material dispersion are critical issues.

Spatial TADPOLE

Now consider the problem of measuring the intensity and phase as a function of *position* as well as time. The TADPOLE technique involves combining at a beam splitter an unknown pulse and a reference pulse characterized by Frequency-Resolved Optical Gating (FROG) and performing spectral interferometry. The measured spectrum of two pulses is:

$$I_{TAD}(\omega) = I_{ref}(\omega) + I_{unk}(\omega) + 2\sqrt{I_{ref}(\omega)I_{unk}(\omega)}\cos[\phi_{unk}(\omega) - \phi_{ref}(\omega) - \omega\tau]$$

where $I_{ref}(\omega)$, $\phi_{ref}(\omega)$, $I_{unk}(\omega)$, and $\phi_{unk}(\omega)$ are the spectra and phases of the reference and unknown pulses, respectively, and τ is the delay between the two pulses. The delay is chosen to yield fringes in the sum spectrum. The individual pulse spectra are measured by blocking one beam and measuring the spectrum of the other and vice versa. $\phi_{unk}(\omega)$ and τ are extracted using a well-known fringe inversion technique.

Because TADPOLE requires measuring only a single spectrum, it uses only one row of pixels in a camera; the remaining rows can then be used to measure $E(t)$ for other slices of the beam. Making a measurement to temporally characterize a pulse along a spatial dimension thus involves simultaneously performing many TADPOLE measurements using an imaging spectrograph.

After splitting the unknown pulse in two (Fig. 3), we spatially filter one pulse to obtain spatially uniform phase fronts and characterize it using FROG. This yields $E(x,y,t)$ for the filtered pulse since there is essentially no variation of E on x or y . We then use TADPOLE at each point along the entrance slit of an imaging spectrograph to characterize the temporal behavior of the pulse at each point of the beam spanned by the slit, yielding $E(x,t)$ for the unknown pulse. By scanning the measurement line in the other two dimensions, the temporal behavior of the pulse field could be mapped in all three spatial dimensions on a multishot basis. Fig. 4 gives examples of measured pulses. We measured the TADPOLE spectrum as a function of position in the beam with and without a slide in one half of the beam. The slide delays the part of the beam that passes through it because of the higher index of refraction of the slide. This delay appears as a phase or time delay of that half of the beam relative to the half of the beam that does not pass through the slide. The image without the slide shows the uniformity of the original pulse in space. In the image with the slide, the slide is delaying the pulse for positions higher than 0.4 cm. Thus, while the left half of the image is the same as that for the beam without the slide, the right half of the image shows much broader fringes than without the slide. This shows that that part of the pulse has been delayed closer to the reference pulse. In addition, some narrow fringes are still visible due to diffraction of the beam from the edge of the slide.

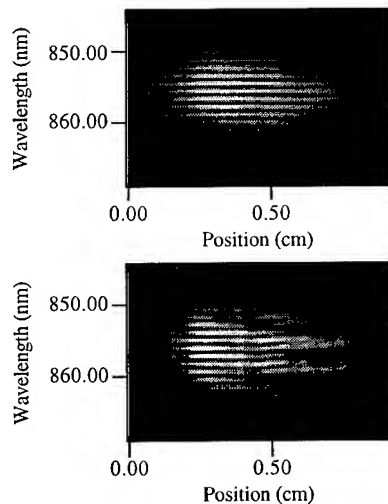


Fig. 4. Spatial TADPOLE measurements of a spatially uniform pulse (top) and of a pulse that is distorted by a glass slide inserted halfway into the beam (bottom). The change in fringe spacing indicates the delay in the half of the pulse that propagates through glass.

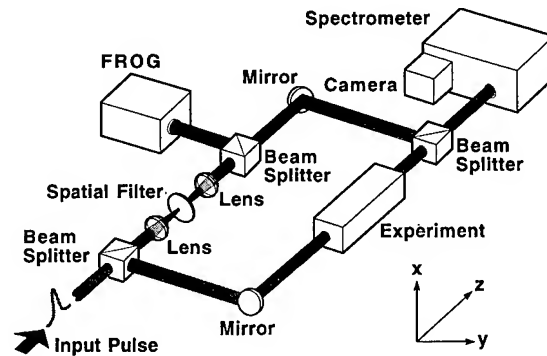


Fig. 3. Experimental setup.

References:

- [1] R. Trebino and D. J. Kane, J. Opt. Soc. Am. A **10** p. 1101-1111 (1993).
- [2] D. J. Kane and R. Trebino, Opt. Lett. **18** p. 823-825 (1993).
- [3] D. J. Kane and R. Trebino, IEEE J. Quantum Electron. **29** p. 571-579 (1993).
- [4] K. W. DeLong, R. Trebino, J. R. Hunter, and W. E. White, J. Opt. Soc. Am. B **11** p. 2206-2215 (1994).
- [5] D. N. Fittinghoff, J. L. Bowie, J. N. Sweetser, R. T. Jennings, M. A. Krumbügel, K. W. DeLong, R. Trebino, and I. A. Walmsley, Opt. Lett. (Submitted).
- [6] T. Tsang, Phys. Rev. A **52** p. 4116 (1995).

Ultrashort Pulse Second-Order Frequency Resolved Optical Gating with Thin Poled Nonlinear Polymers

G. Taft, M. M. Murnane, H. C. Kapteyn

Department of Physics, Washington State University, Pullman, WA 99164-2814

(509) 335-9531, (509) 335-7816 fax

D.R. Yankelevich and A. Knoesen

Department of Electrical and Computer Engineering, University of California, Davis, CA 95616

(916) 752-8023, (916) 752-8428 fax

R. J. Twieg

IBM Research Division, Almaden Research Center, 650 Harry Road, San Jose, CA 95120-6099

(408) 927-1630, (408) 927-3310 fax

Frequency Resolved Optical Gating (FROG) [1] is a newly-developed technique for determining both the amplitude and phase of an ultrashort pulse.[2] Although there are several variations of the FROG technique which use different nonlinear processes, second harmonic generation (SHG) FROG is particularly well suited for measuring un-amplified nJ pulses directly from a modelocked Ti:sapphire oscillator, since SHG produces a much larger signal than the higher order nonlinear processes. In order for SHG FROG to accurately characterize ultrashort pulses, care must be taken to insure the second harmonic signal is not distorted by the nonlinear material. In phase-matched frequency doubling crystals for example, the group velocity mismatch (GVM) can cause severe distortion of the generated pulses over long interaction lengths. Since this finite phase matching bandwidth becomes less of a problem as the crystal thickness is reduced, the thinnest possible crystals ($\approx 50 \mu\text{m}$) are generally used for ultrashort-pulse measurement applications.[3] However, even using such short crystals, the crystal has to be optimally oriented to achieve proper phasematching for a given center frequency. Furthermore, fabricating such phase-matched, polished, ultra-thin crystals is extremely difficult. Thus, an ideal SHG material for short pulse diagnostics is one that can generate an adequate signal intensity while being thin enough to avoid pulse broadening and precise angle tuning.

Such a material is a nonlinear poled polymer film. Recent work with nonlinear poled polymeric films has shown them to be excellent SHG materials for ultrashort pulses. Previously, such films have been used to perform ultrashort pulse autocorrelations [4, 5] and to frequency double 15 fs pulses from an amplified R6G CPM femtosecond dye laser ($\lambda = 625 \text{ nm}$) at peak intensities exceeding 100 GW/cm^2 . [6] In this paper, we report SHG FROG measurements of ultrashort pulses from a Ti:sapphire oscillator using a tricyanovinylaniline (PhTCV) nonlinear poled polymer.

Nonlinear chromophores suitable for ultrashort pulse (USP) SHG applications in poled polymer thin films must possess a number of properties. The material must be sufficiently transparent at both fundamental and second harmonic wavelengths. The chromophore should possess as large a first hyperpolarizability as possible and must be photochemically stable. Photochemical stability is an essential requirement especially in ultrashort pulse applications where the material will be subjected to large peak intensities. We have evaluated a number of nonlinear chromophores based on the suitability of the absorption spectra of a nonlinear chromophore for Ti:sapphire applications. Several were found to be unsuitable for USP applications. The dye julodine/2-thio-pyrimidine trione (X-523) [7, 8, 9] was unstable to room light exposure. Foron Blue [10] decayed during USP SHG due to photochemical changes. Analogs of Foron Brilliant Blue have been recently evaluated for electro-optical applications.[11] We found that the tricyanovinylanilines (TCVs) exhibited the requisite characteristics for Ti:sapphire USP SHG pulse diagnostics. TCVs have been studied as NLO chromophores for some time.[12, 13, 14] The ground state dipole moments and microscopic nonlinearities of TCV's are substantially larger than those of the well known nitroaniline compounds.[13] The tricyanovinyl group is more conjugated and a stronger electron withdrawing group than the nitro group and, as a result, the PhTCV charge transfer (CT) band is red shifted more than 100 nm relative to the nitroaniline. This shift of the CT-band gives rise to a transparency "window" in the 400 nm region. However, the remarkable photochemical stability that some of these PhTCV chromophores possess was not appreciated until our work.

The chromophore N,N-diphenyl-4-tricyanovinylaniline was prepared by the general method of McKusick involving reaction of triphenylamine with tetracyanoethylene in dimethylformamide at 80

^oC.[15] A 5 % by wt. solution of PhTCV in PMMA dissolved on cyclohexanone was spin cast at 1200 rpm on 50 x 25 x 0.7 mm glass substrates. The residual solvent was removed after baking the films for 60 min. at 60 ^oC under vacuum. The films used in the USP-SHG diagnostics were approximately 0.4 μ m thick. The films were corona poled [16] for 15 min. at 100 ^oC. The refractive index and extinction coefficient of a PhTCV/PMMA film are shown in Figure 1. The Figure shows the low absorption at the fundamental (800 nm) and SH wavelengths of the Ti:sapphire laser. Photodegradation effects in the PhTCV/PMMA were not observed following several hours exposure times. The SH signal level remained constant at a fundamental wavelength peak intensity of $I_p=8$ GW/cm² and at an average power density of $I_{ave}=9$ kW/cm². During the FROG measurements these levels were approximately 4 times smaller.

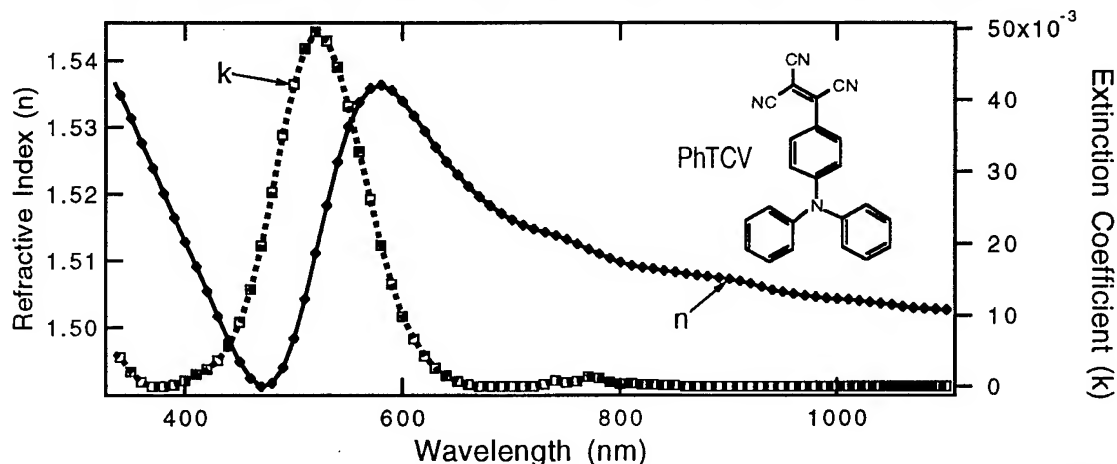


Fig.1. Refractive index and extinction coefficient spectral measurement of a 5% by wt. PhTCV/MMA film. The markers correspond to the ellipsometric data points. The molecular structure of the N,N-diphenyl-4-tricyanovinylaniline (PhTCV) chromophore is shown in the Figure.

A poled PhTCV/PMMA was used in an SHG-FROG setup to characterize 13 fs pulses from a modelocked Ti:sapphire oscillator. After acquisition of the SHG FROG traces, the data is processed using a deconvolution algorithm, which retrieves a unique pulseshape [1, 3] within a few minutes. To avoid dispersive effects from the glass substrate, the fundamental pulses are incident first onto the film, and then the second harmonic pulses propagate through the substrate. As a comparison, FROG measurements were also performed using a KDP crystal of 60 μ m thickness, which is cut for optimal phase matching at 800 nm. As an independent experimental check of the data, we compare the FROG trace with the independently-measured power spectrum of the fundamental light. The frequency marginal of the SHG FROG trace (the trace integrated over time delay) is proportional to the autoconvolution of the fundamental spectrum.[17] Figure 2 shows the comparisons of FROG traces taken with both the PhTCV/PMMA chromophore and the KDP crystal. The good agreement demonstrated in Figure 2 indicates that the data is accurate and self-consistent, even for our very large pulse bandwidths of 90 nm FWHM. It is important to note that such good frequency marginal agreement is much more difficult to achieve for the case of KDP as the SHG medium - the phase matching angle of the crystal needs to be finely adjusted for the center frequency of the pulse in order to obtain the broadest possible phase-matching bandwidth. This means that several test FROG traces must be taken with the KDP, as the angle is tuned to obtain optimal phase matching. For the PhTCV/PMMA on the other hand, this fine tuning is unnecessary. The measured electric field had an intensity envelope of 13 fs FWHM. The electric field of the pulse, measured with both the KDP and the PhTCV/PMMA, were identical, and had FROG algorithm convergence errors of less than 4×10^{-3} .

From these results, it is apparent that for pulses as short as 13 fs, KDP and PhTCV/PMMA perform similarly well. In practice, the KDP is considerably more difficult to use, because of the required angle tuning. The integration time to collect the FROG trace is shorter (by a factor of 4) for the KDP. Index of refraction measurements on the 5% PhTCV/PMMA films performed by a variable angle spectroscopic ellipsometer (see Figure 1) indicate that at the 800 nm fundamental

wavelength the coherence length exceeds 60 nm due to the anomalous phasematching effect [6, 18] and the negligible absorption present. Therefore it is evident that using thicker films, or films with higher chromophore concentrations, the second harmonic intensity can be increased by orders of magnitude. For even shorter pulses, the finite phase-matching bandwidth of KDP will limit the measurable pulsewidth, as will the finite transmission window of the thin poled polymer films. Further work is in progress to determine these limits.

In conclusion, we have shown that thin poled TCV/PMMA films are sufficiently nonlinear and robust to be used in Ti:sapphire ultrashort pulse diagnostics. Since such thin nonlinear films are not limited by phasematching, they hold great promise for extremely short pulse diagnostics.

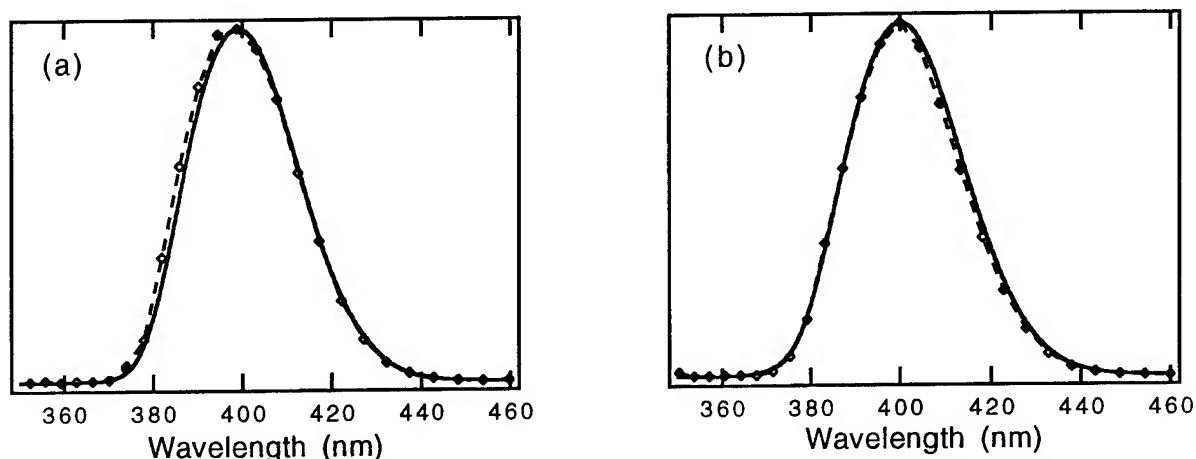


Fig.2. Autoconvolution of fundamental spectrum (solid line) and frequency marginal (dotted line) of SHG FROG trace for a 13 fs pulse measured with (a) PhTCV/MMA film and (b) KDP crystal. The diamond markers correspond to the frequency marginal data points.

References

1. K. W. DeLong, R. Trebino, J. Hunter and W. E. White, *J. Opt. Soc. Am. B* **11**, 2206 (1994).
2. G. Taft, A. Rundquist, M. M. Murnane, H. C. Kapteyn, K. DeLong, R. Trebino, I. Christov, *Opt. Lett.* **20**, 743 (1995).
3. S. Backus, M.T. Asaki, C. Shi, H. C. Kapteyn, and M. M. Murnane, *Opt. Lett.* **19**, 399 (1994).
4. M. A. Mortazavi, D. R. Yankelevich, A. Dienes, A. Knoesen, S. T. Kowel, and S. Djaili, *Appl. Optics* **28**, 3278 (1989).
5. A. Knoesen, N. E. Molau, D. R. Yankelevich, M. A. Mortazavi, and A. Dienes, *Int. J. Nonlin. Opt. Phys.*, **1**, 73 (1991).
6. D. R. Yankelevich, A. Dienes, A. Knoesen, R. W. Schoenlein and C. V. Shank, *IEEE J. of Quantum Elect.* **28**, 2403 (1992).
7. P. A. Cahill, K. D. Singer, *Am. Chem. Soc. Symp. Ser.* **455**, 200 (1991).
8. P. A. Cahill, D. R. Tallant, T. C. Kowalczyk, K. D. Singer, *Proc. SPIE*, **1560**, 130 (1991).
9. T. C. Kowalczyk, K. D. Singer, P. A. Cahill, *Opt. Lett.* **20**, 2273 (1995).
10. P. A. Cahill, K. D. Singer, L. A. King, *Opt. Lett.* **14**, 1137 (1989).
11. M. Ahlheim, M. Barzoukas, P. V. Bedworth, M. Blanchard-Desce, A. Fort, Z. Hu, S. R. Marder, J. W. Perry, C. Runser, M. Staehelin, B. Zysset, *Science* **271**, 335 (1996).
12. J. B. Stamatoff, A. Buckley, G. Calundann, E. W. Choe, R. DeMartino, G. Khanarian, T. Leslie, G. Nelson, D. Stuetz, C. C. Teng, H. N. Yoon, *Proc. SPIE* **682**, 85 (1986).
13. H. E. Katz, K. D. Singer, J. E. Sohn, C. W. Dirk, L. A. King, H. M. Gordon, *J. Amer. Chem. Soc.* **109**, 6561 (1987).
14. K. J. Drost, V. P. Rao, A. K.-Y. Jen, *J. C. S. Chem. Commun.*, 369 (1994).
15. B. C. McKusick, R. E. Heckert, T. L. Cairns, D. D. Coffman, H. F. Mower, *J. Amer. Chem. Soc.* **80**, 2806 (1958).
16. M. A. Mortazavi, A. Knoesen, S. T. Kowel, B. G. Higgins, and A. Dienes, *J. Opt. Soc. Am. B* **6**, 733 (1989).
17. K.W. DeLong, R. Trebino, D.J. Kane, *J. Opt. Soc. Am. B* **11**, 1597 (1994).
18. E. Sidick, A. Dienes, A. Knoesen, *Int. J. Nonlin. Opt. Phys.*, **3**, 543 (1994).

Nonlinear Optical Effects in the Bulk and at the Surface of Acentric Liquids Demonstrating Natural Optical Activity

N.I. Koroteev, V.A. Makarov, A.P. Shkurinov, A.V. Pakulev, A.A. Angeluts,
A.Yu. Resniansky, A.V. Balakin.

International Laser Center and Physics Department, M.V. Lomonosov Moscow State
University, Moscow 119899, Russia
Fax: +(7-095) 939-3113, E-mail: Koroteev@nik.phys.msu.su

Recent experimental results and theoretical investigations are reported concerning sum- and difference frequency generation in the bulk of acentric optically - active liquids comprised of chiral molecules (chiral liquids) as well as SHG and THG of femtosecond pulses reflected from the surface of such liquids. Frequency dependence of second-order optical nonlinearity was studied, for the first time. Dramatic resonant enhancement (more than two orders of magnitude) of multiple - wave mixing processes due to excitation of surface electromagnetic waves at the metallic diffraction gratings are also detected and theoretically explained. Several novel nonlinear optical effects are investigated which are characteristic for the acentric isotropic liquids and solids with natural optical activity, including magnetic field induced SHG, optical rectification, photo-galvanic and photo-refractive effects, BioCARS process.

Tree - wave - mixing processes.

In a non-DC conducting chiral liquids in the presence of two monochromatic (with frequencies ω_1, ω_2 one of which can be tunable) plane (with wave vectors k_1, k_2 respectively) electromagnetic waves with amplitudes E_1, E_2 the bulk second-order nonlinear optical propagation has the following form [1,2]:

$$P(\omega, k) = \frac{1}{2} \chi^{(2)}(\omega_1, \omega_2) [E_1 \times E_2] e^{-i(\omega_1 + \omega_2)t + (k_1 + k_2)r} + c.c. \quad (1)$$

were $\omega = \omega_1 + \omega_2$, $k = k_1 + k_2$, $\chi^{(2)}(\omega_1, \omega_2)$ is a pseudoscalar of second-order nonlinear susceptibility, and $[a \times b]$ states for the vectorial products of the vector a, b . With $\omega_1 \approx \omega_2$ $\chi^{(2)}(\omega_1, \omega_2) \approx \text{const} \cdot (\omega_1 - \omega_2)$, thus vanishing for the case of second harmonic generation (SHG) with $\omega_1 = \omega_2 = \omega/2$ (see refs. [2,3]).

However, nondegenerate sum-frequency generation (SFG) (with $\omega_1 \neq \omega_2$) and/or difference-frequency generation (with $\omega_2 = -|\omega_1| + \omega$) and/or optical rectification (with $\omega_2 = -\omega_1$) are allowed in acentric chiral liquids in the resonance region with either ω_1 or ω_2 being inside the absorption band of the medium [2]. We have succeeded in the experimental investigation of the SFG in several optically active liquids illuminated with focused femtosecond laser pulses. The experiment was performed with 100-fs pulses (energy 100 - 200 μ J) produced by a dye CPM- laser pumped with 5W all-lines Ar-ion-laser and amplified in a 3-stage pulsed dye amplifier chain. The pulses were focused in a cell with an optically active liquid to produce a white-light continuum. The remaining portion of the pump pulse together with the continuum radiation produced inside the cell a nonlinear polarization wave, described by eq.(1), which in turn generated a broadband sum-frequency signal detected, after passing through a polychromator, by a CCD thermoelectrically cooled UV-coating photo-diode-array system (Princeton Instruments TE/CCD 1024 EM/UV) connected to a computer for spectral analysis.

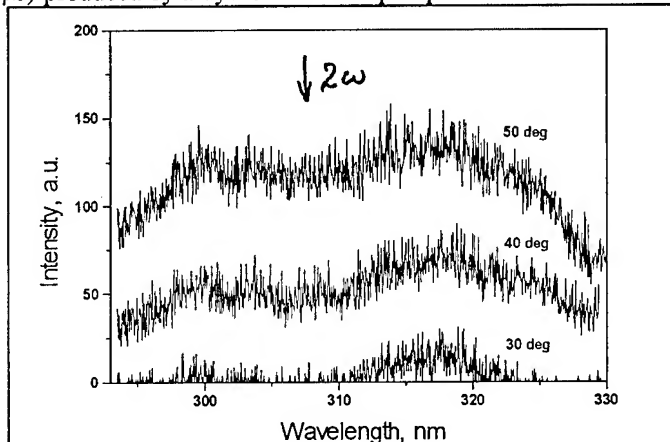


Fig.1. Wavelength dependence of the SFG signal from α -PNEA(+) chiral liquid for various sets of incident polarization angles

The spectrum of the SFG signal is shown at Fig.1 for several sets of the polarizational angles of the incident fs

pulses. The clearly seen dip at the SHG frequency is due to the characteristic spectral behavior of the $\chi^{(2)}$ susceptibility.

We have experimentally investigated the second harmonic generation at reflection of fs laser pulses off the surface of chiral liquids, both in a free space and in the vicinity of a metallic diffraction grating. Due to breaking symmetry at the interface between liquid and air (or liquid and metal), the SHG is allowed in the dipole approximation. The experimental system used is based on fs Ti:Sapphire laser pumped by all-line CW Ar⁺-laser (Innova-310, Coherent). The Ti:S laser output, consisted of a 100 MHz train of 100-fs pulses with average power up to 200 mW, is directed, after proper focusing, to the surface of a chiral liquid. In the presence of metal grating, under specially chosen orientation, a well-pronounced enhancement of SHG is detected due to quasi-resonant excitation of surface electromagnetic waves at the metallic grating Fig. 2 shows the details of the dependence of the SH light on the polarization of incident pulse [4]. THG was also measured both with bare and chiral-liquid-coated aluminum gratings.

There will be discussed first experimental and theoretical results concerning the magnetic-field-

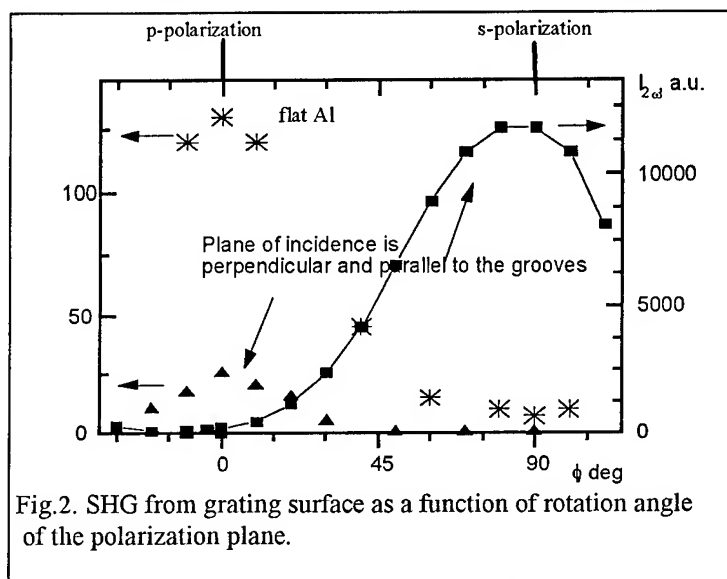


Fig.2. SHG from grating surface as a function of rotation angle of the polarization plane.

induced SHG in the bulk of chiral liquids and in class 432 cubic crystals.

We have theoretically investigated the effect of optical rectification (OR) in the bulk of chiral liquids. With an elliptically polarized plane monochromatic laser beam, the static field-strength induced in the bulk of the material due to the OR effect is expressed as follows:

$$E_{stat} = \hat{k} \frac{64\pi^2}{c\epsilon(0)n(\omega)} I \cdot \sin 2\gamma \cdot \text{Im}\{\chi^{(2)}\},$$

where I is the intensity and γ is ellipticity of the laser radiation. The effect is maximum with circularly polarized light wave ($\gamma = \pm\pi/4$). The

interference pattern created by counter propagating light waves is a periodic static-field grating which can be detected by the diffraction of a probe noncollinear laser beam at the static-electric-field-induced (via linear electro-optic effect) refractive index grating. The back diffracted probe signal intensity is greatly enhanced when the photogalvanic (photovoltaic) effect is taken into consideration [5]. In this case the liquid should be conducting an electric current. Thus, intrinsically conducting (or photoconducting) chiral liquids represent the novel class of photorefractive materials with promising properties.

Five-wave-mixing process

A recent development of the novel higher-order Coherent Anti-stokes Raman Scattering technique to study chiral biomolecules in solution (BioCARS, for short) will be discussed [2,6]. The BioCARS process is based on measurements of the frequency dispersion of fourth-order nonlinear optical susceptibility

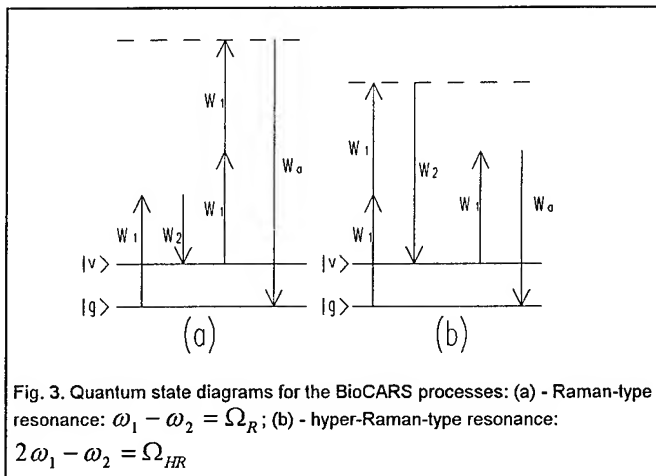


Fig. 3. Quantum state diagrams for the BioCARS processes: (a) - Raman-type resonance: $\omega_1 - \omega_2 = \Omega_R$; (b) - hyper-Raman-type resonance: $2\omega_1 - \omega_2 = \Omega_{HR}$

$\chi_{ijklm}^{(4)}(\omega_a; \omega_1, \omega_1, \omega_1, -\omega_2)$, which is responsible for generation in the solution of the chiral molecules a new spectral component $\omega_a = 3\omega_1 - \omega_2$ when the solution is illuminated simultaneously with two laser beams having frequencies ω_1, ω_2 (tunable). This five-wave-mixing process can be phase-matched in solutions with normal dispersion in a noncollinear geometry - as in ordinary CARS.

The BioCARS technique is background-free, unlike the ordinary CARS, because no signal is produced from the centrosymmetrical solvent (e.g. water), so

the signal of BioCARS is generated exceptionally by mirror-asymmetric chiral biomolecules dissolved in a centrosymmetrical liquid. By tuning the frequency of one of the laser beams (say, ω_2), the dispersion of $|\chi^{(4)}(\omega_a)|^2$ is measured, where Raman-type ($\omega_1 - \omega_2 = \Omega_R$) and/or hyper-Raman-type ($2\omega_1 - \omega_2 = \Omega_{HR}$) resonances are displayed representing the vibrational eigenmodes of the chiral molecules, Ω_R , Ω_{HR} etc. (see Fig.3).

We will describe the recent experimental development of the BioCARS technique together with further microscopical quantum mechanical calculations [7-9]. The selection rules for the BioCARS spectra are found, namely, a molecular vibrational transition displayed in the BioCARS spectrum should be both allowed in Raman and hyper-Raman scattering, with only isotropic and anisotropic irreducible components of the relevant scattering tensors being responsible for the generation of BioCARS signal.

Acknowledgments

The authors acknowledge the useful discussions with C.L.Tang, L.A.Nafie, T.M.II'inova, and S.N.Volkov. This research was partially supported by the Russian Foundation for Basic Research and International Science Foundation.

References

1. N.I.Koroteev, In *Frontiers in nonlinear optics. The Sergei Akhmanov memorial volume*, ed. by H.Walther, N.Koroteev, M.O.Scully, IOP Bristol, 1993, p.228.
2. N.I.Koroteev, *JETP*, **79**, 681 (1994).
3. J.A.Giordmaine. *Phys. Rev. A* **138**, 1599 (1965).
4. A.A.Angelut, I.A.Ozheredov, A.P.Shkurinov and N.I.Koroteev, *JETP Letters*, **63**, N3 (1996).
5. N.I.Koroteev, *JETP Letters*, **61**, 87 (1995).
6. N.I.Koroteev, *Biospectroscopy*, **1**, 341 (1995).
7. A.P.Shkurinov, A.V.Dubrovskii, N.I.Koroteev, *Phys. Rev. Lett.*, **70**, 1085 (1993).
8. N.I.Konovalov, N.I.Koroteev, V.A.Makarov, S.N.Volkov. *Nonlinear optics*, **8**, 231 (1994).
9. S.N.Volkov, N.I.Koroteev, V.A.Makarov, *Quantum Electronics*, **25**, 1198 (1995).

Thursday, July 11, 1996

NLO Poster Session: 3

NThE 9:00 pm-11:00 pm
South Pacific Ballroom

Annealed proton exchange domain inversion erasure in electric-field poled LiNbO₃.

K.Elhadi, M.Sundheimer, P.Baldi, P.Aschieri, M.DeMicheli and
D.B.Ostrowsky

Laboratoire de Physique de la Matière Condensée, Université de Nice-Sophia Antipolis
Parc Valrose, 06108 Nice Cedex 2, France

Tél.: (+33) 92 07 67 57, Fax.: (+33) 92 07 67 54, E-mail: <elhadi@naxos.unice.fr>,

J. Webjörn

Optoelectronics Research Centre, University of Southampton
present address : SDL Inc, San Jose, California, U.S.A

The Quasi-Phase-Matching technique (QPM) [1], in which the ferroelectric domains of a nonlinear material are periodically inverted in order to compensate for dispersion, has become widely used for a number of nonlinear processes [2,3,4]. While bulk experiments in such structures have yielded results close to theoretical predictions, waveguided versions, which offer additional possibilities (higher theoretical efficiencies, electrooptic tuning, etc.) have not attained the predicted efficiencies. In this paper we compare the parametric fluorescence efficiency in both bulk and Annealed Proton Exchange (APE) waveguide configurations in an electric-field poled LiNbO₃ sample, in which the inverted domains exist throughout the entire sample thickness. The results indicate, that even after annealing, the proton exchange process appears to erase the periodic domain inversion, to a depth comparable to that of the exchanged structure, leading to a lack of QPM in that region. Such an effect had already been proposed by Webjörn [5] concerning domains inverted by Ti diffusion at the surface of LiNbO₃. He also noted however, that if an inverted "seed" remained below the surface, annealing could permit regrowth of the inverted structure above the seed. This model would have led one to expect that in materials poled throughout their entire thickness, as in E-field poled LiNbO₃, the seed would always be present allowing appropriate regrowth of the domains during annealing. However, we shall demonstrate that this does not appear to be the case.

The comparison of bulk and waveguide parametric fluorescence is a very attractive method for elucidating this problem since bulk parametric fluorescence does not depend strongly on beam geometry [6], and therefore, yields an unambiguous value of the effective nonlinear coefficient, d_{eff} , taking into account both duty cycle and regularity of the domain structure. On the other hand, careful measurements of the interacting mode profiles permit accurate prediction of the guided fluorescence in a waveguide formed on the same sample.

The sample was prepared by the E-field poling technique to achieve the inverted ferroelectric domains necessary for QPM [7]. The poled crystal, 200 μm thick by 8 mm long, was proton exchanged for 25 mn in a 300 °C bath of benzoic acid containing 1 % lithium benzoate. It was annealed at 350 °C for 4 hours leading to a waveguide with a surface $\delta n_e = 8.10^{-3}$, a 1/e depth of 3 μm and a 1/e half width of 7 μm .

The parametric fluorescence was measured using the experimental apparatus previously described [8]. In the bulk configuration, the geometry sketched in figure 1 was used. For this case, the emitted fluorescence power $P_s(l)$ is given by [9]:

$$P_s(l) = \frac{\beta}{|b|} d_{\text{eff}}^2 l P_p(0) \pi \theta^2$$

with:

$$\beta = \frac{\hbar \omega_i \omega_s^4 n_s}{\pi^2 c^5 n_i n_p \epsilon_0^3}, \quad b = \left(\frac{\partial k_s}{\partial \omega_s} \right)_{\omega_{s0}} - \left(\frac{\partial k_i}{\partial \omega_i} \right)_{\omega_{i0}}$$

where the effective nonlinear coefficient is defined as $d_{\text{eff}} = (2d_{33}/\pi) \sin[\pi a(x)]$, with $a(x)$ expressing the effect of QPM grating shape and duty cycle. The function $a(x) = 1$ for the case of rectangular domains with a 50% duty cycle and 0 for no periodic domain

inversion. $P_p(0)$ is the injected pump power and b , ω , n , l and θ denote the dispersion, the frequency, the index of refraction, the crystal length and the detector acceptance angle, respectively. Quantities associated with pump, signal and idler fields have subscripts p , s and i , respectively. From the fluorescence power dependance on the the square of the detector acceptance angle θ^2 (figure 2), d_{eff} was determined and was close to the expected value of 21 pm/V as shown in table 1. The parametric efficiency, defined as $\eta = P_s(l)/P_p(0)$, was also determined (figure 3).

For the guided parametric fluorescence, the fluorescence power is given by [10]:

$$P_s(l) = \frac{\gamma}{|b|} d_{\text{eff}}^2 P_p(0) I$$

with

$$\gamma = e^{-\alpha_s l} \left(\frac{1 - e^{-\alpha_p l}}{\alpha_p l} \right)^2 \frac{2^2 \hbar \omega_i \omega_s^2 \mu_0^3 c^4}{n_{\text{eff}}^p n_{\text{eff}}^s n_{\text{eff}}^i} \quad I = \frac{\left(\iint E_p(x,y) E_s(x,y) E_i(x,y) dx dy \right)^2}{\iint E_p^2(x,y) dx dy \iint E_s^2(x,y) dx dy \iint E_i^2(x,y) dx dy}$$

where α , n_{eff} and I represent the losses, the effective indices of the guided modes and the overlap integral between the interacting modes, respectively. The parametric fluorescence was measured using both the TM₀₀ and TM₀₁ modes for the pump, corresponding to TM₀₀ modes for both signal and idler, allowing the calculation of d_{eff} and the fluorescence efficiencies for each mode. These results are also shown in table 1 and lead to the following remarks:

- in the bulk case, the measured values of d_{eff} and the fluorescence efficiency η are in excellent agreement with the values calculated based on a 50% duty cycle of domain inversion.

- for the TM₀₀ pump mode, the measured d_{eff} is reduced to 0.02 times the theoretical value, with a corresponding decrease ($4 \cdot 10^{-4}$) in the fluorescence efficiency.

- for the TM₀₁ mode, the reduction of d_{eff} is a factor of 0.3 with the corresponding reduction of efficiency (0.1).

Waveguide loss measurements, made using the optimum end-fire coupling technique [11], indicated losses on the order of 1 dB / cm at the pump wavelength and 0.5 dB / cm at the signal and idler wavelengths, are taken into account in our calculations. Therefore, we conclude that the cause of the enormously reduced TM₀₀ pump efficiency is due to either a reduction of the nonlinear coefficient of the material due to the APE process or to a destruction of domain inversion near the surface. Since annealing has been shown to restore the nonlinear coefficient in APE guides [12], we ascribe the reduction observed here to the destruction of the periodic domain inversion, as suggested in ref. 5. We therefore carried out a numerical simulation to determine to what depth of the structure the periodic domain inversion must be destroyed in order to explain these results. This calculation indicated a depth of nearly 5 microns as shown in the last column of table 1.

In conclusion, we have carried out a comparison between parametric fluorescence in both bulk and APE waveguide configurations in periodically E-field poled lithium niobate. We measure a parametric conversion efficiency 3 orders of magnitude lower than theoretically predicted for the TM₀₀ pump mode in this structure. We attribute this reduction to the erasure of the periodic domain inversion over a depth of approximately 5 microns, which leads to predictions in good agreement with the measured results. Further examinations of the domains structure using both confocal and electron microscopes are underway and the ensuing results will be described.

- [1]: J. A. Armstrong *et al.*, Phys. Rev. **127**, 1918-1939 (1962).
- [2]: M. Y. Yamada *et al.*, Appl. Phys. Lett. **62** (5), (1993).
- [3]: M. L. Bortz *et al.*, CLEO'94, paper CTh D6.
- [4]: L. E. Myers *et al.*, J. Opt. Soc. Am. B. **12**, 2102-2116 (1995).
- [5]: J. Webjörn, Journal of Lightwave Technology. **11** (4), 589-594 (1995).
- [6]: R. L. Byer *et al.*, Physical Review, **168** (3), (1968).

- [7]: V. Pruneri *et al.*, Optics Letters, **20** (23), 2375-2377 (1993).
 [8]: P. Baldi *et al.*, Electron. Lett , **29**, 1539 (1993).
 [9]: Harris *et al.*, Phys. Rev. Letters, **18**, 732 (1967).
 [10]: P. Baldi *et al.*, Journal of Quantum Electronics, **31** (6), 997-1008 (1995).
 [11]: M. Haruna *et al.*, Electronics Letters **28** (17), 1612-1613 (1992).
 [12]: H. Ählfeldt, J. Appl. Phys. **76** (6), 3255-3260 (1994).

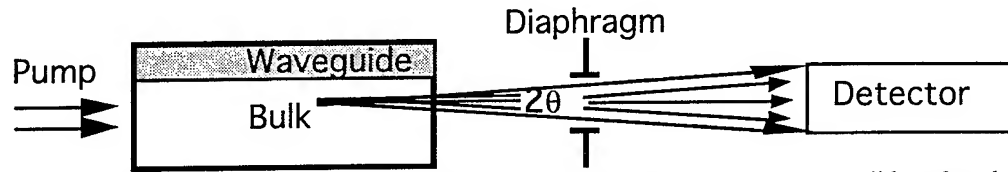


Figure 1: Geometry used for Bulk parametric fluorescence measurements. The solid angle subtended by the detector at the crystal is $\Delta\Omega = \pi\theta^2$. The detector (about 25 mm² of detection area) was placed at 1.50 m from the sample (200 μm thick and 8 mm long).

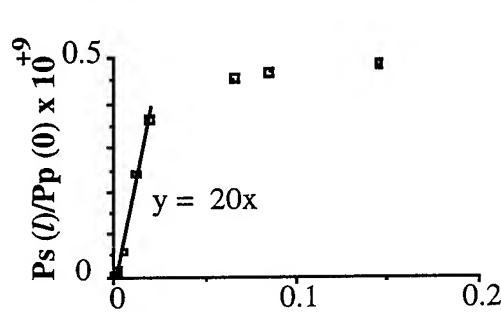


Figure 2: Dependence of the fluorescence power versus the square of the detector acceptance angle. The linear dependance obtained from small angles leads to the d_{eff} . The saturation occurs when all the fluorescence reaches the detector.

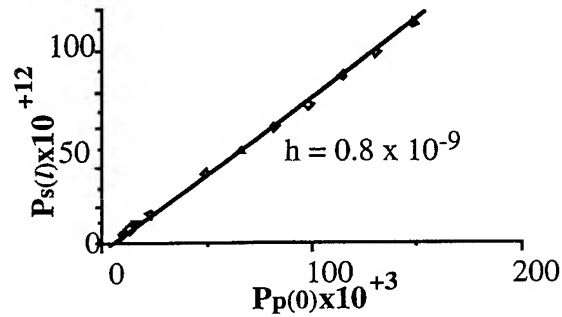


Figure 3: Dependence of the fluorescence power versus the injected pump power for a fixed θ^2 . The slope gives the measured parametric efficiency η

Configuration		d_{eff}^c (pm/V)	d_{eff}^m (pm/V)	η^c (10 ⁻⁹)	η^m (10 ⁻⁹)	η_{hyp}^c (10 ⁻⁹)
Bulk		21	22±2	1	0.8±0.1	1
Waveguide with pump launched in mode	TM ₀₀	21	0.4±0.1	300	0.12±0.1	0.10
	TM ₀₁	21	7±1	100	10±1	10

Table 1: Comparison between theoretical and measured values of d_{eff} and efficiencies for both bulk and waveguide configurations. η_{hyp}^c are the calculated efficiencies for a hypothetical sample taking into account an erasure of the periodic domain inversion over 5 μm. The waveguide index profile is taken gaussian with a surface index increase of $8 \cdot 10^{-3}$, an 1/e depth parameter of 3 μm and an 1/e half width parameter of 7 μm.

Electro-Optic Coefficients of Thin Layers of BaTiO₃

M.J.H. Niesten

*Philips Research Laboratories, Prof. Holstlaan 4, 5656 AA Eindhoven, The Netherlands,
Department of Physics, Eindhoven University of Technology, 5600 MB Eindhoven,
The Netherlands,
tel: +31 40 2742316
fax: +31 40 2743365*

N.J Pulsford

Philips Research Laboratories, Prof. Holstlaan 4, 5656 AA Eindhoven, The Netherlands,

J.F.M. Cillessen

Philips Research Laboratories, Prof. Holstlaan 4, 5656 AA Eindhoven, The Netherlands,

Integrated optics require electro-optic materials with high non-linear coefficients. Oxidic materials have strong electro-optic coefficients and do not deteriorate under high process temperatures or due to aging as e.g. polymers do. Much attention has been paid to the growth of oxidic layers for ferroelectric applications as solid state memories. Layers have been grown by radio frequent sputtering [1], metalorganic vapour deposition [2] and pulsed laser deposition [3]. Some layers have been characterized electro-optically by measuring the birefringence [4] and the effective electro-optic coefficient r_c has been determined from such measurements [5]. In this contribution we present the electro-optic coefficients r_{13} and r_{33} of a layer of BaTiO₃ that we measured with ellipsometry.

We have grown layers of BaTiO₃ by pulsed laser deposition and a bottom electrode of La_{0.5}Sr_{0.5}CoO₃ was grown on a SrTiO₃ substrate. A transparent antimony doped tin oxide (ATO) layer was deposited on the BaTiO₃ layer as a top electrode.

The impedance of the layers has been measured as function of the frequency. Fig.1

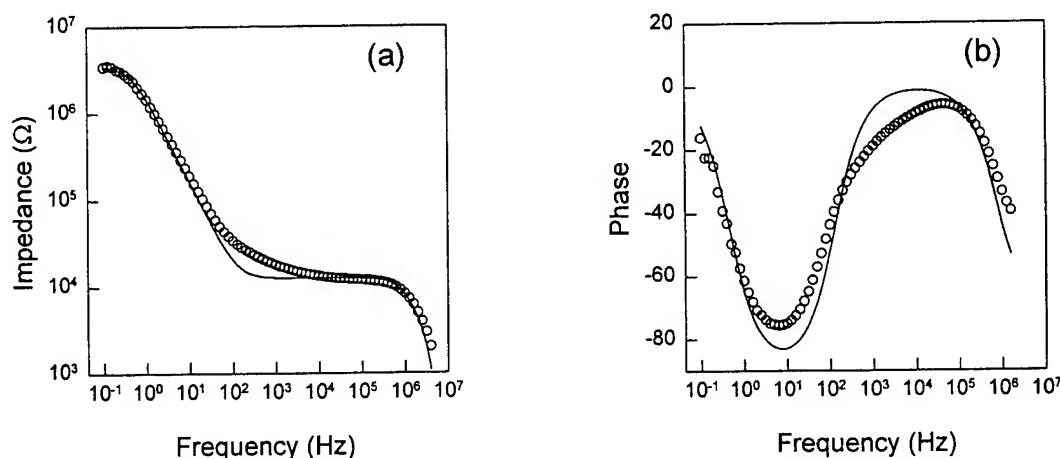


Fig. 1. The impedance (a) and phase (b) of a 620 nm thick BaTiO₃ layer as function of frequency. The measurement is given by the dots, the fit by the solid line.

shows the impedance (a) and phase (b) of a 620 nm thick BaTiO_3 layer as a function of the frequency. The measurement is given by the dots, the fit by the solid line. The impedance starts decreasing at small frequencies, becomes stable at about 200 Hz and decreases again at 0.7 MHz. The curve can be fitted with two RC circuits in series (solid line). This suggests that the layer is split up in two parts which we attribute to the effects of strain, which gives a thin strained layer at the interface and a thick layer that is partially relaxed. By comparing samples with different layer thicknesses we found that the large resistance at small frequencies is the resistance of a thin strained layer at the interface, whereas the smaller resistance of the thick relaxed layer becomes apparent at higher frequencies [6]. The difference in resistance between

the two parts of the layer means that the electric field will not be constant over the BaTiO_3 layer when a voltage is applied. The electric field in the thin strained layer is much larger than that in the thick part where relaxation took place.

We measured the electro-optic effect in an ellipsometric setup shown in fig. 2. A beam with a wavelength of 633 nm enters the ATO layer polarized at 45° with respect to the plane of incidence. The reflected beam passes through a compensator and an analyzer. The reflected signal is measured as function of the compensator angle (dots in figure 3). We calculated the reflection taking into account the multiple reflections at the

interfaces. In this calculation we used the layer thicknesses measured by X-ray diffraction. The result of the calculation is shown as the line in fig. 3. To obtain the electro-optic coefficients a voltage is applied over the BaTiO_3 layer. The change in the reflection is measured as function of the compensator angle. This is shown by the dots in fig. 4. We used the same calculation as for the reflection to fit the electro-optic coefficients. The electric field in the strained and the unstrained part was calculated using the conductances derived from fig. 1. From this fit

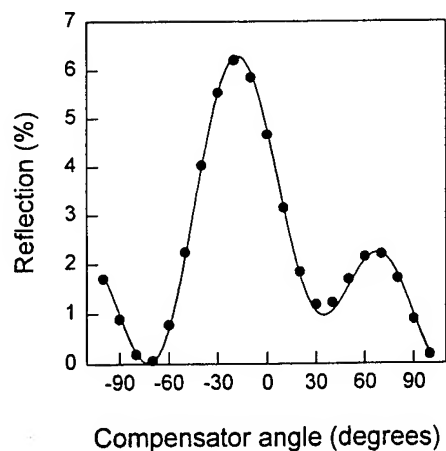


Fig. 3. reflection of a $\text{ATO}/\text{BaTiO}_3/\text{La}_{0.5}\text{Sr}_{0.5}\text{CoO}_3/\text{SrTiO}_3$ multilayer as function of the compensator angle. The measurement is given by the dots, the calculation by the solid line.

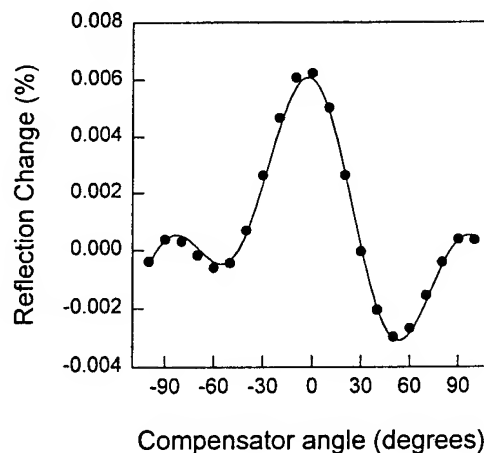


fig. 4. The change in the reflection due to the electro-optic effect of a $\text{ATO}/\text{BaTiO}_3/\text{La}_{0.5}\text{Sr}_{0.5}\text{CoO}_3/\text{SrTiO}_3$ multilayer as function of the compensator angle. The measurement is given by the dots, the calculation by the solid line.

(solid line in fig. 4) the r_{13} and r_{33} coefficients of the unstrained layer are respectively 5.6 ± 1 pm/V and 19.6 ± 5 pm/V and the r_{13} and r_{33} coefficients of the strained layer are respectively -0.5 ± 0.5 pm/V and -14.6 ± 0.5 pm/V. The fit is dominated by the coefficients of the strained part, where the electric field is much larger compared to the partially relaxed part. Recent measurements [7], [8] of the electro-optic coefficients in bulk BaTiO₃ crystals give that the stress free r_{13} is about 10 pm/V and the stress free r_{33} is about 100 pm/V. It is known from bulk crystals that the clamped electro-optic coefficients are smaller than stress free coefficients [8]. Therefore we can assume that strain causes the electro-optic coefficients in the strained part of the BaTiO₃ layer to be lower than in the part that is relaxed. The values of the electro-optic coefficients of the relaxed part of the layer are lower than the bulk values probably because of the poorer crystal quality.

In summary, the electro-optic coefficients r_{13} and r_{33} of a BaTiO₃ layer grown by pulsed laser deposition are measured with ellipsometry. The data can only be fitted when it is assumed that the BaTiO₃ layer is split in two parts which have different electro-optic coefficients.

1. M. Matsuoka, K. Hoshino and K. Ono, J. Appl. Phys. **76**, 1768 (1994).
2. K. Iijima, T. Terashima, K. Yamamoto, K. Hirata and Y. Bando, Appl. Phys. Lett. **56**, 527 (1990).
3. M.G. Norton, C. Scarfone, J. Li, C. B. Carter and J. W. Mayer, J. Mater. Res. **6**, 2022 (1991).
4. D.H. Kim and H.S. Kwok, Appl. Phys. Lett. **67**, 1803 (1995).
5. S.G. Gakh, T.P. Myasnikova, O.A. Bunina and T.A. Yasman, Inorg. Mat. **31**, 345 (1995).
6. M.J.H. Niessen, N.J. Pulsford, J.F.M Cillessen and C.W.T Bulle, submitted to Appl. Phys. Lett.
7. P. Jullien, A. Lahlafi, A. Maillard and G. Ormancey, Ferroelectrics **108**, 147 (1990).
8. M.Zgonik, P. Bernasconi, M. Duelli, R. Schlessler, P.Günter, M.H. Garrett, D. Rytz, Y. Zhu and X. Wu, Phys. Rev. B **50**, 5941 (1994).

Nonlinear Optical Properties of Au Nanocrystals Embedded in Silicate Thin Films

Minyung Lee

Department of Chemistry, Ewha Womans University

Seoul 120-750, Korea

Tel: 02-360-2383 Fax: 02-360-2844

A lot of nanometer-sized metal particles exhibit high optical nonlinearity and fast time response in the surface plasmon absorption region,¹ so they have potential application in nonlinear optical devices in the future. Especially, gold nano crystals were most intensively studied and their linear and nonlinear optical properties are relatively well known.² However, preparation techniques for gold nano particles in inorganic oxide glass are not well established yet and controlling the nanocrystal size has to be elaborated for the systematic study on the nonlinear optical properties of metal nanocrystals.

In this work, gold nano particles were prepared using sol-gel processing, dip-coating, and high temperature heat-treatment.³ Table I summarizes all the experimental conditions for eight samples, which also shows the FWHM of the surface plasmon absorption band. As the heating temperature increases, the absorption maximum shifts to longer wavelength, but it does not vary with the heat-treatment time and withdrawing rate. The maximum heating temperature was limited to 500 °C, due to the low melting point of the substrate (soda-lime glass). The absorption bandwidth rather than the peak position gives direct information on the metal particle size. Assuming the particles are spherical in shape and the size distribution is narrow enough, the particle's mean diameter has been calculated as ca. 10 nm for seven samples showing surface plasmon absorption.²

Table I Absorption characteristics of various Au-SiO₂ thin films.

sample number	withdrawing rate (cm/min)	heating temperature (°C)	heating time (min)	absorption maximum (nm)	maximum absorbance
1	3	100	15	-	-
2	3	250	15	524	0.23
3	3	320	15	528	0.26
4	3	400	15	533	0.29
5	3	500	15	536	0.32
6	3	500	90	537	0.32
7	5	500	15	536	0.40
8	10	500	15	536	0.51

X-ray crystallography gives direct information on whether or not the sample forms a crystal structure. Fig. 1 is the x-ray data of Au-SiO₂ thin films. The data clearly show four peaks which are characteristic of the fcc lattice. Peaks at $2\theta = 38.15^\circ$, 44.24° , and 63.88° correspond to (111), (200), and (220) plane. The fourth peak is more or less blurred but assignable to (311) plane. The lattice parameter, calculated from those angles and four reflection planes was found to be $0.4032 \pm 0.0015\text{nm}$ on average.

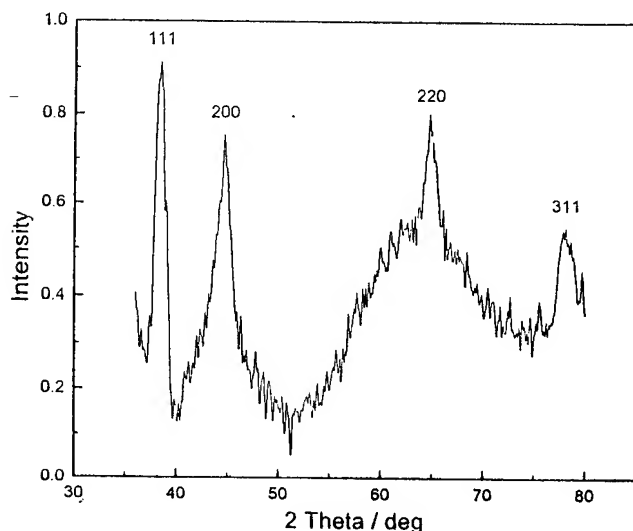


Fig. 1 X-ray diffraction data of Au-SiO₂ thin film.

Table II $\chi^{(3)}$ values of Au nano particles in silicate thin films as a function of laser wavelength

laser wavelength (nm)	absorption coefficient (10^3 cm^{-1})	$\chi^{(3)}$ (10^{-8} esu)
530	2.5	1.6
540	2.6	2.3
550	2.3	1.3
560	1.8	0.7
570	1.4	0.4

Optical nonlinear measurements were performed using the degenerate four wave mixing experiment with two beam configuration. The laser system was a Coumarin 540 dye laser pumped by a nanosecond Q-switched Nd:YAG laser (Spectra-Physics model 150), producing ca. 10 mJ pulse energy at 10Hz. Above a few mJ, it was observed that the dye laser pulses damaged Au-SiO₂ thin films, so they are attenuated and equally split out and recombined on the sample spatially and temporally for DFWM experiment. The diffracted signal was detected by a photodiode or PMT and processed in a boxcar. The diffraction efficiency, the ratio of the signal intensity to the probe beam (I_s/I_p), was plotted in Fig. 2 as a function of the peak intensity of the probe beam in the logarithm scale. Above $1\text{MW}/\text{cm}^2$, the signal begins to saturate. In the unsaturated region, the diffraction efficiency is fairly linear and the slope is 2.04, elucidating square dependence.

For two beam DFWM, the $\chi^{(3)}$ value can be calculated from the following equation:⁴

$$\chi^{(3)} = \frac{n^2 c}{2^5 \pi^3} \lambda \frac{\alpha}{(1-T) T^{1/2}} \frac{\eta^{1/2}}{I_p}$$

where n is the linear refractive index, c the light speed in vacuum, I_p the pump intensity, α the linear absorption coefficient, and η the diffraction efficiency. The transmittance T is given by $\exp(-\alpha l)$ in which l is the sample thickness. Table II shows the calculated $\chi^{(3)}$ values as a

function of laser wavelength. The largest value, 2.3×10^{-8} esu, occurs at 540 nm at room temperature, which is close to the maximum of the surface plasmon absorption band. In the same wavelength region, $\chi^{(3)}$ has been measured at 77 K and it was not different from room temperature values. Table II also shows that the third order optical nonlinearity for gold nanoparticles stems from the surface plasmon resonance because the $\chi^{(3)}$ values are correlated to the absorption coefficient. It has been known that the optical nonlinearity of metal nanocrystals is contributed by three dominated mechanisms: intraband transition including surface plasmon resonance, d-sp interband transtion, and hot-electron effect due to Fermi smearing.⁶ $\chi^{(3)}$ is also a function of volume fraction (p) of metal particles in matrix and the local field factor (f_i): $\chi^{(3)} = p|f_i(\omega)|^2 f_i(\omega)^2 \chi_m^{(3)}$. The third order nonlinear optical coefficient of metal itself was denoted by $\chi_m^{(3)}$. The local field factor and the volume fraction for the samples heat-treated at 500 °C have been calculated as 0.73% and 1.34, respectively. Therefore, the resonant $\chi_m^{(3)}$ for the Au nanocrystals in silicate thin films approaches to the value of 1×10^{-6} esu.

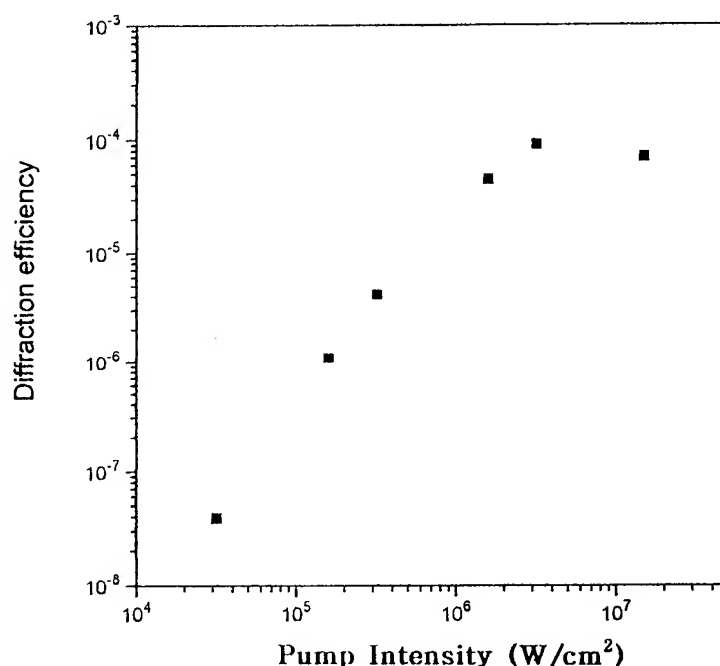


Fig. 2 Diffraction efficiency of Au nanocrystals in silicate thin film.

References

1. U. Kreibig, and L. Genzel *Surf. Sci.* 156, 678, 1985.
2. F. Hache, D. Ricard, C. Flyzannis, and U. Kreibig, *Appl. Phys. A* 47, 347, 1988.
3. H. Kozuka and S. Sakka *Chem. Mater.* 5, 222, 1993.
4. K. Uchida, S. Kaneko, S. Omi, C. Hata, H. Tanji, Y. Asahara, A. J. Ikushima T. Tokizaki, and A. Nakamura *J. Opt. Soc. Am. B* 11, 1236, 1994.
5. J. A. Perenboom, P. Wyder, and F. Meier *Phys. Rep.* 78, 173, 1981.

Third order nonlinear optical properties of metal ion implanted silica at 527nm, 800nm and 1053nm.

Barry Luther-Davies, A. Samoc, M.Samoc[†], Robert H. Magruder^{*}

[†]Laser Physics Centre, RSPHysSE, The Australian National University,
Canberra ACT 0200 Australia.

^{*} Department of Applied and Engineering Sciences, Vanderbilt University, Nashville,
TN 37235, USA

tel (61 62 494244); FAX (61 62 490029); e-mail bld111@rsphy1.anu.edu.au

There is a growing interest in the optical properties of metallic nanocrystals embedded in dielectric hosts particularly since there have been reports of these materials having very large third order optical nonlinearities¹. In this paper we present some results of measurements on materials created by implanting fused silica with various combinations of titanium, antimony, gold and oxygen at doses in the range 10^{16} - 10^{17} atoms/cm³.

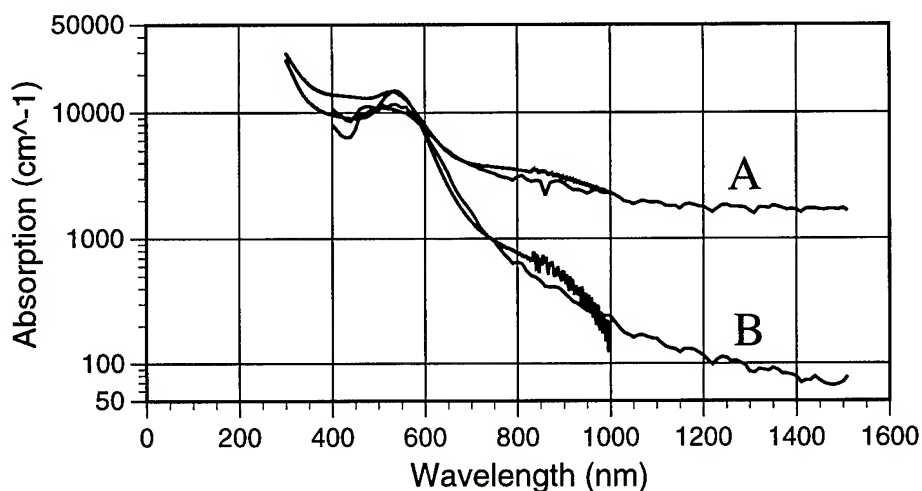


Figure 1: Absorptivity of ion implanted samples containing: A: 1.2×10^{17} Ti ions/cm² and 6×10^{16} Au ions/cm²; B: 1.2×10^{17} Ti ions/cm², 1.42×10^{17} O ions/cm², and 6×10^{16} Au ions/cm².

The measurements have been carried out using low repetition rate lasers (1-30Hz) at 527nm, 800nm and 1053nm. The low repetition rate system was essential in obtaining meaningful data on the optical nonlinearity since these materials were found to be strongly absorbing. Figure 1 shows data taken using a conventional spectrophotometer in the visible (highly absorbing) region combined with data from a high sensitivity photothermal deflection spectrometer for the infra-red for several different films. It should be noted that even at

1.5 μm , well away from the plasmon resonance, the absorption generally exceeds 1000dB/cm! Clearly thermal loading of these films due to linear absorption must be eliminated during nonlinear optical measurements.

To illustrate this point we compared results from z-scan measurements using a chopped train of pulses from a CW model-locked frequency double Nd laser with those from a laser emitting single 35ps pulses at 20Hz. The results are shown in figure 2. The z-scans using the 20Hz laser showed practically no real component of the nonlinearity but an absorptive bleaching effect. The quasi-CW system, on the other hand, indicated a huge positive refractive nonlinearity of thermal origin.

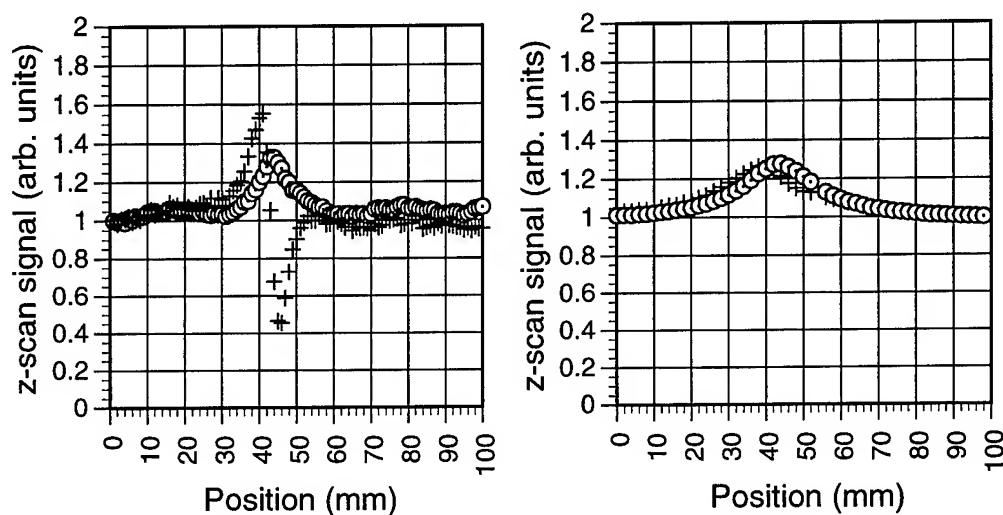


Figure 2: Open and closed (+) aperture z-scans for ion implanted silica samples containing Ti; Au and O using 527nm radiation at high and low repetition rates. LHS using 76MHz chopped radiation from CW mode-locked laser; RHS signals using single pulses at 20Hz. Note the intensity in both cases was $3\text{--}4 \times 10^{-8} \text{W/cm}^2$. The strong "refractive" component in LH figure was due to a thermal nonlinearity whose response time was measured as $\approx 250\mu\text{s}$. (The beam waist size was not the same in these two experiments: hence the different "length" of the z-scan signals)

At 800nm time resolved degenerate four wave mixing was used to evaluate the time response of the optical nonlinearity. The raw data for a fixed laser intensity for several films is shown in figure 3. The laser pulse duration for these measurements was $\approx 2\text{ps}$. As is evident, the DFWM signals from ion implanted samples show response times in the 2-10ps range depending on the dose and combination of implanted ions. An underlying feature is the existence in all samples of a long lived tail with a response time around 10ps. In samples implanted with oxygen as well as the metal ions, a faster response time was also observed (1-2ps).

It proved unhelpful to translate raw data such as shown in figure 3 into meaningful

"numbers" for the third order nonlinearity, since we observed that the DFWM signals did not scale with the cube of the laser intensity as would be required for a Kerr-law material. Similarly z-scan signals indicating a saturable absorption and taken at 527nm did not appear to scale linearly with intensity. It is perhaps worth mentioning, however, that if the scaling "problem" was ignored, the 800nm DFWM data suggested the nonlinearity was in the $10^{-12}\text{cm}^2/\text{W}$ range: several orders of magnitude lower than those reported using higher repetition rate lasers.

Whilst our data did not indicate nonlinearities as large as those reported previously, it should be noted that the methods of preparation of the materials and the existence of clear plasmon features in the spectra suggested that the inclusions were larger than required for quantum confinement effects to become important. Furthermore, more methodical studies of the influence of the different species in multiple ion implants is warranted since our data suggests this has a significant affect on both the magnitude and temporal response of the nonlinearity.

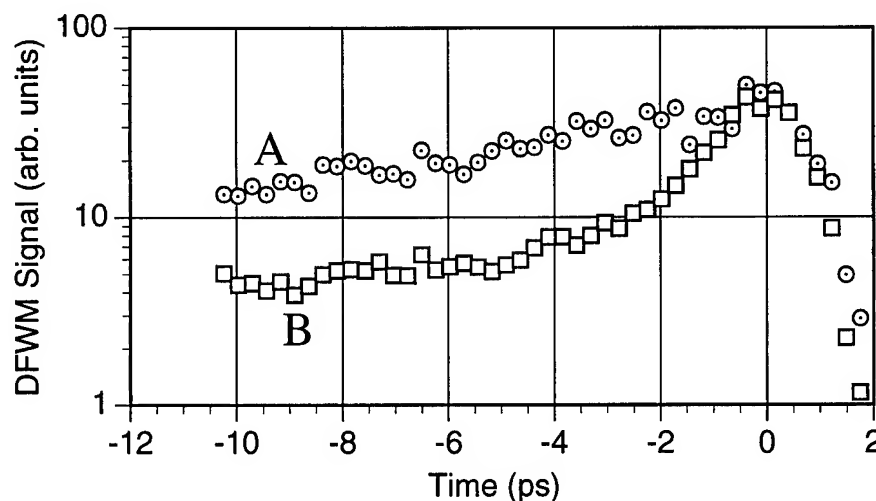


Figure 3: Time resolved DFWM measurements of ion implanted samples containing: A: $1.2 \times 10^{17} \text{Ti ions/cm}^2$ and $6 \times 10^{16} \text{Au ions/cm}^2$; B: $1.2 \times 10^{17} \text{Ti ions/cm}^2$, $1.42 \times 10^{17} \text{O ions/cm}^2$, and $6 \times 10^{16} \text{Au ions/cm}^2$ (negative time corresponds to the probe pulse arriving after the two pumps). Note the single component $\approx 10 \text{ps}$ decay in sample A, whilst two characteristic decay times are apparent for sample B.

¹ see e.g. C.W. White, D.S. Zhou, J.D. Budai, R.A. Zuhr, R.H. Magruder, D.H. Osbourne, **Mat. Res. Soc. Symp. Proc.** **316**, 499-505, (1994).; R.F. Haglund, Jr., D.H. Osbourne, Jr., L. Yang, R.H. Magruder, III, C.W. White, R.A. Zuhr, **Mat. Res. Soc. Symp. Proc.** **316**, 421-432 (1994).

Enhancement of χ^3 in nanoparticle composite media exhibiting electrostriction and quantum confinement

G. Flynn, C. Schwarze, D.A. Pommet and M. A. Fiddy

Department of Electrical Engineering,
University of Massachusetts Lowell, Lowell, MA 01854

508 934 3359; fax 508 934 3027; fiddy@cae.uml.edu

Introduction

A new model is described that combines the interaction between quantum confinement in nanoparticles and electrostriction on the bulk optical nonlinearity of a medium. While modeling the two nonlinear mechanisms independently has been widely reported, there have been few attempts to consider the interplay between two such nonlinearities when both are present and of similar magnitude. We show that local field effects can greatly enhance the bulk nonlinear optical properties of the medium.

Background

There is considerable interest in the use of nanoparticles for nonlinear optical applications because of the advances made in producing large numbers of particles with very uniform size distributions. Careful control of the particle size allows control of its absorption characteristics. Various composite materials have been studied [1,2] such as semiconductor nanocrystals of CdSe and their third order susceptibilities χ^3 have been measured. Various mechanisms are responsible for these large values including thermal effects, exciton mechanisms and electrostriction [3,4]. We consider the intrinsic nonlinearity of the nanoparticles as a primary source of the optical nonlinearity, but incorporate the effect of neighboring particles on the local field around a particle. Since the particles are free to move, then they will move closer together in regions of high electric field, further increasing the local field in the vicinity of any one of these particles. In the limit, a colloidal crystal could be generated which could result in intrinsic bistability or some degree of hysteresis in the bulk χ^3 behavior [5].

Recent work was reported by Guerrero and Mendoza [6] as well as Keller and Garm [7] demonstrating local field enhancements of nonlinear susceptibilities. In our model, we adopt the Clausius-Mossotti relationship to account for the local field at a point in a homogeneous medium bathed in an electric field. Once discrete nanoparticles are introduced, a homogeneous medium of these particles is assumed which generates new local fields in the vicinity of each particle. Assuming one illuminates the medium with a source having a Gaussian intensity profile, the particles will move toward the region of high intensity, as a result of the Lorentz force they experience. This force is directly proportional to the polarizability of the particle and the gradient of the squared local electric field. The polarizability of the particle is modeled to depend on the size and permittivity of the particle. The permittivity of the particle varies because of its intrinsic χ^3 arising from the quantum confinement effect; the Lorentz force experienced by the particle will also change. A mechanism therefore exists to develop a sequential procedure predicting where each particle or cluster of particles will move to after each time step, as a function of the local field generated by the nonlinear particles and the gradient of the electric field.

We have derived the relationships which model this behavior and numerically simulated the movement of the particles, the enhancement of the local field and the change in the bulk refractive index. The numerical simulation begins by assuming a random distribution of particles corresponding to an effectively homogeneous permittivity for the medium. Once the incident field is introduced, instantaneously, the force on each particle is determined; any one particle will move a distance determined by the squared magnitude of the field gradient, the magnitude of the particle's polarizability and the value of the local field. The movement need only be proportional to this quantity since the absolute distance shifted is not important, only the relative motion corresponding to an unspecified period of time between time increments.

The local electric field due to the host and the particles, is given by

$$E_{\text{loc}} = \frac{E(\mathbf{r})}{\left(1 - \frac{4\pi}{3} \alpha_0 N\right) \left(1 - \frac{4\pi}{3} \alpha_1 M\right)}$$

where we assume the nanoparticles are uniformly distributed throughout the medium with number density M . N is the number density of the host material's atoms and their average polarizability is expressed by α_0 ; α_1 is the polarizability of a nanoparticle which is a function of its permittivity

and hence its third order nonlinear susceptibility. Since the applied electric field is non-uniform across the material this equation is only valid provided the electric field does not vary too much within the area surrounding the particle of interest. Also, as the particles' positions change, their distribution will vary, requiring that the value of M to be position dependent. Hence the local field will differ from particle to particle and we can write

$$E_{\text{loc}}(r_i) = \frac{E(r_i)}{\left(1 - \frac{4\pi}{3} \alpha_0 N\right) \left(1 - \frac{4\pi}{3} \alpha_1(r_i) M(r_i)\right)}$$

All particles are moved as a function of the instantaneous local field and when they have all been re-positioned, a new set of local fields is calculated. In this way, each particle's effect on every other is included. We can increment time by choosing a scale factor to control how far a particle moves in any one direction, given that the magnitude of the force determines the relative displacement.

We present numerical results of this model, showing the change in bulk refractive index as a function of particle size, concentration and incident intensity. From these results it is possible to determine the optimal size and concentration to maximize the change in index and minimize the response time. These predictions are compared with experimental results using nanoparticles in water. We discuss the implications of the model for the design of some novel switching devices, which are optimal in the sense that particle sizes and concentrations have been chosen to maximize the magnitude of χ^3 .

References

- [1] R.K. Jain and R. C. Lind, J. Opt. Soc. Am. 73 647 (1983)
- [2] A.E. Neeves and M. H. Birnboim, J. Opt. Soc. Am. B6 787-796 (1989).
- [3] P.W. Smith, A. Ashkin and W.J. Tomlinson, Opt. Lett., 6 284 (1981).
- [4] D. Rogovin, Opt. News 12, 138, (1986).
- [5] J.W. Haus and R. Inguva, Proc. SPIE 1497, 350, (1991)
- [6] A. Guerrero and B. S. Mendoza, Opt. Soc. Am. B12 559 (1995)
- [7] O. Keller and T. Garm, Proc. CQO, Rochester NY (1995).

Second Harmonic Generation Studies of Porous Ice Films: Quantitative Measurements of Multilayer Physical Adsorption On Heterogeneous Surfaces

Jeanne M. Robinson, Bryan F. Henson, and Kevin R. Wilson

Los Alamos National Laboratory, Chemical Sciences and Technology Division, Mail Stop J567, Los Alamos, NM 87545 Phone: 505-665-4834 FAX: 505-665-4817

We present nonlinear light scattering measurements of the equilibrium, multilayer adsorption of molecular species on polycrystalline, porous ice films. The adsorption spectra are quantitatively modeled with the multilayer physical adsorption theory of Brunauer, Emmett and Teller (BET) and an extension based on the Bragg-Williams (BW) formalism which incorporates adsorbate-adsorbate interactions within the first layer. Although the polycrystalline, heterogeneous ice surfaces are likely characterized by adsorption site distributions broad both in energy and the size of local, homogeneous domains, these simple parameterizations model the data to high precision and imply a reduction in the effective complexity of the interface. The ability to quantitatively model adsorption onto a topologically complex, heterogeneous substrate from first principles renders many important systems amenable to quantitative study. For example, we have shown recently [1] that the physical adsorption of H₂O as islands on model polar stratospheric ice surfaces may be a controlling factor in the rates of some surface mediated chemical reactions important in seasonal ozone depletion.

We monitor the second harmonic light [2] generated in reflection from vapor deposited porous ice films of known total surface area during exposure to adsorbates [3]. The intensity of the nonlinear scattering process from an interface with n components can be expressed as a function of surface, coverage θ ,

$$I_{2\omega} = K^2 (I_{\omega})^2 \left(\sum_{n=1}^n \theta_n (\chi_n) \right)^2 \quad (1)$$

where K , I_{ω} , and A are constants describing the laser pulse and θ_n and χ_n are the surface coverage and scattering efficiency of the n^{th} chemical component of the interface [4]. Eqn. 1 simplifies to

$$I_{2\omega} = (\chi\theta)^2, \quad (2)$$

where the optical parameters are combined in χ , when one component dominates the scattering intensity. We use classical theories of physical adsorption to relate $I_{2\omega}$ to the amount of material adsorbed, θ (in units of monolayers). The unique advantage of this probe for studies of multilayer heterogeneous adsorption is the ability to characterize the distribution of adsorbing species among the layers in the adsorbing system. This distribution directly reflects the adsorption energies, as parameterized by the c constant in BET theory (*vide infra*).

The definition of the surface is central to the analysis and interpretation of the data in these experiments, and is not trivial for the high vapor pressure ice substrates under study, which are known to exchange on the order of 1000 monolayers per second with the vapor at these temperatures [5]. We adopt a simplified picture of the interface based on a flat substrate covered by well defined layers of adsorbate, as shown for an expanded pore surface in Fig. 1. Furthermore, in order to apply the BET and BW formalisms, which are essentially lattice treatments, we express the surface concentration as a fractional coverage based on the molecular area of an adsorbing molecule and the measured total surface area of the ice film. Specifically, the fraction of the substrate not covered by adsorbate is denoted θ_0 , and the fraction covered by

adsorbate $1-\theta_0$. The fractional coverage of successive layers is given by θ_i , where $i=1, 2$ denotes the first and second layers, with $\theta_1 = 1-\theta_0$ and $\theta = \sum \theta_i$. Both θ_0 and θ may be determined from the BET theory [6] as

$$\theta = \left(\frac{cx}{(1-x)[1+(c-1)x]} \right) \quad (3)$$

$$\theta_0 = \left(1 + \frac{cx}{(1-x)} \right)^{-1} \quad (4)$$

where $x = P/P_0$, the adsorbate pressure divided by the vapor pressure, and $c \sim \exp((Q_s - Q_a)/RT)$. Q_s and Q_a are the adsorbate-surface and adsorbate-adsorbate energy, and R is the gas constant. The analysis consists of associating $(I_{2\omega})^{1/2}$ with $1-\theta_0$ and fitting the spectra to the BET constant c .

We have measured the spectra for several adsorbates on H_2O ice films. In this summary, we will describe two systems which clearly illustrate BET and BET-BW behavior, namely the adsorption of toluene on water ice at 85K and of HCl on polycrystalline water ice at 160-180 K, respectively. Crystalline toluene melts at 178K, and vapor deposition of toluene ice films at ~ 80 K leads to the formation of a glassy phase with a glass transition at 100K [7] and crystallization at 145K. Adsorption of toluene on H_2O ice at 85K is thus expected to lead to an amorphous phase incommensurate with any substrate structural symmetry that is relatively far from any first order phase transition. We find that this system obeys BET theory, displaying an absorption spectra analogous to the calculated BET curve shown in Fig. 2, with $c=0.2$. This yields $\Delta Q = -0.27$ Kcal/mole, where $\Delta Q = Q_s - Q_a$, which compares favorably with the difference in the aromatic-aromatic and aromatic- H_2O binding energies from simple molecular cluster calculations [8].

HCl adsorption on polycrystalline water ice is a more complex system that is very important in heterogeneous atmospheric chemistry. The adsorption spectra for HCl on H_2O ice at 160 K is shown in Fig. 2. Much stronger dispersion forces are expected, with the formation of stable trihydrate, $HCl(H_2O)_3$, and hexahydrate, $HCl(H_2O)_6$, crystalline phases at these temperatures [9]. This system is also much closer to a first order phase transition, with melting observed near 200K for films grown in our apparatus. In fact, we have tentatively assigned the region of zero signal at low coverage in Fig. 2 to the formation of this 'quasi -liquid' phase on adsorption [9]. The adsorption of HCl on H_2O ice does not exhibit the simple BET behavior that describes toluene adsorption (Fig. 2). The simplest theoretical treatment of two dimensional thermodynamics which predicts a first order phase transition is the BW theory [6]. Proximity to a critical region of the phase diagram should be manifested as an inflection in a plot of pressure against volume, as is well known for the van der Waals equation. From the equation of state for the BET isotherm the surface spreading pressure ϕ , may be expressed as [10]

$$\phi = kT \ln \left(1 + \frac{cx}{(1-x)} \right) \quad (5)$$

Combining (4) and (5), it can be shown that at constant temperature the fraction of substrate covered by adsorbate $(1-\theta_0)$, is approximately equal to the surface pressure $\phi \propto kT(1-\theta_0)$. Plots of $(1-\theta_0)$ against θ are thus equivalent to an isothermal surface pressure-volume plot using the BET equation of state, and the inflections in the adsorption spectra of Fig. 2 are a result of nonideal behavior within an adsorbate layer, where lateral adsorbate-adsorbate interactions must be incorporated. This is completely analogous to the three dimensional result for the van der Waals equation of state. The Bragg-Williams modification of the BET isotherm results in a

modified constant in the normal BET equations, where c is replaced by a modified constant, $c' \sim c \exp(-Q_b \theta(1-x)/RT)$ [6]. The solid curves in Figure 2 are calculated from the BET-BW theory.

The ability to model the complex heterogeneous adsorption spectra in these experiments from first principles opens up a new regime of adsorption systems to experimental study. The intensity dependence in this nonresonant application of harmonic generation has proven sufficient to resolve the mean adsorption energies in these two systems. Resonant applications of second order polarization spectroscopies have been developed [11], and if applied as a scattering technique in transparent, porous matrices of known area, would enable detailed spectroscopic examination of adsorption physics.

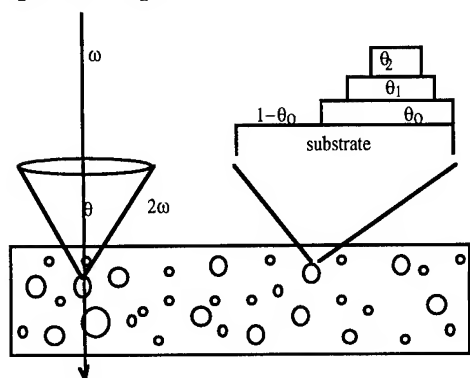


FIG. 1. Schematic of the experiment and the nomenclature describing the interface. The dashed rectangle defines the border of the porous ice film, depicted as circular pores of varying diameter, understood to be connected in a network accessible to the vapor. The film is illuminated by a laser pulse of frequency ω , and second harmonic light scattered from pore surfaces throughout the film is collected. The flat surface description is illustrated as a magnified pore surface covered by layers of adsorbate.

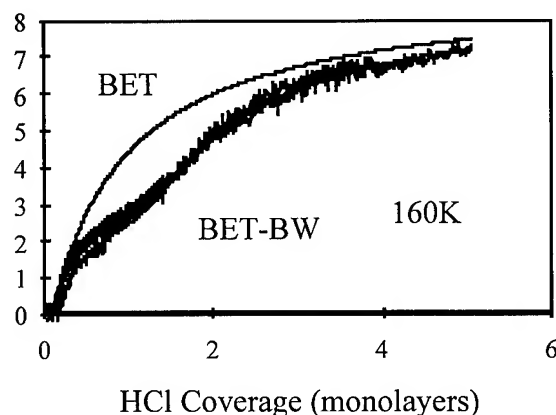


FIG. 2. Adsorption spectra of HCl on 0.5g H_2O at 160K (a), and 180K (b). Three spectra are plotted for $(I_{2\omega})^{1/2}$ as a function of coverage, θ . The solid curve labeled BET was calculated from the BET theory using $c=1.21$. The curves through the spectra, labeled BET-BW, were calculated from the full BET Bragg-Williams adsorption theory using $c=1.21$ and $\exp(Q_b/RT) = 0.10$ and 0.08 .

REFERENCES

- [1] B. F. Henson, K. R. Wilson and J. M. Robinson, *Geophys. Res. Lett.* (submitted)
- [2] Y. R. Shen, *The Principles of Nonlinear Optics* (Wiley-Interscience, Toronto, 1984); Y. R. Shen, *Optical Second Harmonic Generation at Interfaces*, *Ann. Rev. Phys. Chem.* **40**, 327 (1989).
- [3] B. F. Henson, and J. M. Robinson *SPIE Proceedings, Laser Techniques for Surface Science*, 2125, 140 (1994).
- [4] Andrews, D. L., *Molecular Theory of Harmonic Generation*, in *Modern Nonlinear Optics, Part 2*, edited by M. Evans and S. Kielich, *Adv. Chem. Phys.* **85**, 545 (1993).
- [5] D. R. Haynes, N. J. Tro, and S. M. George, *J. Phys. Chem.* **96**, 8502 (1992).
- [6] W. Rudzinski and D. H. Everett, *Adsorption of Gases on Heterogeneous Surfaces*, (Academic Press, San Diego, 1992).
- [8] J. A. Menapace and E. R. Bernstein, *J. Phys. Chem.* **91**(10) 2533-2544 (1987).
- [7] Alba, C., L. E. Busse, D. J. List, and C.A. Angell, *J. Chem. Phys.* **92**(1), 617-624 (1990).
- [9] J. P. D. Abbatt, et al., *J. Geophys. Res.* **97**, 15,819 (1992); D. R. Hanson and A. R. Ravishankara, *J. Phys. Chem.* **96**, 2682 (1992); L. T. Chu, M.-T. Leu, and L. F. Keyser, *J. Phys. Chem.* **97**, 7779 (1993).
- [10] T. L. Hill, *An Introduction to Statistical Thermodynamics*, (Dover, Toronto, 1986).
- [11] Du, Q., E. Freysz, and Y. R. Shen, *Phys. Rev. Lett.* **72**, 238 (1994); Du, Q., R. Superfine, E. Freysz, and Y. R. Shen, *Phys. Rev. Lett.* **70**, 2313 (1993).

A Comparison of Chlorinated Fluoride Glasses for Obtaining Red Upconversion Fluorescence in Praseodymium for a Three-Color Solid-State 3D Display

E. A. Downing, L. Hesselink

Electrical Engineering Dept., Stanford University, Stanford CA 94305-4035

R. M. Macfarlane

IBM Almaden Research Center, 650 Harry Rd, San Jose, CA 95120-6099

N. F. Borrelli, R. Bartholomew, M. Newhouse

Corning Inc., Corning, NY 14831

We have demonstrated an RGB solid-state 3D display based on two-step, two-frequency (TSTF) upconversion in bulk rare earth doped heavy metal halide glasses.^{1,2} Figure 1a shows the basic two-step absorption process and figure 1b shows how two scanned pump lasers are made to intersect inside a bulk sample of active material to create three-dimensional images. Green upconversion fluorescence is obtained by pumping trivalent erbium doped glasses with 1.5 μm and 850 nm, and blue from pumping Tm^{3+} doped glasses with 800 nm and 1120 nm. Figure 2 shows the energy level diagrams of these three ions along with the respective resonant pump wavelengths and emission lines.

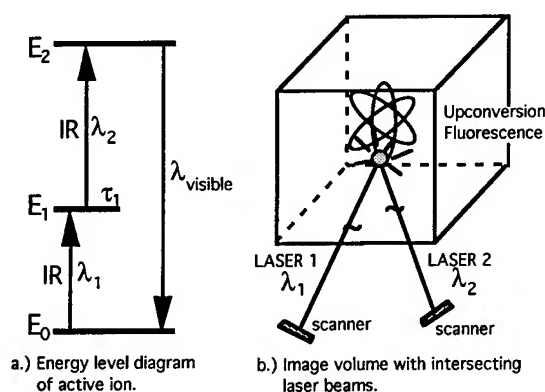


Figure 1. Basic concept.

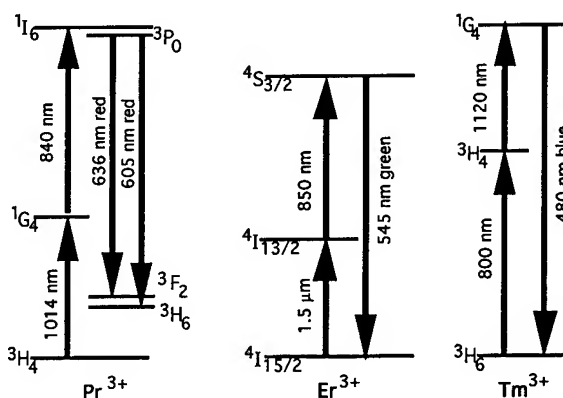


Figure 2. Energy level diagrams of Pr^{3+} , Er^{3+} , and Tm^{3+} .

Red upconversion fluorescence, which is obtained from trivalent praseodymium doped materials, is difficult to induce because of the low absorption associated with the $^3\text{H}_4 - ^1\text{G}_4$ transition. The efficiency of this transition is very sensitive to the composition of the host glass in which the ion is doped. TSTF upconversion to red in Pr^{3+} has been characterized in terms of dopant concentration, ground state absorption cross section, intermediate level lifetime, and pixel brightness in several different host glass compositions. A rate equation analysis of praseodymium, under the excitation conditions required for this display has yielded a figure of merit for quantifying material performance that relies on measurable optical properties.

Figure 3a shows the complete 12-level energy diagram of trivalent praseodymium, and figure 3b shows the simplified 5-level model³ used to analyze the system. Pixel power, P_f , which is defined as the total power emitted from a pixel at the intersection of the two pump laser beams, is described by equation 1. In this equation, P_1 and P_2 are the powers of the two pump laser beams and A is the spot size, \hbar is Planck's constant, ω_{ij} are the transition frequencies between the levels, N_T is the dopant concentration, V is the voxel volume, σ_1 and σ_2 are the ground state and excited state absorption cross sections, and τ_s is the excitation period. The term ξ is the fraction of the light

emitted in the useful bandwidth, and can be obtained from a calculation of the branching ratios to the different final states. Voxel brightness is maximized when the excitation period τ_s is greater than or equal to the intermediate level lifetime τ_1 . Under a consistent set of pumping conditions, the figure of merit (FOM) shown in equation 2 can be used to predict pixel brightness in a particular material system.

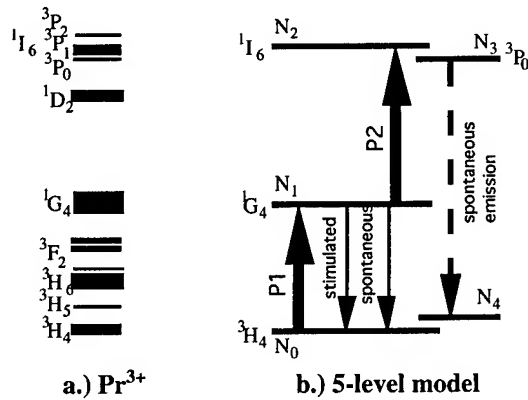


Figure 3. Energy level diagrams of Pr^{3+} .

$$P_f = \xi \left(\frac{P_1 P_2}{A^2} \right) \left(\frac{\hbar \omega_{34}}{\hbar \omega_{01} \hbar \omega_{12}} \right) N_T \tau_s \sigma_1 \sigma_2 V \quad (1)$$

$$\text{FOM} = N_T \tau_s \sigma_1 \sigma_2 \quad (2)$$

Several fluoride glasses were investigated including standard ZBLAN ($53 \text{ ZrF}_4 * 20 \text{ BaF}_2 * (4-x) \text{ LaF}_3 * 3 \text{ AlF}_3 * 20 \text{ NaF} * x \text{ PrF}_3$), ZBLN ($58\% \text{ ZrF}_4 * 15 \text{ BaF}_2 * (6-x) \text{ LaF}_3 * 21 \text{ NaF} * x \text{ PrF}_3$) in which the AlF_3 was completely removed, and variations thereof in which the NaF was systematically replaced with NaCl.⁴ The results of the optical measurements are compiled in table 1. Praseodymium suffers from a weak ($2.1 \times 10^{-21} \text{ cm}^2$) ground state absorption cross section into the $^1\text{G}_4$ level, and glass compositions in which this cross section can be increased provide higher efficiency hosts for applications involving direct pumping of this transition. Chlorinated ZBLN glasses showed longer $^1\text{G}_4$ lifetimes and higher absorption cross sections than did the standard ZBLAN composition with the same dopant concentration. As shown in figure 4, complete substitution of the NaF with NaCl in a chlorinated zirconate glass with no aluminum showed an increase in total emitted pixel power (P_f) of more than a factor of two over the standard ZBLAN composition under the same excitation conditions. These improvements have been attributed to the removal of the light weight AlF_3 which has a high phonon energy, and to the increased non-centrosymmetric environment around the rare earth sites created by the chloride anions.

Glass	Composition (with .1% PrF_3)	% NaCl	$\sigma_1 (\times 10^{-21} \text{ cm}^2)$	$\tau_1 (\mu\text{sec})$	$P_f (\mu\text{W})$
ZBLAN	53ZrF ₄ 20BaF ₂ 3.9LaF ₃ 3AlF ₃ 20NaF	0	1.81	120	.62
ZBLN	58ZrF ₄ 15BaF ₂ 5.9LaF ₃ 21NaF	0	1.87	126	.60
ZBLNa(F/Cl)	58ZrF ₄ 15BaF ₂ 5.9LaF ₃ 15.75NaF 5.25NaCl	5.25	1.91	150	.81
ZBLNa(F/Cl)	58ZrF ₄ 15BaF ₂ 5.9LaF ₃ 10.5NaF 10.5NaCl	10.5	1.98	147	1.03
ZBLNa(F/Cl)	58ZrF ₄ 15BaF ₂ 5.9LaF ₃ 5.25NaF 15.75NaCl	15.75	2.09	144	1.06
ZBLNaCl	58ZrF ₄ 15BaF ₂ 5.9LaF ₃ 21NaCl	21	2.12	183	1.27

Table 1. Measured optical properties of fluorozirconate glasses.

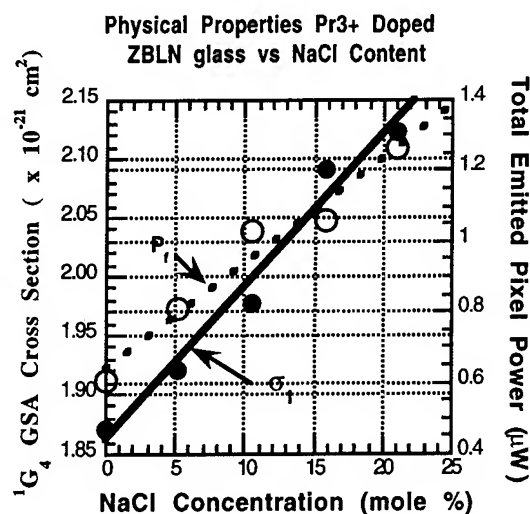


Figure 4. 1G_4 Absorption cross sections and total emitted pixel power vs NaCl content in Pr^{3+} doped ZBLN glass.

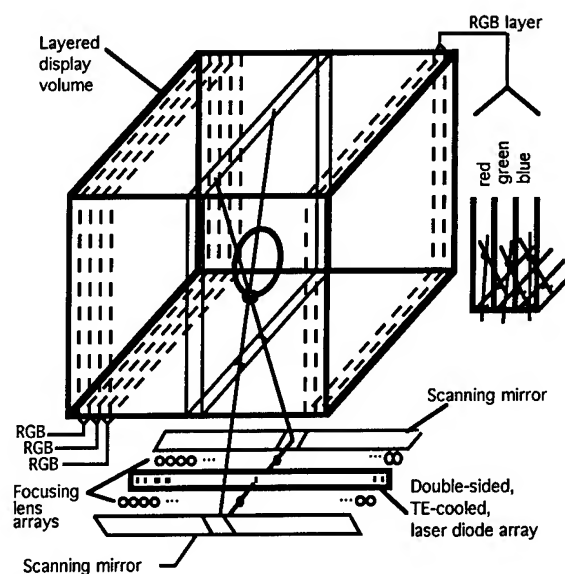


Figure 5. Layered device architecture for obtaining a wavelength-addressable three-color solid-state 3D display.

Figure 5 illustrates the conceptual full scale system architecture of a layered, wavelength-addressable, RGB solid-state 3D display. We have demonstrated a small scale three-color prototype in a single RGB layer. In this system, the individual colors are addressed in separate, parallel layers, each of which has been optimized in terms of host glass composition and dopant concentration for that particular ion. Separation of the ions into different layers is necessary because mixing of all three dopants into a single monolithic bulk medium, at concentrations required to optimize pixel brightness (0.5 mole % per ion), has resulted in cross-relaxation energy transfer processes that reduce upconversion efficiencies. Layering also provides for spatial separation of the pump wavelengths used to address the different colors as erbium, for instance, will undergo single frequency upconversion to green when pumped with 800 nm, which is the first wavelength used to excite blue fluorescence in the Tm^{3+} doped layer. Chlorinated zirconates are processed under the same conditions as ZBLAN and can be readily cast into thicknesses of up to 5 mm. This feature along with their other optical properties make them potential host candidates for obtaining red upconversion fluorescence from praseodymium for solid-state 3D display applications. Host materials with higher cross sections should yield further improvements to device performance.

- ¹ Downing, Hesselink, Klein, Evans, Ralston, Macfarlane, Conference on Lasers and Electro-Optics, CTuE, (1996)
- ² J. D. Lewis, C. M. Verber, and R. B. McGhee, IEEE Trans. Elec. Dev., **ED-18**, 724 (1971).
- ³ A. C. Tropper, J. N. Carter, R. D. T. Lauder, D. C. Hanna, S. T. Davey, and D. Szebesta, J. Opt. Soc. Am. B, **11**, 866, (1994).
- ⁴ S. Inoue, K. Soga, A. Makishima, J. Am. Cer. Soc., **76**, 6, p. 1591 (June 1993).

Excitonic Enhancement of Third-order Optical Nonlinearity in Regioregular Head-to-Tail Coupled Poly(3-Hexylthiophene)

H. Kawahara, Y. Ueno, N. Morito, and K. Ema

Department of Physics, Sophia University
7-1 Kioi-Cho, Chiyoda-Ku, Tokyo 102, Japan
phone;81-3-3238-3432, fax;81-3-3238-3341

M. Rikukawa and N. Ogata

Department of Chemistry, Sophia University
7-1 Kioi-Cho, Chiyoda-Ku, Tokyo 102, Japan

1. Introduction

Conducting polymers are of interest for its application to novel electro-optical devices and ultrafast all-optical devices. Over the past few years it has become apparent that the electrical and optical properties are strongly influenced by their morphology and molecular organization. Although several groups have reported that the control of regularity and orientation in the polymetric structure leads to remarkable enhancements in the electrical properties [1], the enhancement in optical nonlinearity has not been reported. We measure the third-order nonlinearity of regioregular head-to-tail coupled poly(3-hexylthiophene) (HT-PHT) and regiorandom poly(3-hexylthiophene) (R-PHT) using degenerate four-wave mixing (DFWM). we observe the enhancement of third-order optical nonlinearity around exciton resonance in HT-PHT.

2. Preparation of poly(3-hexylthiophene)

We use the thin films of HT-PHT and R-PHT, which are prepared by spin-coating method. HT-PHT and R-PHT are synthesized by following procedures. Structurally homogeneous poly(3-hexylthiophene) is synthesized in a one-flask reaction consisting of metalation of 2-bromo-3-n-hexylthiophene selectively at the 5-position, followed by trapping the 2-bromo-3-n-hexyl-5-lithiothiophene with magnesium bromide etherate to afford 2-bromo-5-(bromomagnesio)-3-n-hexylthiophene. Subsequent treatment of 2-bromo-5-(bromomagnesio)-3-n-hexylthiophene, in situ with bis(1,3-diphenylphosphinopropane)nickel(II) chloride, led to HT-PHT as described by McCullough et al. [2]. R-PHT is also prepared according to the method of Sugimoto et al [3]. The isolated polymer was purified by continuous Soxhlet extractions with methanol and acetone for one week each. The structural regularity of HT-PHT is examined by ^1H NMR spectroscopy. Figure 1 shows the expanded atomic region of ^1H NMR spectra of HT-PHT and R-PHT. Four singlets in the aromatic region of R-PHT can be clearly attributed to the four-protons with each peak representing the different types of

trimeric sequences of HT-HT (δ 6.98), HT-HH (δ 7.00), TT-HT (δ 7.02), and TH-HH (δ 7.05) linked thiophene rings. In constant, only one sharp band of the proton in the 4-position of the thiophene rings, which reveals the HT-HT couplings, is observed in the ^1H NMR spectrum of the HT-PHT obtained. The absorption spectrum are shown in Fig.2. The absorption peak energy of HT-PHT is lower than that of R-PHT, and the spectral width of HT-PHT is narrower than that of R-PHT. This suggests that HT-PHT chain has a more rod-like conformation with longer conjugation length, while R-PHT chain has more coil-like conformation with shorter conjugation length. In the view of solid state physics, these narrow and red-shifted absorption is attributed to Frenkel exciton. In Frenkel exciton model, long conjugation length corresponds to long coherence length of the exciton.

3. Degenerate four-wave mixing experiments

In DFWM experiment, we use 150-fs pulses from optical parametric amplifier (OPA) seeded by amplified mode-locked $\text{Ti:Al}_2\text{O}_3$ laser. Changing the wavelength of the pulses around exciton resonance, we observe resonant enhancement of the DFWM signals as shown in Fig.3. While the DFWM signals of R-PHT even around exciton resonance are so weak that we cannot measure the absolute intensity of them. By scanning the time delay between two pulses, we confirm that the obtained DFWM signals are not caused by thermal effects. The obtained phase relaxation time is shorter than the pulse width. It is known that Frenkel exciton exhibits large optical nonlinearity because of its mesoscopic enhancement of the dipole moment. The effect of the enhancement increases with increasing the coherence length of Frenkel exciton. The observed enhancement of nonlinearity is attributed to long coherence length of the exciton in HT-PHT.

In conclusion, we observe that the control of regularity in the polymetric structure leads to remarkable enhancements in optical nonlinearity.

References

- 1 For example, T.-A. Chen, X. Wu, and R. D. Rieke, *J. Am. Chem. Soc.*, **117**, (1995) 233.
- 2 R. D. McCullough, R. D. Lowe, and M. Jayaraman, and D. L. Anderson, *J. Org.Chem.*, **58**, (1993) 904.
- 3 R.Sugimoto, S. Takeda, H. B. Gu, and K.Yoshino, *Chemical Express*, **1**, (1986) 635.
- 4 E. Hanamura : *Phys. Rev.* **B37** (1988) 1273.
E. Hanamura : *Phys. Rev.* **B38** (1988) 1228.

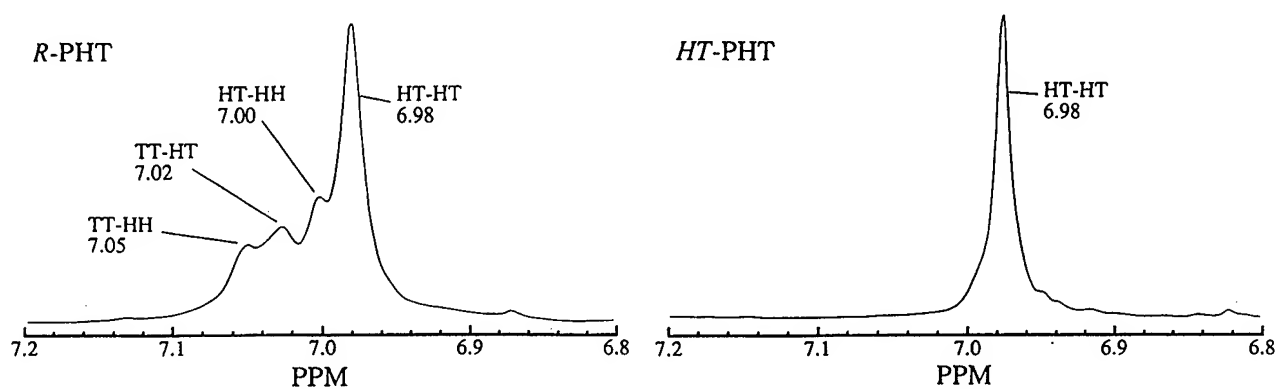


Fig. 1. Expanded ^1H NMR spectra of poly(3-hexylthiophene) aromatic region of HT-PHT and R-PHT

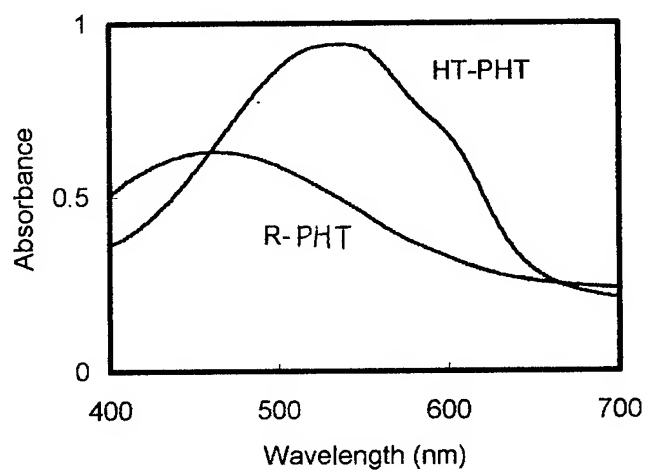


Fig.2. The Absorption Spectrum of HT-PHT and R-PHT

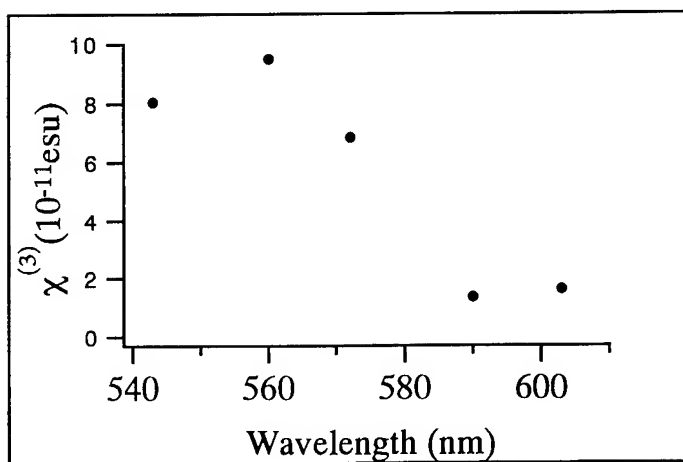


Fig.3. $\chi^{(3)}$ of head-to-tail coupled poly(3-hexylthiophene)

Femtosecond non-degenerate four wave mixing in C₆₀/polymer blends

Eric Maniloff, Duncan McBranch, Hsing Lin Wang, and Ben Mattes

Chemical Science and Technology Division

CST-6

Mail Stop J585

Los Alamos National Laboratory

Los Alamos, NM 87545

ph:(505) 667-9777 fax: 665-4817

Transient holographic gratings using third-order nonlinear optical processes have been suggested as possible elements for a variety of optical applications, particularly in the areas of interconnection networks and optical computing. Many of the materials suggested for applications relating to holographic optical processing rely on effects such as photorefractivity or photo-isomerization, both of which occur on time scales of milliseconds to minutes [1]. While these materials are well suited to applications such as optical storage, faster materials have a higher probability of proving useful for real-time processing. Recently it has been discovered that in certain polymers doped with C₆₀, charge transfer occurs after excitation across the $\pi - \pi^*$ energy gap of the polymer to the dopant C₆₀ molecules [2]. Using transient absorption measurements, it has been shown that this charge-transfer process occurs at times shorter than 300 fs, and can persist up to millisecond time-scales. Since the third order nonlinear optical susceptibility, $\chi^{(3)}$, includes a component which is related to the excited charge distribution, charge transfer to C₆₀ can be used to increase the lifetime of this incoherent contribution to $\chi^{(3)}$ in polymers.

Most studies of $\chi^{(3)}$ in polymer systems are performed using a degenerate four-wave mixing geometry. In this geometry a trade-off in maximizing the signal intensity exists; using a resonant wavelength increases the third order nonlinear response, but also decreases the signal intensity due to the absorption of the probe wave. However, using a non-degenerate four wave mixing geometry, the pump waves can be at a resonant wavelength to increase the value of $\chi^{(3)}$, while the probe wave can be non-resonant to increase the signal intensity. Using this geometry, four wave mixing experiments have been conducted in poly(3-hexyl thiophene) (P3HT) using both pure and C₆₀-doped samples. The second harmonic of a ti:sapphire laser (400 nm) was used to generate two pump waves, incident on the sample with a crossing angle of 7 degrees. The fundamental wavelength (800 nm) was used as forward propagating probe wave, and was delayed relative to the pump waves to monitor the time dynamics. The

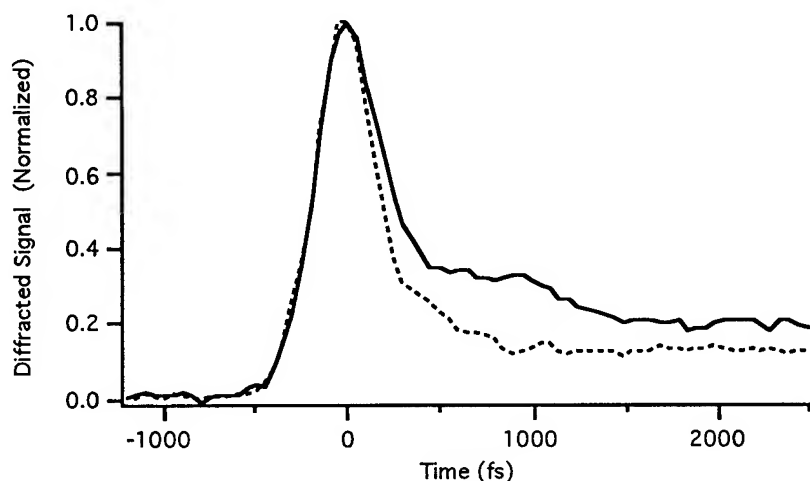


Figure 1: Four wave mixing signals in pure PT (dashed) and 20 wt% C₆₀-doped PT.

800 nm probe light is close to the maximum of the induced absorption arising from the C₆₀⁻ molecules. In addition to the four wave mixing data, transient absorption measurements were taken pumping with 400 nm light and probing with 800 nm light to monitor the dynamics of the charge transfer process. The laser pulse width at the sample was approximately 250 fs.

Fig. 1 shows the four-wave mixing signals in both pure and 20 wt% C₆₀-doped P3HT. The data have been normalized for clarity, however the maxima of the two curves differ by less than 20%. It is evident from these two curves that both are dominated by a rapidly decaying component, completely decaying in less than 400 fs. This rapid decay has previously been observed [3], and has been assigned to a photoinduced exciton with a 100 fs lifetime. In experiments conducted at higher intensities the long lived contribution and the transient absorption signal are observed to saturate, while the peak of the fast component to the four-wave mixing signal continues to increase. This indicates that the fast four-wave mixing signal also includes a large contribution from the coherent part of $\chi^{(3)}$, which continues to increase after the excited state absorption saturates. The addition of C₆₀ to the samples is found to have no observable effect on this component. However, on longer time scales the charge transfer is found to increase the strength of the diffracted signal.

Transient absorption experiments conducted on these samples have clearly demonstrated that the primary contribution to the induced absorption for time scales greater than 500 fs results from the charge transfer to C₆₀. Probing the transient absorption at 800 nm provides a means of monitoring the dynamics of the charge transferred state. The portion of the diffracted signal that results from the induced absorption of the C₆₀⁻ and charged states of the polymer is expected to vary as the square of this

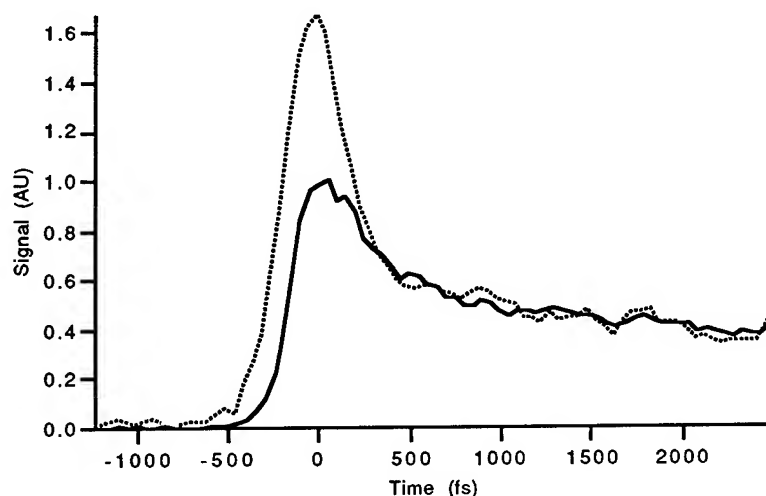


Figure 2: Holographic signal (dotted line) and the square of the transient absorption signal (solid line).

signal. Fig. 2 shows the holographic signal for the 20 % C_{60} -doped sample plotted with the square of the transient absorption signal. These two signals have been scaled such that they are equal at a delay time of 500 fs. As expected, the two signals show similar decay characteristics for times greater than 500 fs. This is a clear indication that the charge transfer results in the primary contribution to the incoherent $\chi^{(3)}$ in this system. The transient absorption signals have been studied in detail for time scales up to 100 ps for a variety of dopant concentrations. It has been observed that for 25 wt % C_{60} -doped P3HT, 70% of the maximum induced absorption remains at a delay time of 100 ps.

These results indicate that C_{60} -doped polymers can be used as third order nonlinear optical materials. Varying the C_{60} doping provides a means of tailoring the nonlinear response for different applications. Additional research is being conducted into similar effects in other charge-transfer systems and in the use of ordered multi-layer structures to enhance the nonlinear effects.

References

- [1] H. Eichler, P. Günter, and D. Pohl, *Laser-Induced Dynamic Gratings* (Springer-Verlag, 1986).
- [2] B. Kraabel, D. McBranch, N. Sariciftci, D. Moses, and A. Heeger, "Ultrafast spectroscopic studies of photoinduced electron transfer from semiconducting polymers to C_{60} ," *Phys. Rev. B* **50**, 543 -551 (1994).
- [3] Y. Pang and P. Prasad, *J. Chem. Phys.* **92**, 2201 - 2206 (1990).

The optical polarizability of excited C₆₀ molecules

Huapeng Guan, Robert W. Hellwarth, Jouni P. Partanen, and Nansheng Tang

Department of Physics, University of Southern California

Los Angeles, CA 90089-0484

Tel: (213) 740 4384, Fax: (213) 740 6653, e-mail: huapeng@physics.usc.edu

Over a dozen reports of optically-induced changes of up to a factor of 5 in the absorption cross-section of the C₆₀ molecule at 532 nm¹ have prompted us to investigate whether there might be a correspondingly large change in the (in-phase) polarizability of C₆₀ at the same wavelength. Unfortunately for nonlinear optical applications, we have found a negative answer: the change is less than 3% for the polarizability of C₆₀ upon excitation to either the lowest singlet or triplet state. In the course of this investigation, we have made, we believe, a more accurate determination of the absorption cross-sections σ_S and σ_T of the lowest excited singlet and triplet states of C₆₀ molecules. This is achieved with a picosecond pump-probe technique not previously applied to C₆₀. Our measurements of the polarizability changes were done with time-delayed degenerate four-wave mixing experiments. Our experiments were performed in a solution of 0.68 g/L of C₆₀ in benzene.

To measure the optically-induced change in absorption, we employ a 30-ps laser 'pump' pulse at 532 nm and observe the transmission of a 30 ps 'probe' pulse at 532 nm that is delayed in steps from the pump pulse by zero to 11 ns. In Fig. 1 we present the results of such pump-probe experiments where the measured transmission of the delayed probe pulse is shown as a function of delay time for various values of the pump-pulse energy flux F . From the data of Fig.1 we can evaluate the difference between excited-state and ground state absorption cross-sections $\sigma_e = \sigma_S = \sigma_T$ and σ_g of C₆₀ molecules using the formula:

$$\ln\left(\frac{T_0}{T_1}\right) = \frac{(\sigma_e - \sigma_g)(1 - T_0)\varepsilon}{h\nu} F \quad (1)$$

Here T_0 and T_1 are the fractional probe transmissions at zero pump flux and pump flux F (mJ/cm²), respectively. The fraction of absorbed photons that create an excited C₆₀ is ε . In Fig.2 $\ln(T_0/T_1)$ is shown as a function of the pump-pulse energy flux F , where the solid center line is a least-square fit to Eq.(1), assuming $\varepsilon = 1$, and gives $\sigma_e - \sigma_g = (8.8 \pm 0.7) \times 10^{-18}$ cm², with the uncertainty here corresponding to the upper and lower thin lines. From the low intensity transmission we find that the absorption cross-section at the ground state to be 3.5×10^{-18} cm²

with similar errors. These results lie near the middle of a variety of reported results that span a range at least three times our uncertainties.¹

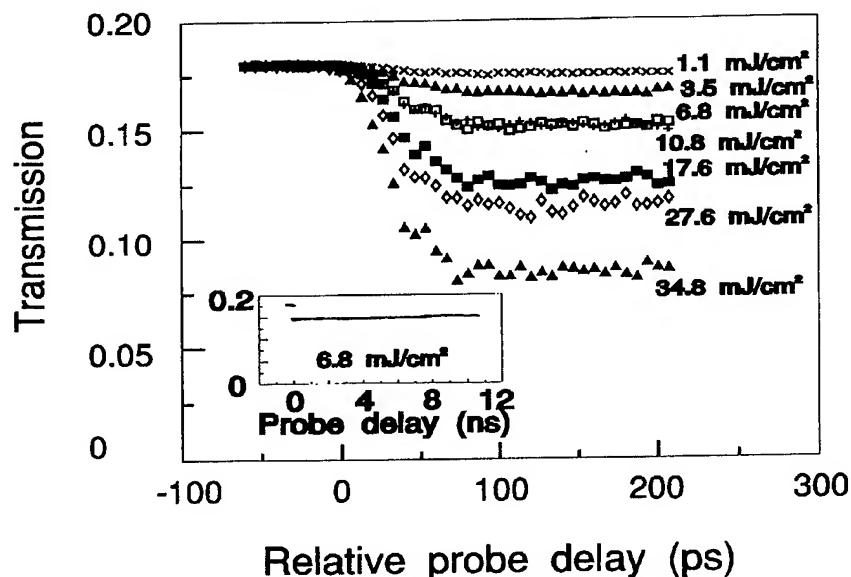


Fig. 1. Transmission of a 'probe' pulse at 532 nm vs its delay from a 'pump' pulse for various fluence F . The insert shows a typical (for the case of 6.8 mJ/cm^2) time dependence in the transmission for longer times.

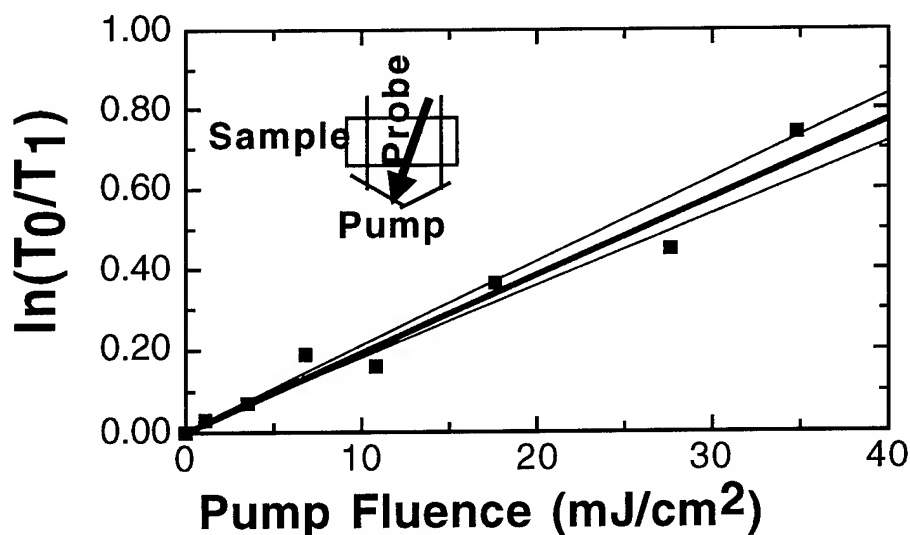


Fig. 2. Logarithm of the normalized transmission $\ln(T_0/T_1)$ as a function of the pump fluence. The center solid line is a least square fit of the data to Eq. (1). The beam configuration for the pump-probe experiment is shown as an insert.

The absorption cross-section is related to the imaginary part of the molecular polarizability. In order to measure the real part of the molecular polarizability of excited state of C₆₀, we perform time-resolved degenerate four-wave mixing experiments with the C₆₀/benzene solution. Fig.3

presents the data of a typical such experiment. We fit the data using a model of diffraction from both an excited-state polarizability grating² and laser-induced acoustic waves³. We find that the real part of the polarizability of the excited state of C₆₀, α_e' , is identical to that of the ground state $\alpha_g' = 92.1 \times 10^{-24} \text{ cm}^3$ within our experimental limits: $-0.3 \times 10^{-24} \text{ cm}^3 \leq \alpha_e' - \alpha_g' \leq 3.3 \times 10^{-24} \text{ cm}^3$. The difference between the imaginary parts of the polarizability α_e'' of the excited state and α_g'' of the ground state is calculated from the pump-probe data to be $\alpha_e'' - \alpha_g'' = 4.4 \times 10^{-24} \text{ cm}^3 \pm 6\%$.

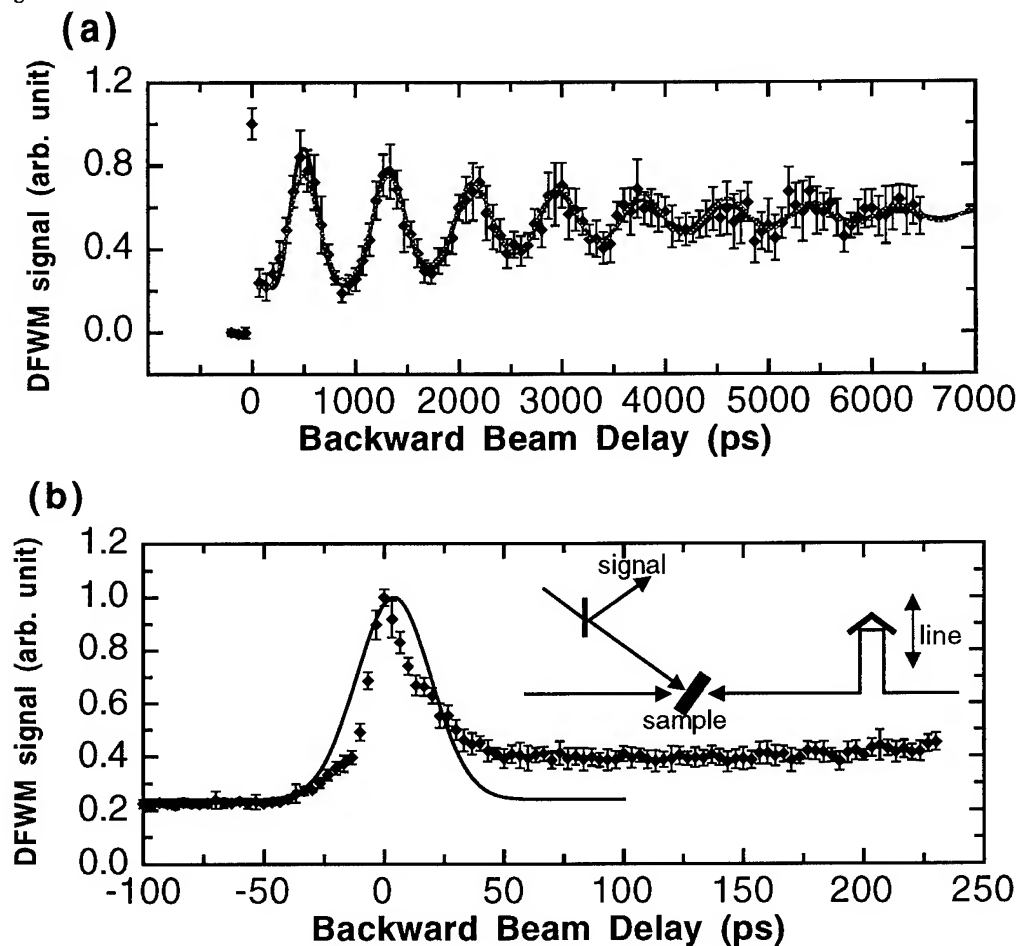


Fig. 3. Degenerate four-wave mixing signal from a C₆₀/benzene solution vs delay of backward beam in the 'phase-conjugating' geometry. The angle between the two forward beams is 17.3°. The schematic of the experimental set-up is shown as an insert in (b). (a) Time range of backward beam delay is ~ 6.5 ns. (b) Data Magnifying the first six points in (a), together with signal from pure CS₂ (solid line) under the same conditions.

References

1. N. Tang, Ph. D. Thesis, U.S.C., 1994.
2. J. R. Saledo, A. E. Siegman, D. D. Dlott, and M.D. Fayer, Phys. Rev. Lett. **41**, 131 (1978).
3. M. D. Fayer, IEEE J. Quantum Electron. **QE-22**, 1437(1986).
4. S. L. Ren, Y. Wang, A. M. Rao, E. McRae, J. M. Holden, T. Hager, K. Wang, W. T. Lee, H. F. Ni, J. Selegue, and P. C. Eklund, Appl. Phys. Lett. **59**, 2678 (1991).

Electric Field Thermopoling of High Dipole Guests when Considered as Ellipsoids

G.H. Cross and D. Healy, University of Durham, Department of Physics, South Road, Durham, UK, DH1 3LE. +44 191 374 2577 (FAX : +44 191 374 3848)

It has become common practice to neglect both the molecule's shape and the features of its polarisability anisotropy when applying local field correction factors to studies of the nonlinear optics of dissolved chromophores. Thus the Lorentz-Lorenz and Onsager local field correction factors in common usage are often expressed, respectively, by the following;

$$f(\omega) = \frac{n^2 + 2}{3} \quad \text{and} \quad f(0) = \frac{\epsilon(n^2 + 2)}{2\epsilon + n^2}, \quad \text{in which } \epsilon \text{ and } n \text{ are taken to be the relative permittivity}$$

and refractive index, respectively of the medium. Thus both the host and the guest are assumed to be optically and electrically identical. Since this is clearly not the case for most of the two-component media studied it is merely fortuitous that this usage returns values which are close to those obtained using a more rigorous approach. Particularly in the case of the optical local field factor, consideration of a spherical guest cavity uniformly occupied by a medium (the guest) of average polarisability identical to that of the host is a good approximation under nearly all situations. Even in the case of the Onsager factor this assumption remains acceptable if not rigorously defensible. In the original discussions of local field factors mostly arising around the middle of this Century however, the evolving descriptions of Debye and Onsager, and others, explicitly required account to be taken of the differing properties of the solvent and solute and of the molecular anisotropy⁽¹⁻⁴⁾. Development of the Onsager approach by Scholte (and Böttcher) to account for the ellipsoidal character of dipolar solutes was taken up recently by Myers and Birge⁽⁵⁾ to provide more accurate determinations of dipole moments from solution dielectric constant measurements. Furthermore, the application of ellipsoidal local field correction factors to studies in organic nonlinear optics may become more commonplace given the recent findings of Dehu et al. correlating self consistent reaction field calculations (assuming ellipsoidal cavity geometries) with Hyper Rayleigh Scattering studies, as a function of reaction field⁽⁶⁾.

We are studying the properties of a range of organic chromophores which appear to possess high ground state dipole moments in solution (solid or liquid phase)⁽⁷⁾. Here, the ellipsoidal cavity assumptions are necessary to adequately describe the local fields but in particular we must further consider the averaging of the local field tensor which in the presence of high force couple between guest dipole and field becomes, itself, field dependent. Such a situation may arise during corona charging of thin films containing these chromophores.

We consider only one component of the macroscopic local field tensor, F_{ZZ} , taken to represent that which influences an applied field, E_Z to produce the local field, E_L acting across the film thickness. F_{ZZ} is assembled from the population averages of the Z-axis projected microscopic local field tensor components of the solution's components. The host medium is taken to be isotropic thus we consider only the guest molecules and, in the initial exercise, take only the diagonal

components of the polarisability tensor, α_{xx} , α_{yy} , α_{zz} , into account. In addition, the molecular frame of reference is defined such that the molecular 'long' axis, the z axis is parallel to the dipole moment. Thus the macroscopic average local field factor becomes

$$F_{ZZ} = \langle f_{xx} \rangle + \langle f_{yy} \rangle + \langle f_{zz} \rangle \quad (1)$$

in which $\langle f_{ij} \rangle$, ($i = j$), are the population orientational averages of the diagonal microscopic local field tensor components. The terms on the right hand side of (1) may be determined assuming the same statistical arguments commonly used to describe orientation processes in EFISH studies or in electric field poling studies of polymers. However, here, we are evaluating the electric field dependence of the local field factor itself, and, furthermore, are explicitly taking account of the two azimuthal components of the molecular polarisability. In our model, we consider that f_{xx} and f_{yy} contribute to F_{ZZ} in statistically equal amounts thus assuming uniaxial symmetry in the bulk sample during poling.

Following Scholte⁽³⁾, the individual microscopic local field tensor components are given in the ellipsoidal model by

$$f_{ij} = \frac{\epsilon}{\epsilon + (n_{ij}^2 - \epsilon)A_i}, (i = j) \quad (2)$$

where ϵ represents the host's relative permittivity and A_i is the ellipsoidal shape factor accounting for the ratio of the lengths of the principle semi-axes of the ellipsoid, a, b and c. Consideration of the polarisability tensor properties is introduced through the 'internal refractive index', n_{ij} , given by

$$n_{ij}^2 = \frac{abc + 3(1 - A_i)\alpha_{ij}}{abc - 3A_i\alpha_{ij}} \quad (3)$$

The population orientation averages of f_{ij} are computed using second order Langevin function solutions to the normalised population orientation distribution integrals and we thus find

$$F_{ZZ} = \left[1 + \frac{2}{p^2} - \frac{2}{p} \coth(p) \right] f_{zz} + \left[\frac{1}{p} \coth(p) - \frac{1}{p^2} \right] [f_{xx} + f_{yy}] \quad (4)$$

in which $p = \frac{\mu E_L}{kT}$. Note, however that $E_L = F_{ZZ} E_Z$, and thus equation 4 requires solution by a method offering self consistency. As a first approximation, we use a seeded iteration technique with the following initial value for the the local field factor

$$F_{ZZ}(0) = \frac{1}{3}(f_{xx} + f_{yy} + f_{zz}) \quad (5)$$

Using computed values for the polarisabilities (MOPAC v6, AM1 Hamiltonian) and molecular modelling to determine approximate dimensions we show below the effect on F_{ZZ} for applied fields up to 200 MVm^{-1} when considering a molecule of dipole moment 30 D and values for the (gas phase) polarisabilities, $\alpha_{xx} = 8 \times 10^{-24} \text{ esu}$, $\alpha_{yy} = 40 \times 10^{-24} \text{ esu}$, $\alpha_{zz} = 150 \times 10^{-24} \text{ esu}$ and molecular dimensions, $a = 3 \text{ \AA}$, $b = 8 \text{ \AA}$, $c = 10 \text{ \AA}$. A medium permittivity, ϵ , of 4 is assumed.

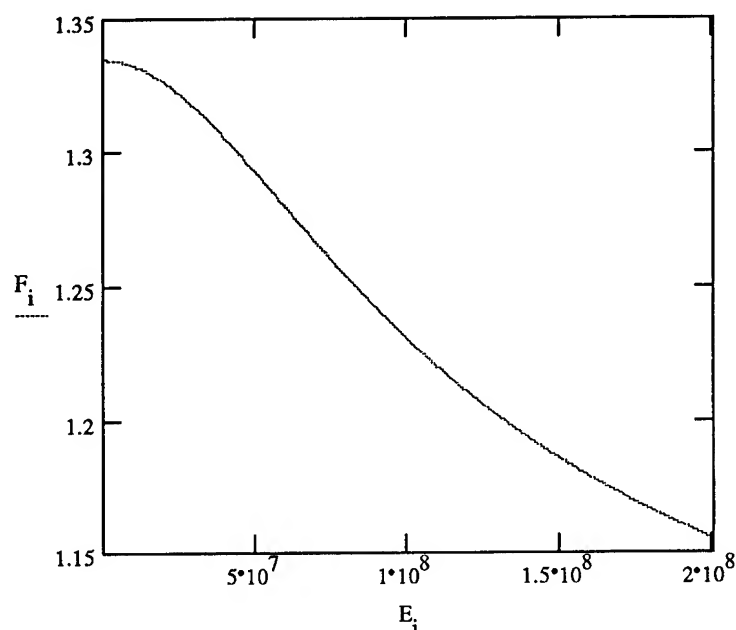


Figure 1: Local field factor, F_i , as a function of applied field (V/m) for an ellipsoidal molecule of dipole moment 42 D.

The extent to which this model may be applied to experimental results will be discussed. In particular, the question is raised over the correct choice of polarisability. The gas phase values used here are clearly not quite what is to be expected from polar molecules surrounded by a polarisable medium. Initial results also show a field dependence on the calculated dipole/field interaction strength which exceeds that predicted using this model. Thus extrinsic processes, such as charge injection during corona charging, may play a more important role.

References

1. P. Debye, *Physik. Z.*, **13**, 97, (1912)
2. L. Onsager, *J. Am. Chem. Soc.*, **58**, 1486, (1936)
3. Th. G. Scholte, *Physica*, **XV**, 450, (1949)
4. C.J.F. Böttcher, "Theory of Electric Polarisation", (Elsevier, Amsterdam, 1973, Vol. 1)
5. A.B. Myers and R.R. Birge, *J. Chem. Phys.*, **74**, 3514, (1981)
6. C. Dehu, F. Meyers, E. Hendrickx, K. Clays, A. Persoons, S.R. Marder and J.L. Brédas, *J. Am. Chem. Soc.*, **117**, 10127, (1995)
7. D. Healy, P.R. Thomas, M. Szablewski and G.H. Cross, *Proc. SPIE*, **2527**, 32, (1995)

Molecular Architectural Approaches to Nonlinear Optical Materials

DeQuan Li, Xiaoguang Yang, and Duncan McBranch

Chemical Sciences and Technology Division (CST-4)

Mail Stop G755

Los Alamos National Laboratory

Los Alamos, NM 87545 (U.S.A.)

Telephone: 505-665-1158

Fax: 505-667-8021

The design and construction of artificial supramolecular architectures on surfaces is of great current interest and represents an important aspect of molecular self-assembly, because self-assembly offers highly ordered mesoscale structures with desired chemical functionalities and physical properties. The fabrication of polar molecular superstructures proves particularly challenging since polar molecular materials are essential to second-order nonlinear optical (NLO) technologies. Several approaches such as the Langmuir-Blodgett technique and liquid crystals have been reported to generate molecular-based materials with organized polar structures. However, the orientation in these materials is maintained by weak bonding or steric hindrance, which lose the polar alignment over time. Recent developments in self-assembly and host-guest chemistry offer a novel route to ordered materials through the design and synthesis of new molecular building blocks that can be organized into supramolecular assemblies. The synthetic approach here is to fix dipole orientation by structural interlocking of NLO chromophores into cone conformation, and then to utilize them to build polar self-assembled monolayers. In this report, we discuss the molecular design of calixarene-based, NLO molecular "pyramids", their monolayer self-assemblies on oxide surfaces, and their spectroscopic second order NLO properties.

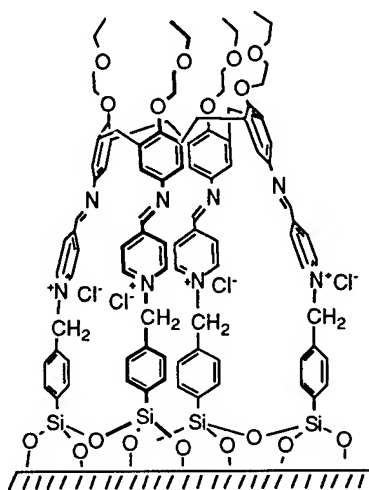


Figure 1. A robust self-assembled calixarene monolayer on silica surfaces.

Organic NLO chromophores are typically π -conjugated molecules with a D- π -A structure, where D and A are electron donor and acceptor, respectively, and π is a π -conjugated segment or sensitizer. This structural feature has been widely used to attain large values of the molecular second-order nonlinear susceptibility, β . By tethering these linear molecular units together through methylene bridges, a calixarene-based NLO chromophoric pyramid is derived. To achieve optimum molecular β , the orientation of each D- π -A unit should be fixed in nearly the same direction. Therefore, our approach involves the synthesis of a calix[4]arene with a frozen "cone" conformation

by substitution at the lower rim with large functional groups. With a molecular building block having rigid structure and fixed dipole orientation, it is expected that self-assembled monolayer (SAM) will have higher alignment, better thermal and structural stability than SAMs using single chromophoric unit. The structure of our calixarene SAMs is summarized in Figure 1.

In order to study the molecular orientation and the NLO response on the surface, spectroscopic second harmonic generation (SHG) was measured on the monolayers of calixarene. These measurements were performed using a modelocked Ti:sapphire laser in either femtosecond (150 fs autocorrelation width) or picosecond (2 ps width) mode with 100 MHz repetition rate, for fundamental wavelengths between 890 nm and 750 nm. Results using femtosecond pulses to generate *p*-polarized SHG from both *p*- and *s*-polarized fundamental are shown in Figure 2 for a fundamental wavelength of 862 nm. An average molecular orientation of $\psi \sim 35 \pm 5^\circ$ was deduced by modeling the angular dependent SHG response ($n_{\text{film}} = 1.7$); an absolute magnitude of $d_{33} \sim 80$ pm/V for monolayers of calixarene was deduced by calibrating to reference Y-cut quartz. The solid lines in Figure 2 are best fits, modulated by an interference term, which has the same physical origin and angular dependence as the well-known Maker fringes in bulk samples. The amplitude of the fringes is much smaller, due to the increased spectral width of the fs pulses; complete destructive (or constructive) interference cannot be achieved across the entire pulse spectrum. For the 1 mm fused silica samples considered here, effects of pulse walkoff due to mismatched group velocities of the fundamental and SH pulses can be neglected.

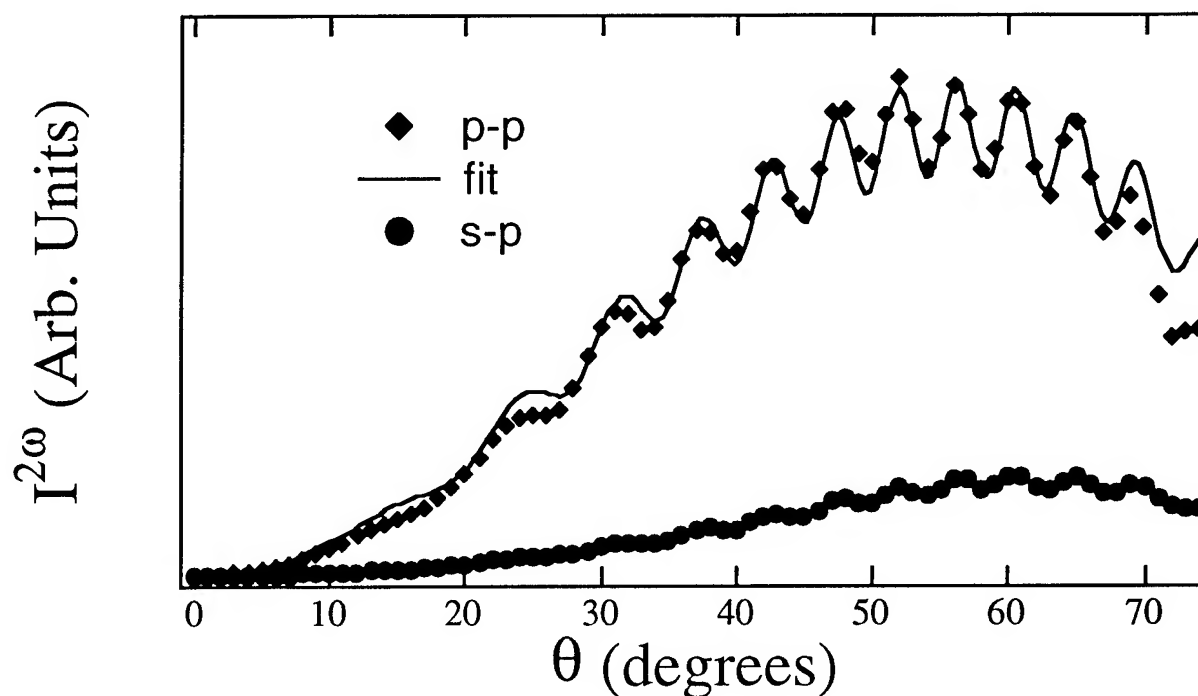


Figure 2. SHG signal vs. incident angle for *p*-polarized SHG from both *p*- (solid diamond) and *s*-polarized (solid circles) fundamental at a wavelength of 862 nm and 150 fs pulsewidth, and best theoretical fit (solid line).

Figure 3 shows the measured values of d_{33} versus fundamental wavelength for monolayer films of calixarene together with the linear absorption spectrum αd taken from the same sample. Here, α and d are the linear absorption coefficient and film thickness, respectively. The nonlinear optical spectrum closely resembles the linear optical absorption spectrum, which is fairly featureless.

The wavelength dependence (fundamental $\lambda = 890\text{--}750\text{ nm}$; harmonic $\lambda = 445\text{--}375\text{ nm}$) indicates a gradual increase of d_{33} as the fundamental moves to shorter wavelength, consistent with normal refractive index dispersion in this spectral region approaching the charge transfer resonance at 390 nm. From Figure 3, the charge transfer resonance is fairly broad; the measured value for d_{33} at the longest wavelength (60 pm/V at 890 nm) is still somewhat resonantly enhanced. We find a value of $d_{33} \sim 110\text{ pm/V}$ at $\lambda = 775\text{ nm}$, indicating a nearly twofold two photon resonant enhancement at the peak of the charge transfer band.

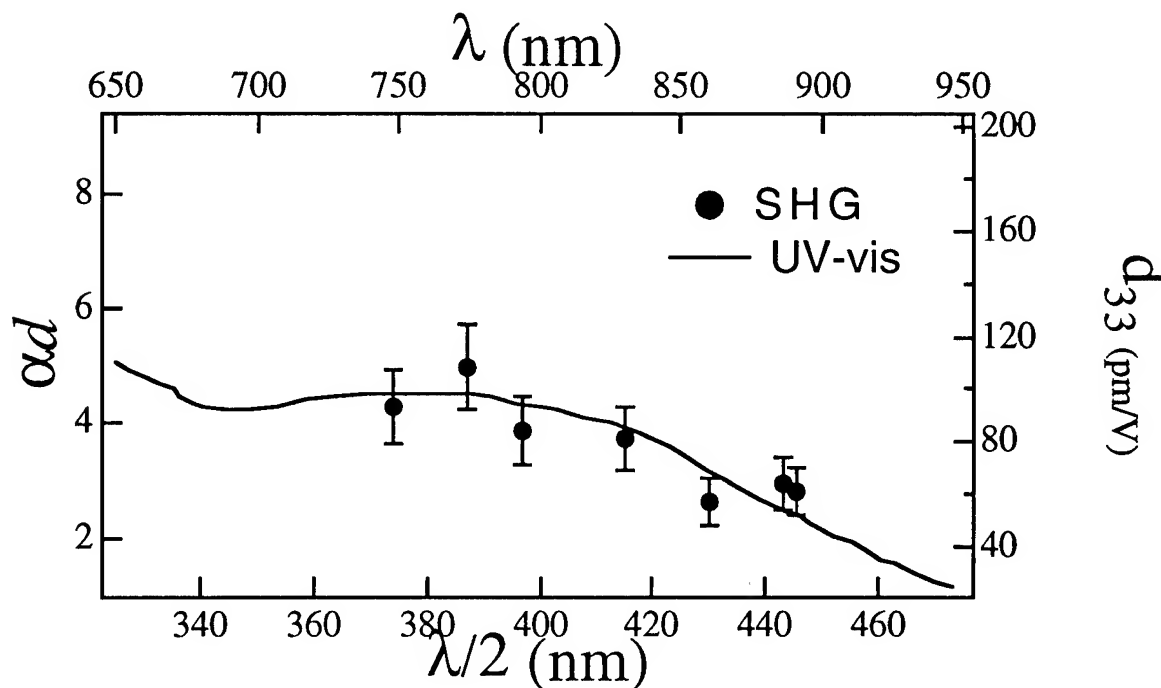


Figure 3. Second-order nonlinear susceptibility d_{33} (solid circles) vs. fundamental wavelength (top and right axes) or second harmonic wavelength (bottom and right axes) along with the linear absorption spectrum αd (solid line) vs. wavelength (bottom and left axes) for a self-assembled monolayer of calixarene. The lowest two photon resonance is at 390 nm corresponding to 780 nm in d_{33} dispersion.

To summarize, we have made a significant step forward in construction of supramolecular architecture by demonstrating the formation of self-assembled monolayers with “pyramid”-like molecular building blocks. Structural interlocking via the bridging methylene groups among the D- π -A units yields films with extremely large second-order nonlinearities ($d_{33} \sim 60\text{ pm/V}$; $\lambda = 890\text{ nm}$), and robust molecular dipole alignment.

Pump-Probe Experiments in Organic Solutions for Optical Limiting

Arthur Dogariu, Paul M. Buck, David J. Hagan and Eric W. Van Stryland

CREOL, University of Central Florida

4000 Central Florida Blvd.

P.O. Box 162700

Orlando, FL 32816-2700, USA

Phone: (407)823-6800

Fax: (407)823-6880

We report a series of picosecond excite-probe and femtosecond continuum excite-probe experiments performed on solutions of organic dyes. These experiments show the dynamics and spectral range of utility for these materials which have shown promise for applications in optical limiting devices. The metallo-organic dye solutions used were: Silicon Naphthalocyanine (SiNc) in methanol, tetrakis(β -cumylphenoxy) Lead Phthalocyanine ($\text{PbPc}(\beta\text{-CP})_4$) in chloroform and Zinc meso-Tetra(p-methoxyphenyl)Tetrabenzporphyrin (ZnTMOTBP) in tetrahydrofuran (THF). Initial studies involved Z-Scan and picosecond pump-probe measurements on these solutions at 532 nm.[1-3] All of these materials exhibited large reverse saturable absorption (RSA), i.e. the excited-state cross-section is larger than that of the ground-state.

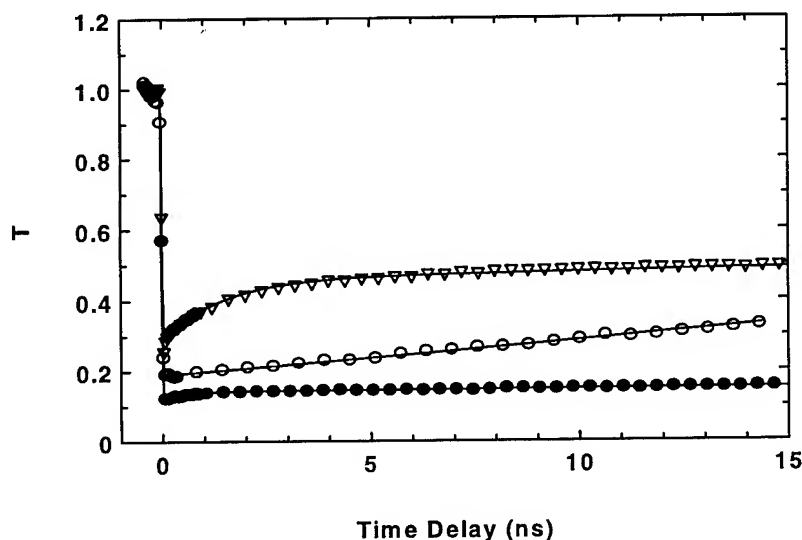


Figure 1. Normalized probe transmittance (T) at 532 nm for SiNc (triangles), $\text{PbPc}(\beta\text{-CP})_4$ (open circles) and ZnTMOTBP (filled circles) as function of time delay.

Figure 1 shows the results of an pump-probe experiment (both at 532 nm) where we observe strong long (i.e. > 10 ns) nonlinear absorption. These long lifetimes, and large excited state absorption (ESA) cross-sections, make these materials good candidates for optical limiting. In order to have a useful limiting device, however, the material must limit over a broad spectrum,

for example the entire visible spectrum. For such studies we have developed a femtosecond continuum source based on an argon ion pumped, Kerr lens modelocked, Ti:sapphire oscillator followed by a Cr:LiSAF regenerative amplifier producing millijoule level, 200 fs pulses around 850 nm. A single pulse is then split to generate a second harmonic (SH) pump at 425 nm and a femtosecond continuum probe that are used in a standard pump-probe geometry. The SH is produced in a thin BBO crystal and the continuum is produced by focusing the 850 nm light into a water cell. Using the femtosecond continuum as probe, the spectral dependence of the ESA response is revealed. Figure 2 shows the normalized transmittance spectra (the spectra obtained after excitation divided by the spectra obtained in the absence of the excitation, i.e., the linear spectra) of these materials at 10 ns after the excitation with the 425 nm pump. The nonlinear response of these materials depends on the linear absorption spectra (i.e., where is the excitation wavelength situated relative to the absorption bands).

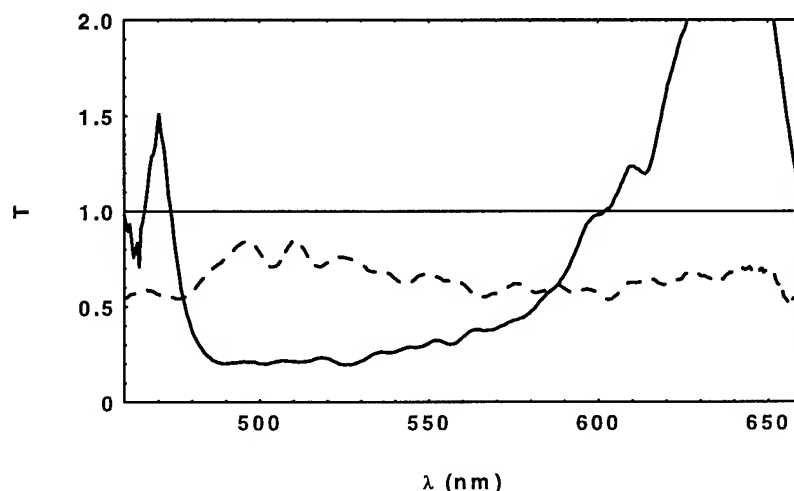


Figure 2. Normalized transmittance spectra for 38 μJ pump at 425 nm. The solid line represents ZnTMOTBP and the dashed line represents SiNc nonlinear response, both 10 ns after excitation.

SiNc is well known to be a good limiter in the visible [1] and from Figure 2 we can see that its nonlinear response is fairly flat in the visible part of the spectrum. However, if limiting is only needed from 480 nm to 600 nm, then the higher excited state absorption cross-section of ZnTMOTBP can be exploited.[2] Note that in the red spectral region ZnTMOTBP is a saturable absorber. By changing the delay between the pump and the probe beam we can observe the dynamics of the nonlinear spectrum. The nonlinear spectra of SiNc and $\text{PbPc}(\beta\text{-CP})_4$ are flat in the visible range, and the decay times do not change with wavelength. ZnTMOTBP, however, has more interesting features, as one can see in Figure 3. Figure 3. a. shows the turn-on of the nonlinearity and one can see that the nonlinear absorption cross-section changes with wavelength. The red part of the nonlinear spectrum shows RSA around zero delay, but, as can be seen in Figure 3. b., for long delay times, ZnTMOTBP becomes a saturable absorber around 630 nm, as expected from Figure 2.

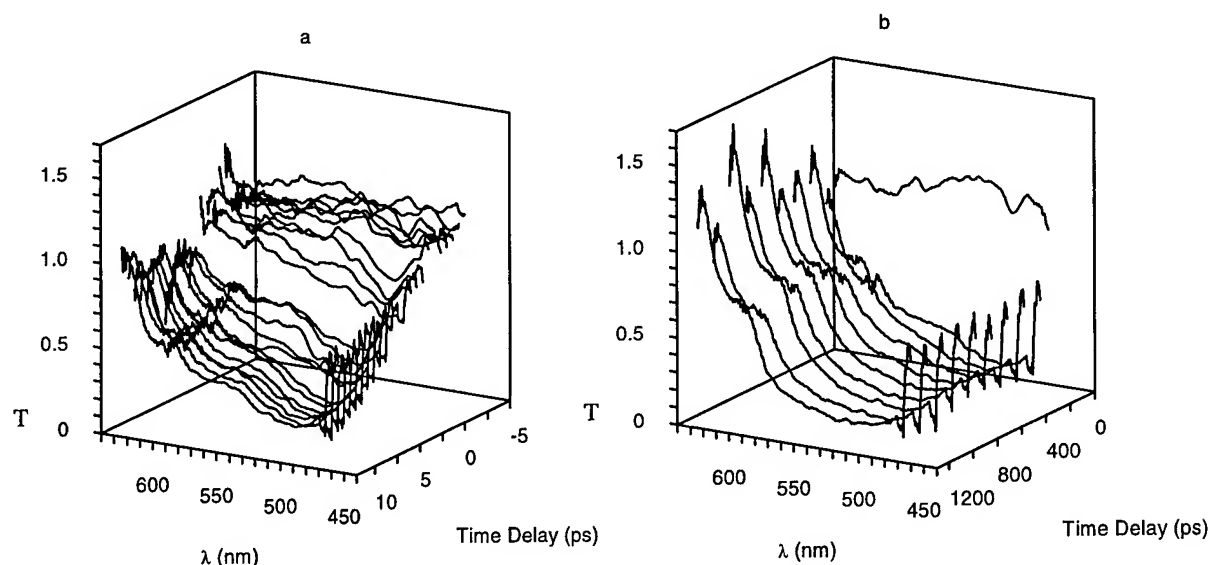


Figure 3. Short (a) and long (b) delay pump-probe experiments on ZnTMOTBP showing the nonlinear absorption spectrum as a function of time delay. The sharp rise at ≈ 450 nm is experimental (near the pump wavelength).

A possible explanation of the change in behavior with time can be that Figure 3. a. shows the singlet excited state absorption spectrum and in Figure 3. b. we see the effect of decay to the triplet excited state absorption spectrum. If the triplet absorption cross-section is smaller than the ground state cross-section at those wavelengths, at delays longer than the inter-system crossing time, the material becomes a saturable absorber as is observed. Analysis of the spectral dynamics may lead to limiters where the nonlinear spectra can be tailored for different pulsewidth inputs by mixing dyes.

References

- [1] H. Wei, D. J. Hagan, M. J. Sence, E. W. Van Stryland, J. W. Perry, and D. R. Coulter, "Direct Measurement of Nonlinear Absorption and Refraction in Solutions of Phthalocyanines," *Applied Physics B*, **54**, 46 (1992).
- [2] A. Said, A. Dogariu, T. Xia, D. J. Hagan, and E. W. Van Stryland, "Nonlinear Optical Characterization of Zinc Tetra (p-methoxyphenyl) Tetrabenzporphyrin," *CLEO*, Baltimore (1995).
- [3] S. R. Flom, J. S. Shirk, R. G. S. Pong, F. J. Bartoli, R. D. George, and A. S. Snow, "Linear and Nonlinear Optical Properties of Phthalcyanine Glasses," *CLEO*, Baltimore (1995).

NONLINEAR EFFECTS IN DYE-DOPED LIQUID CRYSTAL WAVEGUIDES

G. Abbate, L. De Stefano, P. Mormile, G. Scalia, E. Santamato
INFM, Dipartimento di Scienze Fisiche, Pad. 20 Mostra d'Oltremare, 80125, Napoli, Italy

In the nonlinear optics of Liquid Crystals (LC) a new chapter has been opened by the recent discovery that the addition of a small amount of organic dyes, less than 1%w/w, can greatly enhance the LC optical response. In the presence of the dye dopant, the optical torque exerted by light on LC molecules, which is responsible for the nonlinear behaviour, is magnified by a factor η , depending on the dye-LC mixture, on the dye concentration and on the wavelength. This factor may be up to 100 and both positive and negative in sign, leading to both focusing and defocusing nonlinearities¹. This property can be attractive in designing nonlinear optical waveguides, at least for the realisation of quasi-static devices, for which no care is due to the time response. We developed a general model to describe both the light propagation inside the waveguide and the LC response to the guided light, in the plane wave approximation².

We studied both the case of planar and homeotropic alignments. Our results on the planar case have been reported elsewhere², but the case of homeotropic alignment is even more interesting and is reported hereafter. It can be shown that for a TM guided wave no molecular reorientation is induced when η is positive, since the electric field of the light \mathbf{E} is parallel to the nematic director \mathbf{n} ; but, when η is negative, an optical torque arises, above a proper threshold. The numerical results are summarised in Fig. 1. In Fig. 1a the nonlinear propagation constant β is shown vs. the guided power p.u.l. for the first two eigensolutions. These solutions coalesce at some power value, indicating a degeneration also in the module of the field profiles. The effective refractive index and the field amplitude of the first eigensolution inside the LC are plotted in Fig. 1b and 1c, respectively, for three different power p.u.l. values. Due to the induced molecular reorientation above the threshold, the effective index decreases in the middle of the cell, while it remains higher at the cell boundaries because of the strong anchoring conditions. For this reason, the optical field is pushed towards the two sides of the waveguide, assuming a two-peaks symmetric profile. The spatial splitting of the guided beam is more effective at high power and can lead eventually to two spatially separated output beams. We notice that the field distribution of the first mode solution becomes more and more similar to the one of the second mode, apart from a phase factor: the moduli, indeed, become identical for the power p.u.l. values, where the propagation constants β 's of the two modes are equal (points A and B in Fig. 1a). The plot of the threshold power p.u.l. vs. η is reported in Figure 1d.

In order to study these effects experimentally, we made a planar waveguide with glass substrates ($n_s=1.51$), having its core filled in by a mixture of nematic LC (E7 from BDH) and anthraquinone dye (D4 from BDH), exhibiting a negative η factor. We realised different samples with core thickness ranging from 6 to 100 μm , dye concentration from 0.01 to 0.5%w/w, optical path from 0.5 to 2mm. The experimental analysis is not completed yet, but the preliminary results we obtained gave a clear evidence of the mode self-splitting effect. In Figure 2, we report some results for a cell, 100 μm thick, 0.5mm long and with a dye concentration of 0.07%w/w. Figure 2a is a picture, taken with a CCD camera, of the output

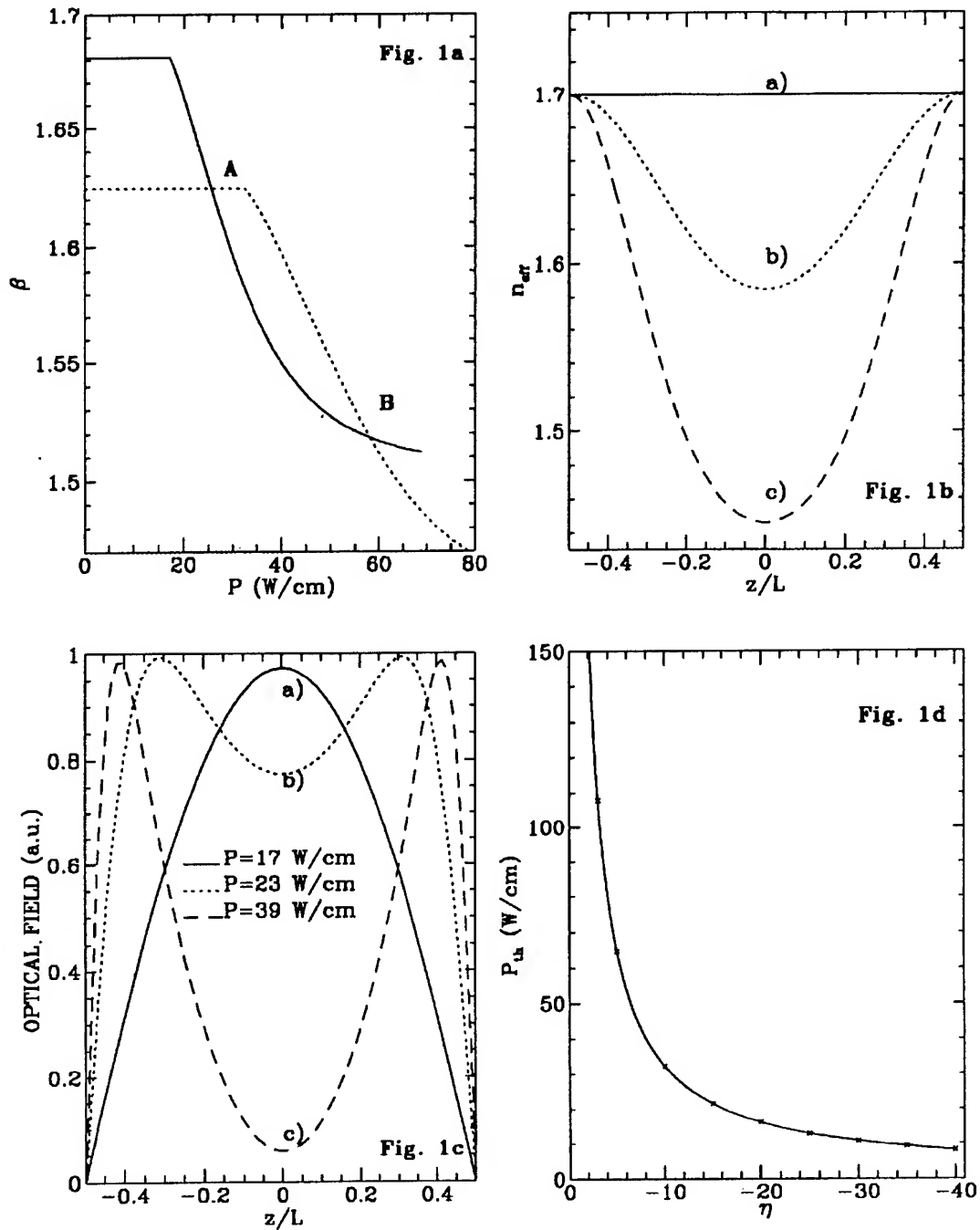


Figure 1 Numerical results for a TM-wave in a homeotropically aligned dye-doped LC waveguide. The propagation constant for the first two modes vs. the power per unit length (1a). The spatial distribution of the effective index (1b) and the field amplitude (1c) for different guided powers. The threshold power vs. the torque amplification factor η (1d).

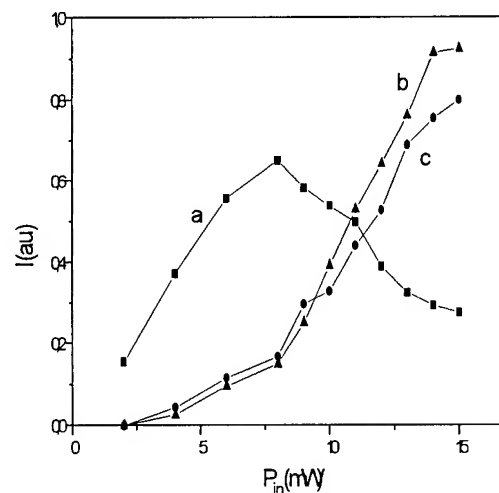
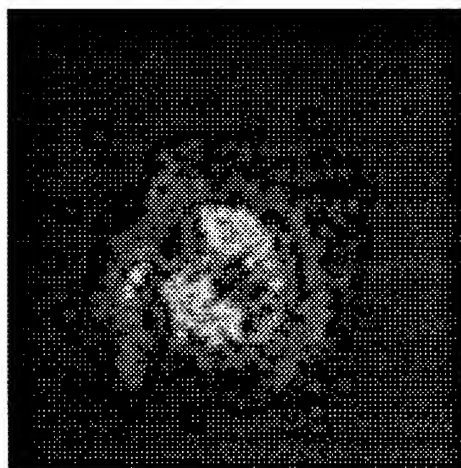


Figure 2 Picture showing the beam self-splitting after traversing the LC waveguide (2a) ; Output intensity of the spots at the centre (a), top (b) and bottom (c) of the output far field as a function of the input power.

far field corresponding to an input power of 15mW, twice the threshold value. The spatial separation of the light beam in two lobes is evident: the guided light intensity is mainly distributed along the core-substrate interfaces, which correspond to the up and down side of the figure. The light intensities measured at the three different spots, up, middle and down, of the far field pattern are plotted in Figure 2b versus the input light power. The threshold for nonlinear effects occurs at 7.5mW. We note, however, that the two lobes are in no way parallel to the waveguide plates: their shapes actually strongly depend on the relative magnitude of the beam waist and the core thickness as well as on the input beam shape. This behaviour cannot be evidently explained in the framework of a plane wave theory: a theoretical model taking into account the finite beam shape appear to be a difficult task, but it seem to be mandatory in the present case.

References

- ¹ I.Jánossy, A.D.Lloyd, B.S.Wherrett, *Mol. Cryst. Liq. Cryst.*, **179**, (1990).
- ² G.Abbate, L.De Stefano, E.Santamato, *J. Opt.Soc. of America B*, in press

Nonlinear cw Pump-Probe Investigations for Semiconductor Microcavities Exhibiting Normal-Mode Coupling

**T. R. Nelson, Jr., G. Khitrova, E. K. Lindmark,
D. V. Wick, J. D. Berger, H. M. Gibbs**

Optical Sciences Center, University of Arizona, Tucson, AZ 85721

Phone: (520) 621-4903 Fax: (520) 621-4323

email: tom@kilimanjaro.opt-sci.Arizona.EDU

K. Tai and Y. Lai

*Institute of Electro-Optical Engineering, National Chiao Tung University,
Hsinchu, Taiwan 30050 Republic of China*

Normal-mode coupling (NMC) or vacuum-field Rabi splitting has been studied for many years. Early experiments used many atoms or even a single atom in a high finesse cavity. Recent observations of NMC in semiconductor microcavities [1] have led to a flurry of investigations. We present here the results of high excitation cw pump-probe experiments which show a new nonlinear behavior, in which the transmission of the two NMC peaks disappears with no appreciable change in NMC splitting.

The samples under investigation consist of either a single 80 Å $\text{In}_{0.03}\text{Ga}_{0.97}\text{As}$ quantum well in the center of a 1λ GaAs spacer which is surrounded by two $R \cong 97.7\%$ distributed Bragg reflector (DBR) mirrors comprised of alternating $\lambda/4$ layers of GaAs and AlAs, or two such quantum wells placed at the intracavity field anti-nodes of a $3\lambda/2$ GaAs spacer with two $R \cong 99.5\%$ DBR mirrors. A key feature of our study is the narrowness of the heavy-hole quantum well exciton absorption lines, about 1 meV (0.6 nm) at 4 K, which yields extremely large NMC splitting-to-linewidth ratios (7 in the two-well sample, and 2.8 in the single-well sample).

The cw pump-probe measurements were performed by using an LED as a broadband probe and a tunable cw Ti:Sapphire laser as the pump. The probe was square-wave modulated at approximately 6.2 kHz, and detected using a lock-in amplifier. Fig. 1a shows the decreasing probe transmission with increasing pump intensity for the two-well sample. Fig. 1b shows the corresponding photoluminescence spectra as detected by a linear array multichannel analyzer. These measurements were performed for a pump wavelength of 787 nm, corresponding to the first minimum above the stopband in the microcavity reflectivity spectrum. The NMC transmission peaks fall to zero with increasing pump intensity with no change in splitting and no formation of new spectral features. Increased pumping results in increasing transmission at the uncoupled wavelength.

More startling is the fact that coherent excitation into either of the NMC peaks shows identical behavior. Fig. 2a is the transmission spectra series for $\lambda_{\text{pump}} = 833.5$ nm, while Fig. 2b is for $\lambda_{\text{pump}} = 836.5$ nm. In both cases, we see decreasing transmission with increasing pump intensity just as for off-resonant pumping. Similar results were also found in the single-well sample.

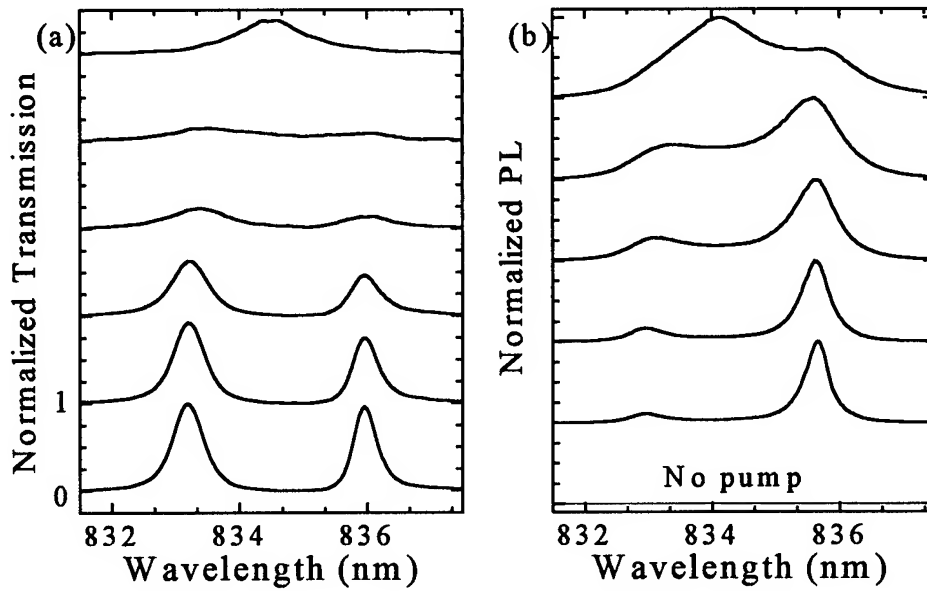


Figure 1. (a) Transmission spectra for the two-well sample (b) corresponding PL spectra. Both spectra series were normalized to one, then offset by 1.0 for clarity. Pump intensity increases from bottom to top.

Modeling of this system was done by means of a transfer-matrix calculation. Experiments were performed on a sample of twenty 80-Å $\text{In}_{0.03}\text{Ga}_{0.97}\text{As}$ quantum wells separated by 920-Å GaAs barriers to determine $\Delta\alpha(\lambda)$ as a function of intensity; see Fig. 3a. Kramers-Krönig transformations then give $\Delta n(\lambda)$ (Fig. 3b). Including the nonlinear susceptibility of the quantum wells in the transfer matrix calculation yields Fig. 3c. The behavior seen is in excellent agreement with our experimental results. With increasing pump intensity, the exciton absorption line is broadened significantly, accompanied by

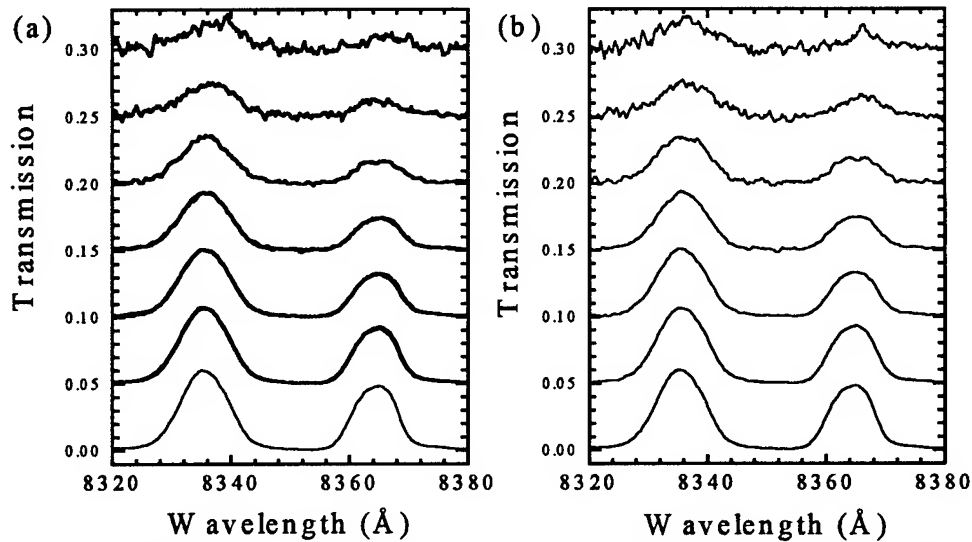


Figure 2 Pump-probe transmission spectra when pumping at (a) 8335 Å and (b) 8365 Å. The spectra have been shifted by 0.05 for clarity.

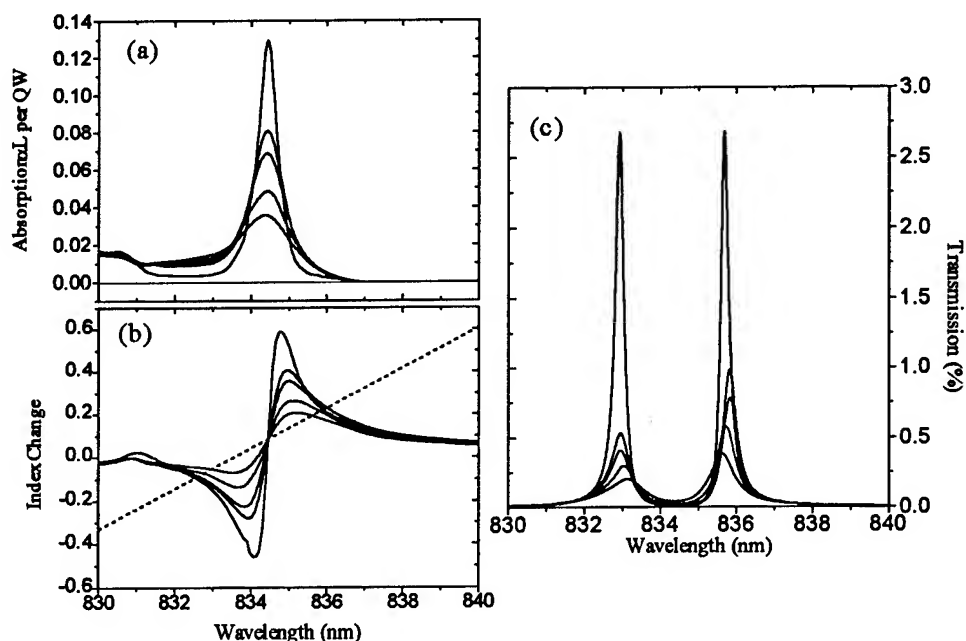


Figure 3 (a) Measured exciton absorption change for increasing pump intensities; (b) Resultant index change via Kramers-Krönig transformation; (c) Transfer matrix calculations using (a) and (b).

some bleaching. This broadening causes increased absorption at the NMC peaks, thereby reducing their transmission. An intersection of the cavity load line (straight line in Fig. 3b) with the nonlinear index curves demonstrates why we see no change in splitting with increasing excitation. Furthermore, fs-pump/cw-probe measurements of the carrier density needed for 50% reduction of the exciton peak on the twenty quantum well sample yielded $N_{sat} \cong 70/\mu\text{m}^2$, from which we determined that roughly $10^5 \hbar\omega$ units of energy were in the microcavity.

In summary, we have carried out a series of cw pump-probe experiments on samples exhibiting very large NMC splitting-to-linewidth ratios. A transfer matrix calculation including an experimentally determined nonlinear susceptibility consistently describes the observed behavior. From this, it is apparent that exciton broadening of the very narrow quantum well exciton absorption line, which was a factor of no import in other nonlinear NMC studies [3,4], plays the key role in the observed nonlinear behavior.

We would like to gratefully acknowledge support from ARPA/ARO, COEDIP, JSOP, NSF Physics and Lightwave Technology, and the Palace Knight Program.

References

- [1] C. Weisbuch, M. Nishioka, A. Ishikawa, and Y. Arakawa, Phys. Rev. Lett. **69**, 3314 (1992).
- [2] J. M. Jacobson, H. Cao, S. Pau, G. Björk, I. Chuang, Y. Yamamoto, and E. Hanamura, QThE2, QELS '95.
- [3] R. Houdré, J. L. Gibernon, P. Pellandini, R. P. Stanley, U. Oesterle, C. Weisbuch, J. O'Gorman, B. Roycroft, and M. Illegems, Phys. Rev. B **52**, 7810 (1995).
- [4] J.-K. Rhee, R. Lai, T. B. Norris, Y. Arakawa, and M. Nishioka, QThI3, QELS'95.

Strong Optical Nonlinearities and Ultrafast Carrier Dynamics in Luminescent and Nonluminescent Porous Silicon

Victor I. Klimov and Duncan McBranch

Chemical Sciences and Technology Division, CST-6, MS-J585,

Los Alamos National Laboratory, Los Alamos, NM 87545

Phone: (505) 665-8284, Fax: (505) 665-4817, e-mail: klimov@lanl.gov

Vladimir A. Karavanskii

Institute of General Physics, 28 Vavilov str., 117942 Moscow, Russia

Since the first experimental observation of efficient visible photoluminescence (PL) from porous silicon (PS) [1] this material has attracted much interest for its possible applications in all-silicon-based optoelectronics. Until now experimental studies of PS have mainly concerned PL, yielding information on the energy structure and population dynamics of the low-energy relaxed states in the material. Time-resolved nonlinear-transmission measurements can provide complementary information to conventional PL spectroscopy, revealing the structure of the higher-lying states and fast carrier dynamics in the initial stage after photoexcitation. In the present paper we report studies of the optical nonlinearities and ultrafast carrier dynamics in free-standing porous silicon films performed by femtosecond pump-probe experiment. The large photoinduced absorption observed in the spectral range 1.2–2.65 eV is attributed to molecular like complexes (clusters) which are most likely intrinsic to PS layers. Comparison of the transient absorption in samples of luminescent and nonluminescent PS shows that PL and photoinduced absorption originate from different species inside PS layers.

Free-standing PS films with different porosities (p) are prepared by a two-stage anodization of p-type (luminescent PS) and n-type (nonluminescent PS) Si substrates with (111) orientation. Films fabricated from p-type silicon exhibit bright red PL with a maximum around 1.75 eV.

Time-resolved differential transmission (DT) is measured in a standard pump-probe set-up. DT is defined as follows: $\Delta T = \Delta T/T_0$, where ΔT is the pump-induced transmission change and T_0 is

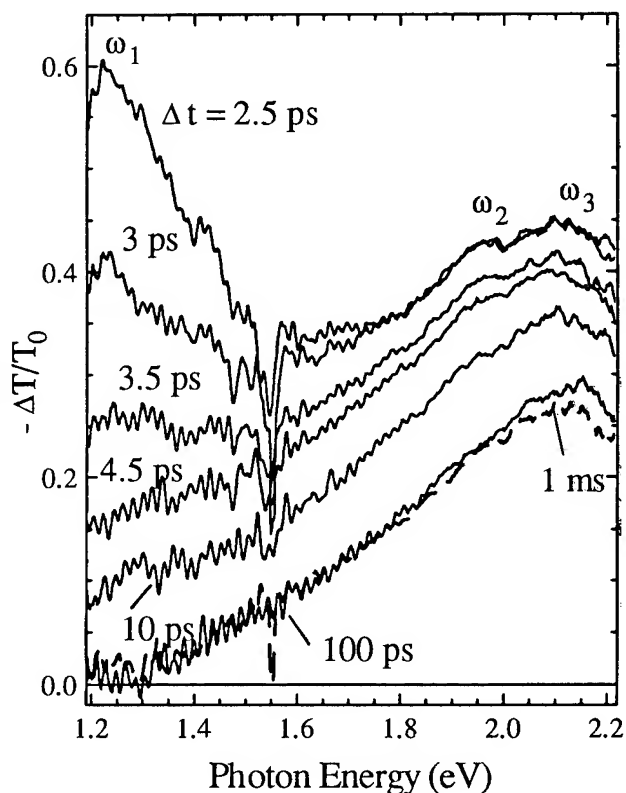


FIG. 1. Time-resolved DT in the PS film ($p = 60\%$) fabricated from n-type Si.

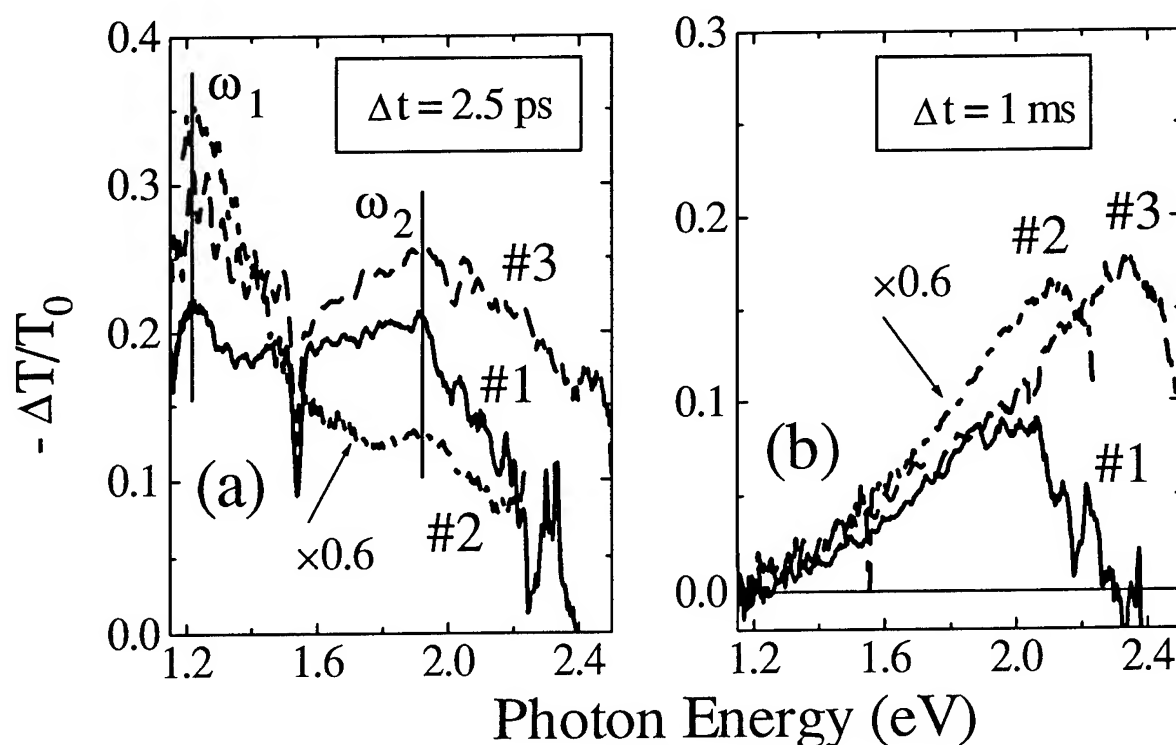


FIG. 2. Fast DT components taken at 2.5 ps (a) and DT measured at 1 ms (b; slow component) in three samples (prepared from n-type Si) of different porosities: $p = 55\%$ (#1), 60% (#2), and 64% (#3). A fast DT component is derived by subtracting the DT measured at 1 ms from that recorded at 2.5 ps.

the linear transmission. The samples are excited at 3.1 eV by frequency-doubled 100-fs pulses from a regeneratively amplified mode-locked Ti-sapphire laser. Photoinduced transmission changes are probed by delayed pulses of a femtosecond continuum generated in a sapphire plate.

Large increased absorption is observed in the spectral range from 1.2 to 2.65 eV for both luminescent and nonluminescent samples (Fig. 1). The measured nonlinear signal has very fast components with relaxation constants from 600 fs to tens of picoseconds superimposed on a slow-relaxing (millisecond) background. The fast picosecond component exhibits two-maxima around 1.2 (ω_1) and 2 eV (ω_2) (Fig. 1). The positions of these maxima are almost independent of sample porosities [Fig. 2 (a)]. The slow relaxing contribution forms a broad band (ω_3) with a peak which shifts to higher spectral energies with increasing sample porosity [see Figs. 1 and 2(b)]. The low-energy band ω_1 is characterized by very fast subpicosecond decay which is accompanied by a complimentary increase of the signal within the ω_2 band (Fig. 3). The decay time of the ω_2 feature is around 3–5 ps. The initial stage of transmission recovery (within the first few picoseconds after excitation) is common for both types of samples – luminescent and nonluminescent ones, whereas the subsequent behavior of transient absorption is different. In the nonluminescent samples the decay of the ω_2 band is accompanied by the complimentary absorption increase at higher spectral energies ($\hbar\omega > 2.5$ eV) (see Fig. 3). In the samples with efficient PL the decay of absorption changes is essentially spectrally uniform in the whole

spectral range from 2 to 2.65 eV.

The shape of the ω_3 band, the correlation between its position and that of the absorption edge as well as very slow (millisecond) relaxation dynamics can be explained by a low-energy shift of the absorption edge resulting from pump-induced heating of the sample. The short-lived DT component has nonthermal origin given its fast relaxation dynamics. However, it can hardly be explained in terms of quantum confinement model, widely accepted for PL from PS (see, *e.g.*, Ref. 1). The spectral structure and relaxation dynamics of the fast DT component can be attributed to molecularlike complexes (clusters) [2, 3] but not Si NC's.

The temporal behavior of the induced absorption in nonluminescent samples reveals the presence of at least three overlapping homogeneously broadened transitions (Fig. 3) with coupled population (depopulation) carrier dynamics which can be explained in terms of interlevel energy relaxation. Two of these transitions (ω_1 and ω_2) are also well manifested in the initial stage of transmission recovery ($\Delta t < 10$ ps) in the luminescent samples that indicates the same (molecular-complexes-mediated) carrier excitation mechanism. The difference seen at longer times after excitation ($\Delta t > 10$ ps) can be explained by carrier transfer to the luminescent species which are not active in DT.

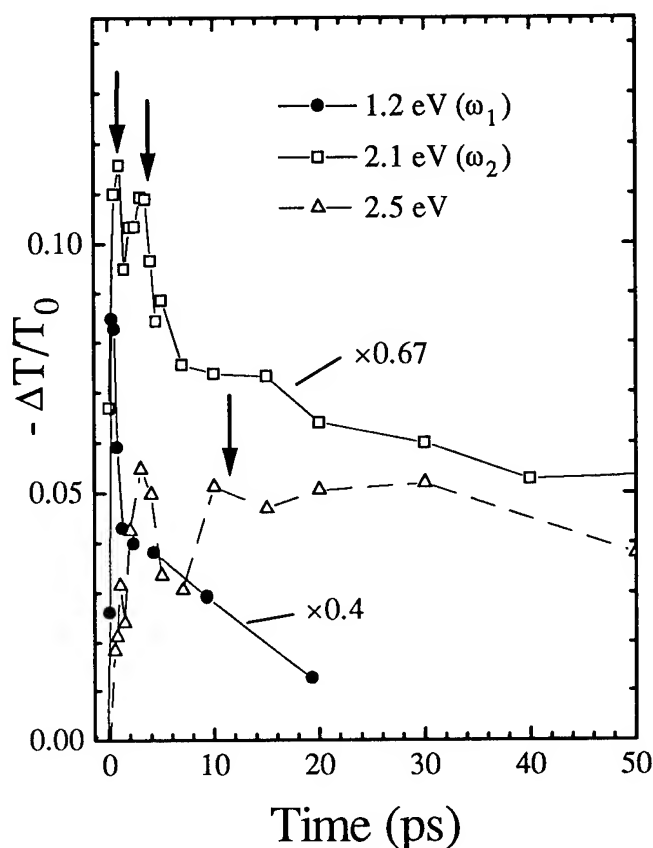


FIG. 3. Time-transients taken at different spectral energies in the PS sample ($p = 64\%$) prepared from n-type Si. Arrows mark the delay times attributed to a population build-up for three different overlapping transitions.

[1] Canham, Appl. Phys. Lett. **57**, 1046 (1990).

[2] S. Sinha, S. Banerjee, and B. M. Arora, Phys. Rev. B **49**, 5706 (1994).

[3] V. Klimov, D. McBranch, and V. Karavanskii, Phys. Rev. B **52**, R16989 (1995).

Ultrafast Optical Nonlinearities in Cu_xS Nanocrystals

Victor I. Klimov

Chemical Sciences and Technology Division, CST-6, MS-J585

Los Alamos National Laboratory, Los Alamos, NM 87545, USA

Phone: (505) 665-8284, Fax: (505) 665-4817, e-mail: klimov@lanl.gov

Vladimir A. Karavanskii

Institute of General Physics, 28 Vavilov str., 117942 Moscow, Russia

Three-dimensional (3D) carrier confinement in semiconductor nanocrystals (NC's) results in size-dependent photoluminescence and absorption spectra and significantly modifies the nonlinear optical properties and carrier dynamics with respect to those in bulk materials. So far, most experimental and theoretical studies have concentrated on NC's formed by direct-gap II-VI semiconductors such as CdS and CdSe. Recently, we reported the preparation, linear and picosecond nonlinear transmission of NC's of a new type: NC's formed by different copper sulfide phases [1]. Depending on the copper deficiency, the energy band gap in copper sulfide varies from 1.2 ($x = 2$) to 1.5 eV ($x = 1.8$) with an accompanying transformation of the semiconductor from indirect-gap to direct-gap one. These interesting properties as well as a small electron mass provide the broad phase/size controlled tuning range and give the opportunity to compare the effects of 3D confinement on nonlinear optical properties in direct and indirect-gap semiconductors.

In the present paper we report on ultrafast carrier dynamics and mechanisms for optical nonlinearities in Cu_xS NC's studied by femtosecond pump-probe techniques. Measurements performed indicate a drastic difference in the nonlinear-optical response in NC's formed by direct and indirect-gap phases of copper sulfide. The extremely fast initial transmission recovery (on the subpicosecond and picosecond time scales) observed in all types of Cu_xS NC's is attributed to ultrafast carrier trapping.

Copper sulfide NC's of 4 nm radius with different copper deficiencies [$x = 1.8$ (digenite), 1.9, 1.96 (djurleite), and 2 (chalcosite)] are prepared by a CdS-to- Cu_xS chemical conversion from glasses originally containing CdS NC's [1]. In the present paper we report three types of samples. Two of them are almost monophase and contain NC's in phases with $x = 2$ (sample 1) and $x = 1.8$ (sample 2), whereas sample 3 is a mixture of NC's in phases with $x = 2$, 1.96, 1.9,

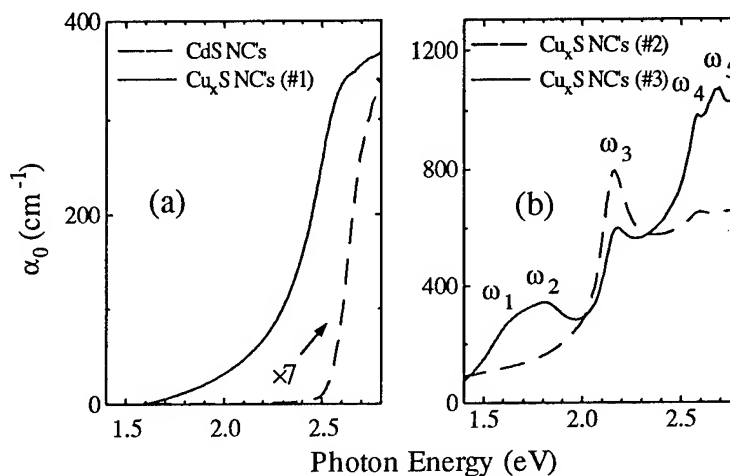


FIG. 1. Linear absorption in Cu_xS NC's (samples 1, 2, and 3) in comparison to that in a CdS-doped source glass.

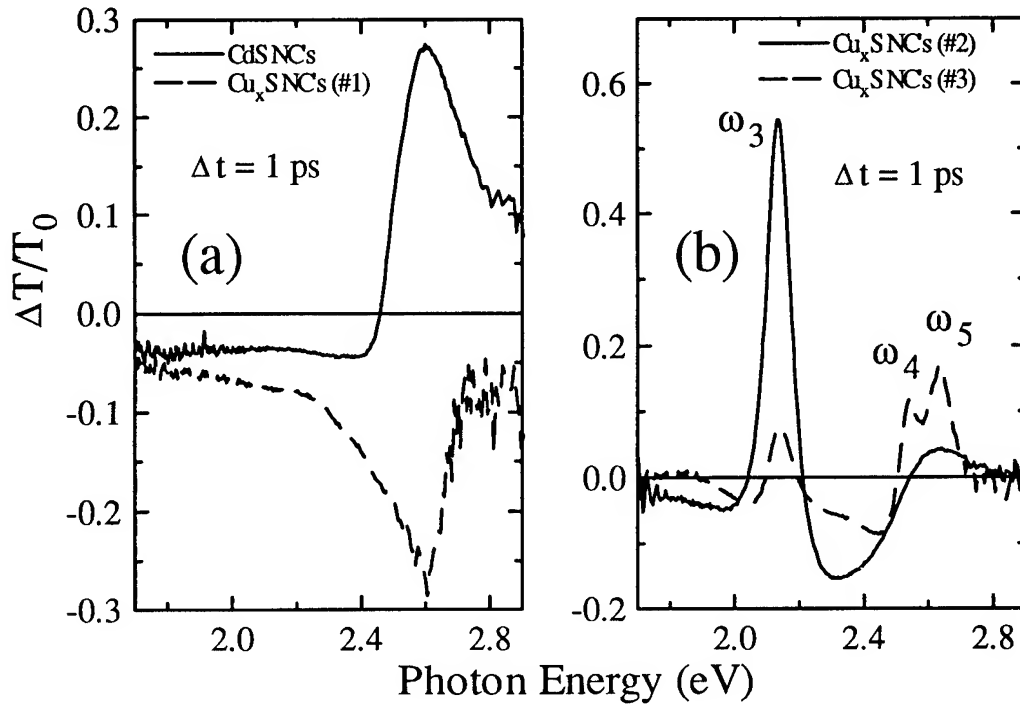


FIG. 2. Differential transmission in Cu_xS [samples 1 (a), 2 (b), and 3 (b)] and CdS NC's (a) taken at $\Delta t = 1$ ps after excitation.

and 1.8.

Time-resolved differential transmission (DT), defined as $\Delta T/T_0$ (ΔT is the pump-induced transmission change and T_0 is the linear transmission), was studied using two different femtosecond pump-probe experiments. First, the transmission of the samples excited at 3.1 eV is probed by broad-band pulses of a femtosecond continuum that provides information on the spectral distribution of absorption changes over a broad spectral range (0.4–1 μm). The other experiment is based on a single wavelength fast-scan technique which allows precise measurements (accuracy up to 10^{-7}) of the build-up and relaxation dynamics of differential transmission with femtosecond time resolution.

Fig. 1 shows absorption spectra in converted glasses in comparison to absorption in a CdS-doped source glass. All three of the converted samples show an increase in the absorption coefficient and a redshift of the absorption edge with respect to that in CdS NC's. The absorption in Cu_2S NC's (indirect-band-gap semiconductor in the bulk form) increases gradually with a photon energy starting at 1.6 eV [Fig. 1(a)] which corresponds to a 400-meV confinement-induced shift of the energy band gap with respect to bulk chalcosite. The NC's formed by direct-band-gap phases ($x = 1.96, 1.9$, and 1.8) exhibit several well-resolved absorption peaks [ω_1 – ω_5 ; Fig. 2(b)] which is a clear indication of size quantization resulting from carrier confinement. The peaks at ω_1 , ω_2 , and ω_3 mark the positions of the lowest optical transitions in NC's formed by phases with $x = 1.96, 1.9$, and 1.8 , respectively.

The DT in a source CdS-doped glass at short delay times after excitation is dominated by a state-filling-induced bleaching (positive DT) of the lowest optical transition [Fig. 2(a), solid line]. The same effect is also observed in DT of samples 2 and 3 as well-pronounced bleaching bands located at the positions of the discrete features seen in linear absorption [compare Figs. 1(b) and 2(b)]. In contrast, DT in the NC's of indirect-gap chalcosite ($x = 2$) does not show any

bleaching but rather indicates large photoinduced absorption peaked at 2.6 eV [Fig. 2(a), dashed line]. This is explained in terms of excited-state absorption on intraband transitions with confinement-enhanced probabilities [2]. This effect is also manifested as a broad negative background in DT of CdS NC's and NC's formed by direct-gap phases of copper sulfide.

The initial stage of transmission recovery in CdS NC's can be fitted to a double exponential decay with time constants of 2 and 30 ps. This is explained in terms of different trapping rates for holes and electrons [3]. The initial DT decay in copper sulfide NC's is monoexponential [time constants from 1 ps ($x = 1.8$) to 3.5 ps ($x = 2$)], which is suggestive of either approximately the same trapping rate for both carriers or a very fast trapping (within less than 200 fs) of one of the carriers, not resolved in the present experiments.

Fast-scan measurements are performed in the spectral range from 1.55 to 1.69 eV on samples 1 and 3 (the signal in sample 2 was below the detection limit). In chalcosite NC's (sample 1), the DT exhibits only weak spectral dependence and is negative for all spectral energies under investigation. In contrast, the temporal behavior of DT in the mixed sample shows strong spectral dependence. It changes gradually from bleaching to increased absorption in going to low spectral energies (Fig. 3). This behavior is due to competition between contributions from phases with direct (djurleite) and indirect (chalcosite) band gaps. The risetime of the bleaching component associated with state-filling is less than our time-resolution (~ 100 fs), whereas the onset of photoinduced absorption is delayed with respect to the pump pulse by about 450 fs, which gives a measure of the intraband relaxation time in chalcosite NC's. The decay constants for both bleaching and increased absorption are about 400 fs. This time is determined by the combined action of intraband energy relaxation and ultrafast carrier trapping.

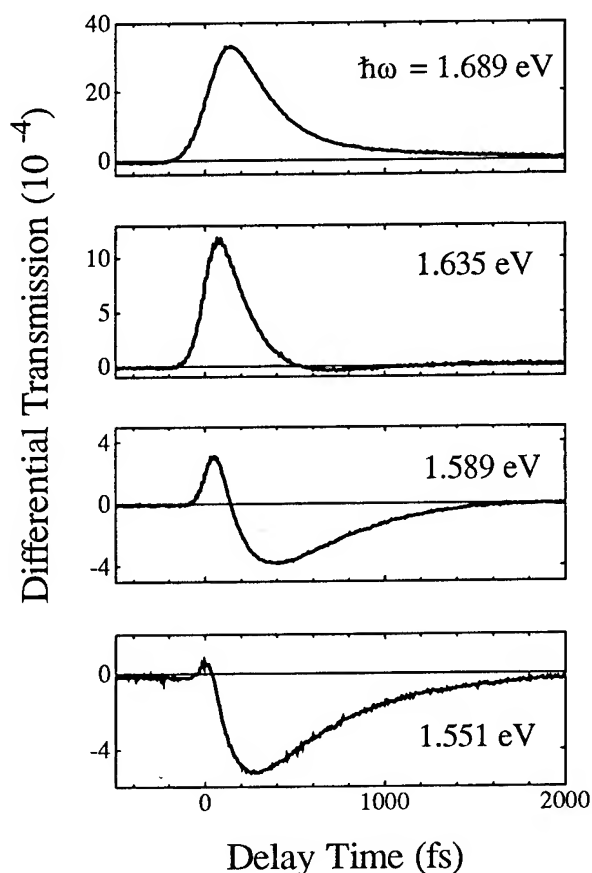


FIG. 3. Time-transients taken in sample 3 at different spectral energies.

[1] V. Klimov et al., *Appl. Phys. Lett.* **67**, 653 (1995).

[2] V. Milanović and Z. Ikonić, *Phys. Rev. B* **39**, 7982 (1989).

[3] V. Klimov et al., *Phys. Rev. B* **53**, 1463 (1996).

Femtosecond Nonlinear Optical Response of CuBr and CuCl Nanocrystals in Glass in the Optically Transparent Region

N. Thantu, J. S. Melinger, and D. McMorrow
Naval Research Laboratory, Code 6613, Washington, DC 20375 (202) 767-8524

B. L. Justus
Naval Research Laboratory, Code 5611, Washington, DC 20375 (202) 767-9468

Because large third-order refractive nonlinearities, γ , are expected, much study on nanocrystal doped glasses has focused on the nonlinear optical properties at or near the single photon resonance.¹ Although γ is smaller in the single-photon transparent region, its temporal response is expected to be pulse-width limited. More importantly, since the potential use of these materials as optical devices depends on the figure-of-merit ratio proportional to $\gamma/(\alpha\tau$ or $\beta\tau)$, where α and β are the linear and nonlinear absorption coefficients, respectively, and τ is the response time, a possibly larger figure of merit in the transparent region warrants studies far from the absorption edge. Recent studies^{2,3,4} performed on photodarkening CuBr nanocrystal doped glasses in the transparent region indicate a sizable two-photon enhanced nonlinearity which should scale with the concentration of CuBr nanocrystals in the glass. Time-resolving the nonlinear optical response³ with 60 fs, 620 nm optical pulses revealed a nearly pulse-width limited response followed by a subpicosecond decay. The CuBr and CuCl nanocrystals with the band edge in the 370-400 nm region are single-photon-transparent to the 620 nm light, but are two-photon-resonant at this wavelength or at 800 nm, the wavelength of interest in this study.

The outstanding issue that we address in this paper is the nature of the nonlinear optical response to excitations near the two-photon band edge in photodarkening and nonphotodarkening nanocrystal doped glasses. The process of photodarkening in nanocrystal doped glasses has been a focus of intense studies. In the I-VII materials of this study photodarkening is thought to originate with an initial sensitization by UV light, which makes the material susceptible to darkening upon further visible irradiation accompanied by the formation of copper colloids.⁵ We report here that the optical response of photodarkening and nonphotodarkening Cu(Cl,Br) nanocrystal doped glasses to the femtosecond, 800 nm excitation appears to be pulse-width limited, and not substantially affected by their photodarkening characteristics. The measured values of nonlinear optical coefficients give a figure-of-merit ratio that is about a factor of 10 greater than the previously reported value for excitations near the single-photon absorption edge.

Optical pulses of 30-45 fs duration centered around 800 nm at 85 MHz repetition rate used for all measurements in our study originates in a passively modelocked Ti:Al₂O₃ laser. The laser powers at the sample in both time-resolved optical heterodyne detected optical Kerr effect (OHD-OKE) and z-scan studies range from 10 mW to 80 mW. In the two beam OHD-OKE configuration, a local oscillator 90° out of phase with the probe field allows independent measurement of the induced transient birefringence associated with the nonlinear refractive index γ .⁶ The single beam z-scan measurements permit determination of the γ and β nonlinear coefficients.⁷ The experimental parameters involved in both configurations are essentially identical. The nanocrystal sizes are in the 30-35 Å range, and their composition in the 0.5 mm to 2 mm thick borosilicate glass host is about 0.1-0.5% by volume fraction. All measurements were performed at room temperature.

Figures 1 and 2 show the OHD-OKE transients of the induced birefringence of a photodarkening CuCl and a nonphotodarkening CuBr nanocrystal doped glass, obtained with femtosecond optical pulses. The transients appear to indicate no substantial dependence on the effects of photodarkening, and are essentially pulse-width limited in contrast to the earlier study using a 620 nm irradiation. Analogous measurements performed on a photodarkening CuBr nanocrystal doped glass revealed a similar behavior. The difference in the absolute signal intensity in the above two measurements is mostly due to the local oscillator field intensity employed in each measurement. The size of the nonlinearity is comparable to that of CS₂, and should scale with the volume fraction of nanocrystals in the glass host. On the other hand, the

measurements performed on a blank glass sample containing just the photodarkening bulk CuBr material indicate a much smaller optical nonlinearity, supporting the common observation in various other nano-structured materials that the enhanced optical nonlinearity is a consequence of quantum confinement.

To verify that the size of the nonlinearity is essentially due to the OKE, and not to a coherent artifact resulting from the diffraction of a probe photon into the signal detector by the pump-probe induced grating, we performed single beam z-scan measurements on the samples.

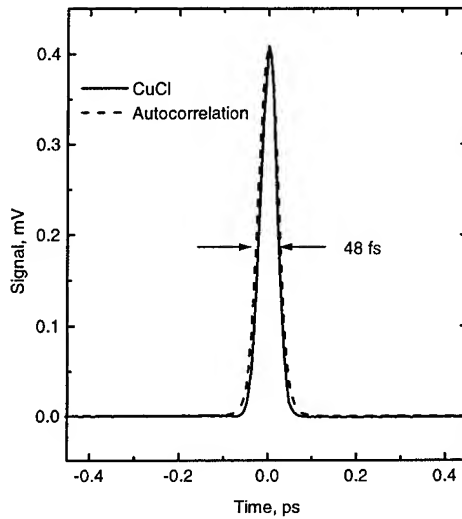


Figure 1. OHD-OKE transient of the induced birefringence of a photodarkened CuCl nanocrystal doped glass.

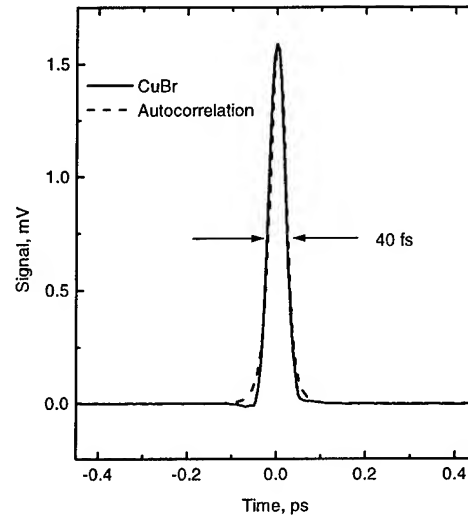


Figure 2. OHD-OKE transient of the induced birefringence of a non-photodarkening CuBr nanocrystal doped glass.

Figures 3 and 4 show typical closed and open aperture z scans performed on a nonphotodarkening CuBr nanocrystal doped glass with femtosecond pulses. The differences in their transmittance (and signal to noise ratio) are due to variations from one measurement to the other in the focal length, detector sensitivity, and spot location on the glass. The on-axis irradiance at the focus is approximately 0.44 GW/cm^2 for the closed aperture scan, and 1.32 GW/cm^2 for the open aperture scan. As explained in reference 7, the open aperture scan may be fitted to the Gaussian beam's normalized transmittance of the form

$$T(z) = \sum_{m=0}^{\infty} \frac{[-\beta I_0 L_{\text{eff}}]^m}{[1 + z^2 / z_0^2][m+1]^{3/2}},$$

where I_0 is the on-axis irradiance at the focus, L_{eff} as defined in the reference 7 for our case is approximately the thickness of the glass sample, and z_0 is the confocal parameter. For a small numerator in the brackets only a few terms in the sum contribute. In this way, we determine the value of β to be about 9 cm/GW . The β values determined from measurements taken with different laser powers agree to within 30% of each other. This β value is then used to obtain the fit, following the procedure outlined in reference 7 for materials which exhibit nonlinear refraction and absorption, for the closed aperture scan yielding $\gamma \sim 3 \times 10^{-14} \text{ cm}^2/\text{W}$. These values are in good agreement with those obtained with 10 Hz, 800 nm, nanosecond pulses of reference 2. The value of γ also is in reasonable agreement with the estimation from the OHD-OKE measurements. To obtain a direct comparison between the figure of merits for wavelengths near the single-photon and two-photon absorption edge, we define the figure of merit as

$$f = \frac{\text{Re } \chi^{(3)}}{\alpha' \tau}$$

where α' is either the linear absorption coefficient α or βI_0 , τ is the response time noted earlier, and $\chi^{(3)}$ is given in the esu units. With the values determined from our measurements for a CuBr nanocrystal doped glass we find f to be about a factor of 10 larger than the value measured at excitation wavelengths near the single-photon absorption edge in reference 1 for glasses doped with comparably sized CuCl nanocrystals at 80K.

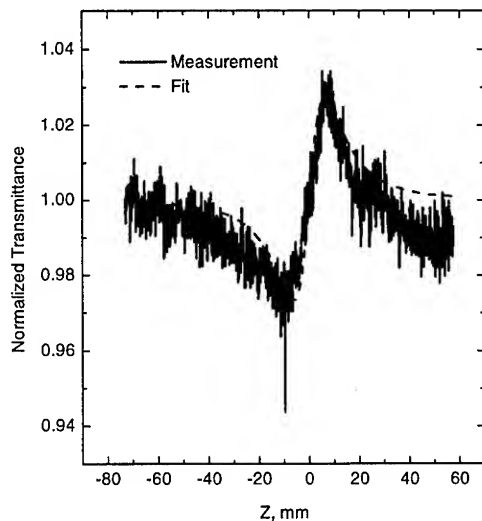


Figure 3. Closed aperture scan taken with a 150mm focusing lens ($I_0=0.44 \text{ GW/cm}^2$).

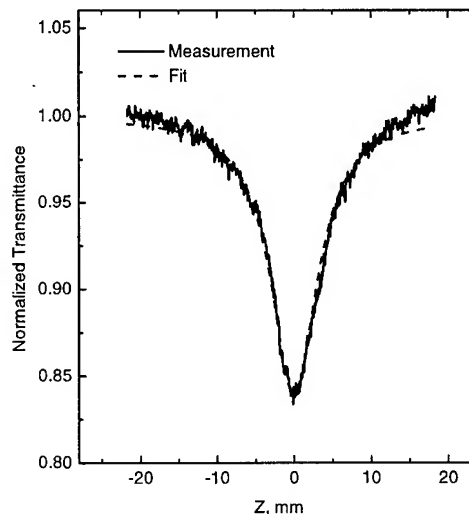


Figure 4. Open aperture scan taken with a 88 mm focusing lens ($I_0=1.32 \text{ GW/cm}^2$).

In summary, our current measurements indicate that the nonlinear properties of CuBr and CuCl nanocrystal doped glasses at excitation wavelengths near the two-photon absorption edge in their photodarkened or nonphotodarkened state appear to be favorable for optical device applications. At the conference we will report, in addition to the data presented here, complete power, wavelength, and laser repetition rate dependent measurements. We also will address questions concerning the degree of two-photon enhancement, the degree of contribution to the nonlinearity arising from the photogenerated carriers, and the degree of thermal effects in a quantitative fashion.

REFERENCES

1. See, for example, T. Tokizaki, T. Kataoka, A. Nakamura, N. Sugimoto, and T. Manabe, *Jpn. J. Appl. Phys.* **32**, 782 (1993).
2. B. L. Justus and J. A. Ruller, *Opt. Materials* **2**, 33 (1993).
3. B. L. Justus, J. A. Ruller, D. McMorro, and J. S. Melinger, 1992 IEEE Nonlinear Optics: Materials, Fundamentals, and Applications, Technical Digest, Paper MD-7, 79 (1992).
4. B. L. Justus, M. E. Seaver, J. A. Ruller, and A. J. Campillo, *Appl. Phys. Lett.* **57**, 1381 (1990).
5. D. L. Morse, *Inorg. Chem.* **20**, 777 (1981).
6. W. T. Lotshaw, D. McMorro, N. Thantu, J. S. Melinger, and R. Kitchenham, *J. Raman Spectros.* **26**, 571 (1995).
7. M. Sheik-Bahae, A. A. Said, T. Wei, D. J. Hagan, and E. W. Van Stryland, *IEEE J. Quant. Elect.* **26**, 760 (1990).

Semiconductor Amplifier as Element of Optical Communication Systems

Marina Settembre, Francesco Matera
Fondazione Ugo Bordonì, Via B.Castiglione 59, 0014 Roma, Italy
tel. +39-6-54802233; fax +39-6-54804402

Volker Hägele,
Universität Kaiserslautern, Postfach 3049, D-67653 Kaiserslautern, Germany

Ildar Gabitov, Arnold Mattheus
Telekom Forschungs- und Technologiezentrum,
Postfach 10 00 03, D-64295 Darmstadt, Germany

Sergei K. Turitsyn
Institut für Theoretische Physik I
Heinrich-Heine-Universität Düsseldorf
40225 Düsseldorf 1, Germany

INTRODUCTION. Recent progress in the fabrication of polarization-insensitive Semiconductor Optical Amplifiers (SOAs) has stimulated interest in investigating transmission systems with in-line SOAs [1-3]. The SOAs cover broad wavelength range from 0.7 to 1.6 μm , they are pumped electrically and are substantially cheaper than fiber amplifiers, therefore, SOA is the natural candidate to be an element of all-optical transparent transmission systems.

The most of presently installed in Europe optical networks are based primarily on conventional Standard Monomode Fibers (SMF) and operate with electro-optical regenerators up to 2.5Gbit/s. The problem of further increasing network capacity has intensively been studied during the last few years. One promising way to upgrade existing networks is to exploit the 1.3 μm optical window using wide-bandwidth SOAs, that have been developed recently [1]. This method takes advantage of both low Group Velocity Dispersion (GVD) of the SMF at this carrier wavelength and attractive features of SOAs.

However, the use of an SOA contributes several negative factors due to the intrinsic nonlinearities: SOAs cause an additional chirp; they are quickly saturated and for high bit rate transmission cannot recover before the next optical pulse in the pattern enters the amplifier. For 10 Gbit/s this is a significant effect leading to the limitation of transmission capacity [2].

In this work we show how these nonlinearities can be suppressed either by additional upgrading of the link by in-line filters or by polarization encoding [4] of the input signal to achieve long-distance, stable transmission. On the other hand the Kerr nonlinearity of the fiber is used to compensate the degradation induced by the GVD. We study here the performance of SMF lines with periodically placed semiconductor amplifiers operating around 1300 μm for both cases of intensity modulation (IM) and polarization modulation (PM). The PM systems show the advantage that all the bits have the same power behaviour; as a consequence the amplification process does not depend on the sequence of "1" and "0" as in IM systems.

MODEL. In the adopted numerical model the propagation is evaluated by solving the coupled nonlinear Schrödinger equations [5] including the effects of the fiber loss, of the GVD, of the Kerr nonlinearity and of the Polarization Mode Dispersion (PMD). The SOA is modelled by following rate equations including noise influence [6]. The random spontaneous emission process is modelled by a complex Gaussian white noise term A_{sp} with zero mean

value. The auto-correlation function of the Gaussian process is described by $\langle A_{sp}(t)A_{sp}^*(t') \rangle = \beta_{sp}P_{sp}(N)\delta(t-t')/T_1$, where β_{sp} is the fraction of the total generated spontaneous emission power $P_{sp}(N)$ coupled into the guided signal mode, N is the carrier density and T_1 the carrier life time. The carrier-induced index change is accounted for through the linewidth enhancement factor α_H , [6]. Its typical values for semiconductor lasers and optical amplifiers are in the range 3-8.

The transmitted message consists of a sequence of 32 bits and the signal can be modulated either in intensity or in polarization (in the PM format the bit "1" and the bit "0" have orthogonal state of polarization).

At the receiver the signal is filtered by an optical Fabry-Perot filter whose bandwidth is $4R$. In the IM case the signals is detected with a direct detection receiver (IM-DD) that consists of a pin photodiode located after the filter and the output electrical signal is filtered by a Second Order Butterworth Filter (SOBF) with a bandwidth, B_R , equal to $0.8R$ [7]. In the PM case the signal is detected with a direct detection (PM-DD) scheme based on a polarimeter, located after the filter, that detects the Stokes parameters $\underline{S}(t)$ of the field; the decision variable is obtained by electrically filtering (with a SOBF with $B_R=0.8R$) the scalar product between $\underline{S}(t)$ with a reference Stokes vector \underline{S}_R obtained by a time average on $\underline{S}(t)$ [8]. The system performance is evaluated in terms of the Q factor, taking into account of the patterning effects [7]. The Q factor was obtained on the basis of 25 simulative runs that differ in the ASE generation and in the random rotation of the fiber birefringence axis. We remember that in the hypothesis of Gaussian distribution of the decision variable $Q>6$ corresponds to an error probability lower than 10^{-9} .

The parameters common in the simulations are: the amplifier spacing (L_{amp}) is 50 km, the fiber loss 0.4 dB/km, the Kerr nonlinearity $2W^{-1}km^{-1}$, the PMD 0.2 ps/ \sqrt{km} and the GVD is $-3 ps^2/km$ ($D=2.5 ps/nm/km$). The amplifier polarization dependent loss 0.2 dB, the spontaneous emission factor (n_{sp}) 5, $\alpha_H=5$, the saturation power 30 mW, $T_1=200 ps$ [1] and the semiconductor loss coefficient, containing the internal and mirror losses, $20 cm^{-1}$. The solitons have a τ_{FWHM} equal to $1/(5R)$ where R is the bit rate, while the filter parameters were chosen as in ref. [7].

RESULTS. In fig.1 the performance of 10 Gbit/s sliding soliton IM-DD and PM-DD systems are evaluated in terms of Q -factor [7] versus input peak power for different distances. All the curves shows a maximum Q value in correspondence of the peak power of the fundamental soliton. For lower power the signal is strongly degraded by the GVD degradation, while for higher power the fiber and SOA nonlinearities dominate. PM-DD systems show better performance than IM-DD ones. This is due to the fact that in the case of IM-DD systems, the transmission of a "0" corresponds to the absence of a pulse during the bit time; conversely, for a PM-DD system the bit energy is constant through the message. Hence, the frequency shift, induced by the SOA gain saturation on each pulse, is strongly dependent on the bit sequence for IM-DD systems, but not for PM-DD systems. As a consequence PM-DD systems result very important to limit the SOA nonlinearities.

In fig. 2 the maximum length, corresponding to $Q>6$, is reported versus the bit rate for soliton IM-DD and PM-DD systems with or without in-line sliding filters. The beneficial effects of the filters is clearly shown. Results on sliding soliton IM-DD systems without amplifier gain saturation are also reported as a comparison. For bit rate higher than $1/T_1$, the advantage of

PM-DD systems is evident until both the systems suffer the degradation mainly induced by the instability effects due to the periodical amplification. For bit rate lower than $1/T_1$, the performance of both the systems are essentially limited by the decreasing of the signal to noise ratio due to the high values of the ASE level compared with the reduced energy of a low bit rate soliton signal [7].

Fig. 2 shows as the use of in-line SOA's can permit the implementation of 10 Gbit/s IM-DD systems in links encompassing step-index fibers for distances up to 500 km without in-line filtering control and such a distance can be increased up to 900 km if PM-DD systems are used. By means of in-line filtering control the maximum propagation distance for 10 Gbit/s systems can be increased up to 800 km for IM-DD systems and 1500 km for PM-DD systems.

CONCLUSIONS. A study on the nonlinearities of SOAs and of optical fibers has been carried out in the case of long optical links. Soliton propagation has been used to suppress the GVD degradation considering both IM-DD and PM-DD systems. Results show how in-line filtering process and soliton PM-DD systems can limit the effect of the SOAs nonlinearities. In particular in the case of soliton PM-DD systems the maximum propagation distance can be increased and in some case even doubled with respect to IM-DD ones. This work was carried out in the framework of ACTS project UPGRADE.

REFERENCES

- [1] C. T. H. F. Liendenbaum, J.J. Reid, L. F. Tiemeijer, A. J. Boot, P. I. Kuindersma, I. Gabitov, and A. Mattheus, proc. of ECOC'94 Florence, Italy 1994, p. 233.
- [2] A. Mecozzi, Opt. Lett. vol. 20 (1995), 1616.
- [3] S. Wabnitz, Opt. Lett. vol. 20 (1995), 1975.
- [4] S. G. Evangelides, L. F. Mollenauer, J. P. Gordon, N. S. Bergano, vol. 10 (1992) p. 28.
- [5] F. Matera, M. Settembre, Optics Letters, vol. 20 (1995) p. 28.
- [6] G. P. Agrawal and N. A. Olsson, IEEE J. of Quan. Electron. vol. 25 (1989) p. 2297.
- [7] F. Matera, M. Settembre J. of Lightwave Technology vol. 14 (1996) p. 1.
- [8] S. Betti, G. De Marchis, E. Iannone, J. Lightwave Tecnology, vol. 10 (1992), p. 1985.

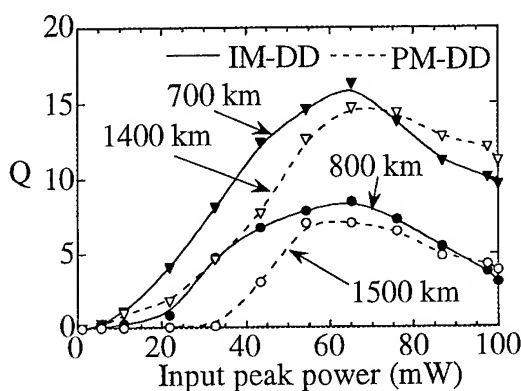


Figure 1: Q vs input peak power for a 10 Gbit/s soliton IM-DD systems (solid line) and PM-DD systems (dashed lines) considering different propagation distances.

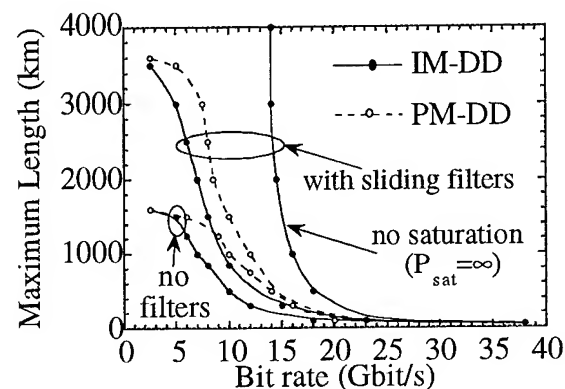


Figure 2: Maximum length vs bit rate for soliton IM-DD (solid line) and PM-DD systems (dashed lines) in the absence and in the presence of optical in-line sliding filters.

High Value of $\chi^{(3)}$ in Fluorine-Phosphate Glass Doped with $\text{CdS}_x\text{Se}_{1-x}$

B. Vaynberg, M. Matusovsky, M. Rosenbluh

Bar-Ilan University, Physics Department, Ramat Gan, Israel

and

A. Lipovskii

Saint Petersburg State Technical University, St. Petersburg, Russia

The non-linear optical properties of semiconductor-doped glass with high semiconductor concentration has been investigated and compared to the optical properties of commercially available color filters(1, 2). We measured the third order nonlinear susceptibility of this new material by observing four wave mixing. We also identify and measure in this glass the onset of competing higher order nonlinear processes, such as six wave mixing. The optical characteristics of all the semiconductor doped glasses are determined by the microcrystals embedded in the glass matrix. The linear and non-linear optical constants of the material can thus be controlled by the proper choice and concentration of the semiconductor dopants, and the size of the microcrystals. Therefore the synthesis of glasses with high concentration of semiconductor microcrystals is important, since this is expected to produce higher optical nonlinearities. The semiconductor concentration is limited by its solubility in the glass. By using a fluorine-phosphate glass matrix(3) we were able to increase this concentration over that of silicate glass color filters, by more than an order of magnitude.

In order to compare the non-linear susceptibility of the phosphate glass with previously studied borosilicate glasses we measured, using a pulsed dye laser, the degenerate four wave mixing (DFWM) signal generated by the new phosphate glass and a Schott OG-590 filter. Both samples are doped by $\text{CdS}_x\text{Se}_{1-x}$, in the same proportion, but had different thickness: 0.2 mm for the phosphate glass and 0.75 mm for the OG-590 filter.

The conjugate beam intensities for each sample are shown in Fig. 1 as a reflectivity, $R(\%)$, of the probe beam as a function of the pump intensity, where each of the two pump beams had the same intensity. For the OG-590 filter we obtain a slope of two for low input intensities with saturation setting in only above 0.1 MW/cm^2 . For the phosphate

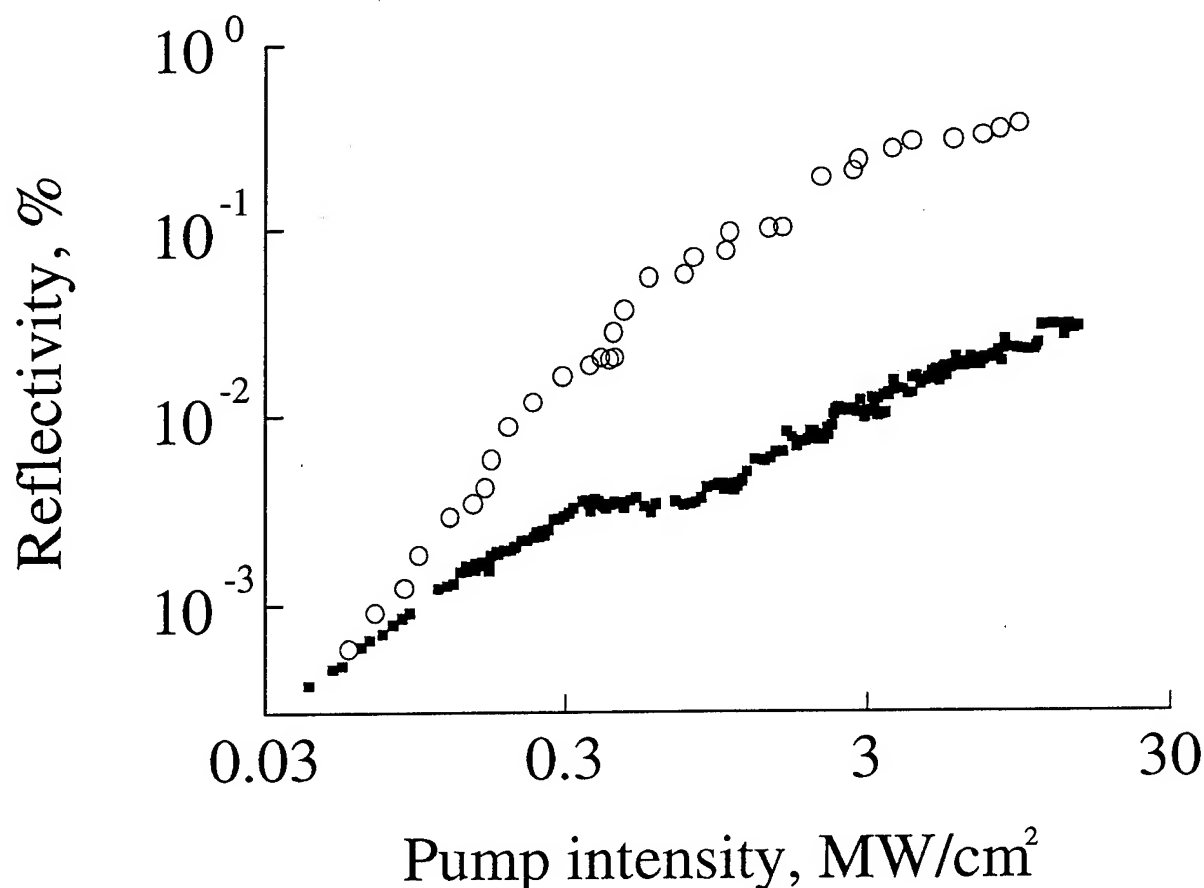


Fig. 1. Four wave mixing reflectivity as a function of pump laser intensity. The laser wavelength was 581 nm, the circles are for a 0.75 mm thick OG-590 filter and the squares are for a 0.2 mm thick, high semiconductor concentration phosphate glass.

glass, saturation is evident even for the lowest input intensities for which signal can be measured. Between 0.1 and 1 MW/cm² the FWM reflectivity becomes nearly constant. This can be explained by the onset of higher order nonlinear processes. Six wave mixing (SWM), which competes with FWM, becomes significant at such input intensities. To demonstrate the onset of SWM, we changed the experimental geometry to enable us to resolve the sixth wave from the probe wave. The sixth wave reflectivity as a function of pump intensity is shown in Fig. 2. Since the slope of this curve is less than four we conclude that SWM is also saturated. At a given pump intensity, the SWM signal is about 10% of the FWM signal thus resulting in the structure of Fig. 1. The influence of even higher orders of wave mixing were not observed in the FWM reflectivity, probably because of the onset of other nonlinear processes, such as free carrier absorption(4).

From the low-intensity part of the data shown in Fig. 1 we evaluate an experimental value for $\chi^{(3)}$ of 2.5×10^{-8} esu for the OG-590 filter. Assuming that for low pump intensities, the third order susceptibility is dominant also in the phosphate glass, and considering the difference in the thickness of the samples, we estimate $\chi^{(3)}$ for the phosphate glass to be at least 1×10^{-7} esu; at least four times larger than for the borosilicate matrix.

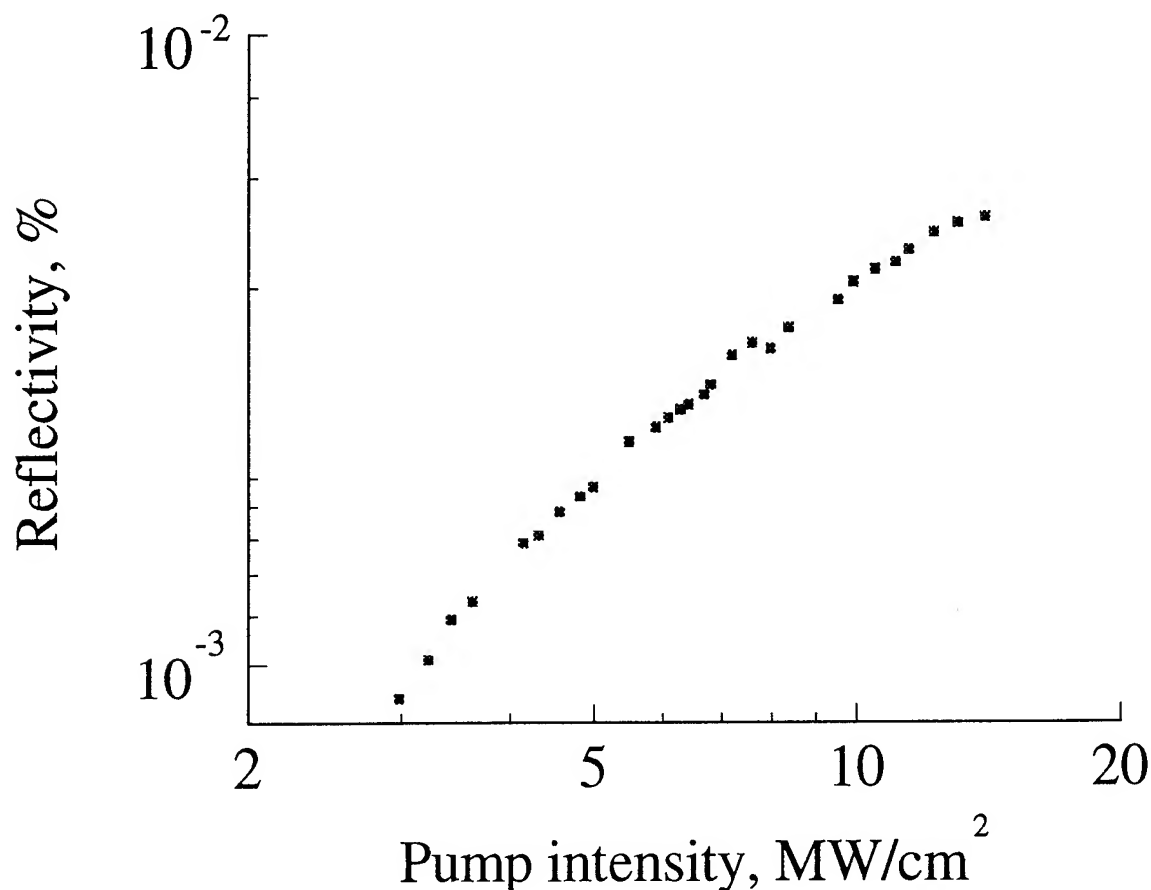


Fig. 2. Six wave mixing reflectivity as a function of pump laser intensity for the high semiconductor concentration phosphate glass.

1. N. Peyghambarian, et al., in *SPIE Critical Reviews* (1994), vol. CR53, pp. 211.
2. C. Flytzanis, F. Hache, M. C. Klein, D. Ricard, P. Roussignol, in *Progress in Optics XXIX* E. Wolf, Ed., (Elsevier Science Pub., 1991) pp. 323.
3. E. Kolobkova, A. Lipovskii, N. Nikonorov, A. Sitnikova, *Phys. Status Sol. B* **147**, K65 (1995).
4. R. Jain, R. Lind, *Journal of the Optical Society of America* **73**, 647 (1983).

Waveguide-Mode Intersubband Second-Harmonic Generation with Separate Active and Phase-Matching Regions

I. Vurgaftman and J. R. Meyer

Code 5613, Naval Research Laboratory, Washington, DC 20375

L. R. Ram-Mohan

Department of Physics,

Worcester Polytechnic Institute, Worcester, MA 01609

We have performed an analysis of the conversion efficiency for waveguide-mode second-harmonic generation (SHG) with detuned intersubband transitions in asymmetric double quantum wells (ADQW). The modeling includes the effects of absorption, saturation of the absorption and SHG, pump depletion, carrier heating, mode confinement, and the loss of phase coherence due to waveguide, bulk and resonant intersubband contributions to the mismatch of the refractive indices at the pump and second-harmonic frequencies. ADQW designs with the optimum detuning of intersubband transition energies from resonance with the pump and second-harmonic photon energies have been derived from a balance between low absorption losses, sufficient nonlinear susceptibility, and adequate compensation of the refractive index mismatch to maintain phase coherence. These have been determined for structures employing the GaAs/AlGaAs, InGaAs/InAlAs and GaSb/InGaSb/AlGaSb material systems, all subject to the constraint that the epitaxial growth thickness should not exceed 10 μm . In the best GaAs/AlGaAs ADQWs, the maximum attainable conversion efficiency at high intensities is limited by the electron transfer to X-valley states whenever the Γ -valley offsets are large enough to permit optimal detuning. Since GaAs-based waveguides also require a thick bottom cladding to isolate the active region from the substrate, the large waveguide dispersion limits the peak conversion efficiency to 2.6%.

Much better performance is predicted for InGaAs/InAlAs ADQW devices, which yield a maximum conversion efficiency of 3.7% at surface incidence for a 10 μm -thick active region. Since this value is limited by the maximum epitaxial thickness, even higher efficiencies can be obtained in waveguides with the InP substrate serving as the bottom cladding and a top cladding layer of InAlAs. The fabrication and handling of such devices is greatly simplified if the waveguide is 200-300 μm long. We have optimized our waveguide design for the absolute maximum conversion efficiency as well as for the highest conversion efficiency with the 200- μm constraint on the minimum waveguide length. In the latter case, the absorption by intersubband transitions in the active region must be minimized by detuning the intersubband transitions far from resonances with the pump and second-harmonic beams. Therefore, the saturated transitions in the active region do not yield a high conversion efficiency unless the loss of phase coherence due to the refractive index mismatch is counteracted. An attractive solution is to incorporate separate phase-matching and active regions into the waveguide core. If the intersubband transition in the phase-matching region is tuned midway between the first and second harmonics, it contributes little absorption, yet it provides sufficient compensation of the index mismatch to allow coherent propagation of pump and second-harmonic beams to distances up to and exceeding 300 μm .

Figure 1 shows phase factors as a function of propagation length for the InGaAs/InAlAs devices without a phase-matching region (dashed curve), and also with the region at zero field and at $F = -32$ kV/cm (solid curves). The figure demonstrates that the ability to maintain phase coherence over long propagation distances is considerably enhanced by the addition of a separate phase-matching region, and also that the coherence length can be tuned electrically. For the same structures and fields, Fig. 2 plots the conversion efficiency as a function of propagation length. For the optimized InGaAs/InAlAs device, $\eta_{max} \approx 16.5\%$ at a propagation length of $72 \mu\text{m}$ and pump-beam intensity of 40 MW/cm^2 . Using the Stark shift of the transition energies, electrical modulation can be used to switch off the second harmonic output for the same device under the same input conditions. A broadband electrically tunable device having a conversion efficiency greater than 1% over the entire wavelength range of $9\text{-}20 \mu\text{m}$ is also described. Electrical tuning can further be used to relax fabrication tolerances, particularly by compensating for fluctuations in the doping density. A modified structure with a similar design of the phase-matching region is predicted to allow phase coherence to be maintained with lengths up to $300 \mu\text{m}$ and to yield a conversion efficiency of 9% at $200 \mu\text{m}$ and 6% at $300 \mu\text{m}$.

A comparison of the results for optimized surface-incidence and waveguide-mode InGaAs/InAlAs and GaSb/InGaSb/AlGaSb ADQWs is shown in Figure 3. Below the saturation intensity (here $\approx 1 \text{ MW/cm}^2$), a double-resonance structure is optimal, whereas detuning leads to considerably better performance above saturation. An optimized GaSb/AlGaSb ADQWs with optically inactive L-valley states serving as a momentum-space reservoir to replenish the depleted subband states is predicted to yield a conversion efficiency exceeding 30%. However, pump-beam intensities of several hundred MW/cm^2 are required, at which point optical damage to the device may be difficult to avoid.

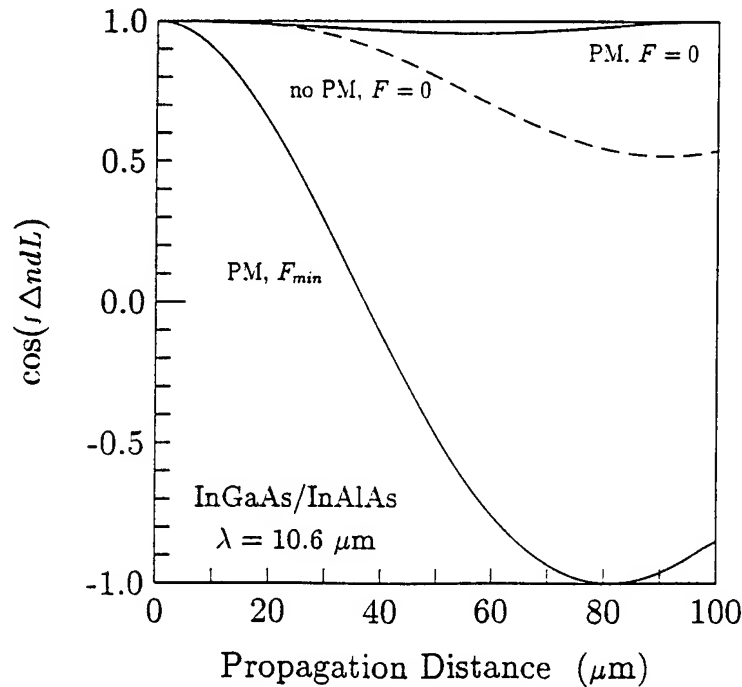


Figure 1. Phase factor vs. propagation distance at applied electric fields of 0 and $F_{min} = -32$ kV/cm for the optimized structures with a phase-matching region (solid curves) and without it at $F = 0$ (dashed curve).

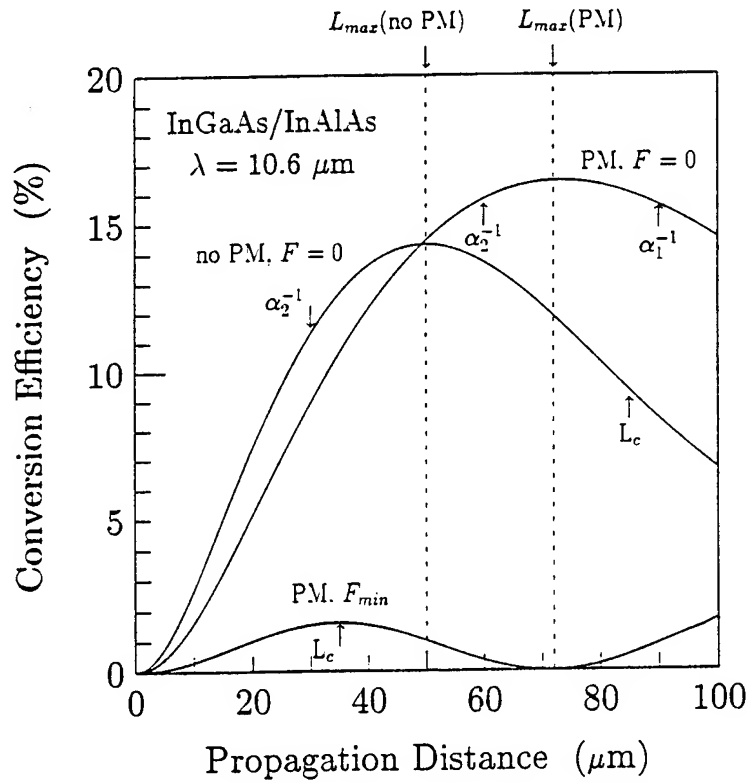


Figure 2. Conversion efficiency for the same structures and fields as in Fig. 1.

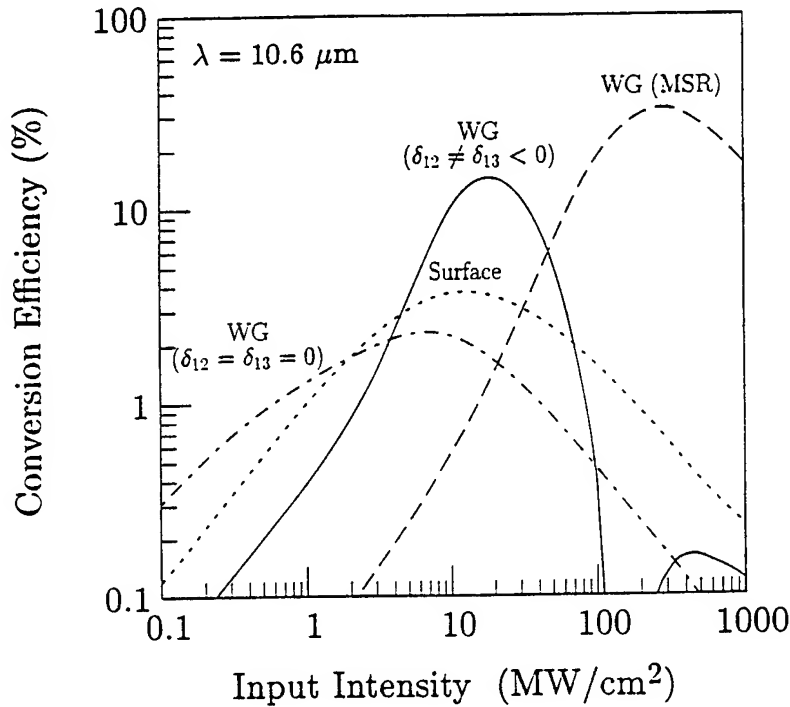


Figure 3. Maximum conversion efficiency vs. pump-beam intensity for the InGaAs/InAlAs detuned ($\delta_{12} \neq \delta_{13} < 0$) and double-resonance ($\delta_{12} = \delta_{13} = 0$) structures optimized for waveguide propagation (WG), an InGaAs/InAlAs single-resonance structure optimized for surface-incidence SHG at 45° (Surface), and a detuned GaSb/InGaSb/AlGaSb momentum-space reservoir (MSR) structure optimized for waveguide propagation.

Intersubband Quantum Box Laser Based on Image Charges

J. B. Khurgin and S. J. Lee

Department of Electrical
Computer Engineering
The Johns Hopkins University
Baltimore, MD 21218
Tel. (410) 516-7518
Fax. (410) 516-5566

Ever since the inception of lasers there has been a consistent effort towards reducing their threshold which in general can be achieved by two means: reduction of the active region size and eliminating the residual absorption. Rapid progress in the reduction of size has culminated in quantum well and microcavity lasers [1]. However, elimination of absorption, long used in NH_3 masers by the "spatial sorting-out" of excited atoms, is clearly not applicable in solid state lasers. It is only recently that "lasing without inversion", in which quantum interference causes reduced absorption, has been suggested for semiconductor quantum wells [2]. This method, however, is inherently complicated for reasons such as requiring separate probe and coupling laser beams, etc.

An ingenious and simple way to eliminate absorption, suggested by Yamanishi *et al.* [3], is to employ "spectral sorting out" i.e. to separate the emission line from the absorption line by a fixed amount of energy, using the quantum-confined Stark effect in biased quantum dots.

In this paper, we propose an improved scheme which, unlike [3], requires no external fields and is applicable to the intersubband transitions. We develop a simple theoretical model which can be used at higher temperatures and in multiple quantum box (QB) structures, and using this model we analyze the threshold of the proposed scheme.

Consider two plane arrays of QB's of different thicknesses formed by GaAs and $\text{Ga}_{1-x}\text{Al}_x\text{As}$, shown in Fig. 1. Two arrays are separated by a thin barrier layer and are thus coupled in the growth direction. On the other hand, the boxes within each array are separated by wide barriers and can be considered completely uncoupled. Therefore, the whole structure can be looked upon as an array of independent elements - asymmetric coupled QB's. If the transverse size of each QB is kept within 100\AA , each element will have no more than two quantized states - state $|1\rangle$ located mostly in the wider well and state $|2\rangle$ located in the narrower one (see Fig. 2). These two states are optically coupled, and in presence of the resonant E-M field and optical feedback provided for example by Bragg mirrors, stimulated emission can commence.

A crucial part of the proposed structure is two highly-doped (or metallic) layers located on both sides of the QB array. As a result, when there is an electron inside the QB situated in the state $|i\rangle$, equilibrium positive image charge densities, $\sigma_{L,i}(\vec{r}_\perp)$ and $\sigma_{R,i}(\vec{r}_\perp)$ develop in two conductive layers. When the electron is in the left well the equilibrium image charge density on the left is larger than on the right,

$$\sigma_{L,1}(\vec{r}_\perp) > \sigma_{R,1}(\vec{r}_\perp) \quad (1)$$

and likewise for the right well.

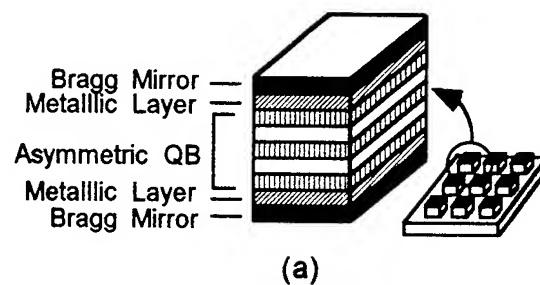


Fig. 1 Asymmetric coupled quantum box array structure.

Let us now describe the image charges by the so-called image distribution function $|\alpha_j\rangle$, ($j = 1, 2$) denoting the state with the equilibrium image charges created by the electron in state $|i\rangle$, and $\langle \alpha_i | \alpha_j \rangle = \delta_{ij}$. A complete state of the system electron-image is described by the function $|\alpha_j, i\rangle$ where j can be both equal and distinct from i . Coulomb attraction then lowers the energy of the above complete state by

$$V_{ij} = \langle \alpha_j, i | \frac{e^2}{\epsilon} \left(\frac{\sigma_{L,j}}{\sqrt{r_L^2 + r_{\perp}^2}} + \frac{\sigma_{R,j}}{\sqrt{r_R^2 + r_{\perp}^2}} \right) | \alpha_j, i \rangle \quad (2)$$

where r_L and r_R are the distances from the left and the right conductive plane. It is easy to see from (1) that diagonal matrix elements V_{ij} are larger than off-diagonal ones,

$$V_{ii} > V_{ij} \quad (3)$$

When the electron is located at the lower state $|1\rangle$ (Fig. 2a) and the image electrons have been allowed to settle into the equilibrium state, the energy of the complete state $|\alpha_1, 1\rangle$ is $E_{\alpha_1, 1} = E_1 - V_{11}$. When the electron absorbs radiation and is transferred instantly into the upper state $|2\rangle$ (Fig. 2b) the image charge still keeps its original distribution α_1 , hence the energy of the upper absorption state is $E_{\alpha_1, 2} = E_2 - V_{12}$. Thus the peak absorption energy is $\hbar\omega_{abs} = E_2 - E_1 + (V_{11} - V_{21})$. Once the electron is in state 2, the image charge density on the right increases while that on the left decreases. Within dielectric relaxation time τ_d the system relaxes into the upper emission state $|\alpha_2, 2\rangle$ (Fig. 2c) with the energy $E_{\alpha_2, 2} = E_2 - V_{22}$. From this state emission takes place with the electron being transferred to the state $|1\rangle$ while the image charge remains in the state α_2 , thus the energy of the lower emission state (Fig. 2d) is $E_{\alpha_2, 1} = E_1 - V_{21}$ and the peak emission energy becomes

$$\hbar\omega_{em} = \hbar\omega_{abs} - (V_{11} + V_{22} - V_{12} - V_{21}) \quad (4)$$

is Stokes-shifted from the peak absorption energy as can be seen from Eq. (3). Following the emission, within τ_d , the system

relaxes back into the lower absorption, or ground state $|\alpha_1, 1\rangle$ and the cycle repeats among the four states. The whole system, therefore, can be represented as a four level system, that can be pumped either optically or electrically.

The amount of Stokes shifts $\hbar\omega_{abs} - \hbar\omega_{em}$ in various GaAs/AlGaAs systems, evaluated using the standard image method, is plotted in Fig. 3. The shift ranges between 3-5 meV and increases for thicker barriers. This can be attributed to the fact that the barrier increase causes the electron wavefunction to be concentrated close to the conductive layers instead of spreading into both wells, thus enhancing the magnitude of V'_{ii} s.

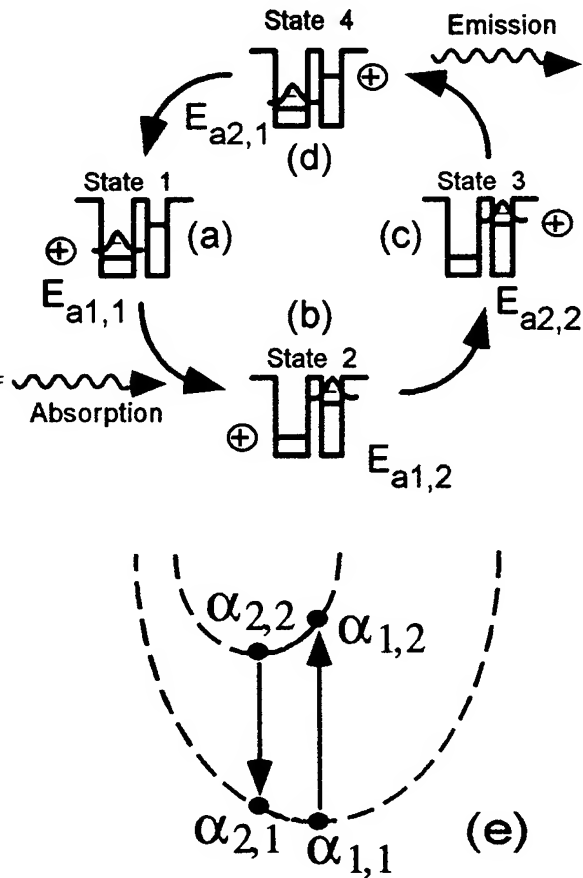


Fig. 2 (a,b,c,d) Four states involved in the absorption/emission. (e) Electronic states in terms of α .

There are two crucial condition that the system must meet; the first is that dielectric relaxation time $\tau_s = \epsilon_s/\sigma$ (~ 0.1 ps in moderately doped GaAs) must be shorter than the upper level lifetime. For transitions dominated by acoustic phonon emission (less than 36 meV), the lifetime is ~ 300 ps. [4]. and thus the above condition can be satisfied easily. Transitions with higher energies, however, are possible only in structures with large barriers where lifetimes are substantially increased.

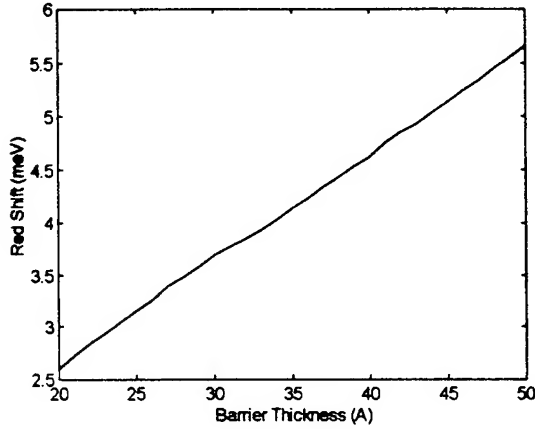


Fig. 3 red shift ($E_{\text{absorption}} - E_{\text{emission}}$) vs. barrier thickness with well sizes of 60 Å and 45 Å using conductive layers with a spacer layer thickness of 60 Å.

More important is the condition that in order to operate the laser with large number of QB's we must ensure that lower emission state is not occupied thermally, i.e. $E_{\alpha_{21}} - E_{\alpha_{11}} = V_{11} - V_{12} > kT$. In fact a better picture appears to be when one assumes that the image charge states have a continuous spectrum of energies, corresponding to all possible charge distributions. The equilibrium charge densities $\sigma_{L,i}(\vec{r}_{\perp})$ and $\sigma_{R,i}(\vec{r}_{\perp})$ correspond to the minima of energy. This convenient representation, reminiscent of any semiconductor laser shown in Fig. 2e, where configuration co-ordinate α describes the state of all the electrons in the conductive plates.

To estimate placed in a microcavity, we can express threshold pump rate by $P_{th} = n_s/\tau_{ph}\beta$ [1] where τ_{ph} is the photon decay time, β is the spontaneous emission coupling efficiency and $n_s \equiv \mathcal{E}_{21}/(\mathcal{E}_{21} - \mathcal{E}_{12})$ is the population inversion factor. Here, \mathcal{E}_{21} (\mathcal{E}_{12}) is the spontaneous emission (absorption) rate at threshold and thus n_s is equal to 1 when absorption is eliminated as in our scheme. For $\tau_{ph} \sim 1$ ps, $\beta \sim 0.1$ and $n_s \sim 1$, the threshold pump rate is of the order of 10^{13} s^{-1} . If carriers are injected, the corresponding threshold current is $\sim 1 \mu\text{A}$, a few orders of magnitude smaller than the currently achieved value ($\sim 100 \mu\text{A}$).

We also note that the concept of using image charges can be also used to without conductive layers in similar configurations. Since the magnitude of image charge depends on a factor $K = (\epsilon_1 - \epsilon_2)/(\epsilon_1 + \epsilon_2)$, materials with low ϵ_s such as AlAs can provide effective dielectric mismatch.

In conclusion, we have considered a practical lasing scheme using intersubband transitions in asymmetric coupled QB's. Ultralow threshold ($\sim 1 \mu\text{A}$) can be obtained by elimination of absorption which results from a Stokes shift between laser lines.

References

- [1] Y. Yamamoto, S. Machida, and G. Björk, Phys. Rev. A **43**, 657 (1991).
- [2] A. Imamoğlu and R. J. Ram, Opt. Lett. **19**, 1744 (1994).
- [3] M. Yamanishi and Y. Yamamoto, Jpn. J. Appl. Phys. **30**, L60 (1991).
- [4] J. Faist, et. al. Appl. Phys. Lett. **64**, 872 (1994).

Second-Order Nonlinear Optical Properties of Wide-Bandgap Semiconductors

Takashi Kondo, Kaoru Morita, and Ryoichi Ito

*Department of Applied Physics, Faculty of Engineering,
The University of Tokyo
7-3-1 Hongo, Bunkyo-ku, Tokyo 113, Japan*

Tel: +81-3-3812-2111 ext. 6842

Fax: +81-3816-7805

E-mail: tkondo@sunflower.t.u-tokyo.ac.jp

There have been growing interest in III-V semiconductors as promising nonlinear optical materials for frequency conversion devices. These devices are based on quasi-phase-matching that is achieved by spatially modulating large quadratic optical nonlinearities of semiconductors [1–5]. In order to exploit the large nonlinearities of semiconductor epitaxial films, we have developed two methods to determine the nonlinear optical coefficients of thin films by reflected second-harmonic measurements [6, 7]. In this paper, we will present nonlinear optical properties of wide-bandgap semiconductors, AlP, ion-implanted GaP and SiC, characterized by the reflected second-harmonic techniques.

A reflected-second-harmonic ellipsometric (RSHE) [7] technique was applied to characterization of an AlP. RSHE measurement involves the measurement of the power and polarization state of the reflected second-harmonic wave. The polarization property of the reflected second-harmonic wave is characterized by two parameters, $\tan \Psi$ and $\cos \Delta$, defined in the following formula:

$$E_p^{2\omega}/E_s^{2\omega} = \tan \Psi \exp(i\Delta),$$

where $E_p^{2\omega}$ and $E_s^{2\omega}$ are p - and s -components of the reflected second-harmonic field, respectively. This method provides information on the complex d coefficient and the film thickness simultaneously. We have measured d_{36} of an epitaxial film of AlP on GaP[100] grown by MBE using an Nd:YAG laser ($\lambda = 1.064 \mu\text{m}$) as a fundamental light source. Second-harmonic power, $\tan \Psi$, and $\cos \Delta$ were measured as functions of the rotation angle of the sample, and the following parameters are determined: $|d_{36}(\text{AlP})| = 0.33 \times |d_{36}(\text{GaP})|$, and the relative phase of $d_{36}(\text{AlP})$ with respect to $d_{36}(\text{GaP})$ is 20 degrees. Simultaneously determined film thickness (650 Å) agreed well with that deduced from the growth parameters. Measurements on AlGaP are now underway. The information on compositional dependence of the nonlinear optical coefficient will be prerequisite for designing quasi-phase-matching devices that can be used in visible region.

We also performed a RSHE measurement on a GaP[100] implanted with 100 keV-Ga⁺ ions at $3 \times 10^{15} \text{ cm}^{-2}$. As a result of ion implantation, the surface region of the GaP substrate is expected to become disordered resulting in reduction in quadratic optical nonlinearity. This measurement was done as the first step of our study toward the intentional control of the nonlinearity with

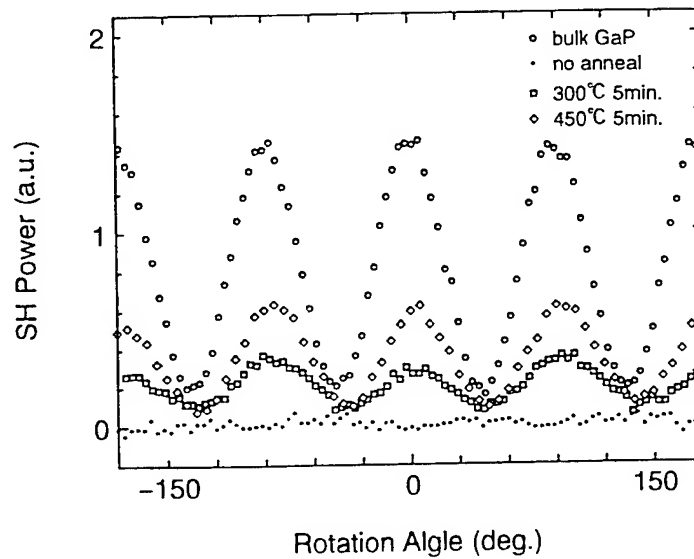


Figure 1 Reflected second-harmonic power of unimplanted, as-implanted, and annealed implanted GaP samples.

possible applications to quasi-phase-matching devices in mind. Figure 1 shows reflected second-harmonic power ($\lambda^w = 1.064 \mu\text{m}$) of unimplanted, as-implanted and annealed implanted GaP samples. It is known that heavily implanted GaP shows strong optical absorption below the bandgap and the absorption can be minimized by annealing after the implantation while the structure remains amorphous even after annealing [8]. The recovery of the second-harmonic power in the annealed samples are *not* due to re-crystallization but to the reduction in the absorption at the second-harmonic wavelength resulting in the transmission of the second-harmonic light from the unimplanted GaP substrate. Actually, RSHE measurements on Ga^+ -implanted GaP revealed that the nonlinear optical coefficient of GaP is dramatically reduced by the ion implantation followed by annealing; d value of the Ga^+ -implanted GaP annealed at 450°C was measured to be only 11% of the unimplanted GaP.

We have also characterized nonlinear optical properties of SiC. Samples we used are cubic 3C-SiC/Si[100] grown by VPE and hexagonal 6H-SiC[0001]. Figure 2 shows the experimental results. GaAs[100] is for the reference. d_{33} value of 6H-SiC was determined to be 11 pm/V in quite good agreement with the previously reported value [9]. On the other hand, no SHG activity was observed in the 3C-SiC/Si[100] sample; reflected second-harmonic power obtained was comparable with that from the surface of Si. This surprising result is believed to be due to the formation of antiphase domains [10] in the 3C-SiC epitaxial layer. Since the adjacent antiphase domains have antiparallel polarization, the formation of micro antiphase domains results in disappearance of macroscopic quadratic nonlinearity. TEM observation revealed that the 3C-SiC/Si[100] grown by VPE actually suffers from antiphase domain formation. Measurements on 3C-SiC samples free from antiphase domains are now underway in order to determine the nonlinear optical coefficient of cubic SiC.

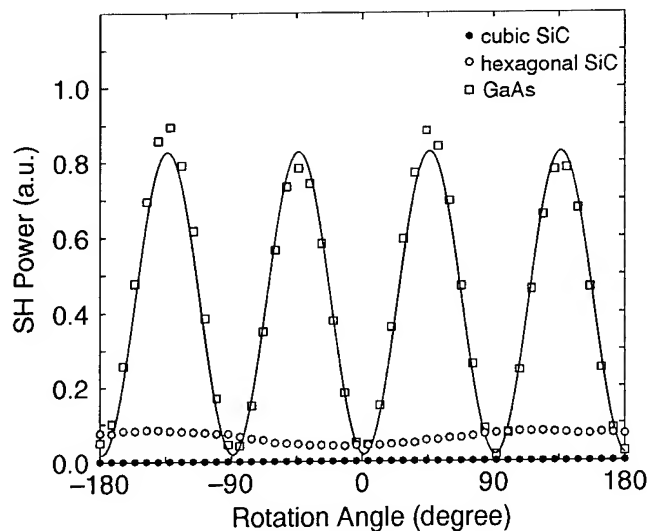


Figure 2 Reflected second-harmonic power of GaAs[100], 3C-SiC/Si[100], and 6H-SiC[0001].

In summary, we have characterized second-order nonlinear optical properties of several wide-bandgap semiconductors. We have also shown that nonlinear optical properties of semiconductor crystals can be controlled by ion implantation. In addition, we believe that “polar-on-nonpolar” epitaxy will play an important role in the future nonlinear optical devices composed of semiconductors, because the domain inversion of semiconductors may become possible by controlling the antiphase domain formation.

References

- [1] R. Normandin, S. Létourneau, F. Chatenoud, and R.L. Williams, *IEEE J. Quantum Electron.* **27**, 1520 (1991).
- [2] D. Vakhshoori and S. Wang, *J. Lightwave Technol.* **9**, 906 (1991).
- [3] H. Takahashi, M. Ohashi, T. Kondo, N. Ogasawara, Y. Shiraki and R. Ito, *Jpn. J. Appl. Phys.* **33**, L1456 (1994).
- [4] M.J. Angell, R.M. Emerson, J.L. Hoyt, J.F. Gibbons, L.A. Eyers, M.L. Bortz and M.M. Fejer, *Appl. Phys. Lett.* **64**, 3107 (1994).
- [5] S.J. Yoo, R. Bhat, C. Caneau and M.A. Koza, *Appl. Phys. Lett.* **66**, 3410 (1995).
- [6] M. Ohashi, T. Kondo, K. Kumata, S. Fukatsu, S.S. Kano, Y. Shiraki and R. Ito, *J. Appl. Phys.* **74**, 596 (1993).
- [7] T. Kondo, S. Koh, T. Tsunoda, A. Okubo, Y. Shiraki and R. Ito, *Tech. Dig. European Quantum Electron.* 262 (1994).
- [8] T. Shimada, Y. Kato, Y. Shiraki and K.F. Komatsubara, *J. Phys. Chem. Solids* **37**, 305 (1976).
- [9] S. Singh, J.R. Potopowicz, L.G. Van Uitert and S.H. Wemple, *Appl. Phys. Lett.* **19**, 53 (1971).
- [10] K. Shibahara, S. Nishino and H. Matsunami, *J. Cryst. Growth* **78**, 538 (1986).

Progress in Reducing Loss of Diffusion Bonded Stacked GaAs for Mid Infra-Red Generation

D. Zheng, L. A. Gordon, Y. S. Wu, R. C. Eckardt,
M. M. Fejer, R. L. Byer and R. S. Feigelson

Edward L. Ginzton Laboratory
Stanford University, CA 94305
Tel. (415) 723-1718
Fax. (415) 723-2666

Mid infra-red (IR) sources between 1 μm and 10 μm have wide applications in spectroscopy, remote sensing and military countermeasures. Established nonlinear IR crystals such as AgGaSe₂, and AgGaS₂ have poor thermal properties, and low damage thresholds. ZnGeP₂ appears promising for high power applications, but its growth technology is still being developed, and crystals are expensive. In comparison, GaAs has a large nonlinear coefficient, good optical transmission between 1 μm and 12 μm , and high optical damage threshold. It also has good chemical stability, good mechanical properties, and a well developed growth technology. Unfortunately, single crystal GaAs is linearly isotropic; therefore, nonlinear interactions cannot be birefringently phase-matched. However, the interacting waves can be quasi-phased-matched (QPM) by periodically modulating the nonlinear coefficient in a stack of rotated plates^{1,2}. By diffusion bonding individual plates together, we can minimize scattering and reflection losses at the air-GaAs interfaces. Preliminary diffusion-bonded-stacked (DBS) GaAs devices demonstrated close to theoretical conversion efficiency^{3,4}, but had high transmission losses. We report improved processing, leading to a significant reduction in the transmission loss to less than 0.2% per layer at 5 μm .

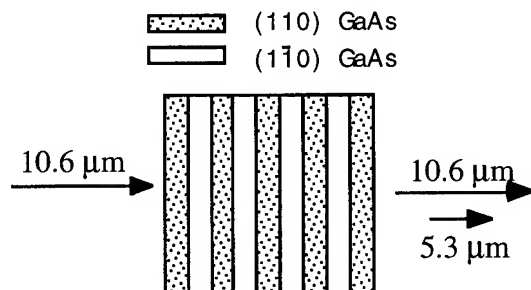


Figure 1. Diffusion-bonded stacked (DBS) GaAs for quasi-phased-matched second harmonic generation of 10.6 μm CO₂ radiation

{110} wafers were chosen to provide the maximum effective nonlinear coefficient for propagation normal to the input face. Each plate is three coherence lengths thick, with adjacent plates rotated 180° to change the sign of the nonlinear coefficient. Stacks are heated to 700-975°C under pressure to achieve diffusion bonding at the interfaces. Figure 1 illustrates second harmonic generation in DBS GaAs. A range of applications become practical for stacks with less than 0.1% additional loss per interface. Losses from both the interfaces and bulk material contribute to the total loss of DBS

GaAs. Incomplete bonding between surfaces leaves microscopic voids and gaps. Scattering due to these irregularities is the dominant loss mechanism for wavelengths less than 3 μm .

Recently, we have discovered that the bulk material undergoes a conversion during the annealing process⁵. Loss in DBS GaAs at longer-wavelengths is a result of bulk p-type free carrier absorption. Semi-insulating wafers can convert to p-type during the annealing step, dependent on soak temperatures and times, and quenching rates⁶. Conversion is also affected by thermal history and composition of wafers; it is, therefore, supplier specific. Our semi-insulating wafers converted to p-type after annealing at 834°C, with a hole concentration of around $10^{16}/\text{cm}^3$. By annealing individual wafers, we found the longer-wavelength loss increased with processing temperatures from 700°C to 834°C, as shown in figure 2. The annealing-induced loss is significantly reduced at 700°C.

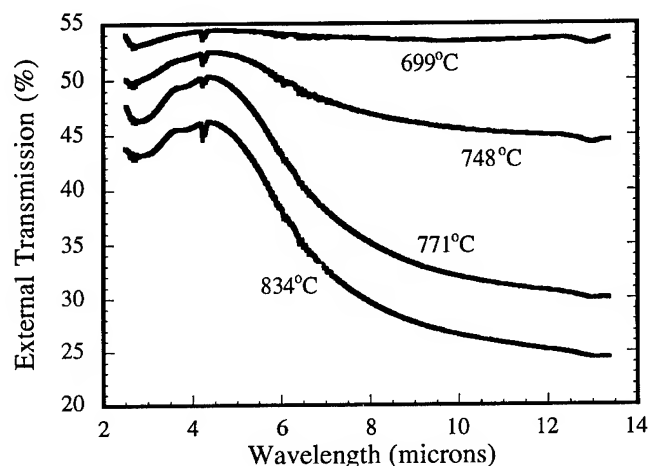


Figure 2. Transmission of a single 320- μm thick GaAs wafers annealed at different temperatures

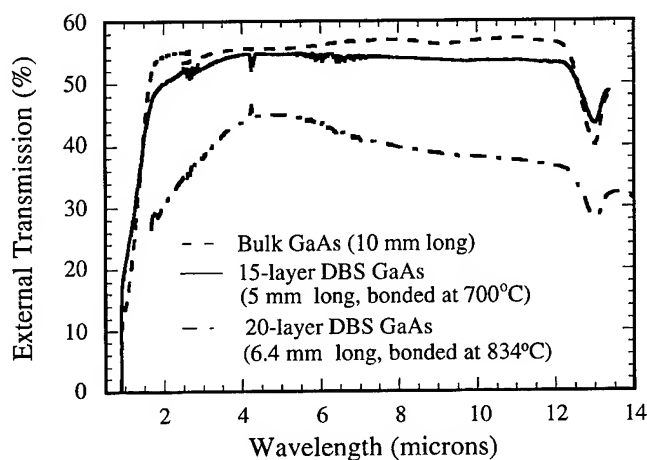


Figure 3. Comparison of the transmission spectra of the 15-layer DBS GaAs (bonded at 700°C), with the 20-layer DBS GaAs (bonded at 834°C), and a 1 cm long unprocessed bulk GaAs crystal

Figure 3 compares the optical transmission of two DBS devices bonded at different temperatures with the transmission of the bulk unprocessed GaAs. All the GaAs is from the same boule. The 20-layer DBS GaAs device, bonded earlier at 834°C, shows transmission is significantly reduced; at 5 μm the internal loss is 0.3 cm^{-1} , corresponding to 1.5% per layer. The recent 15-layer DBS device was bonded at 700°C. Its transmission at wavelengths longer than 3 μm is relatively flat, with a total internal loss of about 0.04 cm^{-1} at 5 μm , corresponding to less than 0.2% per layer. It appears that there could still be some transformation from semi-insulating to p-type doped material even at processing temperatures of 700°C. We should be able to further improve the optical transmission by lowering the temperature again, provided that we are still able to bond the wafers at the lowered temperatures, by requiring specific compositions from manufacturers, or by implementing a post-bonding annealing step. GaAs manufacturers employ multiple annealing steps to ensure high quality, uniformly semi-insulating crystals. Using similar processing techniques, we can regain high quality semi-insulating material.

In summary, a nonlinear frequency conversion device requires low loss. At higher temperatures, semi-insulating GaAs transforms into p-type, resulting in longer-wavelength absorption. By bonding at lower temperatures, we have reduced the loss to less than 0.2% per layer at 5 μm . However, some of the remaining loss is still due to p-type free carrier absorption. We plan to fabricate longer devices and demonstrate efficient second harmonic generation of high power CO₂ laser radiation.

REFERENCES

- [1] A. Szilagy, A. Hordvik and H. Schlossberg, "A Quasi-Phase-Matching Technique for Efficient Optical Mixing and Frequency Doubling," *J. Appl. Phys.* **47**, p. 2025-2032 (1976).
- [2] D. E. Thompson, J. D. McMullen and D. B. Anderson, "Second-Harmonic Generation in GaAs "Stack of Plates" Using High-Power CO₂ Laser Radiation," *Appl. Phys. Lett.* **29**, p. 113-115 (1976).
- [3] L. A. Gordon, G. L. Woods, R. C. Eckardt, R. K. Route, R. S. Feigelson, M. M. Fejer and R. L. Byer, "Diffusion Bonded Stacked GaAs for Quasi-Phase-Matched Second Harmonic Generation of a Carbon Dioxide Laser," *Electron. Lett.* **29**, p. 1942-1943 (1993).
- [4] L. A. Gordon, D. Zheng, Y. C. Wu, R. C. Eckardt, R. K. Route, R. S. Feigelson, M. M. Fejer and R. L. Byer, "Diffusion Bonded Stacked Materials for High Peak and Average Power IR Application", invited paper CLEO Pacific Rim, July 1995
- [5] D. Zheng, L. A. Gordon, R. C. Eckardt, M. M. Fejer and R. L. Byer, "Diffusion Bonding of GaAs Wafers for Nonlinear Optics Applications," *Proceedings of the 189th Electrochemical Society Meeting*, to be published.
- [6] D. C. Look, P. W. Yu, W. M. Theis, W. Ford, G. Mathur, J. R. Sizelove, D. H. Lee and S. S. Li, "semiconducting/ Semi-Insulating Reversibility in Bulk GaAs," *Appl. Phys. Lett.* **49**, p. 1083-1085 (1986).

**Near band gap time resolved reflectivity
studies of ion implanted and MBE grown GaAs:As**

S. Janz and Z.R. Wasilewski

Institute for Microstructural Sciences, National Research Council, Ottawa, Ontario
Canada, K1A 0R6; Telephone: (613)-990-0926, FAX: (613)-952-8701
E-mail: janz@nrcphy1.phy.nrc.ca

U.G. Akano and I.V. Mitchell

Department of Physics, University of Western Ontario, London, Ontario
Canada, N6A 3K7; Telephone: (519)-661-3803, FAX: (519)-661-2033
E-mail: uakano@julian.uwo.ca

Non-stoichiometric GaAs:As with an excess As concentration of approximately 2% has several unique properties including extremely short carrier lifetimes combined with a high mobility, and a large nonlinear optical response with a picosecond recovery time^{1,2}. This combination of properties is believed to arise from either As related defects or Schottky depletion regions surrounding As precipitate inclusions. GaAs:As with an excess As concentration is usually prepared by low temperature molecular beam epitaxy (MBE) (i.e. LT-GaAs), and more recently by As⁺ ion implantation³. Time resolved pump-probe transient reflectivity measurements can provide information not only on carrier lifetime, but also on the carrier induced nonlinear refractive index change, Δn . In this paper, we report the initial results of a comparative study of the transient optical reflectivity for MBE grown LT-GaAs, ion implanted GaAs:As, and semi-insulating GaAs.

Measurements of the optically induced transient reflectivity change, ΔR , were carried out on an semi-insulating GaAs wafer, a GaAs epilayer grown by MBE at 200 C, and a GaAs wafer implanted with 300 keV As⁺ ions at a dose of 1×10^{16} ions cm⁻². Both GaAs:As specimens were annealed at 600 C for 10 minutes. Transient reflectivity measurements were carried out at wavelengths between $\lambda=830$ nm and 900 nm in a conventional pump-probe geometry, using Ti:Sapphire laser with a 150 femtosecond pulse width. At $\lambda=830$ nm, the pump induced carrier density is approximately 10^{18} cm⁻³, and scales with the absorption coefficient α as the wavelength increases.

Fig. 1 shows the variation of ΔR with pump-probe delay for GaAs and LT-GaAs at several wavelengths above and below the band edge. At photon energies near the band edge (e.g. $\lambda=881$ nm), ΔR is positive for GaAs, and decays on a time scale much longer

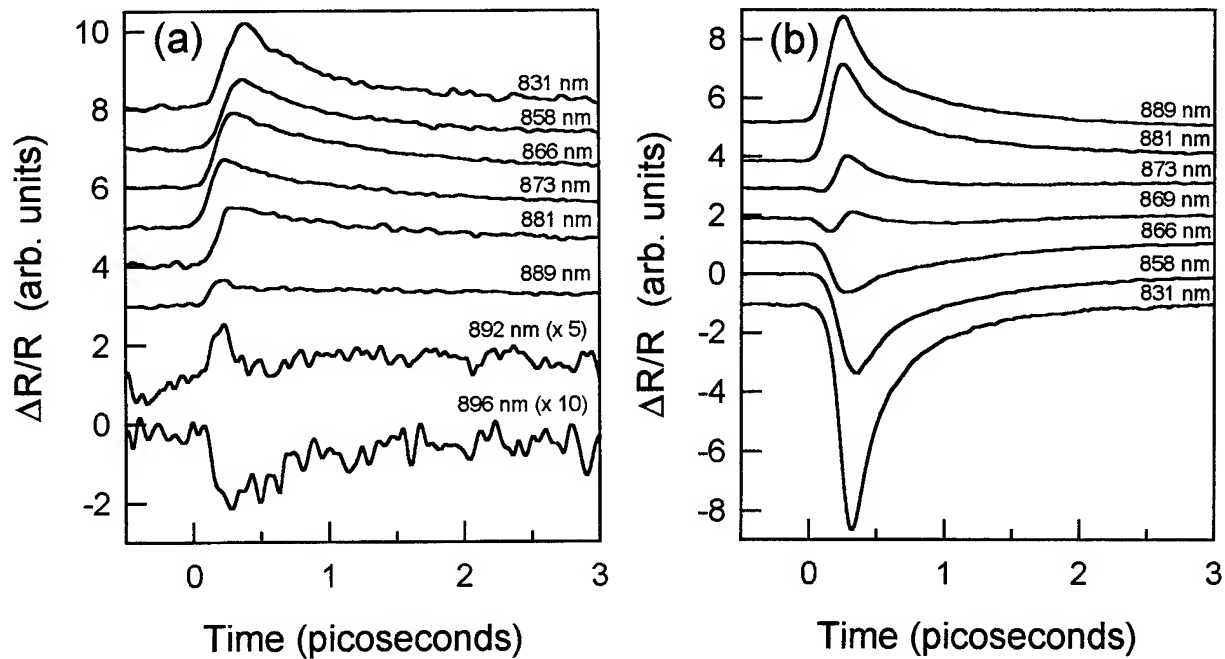


Fig. 1: Time dependence of the transient reflectivity change for (a) semi-insulating GaAs and (b) annealed low temperature grown GaAs:As (LT-GaAs) at wavelengths near the band gap. The curves have been vertically displaced for clarity.

than shown in the figures. The faster decay at higher photon energies can be attributed to the effect of carrier cooling. The variation of ΔR with wavelength is consistent with previous studies of the nonlinear response of GaAs⁴. However, below the band edge the decay of ΔR occurs in less than a picosecond, suggesting that the saturation of rapidly ionized states near the band edge is involved.

The transient reflectivity data shown in Fig. 1b for LT-GaAs, and also in Fig. 2 for ion implanted GaAs:As, differ remarkably from those for GaAs. However, the ion implanted GaAs:As and LT-GaAs exhibit similar behaviour, indicating that both preparation techniques yield As rich material with similar optical properties. The response of the implanted material is smaller, possibly due to residual implantation damage. At $\lambda=831$ nm, the peak ΔR for LT-GaAs is three times larger than that of GaAs and of opposite sign. This demonstrates that annealed GaAs:As has a nonlinear refractive index significantly larger than GaAs. Finally, unlike GaAs, the magnitude of ΔR is almost as large below the band edge as above it. In amorphous or defect rich semiconductors, free carrier absorption results in a negative Δn . However, the observed magnitude and sign change of ΔR (and therefore Δn) in GaAs:As near the band edge cannot be explained

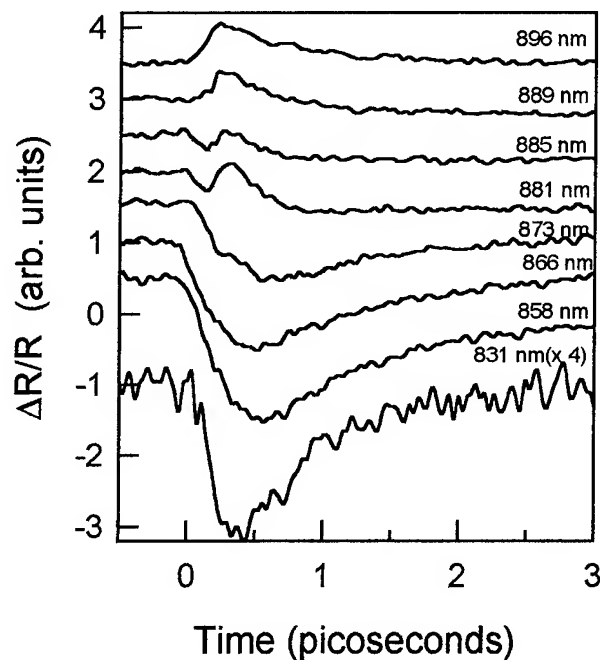


Fig. 2: Time dependence of the transient reflectivity change for As^+ ion implanted GaAs:As. The curves have been vertically displaced for clarity.

by a defect related model alone. Using the Kramers-Kronig relation, the sign change of Δn near the band edge implies an induced absorption peak near the band edge. This may be explained by the effect of band gap renormalization (BGR), which can dominate the nonlinear response if competing processes such as exciton bleaching do not occur⁴. According to the Schottky depletion region model for LT-GaAs, the presence of As precipitates may create an exciton free material, leading to an enhancement of BGR. Whether the multi-component nature of annealed GaAs:As modifies the nonlinear optical properties in some more subtle way is not yet clear.

References

1. G.R. Jacobovitz-Veselka, U. Keller, and M.T. Asom, Opt. Lett. **17**, 1791 (1992).
2. S.D. Benjamin, A. Othonos, and P.W.E. Smith, Electron. Lett. **30**, 1704 (1994).
3. A. Claverie, F. Namavar, Z. Lilliental-Weber, Appl. Phys. Lett. **62**, 1271 (1992).
4. Y.H. Lee, A. Chavez-Pirson, S.W. Koch, H.M. Gibbs, S.H. Park, J. Morhange, A. Jeffrey, N. Peyghambarian, L. Banyai, A.C. Gossard, and W. Wiegmann, Phys. Rev. Lett. **57**, 2246 (1986).

**Materials with Bistable Defects (DX Centers)
As Kerr-Like Media**

Ian Redmond and Richard A. Linke
NEC Research Institute, Inc., 4 Independence Way
Princeton, New Jersey 08540 USA
Phone 609-951-2639, FAX 609-951-2483

Spatially selective ionization of defect sites known as "DX" centers produces phase-type holographic diffraction gratings which have been reported with efficiencies above 10% for grating periods as small as 135nm [1, 2]. Diffraction gratings in Te-doped AlGaAs are persistent for years for sample temperatures below an annealing temperature which is about 70K. The mechanism for grating decay (recapture of electrons into DX centers) is thermally activated with a barrier height of 0.24eV for this material and therefore its rate is a strong function of temperature. We have shown [3] that when operated above the annealing temperature, these DX materials can support dynamic four-wave mixing and optical phase conjugation (PC) using milliwatt infrared beams [4].

Here we describe results of a calculation of the strength of the nonlinearity together with measurements of optical phase conjugation with reflection efficiencies of 2.5% using Te-doped AlGaAs as the nonlinear medium. For this application we hold the crystal at a temperature of 100-120K and operate with decay times in the range of seconds to milliseconds. In order to estimate the magnitude of the nonlinearity in this medium we solve a rate equation for the carrier density as a function of incident intensity and ambient temperature. Since the dependence of refractive index on carrier density is well characterized in semiconductors [6] we can determine the value of n_2 (the change in refractive index per unit intensity change) and thus find the third order nonlinear susceptibility, $\chi^{(3)}$, taking 3.2 as the refractive index of AlGaAs. The results of this calculation are shown in Figure 1 for Te-doped AlGaAs at low incident intensities. We find that the non-linearity can be very large, especially at lower temperatures where the decay time constant becomes long.

We have carried out four-wave mixing experiments on this material using the apparatus shown in Figure 2. This is the classical PC setup with counter-propagating equal-strength pump beams and a third, much weaker, probe beam. All three beams were derived from a diode laser at 0.85 μ m wavelength. The phase-conjugate signal was clearly visible with a reflectivity of 2.5%. The reflection efficiency is shown in Figure 3 as a function of temperature for a fixed pump beam intensity of 32mW/cm² per beam. The reflection efficiency is expected to show a peak in temperature since the nonlinearity is smaller at higher temperatures but the material saturates at low temperatures when recombination can not keep up with pump-induced ionization of DX centers.

To demonstrate that the reflected beam is a phase-conjugate beam we image a mask into the medium and introduce a phase abberator in the path. Figure 4 shows the aberated image and the corrected image before and after phase-conjugate reflection back through the abberator.

References

1. R. A. Linke, T. Thio, J. D. Chadi and G. E. Devlin, *Appl. Phys. Lett.* **65**, 16 (1994).
2. R. A. Linke, R. MacDonald, G. Devlin, T. Thio, J. Chadi and M. Mizuta, Proceedings CLEO'95, May 21-26 (1995).
3. R. L. MacDonald and R. A. Linke, "Optical Phase Conjugation using DX Centers," to be published in *J. Opt. Soc. Am.*, JOSA-B, 1996.
4. B. R. Bennett, R. A. Soref and J. A. Del Alamo, *IEEE J. Quant. Electron.*, **26** 113 (1990).

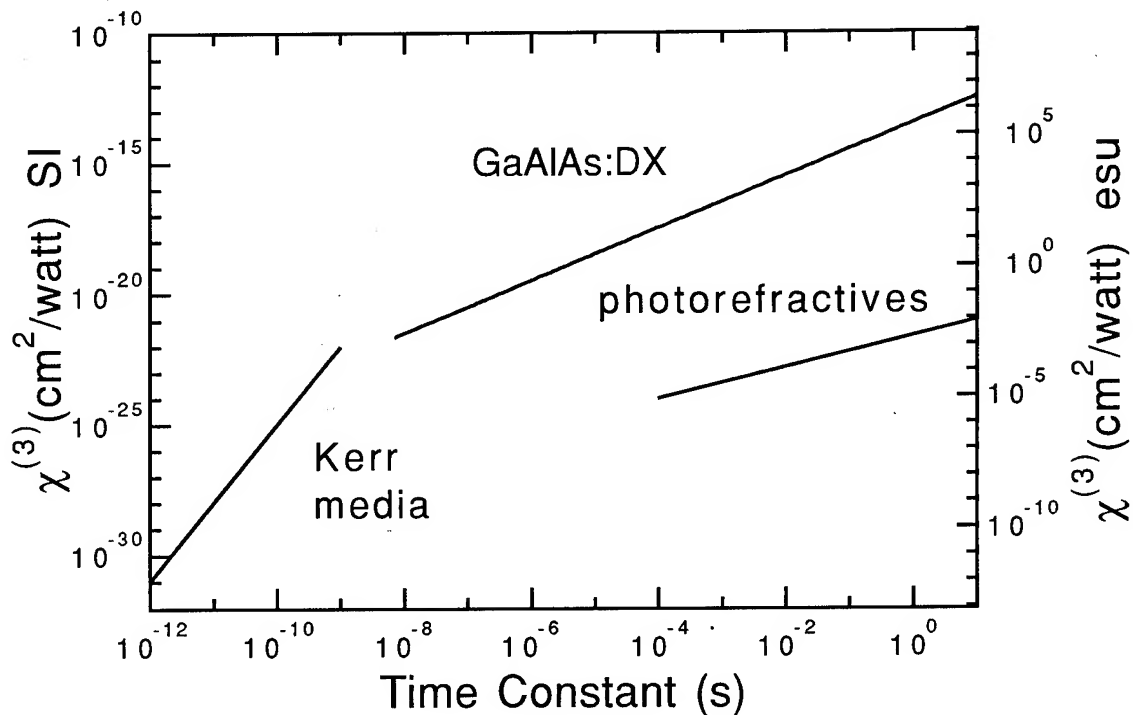


Figure 1. Third order nonlinear susceptibility for the DX material AlGaAs:Te compared with conventional Kerr media and photorefractives.

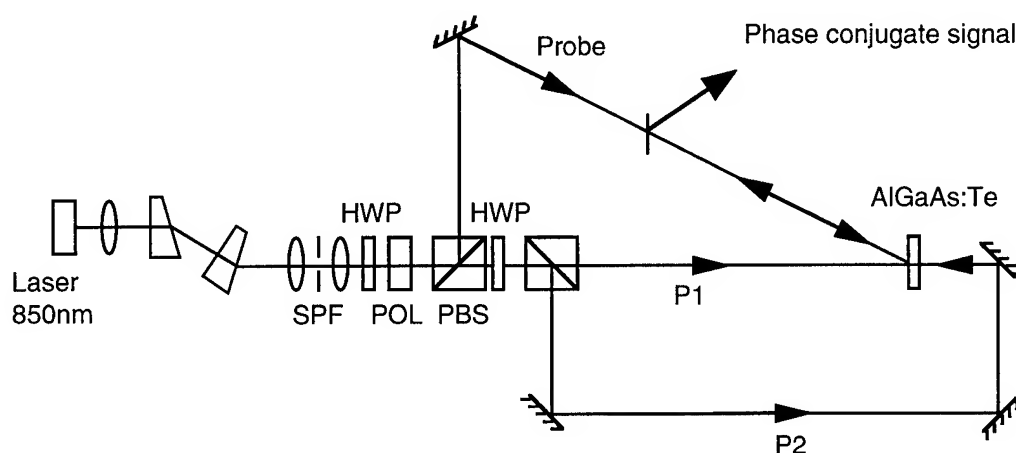


Figure 2. 4-wave mixing experimental setup

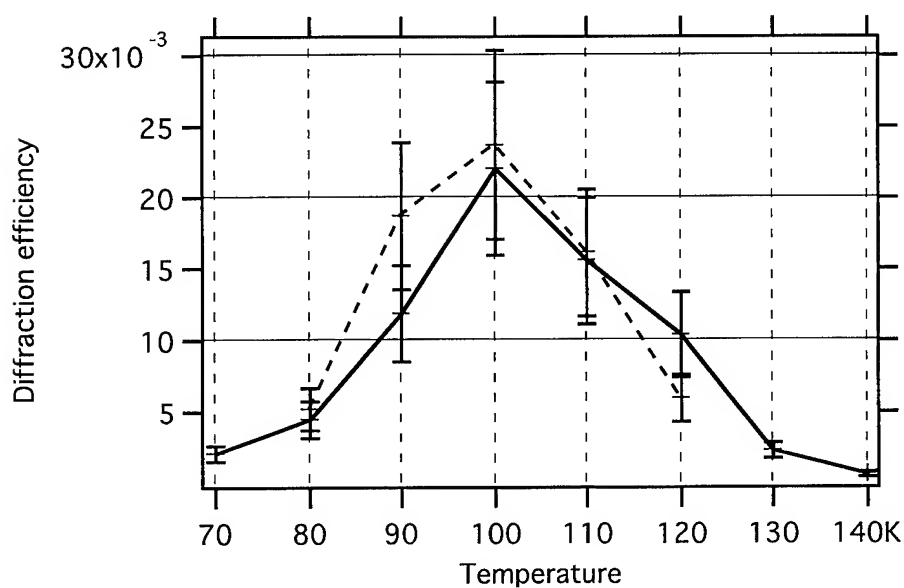


Figure 3. Phase conjugate refractivity data.

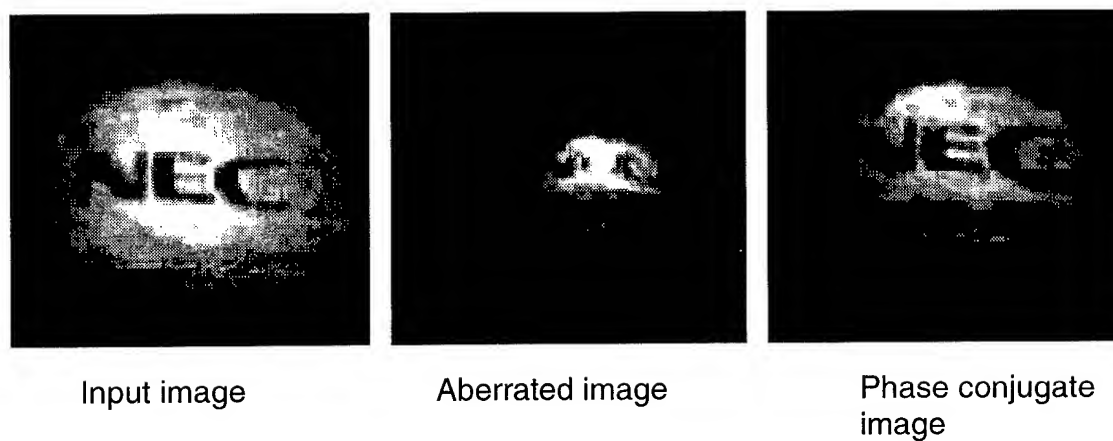


Figure 4. Aberration recovery by phase conjugation in DX material.

Friday, July 12, 1996

NLO of Atomic Systems

NFA 8:00 am-9:40 am
Maile Room

Christopher Clayton, *Presider*
U.S. Air Force Phillips Laboratory

Distinction between lasing without inversion and parametric nonlinear optics.

Thomas W. Mossberg
Department of Physics and Center for Optics in Science and Technology
University of Oregon, Eugene, Oregon 97403
Phone: 541- 346-4779
Fax: 541-346-4791
E-mail: twmoss@oregon.uoregon.edu

Many optical devices have the capacity to amplify light beams. Some of these devices are referred to as lasers. Some are referred to as wavemixing or parametric devices. Still others, such as driven two-level atoms, are frequently described as wavemixing devices but, in many instances, are actually lasers.

To a physicist, a process is well defined when it can be uniquely identified through a specific set of physical measurements. Inasmuch as there is debate over whether a variety of optical gain mechanisms ought to be referred to as laser or parametric processes, it is apparent that these processes have not yet been subjected to rigorous definition. We attempt here to identify the key distinguishing attributes of these processes always keeping in mind that meaningful distinctions lead to unambiguous characterization. We will then examine driven two- and three-level atomic systems, with and without atomic inversion, and show that in many cases the gain generated in these systems cannot be experimentally differentiated from traditional laser gain.

We will also discuss and describe a new mechanism[1] to explain some aspects of the inversionless laser gain[2] observed in driven two- and more-level quantum systems. This mechanism involves stimulated multiphoton transitions wherein one step of the transition always proceeds via spontaneous radiation. The presence of the spontaneous step breaks the complete symmetry between stimulated emissive and absorptive processes characteristic of established laser gain

mechanisms. It is the expected symmetry of emission and absorption that has led us to expect that population imbalance is crucial to determining the dominance of gain or loss. We call the non-symmetric emission process "intrinsically irreversible multiphoton stimulated emission."

In an inverted medium, resonant light amplification by stimulated emission of radiation proceeds in a highly singular manner. Semiclassically, a primary field acts to generate a material polarization. The polarization is uniquely phased so as to emit a secondary field that constructively interferes with the primary. The secondary field automatically and unavoidably assumes the proper constructive phase. The hallmark of classic laser action is the generation of input-field-phase-insensitive optical amplification. There are many laser devices having diverse ancillary properties, e. g. gain bandwidth, energy storage time, inversion pumping mechanism, spectral offset of pump and laser output, etc. However, all lasers based on the familiar stimulated emission mechanism share the same phase insensitive character. We take this physically tangible property as the defining characteristic of laser gain. In the case of classic wavemixing processes, e. g. second harmonic generation, parametric downconversion, etc., an entirely different situation prevails. In the classic wavemixing systems, the optical gain displayed is phase-sensitive. Changing the phase of the signal field, can convert amplification into attenuation.

Within the class of phase insensitive amplifiers, i. e. lasers, additional unique attributes can be identified. One of the most important is the ability to convert incoherent pump energy into

coherent output. In the case of optically pumped lasers, we refer to the incoherent to coherent energy conversion process as “spectral energy condensation.” The extent to which various laser systems exhibit spectral energy condensation is investigated. Contrary to widespread impression, driven two-level-atom lasers are shown[3] to exhibit substantial spectral energy condensation and are thus further distinguished from wavemixing/parametric processes.

In conclusion, we will suggest a systematic and simple means of characterizing optical gain processes based on their fundamental and measurable essential properties. We then review gain mechanisms of current interest and evaluate their character. We will also describe an new class of irreversible stimulated emission processes that provide new insight into the phenomena of inversionless lasing.

Financial support of the U.S. National Science Foundation is acknowledged as are the contributions of P. B. Sellin and G. S. Agarwal.

References:

1. P. B. Sellin, C. C. Yu, J. Bochinski, and T. W. Mossberg (to be published).
2. For a review see: O. Kocharovskaya, *Phys. Rep.* **219**, 175 (1992).
3. P. B. Sellin, T. W. Mossberg, and G. S. Agarwal (to be published)

Bose Einstein Condensation

Eric Cornell
University of Colorado

Summary not available.

Nonlinear Optics Using Electromagnetically-Induced Transparency

K. Hakuta

Department of Applied Physics and Chemistry, and Institute for Laser Science

University of Electro-Communications, Chofu, Tokyo 182, Japan

Phone +81-424-86-2820, Fax. +81-424-85-8960, e-mail: hakuta@pc.uec.ac.jp

Recently, there has been increasing interest on the idea of controlling optical responses using atomic-coherence or quantum-interferences. Typical example may be the concept of electromagnetically-induced transparency (EIT) [1]. The key idea of EIT is to apply a strong-coupling field between a metastable and upper states to dress them equivalently as two states decaying to a common level or continuum, and to induce the transparency at the split-center of Autler-Townes components. This idea of EIT may open new possibilities to various coherent processes, such as lasing without population inversion, enhanced refractive index without absorption], slow group velocity without absorption, enhanced nonlinearity without absorption, etc.

In the present paper, we discuss on the resonantly enhanced nonlinear optical process without absorption loss [2]. The point is to realize resonantly enhanced nonlinear optical susceptibility with keeping linear susceptibility at minimum value through EIT. Sum-frequency generation (SFG) process using atomic hydrogen as a test medium is described theoretically and experimentally. Multiphoton-ionization (MPI) process which may accompany with the SFG process is also discussed, especially on its behavior through quantum interferences.

Figure 1 illustrates the interaction scheme; bare atomic hydrogen states of $1s$, $2s$, and $3p$ are denoted as $|1\rangle$, $|2\rangle$, and $|3\rangle$, respectively. A laser field is applied to strongly couple the metastable-state $|2\rangle$ with the upper state $|3\rangle$, resulting in a pair of dressed states $|2d\rangle$ and $|3d\rangle$. Another laser field is used for the two-photon coupling of the states $|1\rangle$ and $|2\rangle$. Sum-frequency generation occurs at the resonant $3-1$ transition. The optical responses of the atomic system can be calculated by obtaining the susceptibilities through the equations for time-varying single-atom probability

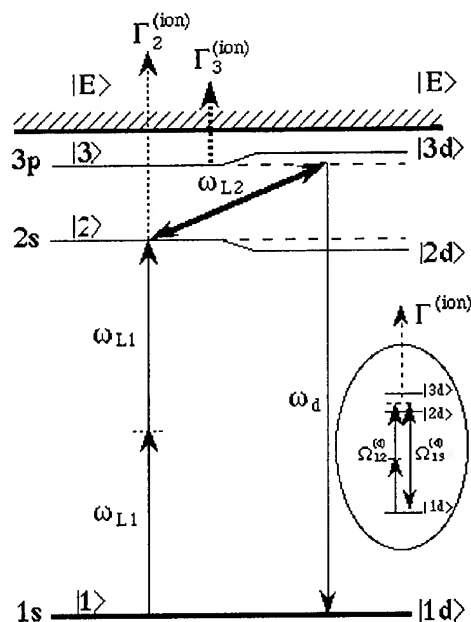


Fig. 1 Energy-level diagram for the SFG-process in atomic hydrogen using EIT.

amplitudes. The MPI-rate may also be calculated as a loss-rate of ground state atoms. We derived the linear and nonlinear optical susceptibilities, and photoionization rate using the dressed-state-basis-set. For numerically calculating the susceptibilities, the susceptibilities were calculated by convolving the Gaussian density of states due to the thermal Doppler-broadening.

Experiments were carried out by using two pulsed single-longitudinal-mode dye lasers, operated at 486 and 656 nm. The 656 nm laser was used to strongly couple the 2s and 3p states. The 486 nm output was frequency-doubled by a BBO crystal for generating 243 nm radiation (2-photon excitation). The 243 and 656 nm laser beams were loosely focused by using two lenses with focal lengths of 1 m and 1.5 m, respectively, and were overlapped spatially with the use of a dichroic mirror. Hydrogen atoms were generated in a microwave discharge at 2.45 GHz using H₂ gas. The

maximum density of atomic hydrogen was estimated to be 10^{15} cm^{-3} .

The calculated tuning characteristics of the generated radiation for four different NL values (product of atom-density and interaction length), versus the detuning of the two-photon frequency $\Delta\omega_1$ are illustrated in Fig. 2(a). The coupling Rabi-frequency was fixed at $\Omega_{23}=10 \text{ cm}^{-1}$. At the relatively low NL value of $2 \times 10^{14} \text{ cm}^{-2}$, the spectrum shows two peaks corresponding to the two dressed states. It is important to note that the intensity at the center remains at half of its peak value. This profile reflects a typical behavior of the nonlinear susceptibility; its value maintains a resonant value at the center due to constructive interference. As NL is increased up to $3.5 \times 10^{15} \text{ cm}^{-2}$, the intensities at the dressed states are quickly saturated, but the intensity at the center can grow quadratically with NL , up to $3.5 \times 10^{15} \text{ cm}^{-2}$. This quadratic enhancement at the center reveals that absorption has been

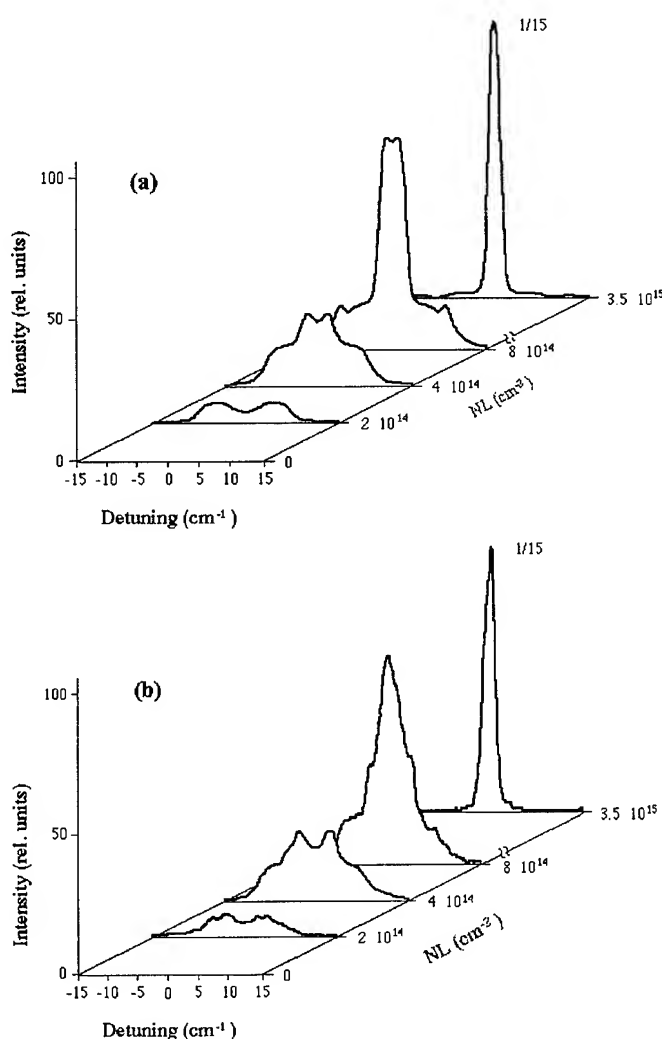


Fig. 2 Tuning characteristics of sum-frequency generation for various NL -values; Calculated characteristics (a) and observed characteristics (b). The Ω_{23} -value is 10 cm^{-1} .

reduced to almost zero at the center, and that the phase-matching condition is simultaneously satisfied.

In Fig. 2(b) are shown the observed tuning characteristics of the generated radiation versus detuning $\Delta\omega_1$ for four different NL values, with the coupling strength Ω_{23} fixed at 10 cm^{-1} . The spectra at $NL = 2 \times 10^{14}$ and $4 \times 10^{14}\text{ cm}^{-2}$ show a two-peak structure, reflecting the profiles of the dressed nonlinear susceptibility. When the NL -value was raised to $8 \times 10^{14}\text{ cm}^{-2}$, the intensity at line center increased by a factor of 16, a quadratic enhancement with increase of NL value. At $NL = 3.5 \times 10^{15}\text{ cm}^{-2}$, the intensity at the center increased about 200 times compared with that at $2 \times 10^{14}\text{ cm}^{-2}$. The observed results are in good agreement with the calculated spectra of Fig. 2(a).

We should note on the spectral profile for the SFG-characteristics at the split center for high- NL region, which is much narrower than the Doppler width observed for low- NL region. This is an important consequence of propagation effect under the strong-coupling condition. Through the interaction during the propagation, the SFG-radiation can only grow up at the split center where EIT-condition is satisfied. On the other hand, since the coupling Rabi-frequency far exceeds the Doppler-tail which decreases much more quickly to the detuning than the Lorentzian tail, the susceptibilities at the split center can basically be described by their Lorentzian-tail behaviors. Consequently, the SFG characteristics behaviors lead to a narrow Doppler-free profile at the center under the high NL -condition. This behavior is transferred to that for MPI-signals which reflect directly the characteristics of SFG-process.

The SFG-process using EIT for the generation of coherent VUV-radiation has been discussed with atomic hydrogen as a test medium. While the present work has demonstrated the possibility of nonlinear optical generation using EIT in the atomic hydrogen, this concept should be applicable to other atomic and molecular systems, as well as fabricated quantum-well structures, and may open new possibilities for generating short-wavelength coherent radiation. The extension of the present method to solid-materials will be discussed.

References

- [1] A. Imamoglu and S. E. Harris, Opt. Lett. **64**, 1107 (1989);
- [2] S. E. Harris, J. E. Field, and A. Imamoglu, Phys. Rev. Lett. **64**, 1107 (1990); K. Hakuta, L. Marmet, and B. P. Stoicheff, Phys. Rev. Lett. **66**, 596 (1991); K. Hakuta, L. Marmet, and B. P. Stoicheff, Phys. Rev. A **46**, 5152 (1992); G. Z. Zhang, K. Hakuta, and B. P. Stoicheff, Phys. Rev. Lett. **71**, 3099 (1993); M. Jain, G.Y. Yin, J.E. Field, and S. E. Harris, Opt. Lett. **18**, 998 (1993); G. Z. Zhang, M. Katsuragawa, K. Hakuta, R. I. Thompson, and B. P. Stoicheff, Phys. Rev. A **52**, 1584 (1995); J. C. Petch, C.H. Keitel, P. L. Knight, and J. P. Marangos, Phys. Rev. A **53**, 543 (1995); M. Katsuragawa, G. Z. Zhang, and K. Hakuta, Opt. Commun, in press.

Enhanced Nonlinear Optics Using an Atomic Local Oscillator

Maneesh Jain, H. Xia, A. J. Merriam, G. Y. Yin, and S. E. Harris.

Edward L. Ginzton Laboratory,
Stanford University,
Stanford, CA 94305-4085.

phone: (415) 725 2259.

fax: (415) 725 4115.

Nonlinear optical mixing of existing laser frequencies to access portions of the spectrum where lasing action is not easily obtainable is common practice today. Although nonlinear solid-state media are available [1] for frequency conversion from just under 200 nm in the ultraviolet to about a few microns in the infrared, the generation of widely-tunable laser radiation in the mid-to-far infrared and VUV regions typically requires four-frequency mixing in atomic vapors. In the past, frequency conversion in atomic vapors suffered from poor conversion efficiencies due to the small magnitude of the third-order nonlinear susceptibility and the difficulty in phasematching. We demonstrate a method [2] for performing four-frequency mixing which overcomes both of these shortcomings, allowing efficient frequency conversion with moderate pump intensities.

Our method is based on preparing an atomic local oscillator. In order to prepare the local oscillator, we use two lasers whose frequencies differ by a Raman resonance [Fig. 1(a)]. These lasers take atoms which are usually in ground state $|1\rangle$, and force a fraction of them into metastable state $|2\rangle$. In doing so, the lasers impose a fixed phase relationship between the atoms in the ground state and those in the metastable state. This new, phased state of the atoms effectively behaves like a $|1\rangle$ - $|2\rangle$ atomic local oscillator. An additional (third) laser frequency input to the system simply beats against this local oscillator and generates sum and difference frequencies [Fig. 1(b)]. The essence of this method is in preparing the atomic local oscillator over sufficiently large density-length products and in phasematching the process by adjusting the phase of the local oscillator. The phase of the local oscillator is controlled by very small detunings of the lasers from two-photon resonance. This requires precise laser technology which has only recently become available.

We work in atomic ^{208}Pb vapor and the laser wavelengths required to create the atomic local oscillator are 406 nm and 283 nm [Fig. 1(a)]. These wavelengths are obtained by frequency doubling and tripling Ti:Sapphire lasers at 812 nm and 850 nm, respectively. The laser systems must also satisfy the following characteristics: High power density ($\sim 10^7 \text{ W/cm}^2$), near-Gaussian spatial mode, smooth pulse envelopes with no phase noise, absolute frequency stability to within several MHz, and continuous tunability of several GHz [3]. These requirements are met by pulse-pumped Ti:Sapphire ring lasers, injection seeded by a continuous-wave master oscillator. Using these laser systems, we have demonstrated, in several experiments, our ability to carefully prepare a local oscillator under realistic conditions. The results include ultra-electromagnetically induced transparency and the elimination of optical self-focusing [4].

We have very recently performed the first nonlinear optics experiments utilizing the local oscillator and demonstrated the ability to carefully phasematch the interaction. The third laser wavelength (425 nm, [Fig. 1(b)]) is NOT special and was chosen for convenience (doubled 850 nm Ti:Sapphire). It should be emphasized that this laser frequency can be tuned freely and can indeed be broadband. The photon-to-photon conversion efficiency from 425 nm to 293 nm for this process (ignoring pump-depletion effects) is given by

$$\eta = |\beta L|^2 |\rho_{12}|^2 \text{sinc}^2(\Delta k L / 2\pi) \quad \dots(1)$$

where βL is the phase shift of the generated frequency, ρ_{12} is a measure of the atomic coherence, and $\Delta k L$ is the phase mismatch. In our experiment, $\beta L = 0.8$. The process was phasematched using very small changes ($\sim 100 \text{ MHz}$) in the 283 nm laser frequency yielding a large-signal conversion efficiencies of about 3% [Fig. 2]. Small-signal conversion efficiencies were near 8%. The laser intensities were all near 5 MW/cm^2 . Our next step is to repeat the experiments at larger densities ($\beta L \sim 2.4$). According to Eq. (1), this will increase the conversion efficiency by a factor of nine, resulting in pump-depletion-limited conversion.

We have demonstrated the use of an atomic local oscillator to obtain efficient frequency conversion in a four-frequency mixing process. Similar experiments which efficiently generate widely-tunable infrared radiation can be performed by difference-frequency mixing with the local oscillator. A Ti:Sapphire laser (λ_b , [Fig. 1(b)]) tuned from 720 nm to 936 nm, will frequency-convert to the infrared (λ_a) from $3 \mu\text{m}$ to $300 \mu\text{m}$. Here, large photon-to-photon conversion efficiencies will require an increase in the density-length product to compensate for the larger detuning.

REFERENCES

- [1]. M. M. Fejer, *Physics Today* **47**, 25 (May 1994).
- [2]. S. E. Harris, *et. al.*, *Phys. Rev. Lett.* **64**, 1107 (1990); K. Hakuta, *et. al.*, *Phys. Rev. Lett.* **66**, 596 (1991); M. Jain, *et. al.*, *Opt. Lett.* **18**, 998 (1993).
- [3]. A. Kasapi, *et. al.*, "A Pulsed Ti:Sapphire Laser Seeded Off the Gain Peak," *Appl. Opt.* (to be published, March 1996).
- [4]. A. Kasapi, *et. al.*, *Phys. Rev. Lett.* **74**, 2447 (1995); M. Jain, *et. al.*, *Phys. Rev. Lett.* **75**, 4385 (1995).

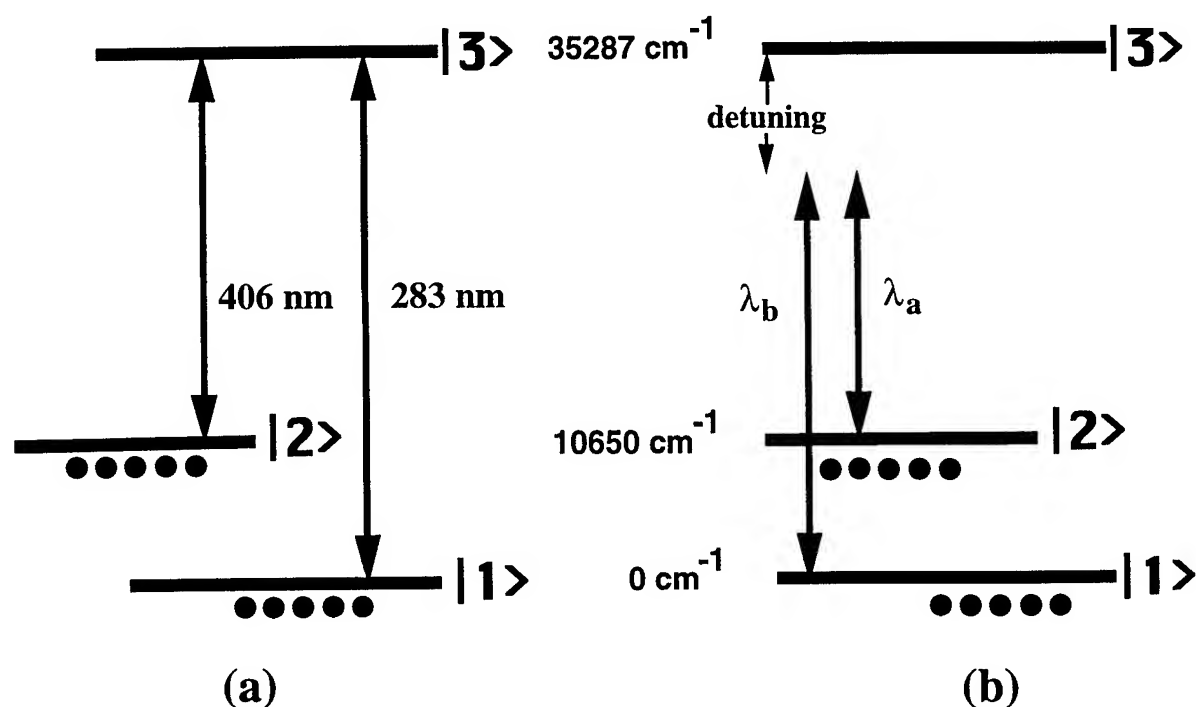


Figure 1. (a) Two lasers at 406 nm and 283 nm prepare the atomic local oscillator. (b) The lasers in (a) are still present, but are not shown for brevity. Here, an input field at λ_a beats against the local oscillator to generate a sum frequency at λ_b . When $\lambda_a = 425 \text{ nm}$ and $\lambda_b = 293 \text{ nm}$, the detuning is 1100 wavenumbers. $|1\rangle$ and $|2\rangle$ denote the ground and metastable state respectively.

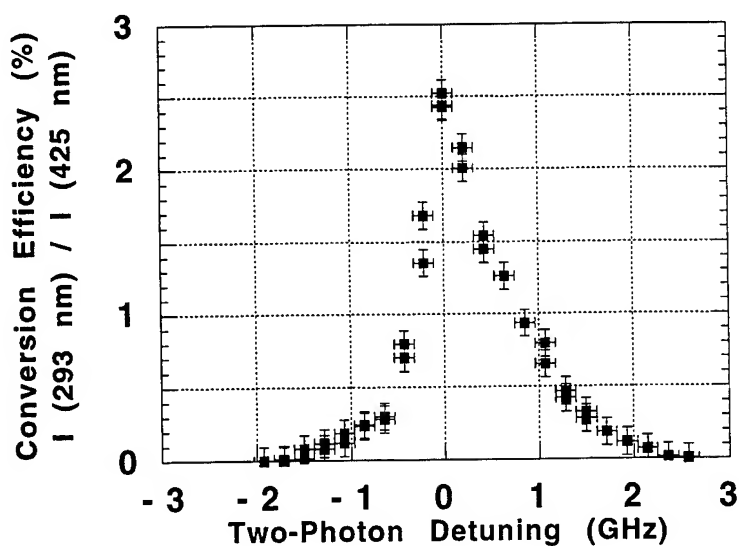


Figure 2. Phasematching Curve. The phase of the local oscillator is controlled by very small laser detunings from two-photon resonance.

Friday, July 12, 1996

Optical Solitons

NFB 10:00 am-11:40 am
Maile Room

Dana Z. Anderson, *Presider*
University of Colorado

Form-stable pulse propagation in 3-level media: adiabatons and matched pulses

Michael Fleischhauer

Sektion Physik, Ludwig-Maximilians-Universität München,
Theresienstraße 37, D-80333 München, Germany
tel: +89 2394 4542, fax: +89 280 52 48
e-mail: mfleisch@mfl.sue.physik.uni-muenchen.de

The resonant interaction of pulse-pairs with multi-level atoms has attracted some attention in recent time because of the possibility of a quasi-loss-free propagation in otherwise optically thick media. The pulse-pair propagation in Λ -type atoms as shown in Figs.1 is here discussed in terms of the adiabatic coupled and decoupled superpositions of the lower levels.

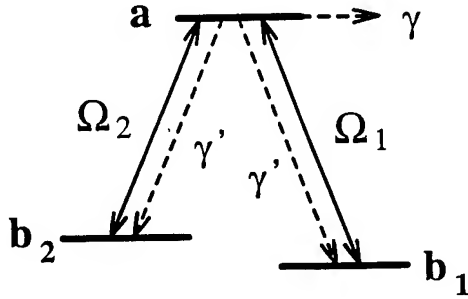


Fig.1 Λ -type atom in bare basis

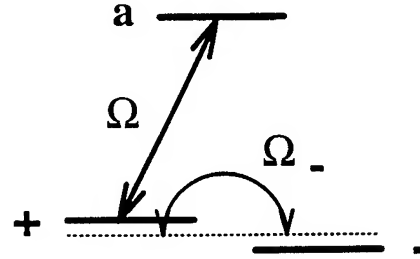


Fig.2 Λ -system in adiabatic dressed basis

We denote by Ω_1 and Ω_2 the real, but time-dependent Rabi-frequencies of the two pulses coupled to the bare-state transitions. It is well known that, when the two pulses change in time very slowly or are cw-fields, the atom-field interaction is best described in terms of the adiabatic dark ($|-\rangle$) and bright states ($|+\rangle$).

$$|+\rangle = \frac{1}{\Omega} \left[\Omega_1 |b_1\rangle + \Omega_2 |b_2\rangle \right], \quad (1)$$

$$|-\rangle = \frac{i}{\Omega} \left[\Omega_2 |b_1\rangle - \Omega_1 |b_2\rangle \right], \quad (2)$$

where $\Omega = [\Omega_1^2 + \Omega_2^2]^{1/2}$ is the total Rabi-frequency. The interaction hamiltonian only couples the levels $|a\rangle$ and $|+\rangle$ while $|-\rangle$ is decoupled from the system in the adiabatic limit.

In order to describe quasi-adiabatic phenomena we use this basis and derive Maxwell-Bloch equations. The explicit time-dependence of the states is thereby fully taken into account. The atomic densitymatrix equations in the new basis correspond again to a 3-level system as shown in Fig.2. Due to non-adiabatic corrections there is a (weak) coupling between the adiabatic bright and dark state in addition to the strong coupling between

the bright state and the upper level. The corresponding formal Rabi-frequency is denoted by

$$\Omega_- = \frac{\dot{\Omega}_1 \Omega_2 - \dot{\Omega}_2 \Omega_1}{\Omega^2}. \quad (3)$$

The Maxwell equations for the 1-dimensional propagation of the two "fields" read in the slowly-varying-amplitude-and-phase approximation

$$c \frac{\partial}{\partial \xi} \Omega(\xi, \tau) = -g^2 N \text{Im}[\rho_{a+}], \quad c \frac{\partial}{\partial \xi} \Omega_-(\xi, \tau) = ig^2 N \frac{\partial}{\partial \tau} \left(\frac{\rho_{a-}}{\Omega} \right). \quad (4)$$

Here g is the atom-field coupling constant and N is the density of atoms. $\xi = z$ and $\tau = t - z/c$ are coordinates in a moving frame.

Full adiabaticity is achieved in the system, when $\Omega_- \equiv 0$. This is the case when

$$\frac{\dot{\Omega}_1}{\Omega_1} = \frac{\dot{\Omega}_2}{\Omega_2}, \quad (5)$$

which implies that both pulses can have arbitrary strength and an arbitrary but identical shape.

If the medium is initially prepared in a coherent superposition of lower levels, such that $\rho_{--}(0) = 1$, pulse pairs that fulfill the condition $\Omega_-(0, \tau) = 0$ will propagate loss-free through the medium, which is optically thick for each of the individual pulses. All population remains in $|-\rangle$ hidden from the interaction. This is the situation of *matched pulses* discovered by Harris [1].

For a pair of pulses with identical shapes and all population initially in the states $|a\rangle$ and $|+\rangle$ instead of $|-\rangle$, the propagation problem reduces to that of a single field of Rabi-frequency Ω interacting with a two level atom. A quasi-formstable propagation in such a situation is possible, if the conditions for self-induced transparency are given. An example is the 2π -hyperbolic secant pulse

$$\Omega(\xi, \tau') = \frac{1}{T} \text{sech} \left[\frac{\tau'}{T} \right], \quad (6)$$

where $\tau' = t - z/v$, v being the group velocity of the soliton. This solution corresponds in the original bare basis to a pair of soliton solutions with identical hyperbolic secant shape, the *simultons* discovered by Konopnicki and Eberly [2].

For a non-vanishing but small non-adiabatic coupling, such that $|\Omega_-| \ll \Omega$, the coupling between the dark and bright state can be treated perturbatively, if the decay from the upper level is taken into account. If again the system starts in the dark state, a coherence between $|a\rangle$ and $|+\rangle$ is build up only in higher order of perturbation. Therefore the total field remains unchanged in first order: $\partial\Omega/\partial\xi = 0$. The equation of motion for the non-adiabatic coupling can then be solved analytically. One finds for the Fourier-transform of Ω_- in the important special case $\Omega = \text{const.}$:

$$\Omega_-(\xi, \omega) \approx \Omega_-(0, \omega) \exp \left\{ -\frac{g^2 N}{\Omega^2} \left[i\omega + \omega^2 \frac{\gamma_{\perp}}{\Omega^2} \right] \frac{\xi}{c} \right\}. \quad (5)$$

The first term corresponds to a linear dispersion and the second one to an absorption of the high-frequency components.

If γ_{\perp}/Ω is sufficiently small the second term can be ignored and Eq.(5) describes the propagation of the "pulse" Ω_{-} in a linear dispersive medium. The physical origin of this is electromagnetically induced transparency of the field Ω_{-} induced by the strong constant field Ω . Hence Ω_{-} propagates formstable with a group velocity $v < c$. In terms of the original field two pulses with complementary adiabatically changing shapes propagate form-stable. These are the *adiabatons* found by Grobe, Hioe and Eberly [3]. An example for an adiabatons propagation is shown in Fig.4 for $\gamma_{\perp}/\Omega = 0.1$. Time is measured in units of Ω^{-1} and the propagation distance in units of the one-photon absorption length. The top curve shows the analytical result, the bottom one that of a numerical beam-propagation code.

For larger values of γ_{\perp}/Ω or larger propagation distances, the second term in Eq.(5) cannot be ignored. It describes the decay of the adiabatons, until eventually $\Omega_{-} \rightarrow 0$, i.e. pulses with identical shape are generated. The decay of the adiabatons is shown for $\gamma_{\perp}/\Omega = 2.5$ in Fig.5. The absorption of high-frequency components is also responsible for a partial reduction of noise in the adiabatons.

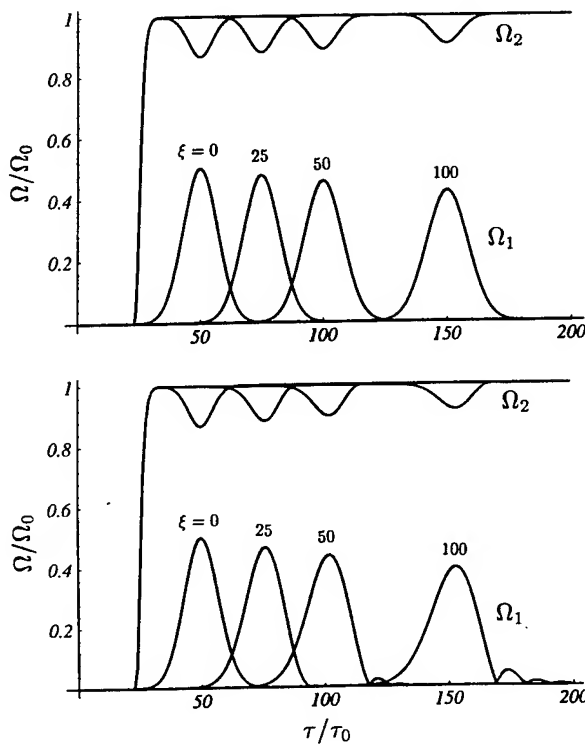


Fig.4 adiabatons propagation, small decay

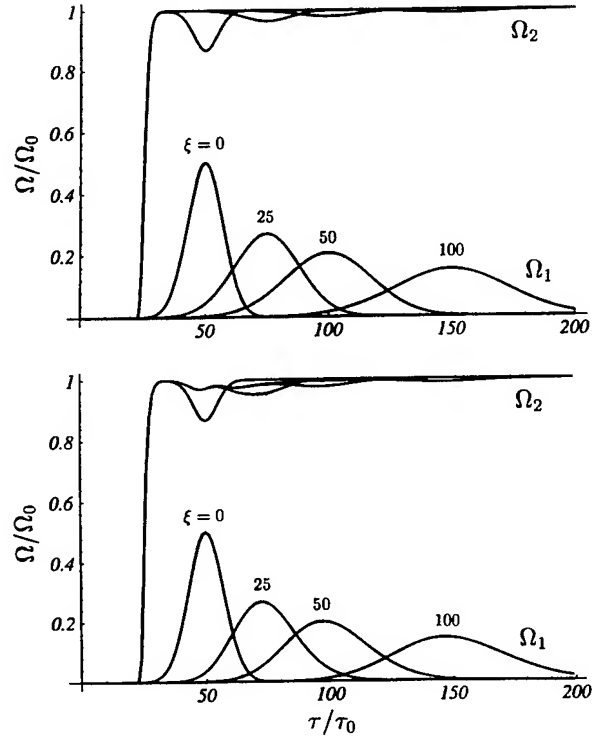


Fig.5 adiabatons decay for larger upper level decay

-
- [1] S.E. Harris, Phys.Rev.Lett. **70**, 552 (1993); *ibid.* **72**, 52 (1994)
 - [2] M.J. Konopnicki, J.H. Eberly, Phys.Rev.A **24**, 2567 (1981)
 - [3] R. Grobe, F.T. Hioe, J.H. Eberly, Phys.Rev.Lett. **73**, 3183 (1995)

Measurements of the Nonlinear Phase Shift from Orthogonally Polarized Solitons Collisions

S.D. Koehler, J. N. Kutz, L. Leng, and K. Bergman

609-258-1174 FAX 609-258-1954

Department of Electrical Engineering, Princeton University
and Advanced Technology Center for Photonics and Opto-Electronic Materials
Room B-312 Engineering Quadrangle, Princeton, NJ 08544

JNK is with the Department of Mathematics, Princeton University

As bitrates in communications and computing systems continue to increase, a demand is created for ultrafast time domain demultiplexing (TDM) components. Much research has recently concentrated on interferometric fiber optic switching, and many of the devices consist of fiber loop mirrors, relying on a non-linear phase shift to induce the switching [1-4]. However, the $\chi^{(3)}$ nonlinearity of fibers is extremely weak long interaction lengths have been a source of severe latency. In order to reduce these latencies, it is desirable to induce large non-linear phase shifts in relatively short fiber lengths without significantly distorting the temporal pulse shape or its spectrum. We present analysis and experiments of a switching scheme based on a collision between two orthogonally-polarized soliton pulses in a highly birefringent polarization-maintaining (PM) optical fiber.

The collision occurs when two pulses are initially delayed with respect to each other such that one pulse, polarized along the fast fiber axis, overtakes a second pulse polarized along the slow axis. If the birefringence is sufficiently large, the collision is quick and the pulses exchange a cross nonlinear phase shift while leaving each other's shape unchanged. Such a switching system has been proposed and demonstrated employing several weak collisions to obtain a net nonlinear phase of π , where the phase shift per collision was much smaller than π [5,6].

We have found through numerical studies and experiments that a nonlinear phase of the order π can be obtained in a single collision between a large control pulse and a weaker signal pulse, yet without affecting the signal's pulse shape. The interaction length for the collision was approximately 20cm, and the total device length which included sufficient initial and final separation between the pulses, was only 2m long. The complete numerical and analytical studies of the soliton collisions [7] produced good agreement between the full numerical coupled nonlinear Schrodinger equations (NLS) partial differential equations (PDE) model, a reduced ordinary differential equations (ODE) model, and an analytic approximation based on a Gaussian approximation of the soliton pulse shape.

We found that the collisional phase shift imparted on the signal pulse depends predominantly on the integrated energy of the pump pulse. Thus, even the simple analytical model remained valid for higher order control pulse solitons, regardless of when the collision occurred during the periodic control soliton evolution. From the analytic Gaussian approximation, the collisional phase shift experienced by the signal is expressed as

$$\sigma_{\text{coll}} = \frac{\lambda^2 |D| A^2}{3 \sqrt{\pi} \Delta n (\tau / 1.76)} , \quad (1)$$

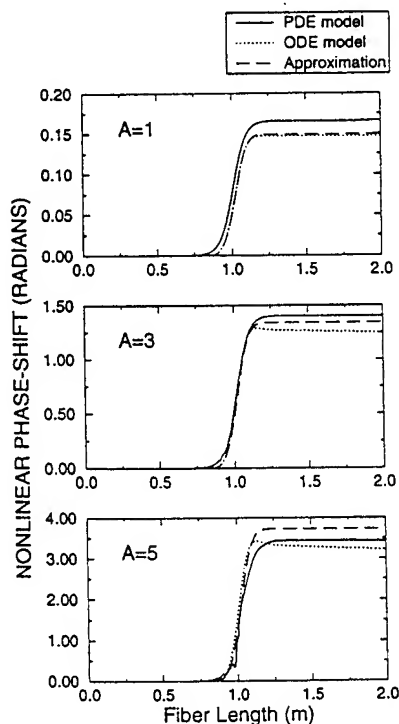


Figure 1: Computed nonlinear collisional phase shift via the full numerical PDE model, (solid line), reduced ODE model (dotted line) and the analytical approximation (dashed line) for $A=1$, 3, and 5.

where λ is the free-space optical wavelength, D is the dispersion parameter, Δn is the fiber birefringence, and A is a coefficient on the pump pulse peak electric field normalized to a first-order soliton. (We use A rather than N because A need not be an integer). In figure 1 we show the predicted collisional nonlinear phase shift imparted on the signal pulse for various values of the control pulse amplitude. We obtain excellent agreement between the full numerical PDE model, the reduced ODE model, and the analytic approximation.

In our experiments, we use Fujikura polarization maintaining (PM) fiber, with D and Δn estimated to be 13 ps/nm/km and 5×10^{-4} , respectively. For a pulse width of $\tau = 200$ fs, the interaction length of the collision is approximately 20 cm. Figure 2 shows the experimental setup used to measure the collisional phase shift in the signal pulse as a function of control pulse power.

An optical parametric amplifier (Coherent OPA 900) pumped by a regeneratively amplified mode-locked Ti:sapphire laser (Coherent Mira and RegA 9000) produces pulses in its idler beam with wavelength $\lambda = 1.55 \mu\text{m}$ and pulse width $\tau = 200$ fs (FWHM) at a repetition rate of 200 kHz. This beam is split into reference, signal, and control pulses as shown, and the polarization of the control beam is rotated by 90° .

The intensity of the control beam can be varied, while the intensities of the signal and reference pulses are held constant. The signal pulse power corresponds to a first-order soliton. The signal and control pulses are delayed with respect to the reference pulse by approximately 1 ns, and the signal is also delayed with respect to the control. The control pulse is chopped at 400 Hz.

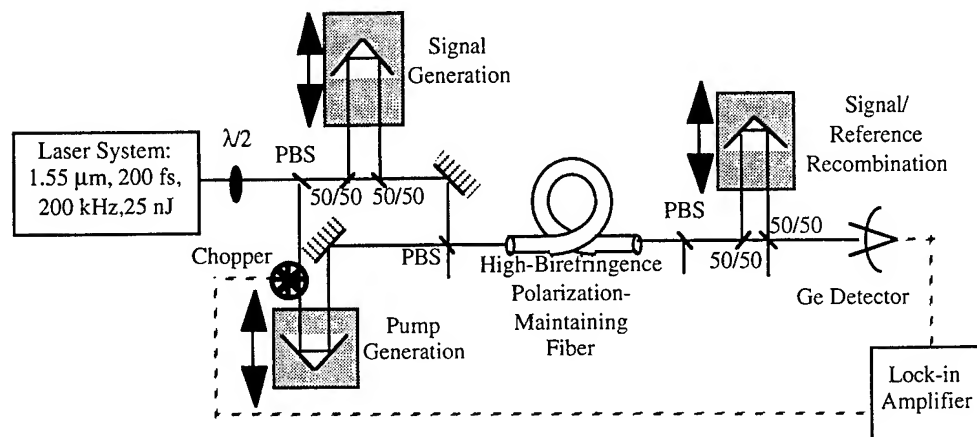


Figure 2: Experimental setup for soliton collision in a birefringent fiber. PBS indicates a polarizing beamsplitter, 50/50 indicates a non-polarizing beamsplitter, $\lambda/2$ is a half-wave plate.

All three beams are launched into 2 m of the PM fiber, with the signal and reference beams along the fast fiber axis and the control pulse along the slow fiber axis. Thus, the control pulse passes through the signal pulse inside the fiber, causing a collisional phase shift in the signal pulse. After the fiber, the control pulse is removed by a polarizing beamsplitter, and the signal and reference pulses are interfered. Since the reference and signal pulses follow the same path, the effects of self-phase modulation and linear phase accumulation are automatically canceled, and only the collisional phase shift caused by the control pulse is measured. The collisional phase shift measurements (Figure 3) show fairly linear dependence with the control pulse intensity, as expected from equation 1.

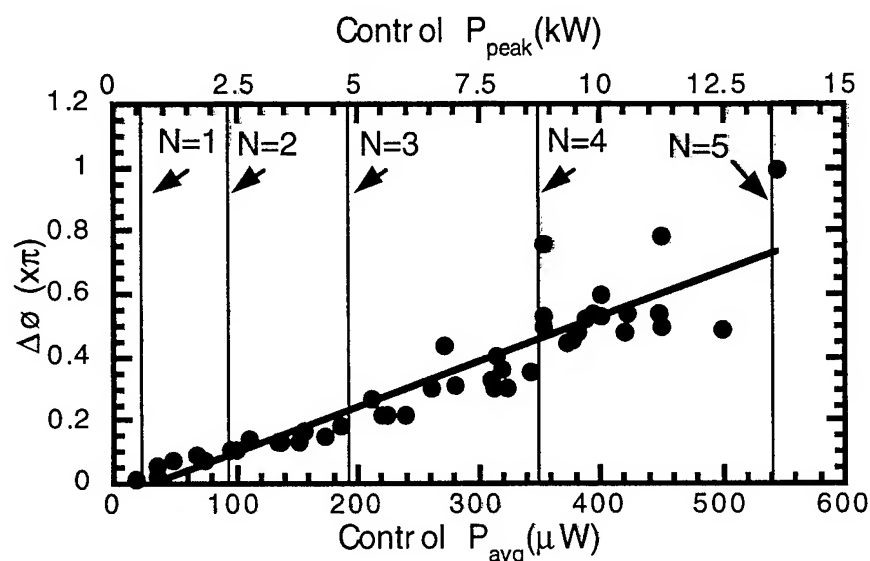


Figure 3: Collisional phase shift on first order signal as a function of control pulse power (average and peak). The solid circles indicate experimental data, and the line is a linear fit (equation 1) to these data. The vertical lines indicate integral soliton orders in the pump pulse.

We gratefully acknowledge support from the National Science Foundation (ECS-9502491). JNK is also with AT&T Bell Laboratories, and acknowledges support from an NSF University-Industry Postdoctoral Fellowship (DMS-9508684).

References:

1. N. J. Doran and D. Wood, *Optics Letters*, **13**, 56 (1988).
2. M. N. Islam, E. R. Sunderman, R. H. Stolen, W. Pleibel, and J. R. Simpson, *Optics Letters*, **14**, 811 (1989).
3. K. J. Blow, N. J. Doran, and B. P. Nelson, *Electronics Letters*, **26**, 962 (1990).
4. N. A. Whitaker, M. C. Gabriel, H. Avramopoulos, and A. Huang, *Optics Letters*, **16**, 1999 (1991).
5. J. D. Moores, K. Bergman, H. A. Haus, and E. P. Ippen, *Journal of the Optical Society of America B*, **8**, 594 (1991).
6. J. D. Moores, K. Bergman, H. A. Haus, and E. P. Ippen, *Optics Letters*, **16**, 138 (1991).
7. J. N. Kutz, S.D. Koehler, L. Leng, and K. Bergman, submitted to *Journal of the Optical Society of America B*.

Optical Bullet-holes in Semiconductors

W. J. Firth, A. Lord and A. J. Scroggie

Department of Physics & Applied Physics

University of Strathclyde, Glasgow G4 0NG, Scotland

Tel (+) 44 141 552 and: (voice 4400 Ext. 3354) (fax 2891)

M. Brambilla, L. A. Lugiato, R. Penco, R. Pregiolato and L. Spinelli

Departmento di Fisica

Universita della Studi di Milano, via Celoria 16, 20133 Milan, Italy

Tel (+) 39 2 239 and: (voice 2264) (fax 2712)

Stable, robust two-dimensional spatial solitons could act as “bits” for parallel information storage and processing. We present analytic and numerical evidence for the existence of stable 2D soliton-like states in optically driven semiconductor cavities. We consider both free-carrier and excitonic nonlinearity, and use parameters appropriate to VCSEL structures. In output these solitons would appear as transparent disks on an absorbing background, formed by aiming a short pulse of light at the target location: hence our term “optical bullet-holes” (OBH) [1]. We demonstrate a self-correcting 2D OBH array memory based on this concept.

Our models are based on the mean-field (high-finesse) cavity model for a two-level medium [2,3]. Generalising this model to allow for diffusion of the excitation permits neglect of grating effects, enabling Fabry-Perot cavities to be handled by such a mean-field model. We thus describe the system by a pair of partial differential equations in the complex field E and normalised population D :

$$\partial_t E = -E[(1 + \alpha_b + i\theta) + 2C(1 - i\Delta)D] + E_I + i\nabla^2 E \quad (1)$$

$$\partial_t D = -\gamma[(1 + |E|^2)D - 1 - d\nabla^2 D] \quad (2)$$

Here time has been scaled to the decay rate of the empty-cavity field, E_I is the external pump field, α_b describes background material absorption, and θ is the cavity mistuning parameter. The transverse coordinates are scaled to the diffraction parameter $a = L_{eff}/k$, with k the optical wave-vector and L_{eff} is the effective cavity length [2]. $2C$ is the coupling strength of the saturable response associated with the excitation D , which has scaled decay rate γ and diffusion coefficient d . The detuning parameter Δ may be associated with a Lorentzian-type resonance such as that of excitons in quantum well cavities [4], or with the linewidth enhancement factor in a free-carrier device. We can handle both cases by a suitable definition of D :

$$D = \frac{N/N_0 - 1}{I/I_0 - 1} \quad (3)$$

Here N and N_0 are respectively the excitation density and its saturation value, at which D vanishes. Allowing for mixed electrical and optical excitation, I and I_0 are the injection current and its transparency value. With $I > I_0$, we can describe an optically-driven VCSEL between transparency and laser threshold.

We consider OBH structures in parameter regions where (1,2) have a *stable* homogeneous background field solution, on which OBH can be created, and sit stably, at any chosen location.

The purely absorptive case $\Delta = d = 0$ of (1,2) is essentially equivalent to the case analysed in [1], and presents phenomena typical of the semiconductor models. Fig. 1a shows a typical OBH for this case. Relative to the background field E_s it has a strong central peak surrounded by a fairly shallow trough. Physically, the OBH acts a self-induced waveguide, with the guidance provided by the (negative) loss profile – there is no linear or nonlinear index profile in the medium in the resonant case $\Delta = 0$.

We have also simulated an optical memory array of 4x4 pixels based on these OBH, with *programmable* pixels created with a small constant spatial phase modulation of the input field E_I [1]. Because the OBH drift up phase gradients, substantial mis-targeting of address "bullets" can be automatically corrected, as Fig. 1b,c shows. Thus the address tolerance here is the pixel pitch, typically several times larger than the island size limiting the address tolerance of material pixels [5].

We observe similar OBH phenomena in the two semiconductor models. For an excitonic nonlinearity we observe stable OBH for Δ up to 1.5, showing OBH to persist into the *self-defocusing* domain ($\Delta > 0$).

In our optically-driven VCSEL model, Δ becomes the linewidth enhancement factor, corresponding between transparency and threshold to a self-focusing nonlinearity. We again find stable OBH over a wide range of experimentally interesting parameters. At 10% below laser threshold, OBH coexist with hexagonal patterns, with other patterns appearing at higher input fields.

In both models we have been able to create and erase the OBH at any location with gaussian address pulses of suitable width and duration (out of phase with the steady input field E_I for erasure). Typical sizes for these OBH are about 15 μm assuming a cavity length of 5 μm and 1% losses. Smaller OBH can be achieved by reducing the cavity length and possibly the diffusion length. The paraxial approximation inherent in our present model is not a real restriction on OBH size, and we are confident that they exist also in non-paraxial generalisations of the above models.

With appropriate design and array geometries, there are good prospects of wavelength-scale parallel information storage and processing based on these OBH.

References

- [1] W. J. Firth and A. J. Scroggie, Phys. Rev. Lett. **76**, 1623 (1996)
- [2] L. A. Lugiato and C. Oldano, Phys.Rev. A **37**, 3896 (1988)
- [3] W. J. Firth and A. J. Scroggie, Europhys. Lett. **26**, 521 (1994)
- [4] V. Pellegrini, F. Fuso, E. Arimondo, F. Castelli, L. A. Lugiato, G. P. Bava and P. Bernardi, Phys.Rev. A **50**, 5219 (1994)
- [5] J. L. Oudar, B. Spez, R. Kuszelewicz, J. C. Michel, R. Azoulay, Phys. Stat. Sol. B **159**, 181 (1990)

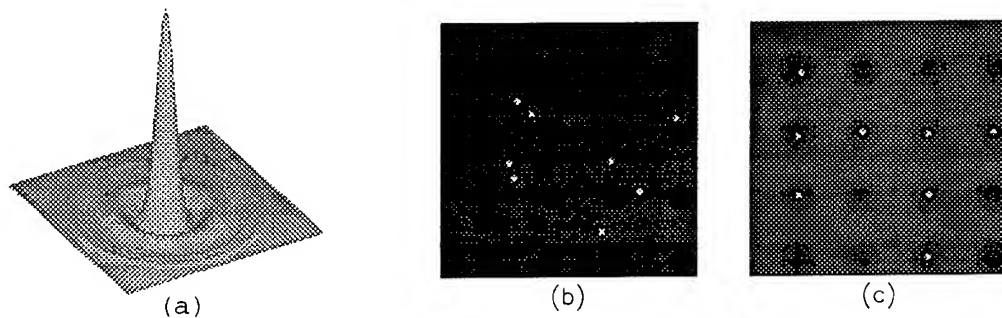


Figure 1: (a) $|E|$ plotted in the transverse plane for a stable OBH. (b) Output image just after addressing of a 4x4 OBH pixel array (deliberately mis-directed). (c) Background phase profile defining pixels has corrected for aiming errors, the letters "IT" are accurately stored in the array.

The Bright Future of Darkness in Nonlinear Optics

G. A. Swartzlander, Jr.
Physics Department
Worcester Polytechnic Institute
Worcester, MA 01609
(508) 831-5420 (voice) -5886 (fax)
<<http://www.wpi.edu/~grovers>>

C. T. Law
Electrical and Computer Engineering Dept.
University of Wisconsin at Milwaukee
Milwaukee, WI 53201
(414) 229-6203 (voice) -6958 (fax)
<lawc@ee.uwm.edu>

Dark solitons are often overshadowed by bright solitons when optical solitons are discussed, perhaps because they have proven more difficult to control and utilize. Whereas a single bright soliton is formed by a simple packet of light, a dark soliton requires a phase difference between two parts of the packet. The extra effort of controlling the phase, however, allows new and unexpected opportunities. For example, arrays of two-dimensional vortex solitons having no bright soliton analogy are possible. When used as bits of information, dark solitons may be more closely spaced than bright solitons in a one-dimensional system. What is more, dark solitons may, in principle, be observed in weakly nonlinear media because there is no threshold intensity. When consideration is given to light-controlling-light, dark solitons have the advantage that a bright signal may be guided or modulated in a dark region. Dark spatial solitons have been mostly investigated in nonlinear refractive media [1], although they have recently been reported in photorefractive media under a voltage bias.

So far soliton-soliton interactions have only been observed in nonlinear-refractive systems. Systems exhibiting one transverse degree of freedom were investigated in both the temporal and spatial domains. Allowing two transverse degrees of freedom was found to support vortex-solitons which have only been observed in the spatial domain [2]. We have observed complex vortex-vortex interactions in our investigations [2-4], but only recently have well-controlled experiments become possible. Recently, vortices on a self-defocusing beam [5] were observed [6] to interact differently than simple linear vortex interactions [7].

What makes the interaction of vortices so interesting is the extra degree of freedom which allows circular motion in the transverse plane. From an application

point-of-view, vortex solitons may therefore be viewed as self-induced waveguides with dynamic trajectories. Each vortex constitutes a graded-index "fiber" whose path may be controlled by other vortices, or by external fields which couple to the refractive index of the nonlinear medium. Until, however, new materials or mechanism are found which achieve small vortex core sizes without a high beam intensity, self-induced waveguiding will be impractical. Never-the-less, the physics is ripe for exploration.

We have approached this frontier by developing (1) computer-generated holograms of arbitrary vortex distributions, (2) diffractive optical elements of vortices, (3) numerical simulations of vortex propagation, and (4) experiments using the highly nonlinear thermal mechanism. Here we will report our latest findings on these fronts, concentrating on vortex-vortex dynamics. This dynamic is effected by both the envelope in which the vortices reside, and the presence of nearby vortices. Phenomena associated with the latter effect are the least understood, and most difficult to observe, owing to an interaction that depends on $1/d^2$, where d is the distance between vortex cores. Computer-generated holograms allow one to fabricate optical masks that create closely spaced vortices having small cores. Figure 1 shows linear propagation when the beam-to-vortex size ratio is 40. While diffractive optical elements allow vortices having a core size of the order of a wavelength, this technology is not yet readily available. The recently formed Honeywell-ARPA Diffractive Optical Element Foundry, may help change that; we will also report on masks made at that facility.

Numerical investigations of vortex-vortex interactions indicate that hydrodynamic-like phenomena may indeed be observable in a system containing vortex solitons. Whereas the continuous rotation of vortices is expected for a beam of infinite extent, finite size beams may approach this limit -- well beyond the linear propagation limit of $\pi/2$. Figure 2 shows the vortex rotation angle as a function of propagation distance for three cases: (a) the classical case given by $\arctan(z/z_0)$, (b) the linear case for a vortex of finite size, and (c) the vortex-soliton case. What is particularly striking is that the rate of rotation is significantly enhanced for the soliton case.

Besides using vortices as dynamic waveguides, we have found other potential applications including dark trapping of low-index particles such as hollow spheres (see Fig. 3). Dark traps have large intensity gradients, as required for transverse trapping, with the additional advantage of low power in the center of the trap. Combined with computer-generated holography, the potential exists to create multiple vortex traps within a single laser beam. We will briefly describe this work, as well as the use of vortex solitons as optical traps.

This work was supported by the National Science Foundation (ECS-9457481).

References

- [1] See the review Y. S. Kivshar, *Dark Solitons in Nonlinear Optics*, IEEE J. Quantum Electron. **29**, 250 (1993).
- [2] G. A. Swartzlander, Jr. and C. T. Law, *Optical vortex solitons observed in Kerr nonlinear media*, Phys. Rev. Lett. **69**, 2503 (1992); *The optical vortex soliton*, Optics & Photonics News, 10 (Dec. 1993).
- [3] C. T. Law and G. A. Swartzlander, Jr., *Optical vortex solitons and the stability of dark soliton stripes*, Opt. Lett. **18**, 586 (1993).
- [4] C. T. Law and G. A. Swartzlander, Jr., *Polarized Optical Vortex Solitons: Instabilities and dynamics in Kerr nonlinear media*, Chaos, Solitons & Fractals **4**, 1759 (1994).
- [5] G. S. McDonald, K. S. Syed, and W. J. Firth, *Optical vortices in beam propagation through a self-defocussing medium*, Opt. Comm. **94**, 469 (1992).
- [6] B. Luther-Davies, R. Powles, and V. Tikhononko, *Nonlinear rotation of three-dimensional dark spatial solitons in a Gaussian laser beam*, Opt. Lett. **19**, 1816 (1994).
- [7] K. Stalinunas, *Dynamics of optical vortices in a laser beam*, Opt. Comm. **90**, 123 (1992).
- [8] K. T. Gahagan and G. A. Swartzlander, Jr., *Optical Vortex Trapping of Particles*, to appear in Opt. Lett.

Figures

Figure 1

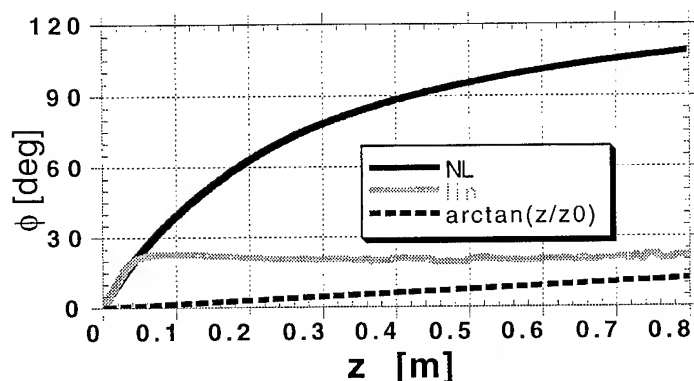
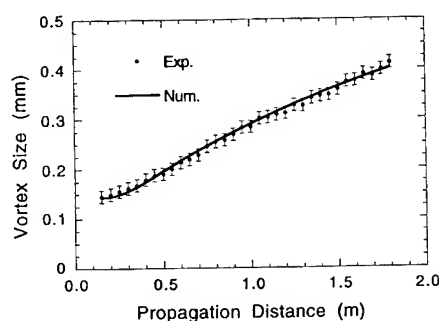
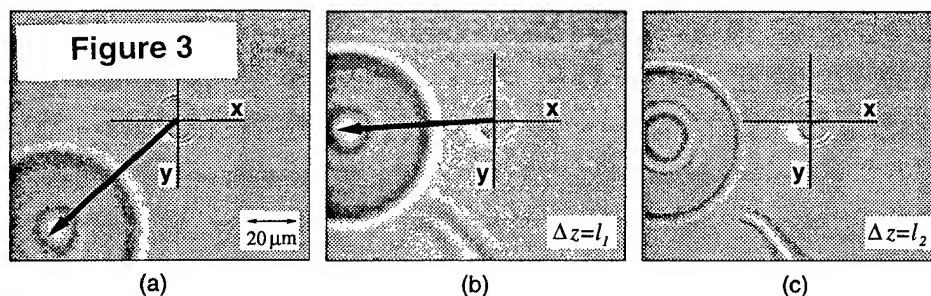


Figure 2



Experiments on spatial solitons in saturating nonlinear media

Vladimir Tikhonenko[†], Jason Christou[†], Barry Luther-Davies[†] and Yuri Kivshar^{*}

[†]Laser Physics Centre, ^{*}Optical Sciences Centre

Research School of Physical Sciences and Engineering

The Australian National University

Canberra ACT 0200 Australia

tel (61 62 494244); FAX (61 62 490029); e-mail bld111@rsphy1.anu.edu.au

The spontaneous creation of spatial patterns in optical beams propagating in nonlinear media has been the subject of considerable research¹. Of particular interest to us has been the formation of stable optical beams or spatial solitons since they may have some relevance to optical switching if the trajectory of those solitons is controllable. In a 3-D geometry bright soliton solutions for a Kerr-law medium are unstable, however, bright solitons can exist when the nonlinearity saturates as is the case for many media such as Rubidium metal vapour used in our experiments. As a result it is possible to study 3-D bright soliton behaviour in such a medium and observe phenomena such as phase-dependent soliton attraction or repulsion²: phenomena which are analogous to those observed in Kerr-media.

Saturation, however, introduces some additional complications. For example, in a Kerr medium the attractive interaction forces between a pair of in-phase solitons lead to periodic oscillations involving elastic collisions with no energy exchange between the individual solitons. In contrast in a saturating medium partial or complete fusion of the solitons occurs creating a new soliton with different properties (energy, momentum, etc)³.

We have studied a number of these phenomena during the propagation of a CW beam from a Ti:sapphire laser through a resonant nonlinear medium consisting of Rubidium vapour contained in a glass cell^{2,3}. By varying the nonlinearity of the medium via the vapour concentration or the laser detuning from resonance we were able to observe attraction, repulsion and fusion of bright spatial solitons. An unusual feature of the experiments was the use of an input beam containing an optical vortex which was used to create pairs of solitons with known relative phase. Such an input beam possesses a finite angular momentum and this momentum was observed to significantly affect the soliton dynamics.

Whilst saturation is not required to stabilise dark spatial solitons, we have used the Rubidium vapour to study some novel behaviour of dark spatial solitons. In our most recent work we have observed the break-up of a black soliton stripe due to the onset of a well-known transverse instability⁴. This instability results in the destruction of the original dark stripe and the creation of pairs of optical vortices which must have opposite charge to conserve topological charge of the field (see figure 1). Whereas in a Kerr medium only one mechanism is known which leads to the instability of the stripe, in a saturating medium, and addition

possibility arises since the black soliton itself is expected to be unstable due to saturation⁵.

Data from experiments to study the dynamics of bright solitons and dark soliton stripes will be presented and compared with the predictions of numerical model.

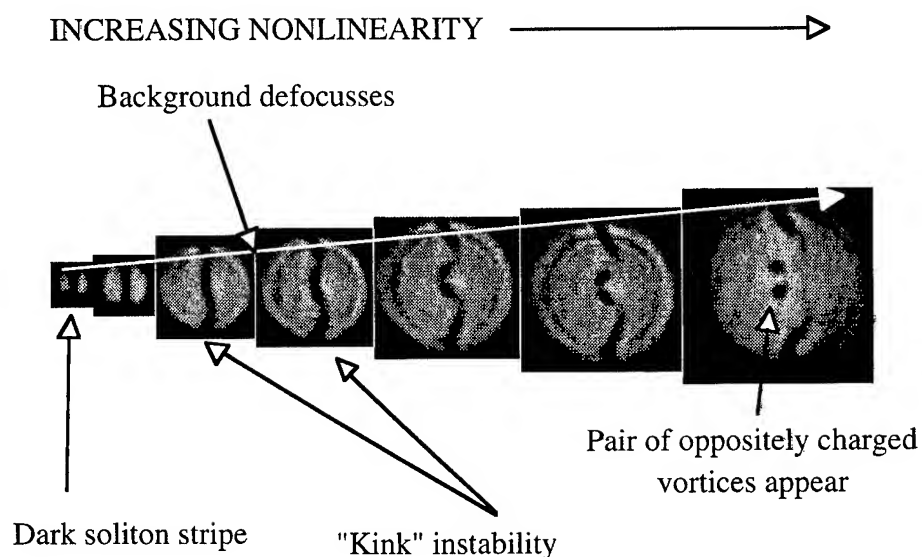


Figure 1: Experimental observation of the break-up of a dark soliton stripe into a pair of oppositely charged vortices.

¹ See for example, L.A. Lugiato, *Chaos, Solitons, Fractals* **4**, 1251 (1994); E. Enfeld, G. Rowlands, "Nonlinear Waves" Cambridge Univ. Press, Cambridge, (1990).

² V. Tikhonenko, J. Christou, B. Luther-Davies, *J. Opt. Soc. Am.-B* **12**, 2046 (1995).

³ V. Tikhonenko, J. Christou, B. Luther-Davies, *Phys. Rev. Letts*, in press.

⁴ E.A. Kuznetsov, S.K. Turitsyn, *Sov. Phys. JETP* **67**, 1583 (1988).

⁵ Y. Kivshar, W. Krolikowski, *Opt. Lett.* **20**, 1527 (1995).

(2+1)-D spatio-temporal solitary-wave dragging

Steve Blair, Kelvin Wagner, and Robert McLeod
 Optoelectronic Computing Systems Center
 University of Colorado, Boulder CO, 80309-0525
 303-492-0886 blair@kona.colorado.edu

The (1+1)-D spatial soliton dragging interaction has been shown numerically to provide large gain with high gate contrast [1, 2] for optical switching applications, and is the spatial analog of temporal dragging in a fiber [3]. In order to retain the best features of both (1+1)-D spatial (short interaction lengths and ease of output state discrimination) and temporal (low energies) solitons, we must look at the dragging interaction between higher-dimensional spatio-temporal solitary waves, such as (3+1)-D light-bullets [4] or their reduced-dimensional counterparts: the (2+1)-D solitary waves in a waveguide. The numerical simulation of (2+1)-D solitary-wave dragging presented here is based upon a vector extension to the split-step algorithm using the exact linear propagation function including the full dispersion relation and nonparaxiality [5].

The dragging interaction occurs by overlapping in space and time a signal and orthogonally-polarized pump solitary wave, as shown in Fig. 1 in the guided-wave configuration. The signal is launched at an internal angle α relative to the pump and, if the angle is small enough, the pump and signal form a bound pair and propagate at a weighted mean angle. We use solitary waves of the same frequency and ignore any temporal walkoff effects due to waveguide birefringence (but we retain space-time coupling - variations in group-velocity with respect to transverse spatial frequency), hence, the main effect we are concerned with is spatial dragging.

In order to describe the propagation and interaction of orthogonal linearly-polarized spatio-temporal solitary waves in higher-order Kerr media, we start with the coupled nonlinear wave equations appropriate for isotropic symmetry [4]

$$\begin{aligned} \frac{\partial^2 A_1}{\partial z^2} + \frac{\partial^2 A_1}{\partial x^2} + k^2 \left(\omega_0 + i \frac{\partial}{\partial t} \right) A_1 + 2k_0^2 \frac{n_2}{n_0} \left[|A_1|^2 + \frac{2}{3} |A_2|^2 \right] A_1 \\ + 2k_0^2 \frac{n_4}{n_0} \left[|A_1|^4 + \frac{3}{5} |A_2|^4 + \frac{6}{5} |A_1|^2 |A_2|^2 \right] A_1 = 0, \end{aligned} \quad (1)$$

with a similar equation for A_2 and where the electric field $E_j = A_j(x, t, z)e^{-i\omega_0 t}$, $k^2(\omega_0 + i\partial/\partial t)$ is interpreted by its Taylor's expansion and represents all orders of linear dispersion [6], $k_0 = k(\omega_0)$, $n_2 = 3\chi_{1111}^{(3)}/8n_0$ is the nonlinear Kerr index and is positive for bright solitary-wave formation, and phase-dependence of the nonlinear polarization, dispersion of the nonlinear index and self-steepening are neglected. Note that weak saturation-like behavior of the nonlinear index (for $|n_4|E|^4| \ll n_2|E|^2$), mediated by ultrafast $n_4 < 0$ in this case, is required in (2+1)-D to ensure stability [4].

The full split-step scheme over a distance Δz (small compared to the confocal distance Z_0) is written

$$A_1(x, t_g, z + \Delta z) = \mathcal{F}^{-1} \left\{ \mathcal{F} \left\{ A_1(x, t_g, z) e^{i\phi_1^{NL}} \right\} e^{i[\sqrt{k^2(\Delta\omega) - k_x^2} - \Delta\omega k'(\omega_0)]\Delta z} \right\}, \quad (2)$$

where $\Delta\omega = \omega - \omega_0$, \mathcal{F} is the spatio-temporal Fourier transform operator ($x \rightarrow k_x$, $t \rightarrow \Delta\omega$), $k_z = \sqrt{k^2(\Delta\omega) - k_x^2} - \Delta\omega k'(\omega_0)$ is the propagation constant, and the equation for A_2 follows. Only unidirectional propagation is considered and the transformation to reduced time, $t_g = t - k'(\omega_0)z$, accounts for the extra term in the transfer function by the Fourier shift theorem. Defining k_f as the free-space propagation constant and ignoring the phase-dependent terms in the nonlinear polarization, the phase applied in real space due to the nonlinear index is

$$\phi_1^{NL} = k_f \Delta z \left\{ n_2 \left[|A_1|^2 + \frac{2}{3} |A_2|^2 \right] + n_4 \left[|A_1|^4 + \frac{3}{5} |A_2|^4 + \frac{6}{5} |A_1|^2 |A_2|^2 \right] \right\}. \quad (3)$$

The fundamental eigenmode of the paraxial (2+1)-D NLS equation is used as the initial signal profile with peak intensity $I_{10} = |E_{10}|^2/2\eta$, while the pump has the same profile with initial peak intensity $I_{20} = rI_{10}$ where r is the initial energy ratio. Since the pump is not launched with the eigenmode profile, it will not

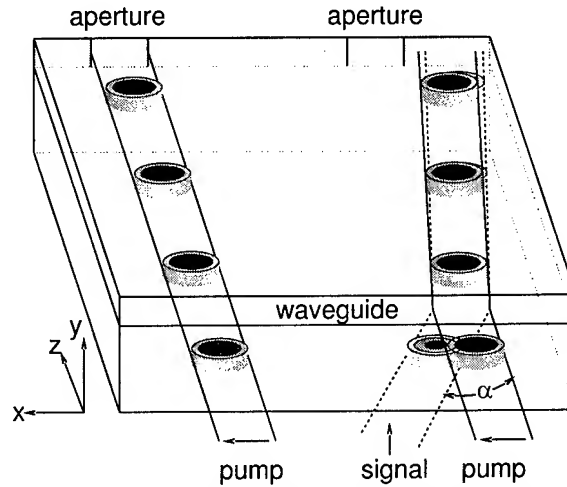


Figure 1: Waveguide configuration used for (2+1)-D spatio-temporal solitary-wave dragging. The pump by itself passes through the aperture, while in the presence of the signal, it is dragged to the side and blocked. The arrows represent the direction of linear polarization.

remain unchanged during propagation. Here, we have set $n_4 = -n_2/16 |E_{10}|^2$, so that the peak index for the signal alone is reduced by a factor 1/16 over the case when $n_4 = 0$.

The simulations were performed using the dispersion parameters and Kerr index n_2 of SiO₂. The full-width at half-maximum (FWHM) spatial width of the signal is $41\mu\text{m}$, resulting in a temporal FWHM of 25 fs (corresponding to $\sim 5\mu\text{m}$ in the material) at $\lambda_0 = 1.8\mu\text{m}$, where $k''(\omega_0) = -64 \text{ ps}^2/\text{km}$. The signal contains about 12nJ of energy for a $2\mu\text{m}$ thick guide; this energy can be reduced many orders of magnitude by using a material with enhanced nonlinearity in a region of strong anomalous group-velocity dispersion.

The results of one simulation are shown in Fig. 2 for an energy ratio of $r = 2$. The pump and signal are initially overlapping at the input (top), with the signal propagating at an angle of $\alpha = 0.69^\circ$ that was chosen for best contrast for this gate length of 22 mm. From the Fourier-domain plot, it can be seen that the two waves are initially well-resolved in linear propagation. The lower two sets of figures show that part of the signal remains bound with the pump and drags the pump out of the aperture, but part of the signal escapes and begins to diffract because α is larger than the critical angle for complete trapping. The contrast achieved by this interaction is 7 and the gain is 2; similar contrast with a gain of 4 is also obtainable with a 34mm gate length. Note that the contrast increases with gate length, so much greater contrast can be achieved with longer gates.

In conclusion, we have briefly demonstrated numerically the dragging interaction between two (2+1)-D spatio-temporal solitary-waves using the full dispersion relation without the use of the paraxial approximation and have shown an interaction in which a gain of 2 is achieved with sufficient contrast for ultrafast, cascable, phase-insensitive all-optical switching.

References

- [1] S. Blair, K. Wagner, and R. McLeod, "Asymmetric Spatial Soliton Dragging," *Optics Letters*, **19**, 1943 (1994)
- [2] S. Blair, K. Wagner, and R. McLeod, "Material figures-of-merit for spatial soliton interactions in the presence of absorption", submitted to *JOSA B*
- [3] M. N. Islam, "All-optical cascable NOR gate with gain," *Optics Letters* **15**, 417 (1990)
- [4] R. McLeod, K. Wagner, and S. Blair, "(3+1)-dimensional optical soliton dragging logic", *Physical Review A* **52**, 3254 (1995)
- [5] J. E. Rothenberg, "Space-time focusing: breakdown of the slowly varying envelope approximation in the self-focusing of femtosecond pulses", *Optics Letters* **17**, 1340 (1992)
- [6] A. C. Newell and J. V. Moloney, *Nonlinear Optics* Addison-Welley (1992)

We wish to acknowledge Prof. Dirk Grunwald at the University of Colorado for the use of an AlphaServer 2100 for the numerical computations.

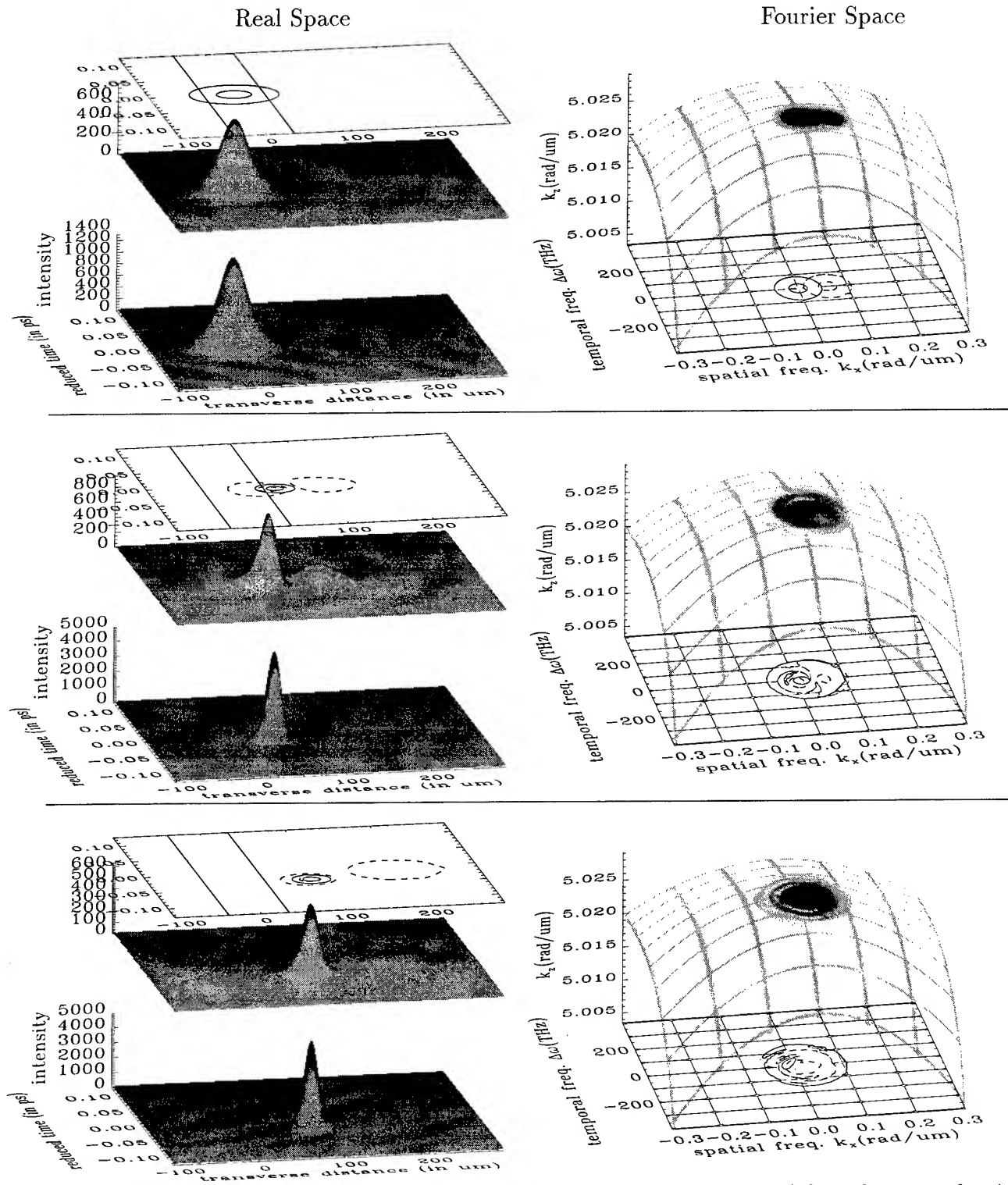


Figure 2: Solitary-wave dragging. The left column is the interaction in real-space (where the top surface is the vertically-polarized signal and the bottom the horizontally-polarized pump) and the right column is the interaction in spatio-temporal Fourier space projected on the allowed $k_z(\Delta\omega, k_x)$ -surface. The interaction angle is $\alpha = 0.69^\circ$ and the initial energy ratio is $r = 2$. The top row is at $z = 0$, the middle at $z = 11\text{mm}$ and the bottom at $z = 22\text{mm}$ and shows that the pump has been dragged out of the aperture (straight lines). The contour levels are at 0.5 and 0.05 of the peak of the signal (dotted) and pump (solid). The group velocity relative to the moving coordinate frame is given by the gradient of the k_z surface.

- Abbate, G. — NThE14
 Abe, Shuji — NWD1
 Aceves, Alejandro B. — NME11
 Agranat, Aharon J. — NTuA3
 Agrawal, Govind P. — NME31
 Akano, U. G. — NThE25
 An, Xin — JTuC1
 Anderson, Dana Z. — NFB
 Anderson, Richard J. — NThA4
 Angelut, A. A. — NThD4
 Arbore, M. A. — NME24, NTuA7
 Aschieri, P. — NThE1
 Assanto, G. — NMB1, NMB2

 Baboiu, D. — NMB1
 Bacher, G. D. — NTuA4
 Backus, S. — NMC5
 Baek, Y. — NMB1, NME9
 Bakker, H. J. — NWA3
 Balakin, A. V. — NThD4
 Balberg, Michal — NTuA3
 Baldi, P. — NMB1, NThE1
 Banerjee, P. P. — NTuA6, NTuA8
 Barbastathis, George — JTuB4
 Barnett, S. M. — NMC3
 Bartholomew, R. — NThE7
 Bashaw, Matthew C. — JTuA1, JTuA3, JTuC3, JTuD3, JTuD4, JTuD7, JTuD8, JTuD9
 Baumann, I. — NMB1
 Behrman, Elizabeth C. — NME2
 Bennett, P. J. — NME25
 Berger, Jill D. — NWA1, NThE15
 Bergman, K. — NFB2
 Betin, Alexander A. — NME17, NThB1
 Bjork, G. — NWA5
 Bjornson, E. S. — JTuD9
 Blair, Steve — NFB6
 Blewett, I. J. — NWA4
 Bloembergen, Nicolaas — NMA1
 Bolger, J. A. — NWA2
 Boothroyd, Simon A. — NME33
 Borrelli, N. F. — NThE7
 Bortz, M. L. — NTuA7
 Botet, R. — NMC7
 Boutton, Carlo — NMD4
 Bowers, M. W. — NME20
 Boyd, Robert W. — NMA, NME20, NThC1

 Brambilla, M. — NFB3
 Brochard, Pascale — NThB2
 Bubeck, Christoph — NMD, NWD3
 Buck, Paul M. — NThE13
 Buckland, Eric L. — NThC1
 Burland, D. M. — JTuB3
 Burr, Geoffrey W. — JTuC1
 Byer, R. L. — NThE24

 Cabanel, Regis — NThB2
 Cao, H. — NWA5
 Catrysse, Peter B. — JTuD8
 Caulfield, H. J. — NTuA6
 Chang, Tallis — JTuA2, JTuB, JTuB4
 Chemla, Daniel — NThD
 Cho, G. C. — NWA3
 Christian, William — JTuA2
 Christou, Jason — NFB5
 Cillessen, J. F. M. — NThE2
 Clayton, Christopher — NFA
 Colvin, James — JTuA3
 Cornell, Eric — NFA2
 Cotts, P. M. — JTuB3
 Crawford, T. M. — NWC4
 Cross, G. H. — NThE11
 Cruz-Cabrera, Alvaro A. — NME2

 Daiber, Andrew — JTuA1, JTuA3
 Dalton, L. R. — NThD1
 De Micheli, M. — NMB1, NThE1
 De Stefano, L. — NThE14
 Dekorsy, T. — NWA3
 Denk, W. — NWC3
 Denz, Cornelia — NThA6
 DeVoe, R. G. — JTuB3
 Dewar, Susan V. — NME1
 Dhanjal, S. — NME25
 Dimmock, J. O. — NTuA6
 Ding, Yujie J. — NME18
 Dogariu, Arthur — NThE13
 Domash, Lawrence H. — JTuD6
 Dorsinville, Roger — NWD4
 Downer, Michael — NWC1
 Downing, E. A. — NThE7
 Dunlop, A. M. — NME21
 Dunning, G. J. — NME6, NThA5

 Ebrahimzadeh, M. — NME14
 Eckardt, R. C. — NThE24

 Eger, D. — NTuA7
 Elhadi, K. — NThE1
 Ema, K. — NME35, NThE8
 Erbach, Peter S. — JTuD12
 Erdogan, Turan — JTuB2
 Erneux, T. — NME3
 Ewbank, M. D. — NMC4

 Fedotov, A. B. — NMC6
 Feigelson, R. S. — NThE24
 Feinberg, Jack — NTuA4, NThA1
 Fejer, M. M. — NMC1, NME24, NTuA7, NThE24
 Feller, G. S. — NME5
 Fiddy, M. A. — NThE5
 Firth, W. J. — NME21, NME28, NFB3
 Fittinghoff, David N. — NThD2
 Fleischhauer, Michael — NFB1
 Flynn, G. — NThE5
 French, S. — NME14
 Fuerst, R. — NMB1
 Fujimura, M. — NMC2

 Gabitov, Ildar — NThE19
 Galbraith, I. — NWA4
 Galstyan, T. — JTuD1
 Garay, R. O. — NWD3
 Garcia-Weidner, Alfonso — NThA3
 Gatti, A. — NMC3
 Gavrielides, A. — NME3
 Geatches, Rachel M. — NME1
 Geletneky, C. — JTuB3
 Gibbs, Hyatt M. — NWA1, NThE15
 Gomatam, Badri N. — JTuD6
 Goorjian, Peter M. — NME31
 Gordon, L. A. — NThE24
 Granger, A. — JTuD1
 Gregory, Don A. — JTuD12
 Greiner, U. J. — NME22
 Grigorova, M. — NMD3
 Grolier, Valerie — NThB2
 Grynberg, G. — NME10
 Gu, Claire — JTuA5, JTuC5
 Guan, Huapeng — NThE10
 Guenter, Peter — NWD2
 Guenther, B. D. — NThC3
 Guibal, S. — NME10
 Guidoni, L. — NME10
 Gurkan, Korhan — JTuA4
 Gusev, V. E. — NThB3

- Haelterman, Marc — NME19
 Hagan, David J. — NMB2, NThE13
 Hagele, Volker — NThE19
 Hakuta, K. — NFA3
 Hankla, A. K. — NME20
 Harkness, G. K. — NME27
 Harris Jr., J. S. — NWB4
 Harris, S. E. — NFA4
 Harvey, J. D. — NThC2
 Haus, H. A. — NThC4
 Healy, D. — NThE11
 Heanue, John F. — JTuA1, JTuA3, JTuA4, JTuB1, JTuC3, JTuD3, JTuD4, JTuD7, JTuD8, JTuD9
 Hellwarth, Robert W. — NThD1, NThE10
 Hemphill, Daniel — NTuA2
 Henson, Bryan F. — NThE6
 Hesselink, Lambertus — JTuA1, JTuA3, JTuA4, JTuB1, JTuC3, JTuD3, JTuD4, JTuD7, JTuD8, JTuD9, NThE7
 Honda, Tokuyuki — NTuA6, NThA6
 Hong, John — JTuA2, JTuA5, JTuB4
 Horsburgh, G. — NWA4
 Houbrechts, Stephan — NMD4
 Howells, S. C. — NWB3
 Hsu, Wei-Feng — JTuC2
 Hudson, Tracy D. — JTuD5, JTuD12
 Hunsche, S. — NWA3

 Ishi, J. — NME35
 Ito, Ryoichi — NME29, NThE23

 Jain, Maneesh — NFA4
 Jain, R. K. — NME5, NWA
 Janz, S. — NWB1, NThE25
 Jarem, J. M. — NTuA8
 Jeong, Jong Sool — NME8
 Johnson, K. — JTuD13
 Justus, B. L. — NThE18

 Kaatz, Philip — NME30
 Kamshilin, Alexei A. — NThA3
 Kapteyn, H. C. — NMC5, NThD3
 Kar, A. K. — NWA4
 Karavanskii, Vladimir — NThE16, NThE17
 Kauranen, Martti — NMD2, NMD4
 Kawahara, H. — NThE8

 Ketchel, Brian P. — NThA4
 Khitrova, Galina — NWA1, NThE15
 Khomenko, Anatoli V. — NThA3
 Khoo, I.-C. — NThC3
 Khoshnevisan, Monte — JTuA2
 Khurgin, Jacob B. — NME18, NME26, NME32, NWB2, NThE22
 Kilby, Gregg — JTuD6
 Kim, S. — NMB2
 Kim, Y. K. — NWC4
 Kintaka, K. — NMC2
 Kitahara, R. — NME35
 Kitamoto, A. — NME29
 Kivshar, Yuri — NFB5
 Klein, Marvin B. — NME6, NTuA4, NThA1, NThA5
 Klimov, Victor I. — NMD3, NThE16, NThE17
 Klingenberg, H. H. — NME22
 Knittel, Joachim — NME12
 Knoesen, A. — NThD3
 Knox, W. H. — NWC3, NThC
 Koch, Karl — NME16
 Koehler, S. D. — NFB2
 Kondo, Takashi — NME29, NThE23
 Koroteev, N. I. — NMC6, NThD4
 Koskelo, A. — NMD3
 Kovanis, V. — NME3
 Kransteuber, Amy S. — JTuD5, JTuD12
 Krijnen, G. — NME9
 Krumbugel, Marco A. — NThD2
 Krylov, V. N. — NMC6
 Kukhtarev, N. V. — NTuA6
 Kume, T. — JTuB5
 Kung, A. H. — NME12, NME23
 Kurz, H. — NWA3, NWC2
 Kutz, J. N. — NFB2

 Lahrichi, A. — JTuD13
 Lai, Y. — NThE15
 Lande, D. — JTuC3
 Lang, Robert J. — NThA1
 Law, C. T. — NFB4
 Lawrence, B. — NMB1
 Lee, El-Hang — NME8
 Lee, M. — NThC3
 Lee, Minyung — NThE3
 Lee, S. J. — NME26, NThE22
 Lega, J. — NME27

 Leger, James — JTuD6
 Leng, L. — NFB2
 Lessard, R. A. — JTuD1
 Li, Chunfei — NME7
 Li, DeQuan — NThE12
 Lin, Shiuan-Hui — JTuC5
 Lindmark, E. K. — NThE15
 Linke, Richard A. — NThE26
 Lipovskii, A. — NThE20
 Liu, A. Y. — JTuD3, JTuD4
 Loffler, T. — NWC2
 LoPresti, Peter G. — NTuA2
 Lord, A. — NFB3
 Lowenthal, Dennis D. — NME4
 Loy, M. M. T. — NMC6
 Lugiato, L. A. — NMC3, NFB3
 Lundquist, P. — JTuB3
 Lupke, G. — NWC2
 Luther-Davies, Barry — NThE4, NFB5
 Lyngnes, Ove — NWA1

 Ma, Jian — JTuA2, JTuB4
 MacCormack, Stuart — NTuA4, NThA1
 Macfarlane, R. M. — NThE7
 Magruder, Robert H. — NThE4
 Makarov, V. A. — NThD4
 Maki, Jeffery J. — NMD2
 Mangir, M. S. — NME17
 Maniloff, Eric — NThE9
 Martin, R. — NME28
 Marzoli, I. — NMC3
 Matera, Francesco — NThE19
 Mattes, Ben R. — NMD3, NThE9
 Mattheus, Arnold — NThE19
 Matthews, S. C. — NME17
 Matusovsky, M. — NThE20
 McBranch, Duncan — NMD3, NME13, NThE9, NThE12, NThE16
 McLeod, Robert — NFB6
 McMichael, Ian — JTuA2
 McMillen, Deanna K. — JTuD5, JTuD12
 McMorrow, D. — NThE18
 Melinger, J. S. — NThE18
 Mercer, J. — NMC7
 Merriam, A. J. — NFA4
 Meyer, C. — NWC2
 Meyer, J. R. — NMC, NThE21
 Miller, A. — NME14
 Mitchell, I. V. — NThE25

Mitchell, P. V. — NME6, NThA5
 Mok, Fai H. — JTuC1
 Moore, Gerald T. — NME16
 Morita, Kaoru — NThE23
 Morito, N. — NThE8
 Mormile, P. — NThE14
 Morozov, Valentine — JTuD13, JTuD14
 Mossberg, Thomas W. — NFA1
 Moylan, C. R. — JTuB3
 Mullen, K. — NWD3
 Murdoch, S. G. — NThC2
 Murnane, M. M. — NMC5, NThD3

Namiki, S. — NThC4
 Nelson, C. C. — NTuA4
 Nelson Jr., T. R. — NThE15
 Neurgaonkar, Ratnakar R. — JTuB4
 Newell, T. — NME3
 Newhouse, M. — NThE7
 Ni, C. K. — NME23
 Niesten, M. J. H. — NThE2
 Nishihara, H. — NMC2
 Nonaka, Koutarou — JTuB5, JTuD2
 Nostrand, M. C. — NME5

O'Brien, Steve — NThA1
 O'Meara, T. R. — NME6, NThA5
 Ogata, N. — NThE8
 Ohlhoff, C. — NWC2
 Oppo, G. L. — NMC3, NME27, NME28
 Ostrowsky, D. B. — NMB1, NThE1
 Ottusch, John — NThB

Pakulev, A. V. — NThD4
 Paraschis, L. — JTuD3, JTuD4
 Park, Sahnggi — NWA1
 Partanen, Jouni P. — NThE10
 Pau, S. — NWA5
 Paul, A. E. — NWA2
 Peatross, J. — NMC5
 Penco, R. — NFB3
 Penty, Richard V. — NME1
 Pepper, David M. — NMB, NME6, NThA5
 Persoons, Andre — NMD2, NMD4
 Pfeifer, T. — NWC2
 Pham, V. P. — JTuD1
 Pletcher, David — JTuA2
 Poga, C. — JTuB3

Pommet, D. A. — NThE5
 Popov, S. V. — NThB3
 Pregolato, R. — NFB3
 Priestley, Richard — NWD4
 Prineas, John — NWA1
 Prior, K. A. — NWA4
 Psaltis, Demetri — JTuA6, JTuB4, JTuC1
 Pu, Allen — JTuA6
 Pulsford, N. J. — NThE2

Ram-Mohan, L. R. — NThE21
 Rauch, Torsten — NThA6
 Razvag, Meir — NTuA3
 Read, K. — NMC5
 Rebane, A. K. — NMC6
 Redmond, Ian — NThE26
 Reed, Murray K. — NME15
 Rendulic, Traci L. — NTuA5
 Resniansky, A. Yu. — NThD4
 Rikukawa, M. — NThE8
 Robinson, Jeanne M. — NMD3, NME13, NThE6
 Rogers, C. T. — NWC4
 Rosenbluh, M. — NThE20
 Rosencher, Emmanuel — NME32
 Rosker, M. J. — NMC4
 Roskos, H. G. — NWC2

Safonov, V. P. — NMC7
 Salamo, Gregory J. — NThA4
 Samoc, A. — NThE4
 Samoc, M. — NThE4
 Samyn, Celest — NMD4
 Santagiustina, Marco — NME11
 Santamato, E. — NThE14
 Sawchuk, Alexander A. — JTuC2
 Sayano, Koichi — JTuC4, JTuD10, JTuD11
 Scalia, G. — NThE14
 Schiek, R. — NMB1, NME9
 Schlie, L. A. — NWB3
 Schroder, T. — NME22
 Schwarze, C. — NThE5
 Scroggie, A. J. — NME28, NFB3
 Sedlatschek, Markus — NThA6
 Settembre, Marina — NThE19
 Shakin, V. A. — NWD1
 Shalaev, Vladimir M. — NMC7
 Shatwell, I. R. — NThB3

Shelton, David P. — NME30
 Shirane, M. — NME29
 Shkurinov, A. P. — NThD4
 Shoji, I. — NME29
 Si, Jinhai — NME7
 Sibbett, Wilson — NThB4
 Silva, T. J. — NWC4
 Simkin, David J. — NME33
 Sincerbox, Glenn T. — JTuA, JTuB1
 Skinner, Steven R. — NME2
 Skirtach, Andrei G. — NME33
 Smilowitz, Laura — NMD3, NME13
 Smirl, Arthur L. — NWA2, NWB
 Snyder, R. — JTuA1, JTuA3
 Sohler, W. — NMB1
 Song, Seok Ho — NME8
 Sornat, Gregory — JTuA5
 Spinelli, L. — NFB3
 Srinivasan, B. — NME5
 Statman, David — NTuA5
 Steck, James E. — NME2
 Steele, T. A. — NWA4
 Stegeman, G. I. — NMB1, NME9, NWC
 Steiner-Shepard, Michael K. — NME15
 Strohkendl, F. P. — NThD1
 Suhara, T. — NMC2
 Sukow, D. — NME3
 Sundheimer, M. — NThE1
 Svirko, Yu. P. — NME25
 Svoboda, K. — NWC3
 Swartzlander Jr., G. A. — NFB4
 Sweetser, John N. — NThD2

Taft, G. — NThD3
 Tai, K. — NThE15
 Tang, Nansheng — NThE10
 Thantu, N. — NThE18
 Tikhonenko, Vladimir — NFB5
 Tookey, A. — NWA4
 Torner, L. — NMB1
 Torruellas, W. E. — NMB1
 Trebino, Rick — NThD2
 Trevino-Palacios, C. — NMB1
 Triche, C. — NME10
 Trillo, Stefano — NME19, NME34
 Tsang, Thomas — NThD2
 Tschudi, Theo — NThA6
 Tsuda, S. — NWC3

- Turitsyn, Sergei K. — NThE19
 Twieg, R. J. — JTuB3, NWD, NThD3

 Ueberhofen, K. — NWD3
 Ueno, Y. — NThE8

 Van Stryland, Eric W. — NMB2, NThE13
 Vaynberg, B. — NThE20
 Verbiest, Thierry — NMD2, NMD4
 Verkerk, P. — NME10
 Vurgafman, I. — NThE21

 Wagner, Kelvin — NFB6
 Walser, Ardie D. — NWD4
 Wang, Hsing Lin — NThE9
 Wang, K. — NThC3
 Wang, Yuxiao — NME7
 Wang, Z. — NMB2
 Wasilewski, Z. R. — NThE25

 Webjorn, J. — NThE1
 Wechsler, Barry A. — NTuA4, NThA1
 Wherrett, B. S. — NWA4
 Wick, D. V. — NThE15
 Wiedemann, H. — NMC3
 Wilson, Kevin R. — NThE6
 Wong, W. S. — NThC4
 Wood, Gary L. — NThA, NThA4
 Wood, M. — NThC3
 Wortmann, R. — JTuB3
 Wright, E. M. — NME21
 Wu, Y. S. — NThE24
 Wu, Weishu — NTuA1

 Xia, H. — NFA4
 Xiao, X. — NMC6
 Xu, D. Y. — NWD4

 Yamamoto, Manabu — JTuB5, JTuC
 Yamamoto, Y. — NWA5

 Yang, Changxi — JTuC5, NThA2
 Yang, Miao — NME7
 Yang, Nan-Loh — NWD4
 Yang, Xiaoguang — NThE12
 Yankelevich, D. R. — NThD3
 Yeh, Pochi — NTuA1, JTuC5, NThA2
 Yi, Xianmin — JTuC5, NThA2
 Yin, G. Y. — NFA4
 Yin, Shizhuo — JTuD5
 Yu, Francis T. S. — JTuD5
 Zabel, Cynthia G. — JTuD12
 Zeek, E. — NMC5
 Zhao, Feng — JTuC4, JTuD10, JTuD11
 Zheltikov, A. M. — NMC6
 Zheludev, N. I. — NME25, NThB3
 Zheng, D. — NThE24
 Zou, W. K. — NWD4
 Zyss, Joseph — NMD1

1996 NONLINEAR OPTICS: MATERIALS, FUNDAMENTALS, AND APPLICATIONS
TECHNICAL PROGRAM COMMITTEE

Richard Lind, *Hughes Research Laboratories, USA, General Co-Chair*
C. L. Tang, *Cornell University, USA, General Co-Chair*
Robert W. Boyd, *University of Rochester, USA, Program Co-Chair*
Ian C. McMichael, *Rockwell International, USA, Program Co-Chair*
Dana Z. Anderson, *University of Colorado, USA*
Christoph Bubeck, *Max Planck Institute, Germany*
Tallis Y. Chang, *Rockwell International, USA*
Daniel Chemla, *University of California, Berkeley, USA*
Gilbert Grynberg, *University of Paris, France*
Eiichi Hanamura, *University of Tokyo, Japan*
Stephen E. Harris, *Stanford University, USA*
Ravi Jain, *University of New Mexico, USA*
Wayne Knox, *AT&T Bell Laboratories, USA*
Jerry R. Meyer, *Naval Research Laboratory, USA*
John Ottusch, *Hughes Research Laboratories, USA*
Demetri Psaltis, *California Institute of Technology, USA*
Arthur L. Smirl, *University of Iowa, USA*
Robert Twieg, *IBM Almaden Research Center, USA*
Gary Wood, *Army Research Laboratory, USA*
Boris Zel'dovich, *University of Central Florida, USA*
John D. Harvey, *University of Auckland, New Zealand, IQEC Coordinator*

Domestic Advisory Committee

Christopher Clayton, *US Air Force Phillips Laboratory, USA*
L. N. Durvasula, *ARPA, USA*
Hyatt Gibbs, *University of Arizona, USA*
Robert Guenther, *Army Research Office, USA*
I. C. Khoo, *Pennsylvania State University, USA*
David Pepper, *Hughes Research Laboratories, USA*
Herschel Pilloff, *Office of Naval Research, USA*
Howard Schlossberg, *AFOSR, USA*
Y. R. Shen, *University of California, Berkeley, USA*
Pochi Yeh, *University of California, Santa Barbara, USA*

International Advisory Committee

H. J. Eichler, *Technische Universitaet Berlin, Germany*
W. J. Firth, *University of Strathclyde, UK*
Christos Flytzanis, *CNRS Lab., Palaiseau, France*
Peter Guenter, *ETH-Hoenggerberg, Switzerland*
Nikolai Koroteev, *Moscow State University, Russia*
B. Luther-Davis, *National University of Australia*
Seizo Miyata, *Tokyo University of Agriculture and Technology, Japan*
C. L. Pan, *National Chiao Tung University, China*
A. Persoons, *University of Leuven, Belgium*
Hiroyuki Sasabe, *RIKEN, Japan*
Francesco Simoni, *Universita di Ancona, Italy*
Daniel Walls, *University of Auckland, New Zealand*
Herbert Walther, *Max Planck Institute fur Quantenoptik, Germany*
Guo-Zheng Yang, *Academia Sinica, China*
Zhi-Ming Zhang, *Fudan University, China*